ASME
SETTING THE STANDARD

Journal of Applied Mechanics

Published Bimonthly by ASME

VOLUME 74 • NUMBER 2 • MARCH 2007

Transactions of the ASME, Journal of Applied Mechanics (ISSN 0021-8936) is published bimonthly (Jan., Mar., May, July, Sept., Nov.) by The American Society of Mechanical Engineers, Three Park Avenue, New York, NY 10016. Periodicals postage paid at New York, NY and additional mailing offices. POSTMASTER: Send address changes to Transactions of the ASME, Journal of Applied Mechanics, c/o THE AMERICAN SOCIETY OF MECHANICAL ENGINEERS, 22 Law Drive, Box 2300, Fairfield, NJ 07007-2300.
CHANGES OF ADDRESS must be received at Society headquarters seven weeks before they are to be effective. Please send old label and new address.
STATEMENT from By-Laws. The Society shall not be responsible for statements or opinions advanced in papers or printed in its publications (B7.1, Para. 3).

TECHNICAL PAPERS

(Contents continued on inside back cover)

This journal is printed on acid-free paper, which exceeds the ANSI Z39.48-1992 specification for permanence of paper and library materials. ♾™
♻ 85% recycled content, including 10% post-consumer fibers.

Journal of Applied Mechanics Volume 74, Number 2 MARCH 2007

TECHNICAL BRIEFS

The ASME Journal of Applied Mechanics is abstracted and indexed in the following:

Alloys Index, Aluminum Industry Abstracts, Applied Science & Technology Index, Ceramic Abstracts, Chemical Abstracts, Civil Engineering Abstracts, Compendex (The electronic equivalent of Engineering Index), Computer & Information Systems Abstracts, Corrosion Abstracts, Current Contents, EEA (Earthquake Engineering Abstracts Database), Electronics & Communications Abstracts Journal, Engineered Materials Abstracts, Engineering Index, Environmental Engineering Abstracts, Environmental Science and Pollution Management, Fluidex, Fuel & Energy Abstracts, GeoRef, Geotechnical Abstracts, INSPEC, International Aerospace Abstracts, Journal of Ferrocement, Materials Science Citation Index, Mechanical Engineering Abstracts, METADEX (The electronic equivalent of Metals Abstracts and Alloys Index), Metals Abstracts, Nonferrous Metals Alert, Polymers Ceramics Composites Alert, Referativnyi Zhurnal, Science Citation Index, SciSearch (Electronic equivalent of Science Citation Index), Shock and Vibration Digest, Solid State and Superconductivity Abstracts, Steels Alert, Zentralblatt MATH

Hydromagnetic Fluctuating Flow of a Viscoelastic Fluid in a Porous Channel

Sushil Kumar Ghosh
Department of Mathematics,
Garhbeta College,
Paschim Medinipur 721127,
West Bengal, India

An exact periodic solution for the time dependent flow of a viscoelastic fluid in the presence of transverse magnetic field is derived. It is assumed that on one plate the fluid is injected with certain velocity and that it is sucked off at the other plate with the same velocity. Both plates are oscillating with a known velocity in their own plane. A perturbation method has been employed by treating the viscoelastic parameter to be small. Effects of viscoelastic parameter, cross-flow Reynolds number, frequency parameter, and Hartmann number on the velocity as well as wall shear stress of the flow are discussed here with graphs. [DOI: 10.1115/1.2062828]

Introduction

Influence of the magnetic field on the non-Newtonian fluid flow has wide applications in chemical engineering, metallurgical engineering, and various industries. Researchers have considerable interest in the study of flow phenomenon between two parallel plates. Because of its occurrence in rheometric experiments to determine the constitutive properties of the fluid, in lubrication engineering, and in transportation and processing encountered in chemical engineering, the flow on non-Newtonian viscoelastic fluid is worthwhile to investigate.

Gupta [1] developed the stability analysis of viscoelastic fluid over an infinite flat plate and achieved a wide range of significant conclusions regarding that problem. Bhatnagar [2] considered the pulsatile flow of viscoelastic fluid through a porous channel with permeable walls. He made an analysis by using a perturbation scheme, considering a small perturbation parameter with a valid reason related to his problem. Assuming the fluid is an electrically conducting and incompressible, Balaram [3] suggested that the applied transverse magnetic field exerts a strong stabilizing influence on the fluid motion and investigated the growth of small random motion in the fluid flow. He has investigated the impulsive motion of fluid between parallel planes. Bujurke et al. [4] extended the Bhatnagar's [2] problem by considering the time dependent flow (evaluated by Laplace transform) when the motion is impulsive. Mukhopadhya and Chaudhury [5] discussed the flow of viscoelastic fluid of the Oldroyd type over an infinite porous plate due to fluctuation in the main flow. Ray et al. [6] derived an exact solution for a hydromagnetic flow of second-order fluid in a channel using a method applied by Vajravelu [7].

The present investigation is undertaken for two reasons. First, researchers have studied the impulsive motion of Newtonian fluid in the presence of magnetic field and stabilized the random motion, however, for non-Newtonian fluid it is unknown. Second, velocity profiles for viscoelastic fluid for porous channel flow is known but in the presence of magnetic field it is yet to be determined. The perturbation technique used by Bhatnagar [2] will be followed in the present analysis and the result is verified with small values of viscoelastic parameter for validity.

Contributed by the Applied Mechanics Division of THE AMERICAN SOCIETY OF MECHANICAL ENGINEERS for publication in the ASME JOURNAL OF APPLIED MECHANICS. Manuscript received by the Applied Mechanics Division, January 16, 2003; final revision, August 4, 2005. Review conducted by D. A. Siginer. Discussion on the paper should be addressed to the Editor, Prof. Robert M. McMeeking, Journal of Applied Mechanics, Department of Mechanical and Environmental Engineering, University of California—Santa Barbara, Santa Barbara, CA 93106-5070, and will be accepted until four months after final publication of the paper itself in the ASME JOURNAL OF APPLIED MECHANICS.

Basic Equations

The Rivlin-Ericksen model for viscoelastic fluid is described as [2]

$$\tau_{ij} = -p\delta_{ij} + 2\phi_1 E_{ij} + \phi_2 D_{ij} + 4\phi_3 E_i^m E_{mj}$$

$$E_{ij} = \tfrac{1}{2}(U_{i,j} + U_{j,i})$$

$$D_{ij} = a_{i,j} + a_{j,i} 2U_{m,j}U^m_{,j}$$

$$a^i = \frac{\partial U^i}{\partial t} + U^m U^i_{,m} \tag{1}$$

Here τ_{ij}, E_{ij}, δ_{ij}, D_{ij}, U_i, and a_i respectively denote the stress tensor, rate of strain tensor, Koneckor delta, acceleration gradient tensor, velocity, and acceleration vector. ϕ_1 and ϕ_2 represent the Newtonian viscosity and viscoelasticity, whereas ϕ_3 accounts for the cross viscosity. The fluid flow performs under the respective mass and momentum conservation laws

$$U_{i,i} = 0 \tag{2}$$

$$\rho\left(\frac{\partial U_i}{\partial t} + U^m U_{i,m}\right) = \tau_{ij,j} \tag{3}$$

where ρ is the density of the fluid.

Formulation of the Problem

It has been considered that fluid is driven by fluctuating pressure gradient

$$\frac{1}{\rho}\frac{\partial p}{\partial x} = A + Be^{i\omega t} \tag{4}$$

where A and B are known constants and ω is the circular frequency. Let us take both plates are in motion with a constant mean velocity U_0. Through the lower plate the fluid is injected with a constant velocity V perpendicular to it and that is sucked off with the same velocity at the upper plate. We assume that the thickness of the channel is h. The uniform magnetic field is applied perpendicular to the plates where the magnetic Reynolds number is small and induced magnetic field is negligible. The motion of highly viscous fluid is slow. Consequently the governing equations reduce to one-dimensional having no convective terms.

The equation of motion (3) by Eq. (1) is then [2,3,5]

$$\frac{\partial u}{\partial t} + V\frac{\partial u}{\partial y} = -\frac{1}{\rho}\frac{\partial p}{\partial x} + \alpha\frac{\partial^2 u}{\partial y^2} + \beta\left(\frac{\partial^2 u}{\partial y \partial t} + V\frac{\partial^3 u}{\partial y^3}\right) - \frac{\sigma H_0^2 \mu^2}{\rho}u + \frac{\sigma H_0^2 \mu^2}{\rho}uI^* \tag{5}$$

where $\alpha = \phi_1/\rho$, $\beta = \phi_2/\rho$, u velocity along x axis, μ is the magnetic permeability, σ is the electrical conductivity, H_0 is the constant magnetic field strength, uI^* is the impulsive fluid velocity.

Boundary conditions are

$$u = U_0 e^{i\omega t} \text{ at } y = 0 \text{ and } y = h \tag{6}$$

Analysis

Equation (5) is a linear partial differential equation and pressure is the sum of steady and pulsatile part. Then we can write

$$u = u_S + u_f$$

$$u(y,t) = \bar{u}(y) + \bar{f}(y)e^{i\omega t} \tag{7}$$

Using Eq. (7) in Eq. (5) and making nondimensional, we note that Eq. (5) can be written as

$$u'' - Ru' - M^2 u = R - M^2 uI - KRu''' \tag{8}$$

$$f'' - Rf' - (M^2 + iF^2)f = 1 - K(iF^2 f' + Rf''') \tag{9}$$

where dash denotes differention with respect to r *and* $r = y/h$, $u = \bar{u}/(Ah/V)$ and $f = \bar{f}/(Bh^2/V)$,

$K = \beta/h^2$ (viscoelastic parameter);

$R = Vh/\alpha$ (cross-flow Reynolds number);

$F = \sqrt{h^2\omega/\alpha}$ (frequency parameter); $M = \sqrt{\sigma H_0^2 \mu^2/\rho}$

Equations (8) and (9) are to be solved with the boundary condition

$$u = 0 \quad \text{at } r = 0; \quad u = 0 \text{ at } r = 1.0 \tag{10}$$

$$f = U_0 \text{ at } r = 0; \quad f = U_0 \text{ at } r = 1.0 \tag{11}$$

We then look for a solution of the form

$$u = u_0 + Ku_1 + K^2 u_2 + K^3 u_3 + \ldots \tag{12}$$

$$f = f_0 + Kf_1 + K^2 f_2 + K^3 f_3 + \ldots \tag{13}$$

Substituting Eqs. (12) and (13) into Eqs. (8) and (9), respectively, and equating the like power of K we get six equations for u_0, u_1, u_2, f_0, f_1, and f_2. By making use of Eqs. (10) and (11), we obtain

$$u_0 = c_{11}\cosh(m_1 r) + c_{12}\sinh(m_2 r) + \frac{M^2 uI - R}{M^2} \tag{14}$$

$$u_1 = c_{21}\cosh(m_1 r) + c_{22}\sinh(m_2 r) - Rc_{11}m_1^3\cosh(m_1 r)\frac{r}{m_1 - m_2} + Rc_{12}m_2^3\sinh(m_2 r)\frac{r}{m_1 - m_2} \tag{15}$$

$$u_2 = c_{31}\cosh(m_1 r) + c_{32}\sinh(m_2 r) - Rc_{21}m_1^3\cosh(m_1 r)\frac{r}{m_1 - m_2} + Rc_{22}m_2^3\sinh(m_2 r)\frac{r}{m_1 - m_2} - 3R^2 c_{11}m_1^5 r\frac{\cosh(m_2 r)}{(m_1 - m_2)^2} + 3R^2 c_{12}m_2^5 r\frac{\sinh(m_2 r)}{(m_1 - m_2)^2} - R^2 c_{11}m_1^6\frac{\cosh(m_1 r)}{m_1 - m_2}\left\{\frac{r^2}{2} - \frac{r}{m_1 m_2}\right\} + R^2 c_{12}m_2^6\frac{\sinh(m_2 r)}{m_1 - m_2} \times \left\{\frac{r^2}{2} - \frac{r}{m_1 - m_2}\right\} \tag{16}$$

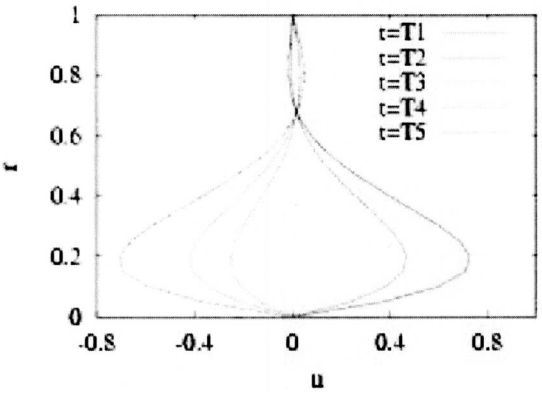

Fig. 1 Axial velocity at different instants of time

$$f_0 = e^{n_1 r}\{D_{11}\cos(n_2 r) + D_{12}\sin(n_2 r)\} + \frac{1}{n_1 n_2} \tag{17}$$

$$f_1 = e^{n_1 r}\{(D_{21} + X_1 Y_1 + X_2 Y_2)\cos(n_2 r) + (D_{22}X_2 Y_1 + X_1 Y_2)\sin(n_2 r)\} \tag{18}$$

$$f_2 = e^{n_1 r}\{(D_{31} + X_3 Y_3 + X_4 Y_4)\cos(n_2 r) + (D_{32} + X_3 Y_4 + X_4 Y_3)\sin(n_2 r)\} \tag{19}$$

where all the constants $c_{11}, c_{12}, c_{21}, c_{22}, c_{31}, c_{32}, D_{11}, D_{12}, D_{21}, D_{22}, D_{31}, D_{32}$ are given in the Appendix. The shear stress at the wall, i.e., on the plate, is defined as

$$\tau = \alpha\frac{\partial^2 u}{\partial r^2} + \beta\left(\frac{\partial^3 u}{\partial r^3} + \frac{\partial^3 u}{\partial t \partial r^2}\right) \tag{20}$$

Results and Discussions

For convenient representation of figure we denote 0, $2\pi/3$, $2\pi/4$, π, $\pi/3$ as T1, T2, T3, T4, T5, respectively.

At different instants of time, the axial fluid velocity has been represented in Fig. 1 ($M=5.0$, $R=2.0$, $K=-0.05$, $U_0=0.0$, $uI=0.1$, $F=2.0$). It shows the distribution of velocity in various instants of time at different points on the thickness of the channel. It is found that there is a back flow for the instant $t=0$, $t=2\pi/3$ surrounding the upper wall; but on the lower wall where the fluid is injected, the fluid in the channel space has increased its axial velocity substantially toward the forward direction. It may be concluded that the Richardson's annular effect can be suppressed by a transverse magnetic field when the fluid is electrically conducting.

In Fig. 2 ($M=2.0$, $R=10.0$, $K=-0.05$, $U_0=0.0$, $uI=0.1$, $F=2.0$), a change has been made on R and observed a significant difference between this and Fig. 1. In this case back flow is higher in magnitude and the shape is not at all parabolic. Hence the cross-flow Reynolds number has a significant effect on the flow. A comparison with Bhatnagar [2] shows that the magnetic field induces the back flow surrounding the upper wall. Moreover, in these studies the velocity profile has forward and backward flow in the same instant of time ($t=0$, $t=2\pi/3$).

The above two figures are represented for nonoscillating walls. Figure 3 ($M=5.0$, $R=2.0$, $U_0=0.05$, $uI=0.1$, $F=2.0$, $t=2\pi/3$) depicted for different elastic parameter for the instant $t=2\pi/3$. The configuration is similar to Fig. 1. The figure shows that if the values of K decrease the velocity response significantly. Although two walls have the same pulsating velocities the magnitude of fluid velocities on the upper and lower plates are different. This may be the cause of suction and injection.

The effect of magnetic field on the fluid flow having non-Newtonian character has been incorporated in Fig. 4 ($R=2.0$, $K=-0.02$, $F=2.0$, $U_0=0.05$, $uI=0.1$, $t=0.0$). The graphs are for dif-

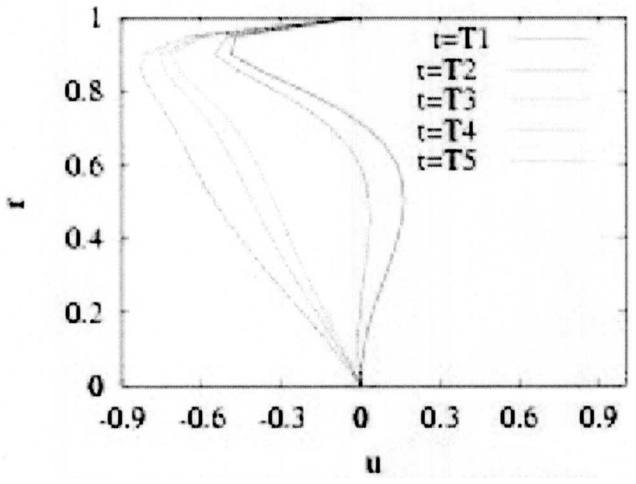

Fig. 2 Axial velocity at different instants of time

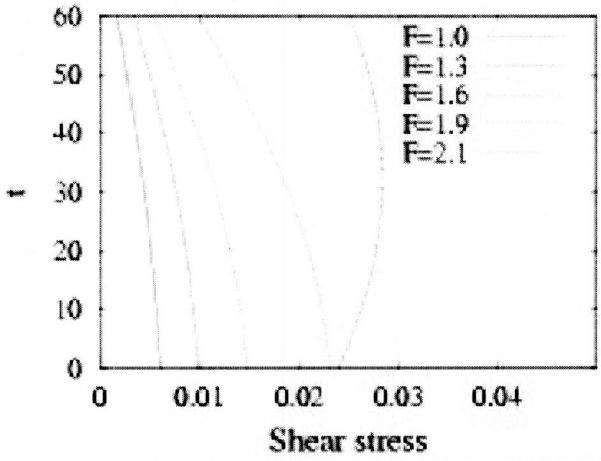

Fig. 5 Distribution of shear stress with t

ferent values of M. By interpretation of the figure, it may be found that by increasing values up to $M=16$, the fluid velocity increases and then decreases in the given set of values of different parameters. Also, it has been observed that the values of M on the velocity profile are very sensitive and the values of M less than 10 introduce back flow along the axis of the channel. In Fig. 5 ($M=10.0$, $R=10.0$, $K=-0.02$, $U_0=0.05$, $uI=0.1$, $t=2\pi/3$) graphs indicate the wall shear stress for different values of frequency parameter at various instants of time. From the previous figure it is clear that the shear stress increased with the increasing values of frequency parameter. Reasons behind this may be interpreted as the greater values of ω sharply diminish the axial velocity and enhance the frictional resistance between the layers, so the shear stress increased in a significant manner.

An important prediction of wall shear stress for various elastic parameters has been introduced by Fig. 6 ($M=10.0$, $R=10.0$, $U_0=0.05$, $uI=0.1$, $F=2.0$, $t=2\pi/3$). Graphs are nearly symmetric about $t=\pi/3$ (except $K=-0.03$). It is to be noted that first it decreases sharply and then increases symmetrically. Figure 7 ($M=10.0$, $K=-0.05$, $F=2.0$, $U_0=0.05$, $uI=0.1$) is the graphical representation of the wall shear stress with cross flow Reynolds numbers. Graphs in Fig. 7 are for different t and it produces the result that the higher values of R sweep out the existing differences between the graphs of different t. The graphical results of the velocity also predict the similar observation, which is obvious and expected. As the impulsive motion has been inducted into the fluid motion, therefore its effective impacts are also to be studied. To study the impact of impulsive velocity we take the assistance of Fig. 8 ($M=10.0$, $K=-0.05$, $F=2.0$, $U_0=0.05$, $uI=0.1$, $t=\pi$). A careful investigation may lead to the conclusion of Fig. 8 that an appreciable increase in the impulsive velocity ensures the enrich-

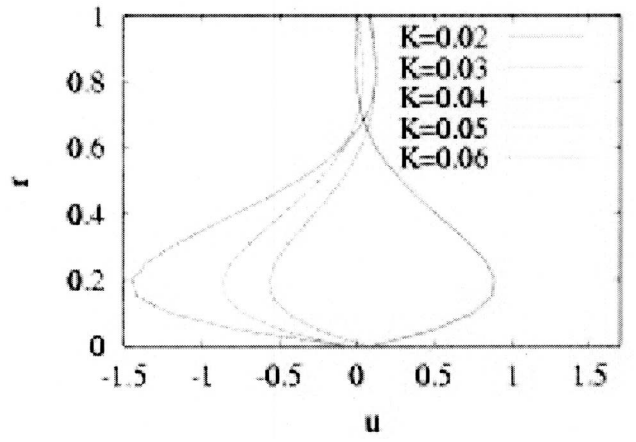

Fig. 3 The axial velocity for different values of K

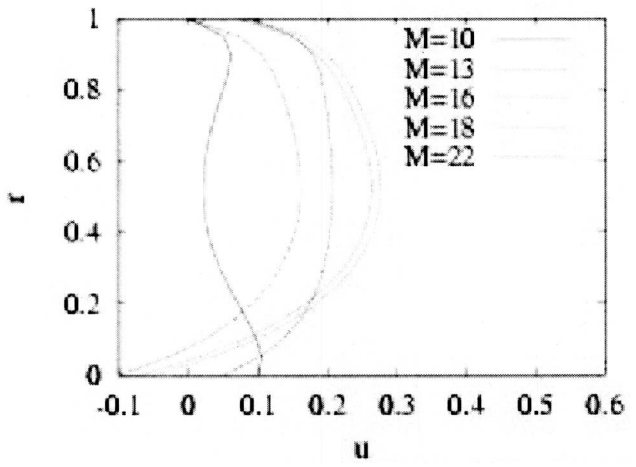

Fig. 4 Axial velocity distribution at different channel heights

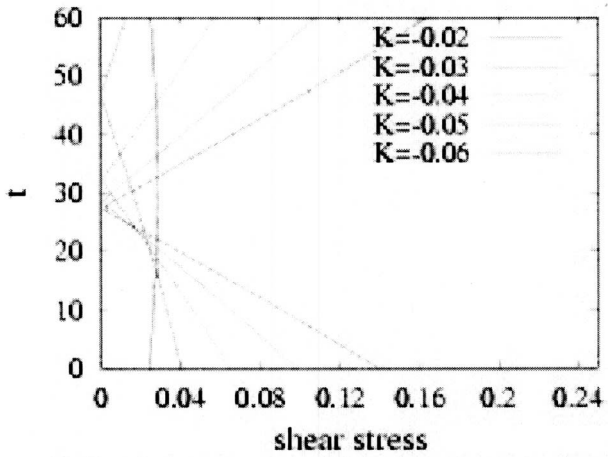

Fig. 6 Shear stress distribution at the wall with t

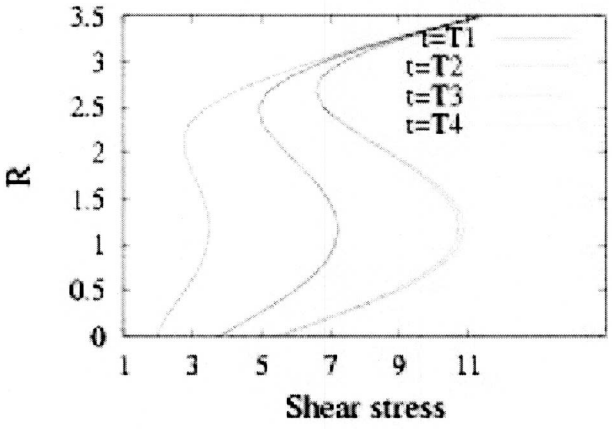

Fig. 7 Wall shear stress versus *R* for different *t*

ment of the wall shear stress. Thus, it may put forward that a moderate value of impulsive velocity can bring down the wall shear stress in the expected manner.

Conclusions

This study is analogous to Bhatnagar [2] and here along with oscillating plates we have applied a transverse magnetic field. It is observed that the back flows in moderate magnitude occur because of the plate's oscillation. The Loretz force due to the presence of magnetic field suppresses the back flow in high Hartmann number and reduces Richardson's annular effect. Besides, the impulsive velocity disturbs the original motion and substantially increases the wall shear stress.

Acknowledgments

This research was carried out at the Center for Theoretical Studies, Indian Institute of Technology, Kharagpur-721302, India and author is grateful to the convener, CTS for giving financial assistance under visiting faculty program.

Appendix

$$n_1, n_2 = \left\{ \frac{R}{2} + \frac{1}{2\sqrt{2}} \sqrt{\sqrt{A^2 + B^2} + A} \right\} + i \left\{ \frac{1}{2\sqrt{2}} \sqrt{\sqrt{A^2 + B^2} - A} \right\}$$

$$A = R^2 + 4M$$

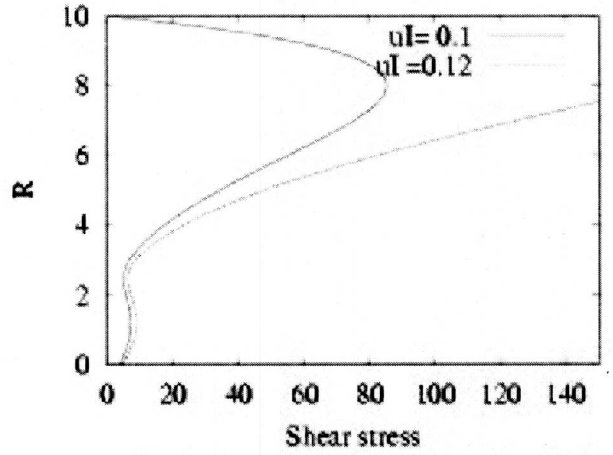

Fig. 8 The effect of impulsive fluid velocity on wall shear stress

$$B = 4F; \quad m_1, m_2 = \frac{R \pm \sqrt{R^2 + 4M^2}}{2}, \quad C_{11} = \frac{R - M^2 uI}{M^2},$$

$$C_{12} = \frac{R - M^2 uI}{M^2} \left(\frac{\cosh(m_1) - 1}{\sinh(m_2)} \right)$$

$$C_{22} = \frac{R}{m_1 - m_2} \left(\frac{C_{11} m_1^3 \sinh(m_1) - C_{12} m_2^3 \cosh(m_2)}{\sinh(m_2)} \right)$$

$$C_{21} = 0, \quad C_{31} = 0$$

$$C_{32} = \frac{1}{\sinh(m_2)} \left[RC_{21} m_1^3 \cosh(m_1) \frac{1}{m_1 - m_2} + RC_{22} m_2^3 \sinh(m_2) \frac{1}{m_1 - m_2} - 3R^2 C_{11} m_1^5 \frac{\cosh(m_2)}{(m_1 - m_2)^2} + 3R^2 C_{12} m_2^5 \frac{\sinh(m_2)}{(m_1 - m_2)^2} - R^2 C_{11} m_1^6 \frac{\cosh(m_1)}{(m_1 - m_2)} \left\{ \frac{1}{2} - \frac{1}{m_1 - m_2} \right\} + R^2 C_{11} m_2^6 \frac{\sinh(m_2)}{m_1 - m_2} \left\{ \frac{1}{2} - \frac{1}{m_1 - m_2} \right\} \right]$$

$$X_1 = -[iF^2 \{D_{11} n_1 + n_2 D_{12}\} + R\{D_{11}(n_1^3 - 3n_1 n_2^2) + D_{12}(3n_1^2 n_2 - n_2^3)\ ]$$

$$X_3 = -[iF^2 \{D_{21} n_1 + D_{22} n_2\} + R\{D_{21}(n_1^3 - 3n_1 n_2^2) + D_{22}(3n_1^2 n_2 - n_2^3)\ ]$$

$$X_4 = -[iF^2 \{D_{22} n_1 - n_2 D_{21}\} + R\{D_{22}(n_2^3 - 3n_2 n_1^2) - D_{21}(3n_2^2 n_1 - n_1^3)\ ]$$

$$Y_1 = \frac{(n_1^2 - n_2^2 - Rn_2 - M^2)}{(2n_1 n_2 - Rn_2 + F^2)^2 + (n_1^2 - n_2^2 - Rn_1 - M^2)^2}$$

$$Y_2 = \frac{2n_1 n_2 - Rn_2 + F^2}{(2n_1 n_2 - Rn_2 + F^2)^2 + (n_1^2 - n_2^2 - Rn_1 - M^2)^2}$$

$$D_{11} = 2U_0 + \frac{1}{n_1 n_2},$$

$$D_{12} = \frac{1}{\sin(n_2)} U_0 e^{-n_1} - D_{11} \cot(n_2) - \frac{1}{n_1 n_2} e^{-n_1} \cos ec(n_2)$$

$$D_{21} = -(X_1 Y_1 + X_2 Y_2), \quad D_{22} = -(X_2 Y_1 + X_1 Y_2)$$

$$D_{31} = -(X_3 Y_1 + X_4 Y_2)$$

$$D_{32} = -(X_4 Y_1 + X_3 Y_2)$$

References

[1] Gupta, A. S., 1967, "Stability of a Viscoelastic Liquid Film Flowing Down an Inclined Plane," J. Fluid Mech., **28**, pp. 17–28.
[2] Bhatnagar, R. K., 1979, "Fluctuating Flow of a Viscoelastic Fluid in a Porous Channel," J. Appl. Mech., **46**, pp. 21–25.
[3] Balaram, M., 1975, "Impulsive Magnetohydrodynamic Flows between Parallel Plane," J. Appl. Mech., **42**, pp. 886–887.
[4] Bujurke, N. M., Hiremath, P. S., and Biradar, S. N., 1988, "Impulsive Motion of a Non-Newtonian Fluid between Two Oscillating Plates," Appl. Sci. Res., **45**, pp. 211–231.
[5] Mukhopadhyay, D. N., and Chaudhury, T. K., 1982, "On the Flow of a Viscoelastic Liquid Past an Infinite Porous Plate due to Fluctuation in the Main Flow," J. Appl. Mech., **49**, pp. 644–646.
[6] Ray, R. N., Samad, A., and Chaudhury, T. K., 1999, "An Exact Periodic Solution of a Hydromagnetic Flow of an Oldroyd Fluid in a Channel," J. Appl. Mech., **66**, pp. 974–977.
[7] Vajravelu, K., 1988, "An Exact Periodic Solution of a Hydromagnetic Flow in a Horizontal Channel," J. Appl. Mech., **55**, pp. 981–989.

Xian-Fang Li
Institute of Mechanics and Sensor Technology,
School of Civil Engineering and Architecture,
Central South University,
Changsha, Hunan 410083,
China

L. Roy Xu[1]
Department of Civil and Environmental Engineering,
Vanderbilt University,
Nashville, TN 37235
e-mail: l.roy.xu@vanderbilt.edu

T-Stresses Across Static Crack Kinking

This paper is concerned with the T-stress change before and after crack kinking in two-dimensional elastic solids. By using asymptotic analysis and the Westergaard stress function method, approximate analytical formulas for calculating the T-stress as well as stress intensify factors of an infinitesimal kink are given. Contributions from the T-stress before crack kinking, to the T-stress and the stress intensity factors of the kinked crack, are clearly described. It is noted that since the sign of the T-stress of a kinked open crack might be different from that of a main crack, simply using the sign of the T-stress before crack kinking is not sufficient to determine crack growth stability as observed in recent experiments. [DOI: 10.1115/1.2188016]

1 Introduction

A crack will propagate off its original path due to change in local fracture mode mixity (a mechanics factor) or fracture toughness (a material factor). This type of crack phenomena is often called "crack kinking" [1–3]. According to recent experimental observations by Xu and Rosakis [4] as seen in Fig. 1(*a*), when two dynamic mode-I cracks passed through a weak interface (lower interfacial fracture toughness than the matrix material, Homalite-100, a brittle polymer), one crack completely kinked from its original path and transformed into a mixed-mode interfacial crack. We may call this type of crack kinking "material-induced kinking." Whereas, another crack propagated across the interface and suffered a crack kink probably due to the reflected stress wave from specimen edges, this type of crack kinking may be called "load-induced kinking." The kinked crack and the main crack (or mother/parent crack) formed a smooth kinking angle, which is in contrast to a sharp kinking angle formed in the "material-induced kinking" case. With extensive applications of composite/layered materials and in-depth research of earthquakes [5–9], investigation of material interfaces has become vital and hence more attention needs to be given to the material-induced crack kinking phenomena [10–12].

Here, we only consider static crack kinking cases and explore some necessary conditions based on different scenarios of crack kinking paths, rather than the sufficient conditions, such as stress or energy criterion to predict crack kinking initiation [13,14]. For a two-dimensional elastic material, the full-field stress tensor of a mixed-mode main crack as seen in Fig. 1, can be expressed in a polar coordinate system [15]

$$\sigma_{ij}^{m}(r,\theta)=\frac{K_I^m}{\sqrt{2\pi r}}\sum_{ij}^{I}(\theta)+T\delta_{i1}\delta_{j1}+\frac{K_{II}^m}{\sqrt{2\pi r}}\sum_{ij}^{II}(\theta)+O(r^{1/2})\quad(i,j=1,2)\tag{1}$$

where m and k denotes "main crack" and "kinked crack." K_I and K_{II} are mode I and mode II stress intensity factors; T is a nonsingular term, $O(r^{1/2})$ represents higher-order terms of length scale r and will be dropped if the kinked daughter crack length l is very small; and known functions $\Sigma_{ij}^{I}(\theta),\Sigma_{ij}^{II}(\theta)$ represent the angular variations of stress components. Previous research on crack kinking was focused on the relation between the stress intensity factors before and after crack kinking, which can be expressed in a united way [16,17]

$$K_{\mathrm{I}}^{k}=c_{11}K_{\mathrm{I}}^{m}+c_{12}K_{\mathrm{II}}^{m}+b_1T\sqrt{l}\tag{2}$$

$$K_{\mathrm{II}}^{k}=c_{21}K_{\mathrm{I}}^{m}+c_{22}K_{\mathrm{II}}^{m}+b_2T\sqrt{l}\tag{3}$$

The above relation could also be obtained using dimensional analysis, and numerous results have been reported to determine the coefficients c_{ij} and b_i $(i,j=1,2)$. From the above relations, it is obvious that the stress intensity factors of the kinked crack depend not only on the stress intensity factors of the main crack, but also on the T-stress of the main crack. However, similar to the main crack, the kinked crack should have its own T-stress field, which should be related to the T-stress of the main crack. Therefore, a new issue that we are raising will be the change of "the T-stress" before and after crack kinking, and to the authors' knowledge this has not been dealt with in the open literature. The T-stress is the constant term in William's series solutions [18], which is acting along the main crack surface and is only determined by the far-field load. According to the stress tensor decomposition principle, for the kinked crack, there will be three nonsingular, constant stress terms in a polar coordinate system as seen in Fig. 1(*b*)

$$T_{rr}=T\cos^2\theta\quad T_{\theta\theta}=T\sin^2\theta\quad T_{r\theta}=-T\cos\theta\sin\theta\tag{4}$$

Note that these terms are defined before the crack kinking initiation. There have also been no systematic results reported regarding the contributions of these different constant stress terms to the kinked crack if the original T-stress of the main crack is very large [19].

A number of experiments have demonstrated that besides the usual stress intensity factors at a crack tip describing the singular elastic stress field, the T-stress plays a crucial role in determining crack growth direction [20–24] and the apparent fracture toughness [25,26], even for a pure mode-I crack subjected to biaxial loading. Now two parameters, the stress intensity factor and the T-stress, have been accepted as a two-parameter fracture criterion in predicting the crack propagation direction and the shape and size of small-scale yielding [27–29]. Computational methods for determining the T-stress have been extensively published. For example, in addition to standard Williams' expansion method, other methods for determining T-stress contain Eshelby's path-independent integral technique [30], higher-order weight function method [31], stress difference method [32], finite element method [33], and boundary element method [34]. Moon and Earmme [35] calculated the T-stress at the interface crack tip for in-plane deformation and antiplane deformation. Numerical studies have been

[1]Author to whom correspondence should be addressed.

Contributed by the Applied Mechanics Division of ASME for publication in the JOURNAL OF APPLIED MECHANICS. Manuscript received May 9, 2005; final manuscript received January 20, 2006. Review conducted by H. Gao. Discussion on the paper should be addressed to the Editor, Prof. Robert M. McMeeking, Journal of Applied Mechanics, Department of Mechanical and Environmental Engineering, University of California—Santa Barbara, Santa Barbara, CA 93106-5070, and will be accepted until four months after final publication of the paper itself in the ASME JOURNAL OF APPLIED MECHANICS.

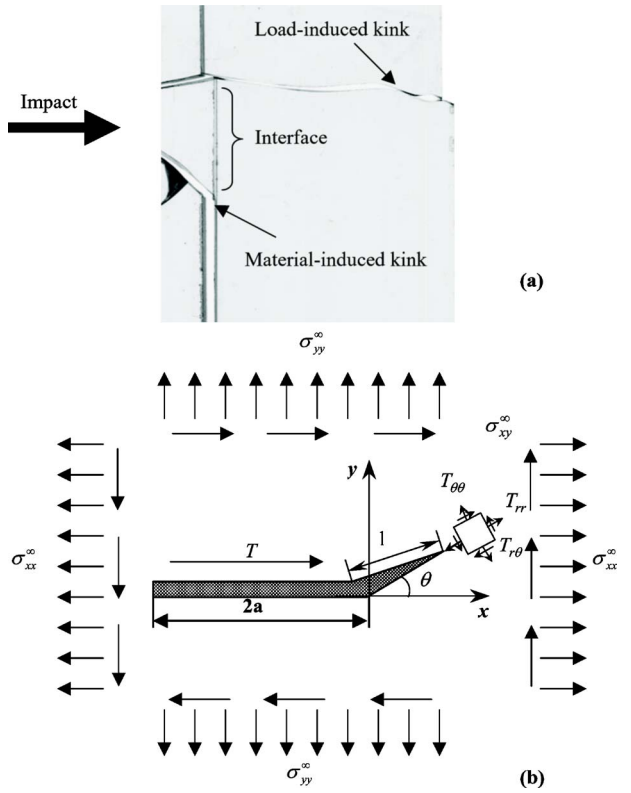

Fig. 1 (*a*) Conceptions of "load-induced kinking" and "material-induced kinking" as observed in a brittle polymer plate with a weak interface after projectile impact [4]. (*b*) schematic of a kinked crack from a main crack along with two coordinate systems.

carried out by Jayadevan et al. [36] to determine the T-stress caused by dynamic loading. The effect of the T-stress on the crack propagation in a functionally graded material has been analyzed by Becker et al. [17] and Paulino and Kim [37].

Numerous researchers have investigated the crack kinking or crack branching problem both theoretically and experimentally. They included Bilby and Cardew [38], Lo [39], Cotterell and Rice [40], Hayashi and Nemat-Nasser [41], Gu and Asaro [42], among others. Furthermore, a kink of a preexisting crack in an anisotropic elastic plane has been dealt with by Gao and Chiu [43] via a perturbation analysis, and Azhdari and Nemat-Nasser [14] analyzed this problem using stress and energy-based fracture criteria. He et al. [16] showed that the residual stress parallel to the interface strongly influences the energy release rate of the kinked crack, for an interfacial crack with a small kink out of an interface between two dissimilar elastic bodies. This work was further modified by Geubelle and Knauss [44]. In addition, dynamic crack growth path involving kinking in general anti-plane loading has been investigated by Adda-Bedia and Arias [45]. Very recently, a crack with a kink in an anisotropic medium subjected to thermomechanical loading has also been dealt with by Li and Kardomateas [46]. However, most of the above-mentioned work is focused on the stress intensity factors at the kink tip and very little work involving the T-stress at the kink tip can be found. Only Selvarathinam and Goree [47] studied the T-stress at the kink tip of a main crack embedded in an isotropic medium under biaxial tension, and Yang and Yuan [48] briefly investigated the T-stress for a kinked crack in an anisotropic elastic medium under mixed mode loading. Indeed, the effect of the T-stress on the crack growth is very important. For instance, if a kinked crack is subjected to mixed mode loading, the kink surfaces may be completely or partially closed under the action of a large compressive

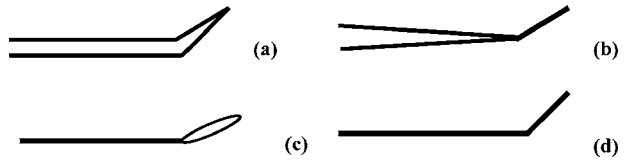

Fig. 2 Possible formats of main cracks and their kinks (*a*,*b*), main cracks are open and their kinks are open in (*a*) and closed in (*b*); and (*c*,*d*) main cracks are closed and their kinks are open in (*c*) and closed in (*d*)

T-stress (see Eq. (2)). Once this takes place, crack growth could be arrested and the failure due to cracks can be controlled effectively. Lauterbach and Gross [49] considered the effect of the kink curvature on the stress intensity factors. Leblond and Frelat [50] studied the stability of crack growth path for an initially closed main crack with an open kink, and Isaksson and Ståhle [51] studied the crack growth path for an initial closed crack with a closed kink.

This investigation is mainly concerned with a systematic analysis of a main crack with a kink of a small kink angle and a kink length. The conditions for an open kink or closed kink will be carefully analyzed. We propose an approach to determine the T-stress for an open or completely closed kink. This approach is applicable for small kink lengths and angles. A comparison of the results of the stress intensity factors obtained by our proposed method with the other previous results will be made. In addition, by adopting an asymptotic analysis, an approximate and a modified expression for the T-stress at the kink tip will be obtained. Finally, some new results showing the influence of the sign of the T-stress on the crack growth stability are given.

2 Statement of a General Crack Kinking Problem

Consider a kinked crack of an arbitrary length and kinking angle embedded in an infinite elastic medium, as shown in Fig. 1(*b*). It is assumed that the lengths of the main crack and the kinked crack are $2a$ and l, respectively, and the kink is inclined at a kinking angle θ to the main crack. We are interested in cases where the kink angle lies in the range from 0 to $\pi/2$ or $-\pi/2$ to 0. Obviously, the analysis for the two cases is similar; thus, we will only deal with the former case. Similar to the previous crack kinking models, one of the coordinate systems is denoted as (x,y) and is established so that the main crack lies along the negative x-axis and the origin is located at the right main crack tip. The other is denoted as (ξ,η), which is chosen so that the kink lies along the negative ξ-axis and the origin is at the right kink tip. Thus, the main crack occupies the region $-2a<x<0, y=0$, and the kink occupies the region $-l<\xi<0, \eta=0$.

Assume that the infinite elastic medium with a kinked crack is subjected to uniform mixed-mode loading at infinity, i.e.,

$$\sigma_{xx}\to\sigma_{xx}^{\infty},\quad \sigma_{yy}\to\sigma_{yy}^{\infty},\quad \sigma_{xy}\to\sigma_{xy}^{\infty},\quad \text{as}\quad x,y\to\infty \tag{5}$$

Under such circumstances, the stress intensity factors and T-stress at the kink tip can be determined exactly by using the dislocation array model [39,52]. To describe the analytical dependence of the T-stress and the stress intensity factors at the kink tip, on those at the main crack tip, it is desirable to give explicit analytical expressions for these physical quantities, even if they are in approximate form. In this paper, we will present a method to approximately determine the closed-form solutions for the T-stress of an infinitesimal kink with a small kink angle. Four possible cases, as illustrated in Fig. 2, will be considered:

1. Both the main crack and the kink surfaces are free of traction (see Fig. 2(*a*)), and the boundary conditions for this case is as stated below

$$\sigma_{yy}(x,0)=0,\quad \sigma_{xy}(x,0)=0,\quad -2a<x<0 \tag{6}$$

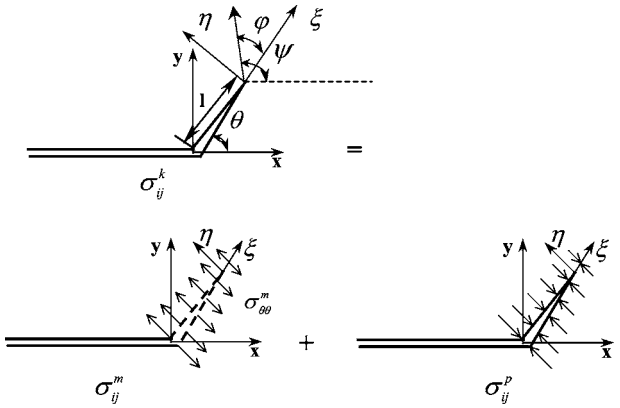

Fig. 3 Schematic of superposition of elastic field for a crack with a small kink (only $\sigma_{\theta\theta}$ is depicted)

$$\sigma_{\eta\eta}(\xi,0)=0, \quad \sigma_{\xi\eta}(\xi,0)=0, \quad -l<\xi<0 \tag{7}$$

2. The main crack surfaces are traction-free, and the kink surfaces are in frictionless contact (closed, see Fig. 2(*b*)), the corresponding boundary conditions can be written as

$$\sigma_{yy}(x,0)=0, \quad \sigma_{xy}(x,0)=0, \quad -2a<x<0 \tag{8}$$

$$\sigma_{\xi\eta}(\xi,0)=0, \quad -l<\xi<0 \tag{9}$$

3. The main crack surfaces are in contact without friction, and the kink surfaces are traction-free (see Fig. 2(*c*)), so the corresponding boundary conditions are

$$\sigma_{xy}(x,0)=0, \quad -2a<x<0 \tag{10}$$

$$\sigma_{\eta\eta}(\xi,0)=0, \quad \sigma_{\xi\eta}(\xi,0)=0, \quad -l<\xi<0 \tag{11}$$

4. When both the main crack and the kink surfaces are closed, and the surface contact is frictionless (see Fig. 2(*d*)), then the boundary conditions are given by

$$\sigma_{xy}(x,0)=0, \quad -2a<x<0 \tag{12}$$

$$\sigma_{\xi\eta}(\xi,0)=0, \quad -l<\xi<0 \tag{13}$$

It is worth pointing out that the above four cases take place depending on certain remote boundary conditions. Here a closed kink refers to kink surfaces that are completely in contact.

3 Approximate Solution for Crack Kinking With Small Kinking Angles

3.1 Case 1: An Open Kink From an Open Main Crack. The entire elastic stress field around the kink tip σ_{ij}^k after crack kinking can be obtained by superposition of σ_{ij}^m and σ_{ij}^p, i.e.,

$$\sigma_{ij}^k=\sigma_{ij}^m+\sigma_{ij}^p \tag{14}$$

where σ_{ij}^m stands for the elastic stress field around the main crack tip before crack kinking (as if crack kinking is absent) and σ_{ij}^p represents the perturbed elastic stress field induced by the kink, where the kink surfaces are loaded by the negative values of σ_{ij}^m. At the onset of crack kinking, the length of a kink is very small when compared to that of the main crack, hence the main crack is taken to be semi-infinite, as shown in Fig. 3.

We follow the same treatment of Cotterell and Rice [40], who employed the perturbation technique to establish a formula for calculating the stress intensity factors at the tip of an infinitesimal kink,

$$\begin{pmatrix} K_I^k \\ K_{II}^k \end{pmatrix}=\sqrt{\frac{2}{\pi}}\int_0^l \begin{pmatrix} \sigma_{\theta\theta} \\ \sigma_{r\theta} \end{pmatrix}\frac{\mathrm{d}r}{\sqrt{l-r}} \tag{15}$$

which is accurate to the first order. It is noted that with the aid of the Green's function for a semi-infinite crack subjected to a pair of concentrated forces at the crack surfaces [53], the above formula is equivalent to superposition of the stress intensity factors caused by the distributed stresses applied on the crack surfaces. Now we employ the following Westergaard stress functions for a semi-infinite crack lying at $x<0, y=0$, opened by a pair of concentrated tensile (shear) forces $P(Q)$ at an arbitrary position b away from the crack tip

$$\begin{pmatrix} Z_I(z) \\ Z_{II}(z) \end{pmatrix}=\begin{pmatrix} P \\ Q \end{pmatrix}\frac{1}{\pi(z+b)}\sqrt{\frac{b}{z}} \tag{16}$$

where $z=x+iy$, from which the induced elastic stress field can be expressed in terms of Z_I and Z_{II} [54], i.e.,

$$\sigma_{xx}=\mathrm{Re}[Z_I(z)+yZ_{II}'(z)]-\mathrm{Im}[yZ_I'(z)-2Z_{II}(z)] \tag{17}$$

$$\sigma_{yy}=\mathrm{Re}[Z_I(z)-yZ_{II}'(z)]+\mathrm{Im}[yZ_I'(z)] \tag{18}$$

$$\sigma_{xy}=-\mathrm{Re}[yZ_I'(z)-Z_{II}(z)]-\mathrm{Im}[yZ_{II}'(z)] \tag{19}$$

where the prime denotes differentiation with respect to z. Therefore, in order to obtain the perturbed elastic stress field caused by a kink, it is sufficient to superpose the induced elastic stress field produced by the distributed stresses at the kink surfaces with the fundamental Westergaard functions for concentrated loading. On the other hand, with the knowledge of $-\sigma_{ij}^m$ applied on the kink surfaces, we can obtain the corresponding Westergaard functions in the (ξ,η) coordinate system (see Fig. 3),

$$\begin{pmatrix} Z_I(\varsigma) \\ Z_{II}(\varsigma) \end{pmatrix}=-\frac{1}{\pi}\int_0^l \begin{pmatrix} \sigma_{\theta\theta}^m \\ \sigma_{r\theta}^m \end{pmatrix}\frac{1}{\varsigma+l-r}\sqrt{\frac{l-r}{\varsigma}}\mathrm{d}r \tag{20}$$

where $\varsigma=\xi+i\eta, r$ is the distance from the main crack tip, and $l-r$ corresponds to b in Eq. (16) and denotes the distance from the kink tip. By using the reside theorem, the following results are readily obtained

$$\frac{1}{\pi}\int_0^l \frac{1}{\varsigma+l-r}\sqrt{\frac{l-r}{r}}\mathrm{d}r=1-\sqrt{\frac{\varsigma}{\varsigma+l}} \tag{21}$$

$$\frac{1}{\pi}\int_0^l \frac{1}{\varsigma+l-r}\sqrt{l-r}\,\mathrm{d}r=\frac{2}{\pi}\left(\sqrt{l}-\sqrt{\varsigma}\tan^{-1}\sqrt{\frac{l}{\varsigma}}\right) \tag{22}$$

Therefore, the stress field at the main crack tip can be obtained if all higher-order terms are omitted

$$\sigma_{rr}^m=\frac{1}{\sqrt{2\pi r}}[C_{01}(\theta)K_{\mathrm{I}}^m+C_{02}(\theta)K_{II}^m]+T^m\cos^2\theta \tag{23}$$

$$\sigma_{\theta\theta}^m=\frac{1}{\sqrt{2\pi r}}[C_{11}(\theta)K_{\mathrm{I}}^m+C_{12}(\theta)K_{\mathrm{II}}^m]+T^m\sin^2\theta \tag{24}$$

$$\sigma_{r\theta}^m=\frac{1}{\sqrt{2\pi r}}[C_{21}(\theta)K_{\mathrm{I}}^m+C_{22}(\theta)K_{\mathrm{II}}^m]-T^m\sin\theta\cos\theta \tag{25}$$

where K_{I}^m and K_{II}^m denotes the mode-I and mode-II stress intensity factors at the main crack tip, T^m is the T-stress at the main crack tip, parallel to the crack plane, and

$$C_{01}(\theta)=\frac{1}{2}(3-\cos\theta)\cos\frac{\theta}{2}, \quad C_{02}(\theta)=\frac{1}{2}(3\cos\theta-1)\sin\frac{\theta}{2} \tag{26}$$

$$C_{11}(\theta)=\frac{1}{2}(1+\cos\theta)\cos\frac{\theta}{2},\quad C_{12}(\theta)=-\frac{3}{2}(1+\cos\theta)\sin\frac{\theta}{2} \tag{27}$$

$$C_{21}(\theta)=\frac{1}{2}(1+\cos\theta)\sin\frac{\theta}{2},\quad C_{22}(\theta)=\frac{1}{2}(3\cos\theta-1)\cos\frac{\theta}{2} \tag{28}$$

substituting the above results into Eq. (20), one can easily show that

$$Z_{\mathrm{I}}(\varsigma)=\frac{C_{11}(\theta)K_{\mathrm{I}}^{m}+C_{12}(\theta)K_{\mathrm{II}}^{m}}{\sqrt{2\pi\varsigma}}+\frac{2}{\pi}\sqrt{\frac{l}{\varsigma}}T^{m}\sin^{2}\theta-\left[\frac{C_{11}(\theta)K_{\mathrm{I}}^{m}+C_{12}(\theta)K_{\mathrm{II}}^{m}}{\sqrt{2\pi(\varsigma+l)}}+\frac{2}{\pi}T^{m}\sin^{2}\theta\tan^{-1}\sqrt{\frac{l}{\varsigma}}\right] \tag{29}$$

$$Z_{\mathrm{II}}(\varsigma)=\frac{C_{21}(\theta)K_{\mathrm{I}}^{m}+C_{22}(\theta)K_{\mathrm{II}}^{m}}{\sqrt{2\pi\varsigma}}-\frac{2}{\pi}\sqrt{\frac{l}{\varsigma}}T^{m}\sin\theta\cos\theta-\left[\frac{C_{21}(\theta)K_{\mathrm{I}}^{m}+C_{22}(\theta)K_{\mathrm{II}}^{m}}{\sqrt{2\pi(\varsigma+l)}}-\frac{2}{\pi}T^{m}\sin\theta\cos\theta\tan^{-1}\sqrt{\frac{l}{\varsigma}}\right] \tag{30}$$

Since the stress intensity factors and the T-stress are dependent on the elastic stress field ahead of the immediate vicinity of the propagating crack or kink tip, consequently, from the relations (17)–(19), the perturbed elastic stress field along the propagating kink is given by

$$\sigma_{\xi\xi}^{p}=\sigma_{\eta\eta}^{p}=\frac{C_{11}(\theta)K_{\mathrm{I}}^{m}+C_{12}(\theta)K_{\mathrm{II}}^{m}}{\sqrt{2\pi\xi}}+\frac{2}{\pi}\sqrt{\frac{l}{\xi}}T^{m}\sin^{2}\theta-\left[\frac{C_{11}(\theta)K_{\mathrm{I}}^{m}+C_{12}(\theta)K_{\mathrm{II}}^{m}}{\sqrt{2\pi(\xi+l)}}+\frac{2}{\pi}T^{m}\sin^{2}\theta\tan^{-1}\sqrt{\frac{l}{\xi}}\right] \tag{31}$$

$$\sigma_{\xi\eta}^{p}=\frac{C_{21}(\theta)K_{\mathrm{I}}^{m}+C_{22}(\theta)K_{\mathrm{II}}^{m}}{\sqrt{2\pi\xi}}-\frac{2}{\pi}\sqrt{\frac{l}{\xi}}T^{m}\sin\theta\cos\theta-\left[\frac{C_{21}(\theta)K_{\mathrm{I}}^{m}+C_{22}(\theta)K_{\mathrm{II}}^{m}}{\sqrt{2\pi(\xi+l)}}-\frac{2}{\pi}T^{m}\sin\theta\cos\theta\tan^{-1}\sqrt{\frac{l}{\xi}}\right] \tag{32}$$

On the other hand, owing to the assumption of an infinitesimal length of the kink at an angle θ to the crack plane, the elastic stress field around the kink tip can be directly written by those around the main crack tip prior to crack kinking, which has the same expression as (23)–(25) but with a substitution $r=\xi+l$. Therefore, based on Eq. (14), the entire elastic stress field σ_{ij}^{k}, around the kink tip posterior to crack kinking is given by the sum of σ_{ij}^{m} and σ_{ij}^{p}

$$\sigma_{\xi\xi}^{k}=\frac{C_{11}(\theta)K_{\mathrm{I}}^{m}+C_{12}(\theta)K_{\mathrm{II}}^{m}}{\sqrt{2\pi\xi}}+\frac{2}{\pi}\sqrt{\frac{l}{\xi}}T^{m}\sin^{2}\theta+\frac{1}{\sqrt{2\pi(\xi+l)}}\{[C_{01}(\theta)-C_{11}(\theta)]K_{\mathrm{I}}^{m}+[C_{02}(\theta)-C_{12}(\theta)]K_{\mathrm{II}}^{m}\}+T^{m}\cos2\theta+T^{m}\sin^{2}\theta\left[1-\frac{2}{\pi}\tan^{-1}\sqrt{\frac{l}{\xi}}\right] \tag{33}$$

$$\sigma_{\eta\eta}^{k}=\frac{C_{11}(\theta)K_{\mathrm{I}}^{m}+C_{12}(\theta)K_{\mathrm{II}}^{m}}{\sqrt{2\pi\xi}}+\left[\frac{2}{\pi}\sqrt{\frac{l}{\xi}}+1-\frac{2}{\pi}\tan^{-1}\sqrt{\frac{l}{\xi}}\right]T^{m}\sin^{2}\theta \tag{34}$$

$$\sigma_{\xi\eta}^{k}=\frac{C_{21}(\theta)K_{\mathrm{I}}^{m}+C_{22}(\theta)K_{\mathrm{II}}^{m}}{\sqrt{2\pi\xi}}-\left[\frac{2}{\pi}\sqrt{\frac{l}{\xi}}+1-\frac{2}{\pi}\tan^{-1}\sqrt{\frac{l}{\xi}}\right]T^{m}\sin\theta\cos\theta \tag{35}$$

With the above elastic stress field ahead of the kink tip determined, stress intensity factors are readily found to be

$$K_{\mathrm{I}}^{k}=C_{11}(\theta)K_{\mathrm{I}}^{m}+C_{12}(\theta)K_{\mathrm{II}}^{m}+2T^{m}\sqrt{\frac{2l}{\pi}}\sin^{2}\theta \tag{36}$$

$$K_{\mathrm{II}}^{k}=C_{21}(\theta)K_{\mathrm{I}}^{m}+C_{22}(\theta)K_{\mathrm{II}}^{m}-2T^{m}\sqrt{\frac{2l}{\pi}}\sin\theta\cos\theta \tag{37}$$

This is in agreement with the results obtained by He et al. [16] and Fett et al. [55]. Obviously, if the terms involving the T-stress are neglected, the results given by Cotterell and Rice [40] are recovered. It should be noted that the stress intensity factors at the kink tip depend not only on the stress intensity factors at the main crack tip, but also the T-stress at the main crack, especially if the T-stress is very large. Moreover, the length of the kink has a pronounced influence on the stress intensity factors at the kink tip when the T-stress is taken into account. From the obtained asymptotic stress field ahead of the kink tip, the T-stress of the kink tip could be expressed in terms of the stress intensity factors and the T-stress at the main crack tip as follows:

$$T^{k}=\frac{1}{\sqrt{2\pi l}}[N_{1}(\theta)K_{\mathrm{I}}^{m}+N_{2}(\theta)K_{II}^{m}]+n(\theta)T^{m} \tag{38}$$

where

$$N_{1}(\theta)=\sin\theta\sin\frac{\theta}{2},\quad N_{2}(\theta)=(1+3\cos\theta)\sin\frac{\theta}{2},\quad n(\theta)=\cos2\theta \tag{39}$$

which indicates that in addition to the T-stress at the main crack tip, the stress intensity factors of the main crack strongly affect the T-stress at the kink tip. Also, the T-stress is related to the angle and length of the kink. In particular, when a crack advances in a self-similar manner, which means when $\theta=0$, we have $T^{k}=T^{m}$, in agreement with that for a single straight crack.

In order to further analyze the T-stress as expressed in Eq. (38), we split T^{k} into three parts: the first part comes from K_{I}^{m}, the second part is from K_{II}^{m}, and the third is due to T^{m}. Particularly, for the third part, when a crack kinks at a 45 deg angle to the main crack plane, it vanishes. When a crack kinks perpendicular to the main crack plane, it yields the negative value of T^{m} at the main crack tip. This is attributed to the fact that a uniaxial tension perpendicular to the crack plane produces a negative T-stress of the same magnitude as tension, and by setting $\sigma_{xx}^{\infty}=0$ for a single isolated straight crack, one gets $T=-\sigma_{yy}^{\infty}$. After a crack kinks at a 90 deg angle to the main crack, T^{m} is just applied on the kink surfaces normal to the kink direction, so that it produces $-T^{m}$ near the kink tip. Of course, it should be pointed out that Eq. (38) is valid only for a small kink angle (see Fig. 3), and its accuracy will be examined in Sec. 3.2. In contrast, the contributions of the first and second parts are apparently due to the consequence of relaxation of tensile stress at the cracked plane without kink. The traction-free boundary conditions at the kink surfaces enforce partial stress to convert the T-stress at the kink tip. For these three parts, the corresponding angle functions $N_{1}(\theta)$, $N_{2}(\theta)$, and $n(\theta)$

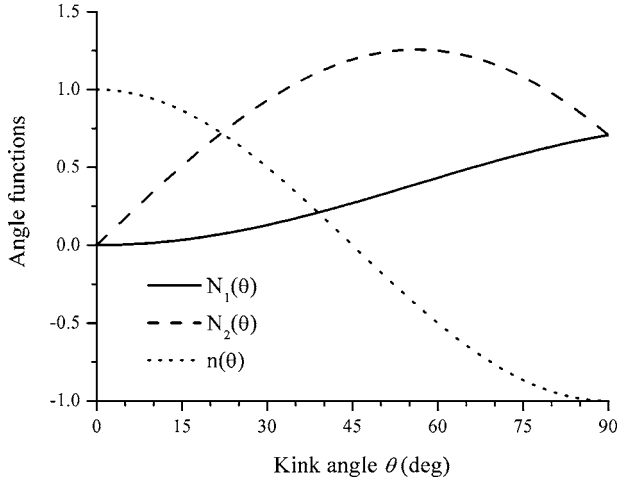

Fig. 4 Variation of three angle functions with respect to kink angles

are plotted in Fig. 4.

We now study the contribution of each decomposed T-stress component on a kinked open crack. The T-stress of the main crack is decomposed into three components as shown in Fig. 1. The one acting perpendicular to the kinked crack is $T^m \sin^2(\theta)$, which contributes to the mode I stress intensity factor of the kinked crack, expressed in Eq. (36). While the component parallel to the kink is $-T^m \sin(\theta)\cos(\theta)$, which further gives rise to the mode-II stress intensity factor of the kinked crack and is expressed in Eq. (37), the last one directly acting along the kinked crack path is $T^m \cos^2\theta$ and makes a part of the T-stress of the kinked crack (see Eq. (38)). The above results are based on an open kink initiating from an open main crack. For different main cracks and kinks as illustrated in Fig. 2, it would be interesting to see how the role of each decomposed T-stress component quite differs.

3.2 Other Cases. Now we turn our attention to the case of completely closed crack surfaces. First we consider case 2, i.e., the main crack is open and the kink is closed as seen in Fig. 2(*b*). This case does not change the conditions of the main crack, but change the boundary conditions at the kink surfaces. For example, under $\sigma^{\infty}_{yy}>0$ and $\sigma^{m}_{\theta\theta}<0$, the crack tip region is in a state of compression since the former corresponds to an open main crack and the latter indicates that the normal stress at the kink surfaces is compressive. Thus, for the closed kink, due to the presence of the normal stress, by superposition it is easily found that the perturbed elastic stress field induced by the kink is only caused by $-\sigma^{m}_{r\theta}$. In other words, as compared to the treatment of the open kink, the corresponding Werstergaard stress function Z_{II} is the same, while the other function Z_I must vanish. Omitting a detailed procedure, we get the elastic stress field of a closed kink, as follows:

$$\sigma^{k}_{\xi\xi}=\frac{1}{\sqrt{2\pi(\xi+l)}}[C_{01}(\theta)K^{m}_{\mathrm{I}}+C_{02}(\theta)K^{m}_{\mathrm{II}}]+T^m\cos^2\theta \quad (40)$$

$$\sigma^{k}_{\eta\eta}=\frac{1}{\sqrt{2\pi(\xi+l)}}[C_{11}(\theta)K^{m}_{\mathrm{I}}+C_{12}(\theta)K^{m}_{\mathrm{II}}]+T^m\sin^2\theta \quad (41)$$

$$\sigma^{k}_{\xi\eta}=\frac{C_{21}(\theta)K^{m}_{\mathrm{I}}+C_{22}(\theta)K^{m}_{II}}{\sqrt{2\pi\xi}}-\left[\frac{2}{\pi}\sqrt{\frac{l}{\xi}}+1-\frac{2}{\pi}\tan^{-1}\sqrt{\frac{l}{\xi}}\right]T^m\sin\theta\cos\theta \quad (42)$$

Therefore, the mode-II stress intensity factor for a closed kink coincides with those for an open kink, and the mode-I stress intensity factor reduces to zero. Furthermore, we find that due to the closure of the kink surface, there are two nonsingular stress components at the kink tip, parallel and perpendicular to the kink surfaces, denoted as T^k_{I} and T^k_{II}, respectively. Setting $\xi\to 0$ results in two T-stresses at the kink tip, respectively,

$$T^k_I=\frac{1}{\sqrt{2\pi l}}[C_{01}(\theta)K^{m}_{\mathrm{I}}+C_{02}(\theta)K^{m}_{\mathrm{II}}]+T^m\cos^2\theta \quad (43)$$

$$T^k_{II}=\frac{1}{\sqrt{2\pi l}}[C_{11}(\theta)K^{m}_{\mathrm{I}}+C_{12}(\theta)K^{m}_{\mathrm{II}}]+T^m\sin^2\theta \quad (44)$$

Clearly, this is a significant difference with the result of an open kink initiating from an open main crack. This is because for an open kink, there is only one nonsingular stress component along the kink plane. Here, besides the T-stress T^k_{I} parallel to the kink plane, there is another T-stress perpendicular to the kink plane T^k_{II} for a closed kink. Furthermore, one can find that for a closed kink, $T^k_{\mathrm{II}}<0$, equal to the compressive stress at the kink tip perpendicular to the kink surfaces [56]. It is noted that

$$T^k_{\mathrm{I}}-T^k_{\mathrm{II}}=T^k \quad (45)$$

where T^k is the T-stress of an open kink as shown in Eq. (38).

In the remainder of the section, we turn our attention to closed main cracks with closed and open kinks. For case 3, where the kink is open and is illustrated in Fig. 2(*c*), the stability of crack growth path has been considered by Leblond and Frelat [50]. Here our emphasis is to derive the T-stress as well as the stress intensity factors at the kink tip. It is obvious that for the main crack $K_{\mathrm{I}}=0$ owing to $\sigma^{\infty}_{yy}<0$. Furthermore, through a simple derivation, the asymptotic stress field of a main crack tip is no longer given by Eqs. (23)–(25), but expressed as

$$\sigma^{m}_{rr}=\frac{1}{\sqrt{2\pi r}}C_{02}(\theta)K^{m}_{\mathrm{II}}+T^m\cos^2\theta+\sigma^{\infty}_{yy} \quad (46)$$

$$\sigma^{m}_{\theta\theta}=\frac{1}{\sqrt{2\pi r}}C_{12}(\theta)K^{m}_{\mathrm{II}}+T^m\sin^2\theta+\sigma^{\infty}_{yy} \quad (47)$$

$$\sigma^{m}_{r\theta}=\frac{1}{\sqrt{2\pi r}}C_{22}(\theta)K^{m}_{\mathrm{II}}-T^m\sin\theta\cos\theta \quad (48)$$

for $\sigma^{\infty}_{yy}<0$, where $T^m=\sigma^{\infty}_{xx}-\sigma^{\infty}_{yy}$. Here, we observe again that there are two nonsingular stress components along the x- and y-axes near the closed crack tip: σ^{∞}_{xx} and σ^{∞}_{yy}. Since the kink surfaces are free of traction, an analogous procedure leads to the stress intensity factors and the T-stress at the tip of an open kink from a closed main crack

$$K^k_{\mathrm{I}}=C_{12}(\theta)K^{m}_{\mathrm{II}}+2\sqrt{\frac{2l}{\pi}}(T^m\sin^2\theta+\sigma^{\infty}_{yy}) \quad (49)$$

$$K^k_{\mathrm{II}}=C_{22}(\theta)K^{m}_{\mathrm{II}}-2\sqrt{\frac{2l}{\pi}}T^m\sin\theta\cos\theta \quad (50)$$

$$T^k=\frac{K^{m}_{\mathrm{II}}}{\sqrt{2\pi l}}(1+3\cos\theta)\sin\frac{\theta}{2}+T^m\cos 2\theta \quad (51)$$

In addition, for a closed main crack as seen in Fig. 2(*d*), if the kink is also closed under certain conditions, the final results are slightly different

$$K^k_{\mathrm{II}}=C_{22}(\theta)K^{m}_{\mathrm{II}}-2\sqrt{\frac{2l}{\pi}}T^m\sin\theta\cos\theta \quad (52)$$

$$T^k_{\mathrm{I}}=\frac{1}{\sqrt{2\pi l}}C_{02}(\theta)K^{m}_{\mathrm{II}}+T^m\cos^2\theta+\sigma^{\infty}_{yy} \quad (53)$$

Table 1 Coefficients $N_1(\theta)$, $N_2(\theta)$ and $n(\theta)$ for the T-stress at the kink tip

θ deg	$N_1(\theta)$		$N_2(\theta)$		$n(\theta)$	
	Numerical	Analytic	Numerical	Analytic	Numerical	Analytic
0	0	0	0	0	1	1
15	0.0337	0.0338	0.4495	0.5088	0.8729	0.8660
30	0.1285	0.1294	0.7975	0.9312	0.5287	0.5000
45	0.2672	0.2706	0.9662	1.1945	0.0678	0
60	0.4271	0.4330	0.9167	1.2500	−0.3752	−0.5000
75	0.5878	0.5880	0.6530	1.0814	−0.6691	−0.8660
90	0.7444	0.7071	0.2146	0.7071	−0.7166	−1

$$T_{\mathrm{II}}^{k}=\frac{1}{\sqrt{2\pi l}}C_{12}(\theta)K_{\mathrm{II}}^{m}+T^{m}\sin^{2}\theta+\sigma_{yy}^{\infty} \tag{54}$$

However, these two T-stresses after crack kinking also satisfy the following relation:

$$T_{\mathrm{I}}^{k}-T_{\mathrm{II}}^{k}=T^{k} \tag{55}$$

4 Results and Discussions

In this section, we will validate our approximate approaches by comparing our results to exact results using the dislocation layer technique [39,52]. Furthermore, we will also address the issue of using the sign of the T-stress to predict crack stability. In our numerical calculation, we adopt the Lobatto-Chebyshev collocation method with $N=20$ for solving a resulting singular integral equation.

4.1 Comparison of Approximate and Exact T-Stress Values. Since the T-stress strongly affects the direction of crack growth, it is important to understand the variation of the T-stress at the kink tip, rather than the T-stress of the main crack before crack kinking. Our major focus is an open kink, and we only compare the approximate analytical results to the exact ones for the T-stress calculation. Table 1 shows the analytical and numerical results of the coefficients $N_1(\theta)$, $N_2(\theta)$, and $n(\theta)$ in Eq. (38), where the analytical results are from Eq. (39) and the numerical procedure is similar to Lo [39] and Broberg [52], and is omitted here. From Table 1, it is found that for a biaxial tension case with K_{I}^{m} present and T^{m} absent, the approximate closed-form expression for the T-stress at the kink tip provides quite accurate results as compared to the exact ones. Even for a large kink angle, $\theta=90$ deg, the difference is within 5%; and for $\theta<75$ deg, the difference is $<1.5\%$. However, the combined influence of shear loading and the T-stress of the main crack on the T-stress at the kink tip does not seem to be described satisfactorily by Eq. (38), since there is evident difference between the two kinds of results, and, furthermore, when $\theta>15$ deg, the error of the approximate analytical results is enlarged. In what follows our discussions are limited to a small kink angle such as $\theta<15$ deg.

4.2 Effects of T-Stress After Crack Kinking on the Crack Growth Stability. As we know, the analysis of crack growth stability depends strongly on the adopted fracture criteria. In general, common brittle fracture criteria include the maximum hoop stress criterion, maximum energy release rate criterion, vanishing K_{II} criterion, etc. In this investigation, we choose the maximum hoop stress criterion [13] since it contains both the stress intensity factors and T-stresses when high-order terms are involved. Therefore, at a kinked crack tip one can write the hoop stress

$$\sigma_{\varphi\varphi}^{k}=\frac{1}{\sqrt{2\pi r}}\cos\frac{\varphi}{2}\left[K_{I}^{k}\cos^{2}\frac{\varphi}{2}-\frac{3}{2}K_{II}^{k}\sin\varphi\right]+T^{k}\sin^{2}\varphi+O(r^{1/2}) \tag{56}$$

where φ is an angle to the kink, as shown in Fig. 3. For simplicity, we assume the kink length l as a characteristic length, and denote $\alpha=l/2a$. At the characteristic length, one can evaluate the hoop stress at the kink tip $\sigma_{\varphi\varphi}^{k}$, and the maximum value of $\sigma_{\varphi\varphi}^{k}$ will determine the direction of the kinked crack path. Figures 5(*a*) and 5(*b*) show the variation of $\alpha\sigma_{\varphi\varphi}^{k}$ against $\psi(\psi=\theta+\varphi$, for convenience) in the absence of mode II stress intensity factors ($\alpha=0.01$ and $\theta=10$ deg), when we neglect T^{k} or take into account the presence of T^{k}. From Fig. 5(*a*), we find that if neglecting the T-stress at the kink tip T^{k}, the curves of $\sigma_{\varphi\varphi}^{k}$ nearly intersect about $\psi=-6.5$ deg. Moreover, the maximum value of $\sigma_{\varphi\varphi}^{k}$ occurs in the

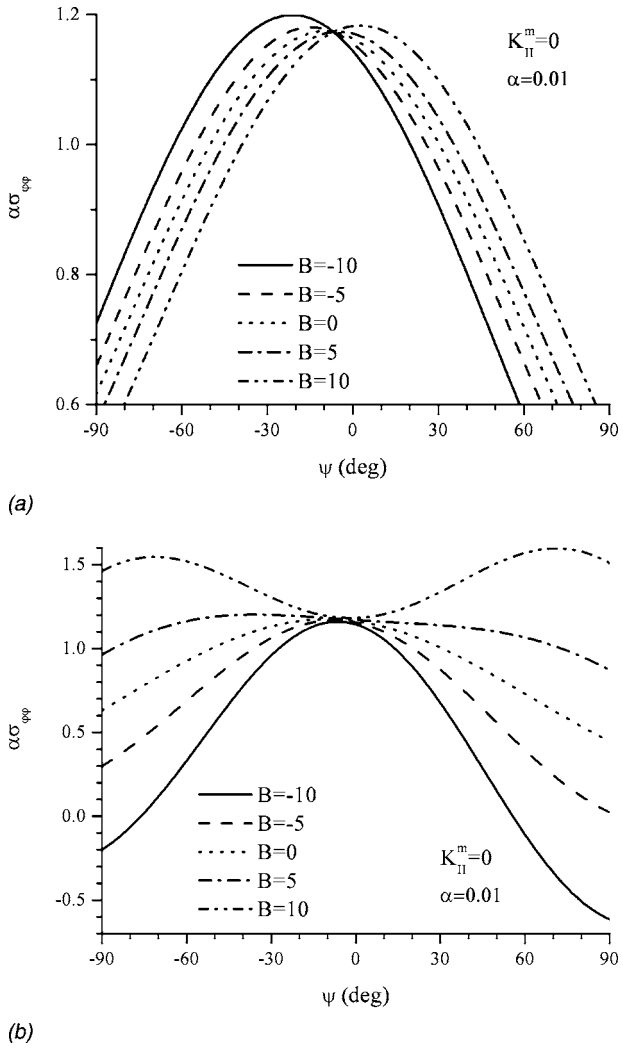

Fig. 5 Hoop stresses $\alpha\sigma_{\phi\phi}^{k}$ at the kink tip with $\alpha=0.01$ and $\theta=10$ deg in the absence of mode-II stress intensity factors $K_{\mathrm{II}}=0$: (*a*) neglecting T^{k} and (*b*) taking T^{k} into account

range of $\psi<0$ deg (or $\varphi<-10$ deg) for a generalized biaxiality ratio $B\leqslant 0$, where

$$B = T\sqrt{\pi a}/\sqrt{K_{\mathrm{I}}^2 + K_{\mathrm{II}}^2} \tag{57}$$

is introduced by Leevers and Radon [57] and Smith et al. [25]. Therefore, a negative T-stress makes crack growth stable. On the other hand, for $B>0$, the maximum value of $\sigma_{\varphi\varphi}^k$ takes place at $\psi>0$ deg, inferring cracking away from the main crack plane. Usually, a positive T-stress often causes unstable crack growth, while a negative one leads to stable crack growth, which generally agree with those results from Cotterell and Rice [40]. However, a small positive T-stress still can lead to stable crack growth. In order to compare the above results, we consider the presence of the T-stress at the kink tip, and the corresponding curves are plotted in Fig. 5(*b*). Clearly, similar trends can be observed for $B<0$ in Fig. 5(*a*). That is, crack growth is stable for negative T-stresses. However, for positive B, one can find that there are two possible cases. One is that the crack path is stable for certain small positive T-stresses, and the other case is that the crack path is unstable for large positive T-stresses. This trend can be seen in Fig. 5(*b*), where a curve corresponding to $B=5$ possesses only a peak at about $\psi=-36$ deg, while a curve corresponding to $B=10$ possesses only two local peaks at about $\psi=\pm 71$ deg, respectively. The former case ($\alpha\sigma_{\varphi\varphi}^k=1.546$ at about $\psi=-36$ deg) indicates a stable crack extension path since the crack advances toward the original crack plane. The latter case ($\alpha\sigma_{\varphi\varphi}^k=1.60$ at about $\psi=\pm 71$ deg) infers the occurrence of crack branch with one branch ($\psi=-71$ deg) propagating toward the original crack plane, and the other ($\psi=71$ deg) propagating off the original crack plane.

In the presence of mode-II stress intensity factors, the variation of $\alpha\sigma_{\varphi\varphi}^k$ against ψ are displayed in Figs. 6(*a*) and 6(*b*) with $\alpha=0.01$ and $\theta=10$ deg for both positive and negative K_{II}^m. One can observe that the locus of the peak of $\alpha\sigma_{\varphi\varphi}^k$ commonly takes place in the range of $\psi<0$ deg for the case of $K_{\mathrm{II}}^m/K_{\mathrm{I}}^m=0.5$ in Fig. 6(*a*), whereas it takes place about $\psi=-26$ deg when $B=-5$, and $\psi=27$ deg, and 66 deg when $B=0,5$, respectively for the case of $K_{\mathrm{II}}^m/K_{\mathrm{I}}^m=-0.5$ in Fig. 6(*b*). This indicates that when the initial kink angle is larger than zero, a positive K_{II}^m enhances crack path stability, where a negative K_{II}^m enhances crack path instability. Note that in this case the initial kink angle is crucial in the presence of K_{II}^m. The above theoretical predictions agree well with recent experiments and modeling. Melin [58] showed that when $T>0$, the crack path was still stable and certain length dimensions or loading configurations are more important while considering the crack path directional stability rather than considering only the T-stress. This was also pointed out by Yang and Ravi-Chandar [59] who found the criterion $T=0$ inappropriate for predicting the directional stability for the case of thermally driven fracture processes in quenched glass plates. Richardson and Goree [60] observed that in PMMA specimens of different dimensions, the crack did not kink immediately if the T-stress became positive. In our dynamic fracture experiments [12], even though the T-stress was always greater than zero for a dynamic mode-I crack [61], the crack path was pretty stable. We note that the T-stress before crack kinking was mainly considered by Cotterell and Rice [40] and He et al., [16], while the T-stress after crack kinking is taken into account in this paper.

4.3 Comparison of T-Stress Before and After Crack Kinking. Since a small mode-II component will lead to a "load-induced kink," and even a pure mode-I crack will kink from its original path to form a "material-induced kink," we tend to assume $K_{\mathrm{II}}^m=0$ and use Eq. (57) to get a ratio of the T-stresses before and after crack kinking: $T^k/T^m=N_1(\theta)/(\sqrt{2\alpha}B)+n(\theta)$, which is mainly related to three parameters: (i) kinking angle θ; (ii) characteristic length α; and (iii) the biaxial ratio B. To compare the relative magnitude of the two terms in T^k/T^m, we employed another function

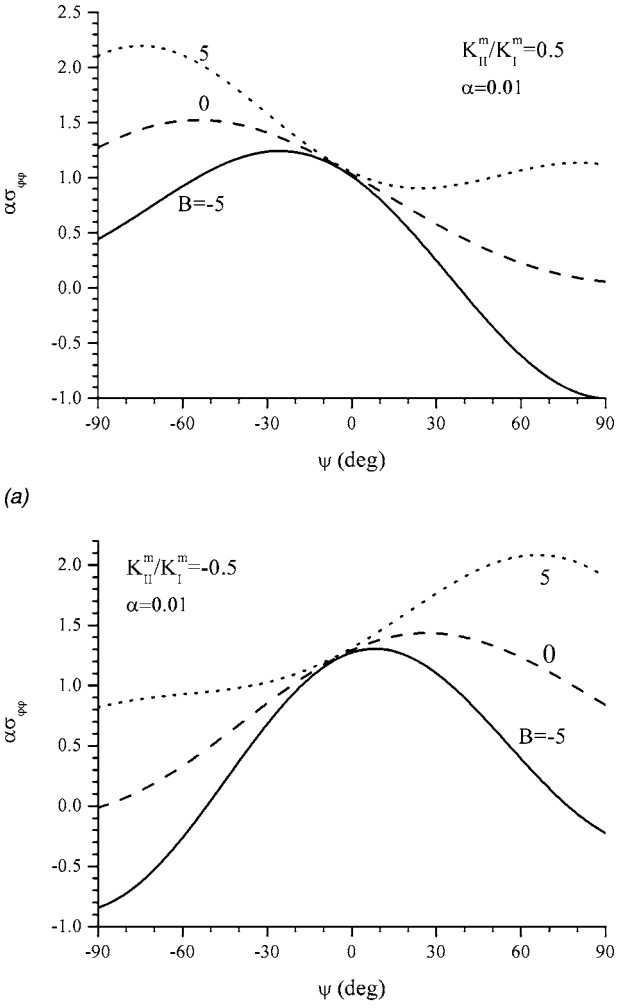

Fig. 6 Hoop stresses $\alpha\sigma_{\phi\phi}^k$ at the kink tip with $\alpha=0.01$ and $\theta=10$ deg in the presence of mode-II stress intensity factors: (*a*) $K_{\mathrm{II}}^m/K_{\mathrm{I}}^m=0.5$ and (*b*) $K_{\mathrm{II}}^m/K_{\mathrm{I}}^m=-0.5$

$$F = \frac{\sqrt{2\alpha}n(\theta)B}{N_1(\theta)} \tag{58}$$

Interesting results on the T-stresses across crack kinking are shown in Figs. 7 and 8. Usually, the magnitude of the T-stress after crack kinking is always larger than that of the T-stress before crack kinking, especially if the kinking angle is large (>45 deg) as seen in Fig. 7(*a*). This is similar to making a turn of a car, i.e., a higher support force will be needed compared to a car moving straight with balanced support force from the ground. Of course, unlike a moving car, a moving crack carries no kinetic energy. As shown in Fig. 7(*b*), it is also easy to understand that the T-stress right after crack kinking is very large because the singular term is related to the kinked crack length (see Eq. (38)). Since there is another nonsingular term related to the T-stress before crack kinking in Eq. (38), a comparison of these two terms (see Eq. (58)) will be helpful to analyze the T-stress change. Figure 8(*a*) shows that for the same small crack kink length ($\alpha=0.01$), the nonsingular term related to the T-stress before crack kinking will dominate for small kinking angles, whether the biaxiality ratio is small or large. With increasing kink crack lengths, the nonsingular term will dominate again for the same kinking angle and the biaxiality ratio, as shown in Fig. 8(*b*).

The variation of T^k/T^m against the kinking angle is plotted for

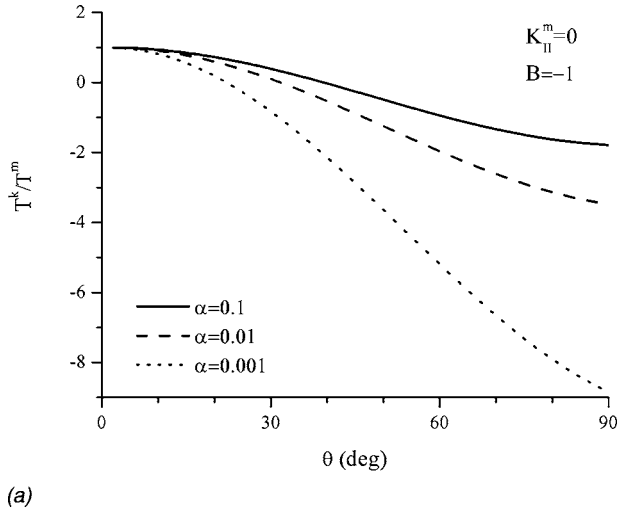

(a)

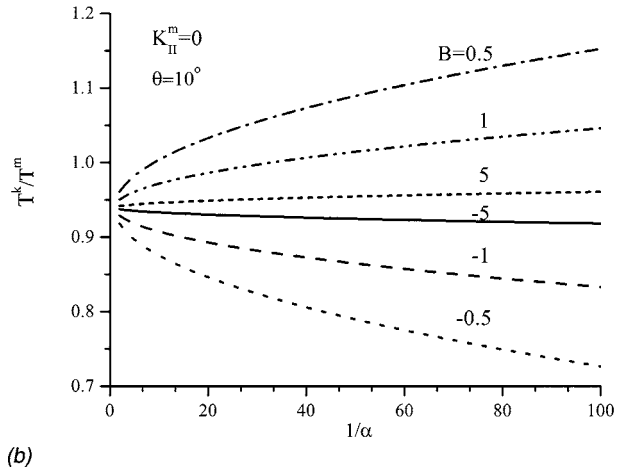

(b)

Fig. 7 (*a*) Variation of T^k/T^m with crack length ratio and kink angle for $B=-1$ and (*b*) variation of T^k/T^m with crack length ratio and biaxiality ratio for kink angle $\theta=10$ deg

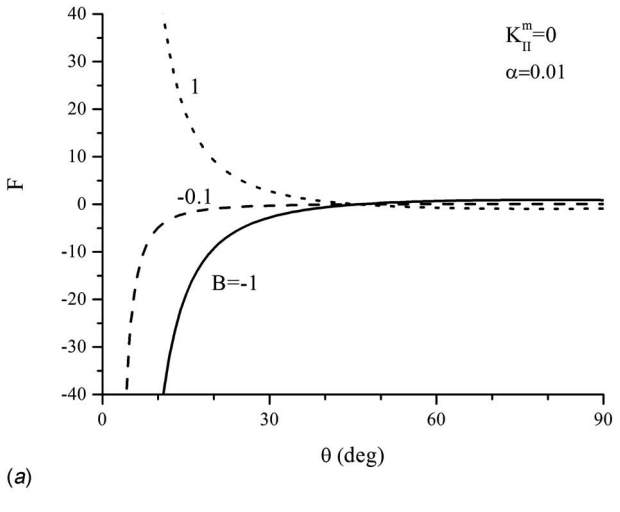

(a)

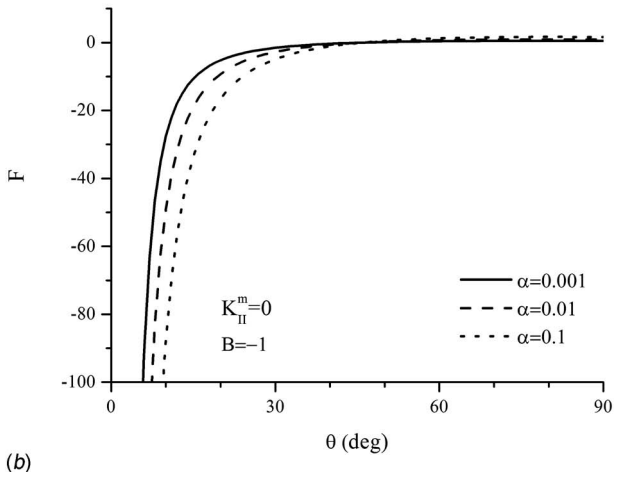

(b)

Fig. 8 (*a*) Variation of F with biaxiality ratio B and kink angle for $\alpha=0.01$ and (*b*) variation of F with crack length ratio and kink angle for $B=-1$

various B with $\alpha=0.01$ in Fig. 9, which gives an important result that the sign of the T-stresses before and after crack kinking would be altered under certain conditions. Here, we consider a specific case with small kink lengths ($\alpha=0.01$) and common ranges of the biaxiality ratios. The ratio of the T-stresses is always positive (implying the same sign for the T-stresses before and after crack kinking) if the biaxiality ratio is positive. However, this ratio will become negative (implying different signs for the T-stresses before and after crack kinking), if the biaxiality ratio is a small negative number (e.g., −0.5) even for small kinking angles (20–30 deg).

4.4 Opening and Closing Conditions of Kinks Due to Applied Loading. It is noted that the above discussion is based on the assumption of an open kink tip, or $K_I^k>0$. Once $K_I^k=0$, the crack surfaces are either partially or entirely in contact. Consequently, for a larger compressive σ_{xx}^∞, the singularity of the kink tip disappears and $K_I^k=0$. For the closed kink, we only deal with a simple case, i.e., the entire or partial kink surfaces are just in contact (the normal stress along the crack surface just changes its sign from zero to a very small negative value). Thus, there is no opening singularity at the kink tip ($K_I^k=0$). Applying a compressive load may lead to the vanishing of the kink tip singularity, similar to that of a Dugdale-type crack [62]. From the expression (36) for K_I^k, we can solve for the required T-stress such that $K_I^k=0$, which is dependent on the stress intensity factors of the main crack tip and the kink angle. For example, for $\alpha=0.01$ together with $K_{II}^m=0$, if we set $K_I^k=0$, we can get T^m/σ_{yy}^∞ equal to about −28 and −7, corresponding to $\sigma_{xx}^\infty/\sigma_{yy}^\infty\approx-27$ and −6, for $\theta=30$ deg and 60 deg, respectively.

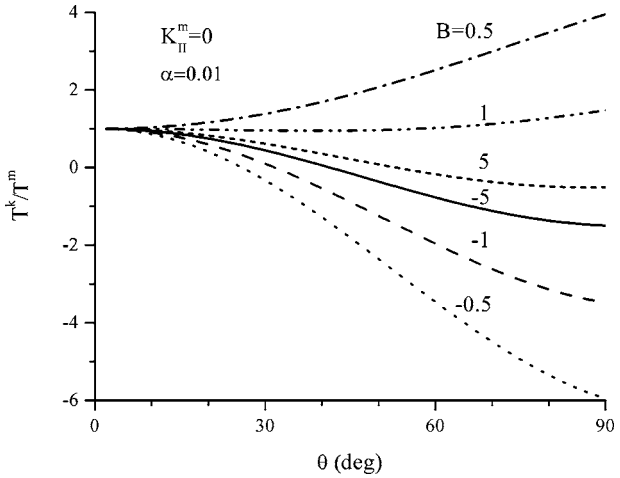

Fig. 9 Variation of T^k/T^m with biaxiality ratio B and kink angle for $\alpha=0.01$

5 Conclusions

We have systematically explored the possible static crack kink cases to determine the necessary T-stress formats. The change of the T-stresses before and after crack kinking and its relation with the crack growth stability is highlighted. For an open main crack, there is only one T-stress term along the main crack in the rectangular coordinate system. This T-stress before crack kinking could be decomposed into three terms in a polar coordinate system based on a possible kink direction, i.e., (i) normal T-stress along the kinking path, $T_{rr}=T\cos^2\theta$; (ii) normal T-stress perpendicular to the kinking path, $T_{\theta\theta}=T\sin^2\theta$; (iii) shear T-stress along the kinking path, $T_{r\theta}=-T\cos\theta\sin\theta$. These three terms make different contribution to the mechanics parameters of the kinked crack. If the kinked crack is open (or free of surface traction), the normal T-stress perpendicular to the kinking path before crack kinking affects the mode-I stress intensity factor of the kinked crack (Eq. (36)); the shear T-stress along the kinking path contributes to the mode-II stress intensity factor of the kinked crack (Eq. (37)), whereas the T-stress of the kinked crack only has one term for a two-dimensional solid, which is determined by (i) normal T-stress along the kinking path and (ii) normal T-stress perpendicular to the kinking path, as expressed in Eq. (38). The T-stress for an open kink is a function of the kinked crack length and the stress intensity factors of the main crack, and is different from the T-stress before crack kinking. If the kinked crack is closed, i.e., its mode-I stress intensity factor is zero, then two T-stress terms for the kinked crack are necessary as expressed in Eqs. (43) and (44), which are contributed by the (i) normal T-stress along the kinking path and (ii) normal T-stress perpendicular to the kinking path before crack kinking. Of course, the shear T-stress along the kinking path before crack kinking still contributes to the mode-II stress intensity factor of the kinked crack.

Therefore, it is easily understood that the T-stress formats of a closed main crack with two possible kink types. There are also two nonsingular T-stresses for the closed main crack. For an open kink, only one T-stress term and two stress intensity factors are involved, whereas for a closed kink, two T-stress terms and one stress intensity factor are important from mechanics viewpoint. These results will be very helpful to analyze a crack kinking along a material interface. It is also noted that simply using the sign of the T-stress before crack kinking is not sufficient to determine crack growth stability as observed in recent experiments.

Acknowledgments

The authors gratefully acknowledge support from the Office of Naval Research Young Investigator Program (Grant No. N00014-03-1-0505, Dr. Roshdy G. S. Barsoum, Program Officer), and the National Science Foundation (Grant Nos. CMS-0409665 and CMS-0456807). Helpful discussions with Professor K. Ravi-Chandar of the University of Texas in Austin and P. Wang of Vanderbilt University are appreciated.

References

[1] He, M.-Y., and Hutchinson, J. W., 1989, "Crack Deflection at an Interface Between Dissimilar Elastic Materials," Int. J. Solids Struct., **25**, pp. 1053–1067.
[2] Broberg, K. B., 1999, *Cracks and Fracture*, Academic Press, New York.
[3] Kimberley, J., and Lambros, J., 2004, "Dynamic Crack Kinking from a PMMA/Homalite Interface," Exp. Mech., **44**, pp. 158–166.
[4] Xu, L. R., and Rosakis, A. J., 2003, "An Experimental Study of Impact-Induced Failure Events in Homogeneous Layered Materials Using Dynamic Photoelasticity and High-Speed Photography," Opt. Laser Technol., **40**, pp. 263–288.
[5] Sun, C. T., and Jih, C. J., 1987, "On Strain Energy Release Rates for Interfacial Cracks in Bimaterial Media," Eng. Fract. Mech., **28**(1), pp. 13–20.
[6] Lee, O. S., and Knauss, W. G., 1989, "Dynamic Crack Propagation Along a Weakly Bonded Planes in a Polymer," Exp. Mech., **29**, pp. 342–345.
[7] Gupta, V., Argon, A. S., and Suo, Z., 1992, "Crack Deflection at an Interface Between Two Orthotropic Materials," ASME J. Appl. Mech., **59**, pp. S79–S87.
[8] Hutchinson, J. W., and Suo, Z., 1992, "Mixed Mode Cracking in Layered Materials," Adv. Appl. Mech., **29**, pp. 63–191.
[9] Rosakis, A. J., 2002, "Intersonic Shear Cracks and Fault Ruptures," Adv. Phys., **51**, pp. 1189–1257.
[10] Xu, L. R., and Rosakis, A. J., 2002, "Impact Failure Characteristics in Sandwich Structures, Part II: Effects of Impact Speed and Interfacial Strength," Int. J. Solids Struct., **39**, pp. 4237–4248.
[11] Rousseau, C.-E., and Rosakis, A. J., 2003, "On the Influence of Fault Bends on the Growth of Sub-Rayleigh and Intersonic Dynamic Shear Ruptures," J. Geophys. Res., **108**, pp. 2411–2431.
[12] Xu, L. R., Huang, Y. Y., and Rosakis, A. J., 2003, "Dynamic Crack Deflection and Penetration at Interfaces in Homogeneous Materials: Experimental Studies and Model Predictions," J. Mech. Phys. Solids, **51**, pp. 461–486.
[13] Erdogan, F., and Sih, G. C., 1963, "On the Crack Extension in Plates Under Plane Loading and Transverse Shear," ASME J. Basic Eng., **85**, pp. 519–527.
[14] Azhdari, A., and Nemat-Nasser, S., 1996, "Energy-Release Rate and Crack Kinking in Anisotropic Brittle Solids," J. Mech. Phys. Solids, **44**, pp. 929–951.
[15] Anderson, T. L., 1995, "*Fracture Mechanics*, 2nd ed., CRC Press, Boca Raton.
[16] He, M.-Y., Bartlett, A., Evans, A. G., and Hutchinson, J. W., 1991, "Kinking of a Crack Out of an Interface: Role of In-Plane Stress," J. Am. Ceram. Soc., **74**, pp. 767–771.
[17] Becker, T. L. Jr., Cannon, R. M., and Ritchie, R. O., 2001, "Finite Crack Kinking and T-Stresses in Functionally Graded Materials," Int. J. Solids Struct., **38**, pp. 5545–5563.
[18] Williams, M. L., 1957, "On the Stress Distribution at the Base of Stationary Crack," ASME J. Appl. Mech., **24**, pp. 109–114.
[19] Selvarathninam, A. S., 1995, "A Generalized Linear Elastic Fracture Mechanics Model for Advanced Materials," Ph.D. thesis, Clemon University.
[20] Williams, J. G., and Ewing, P. D., 1972, "Fracture Under Complex Stress—The Angled Crack Problem," Int. J. Fract., **8**, pp. 441–446.
[21] Maccagno, T. M., and Knott, J. F., 1989, "The Fracture Behaviour of PMMA in Mixed Modes I and II," Eng. Fract. Mech., **34**, pp. 65–89.
[22] Haefele, P. M., and Lee, J. D., 1995, "The Constant Stress Term," Eng. Fract. Mech., **50**, pp. 869–882.
[23] Chao, Y. J., Liu, S., and Broviak, B. J., 2001, "Brittle Fracture: Variation of Fracture Toughness with Constraint and Crack Curving Under Mode I Conditions," Exp. Mech., **41**, pp. 232–241.
[24] Maleski, M. J., Kirugulige, M. S., and Tippur, H. V., 2004, "A Method for Measuring Mode I Crack Tip Constraint Under Static and Dynamic Loading Conditions," Exp. Mech., **44**, pp. 522–532.
[25] Smith, D. J., Ayatollahi, M. R., and Pavier, M. J., 2001, "The Role of T-Stress in Brittle Fracture for Linear Elastic Materials Under Mixed-Mode Loading," Fatigue Fract. Eng. Mater. Struct., **24**, pp. 137–150.
[26] Ayatollahi, M. R., Pavier, M. J., and Smith, D. J., 2002, "Mode I Cracks Subjected to Large T-Stresses," Int. J. Fract., **117**, pp. 159–174.
[27] Larsson, S. G., and Carlsson, A. J., 1973, "Influence of Non-Singular Stress Terms and Specimen Geometry on Small Scale Yielding at Crack Tips in Elastic-Plastic Materials," J. Mech. Phys. Solids, **21**, pp. 263–277.
[28] Rice, J. R., 1974, "Limitations to Small-Scale Yielding Approximation for Crack Tip Plasticity," J. Mech. Phys. Solids, **22**, pp. 17–26.
[29] Dodds, R. H., Shih, C. F., and Anderson, T. L., 1993, "Continuum and Micromechanics Treatment of Constraint in Fracture," Int. J. Fract., **64**, pp. 101–133.
[30] Kfouri, A. P., 1986, "Some Evaluations of the Elastic T-Term Using Eshelby's Method," Int. J. Fract., **30**, pp. 301–315.
[31] Sham, T. L., 1991, "The Determination of the Elastic T-Term Using Higher Order Weight Functions," Int. J. Fract., **48**, pp. 81–102.
[32] Yang, B., and Ravi-Chandar, K., 1999, "Evaluation of Elastic T-Stress by the Stress Difference Method," Eng. Fract. Mech., **64**, pp. 589–605.
[33] Xiao, Q. Z., and Karihaloo, B. L., 2002, "Coefficients of the Crack Tip Asymptotic Field for a Standard Compact Tension Specimen," Int. J. Fract., **118**, pp. 1–15.
[34] Olsen, P. C., 1994, "Determining the Stress Intensity Factors K_I and K_{II} and the T-Term via the Conservation Laws Using Boundary Element Method," Eng. Fract. Mech., **49**, pp. 49–60.
[35] Moon, H. J., and Earmme, Y. Y., 1998, "Calculation of Elastic T-Stresses Near Interface Crack Tip Under In-Plane and Anti-Plane Loading," Int. J. Fract., **91**, pp. 179–195.
[36] Jayadevan, K. R., Narasimhan, R., Ramamurthy, T. S., and Dattaguru, B., 2001, "A Numerical Study of T-Stress in Dynamically Loaded Fracture Specimens," Int. J. Solids Struct., **38**, pp. 4987–5005.
[37] Paulino, G. H., and Kim, J.-H., 2004, "A New Approach to Compute T Stress in Functionally Graded Materials by Means of the Interaction Integral Method," Eng. Fract. Mech., **71**, pp. 1907–1950.
[38] Bilby, B. A., and Cardew, G. E., 1975, "The Crack With a Kinked Tip," Int. J. Fract., **11**, pp. 708–812.
[39] Lo, K. K., 1978, "Analysis of Branched Cracks," ASME J. Appl. Mech., **45**, pp. 797–802.
[40] Cotterell, B., and Rice, J. R., 1980, "Slightly Curved or Kinked Cracks," Int. J. Fract., **16**, pp. 155–169.
[41] Hayashi, K., and Nemat-Nasser, S., 1981, "On Branched, Interface Cracks," ASME J. Appl. Mech., **48**, pp. 529–533.
[42] Gu, P., and Asaro, R. J., 1997, "Cracks in Functionally Graded Materials," Int. J. Solids Struct., **34**(1), pp. 1–17.
[43] Gao, H., and Chiu, C., 1992, "Slightly Curved or Kinked Cracks in Anisotropic Elastic Solids," Int. J. Solids Struct., **29**, pp. 947–972.
[44] Geubelle, P. H., and Knauss, W. G., 1994, "Crack Propagation at and Near

Bimaterial Interfaces: Linear Analysis," ASME J. Appl. Mech., **61**, pp. 560–566.
[45] Adda-Bedia, M., and Arias, R., 2003, "Brittle Fracture Dynamics With Arbitrary Paths, I. Kinking of a Dynamic Crack in General Antiplane Loading," J. Mech. Phys. Solids, **51**, pp. 1287–1304.
[46] Li, R., and Kardomateas, G. A., 2005, "Thermo-Elastic Crack Branching in General Anisotropic Media," Int. J. Solids Struct., **42**, pp. 1091–1109.
[47] Selvarathinam, A. S., and Goree, J. G., 1998, "T-Stress Based Fracture Model for Cracks in Isotropic Materials," Eng. Fract. Mech., **60**, pp. 543–561.
[48] Yang, S., and Yuan, F.-G., 2000, "Kinked Crack in Anisotropic Bodies," Int. J. Solids Struct., **37**, pp. 6635–6682.
[49] Lauterbach, B., and Gross, D., 1998, "Crack Growth in Brittle Solids Under Compression," Mech. Mater., **29**, pp. 81–92.
[50] Leblond, J.-B., and Frelat, J., 2000, "Crack Kinking From an Initially Closed Crack," Int. J. Solids Struct., **37**, pp. 1595–1614.
[51] Isaksson, P., and Ståahle, P., 2002, "Prediction of Shear Crack Growth Direction Under Compressive Loading and Plane Strain Conditions," Int. J. Fract., **113**, pp. 175–194.
[52] Broberg, K. B., 2005, "A Note on T-Stress Determination Using Dislocation Arrays," Int. J. Fract., **131**, pp. 1–14.
[53] Tada, H., Paris, P. C., and Irwin, G. R., 2000, *The Stress Analysis of Cracks Handbook*, ASME, New York.
[54] Sanford, R. J., 2003, *Principles of Fracture Mechanics*, Prentice-Hall, Englewood Cliffs, NJ.
[55] Fett, T., Pham, V.-B., Bahr, H.-A., 2004, "Weight Functions for Kinked Semi-Infinite Cracks," Eng. Fract. Mech., **71**, pp. 1987–1995.
[56] Deng, X., 1994, "An Asymptotic Analysis of Stationary and Moving Cracks With Frictional Contact Along Bimaterial Interfaces and in Homogeneous Solids," Int. J. Solids Struct., **31**, pp. 2407–2429.
[57] Leevers, P. S., and Radon, J. C., 1982, "Inherent Stress Biaxiality in Various Fracture Specimen Geometries," Int. J. Fract., **19**, pp. 311–325.
[58] Melin, S., 2002, "The Influence of the T-Stress on the Directional Stability of Cracks," Int. J. Fract., **114**, pp. 259–265.
[59] Yang, B., and Ravi-Chandar, K., 2001, "Crack Path Instabilities in a Quenched Glass Plate," J. Mech. Phys. Solids, **49**, pp. 91–130.
[60] Richardson, D. E., and Goree, J. G., 1993, "Experimental Verification of a New Two Parameter Fracture Model," Fracture Mechanics: 23 Symposium, ASTM, Philadelphia, STP 1189, pp. 738–750.
[61] Xu, L. R., and Wang, P., 2006, "Dynamic Fracture Mechanics Analysis of Failure Mode Transitions Along Weakened Interfaces in Elastic Solids," (in press).
[62] Dugdale, D. S., 1960, "Yielding of Steel Sheets Containing Slits," J. Mech. Phys. Solids, **8**, pp. 100–104.

Exploring Effective Methods for Simulating Damaged Structures With Geometric Variation: Toward Intelligent Failure Detection

Daniel A. McAdams[1]
e-mail: dmcadams@umr.edu

David Comella

Department of Mechanical and Aerospace Engineering,
University of Missouri—Rolla,
Rolla, MO 65409-0050

Irem Y. Tumer
Complex Systems Design Group,
Intelligent Systems Division,
NASA Ames Research Center,
Moffett Field, CA 94035-1000
e-mail: itumer@mail.arc.nasa.gov

Inaccuracies in the modeling assumptions about the distributional characteristics of the monitored signatures have been shown to cause frequent false positives in vehicle monitoring systems for high-risk aerospace applications. To enable the development of robust fault detection methods, this work explores the deterministic as well as variational characteristics of failure signatures. Specifically, we explore the combined impact of crack damage and manufacturing variation on the vibrational characteristics of beams. The transverse vibration and associated eigenfrequencies of the beams are considered. Two different approaches are used to model beam vibrations with and without crack damage. The first approach uses a finite difference approach to enable the inclusion of both cracks and manufacturing variation. The crack model used with both approaches is based on a localized decrease in the Young's modulus. The second approach uses Myklestad's method to evaluate the effects of cracks and manufacturing variation. Using both beam models, Monte Carlo simulations are used to explore the impacts of manufacturing variation on damaged and undamaged beams. Derivations are presented for both models. Conclusions are presented on the choice of modeling techniques to define crack damage, and its impact on the monitored signal, followed by conclusions about the distributional characteristics of the monitored signatures when exposed to random manufacturing variations. [DOI: 10.1115/1.2188535]

Introduction

Background and Motivation. Effective failure detection requires a good understanding of the characteristics of the monitored data and a good sample of failure data. In the absence of a statistically significant sample of failure data, vehicle health monitoring systems for high-risk aerospace applications have to rely on anomaly detection algorithms that work around this problem. Prior work has shown that such algorithms work poorly for engineered systems operating in a highly variable environment. For anomaly detection algorithms to work effectively, a more comprehensive framework must be established to represent known sources of design, manufacturing, operational, and random variation. In the case of anomaly detection, it is necessary to understand the probabilistic footprint of all these combined effects on the signals being measured.

In the actual operating environment, aerospace systems exhibit significant variability [1–3]. Furthermore, variations introduced during design, manufacturing, and assembly significantly influence the final response characteristics of such systems [4,2]. Ongoing research at NASA Ames Research Center and at the University of Missouri—Rolla explores an empirical and simulation-based approach to help develop deterministic and probabilistic models of healthy and faulty data.

Previous work has been published which describes the attempt to capture the influence of design variations for dynamic systems using probabilistic models [5], as well as to reduce the effects of operational variations due to maneuvering on decisions about the vehicle's health [1]. Current efforts focus on modeling rare failure signatures to determine their distributional characteristics using both empirical and simulation-based data.

More specifically, health monitoring of gas turbine engines is of great interest due to the use of the engines as the source of primary propulsion and power in many aerospace and military applications. The unexpected failure of a gas turbine can stop missions and in the worst case result in the death of crew members. Health monitoring is an integral part of many maintenance plans; accurate and reliable health monitoring can result in significant cost savings.

As a result, this paper is building a knowledge base for the operational detection of cracked turbine blades in zero allowable fault systems. A crack in a blade rotating at high speed can devastate an engine beyond repair. An extensive postfracture failure analysis of a wind tunnel compressor blade was made by Hampton and Nelson [6] and reveals much about crack initiation and growth but this is far too late for many applications. Ganesan et al. [7] use a finite element method to study the dynamic response of high speed rotors with variation in elastic modulus and mass density. Turbine blades have complex geometries and are subject to complex excitation signals. With a long term goal to completely understand the vibrational response of healthy and damaged turbine blades subject to different excitations, we begin with the simpler problem of understanding the impact of design and manufacturing variations on healthy and damaged simple beams. As basic knowledge is developed, future work will explore the more complex turbine blade problem.

Paper Focus. In the first publication on the results of this work, the authors presented a feasibility study on the use of probabilistic methods (e.g., Monte Carlo simulation) using a simple example in design, and compared these methods to more traditional variation analysis techniques [5]. A case study was presented, focusing on

[1]Author to whom correspondence should be addressed.

Contributed by the Applied Mechanics Division of ASME for publication in the JOURNAL OF APPLIED MECHANICS. Manuscript received September 9, 2004; final manuscript received January 25, 2006. Review conducted by S. Govindjee. Discussion on the paper should be addressed to the Editor, Prof. Robert M. McMeeking, Journal of Applied Mechanics, Department of Mechanical and Environmental Engineering, University of California—Santa Barbara, Santa Barbara, CA 93106-5070, and will be accepted until four months after final publication of the paper itself in the ASME JOURNAL OF APPLIED MECHANICS.

the analysis of a lumped parameter dynamic model for a complex cam-follower, followed by an analysis of vibration data obtained from such a model. The Monte Carlo simulation technique was used to vary a subset of the design parameters. The effect on the vibration response was explored to determine whether probabilistic methods can be used to model the inherent variations observed in the dynamic response of complex systems [5]. Manufacturing process capability variations on as little as one of the modeling elements (e.g., the spring constant) were shown to cause significant variations in the acceleration signature of the cam-follower system.

A next set of publications addressed the question of whether these variations, caused by variations in the manufacturing process, would have an impact on the monitored signature when combined with a failure signature. A key effort required was the modeling of cracks in conjunction with variability. A modal analysis approach was presented in that work to explore the effect of variability and cracks together [8]. The results of the previous work indicated that the type of variation that can occur from standard manufacturing processes can cause complications in identifying damaged beams. Though the comparison of a damaged beam to an undamaged beam still results in the same trend (the eigenfrequencies of the damaged beam decrease as compared to the undamaged beam), the geometric variations result in a variation in eigenfrequencies on a scale similar to that resulting from damage.

To thoroughly simulate turbine blades, variations in material properties need to be included as well as variations in geometry. In addition, realistic turbine blade geometries need to be simulated as opposed to simple prismatic beams. Performing Monte Carlo simulations on more complex geometries with more sources of variation will be computationally expensive. Thus, determining an effective method for calculating the eigenfrequencies of damaged beams is important. In a previous effort, we discovered that using a direct modal approach had difficulty in calculating high-order eigenfrequencies [8]. In this paper, damage simulation is explored further by using two different modeling approaches to generate the failure signatures, and exploring their variational characteristics when combined with inherent variations in the system and/or its components. Specifically, models are derived to study the combined impact of crack damage and manufacturing variation on the vibrational characteristics of simple beams. The transverse vibration and associated eigenfrequencies of the beams are considered as the candidate monitoring signature.

Specifically, we are interested in methods that are computationally efficient and allow the inclusion of damage in the model formulation. The first approach uses a finite difference approach, initially presented in [8], to enable the inclusion of both cracks and manufacturing variation to be considered. The crack model used with both approaches is based on a localized decrease in Young's modulus. The second approach uses Myklestad's method. This method uses a lumped model of the beam to create a frequency equation which can then be solved to find the natural frequencies. Using both beam models, Monte Carlo simulations are used to explore the impact of manufacturing variation on damaged and undamaged beams.

Finite element method (FEM) approaches, such as cohesive zone finite element modeling, are not explored in this article. Finite element methods are perhaps the most versitile and effective approach to the analysis of dynamic structures. However, when applied to structures with uncertain properties, including geometry and material properties, the FEM faces some difficulties. To perform a Monte Carlo simulation each sample requires the generation of a different geometric structure with spatially random properties. After generating the structure, it needs to be decomposed or meshed, then solved and relevant information recorded. In many cases, meshing requires almost as much computation time as the solution. If 10,000 samples are needed to generate a sufficiently accurate simulation, the computational time becomes large.

In the following sections, detailed derivations are presented for both models, followed by their application to an example problem to determine the distributional characteristics. Conclusions are presented on the choice of modeling techniques to define crack damage, and its impact on the monitored signal, followed by conclusions about the distributional characteristics of the monitored signatures when exposed to random manufacturing variations.

Fault Detection and Health Monitoring Overview. The general problem of fault detection is reviewed by Lefas et al. [9]. Fault detection is conducted by checking that measured or estimated parameters are within set tolerances. Models are needed to relate directly measurable parameters to physical problems within the device. For instance, if the natural frequency of a beam can be measured, a model can be used to determine whether the beam is cracked. Using the model, the tolerance for the natural frequency can be set such that, if the natural frequency is outside the tolerance, confidence is high that a crack is present.

The final design of a health monitoring system for any turbomachinery is influenced by the maintenance philosophy which will be employed for the machines lifetime and the specific needs of the application. Four maintenance philosophies are reviewed by Pusey and Roemer [10]. The design of a health monitoring system requires the careful study of potential failure modes, their effects, and criticality of those effects. Banks et al. [11] review this process for the U.S. Marine Corps Advanced Amphibious Assault Vehicle (AAAV). Functional models and good system response models are needed to determine where a particular failure mode's symptoms would occur and how it could be measured [12,13]. Set points for alarms and automated responses can be established for the measured parameters. The costs and benefits must then be evaluated for the particular needs of an application. The trade off between false alarm rate and missed detection rate is one of the most difficult problems that must be balanced [14].

With respect to the current focus on turbine blades, the most commonly measured parameters for gas turbines are vibration, lubrication oil quality, and performance. Performance is calculated from the measured parameters of temperature, pressure, and flow rate [15]. Lifson et al. [16] analyze the practices, benefits, and limitations of several types of vibration monitoring systems used with industrial gas turbines.

This paper is building a knowledge base for the operational detection of cracked turbine blades in zero allowable fault systems. Blading problems are responsible for 42% of failures in gas turbines [17]. A crack in a blade rotating at high speed can devastate an engine beyond repair. Case studies have shown that common existing vibration monitoring systems on operating engines cannot detect a fatigue crack until a critical problem occurs [18]. Several methods of measuring the blade vibration have been reviewed by Al-Bedoor [19], including strain gauges, laser Doppler, lateral vibration, pressure fluctuations, torsional vibration, and piezoelectric materials. Most of these methods are still under investigation and are not intended for use on production engines. An extensive postfracture failure analysis of a wind tunnel compressor blade was made by Hampton and Nelson [6] and reveals much about crack initiation and growth but this is far too late for many applications. Ganesan et al. [7] use a finite element method to study the dynamic response of high speed rotors with variation in elastic modulus and mass density.

Turbine blades have complex geometries and are subject to complex excitation signals. With a long term goal to completely understand the vibrational response of healthy and damaged turbine blades subject to different excitations, we begin with the simpler problem of understanding the impact of manufacturing variations on healthy and damaged simple beams. As basic knowledge is developed and effective solution methods established, future work will explore the more complex turbine blade problem.

Modeling Vibration in Damaged Beams

A critical and observable impact of fractures on beam vibrational response is the difference in the eigenfrequencies for the damaged and undamaged beams. Most theoretical models of cracked beams begin with a Euler-Bernoulli beam and develop special considerations to model crack damage. Here, the Euler-Bernoulli beam is developed with considerations for manufacturing variation. Crack models are added to the resultant model to explore the impacts of both manufacturing variation and structural damage.

In the following sections, two different approaches are explored to model crack damage in simple beams. The derivations of the models are presented for each, followed by simulation results to explore the distributional characteristics of the vibrational response of cracked and uncracked beams when combined with manufacturing variations.

Damaged Models and Related Work. A large effort has been made to explore the vibrational characteristics of damaged beams. Doebling et al. [20] present a review of vibration-based damage identification methods. Damage identification methods can be classified as linear and nonlinear. Linear methods can be divided into model- and non-model-based methods. They can also be classified by the four levels of information they can provide:

Level 1: Determination that damage is present
Level 2: Level 1 plus the location of the damage
Level 3: Level 2 plus quantification of the severity of the damage
Level 4: Level 3 plus a prediction of the remaining life of the structure

There are three common types of crack models [21]; local stiffness reduction, discrete spring models, and complex models in two or three dimensions. Hu and Liang [22] use an integrated approach of a massless spring and a continuum damage concept to develop a crack detection technique. Gudmundson [23] developed models that enable the simulation of natural frequency changes of structures due to cracks and other geometrical changes. In Gudmundson [23] the models are benchmarked against finite element analysis and experimental results from Wetland [24]. Chondros et al. [25] developed a continuous vibration model for the lateral vibration of a cracked Euler-Bernoulli beam with open edge cracks. Chondros et al. have also explored a crack model for transverse, longitudinal, and other vibrations as well as beams with different end conditions [26–28]. Mengcheng [29] and Yokoyama [30] used a theoretical line-spring model and Euler-Bernoulli beam theory to approximate the response of cracked beam vibrations. Maiti [31] developed theoretical models for the vibration characteristics of cracked beams with a linearly variable cross section (wedge shaped beams). Zheng and Fan [32] developed a method to calculate the natural frequency of beams with an arbitrary number of cracks and a nonuniform cross section using a modified Fourier series. Using experimental methods, Ju et al. [33] diagnosed the fracture damage of structures using modal frequency methods. Kuang and Huang [34] tackled the problem of a blade crack on a rotating disk with many shrouded blades.

Most works with cracks use a linear open crack model where the opposing crack faces do not come in contact at any point during the vibration. There has been some recent work with nonlinear breathing or closing crack models [35–37]; these all indicate that the closing reduces the change in natural frequency reduction compared to the open crack models, making the practical problem of damage detection more difficult.

Despite the effort expended in developing models that can be used to simulate the vibrational characteristics of fractured beams, each of the models assumes a beam with ideal geometry and material properties. Little work has been done to determine the combined effects of manufacturing variation and fractures on vibrational characteristics of structures. Two such such models are developed in this article and are presented next. The fault detection models developed will provide level 1 information and use a stiffness reduction method to model damage.

A Finite Difference Approach. On approach to determining the vibration characteristics of a cracked beam with manufacturing variation is developed here. This approach uses a finite difference method to produce the complete spatial and time solution to the beam. To produce the specific frequency information needed to identify a crack, a fast Fourier transform (FFT) is used to extract frequency information from the complete solution. To model a crack, a local reduction in material stiffness is used to model the crack [38].

Problem Formulation. The derivation of the model begins with the Euler-Bernoulli beam equation:

$$\rho A\frac{\partial^2 w}{\partial t^2}+\frac{\partial^2}{\partial x^2}\left(EI\frac{\partial^2 w}{\partial x^2}\right)=f(x,t). \tag{1}$$

In the development of the finite difference equations in this section, the products ρA and EI will be kept together as a single term. Also, the explicit functional dependency of w on space and time is not shown to simplify notation. To allow geometric variation to enter the model, also, ρA and EI have spatial dependency. We are interested in the free response as only frequency information is needed, thus $f(x,t)=0$. Given this construction, the multiplication rule can be applied to give

$$\rho A\frac{\partial^2 w}{\partial t^2}+\frac{\partial^2 EI}{\partial x^2}\frac{\partial^2 w}{\partial x^2}+EI\frac{\partial^4 w}{\partial x^4}=0. \tag{2}$$

Equation (2) is a model of beam vibration that allows geometric variation to be included in the simulation. For the case presented here, a pinned-pinned beam will be simulated. The boundary conditions for the simply supported (pinned-pinned) case for the left end are that the deflection is zero,

$$w|_{x=0}=0, \tag{3}$$

and that the moment is zero,

$$EI\frac{\partial^2 w}{\partial x^2}\bigg|_{x=0}=0. \tag{4}$$

Similarly, for the right end the boundary conditions are that the deflection is zero,

$$w|_{x=L}=0 \tag{5}$$

and the moment is zero,

$$EI\frac{\partial^2 w}{\partial x^2}\bigg|_{x=L}=0. \tag{6}$$

The frequency behavior of damaged and undamaged beams will be extracted by applying an FFT to the complete solution of the finite difference model. To produce motion, initial conditions must be applied. The beam will be bent to an initial shape and then allowed to vibrate from rest. This results in the following initial conditions of

$$w|_{t=0}=w_0 \tag{7}$$

and

$$\frac{\partial w}{\partial t}\bigg|_{t=0}=0 \tag{8}$$

where w_0 is the initial beam shape. The problem is now fully formulated. We apply finite difference techniques in the next section.

Application of Finite Difference Techniques. To formulate algorithms for a computer program to solve, approximations for

the fourth- and second-order terms in Eq. (2) must be substituted. The second-order accurate approximation for the fourth-order term from Lapidus [39] is

$$\frac{\partial^4 w}{\partial x^4} = \frac{w_{i+2,j} - 4w_{i+1,j} + 6w_{i,j} - 4w_{i+1,j} + w_{i-2,j}}{(\Delta x)^4} \tag{9}$$

where i and j are integers representing the spatial step and the time step, respectively. The second-order accurate approximation for the second derivative of deflection with respect to x is

$$\frac{\partial^2 w}{\partial x^2} = \frac{w_{i+1,j} - 2w_{i,j} + w_{i-1,j}}{(\Delta x)^2} \tag{10}$$

Similar approximations are used for the second derivative of deflection with respect to time and the second derivative of EI with respect to x. The result is

$$\frac{\partial^2 w}{\partial t^2} = \frac{w_{i,j+1} - 2w_{i,j} + w_{i,j-1}}{(\Delta t)^2} \tag{11}$$

and

$$\frac{\partial^2 EI}{\partial x^2} = \frac{EI_{i+1} - 2EI_i + EI_{i-1}}{(\Delta x)^2}. \tag{12}$$

Substituting Eqs. (10)–(12) into Eq. (2) yields

$$\rho A_i \frac{(w_{i,j+1} - 2w_{i,j} + w_{i,j-1})}{(\Delta t)^2} + \left(\frac{EI_{i+1} - 2EI_i + EI_{i-1}}{(\Delta x)^2}\right) \times \left(\frac{w_{i+1,j} - 2w_{i,j} + w_{i-1,j}}{(\Delta x)^2}\right) + EI_i\left(\frac{w_{i+2,j} - 4w_{i+1,j} + 6w_{i,j} - 4w_{i-1,j} + w_{i-2,j}}{(\Delta x)^4}\right) = 0. \tag{13}$$

Solving for the $w_{i,j+1}$ term gives

$$w_{i,j+1} = 2w_{i,j} - w_{i,j-1} - \frac{(\Delta t)^2}{\rho A_i (\Delta x)^4}[(EI_{i+1} - 2EI_i + EI_{i-1})(w_{i+1,j} - 2w_{i,j} + w_{i-1,j}) + EI_i(w_{i+2,j} - 4w_{i+1,j} + 6w_{i,j} - 4w_{i-1,j} + w_{i-2,j})]. \tag{14}$$

Equation (14) can be used to calculate the deflection at a point on the beam at a time step, given knowledge of the deflection at that point at the two previous time steps, as well as knowledge of the deflection two spatial time steps to the left and to the right at the previous time step. This is an explicit finite difference form.

In addition to the general formulation of Eq. (14), finite difference expressions are needed for the boundary conditions and time and spatial steps where the two previous time steps are not known and the spatial steps are at the physical ends of the beam. Using a Taylor series expansion, the deflection at the first time step can be represented by

$$w_{i,1} = w_{i,0} + \Delta t \left.\frac{\partial w}{\partial t}\right|_{i,0} + (\Delta t)^2 \frac{1}{2} \left.\frac{\partial^2 w}{\partial t^2}\right|_{i,0}. \tag{15}$$

The first two terms on the right-hand side of Eq. (15) are known from the initial conditions, Eqs. (7) and (8). Substituting the initial conditions and solving for the second derivative with respect to time gives

$$\left.\frac{\partial^2 w}{\partial t^2}\right|_{i,0} = \frac{2(w_{i,j} - w_{i,0})}{(\Delta t)^2}. \tag{16}$$

Substituting Eqs. (16), instead of (11), along with Eqs. (9), (10), and (12) into Eq. (2) and solving for the deflection at the first time step gives

$$w_{i,1} = w_{i,0} - \frac{1}{2}\frac{(\Delta t)^2}{\rho A_i (\Delta x)^4}[(EI_{i+1} - 2EI_1 + EI_{i-1})(w_{i+1,0} - 2w_{i,0} + w_{i,0}) + EI_i(w_{i+2,0} - 4w_{i+1,0} + 6w_{i,0} - 4w_{i-1,0} + w_{i-2,0})]. \tag{17}$$

Equation (17) gives the deflection of the first time step for any point on the beam except the first and second points from the left or right where the terms $i+2$, $i+1$, $i-1$, and $i-2$ could have no meaning as those points do not exist on the beam. The boundary conditions must be used to give information about those points.

From the deflection boundary conditions (3) and (5), the deflection for the left and right ends of the beam is zero for all time steps

$$w_{1,j} = 0 \tag{18}$$

and

$$w_{n,j} = 0 \tag{19}$$

where $w_{n,j}$ represents the right end ($x=L$) and $w_{1,j}$ represents the left end ($x=0$).

Next, an expression for the second point from the left and right must be found from the other two boundary conditions (4) and (6). Writing Eq. (10) for the end points (1 and n) and using the boundary conditions to set the second derivative equal to zero yields

$$EI_1\left(\frac{w_{0,j} - 2w_{1,j} + w_{2,j}}{(\Delta x)^2}\right) = 0 \tag{20}$$

and

$$EI_n\left(\frac{w_{I+1,j} + 2w_{I,j} - w_{I-1,j}}{(\Delta x)^2}\right) = 0. \tag{21}$$

Substituting the values from Eqs. (18) and (19) into those above gives

$$w_{0,j} = -w_{2,j} \tag{22}$$

and

$$w_{n+1,j} = -w_{n-1,j}. \tag{23}$$

Writing Eq. (17) for the points 2 and $n-1$ and substituting into Eq. (18), (19), (22), and (23) results in expressions for these second points at the first time step. These expressions are

$$w_{2,1} = w_{2,0} - \frac{1}{2}\frac{(\Delta t)^2}{\rho A_2 (\Delta x)^4}[EI_2(w_{4,0} - 4w_{3,0} + 5w_{2,0}) + (EI_3 - 2EI_2 + EI_1)(w_{3,0} - 2w_{2,0})] \tag{24}$$

and

$$w_{n-1,1} = w_{n-1,0} - \frac{1}{2}\frac{(\Delta t)^2}{\rho A_2 (\Delta x)^4}[(EI_n - 2EI_{n-1} + EI_{n-2})(-2w_{n-1,0} + w_{n-2,0}) + EI_{n-1}(5w_{n-1,0} - 4w_{n-2,0} + w_{n-3,0})]. \tag{25}$$

Also, writing Eq. (14) about the same points as above but for any time step $j+1$ yields

$$w_{2,j+1} = 2w_{2,j} - w_{2,j-1} + \frac{(\Delta t)^2}{\rho A_2 (\Delta x)^4}[(EI_3 - 2EI_2 + EI_1)(w_{3,j} - 2w_{2,j}) + EI_2(w_{4,j} - 4w_{3,j} + 5w_{2,j})] \tag{26}$$

and

$$w_{n-1,j+1} = 2w_{n-1,j} - w_{n-1,j-1} + \frac{(\Delta t)^2}{\rho A_{n-1} (\Delta x)^4}[(EI_n - 2EI_{n-1} + EI_{n-2}) \times (-2w_{n-1,j} + w_{n-2,j}) + EI_{n-1}(5w_{n-1,j} - 4w_{n-2,j} + w_{n-3,j})]. \tag{27}$$

Equations (7), (17), (24), and (25) are used in a program to give a complete data set for the initial deflection of the beam and the

Table 1 Properties of the simulated beam.

Property	Value
Length	1 m
Nominal base	10 cm
Nominal base	10 cm
Nominal height	10 cm
E_0	93750 Pa
Density	1 kg/m^3
Crack depth	10 mm
Crack location	Midpoint

deflection of the first time step. Equations (26) and (27) are then calculated for a time step; Eq. (14) is then calculated for each internal point on the beam.

Since this is an explicit formulation, the choice of step sizes must meet the following stability criterion [40]:

$$2\sqrt{\frac{EI}{\rho A}}\frac{(\Delta t)}{(\Delta x)^2} \leq 1. \tag{28}$$

Parameter Variation and Crack Modeling. Using the finite difference technique developed above, solutions to Euler-Bernoulli beams with variation in the material properties and geometry can be found. This section will consider how the variation due to manufacturing tolerances and cracks was modeled. The *McGraw-Hill Machining and Metal Working Handbook* [41] gives tolerances for many manufacturing techniques and for different parts. Rarely do these tolerances exceed 1% of the nominal dimension. We will use this variation as to approximate geometric variations in the beam simulations below.

This paper considers a beam with a square cross section. To model manufacturing variation, the base and height may differ at any point on the beam's length by ±1% from the nominal dimension. Using the standard practice [42], a tolerance is equal to three times the standard deviation of a normal distribution. To generate these differences a random number generator was used with the base diminsion as the mean and a standard deviation of one third of the tolerance. Then, the base and height were generated for each of the desired subdivisions of the length and then substituted into the formulas for I and A. When multiplied by modulus of elasticity and density, this results in data for the $EI(x)$ and $pA(x)$ functions, thus providing a randomly varying geometry for the beam.

As discussed above, there are numerous crack and damage models in the literature. Here, the influence of the crack was modeled using the damage mechanics approach by DiPasquale [43]. The damage parameter is defined as

$$d = \frac{A_d}{A_T} \tag{29}$$

where $A_d = b \times a$.

Using the damage parameter the stiffness degradation in the area near the crack can be calculated as

$$E = (1 - d)E_0. \tag{30}$$

This degraded E is substituted into the EI formula for the node corresponding to the crack location. This incorporates the influence of the crack into the varying properties of the beam.

Example. The finite difference equations and crack model developed above were used to simulate the vibrational behavior of a cracked beam. The specific properties of the beam are shown in Table 1. Results of the distribution of the first five natural frequencies are presented for both a healthy and damaged beam below.

Results. A time marching program was developed in MATLAB utilizing the equations presented above to solve the Euler-Bernoulli beam. Ten thousand Monte Carlo simulates were run for an uncracked beam with a randomly varying geometry. The first five natural frequencies were recovered using fast Fourier transforms for each iteration. However, in a final detailed simulation, more than 10,000 runs would be used to create more accurate models. In this article we are only comparing the two methods so 10,000 samples is deemed sufficient. The histograms for the uncracked beam are shown in Figs. 1–5.

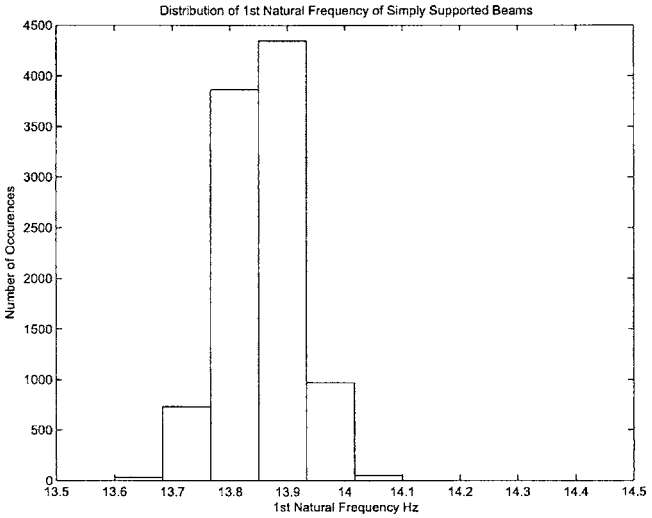

Fig. 1 Histogram for the first natural frequency of the uncracked beam (finite difference method)

The program was next modified to take into account the influence of a crack at the midpoint with a depth of 10 mm using the local stiffness degradation model presented above. Histograms for the first five natural frequencies are presented in Figs. 6–10.

Table 2 shows values for the mean and the standard deviation of the five recovered natural frequencies for the damaged and undamaged beams. The mean decreased as expected when the beam is cracked for the first, third, and fifth natural frequencies, but increased for the second and fourth natural frequencies. The increase in the second and fourth natural frequencies is inconsistent with both the experimental and theoretical literature on damaged beams. The increase in these natural frequencies represents an error in the simulation approach. The difference in standard deviation of the natural frequencies between cracked and uncracked

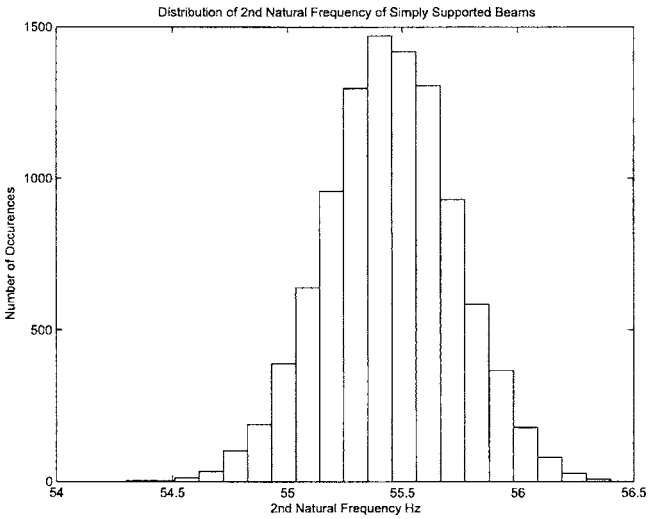

Fig. 2 Histogram for the second natural frequency of the uncracked beam (finite difference method)

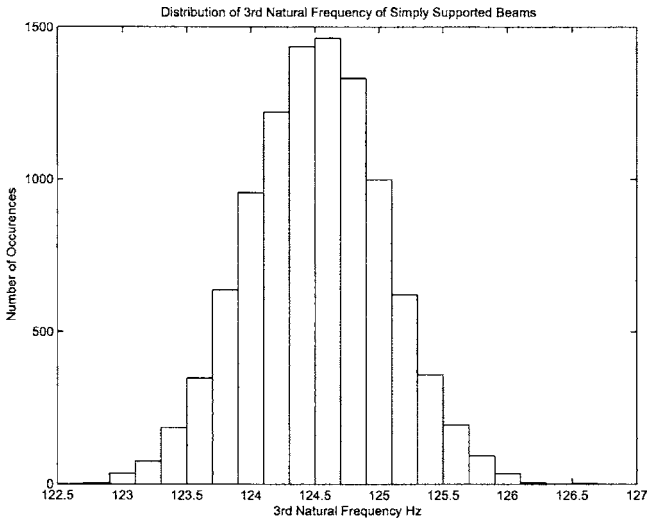

Fig. 3 Histogram for the third natural frequency of the uncracked beam (finite difference method)

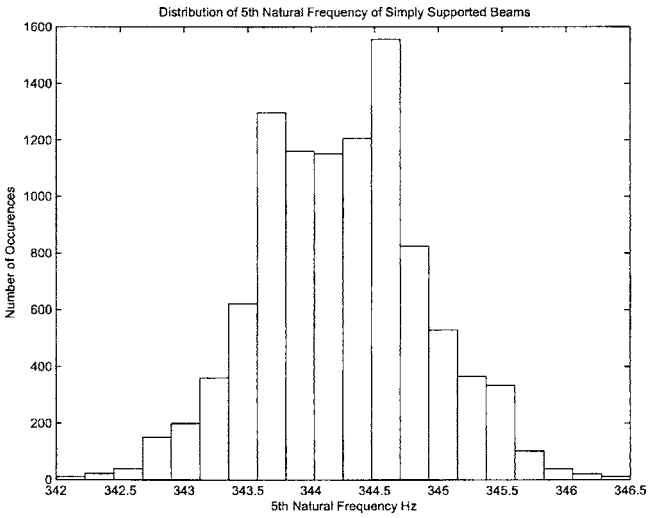

Fig. 5 Histogram for the fifth natural frequency of the uncracked beam (finite difference method)

cases was small for all frequencies except the first, which nearly doubled when cracked. The addition of manufacturing variations on the beam had little impact on the changes in natural frequency as compared to a beam of ideal geometry. Using this model, the conclusion would be that a shift in natural frequencies would be observable even under conditions of geometric variation. Also, the standard deviations are largely the same for uncracked and cracked beams.

The Myklestad Approach. A second approach to determining the vibration characteristics of a cracked beam with manufacturing variation is developed here. Myklestad [44] used a tabular method to perform the calculations. Here, we will use Myklestad's method with the transfer matrix approach developed by Thomson [45] and augmented by Pestel and Leckie [46]. In this approach a lumping method will create a model of the beam with point masses and stiffness fields. Transfer matrices will be written for each segment of the lumped beam. The matrices are then multiplied together to form an overall transfer matrix for the entire beam. Next, boundary conditions are then applied to produce the frequency equation. Finally, the roots of the frequency equation can then be solved to yield the natural frequencies.

Problem Formulation. Myklestad's method for bending vibration is effective for determining natural frequencies for a structure. This paper uses the notation and approach of Meirovitch [47]. First, a lumped model of the pinned-pinned beam must be constructed. The beam will be divided into ten equal increments with the lumped zero inertia masses placed in the center as shown in Fig. 11. Ten increments were used to satisfy the rule [48] that the number of concentrated masses should be at least twice the number of frequencies to be obtained.

The masses will be called "stations" and the space in between them will be referred to as "fields." Utilizing a free body diagram of a station, as shown in Fig. 12, and the equations of motion, a system of equations for the variables on the right can be written in matrix form

$$\begin{bmatrix} Y \\ \Psi \\ M \\ Q \end{bmatrix}_i^R = \begin{bmatrix} 1 & 0 & 0 & 0 \\ 0 & 1 & 0 & 0 \\ 0 & 0 & 1 & 0 \\ -\omega^2 m_i & 0 & 0 & 1 \end{bmatrix} \begin{bmatrix} Y \\ \Psi \\ M \\ Q \end{bmatrix}_i^L = T_{S,i} \begin{bmatrix} Y \\ \Psi \\ M \\ Q \end{bmatrix}_i^L . \quad (31)$$

Now an equation for the field will be developed from the free body diagram as shown in Fig. 13. Regarding the left end of the

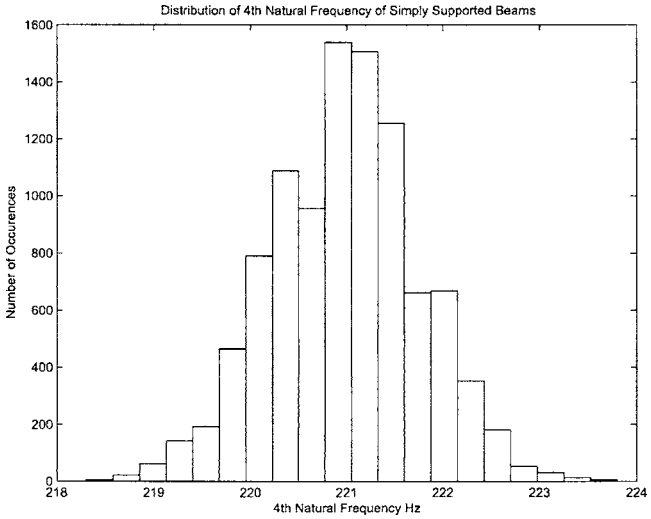

Fig. 4 Histogram for the fourth natural frequency of the uncracked beam (finite difference method)

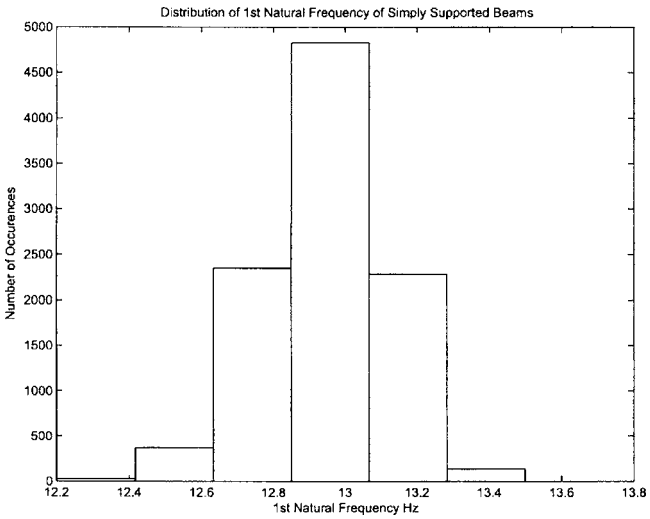

Fig. 6 Histogram for the first natural frequency of the cracked beam (finite difference method)

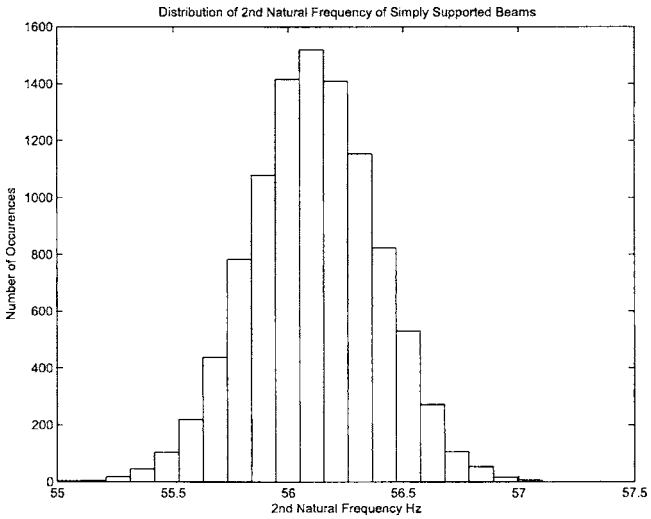

Fig. 7 Histogram for the second natural frequency of the cracked beam (finite difference method)

field as clamped, the equivalent spring equations for cantilevered beams can be introduced in the equations for deflection and angle. These relations coupled with equations of motion yield the following transfer matrix for the ith field.

$$\begin{bmatrix} Y \\ \Psi \\ M \\ Q \end{bmatrix}_{i+1}^{L} = \begin{bmatrix} 1 & \Delta x_i & (\Delta x_i)^2/2EI_i & -(\Delta x_i)^3/6EI_i \\ 0 & 1 & \Delta x/EI_i & -(\Delta x_i)^2/2EI_i \\ 0 & 0 & 1 & -\Delta x_i \\ 0 & 0 & 0 & 1 \end{bmatrix} \begin{bmatrix} Y \\ \Psi \\ M \\ Q \end{bmatrix}_{i}^{R} = T_{F,i} \begin{bmatrix} Y \\ \Psi \\ M \\ Q \end{bmatrix}_{i}^{R} . \quad (32)$$

Substituting Eq. (31) into Eq. (32) yields the transfer equation for the station vector of the left side of station $i+1$ to the station vector on the left side of station i

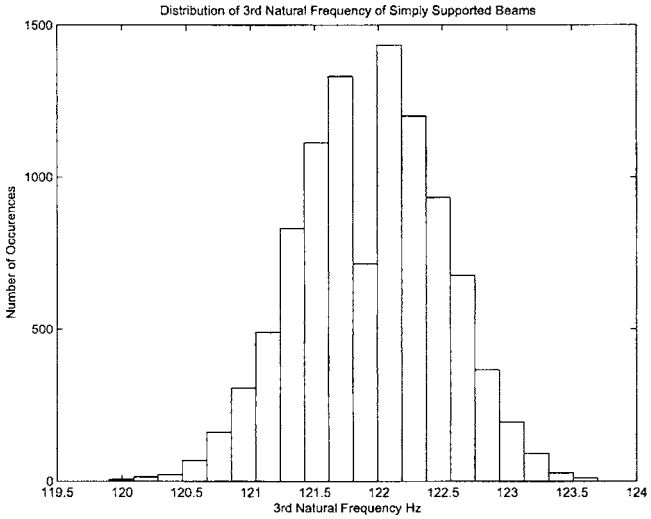

Fig. 8 Histogram for the third natural frequency of the cracked beam (finite difference method)

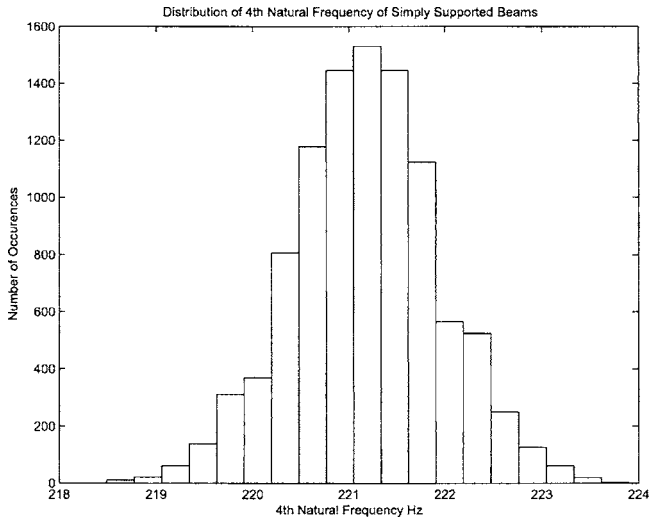

Fig. 9 Histogram for the fourth natural frequency of the cracked beam (finite difference method)

$$\begin{bmatrix} Y \\ \Psi \\ M \\ Q \end{bmatrix}_{i+1}^{L} = T_i \begin{bmatrix} Y \\ \Psi \\ M \\ Q \end{bmatrix}_{i}^{L} , \quad (33)$$

where T_i is the transfer matrix for the ith combination of station and field given by the product of the two matrixes

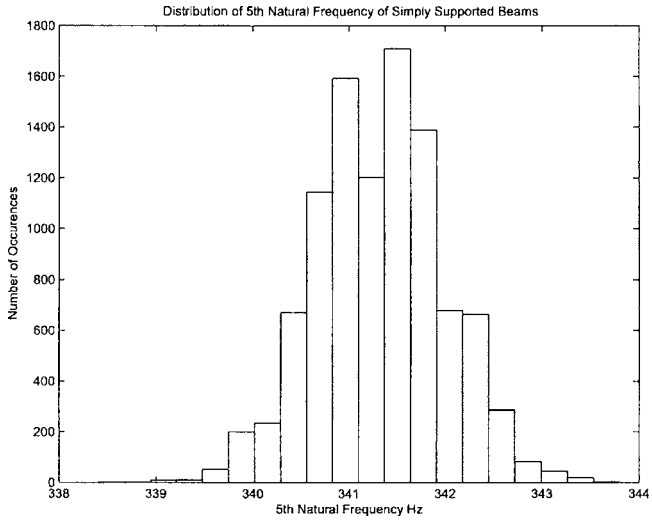

Fig. 10 Histogram for the fifth natural frequency of the cracked beam (finite difference method)

Table 2 The mean and standard deviation for the five natural frequencies (f_n) recovered

	Undamaged	Cracked
f_{n1} Mean	13.8505	12.9380
f_{n1} StDev	0.0799	0.1585
f_{n2} Mean	55.4427	56.109
f_{n2} StDev	0.2702	02638
f_{n3} Mean	124.5604	121.9362
f_{n3} StDev	0.5343	0.5561
f_{n4} Mean	220.9936	221.1734
f_{n4} StDev	0.7692	0.7672
f_{n5} Mean	344.2524	341.3335
f_{n5} StDev	0.6542	0.6590

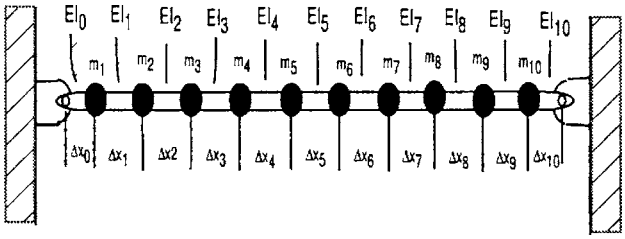

Fig. 11 Lumped model for a pinned-pinned beam

$$T_i = T_{F,i}T_{S,i} = \begin{bmatrix} 1+\omega^2 m_i(\Delta x_i)^3/6EI_i & \Delta x_i & (\Delta x_i)^2/2EI_i & -(\Delta x_i)^3/6EI_i \\ \omega^2 m_i(\Delta x_i)^2/2EI_i & 1 & \Delta x_i/EI_i & -(\Delta x_i)^2/EI_i \\ \omega^2 m_i \Delta x_i & 0 & 1 & -\Delta x_i \\ -\omega^2 m_i & 0 & 0 & 1 \end{bmatrix}. \tag{34}$$

Now the overall transfer matrix for the whole beam can be written by multiplying all of the individual transfer matrices together with the first field matrix

$$T = T_n T_{n-1} \cdots T_2 T_1 T_{F,0}. \tag{35}$$

The overall transfer matrix is a 4×4 matrix whose terms are functions of the eigenvalues, expressed in generic terms as

$$T = \begin{bmatrix} T_{1,1}(\omega^2) & T_{1,2}(\omega^2) & T_{1,3}(\omega^2) & T_{1,4}(\omega^2) \\ T_{2,1}(\omega^2) & T_{2,2}(\omega^2) & T_{2,3}(\omega^2) & T_{2,4}(\omega^2) \\ T_{3,1}(\omega^2) & T_{3,2}(\omega^2) & T_{3,3}(\omega^2) & T_{3,4}(\omega^2) \\ T_{4,1}(\omega^2) & T_{4,2}(\omega^2) & T_{4,3}(\omega^2) & T_{4,4}(\omega^2) \end{bmatrix}. \tag{36}$$

The relationship between the two pinned ends ($i=0$ and $i=11$) can now be expressed as

$$\begin{bmatrix} Y \\ \Psi \\ M \\ Q \end{bmatrix}_{n+1} = T \begin{bmatrix} Y \\ \Psi \\ M \\ Q \end{bmatrix}_0. \tag{37}$$

For the pinned-pinned case the deflection and bending moments are zero at the ends giving end conditions of

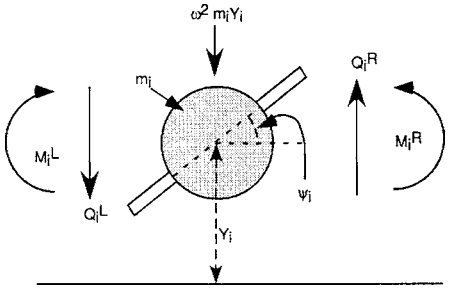

Fig. 12 Free-body diagram for station I

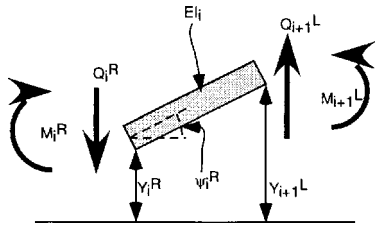

Fig. 13 Free-body diagram for station I

$$Y_0 = 0, \quad M_0 = 0, \quad Y_{n+1} = 0, \quad M_{n+1} = 0. \tag{38}$$

Substituting the values of Eq. (38) and the generic terms of Eq. (36) into Eq. (37) gives

$$0 = T_{1,2}(\omega^2)\Psi_0 + T_{1,4}(\omega^2)Q_0, \tag{39}$$

$$\Psi_{n+1} = T_{2,2}(\omega^2)\Psi_0 + T_{2,4}(\omega^2)Q_0, \tag{40}$$

$$0 = T_{3,2}(\omega^2)\Psi_0 + T_{3,4}(\omega^2)Q_0, \tag{41}$$

$$Q_{n+1} = T_{4,2}(\omega^2)\Psi_0 + T_{4,4}(\omega^2)Q_0. \tag{42}$$

The system of equations from Eqs. (39)–(41) have a nontrivial solution if

$$\det\begin{bmatrix} T_{1,2}(\omega^2) & T_{1,4}(\omega^2) \\ T_{3,2}(\omega^2) & T_{3,4}(\omega^2) \end{bmatrix} = T_{1,2}(\omega^2)T_{3,4}(\omega^2) - T_{1,4}(\omega^2)T_{3,2}(\omega^2) = 0. \tag{43}$$

Finding the roots of Eq. (43) gives the eigenvalues whose square roots are the natural frequencies or natural frequencies. In order to determine the roots, we have to generate sets of the lumped parameters m, EI, and a step size (Δx), then substitute that data into the equations above and find the roots of the frequency equation (43). The process of developing the variable parameters is described in the next section.

Parameter Variation and Crack Modeling. The reason for using Myklestad's method was to find solutions to Euler-Bernouilli beams with variation in the material properties and geometry. This section will consider how the variation due to manufacturing tolerance and cracks can be modeled and included in the Myklestad's formulation.

Again, we will use a ±1% tolerance on geometric variation. Also, the tolerance is considered equal to three times the standard deviation of a normally distributed parameter. Using the same beam as above, we consider a beam with a square cross section but the base and height may differ at any point on the beam's length. To generate these differences a random number generator was used with the base dimension as the average and a variance based on the 1% tolerance.

The base and hight were generated separately for a number of desired subdivisions of the length and then substituted into the formulas for I and A. When I is multiplied by the modulus of elasticity it produces the stiffness field parameter EI for that field. The value for A is multiplied by density and step size to give the value of the local lumped mass (m_i). Also, as used for the finite difference formulation, the influence of the crack was modeled using the same local stiffness degradation method as was used in the finite difference section.

Results. A program was developed in MATLAB to solve the same beam as presented in Table 1 in the finite difference section. Ten thousand Monte Carlo simulations were run for the uncracked beam with a randomly varying geometry. In a final detailed simulation, more than 10,000 runs would be used to create more accurate models. In this article we are only comparing the two methods so 10,000 samples is deemed sufficient. The first five natural frequencies were solved for each iteration. The histograms for the uncracked beam are shown in Figs. 14–18.

The program was next modified to take into account the influence of a crack at the midpoint with a depth of 10 mm using the local stiffness degradation model presented above. Histograms for the first five natural frequencies are presented in Figs. 19–23.

Table 3 shows values for the mean and the standard deviation of the first five natural frequencies for the damaged and undamaged beams. The mean decreased as expected when the beam is cracked for all natural frequencies. This result is consistent with both the experimental and theoretical literature on damaged and cracked beams. The standard deviation increased for the odd natural frequencies but decreased for the even ones. Again, the addition of

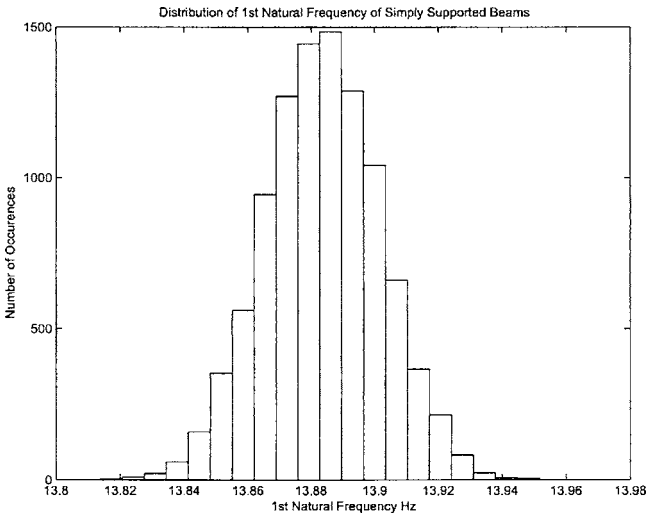

Fig. 14 Histogram for the first natural frequency of the uncracked beam (Myklestad's method)

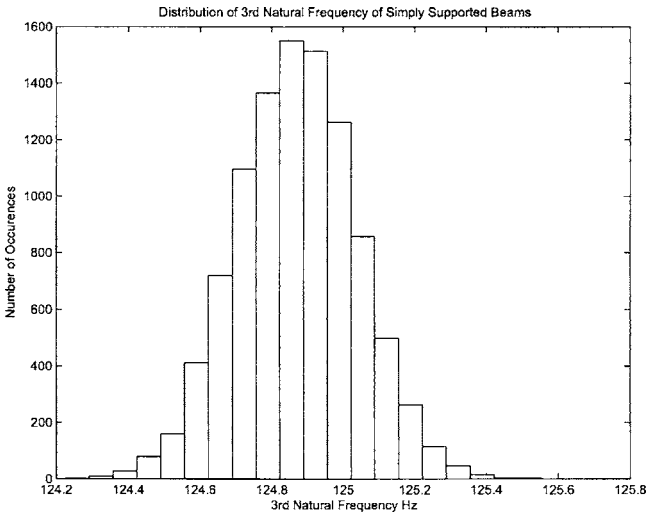

Fig. 16 Histogram for the third natural frequency of the uncracked beam (Myklestad's method)

manufacturing variations on the beam had little impact on the changes in natural frequency as compared to a beam of ideal geometry. Also, the standard deviations are largely the same for uncracked and cracked beams.

Discussion: Comparison of Modeling Approaches. To perform Monte Carlo simulations of a damaged turbine blade with the inclusion of variations in the model requires methods that run quickly and provide quantitative results consistent with the experimental and theoretical literature. Here the finite difference approach and Myklestad's method are compared with respect to their future applicability to realistic turbine blades.

Comparing the modeling approaches, both give largely the same results for the vibrational behavior of the beam. It does appear that the finite difference method introduces some numerical error with respect to the appropriate trends in natural frequency behavior. Myklestad's method can run much faster than the finite difference technique (more than 800 times faster). This is because the finite difference approach has to calculate the behavior of the beam for all points in space and a large enough sample length in time to recover the natural frequencies. Myklestad's method only requires solving the frequency equation for the number of natural frequencies desired.

Another advantage of Myklestad's method is its flexibility. The nominal properties of the beam analyzed in this paper were intentionally selected to have an unrealistically low modulus of elasticity. Common structural materials have modulus measured in GPa. To analyze beams with such high nominal modulus would require extremely small time step sizes to meet the stability criterion and the sampling frequency requirements. This would increase the already large computational time and memory requirements to prohibitive levels for the common personal computer.

The finite difference approach has the disadvantage that it does not directly supply frequency information. An FFT is used to extract the frequency information from the complete response. The frequency resolution of the recovered frequencies is dependent on the length of time the FFT samples. The larger the amount of time simulated, the better (i.e., smaller) the resolution. However, increasing the amount of data generated increases the demand on computer resources. Another problem with the recovery of frequency information by FFT is the leakage phenomena. Because the dimensions of the beam are randomly generated it is impossible to match the sampling period (i.e., record length) to the natural frequencies of the beam. This mismatch causes false natu-

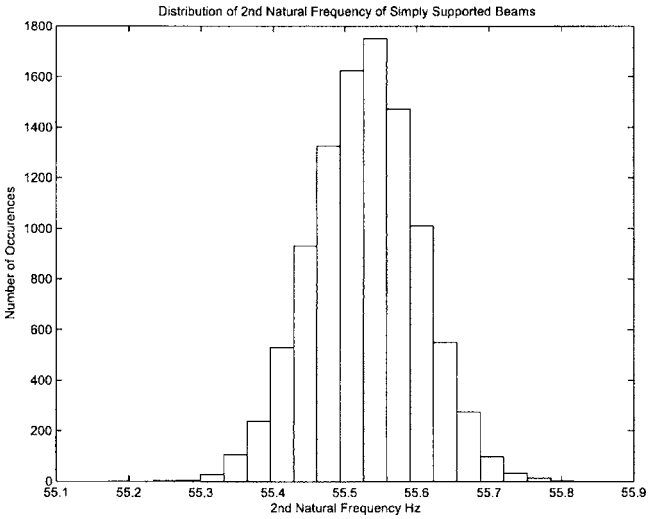

Fig. 15 Histogram for the second natural frequency of the uncracked beam (Myklestad's method)

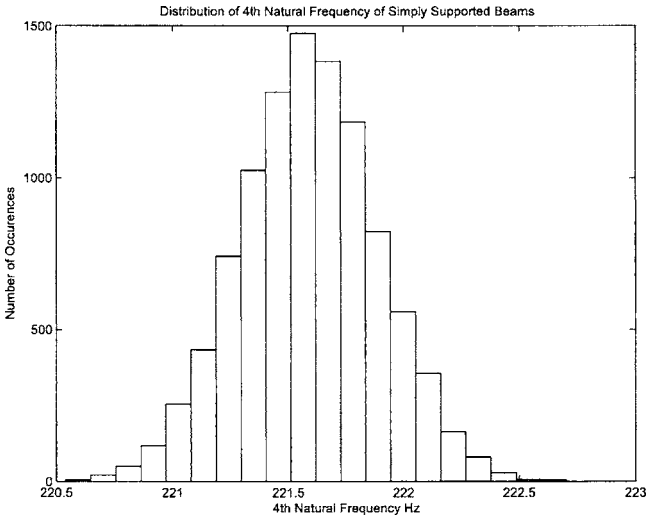

Fig. 17 Histogram for the fourth natural frequency of the uncracked beam (Myklestad's method)

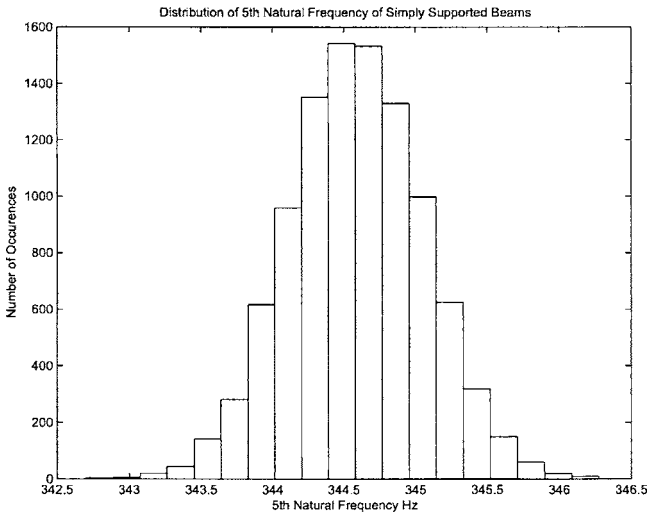

Fig. 18 Histogram for the fifth natural frequency of the uncracked beam (Myklestad's method)

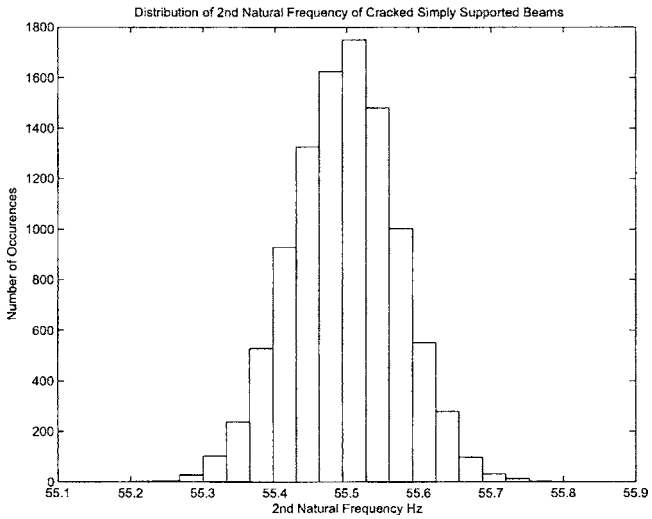

Fig. 20 Histogram for the second natural frequency of the cracked beam (Myklestad's method)

ral frequencies to be recorded near true natural frequencies. The false natural frequencies must be filtered out before meaningful interpretation of the data can be conducted. Myklestad's method has none of these problems as the natural frequencies are directly solved for.

Myklestad's method is superior to the finite difference method for the purposes of analyzing realistic structures with limited computing resources. This makes it the method of choice for simulating damaged structures. From both of these methods, we can conclude that geometric variation due to manufacturing tolerances alone is not likely to mask our ability to detect the presence of a crack that penetrates to 10% or more of the beam's depth by measuring the natural frequencies. The decrease in the natural frequencies in the damaged beams exceeds the standard deviation of the undamaged beams. Additional work to confirm this hypothesis will be discussed in the next section.

Summary and Future Work

In this article, the impact of manufacturing variations on the vibrational behavior of healthy and damaged pinned-pinned beams was explored. These modeling methods are being developed toward a long term goal of generating a complete understanding of realistic turbine blade behavior with respect to health monitoring. Specifically, we are interested in determining the way in which geometric and material variations interact with the vibrational behavior of the turbine blade and obfuscate fault detection.

Two solution methodologies are employed. The first uses a finite difference method to produce a complete solution to an undamaged and damaged beam. Fast Fourier transforms are used to extract frequency information from the complete response. The second develops a lumped beam model and uses transfer matrices to construct a frequency equation that can be solved to find the characteristics of the damaged and undamaged beam. Both solution methods gave similar results. The inclusion of manufacturing variation on a pinned-pinned beam of the nominal characteristics simulated here has minimal impact on changes in natural frequencies as compared to a significant crack.

Additional other methods in computational fracture mechanics still need to be explored, for example, the stochastic finite element method (SFEM). The SFEM has the advantage that it extends simply to structures of high geometric complexity. Also, developing efficient computational methods is facilitated by the wealth of existing numerical solution approaches. Also the SFEM integrates

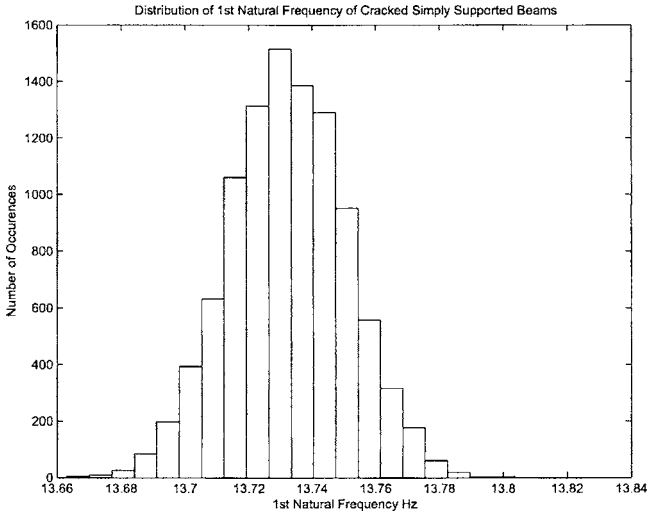

Fig. 19 Histogram for the first natural frequency of the cracked beam (Myklestad's method)

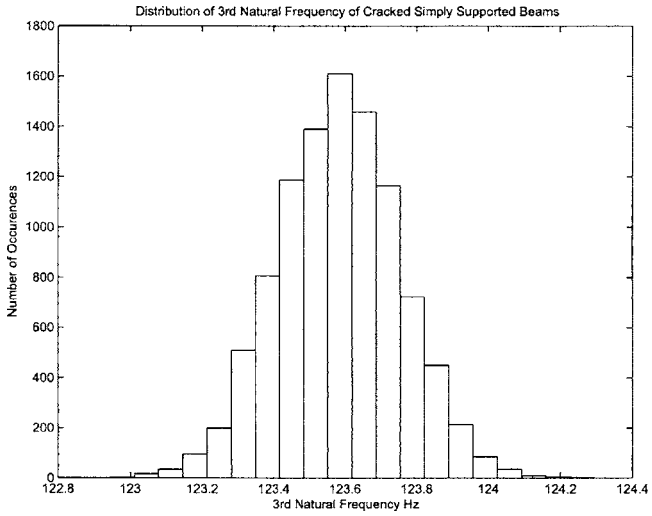

Fig. 21 Histogram for the third natural frequency of the cracked beam (Myklestad's method)

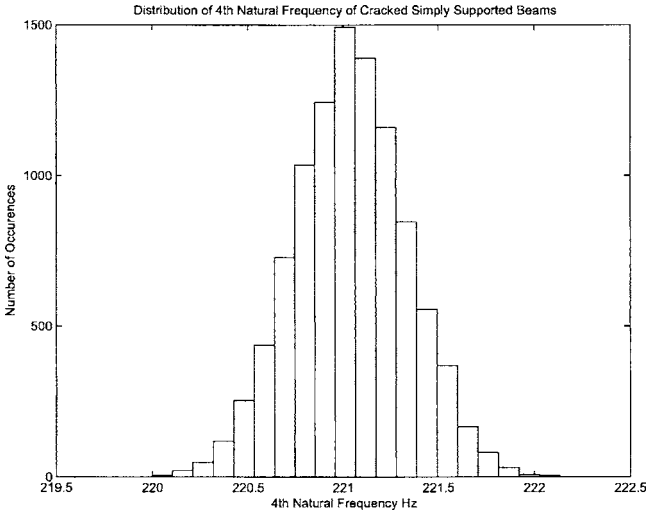

Fig. 22 Histogram for the fourth natural frequency of the cracked beam (Myklestad's method)

well with many of the crack models that are modeled using FEM techniques. One of the key advantages of the SFEM is that it does not require Monte Carlo simulation, thus it is computationally inexpensive compared to Monte Carlo based simulations. Also, multi-scale methods need to be explored.

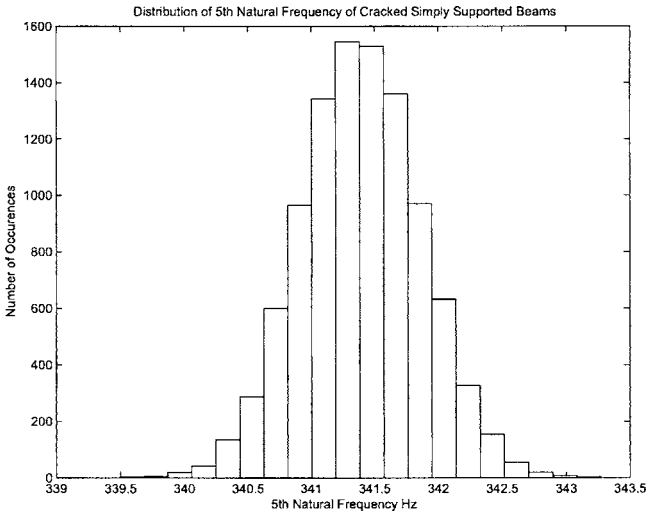

Fig. 23 Histogram for the fifth natural frequency of the cracked beam (Myklestad's method)

Table 3 The mean and standard deviation for the five natural frequencies (f_n)

	Undamaged	Cracked
f_{n1} Mean	13.8835	13.7324
f_{n1} StDev	0.0181	0.184
f_{n2} Mean	55.5284	55.49
f_{n2} StDev	0.0739	0.0738
f_{n3} Mean	124.8702	123.5825
f_{n3} StDev	0.1672	0.1694
f_{n4} Mean	221.5910	221.0384
f_{n4} StDev	0.2995	0.2968
f_{n5} Mean	344.5878	341.3925
f_{n5} StDev	0.4688	0.4710

To more realistically simulate actual turbine blades, critical future work includes developing models that allow the inclusion of variations in material properties such as density and Young's modulus. Additionally, more accurate representations of realistic turbine blade geometry need to be simulated. The current work has been limited to prismatic beams. The interaction between damaged and the more complex geometries of turbine blades needs to be explored.

Once the theoretical work has been developed to allow realistic turbine blades to be simulated, experimental validation is required. Experimental validation will begin with benchmarking theoretical models against simple prismatic structures and turbine blade geometries. Additionally, different crack models need to be explored and compared to determine which give the most accurate results when the models include damage.

Acknowledgment

This research was supported by NASA's Intelligent Data Understanding project of the Intelligent Systems/CICT program, and funded through a cooperative agreement NCC 2-5490.

Nomenclature

a = crack depth
b = width of beam
c = local compliance of the damaged beam
d = damage parameter
$f(x,t)$ = external force applied to a beam
h = height of a beam's cross section
i = integer multiplier for axial location
j = integer multiplier for time
n = denotes the left end of the beam
t = time
w = lateral deflection of the beam as a function of space and time
$w_0(x)$ = initial deflection of the beam
x = horizontal coordinate
A = cross-sectional area of the beam cross section
A_d = area of a beam's cross section affected by damage
A_t = total area of a beam's cross section
E = Young's modulus of elasticity
E_o = undamaged or ideal Young's modulus of elasticity
EI = flexural stiffness of a beam
I = area moment of inertia
L = length of beam
β = nondimensional horizontal crack location
λ = ratio of crack depth to beam height
ν = Poisson's ratio
ρ = density
I = area moment of inertia
ρA = mass per unit length of a beam
Δt = uniform time step size
Δx = uniform axial step size
Y = vertical position of a beam segment
Ψ = angle of a deflected beam
M = bending moment
Q = shearing force
T = transfer matrix
ω^2 = eigenvalue
m = mass of a beam segment

References

[1] Oza, N., Tumer, I., Tumer, K., and Huff, E., 2003, "Classification of Aircraft Maneuvers for Fault Detection," *Proceedings of the Multiple Classifier Systems (MCS) Workshop*.
[2] Tumer, I., and Huff, E., 2002, "On the Effects of Production and Maintenance

Variations on Machinery Performance," J. Qual. Maint. Eng., **8**(3), pp. 226–238.
[3] Tumer, I., and Huff, E., 2002, "Analysis of Triaxial Vibration Data for Health Monitoring of Helicopter Gearboxes," ASME J. Vibr. Acoust., **125**(1), pp. 120–128.
[4] Huff, E., Tumer, I., Barszcz, E., Dzwonczyk, M., and McNames, J., 2002, "Analysis of Maneuvering Effects on Transmission Vibrations in an AH-1 Cobra Helicopter," J. Am. Helicopter Soc., **47**(1), pp. 42–49.
[5] McAdams, D., and Tumer, I., 2002, "Towards Failure Modeling in Complex Dynamic Systems: Impact of Design and Manufacturing Variations," ASME Design for Manufacturing Conference, Vol. DETC2002/DFM-34161.
[6] Hampton, R., and Nelson, H. G., 1986, "Failure Analysis of a Large Wind Compressor Blade," ASTM Spec. Tech. Publ., **918**, pp. 153–180.
[7] Ganesan, R., Ramu, S., and Sankar, T., 1993, "Stochastic Finite Element Analysis for High Speed Rotors," ASME J. Vibr. Acoust., **115**(3), pp. 59–64.
[8] McAdams, D. A., Comella, D., and Tumer, I. Y., 2003, "Developing Variational Vibration Models of Damaged Beams: Toward Intelligent Failure Detection," *Proceedings ASME International Mechanical Engineering Congress and Expo*, No. IMECE 2003-42540, ASME, New York.
[9] A. Pouliezos, G. S., and Lefas, C., 1989, "Fault Detection Using Parameter Estimation," Qual. Reliab. Eng. Int, **5**, pp. 283–290.
[10] Pusey, H. C., and Roemer, M. J., 1999, "An Assessment of Turbomachinery Condition Monitoring and Failure Prognosis Technology," Shock Vib. Dig., **31**(5), pp. 365–371.
[11] Banks, J., Reichard, K., and Brought, M., 2002, "Development of the Asset Health Management System for the Marine Corps Advanced Amphibious Assult Vehicle," Proc. Society Mach. Failure Prevention Technol., **56**(2), pp. 277–286.
[12] Roemer, M. J., Kacprzynski, G. J., and Hess, A. J., 2002, "Health Management System Design: Development, Simulation and Cost/Benefit Optimization," *Proceedings of IEEE Conference*, Vol. 6, March, IEEE, Piscataway, NJ, pp. 3065–3072.
[13] Roemer, M. J., Kacprzynski, G. J., and Hess, A. J., 2001, "Extending FMECA-Health Management Design Optimization for Aerospace Applications," *Proceedings of IEEE Conference*, Vol. 6, March, IEEE, Piscataway, NJ, pp. 3105–3065.
[14] Ding, S. X., Frank, P. M., Ding, E., and Jeinsch, T., 2000, "Fault Detection System Design Base on a New Trade-off Strategy," *Proceedings of the 39th IEEE Conference on Decision and Control*, Vol. 4, December, IEEE, Piscataway, NJ, pp. 4144–4149.
[15] Phillips, J. N., Levine, P., and Tustain, S., 2000, "Performance Monitoring of Gas Turbine," *CO-MADE'2000 Proceedings of the 13th International Congress on Condition Monitoring and Diagnostic Engineering*, Houston, December 3–8, pp. 527–536.
[16] Lifson, A., Quentin, G., Smalley, A., and Knauf, C., 1989, "Assessment of Gas Turbine Vibration Monitoring," ASME J. Eng. Gas Turbines Power, **111**(2), pp. 257–263.
[17] Meher-Homji, C. B., and Gabriles, G., 1998, "Gas Turbine Blade Failure—Causes, Avoidance, and Troubleshooting," *Turbomachinery Symposium 1998: Proceedings of the Twenty-Seventh Turbomachinery Symposium*, Houston, September 20–24, pp. 129–179.
[18] Kumar, A., Kumar, V., and Hazara, U., 1996, "Effective Failure Analysis of Gas Turbine—A Need of Improved Monitoring System (A Case Study)," *COMADE'96 Proceedings of the Diagnostic Engineering Management Conference*, Sheffield, UK, June, pp. 905–915.
[19] Al-Bedoor, B. O., 2002, "Blade Vibration Measurement in Turbo-Machiner: Current Status," Shock Vib. Dig., **34**(6), pp. 455–461.
[20] Doebling, S. W., Farrar, C. R., and Prime, M. B., 1998, "A Summary Review of Vibration-Based Damage Identification Methods," Shock Vib. Dig., **30**(2), pp. 91–105.
[21] Friswell, M. I., and Penny, J. E. T., 2002, "Crack Modeling for Structural Health Monitoring," Struct. Health Monit., **1**(2), pp. 139–148.
[22] Hu, J., and Liang, Y., 1993, "An Integrated Approach to Detection of Cracks Using Vibration Characteristics," J. Franklin Inst., **330**(5), pp. 841–853.
[23] Gudmundon, P., 1982, "Eigenfrequency Changes of Structures Due to Cracks, Notches or Other Geometrical Changes," J. Mech. Phys. Solids, **30**(5), pp. 339–353.
[24] Wetland, D., 1972, "Aenderung der Biegeeigenfrequenzen einer idealisierten Schaufel durch Risse," Ph.D. thesis, University of Karlsruhe.
[25] Chondros, T. G., Dimarogonas, A. D., and Yao, J., 1998, "A Continuous Cracked Beam Vibration Theory," J. Sound Vib., **215**(1), pp. 17–34.
[26] Chondros, T. G., and Dimarogonas, A. D., 1998, "Vibration of a Cracked Cantilever Beam," Trans. ASME, J. Vib. Acoust., **120**(2), pp. 742–746.
[27] Chondros, T. G., Dimarogonas, A. D., and Yao, J., 1998, "Longitudinal Vibration of a Continuous Cracked Bar," Eng. Fract. Mech., **61**(5–6), pp. 593–606.
[28] Chondros, T. G., 2001, "The Continuous Crack Flexibility Model for Crack Identification," Fatigue Fract. Eng. Mater. Struct., **24**(10), pp. 643–650.
[29] Mengcheng, C., and Renji, T., 1997, "An Approximate Method of Response Analysis of Vibrations for Cracked Beams," Appl. Math. Mech., **18**(3), pp. 221–228.
[30] Yokoyama, T., and Chen, M.-C., 1998, "Vibration Analysis of Edge-Cracked Beams Using a Line-Spring Model," Eng. Fract. Mech., **59**(3), pp. 403–409.
[31] Chaudhari, T. D., and Maiti, S. K., 1999, "Modelling of Transverse Vibration of Beam of Linearly Variable Depth With Edge Crack," Eng. Fract. Mech., **63**(4), pp. 425–445.
[32] Zheng, D. Y., and Fan, S. C., 2001, "Natural Frequencies of a Non-Uniform Beam With Multiple Cracks Via Modified Fourier Series," J. Sound Vib., **242**(5), pp. 701–717.
[33] Ju, F. D., and Mimovich, M. E., 1988, "Experimental Diagnosis of Fracture Damage in Structures by the Modal Frequency Method," Trans. ASME, J. Vib. Acoust., **110**(4), pp. 456–463.
[34] Kuang, J. H., and Huang, B. W., 1999, "The Effect of Blade Crack on Mode Localization in Rotating Bladed Disks," J. Sound Vib., **227**(1), pp. 85–103.
[35] Chondross, T. G., Dimarogonas, A. D., and Yao, J., 2001, "Vibration of a Beam With a Breathing Crack," J. Sound Vib., **239**(1), pp. 57–67.
[36] Bovsunovsky, A. P., and Matveev, V. V., 2000, "Analytical Approach to the Determination of Dynamic Characteristics of a Beam With a Closing Crack," J. Sound Vib., **235**(3), pp. 415–434.
[37] Surace, N. P. C., and Ruotolo, R., 2000, "Evaluation of the Non-Linear Dynamic Response to Harmonic Exitation of a Beam With Several Breathing Cracks," J. Sound Vib., **235**(5), pp. 749–762.
[38] Kachanov, L., 1986, *Introduction to Continuum Damage Mechanics*, Martinus Nijhoff Publishers, Dordrecht, The Netherlands.
[39] Lapidus, L., and Pinder, G., 1982, *Numerical Solution of Partial Differential Equations in Science and Engineering*, John Wiley and Sons, New York.
[40] Bilbao, S., 2002, "Wave and Scattering Methods for the Numerical Integration of Partial Differential Equations," Ph.D. thesis, Stanford University.
[41] Walsh, R., 1999, *McGraw-Hill Machining and Metal Working Handbook*, McGraw-Hill, New York.
[42] Bowker, A. H., and Lieberman, G. J., 1959, *Engineering Statistics*, Prentice-Hall, Englewood Cliffs, NJ.
[43] Dipasquale, E., Ju, J., Askar, A., and Cakmak, A., 1990, "Relation Between Global Damage Indices and Local Stiffness Degradation," J. Struct. Eng., **116**(5) [May.], pp. 1440–1456.
[44] Myklestad, N. O., 1944, "A New Method of Calculating Natural Modes of Uncoupled Bending Vibration of Airplane Wings and Other Types of Beams," J. Aeronaut. Sci., **12**, pp. 153–162.
[45] Thomson, W. T., 1972, *Theory of Vibrations with Applications*, Prentice-Hall, Englewood Cliffs, NJ.
[46] Pestel, E. C., and Leckie, F. A., 1963, *Matrix Methods in Elastomechanics*, McGraw-Hill, New York.
[47] Meirovitch, L., 2001, *Fundamentals of Vibrations*, McGraw Hill, New York.
[48] Myklestad, N., 1944, *Vibration Analysis*, McGraw-Hill, New York.

Modeling Heterogeneous Media With Microstructures of Different Scales

C. T. Sun
e-mail: sun@ecn.purdue.edu

G. L. Huang

School of Aeronautics and Astronautics,
Purdue University,
West Lafayette, IN 47907

The objective of this paper is to extend the framework of the continuum theory so that it can capture the properties that are embedded in the microstructure or nanostructure and still keep its simplicity and efficiency. The model thus developed is capable of accounting for local deformation of microstructures in solids especially their micro- (local) inertia effect. The essence underlying this approach is the introduction of a set of bridging functions that relate the local deformation of microstructures to the macrokinematic variables. Once the solution of the macroscopically homogeneous continuum is obtained, the solutions in the microstructures are obtained through the use of these bridging functions. Propagation of waves of different wavelengths is considered and the dispersion curve is used to evaluate the accuracy of the model. The model is also employed to study wave reflection and transmission at the boundary of two media with microstructures of very different scales. [DOI: 10.1115/1.2188536]

1 Introduction

The design and application of micro-heterogeneous materials and nanostructured materials require efficient and accurate modeling and analysis tools. For nanostructured materials, the use of molecular dynamics (MD) may be a potential solution in the long run. However, it is well known that the MD approach is beset with prohibitive computing time and an astronomical amount of data generated in the calculation. As a result, its usefulness will be limited to describing behavior at the atomic scale. For bulk media that contain heterogeneous microstructures or nanostructured materials such as many nanocomposites, the basic framework of continuum mechanics is highly desirable.

The conventional approach in treating heterogeneous solids has been to replace the original solid with an equivalent continuum in which the heterogeneous microstructure is no longer present. Such an approach (often referred to as effective modulus theory) yields great simplifications and has been widely adopted for analyses of heterogeneous materials such as many forms of composite materials. However, classical continuum models become inadequate in describing the response of heterogeneous solids when the characteristic length (or wavelength) of deformation becomes comparable to or smaller than the dimensions of heterogeneity. The main reason for this deficiency of the classical continuum model can be attributed to its inability to account for the local motion of the microstructure.

One common way to solve the above-mentioned problem is to employ additional kinematic variables to describe the nonhomogeneous local deformation in the microstructure of the solid. This approach leads to Cosserat continuum models [1] or micropolar models [2–4] or the like [5,6]. Some authors have even attempted to use the Cosserat type of model (micromorphic theory) to bridge continuum theory and molecular dynamics at the atomic scale [7]. Common to all the above models is that, in addition to the usual translational displacement vector to describe the average displacement, additional deformation kinematic variables are introduced to describe the nonhomogeneous deformation. It is evident that additional kinematic variables would increase the complexity of the resulting model.

Another approach is the homogenization by Kunin's integral transform [8], which involves the introduction of a nonlocal constitutive law which allows stresses to depend on strains at distant points of the continuum, albeit with weight decreasing with distance from the point of interest. This homogenization was achieved by trigonometric interpolation of the discrete field and the particle centers are assumed to be situated at the nodes of a regular grid. The kernels of the nonlocal relationship are expressed through Kunin's analog of the Dirac-delta function. Recently, Pasternak and Muhlhaus [9] compared the Cosserat continuum theory with Kunin's integral homogenization theory for homogeneous discrete systems of translational springs with an additional rotational degree of freedom. According to Ref. [9], Kunin's integral homogenization theory yields the exact solution, but does not offer any real simplification in the solution of the model equations as compared to the original discrete system. Nesterenko [10] solved wave propagation problems of compressed chains of particles for linear and nonlinear cases using Taylor expansions of displacements. Results of the resulting higher space gradient continuum description show good agreement with the corresponding discrete systems and experiments on the length scales of about five particle sizes.

Recently, Wang and Sun [11] have introduced a continuum model with microinertia that retains the simplicity of the classical continuum mechanics while capturing the characteristics of the microstructure. In this formulation, the microstructural effect is included in an effective body force term that appears in the equations of motion and the boundary conditions. The effective body force term is a function of the first and second time derivatives of the macrostrain and is responsible for the dispersive behavior of harmonic waves. By combining this effective body force term with the macrostress, this continuum model has the form of the classical elasticity theory.

The emerging nanotechnology has given rise to great interest in modeling material behavior at nanoscale. One of the unavoidable issues facing researchers in this new field is dealing with multiple scales, or the so-called "hand-shaking" techniques. Methodologies for linking a continuum to an atomistic domain can be found in the literature as early as 1971 [12]. Finite element methods were later employed by Mullins and Dokainish [13] using a numerically decoupled domain approach with spatially overlapping ato-

Contributed by the Applied Mechanics Division of ASME for publication in the JOURNAL OF APPLIED MECHANICS. Manuscript received July 2, 2005; final manuscript received January 24, 2006. Review conducted by H. D. Espinosa. Discussion on the paper should be addressed to the Editor, Prof. Robert M. McMeeking, Journal of Applied Mechanics, Department of Mechanical and Environmental Engineering, University of California—Santa Barbara, Santa Barbara, CA 93106-5070, and will be accepted until four months after final publication of the paper itself in the ASME JOURNAL OF APPLIED MECHANICS.

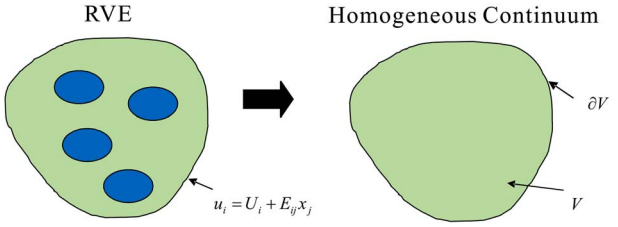

Fig. 1 Representation of a representative volume element of a heterogeneous solid by a homogeneous solid

mistic and continuum regions. Among these early analytic and computational studies, frequent issues regarding the treatment of the interface arose which were primarily handled through creative use of kinematic constraints. More recently Tadmor et al. [14] developed a finite element (FE) based formulation, the so-called quasi-continuum method. Similar efforts were made through the so-called handshaking or coupling-of-length-scales (CLS) method by Broughton et al. [15] by increasing the atomic resolution to account for electron degrees of freedom via the tight-binding (TB) method. The dynamic problem was studied with a generalized scaling approach in coarse-grained molecular dynamics by Rudd and Broughton [16] to better handle the propagation of waves through the atomistic FE interface and the FE far field. The method is based on eliminating the high-frequency components moving from fine mesh to coarse mesh. Along a similar line, E and Huang [17] have developed nonreflecting interfaces by constructing time integration formulas that eliminate spurious reflections. A different approach was proposed by Wagner and Liu [18] who have developed a multiscale method in which the molecular displacements are decomposed into fine and coarse scales throughout the domain. Another bridging domain method for coupling continuum models with molecular models has recently been proposed by Xiao and Belytschko [19]. However, most of these methods are numerical in nature and the "hand shaking" between materials of different scales is actually performed at the nano scale.

In the present paper, we employ a continuum model developed based on the micro-inertia modeling technique to describe the mechanical behavior of discrete lattice systems. For simple illustrations of this approach, we consider only one-dimensional systems for which the exact solution can be worked out and used to evaluate the present model. The effectiveness of interscale connection (or hand shaking) between the lattice system and a homogeneous medium is examined. Different from other numerical approaches, the connection between the lattice and the homogeneous medium is at the continuum level. Following a similar approach, we investigate the hand-shaking between a thinly layered medium and a homogeneous solid simulating composites containing regions of microstructures of very different scales.

2 Continuum Model With Microinertia

The formulation of the microinertia model can be illustrated with the representative volume element (RVE) for a heterogeneous solid as shown in Fig. 1. Using the classical micromechanics approach, the macro-strain and -stress are defined, respectively, as the volume averages of the strain and stress fields in the RVE, i.e.,

$$E_{ij} = \frac{1}{|\Omega|}\int_{\Omega} \varepsilon_{ij} d\Omega = \langle \varepsilon_{ij} \rangle \quad i,j = 1,2,3 \tag{1}$$

$$\Sigma_{ij} = \frac{1}{|\Omega|}\int_{\Omega} \sigma_{ij} d\Omega = \langle \sigma_{ij} \rangle \quad i,j = 1,2,3 \tag{2}$$

where σ_{ij} and ε_{ij} denote the actual local stress and strain fields in the original heterogeneous medium, respectively, $\langle \cdot \rangle$ denotes the volume average, and $|\Omega|$ is the volume of the RVE. Note that the macrodisplacement vector U_i is defined from the relation $E_{ij} = \frac{1}{2}(\partial U_i/\partial X_j + \partial U_j/\partial X_i)$.

Underlying the development of the microinertia continuum theory is the establishment of the relation between the local displacement field u_i and the macrostrain E_{ij}. In a RVE, the relation can be expressed in a general form as

$$u_i = U_i(X_p) + \hat{u}_{ijk}(x_p)E_{jk}(X_p) \quad \text{in an RVE} \tag{3}$$

in which x_p and X_p are axes of the local and global coordinate systems, respectively, and a set of bridging functions $\hat{u}_{ijk}(x_p)$ describes the local displacement field, which is required to match the macrodisplacement at the boundary ∂V of the region occupied by the RVE, i.e.,

$$u_i = U_i(X_p) + E_{ij}x_j \quad \text{at } \partial V \tag{4}$$

The above matching condition is necessary in order to satisfy the energy equivalence between the RVE and the representative homogeneous continuum [11]. This boundary conditions on the RVE (see Fig. 1) are used to find the candidate bridging functions $\hat{u}_{ijk}(x_p)$ for the approximate local displacement field. As a result of this relation given by Eq. (4), the local strains and stresses can be estimated from the global solution of the homogenized medium once bridging functions $\hat{u}_{ijk}(x_p)$ are established. Using Eq. (3), the local strains can be calculated and the local stresses can be obtained from the stress-strain relations. Subsequently, the average strain energy density of the RVE is obtained as

$$W = \left\langle \tfrac{1}{2}\sigma_{ij}\varepsilon_{ij} \right\rangle = \tfrac{1}{2}\Sigma_{ij}E_{ij} + W' \tag{5}$$

where

$$W' = -\left\langle \tfrac{1}{2}\rho\ddot{u}_i(u_i - E_{ij}x_j) \right\rangle = W'(E,\ddot{E}_{ij})$$

In a similar manner, the kinetic energy density of the RVE

$$T = \left\langle \tfrac{1}{2}\rho\dot{u}_i\dot{u}_i \right\rangle = \tfrac{1}{2}\langle\rho\rangle\dot{U}_i\dot{U}_i + T' \tag{6}$$

in which

$$T' = \langle \rho\dot{u}_i'\dot{E}_{ij}x_j \rangle + \left\langle \tfrac{1}{2}\rho\dot{u}_i'\dot{u}_i' \right\rangle = T'(\dot{E}_{ij})$$

$$u_i' = u_i - (U_i + E_{ij}x_j) = (\hat{u}_{ijk} - x_j\delta_{ik})E_{kj}(X_p)$$

The Hamilton's principle

$$\delta\int_{V,t}(W - T)dVdt = \int_{V,t} T_i\delta U_i dSdt \tag{7}$$

yields the macroequations of motion,

$$\frac{\partial\Sigma_{ij}}{\partial X_j} + F_i = \langle\rho\rangle\ddot{U}_i \tag{8}$$

where F_i is an effective body force that contains the effect of microinertia and is given formally as

$$F_i = \frac{\partial H_{ij}}{\partial X_j} \tag{9}$$

In Eq. (9), H_{ij} are functions of E_{ij} and time derivatives of E_{ij} and can be obtained from

$$H_{ij} = \frac{\partial U'}{\partial E_{ij}} + \frac{\partial^2}{\partial t^2}\left(\frac{\partial U'}{\partial \ddot{E}_{ij}}\right) + \frac{\partial}{\partial t}\left(\frac{\partial T'}{\partial \dot{E}_{ij}}\right) \tag{10}$$

The natural boundary conditions are given in the form

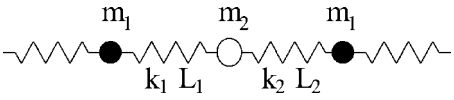

Fig. 2 The lattice system

$$(\Sigma_{ij} + H_{ij})n_j = T_i \quad \text{on } \partial V \tag{11}$$

Without considering the effective body force term that contains microinertia, this model appears to be the same as the classical continuum model except that the stresses and strains must be properly interpreted as the macromechanical quantities. The effective body force is the result of the local motion that deviates from the global average motion in the RVE and usually can be explicitly expressed in a rather simple form.

It is of interest to note that, if a new macrostress defined as $\Sigma^*_{ij}=\Sigma_{ij}+H_{ij}$ is introduced, the equations of motion as well as the traction boundary condition can be written exactly as the classical elasticity model. However, such a definition of stress is quite different from the conventional definition of Cauchy stress in continuum mechanics as it contains time derivatives of displacement. This type of definition is analogous to the so-called virial stress in molecular dynamics [20–23], which also includes particle velocity terms.

3 Microinertia Model for Lattice Systems

In this section, we employ the procedure for developing the microinertia model as described in Sec. 2 to derive an equivalent continuum model for lattice systems. For clarity, we consider a one-dimensional lattice consisting of two alternating masses m_1 and m_2 as shown in Fig. 2. The pairwise interactions are represented by elastic springs with spring constants k_1 and k_2, respectively. The spacings between the adjacent periodic masses are L_1 and L_2 as shown in Fig. 2. This periodic chain of masses is viewed as a typical chain in a three-dimensional lattice system with a unit cross section.

Consider a unit cell of the lattice system as shown in Fig. 3 in which x denotes the local coordinate axis and X is the macrocoordinate axis. The total deformation energy and kinetic energy in the unit cell can be readily obtained in terms of the displacements of the two masses. Assume that the unit cell has a unit cross-sectional area. Then the deformation and kinetic energy densities are

$$W = \left(\frac{k_1}{2}(u_0-u_1)^2 + \frac{k_2}{2}(u_2-u_0)^2\right) \Big/ L, \tag{12}$$

and

$$T = \left(\frac{m_1}{2}(\dot{u}_1)^2 + \frac{m_2}{2}(\dot{u}_0)^2\right) \Big/ L \tag{13}$$

respectively. In Eqs. (12) and (13), $L=L_1+L_2$, u_0 is the displacement at mass 2, and u_1 and u_2 are the displacements at the left and right ends of the unit cell, respectively.

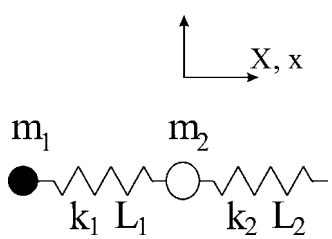

Fig. 3 Representative unit cell of the lattice system

To represent the unit cell as an equivalent homogeneous continuum element, we define the macrostrain E and macrostress Σ as the volume average of the local strains and stresses, respectively, i.e.,

$$E = \frac{L_1\varepsilon^{(1)} + L_2\varepsilon^{(2)}}{L_1+L_2}, \quad \sum = \frac{L_1\sigma^{(1)} + L_2\sigma^{(2)}}{L_1+L_2} \tag{14}$$

where $\varepsilon^{(1)}=(u_0-u_1)/L_1$, $\varepsilon^{(2)}=(u_2-u_0)/L_2$, $\sigma^{(1)}=k_1(u_0-u_1)$, and $\sigma^{(2)}=k_2(u_2-u_0)$. The macrodisplacement U of the continuum is defined from the relation $E=\partial U/\partial X$.

For the local displacement field in the unit cell, we assume the linear approximation form as

$$u_1 = u_0 + a_1 x, \quad u_2 = u_0 + b_1 x \tag{15}$$

Applying static force equilibrium at mass point m_2 within the unit cell and the boundary matching condition given by Eq. (4) at the two ends of the unit cell leads to

$$u_0 = \frac{k_2L_2 - k_1L_1}{k_1+k_2}E + U, \quad a_1L_1 = \frac{k_2L}{k_1+k_2}E, \quad b_1L_2 = \frac{k_1L}{k_1+k_2}E \tag{16}$$

Substituting Eq. (16) in (15) and then in Eqs. (12) and (13), we obtain the strain energy and kinetic energy densities, respectively, for the equivalent continuum:

$$W = \frac{L}{2}\frac{k_1k_2}{k_1+k_2}E^2 \tag{17}$$

and

$$T = \frac{m_1}{2}(\dot{U} - L_1\dot{E})^2 + \frac{m_2}{2}\left(\dot{U} + \frac{k_2L_2 - k_1L_1}{k_1+k_2}\dot{E}\right)^2 = \frac{1}{2}(m_1+m_2)(\dot{U})^2 + T' \tag{18}$$

where

$$T' = \frac{m_1}{2}(-2L_1\dot{U}\dot{E} + L_1^2\dot{E}^2) + \frac{m_2}{2}\left[2\frac{k_2L_2 - k_1L_1}{k_1+k_2}\dot{U}\dot{E} + \left(\frac{k_2L_2 - k_1L_1}{k_1+k_2}\dot{E}\right)^2\right] \tag{19}$$

is the term that contains the local inertia. The corresponding macrostress can be expressed as

$$\Sigma = \frac{\partial W}{\partial E} = kE \tag{20}$$

in which the elastic constant k is

$$k = \frac{Lk_1k_2}{k_1+k_2} \tag{21}$$

The equation of motion can be obtained using Hamilton's principle with the result

$$\frac{\partial \Sigma}{\partial X} + F = \rho_0\ddot{U} \tag{22}$$

where

$$\rho_0 \equiv \langle\rho\rangle = \frac{m_1+m_2}{L}, \quad F = \frac{1}{L}\left[\frac{\partial}{\partial t}\left(\frac{\partial T'}{\partial \dot{U}}\right) + \frac{\partial^2}{\partial t\partial X}\left(\frac{\partial T'}{\partial \dot{E}}\right)\right]$$

$$F = \frac{\partial H}{\partial X}, \quad H = H_0\frac{\partial \ddot{U}}{\partial X}$$

$$H_0 = \left[m_1 L_1^2 + m_2 \left(\frac{k_2 L_2 - k_1 L_1}{k_1 + k_2} \right)^2 \right] \Big/ L. \tag{23}$$

The corresponding traction boundary condition is

$$\sigma = \Sigma + H \tag{24}$$

where σ is the prescribed traction. It is interesting to note that in Eq. (24) the traction boundary condition included an inertia term.

4 Wave Propagation in Lattice Systems

We consider the harmonic wave propagation in the one-dimensional lattice system of infinite extent as shown in Fig. 2. For the jth unit cell the equations of motion are

$$m_1 \ddot{u}_1^j = k_1 (u_2^j - u_1^j) - k_2 (u_1^j - u_2^j) \tag{25}$$

$$m_1 \ddot{u}_2^j = k_2 (u_1^{j+1} - u_2^j) - k_1 (u_2^j - u_1^j) \tag{26}$$

where u_i^j is the displacement at mass m_i in the jth unit cell. The harmonic wave assumes the form

$$u_1^j = B_1 e^{iq(x_1 - c_p t)}, \quad u_2^j = B_2 e^{iq(x_1 + L_1 - c_p t)} \tag{27}$$

where q denotes the wave number, c_p is the phase velocity, and x_1 is the position of mass m_1. Substitution of Eq. (27) in Eqs. (25) and (26) yields two homogeneous equations for B_1 and B_2 as

$$\begin{bmatrix} m_1 c_p^2 q^2 - (k_1 + k_2) & k_1 e^{iqL} + k_2 \\ k_1 e^{-iqL} + k_2 & m_2 c_p^2 q^2 - (k_1 + k_2) \end{bmatrix} \begin{Bmatrix} B_1 \\ B_2 \end{Bmatrix} = \begin{Bmatrix} 0 \\ 0 \end{Bmatrix} \tag{28}$$

The dispersion equation is obtained by setting the determinant of the coefficient matrix in the above system of equations to zero. We have

$$\left(\frac{c_p}{c_0} \right)^2 = \frac{(m_1 + m_2)^2 (k_1 + k_2)^2}{2 k_1 k_2 m_1 m_2 q^2 L^2} \left(1 \pm \sqrt{1 - \frac{8 k_1 k_2 m_1 m_2 (1 - \cos qL)}{(m_1 + m_2)^2 (k_1 + k_2)^2}} \right) \tag{29}$$

where

$$c_0 = L \sqrt{\frac{k_1 k_2}{(k_1 + k_2)(m_1 + m_2)}} \tag{30}$$

is the limiting phase velocity at vanishing wave numbers ($q \to 0$).

The dispersion curve for harmonic waves in the equivalent continuum with microinertia can be obtained in a similar manner by assuming the wave form:

$$U = A e^{iq(X - c_p t)}$$

The result is

$$\left(\frac{c_P}{c_0} \right)^2 = \frac{m_1 + m_2}{(m_1 + m_2) + \left[m_1 L_1^2 + m_2 \left(\frac{k_2 L_2 - k_1 L_1}{k_1 + k_2} \right)^2 \right] q^2} \tag{31}$$

Figure 4 shows the comparison of the lowest dispersion curves obtained according to Eqs. (29) and (31), respectively, for $L_2/L_1 = 1$, $m_2/m_1 = 4$, and $k_2/k_1 = 0.5$. It is found that the microinertia continuum model is reasonably accurate for $qL < 2.0$. It is noted that, for long waves, $q \to 0$ and $c_p \to c_0$. This means that, for long waves, the microinertia effect diminishes ($F = 0$ in Eq. (22)) and the microinertia model reduces to a classical homogeneous solid.

5 Transmission/Reflection of Waves Between a Lattice System and a Homogeneous Continuum

When waves propagate over materials composed of micro/nanostructures of very different scales, reflections occur and energy transmitted across the boundary of the two regions is affected. When a homogeneous continuum is used to represent a microscopically heterogeneous medium, these wave reflection/transmission characteristics should be accurately preserved. With the foregoing in mind, we consider a one-dimensional lattice system which is connected to a homogeneous elastic solid as shown in Fig. 5 in which ρ_* and c_* are the mass density and longitudinal wave velocity of the homogeneous solid, respectively.

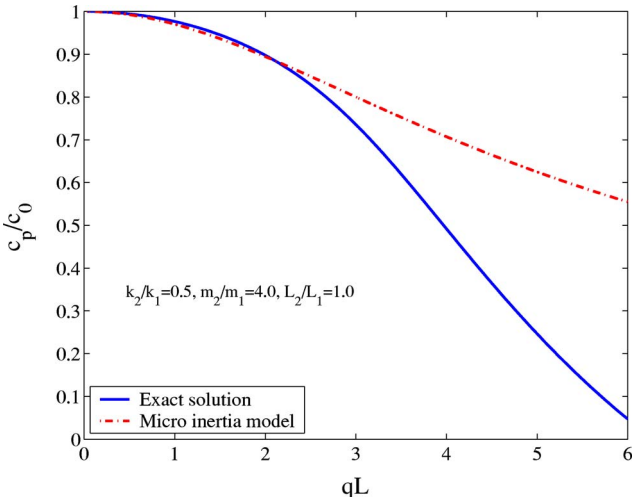

Fig. 4 Comparison of the dispersive curves obtained with the lattice model and the microinertia continuum model

An incident harmonic wave traveling over the lattice system toward the homogeneous solid is first studied. Subsequently, the same problem is studied with the lattice system replaced by an equivalent continuum with microinertia.

When a wave reaches the interface separating two media of different acoustic impedances, two boundary conditions requiring continuities in displacement and stress must be met. In general, these conditions can be expressed as

$$u^I + u^R = u^T, \tag{32}$$

$$\sigma^I + \sigma^R = \sigma^T \tag{33}$$

where superscript "I" indicates incident wave, "R" reflected wave, and "T" transmitted wave. Implicit in the continuity conditions is the condition that the angular frequencies of the incident and all the induced waves must be identical.

5.1 A Lattice System Connected to a Homogeneous Elastic Solid. In the lattice/solid model, the solution for harmonic waves in the lattice system is given by Eq. (27) in conjunction with Eq. (28). From Eq. (28), we obtain

$$B_2 = \kappa B_1 = - \frac{m_1 c_p^2 q^2 - (k_1 + k_2)}{k_1 e^{iqL} + k_2} B_1 \tag{34}$$

where c_p represents the phase velocity in the lattice system. As a result, the incident and reflected waves in the lattice system can be written, respectively, in terms of the displacement of m_1 as

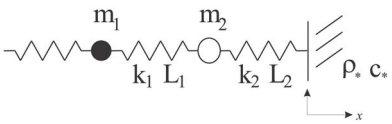

Fig. 5 A lattice system connected to a homogeneous elastic solid

$$u_1^I = B^I e^{iq(x-c_p t)}, \quad u_1^R = B^R e^{-iq(x+c_p t)} \tag{35}$$

The transmitted wave in the homogeneous elastic solid is

$$u^T = B^T e^{iq_*(x-c_* t)} \tag{36}$$

in which q_* is the wave number and c_* is the phase velocity for the homogeneous solid.

If the lattice system is connected to the homogeneous solid as shown in Fig. 5, then the corresponding stresses of the waves at the boundary can be expressed as

$$\sigma^I = k_2(u_1^I - u_2^I), \quad \sigma^R = k_2(u_1^R - u_2^R), \quad \sigma^T = -\rho_* c_* \dot{u}^T \tag{37}$$

where u_1 is the displacement of m_1 at the interface and u_2 is the displacement of m_2 that is adjacent to the interface. It is found that interchanging the positions of m_1 and m_2 at the interface does not affect the result of wave transmission/reflection.

The continuity conditions (32) and (33) yield

$$B^R = \frac{k_2(1-\kappa) - iqc_p\rho_* c_*}{k_2(\bar{\kappa}-1) + iqc_p\rho_* c_*} B^I \tag{38}$$

$$B^T = \frac{k_2(\bar{\kappa}-\kappa)}{k_2(\bar{\kappa}-1) + iqc_p\rho_* c_*} B^I \tag{39}$$

where $\bar{\kappa}$ is the complex conjugate of κ given in Eq. (34). Thus, the solutions of the reflected and transmitted waves can be obtained in terms of the incident wave. The ratio of the stresses of the transmitted wave and the incident wave at the interface is obtained as

$$\frac{\sigma^T}{\sigma^I} = \frac{i\rho_* c_* q c_p(\bar{\kappa}-\kappa)}{(1-\kappa)[k_2(\bar{\kappa}-1) + i\rho_* c_* q c_p]} \tag{40}$$

It should be noted that the above stress ratio is a complex number, indicating that both amplitude and phase angle are altered during wave transmission.

5.2 The Microinertia Model Connected to a Homogeneous Elastic Solid. We now consider the problem of Sec. 5.1 using the proposed microinertia continuum model to represent the lattice system. The incident and reflected harmonic waves are given by

$$U^I = B^I e^{iq(X-c_p t)} \quad \text{and} \quad U^R = B^R e^{-iq(X+c_p t)}, \tag{41}$$

respectively. The transmitted wave in the homogeneous solid can be expressed as

$$U^T = B^T e^{iq_*(X-c_* t)} \tag{42}$$

Note that, in the homogeneous solid, there is no distinction between the local displacement u and macrodisplacement U. It is important to note also that, in satisfying continuity condition (33), the stresses σ^I and σ^R of the incident and reflected waves must be interpreted according to Eq. (24). From continuity conditions (32) and (33) we obtain the reflected and transmitted displacement fields in terms of the incident displacement, i.e.,

$$B^R = \frac{q(k-\omega^2 H_0) - \omega\rho_* c_*}{q(k-\omega^2 H_0) + \omega\rho_* c_*} B^I \tag{43}$$

$$B^T = \frac{2q(k-\omega^2 H_0)}{q(k-\omega^2 H_0) + \omega\rho_* c_*} B^I \tag{44}$$

in which ω is angular frequency, and k and H_0 are given in Eqs. (21) and (23), respectively. With the aid of the above relations, the stress response of the transmitted wave in the homogeneous solid can be obtained and the following ratio of stresses at the interface is readily obtained.

$$\frac{\Sigma^T}{\Sigma^I} = \frac{2\omega\rho_* c_*(k-\omega^2 H_0)}{k[q(k-\omega^2 H_0) + \omega\rho_* c_*]} \tag{45}$$

Figure 6 shows the ratio of stresses of the incident wave and transmitted wave at the interface of a lattice system connected to a homogeneous solid. The curve labeled as "exact solution" is calculated according to Eq. (40); the "microinertia model" curve is obtained from Eq. (45). The material properties used in the calculations are $\rho_*/\rho_0=2$, $c_*/c_0=5$, and Poisson's ratio $\nu_*=0.3$ for the homogeneous solid, and $L_2/L_1=5$, $m_2/m_1=0.2$, and $k_2/k_1=2$ for the lattice system. The result of Fig. 6 indicates that the microinertia model is excellent for nondimensional wave numbers at least up to $qL=1.5$, which is equivalent to a wavelength equal to four times the unit cell dimension of L.

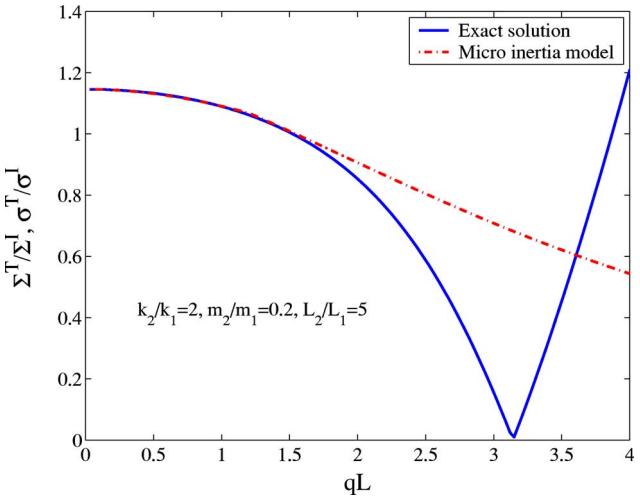

Fig. 6 Ratio of stresses of the incident and transmitted waves at the interface in the lattice/homogeneous solid system

5.3 Effect of Microinertia. The effectiveness of the microinertia model to represent a lattice system can be evaluated by studying transmission of harmonic waves through the lattice/microinertia continuum system similar to that considered in Sec. 5.1. If there is little wave reflection, then the representation is good. The analysis procedure for this case follows that described in Sec. 5.1. If the microinertia terms F in Eq. (22) and H in Eq. (24) are set equal to zero, then the microinertia model reduces to a classical elastic solid or the so-called effective modulus theory. We consider both cases with the lattice connected to the microinertia continuum (that represents the lattice) and a continuum without microinertia (the effective modulus theory). The numerical results are shown in Fig. 7 for $L_2/L_1=5$, $m_2/m_1=0.2$, and $k_2/k_1=2$. From these results it is evident that the effective modulus

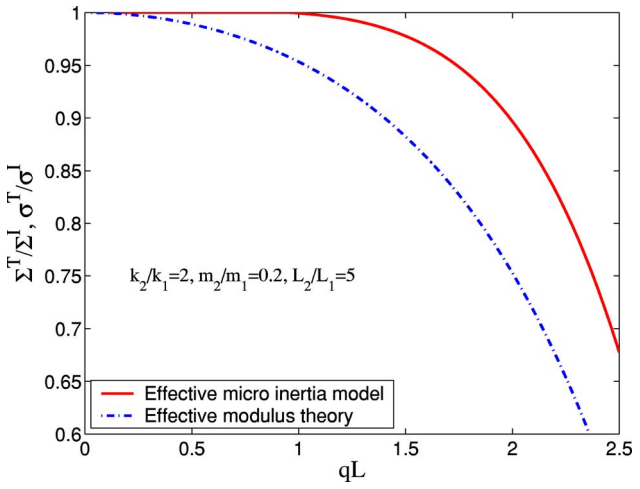

Fig. 7 Effectiveness of wave transmission in lattice/representative continuum system

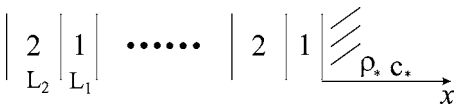

Fig. 8 A layered medium attached to an elastic medium

theory is adequate in representing the lattice system only for long waves. On the other hand, the microinertia model allows almost perfect transmission of waves across the lattice/microinertia continuum boundary for wavelengths up to six times the size of the unit cell.

6 Wave Propagation Between a Layered System and a Homogeneous Elastic Medium

Wave reflection and transmission are also considered for layered media attached to a homogeneous elastic medium as shown in Fig. 8. The microinertia model developed by Wang and Sun [8] is adopted here. The thicknesses for layer 1 and layer 2 are denoted as L_1 and L_2, respectively, and the total length for each cell is $L=L_1+L_2$. In the study, layer 1 is assumed to be attached to the elastic medium.

6.1 The Original System. The longitudinal harmonic wave propagating in the direction normal to the layers is a one-dimensional problem for which the nonvanishing displacement field can be derived from a scalar potential function ϕ, i.e., $u=\partial\phi/\partial x$ with ϕ satisfying the wave equation

$$\frac{\partial^2\phi_k}{\partial x^2}=\frac{1}{c_k^2}\frac{\partial^2\phi_k}{\partial t^2} \tag{46}$$

where $k=1,2$ indicating layer 1 and layer 2, respectively, $c_k=\sqrt{(\lambda_k+2\mu_k)/\rho_k}$ is the longitudinal wave velocity in layer k, and λ and μ are the Lamé constants. The general forms of the incident and reflected harmonic waves in layer 1 can be expressed as [5]

$$\phi_1^I=(A_1^I e^{-iqx(1+c_p/c_1)}+B_1^I e^{-iqx(1-c_p/c_1)})e^{iq(x-c_pt)},$$

$$\phi_1^R=(A_1^R e^{iqx(1+c_p/c_1)}+B_1^R e^{iqx(1-c_p/c_1)})e^{-iq(x+c_pt)} \tag{47}$$

where c_p is the phase velocity for the layered medium. Similar expressions for the incident and reflected waves in layer 2 can be obtained from Eq. (47) by replacing subscript "1" with "2." The transmitted wave in the homogeneous elastic solid is

$$\phi^T=A^T e^{iq_*(x-c_*t)} \tag{48}$$

In view of the periodicity of the layered medium, we conclude from Floquet's theorem that the scalar functions ϕ_k are periodic with a period L [5]. By using this periodic condition and continuity conditions between layers 1 and 2, we obtain the following relation

$$B_1^I=nA_1^I$$

$$=\frac{e^{i(c_p/c_1)L_1}e^{iqL}-\frac{1}{2}(1+p)e^{-iq(c_p/c_2)L_2}+\frac{1}{2}(p-1)e^{iq(c_p/c_2)L_2}}{e^{-i(c_p/c_1)L_1}e^{iqL}+\frac{1}{2}(p-1)e^{-iq(c_p/c_2)L_2}-\frac{1}{2}(1+p)e^{iq(c_p/c_2)L_2}}A_1^I \tag{49}$$

where $p=(\lambda_1+2\mu_1)c_2/(\lambda_2+2\mu_2)c_1$. In a similar manner, B_1^R can be expressed in terms of A_1^R as $B_1^R=\bar{n}A_1^R$.

Thus, the incident, reflected, and transmitted waves can all be expressed in terms of a single arbitrary amplitude. From continuity conditions (32) and (33) at the interface between layer 1 and the attached homogeneous elastic medium, we have

$$A^T=\frac{2p_*c_*(1-\bar{n}n)}{c_1[(1-\bar{n})-p_*(1+\bar{n})]}A_1^I \tag{50}$$

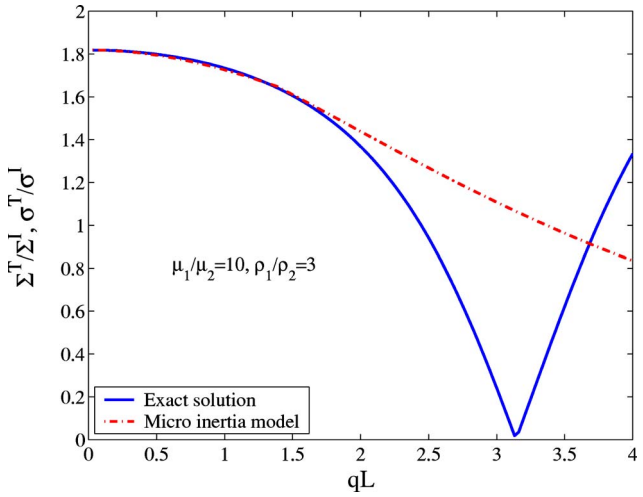

Fig. 9 Ratio of stresses of the incident and transmitted waves at the interface of the layer medium/homogeneous solid system

in which $p_*=(\lambda_1+2\mu_1)c_*/(\lambda_*+2\mu_*)c_1$ and $c_*=\sqrt{(\lambda_*+2\mu_*)/\rho_*}$.

Subsequently, the following ratio of stresses at the interface is obtained.

$$\frac{\sigma^T}{\sigma^I}=\frac{2(1-n\bar{n})}{(1+n)[(1-\bar{n})-p_*(1+\bar{n})]} \tag{51}$$

6.2 The Continuum Representation. Consider the system of Fig. 8 with the layered medium being replaced by the microinertia model. According to [11], for the one-dimensional wave motion, the macroequation of motion can be obtained as

$$\frac{\partial\Sigma}{\partial X}+F=\rho_0\ddot{U}$$

where $\rho=\rho_1f_1+\rho_2f_2$, $f_1=L_1/L$, $f_2=L_2/L$ and $F=\partial H/\partial X$ with

$$H=H_0\frac{\partial\ddot{U}}{\partial X} \quad \text{and} \quad H_0=\frac{1}{6}\frac{f_1f_2(\gamma\delta_1-\delta_2)(bf_1^2-f_2^2)}{(\delta_2f_1+\gamma\delta_1f_2)}.$$

The problem of transmission of harmonic wave propagation from the microinertia model to the homogeneous elastic medium can be readily solved. We obtain the ratio of stresses at the interface as

$$\frac{\Sigma^T}{\Sigma^I}=\frac{2\omega\rho_*c_*(\eta-\omega^2H)}{\eta[q(\eta-\omega^2H)+\omega\rho_*c_*]} \tag{52}$$

where

$$\eta=\frac{\mu_1\delta_1\delta_2}{(\gamma f_2\delta_1+f_1\delta_2)}, \quad \delta_1=\frac{2(1-v_1)}{1-2v_1}, \quad \delta_2=\frac{2(1-v_2)}{1-2v_2},$$

$$b=\frac{\rho_1}{\rho_2}, \quad \gamma=\frac{\mu_1}{\mu_2}.$$

Figure 9 shows the numerical results for Eqs. (51) and (52) with $\rho_*/\rho_2=4$, $c_*/c_2=5$, and $v_*=0.3$ for the homogeneous solid, and $L_1/L_2=4$, $\mu_1/\mu_2=10$, $\rho_1/\rho_2=3$, $v_1=0.3$, and $v_2=0.35$ for the layered medium. The result of Fig. 9 indicates that the microinertia model yields excellent agreement with the exact solution (Eq. (51)) up to $qL=2.0$. A numerical simulation is also performed for the case in which layer 2 is connected to the homogeneous solid. No variance with the result of Fig. 9 is noticed.

6.3 Effect of Microinertia. Analogous to the lattice system discussed in Sec. 5.3, we now consider the system of a layered medium connected to the microinertia continuum that represents

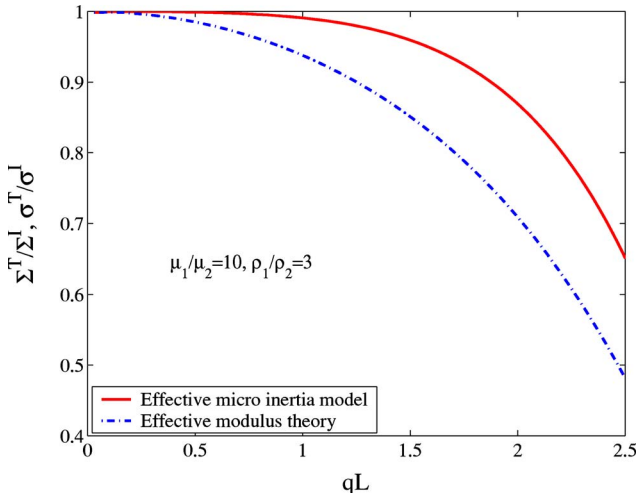

Fig. 10 Effectiveness of wave transmission in layered medium/representative continuum system

the layered medium. The numerical results are shown in Fig. 10 for $L_1/L_2=4$, $\mu_1/\mu_2=10$, $\rho_1/\rho_2=3$, $v_1=0.3$, and $v_2=0.35$. For comparison, the result obtained by dropping the microinertia (i.e., the effective modulus theory) is also presented in the figure. It is easy to see that the microinertia model allows almost perfect transmission of waves across the interface for wavelengths up to six times the size of the unit cell. This implies that, in this range of wavelength, the microinertia model can accurately describe the dynamic characteristics of the layered medium.

7 Concluding Remarks

It has been demonstrated that, by including the microinertia effect, a homogeneous continuum model can effectively represent a locally heterogeneous continuous media. A similar approach can also be used to develop continuum models for nonhomogeneous lattice systems. It was shown that the microinertia term appears in the equations of motion as a body force. Moreover, the traction boundary condition in the continuum model (with microinertia) also involves the contribution of the microinertia. To check the accuracy of the continuum representation, the model was employed to study wave reflection and transmission at the boundary of two media (continua and lattices) with microstructures of very different scales. It was found that, in general, the continuum model with microinertia is accurate in representing the original heterogeneous media or lattice systems up to wavelengths that are of the same order of magnitude of the size of the representative volume element.

References

[1] Cosserat, E., and Cosserat, F., 1909, *Theorie des Corps Deformables*, A. Hermann & Fils, Paris.
[2] Toupin, R. A., 1962, "Elastic Materials With Couple-Stresses," Arch. Ration. Mech. Anal., **11**, pp. 385–414.
[3] Mindlin, R. D., 1964, "Micro-Structure in Linear Elasticity," Arch. Ration. Mech. Anal., **16**, pp. 51–78.
[4] Eringen, A. C., and Suhubi, E. S., 1964, "Nonlinear Theory of Micro-Elastic Solids," Int. J. Eng. Sci., **2**, pp. 189–203.
[5] Sun, C. T., Achenbach, J. D., and Herrmann, G., 1968, "Continuum Theory for a Laminated Medium," ASME J. Appl. Mech., **35**, pp. 467–475.
[6] Achenbach, J. D., Sun, C. T., and Herrmann, G., 1968, "On the Vibrations of a Laminated Body," ASME J. Appl. Mech., **35**, pp. 689–696.
[7] Chen, Y. P., and Lee, J. D., 2003, "Connecting Molecular Dynamics to Micromorphic Theory. (I). Instantaneous and Averaged Mechanical Variables," Physica A, **322**, pp. 359–376.
[8] Kunin, I. A., 1982, *Elastic Media with Microstructure I, One Dimensional Models*, Springer-Verlag, Berlin.
[9] Pasternak, E., and Muhlhaus, H. B., 2005, "Generalised Homogenisation Procedures for Granular Materials," J. Eng. Math., **52**, pp. 199–229.
[10] Nesterenko, V. F., 2001, *Dynamics of Heterogeneous Materials*, Springer-Verlag, New York.
[11] Wang, Z. P., and Sun, C. T., 2002, "Modeling Micro-Inertia in Heterogeneous Materials under Dynamic Loading," Wave Motion, **36**, pp. 473–485.
[12] Sinclair, J., 1971, "Improved Atomistic Model of a bcc Dislocation Core," J. Appl. Phys., **42**, pp. 5321–5329.
[13] Mullins, M., and Dokainish, M. A., 1982, "Simulation of the (0 0 1) Plane Crack in a-Iron Employing a New Boundary Scheme," Philos. Mag. A, **46**, pp. 771–787.
[14] Tadmor, E. B., Ortiz, M., and Phillips, R., 1996, "Quasicontinuum Analysis of Defects in Solids," Philos. Mag. A, **73**, pp. 1529–1563.
[15] Broughton, J. Q., Abraham, F. F., Bernstein, N., and Kaxiras, E., 1999, "Concurrent Coupling of Length Scales: Methodology and Application," Phys. Rev. B, **60**, pp. 2391–2403.
[16] Rudd, R. E., and Broughton, J. Q., 2000, "Concurrent Coupling of Length Scales in Solid State Systems," Phys. Status Solidi B, **217**, pp. 251–291.
[17] E, W. N., and Huang, Z. Y., 2001, "Matching Conditions in Atomistic-Continuum Modeling of Materials," Phys. Rev. Lett., **87**, p. 135501.
[18] Wagner, G. J., and Liu, W. K., 2003, "Coupling of Atomic and Continuum Simulations using a Bridging Scale Decomposition," J. Comput. Phys., **190**, pp. 249–274.
[19] Xiao, S. P., and Belytschko, T., 2004, "Coupling Methods for Continuum Model With Molecular Model," Comput. Methods Appl. Mech. Eng., **193**, pp. 1645–1669.
[20] Irving, J. H., and Kirkwood, J. G., 1950, "The Statistical Mechanical Theory of Transport Processes," J. Chem. Phys., **18**, pp. 817–829.
[21] Lutsko, J. F., 1988, "Stress and Elastic Constants in Anisotropic Solids: Molecular Dynamic Techniques," J. Appl. Phys., **64**, pp. 1152–1164.
[22] Cormier, J., Rickman, J. M., and Delph, T. J., 2001, "Stress Calculation in Atomistic Simulations of Perfect and Imperfect Solids," J. Appl. Phys., **89**, pp. 99–104.
[23] Zhou, M., 2003, "A New Look at the Atomic Level Virial Stress: on Continuum-Molecular System Equivalence," Proc. R. Soc. London, Ser. A, **459**, pp. 2347–2392.

Some Applications of Integrated Elasticity

A. T. Assaad
Blue Slide Systems LLC,
Pittsburgh, PA 15219-3120

G. B. Sinclair[1]
Department of Mechanical Engineering,
Louisiana State University,
Baton Rouge, LA 70803-6413
e-mail: glennsinclair@cox.net

This paper examines the effects of relaxing the assumption of classical linear elasticity that the loads act in their entirety on the undeformed shape. Instead, loads here are applied incrementally as deformation proceeds, and resulting fields are integrated. A formal statement of the attendant integrated elasticity theory is provided. A class of problems is identified for which this formulation is amenable to solution in closed form. Some results from these configurations are compared with linear elasticity and experimentally measured data. The comparisons indicate that, as deformation increases, integrated elasticity is capable of tracking the physical response better than linear elasticity. [DOI: 10.1115/1.2188537]

1 Introduction

The classical theory of elasticity is founded on three linearizations. The first linearization stipulates that the relationship between stresses and strains is linear: that is, the stresses are small in a sense. The second linearization requires that the strains depend in a linear fashion on the displacement gradients: that is, the displacement gradients are small. The third linearization has that all loads act on the undeformed shape throughout the entire loading process: that is, the deflections are small. The primary objective of this paper is to consider what happens when we relax this last linearization.

In his monograph [1], Frisch-Fay provides an indication of how significant relaxing the third linearization can be. In Ref. [1], on p. 1, a cantilever beam of length "100 in." and bending stiffness "1000 lbf in^2," subjected to a transverse concentrated end load of "1 lbf," is first treated via traditional beam theory. That is, within the context of classical one-dimensional elasticity. This results in a vertical tip deflection of "333 in." with no horizontal displacement, implying strains of the order of 300%, and thus seemingly suggesting gross yielding and even rupture of the beam. Subsequently in Ref. [1], on p. 39, the same beam is analyzed by tracking its deformation and applying loads to its deformed shape. That is, within the context of nonlinear beam theory. The result is a tip deflection of "81 in." vertically and "56 in." horizontally, and stresses and strains that can be well within the elastic regime. Hence, physically sensible results are obtained by merely remitting the small deflection assumption, while still adhering to the other two linearizations of linear elasticity. This example was no doubt chosen by Frisch-Fay to dramatically demonstrate the potential impact of taking into account deflections during loading. Typically such large differences in results are not to be expected. Nonetheless, it would seem worthwhile to investigate the effects of relaxing the third linearization in general, and such is the intent of the present work.

Arguably the simplest approach to relaxing the small deflection assumption is to apply loads incrementally, then add the result of successive increments. One means of actually implementing such an approach is to use the linear elastic deflections produced by each load increment to update the body's positions and the points of application of the loads. The outcome of summation is then an accumulation of infinitesimal elasticity responses. Such an accumulation might reasonably be termed *integrated* elasticity.

The approach is not new. Griffith applied it to a single configuration in 1920 (see Ref. [2]). Truesdell [3] quotes Murnaghan as explicitly advancing this possibility in general in Ref. [4] in 1949, while Truesdell himself pursues it in its simplest form in Ref. [3], Sec. 56.[2] Under favorable circumstances, updating the geometry of the body reduces to simple integration of the linear elastic fields with respect to loading alone. Further, when it is possible to carry out the integration in closed form, such an approach combines tractability with the promise of capturing the physics better as deformation proceeds. Unfortunately, the progressively larger loads can engender rotational deformations that are no longer infinitesimal, even with a linear elastic response assumed for each load increment. Accordingly, some care must be exercised in the application of integrated elasticity.

In this paper, we identify a class of configurations that do admit to solution simply by direct integration. We proceed to analyze a number of members of this class of problems, and examine them with respect to the effects, if any, of accumulated rotations. We then compare results with linear elasticity and some physical measurements. We also make some comparisons with a neo-Hookeon constitutive law from rubber elasticity. Specifically, we begin in Sec. 2 by providing a formal statement of the integrated elasticity theory to be used, and discussing its limitations. In Sec. 3, we consider the application of the theory to the uniaxial tension (or compression) of a prismatic bar. Next, in Sec. 4, we apply it to thin-walled pressure vessels (a companion analysis of thick-walled vessels is given in an Appendix). In Sec. 5, we provide a limited treatment of a plate under tension weakened by an elliptical hole. Finally, we offer some concluding remarks in Sec. 6.

2 General Formulation of Integrated Elasticity

Consider an elastic body occupying an open regular region R_0 with a boundary ∂R_0 in an initial stress-free and undeformed state (Fig. 1(*a*): herein and henceforth, a hairline dashed outline indicates an undeformed shape). We use rectangular Cartesian coordinates X_i $(i=1,2,3)$ with corresponding unit vectors $\mathbf{e}_i$ and origin O to describe this region. At the conclusion of the loading history, R_0 deforms into the ultimate region R_u, with boundary ∂R_u. We employ new Cartesian coordinates x_i $(i=1,2,3)$, sharing the same unit vectors and origin, to describe this deformed region. During loading, after a number of intervening load increments, R_0 deforms into an intermediate R, with boundary ∂R (Fig. 1(*b*)). In the

[1]Author to whom correspondence should be addressed.

Contributed by the Applied Mechanics Division of ASME for publication in the JOURNAL OF APPLIED MECHANICS. Manuscript received February 18, 2005; final manuscript received November 30, 2005. Review conducted by E. M. Arruda. Discussion on the paper should be addressed to the Editor, Prof. Robert M. McMeeking, Journal of Applied Mechanics, Department of Mechanical and Environmental Engineering, University of California – Santa Barbara, Santa Barbara, CA 93106-5070, and will be accepted until four months after final publication of the paper itself in the ASME JOURNAL OF APPLIED MECHANICS.

[2]This sort of approach belongs to a class of rate-of-deformation theories, early versions of which were also advanced in Jaumann [5] and Hencky [6].

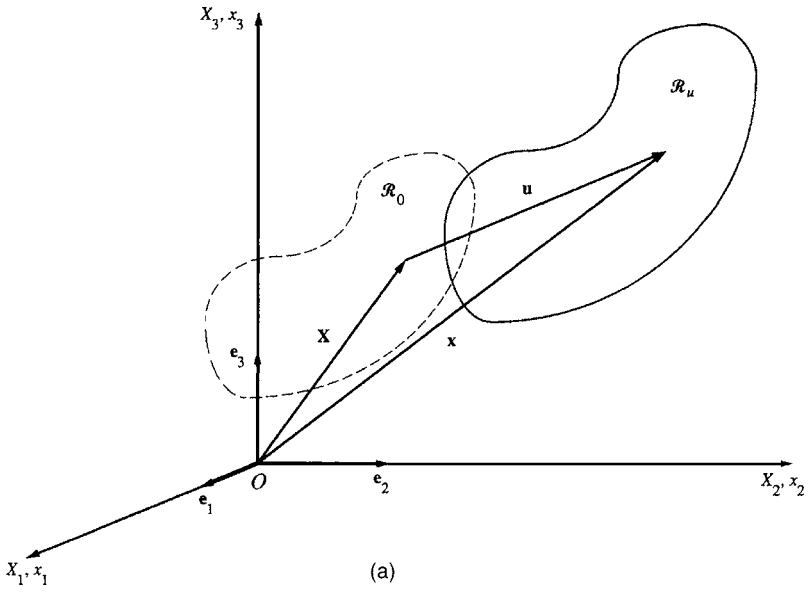

(a)

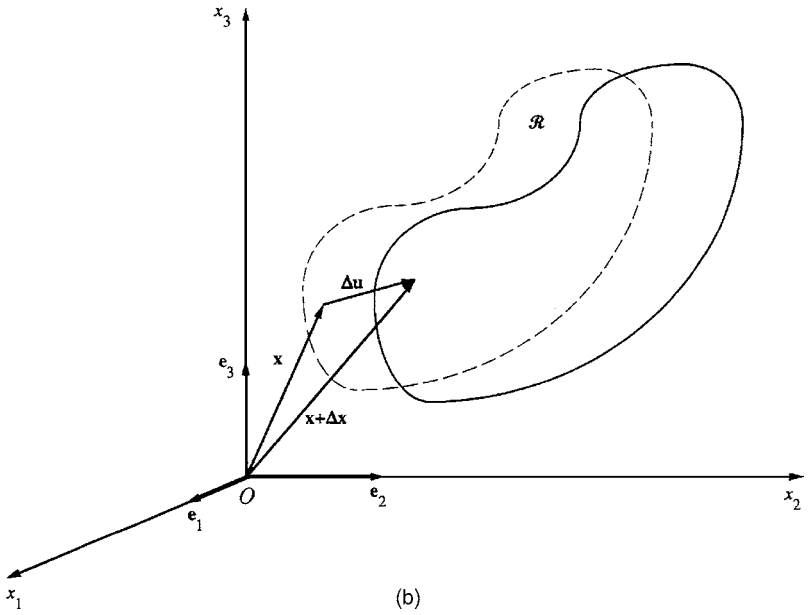

(b)

Fig. 1 Coordinate systems for elastic regions: (*a*) initial and final regions, (*b*) intervening regions for successive load increments

interest of keeping distinct notations to a minimum, we continue to use the Cartesian coordinates x_i to designate this intermediate state. Thus **X** is the position vector of a point initially in R_0, and **x** is the corresponding position vector in both R and R_u. We denote the displacements associated with **x** by **u**. Again, **u** designates displacement in R, an intermediate stage, and in R_u, the ultimate configuration. The differences in **x** and **u** between successive load increments are denoted by $\Delta\mathbf{x}$ and $\Delta\mathbf{u}$. For the present, we limit consideration to configurations loaded only by tractions, and where load is controlled by a single parameter. With these preliminaries in place, we can furnish the following formal statement of an integrated theory of elasticity.

In general, we seek the stresses σ_{ij}, strains ϵ_{ij}, and displacements u_i $(i,j=1,2,3)$, throughout R_u as functions of position **x**, resulting from the accumulation over the entire loading history of corresponding increments in accordance with

$$\sigma_{ij} = \int_0^\sigma \Delta\sigma_{ij} d\sigma, \quad \epsilon_{ij} = \int_0^\sigma \Delta\epsilon_{ij} d\sigma, \quad u_i = \int_0^\sigma \Delta u_i d\sigma \tag{1}$$

throughout R_u, wherein $\Delta\sigma_{ij}$, $\Delta\epsilon_{ij}$, and Δu_i are the stress, strain, and displacement increments, respectively, and the integration variable σ is a single, controlling, loading parameter. Further, the increments are to satisfy the following field equations of linear elasticity

$$\frac{\partial(\Delta\sigma_{ij})}{\partial x_j} = 0$$

$$\Delta\sigma_{ij} = \frac{E}{1+\nu}\left[\frac{\nu}{1-2\nu}\Delta\epsilon_{kk}\delta_{ij} + \Delta\epsilon_{ij}\right]$$

$$\Delta\epsilon_{ij} = \frac{1}{2}\left(\frac{\partial(\Delta u_i)}{\partial x_j} + \frac{\partial(\Delta u_j)}{\partial x_i}\right) \tag{2}$$

on R. Here E is Young's modulus, ν is Poisson's ratio, and δ_{ij} is the Kronecker delta. For boundary conditions, we subject a portion of the boundary, $\partial_1 R$, to traction increments, the magnitudes of which depend on $\Delta\sigma$ alone with the understanding that the limit $\Delta\sigma \to 0$ is employed in Eq. (1). These traction increments remain in fixed proportion with respect to one another. Accordingly

$$\Delta\sigma_{ij} n_j = \Delta\sigma s_i \tag{3}$$

on $\partial_1 R$, where n_j are the components of the unit vector normal to ∂R_0 and s_i are the fixed components of a unit vector. On the remainder of the boundary, $\partial_2 R$, we prescribe displacement boundary conditions such that

$$\Delta u_i = 0 \tag{4}$$

on $\partial_2 R$. For Eqs. (3) and (4), $\partial_1 R \cup \partial_2 R = \partial R$, and $\partial_1 R \cap \partial_2 R = \emptyset$.

Several comments on the foregoing formulation of integrated elasticity are in order. First, we observe that loading has been assumed to be slow enough that any problem can be considered quasi-static. Second, the integration of the familiar infinitesimal strain is, in effect, defined as our measure of the accumulated strain in the final state. Third, the elastic moduli are taken to be constant and independent of the loading. Fourth, the loading process is controlled by changing the value of a single scalar parameter, here σ. That is, loading directions are fixed. With this proviso, the present formulation is equally applicable to loading via a single controlling displacement. Fifth, there are limitations imposed by the effects of rigid-body rotations and of rotational deformations accumulating during loading. These merit discussion in greater detail.

To be of completely general applicability, a theory dealing with elastic deformations must produce correct results under rigid-body rotations. Provided they are undertaken quasi-statically, such rotations should not change the state of stress or strain within the body. Fortunately, $\Delta\epsilon_{ij}$ of Eq. (2) are guaranteed to vanish identically under such rotations. However, in terms of the fixed coordinate systems X_i or x_i, neither $\Delta\epsilon_{ij}$ nor $\Delta\sigma_{ij}$ take on appropriate values under a simple rotation of the frame of reference (Fung [7], p. 447, gives a demonstration of this). Consequently, the present formulation lacks material frame indifference, as does classical linear elasticity whence it derives. It is therefore necessary to restrict the use of this formulation to loading situations wherein rigid-body rotations are precluded.

The possibility of rotational deformations accumulating throughout the loading process results in further limitations on the applicability of the current formulation. Nevertheless, when rotations accumulate no more than in the corresponding linear elasticity treatment, integrated elasticity promises to do no worse than linear elasticity in this regard. Further, in such instances, integrated elasticity can capture the physics more accurately, as it tracks the action of the load on the deforming shape.

That said, there is the question of why we consider the present approach instead of one of the treatments available in the literature that can handle rotational deformations exactly. The answer lies in the tractability of the present formulation of integrated elasticity, which can yield closed-form solutions under favorable circumstances. One such favorable circumstance occurs when the deformed shape exhibits a weak form of geometric similarity to its undeformed antecedent. Here weak geometric similarity admits more than one scaling parameter, as is the case for hollow spheres. This is in contrast to the usual definition of strict geometric similarity for triangles in a plane which have but one scaling parameter. For deformed shapes that are weakly geometrically similar to their undeformed shapes, with loading directions being fixed as in Eq. (3), one can directly write down integrals for the outcome of an integrated elasticity analysis. Moreover, on occasion, such integrals can be evaluated exactly to furnish solutions involving elementary functions. In what follows, we identify configurations with the foregoing attributes for facilitating solution and seek to exploit them.

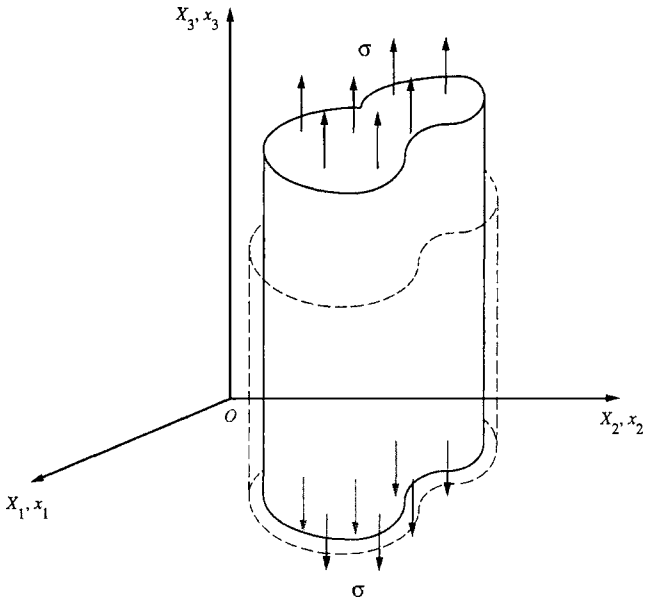

Fig. 2 Cylindrical bar under uniaxial tension

3 Uniaxial Tension of a Cylindrical Bar

We begin with one of the simplest configurations to analyze, namely a cylindrical bar held at one end and subjected to a uniform tensile traction σ at the other (Fig. 2). We derive the stresses, strains, and displacements predicted by integrated elasticity under such loading; we then compare them with those of linear elasticity and some experimental data.

The bar has an undeformed cross section of constant area A_0 which lies in the X_1X_2 plane (Fig. 2). Initially, the bar occupies an open region R_0 along with its closure, where

$$R_0 = \{(X_1, X_2, X_3) | X_1, X_2 \in S_0, 0 < X_3 < L_0\}$$

and L_0 is the length of the bar in the undeformed state, while S_0 is the open set of points comprising A_0. When loaded parallel to the X_3 axis, the bar deforms such that plane cross sections remain plane. It occupies a deformed region R described in the x_1, x_2, x_3-coordinate system by

$$R = \{(x_1, x_2, x_3) | x_1, x_2 \in S, 0 < x_3 < L\}$$

where L is the deformed length of the bar and S the open set of points comprising the deformed cross section A.

For a single first increment of uniaxial tensile loading, linear elasticity has that the only normal stress component induced is the longitudinal stress. Moreover, the accompanying displacement components are functions of the coordinates aligned with their direction alone. The occurrence of this response for an initial increment suggests that it may persist for a sequence of increments. Accordingly, we seek fields of this type in what follows.

Thus we seek throughout R the longitudinal stress σ_{33}, the normal strains ϵ_{ii} (no sum), and the displacements u_i, for $i = 1, 2, 3$. These result from the accumulation of corresponding increments, under a gradually applied traction σ, in accordance with

$$\sigma_{33} = \int_0^{\sigma} \Delta\sigma_{33} d\sigma, \quad \epsilon_{ii} = \int_0^{\sigma} \Delta\epsilon_{ii} d\sigma \text{ (no sum)}, \quad u_i = \int_0^{\sigma} \Delta u_i d\sigma \tag{5}$$

on R, wherein $\Delta\sigma_{33}$, $\Delta\epsilon_{ii}$ (no sum), and Δu_i are the stress, strain, and displacement increments, respectively. At any stage of deformation, an additional increment of traction $\Delta\sigma$ engenders these increments such that they satisfy: the stress equation of equilibrium

$$\frac{\partial(\Delta\sigma_{33})}{\partial x_3} = 0 \tag{6}$$

on R; the stress and strain relations

$$\Delta\sigma_{33} = \frac{E}{(1+\nu)(1-2\nu)}[(1-\nu)\Delta\epsilon_{33} + \nu(\Delta\epsilon_{11} + \Delta\epsilon_{22})]$$

$$\Delta\epsilon_{11} = \Delta\epsilon_{22} = -\nu\Delta\epsilon_{33} \tag{7}$$

on R; the strain-displacement relations

$$\Delta\epsilon_{ii} = \frac{d(\Delta u_i)}{dx_i} \text{(no sum)} \tag{8}$$

on R; the end condition prescribing the application of the traction

$$\Delta\sigma_{33} = \Delta\sigma \tag{9}$$

at $x_3 = L$ for $x_1, x_2 \in S$; the displacement end condition

$$\Delta u_3 = 0 \tag{10}$$

at $x_3 = 0$ for $x_1, x_2 \in S$; and the supplementary boundary conditions to prevent rigid-body translations

$$\Delta u_1 = \Delta u_2 = 0 \tag{11}$$

at $x_1 = x_2 = x_3 = 0$.

The formulation for the incremental fields is identical to that of linear elasticity for uniaxial tension of a prismatic bar. Therefore, we can draw on the linear elasticity results to write expressions for the longitudinal stress, strain, and displacement, and the attendant lateral strains and displacements (see, e.g., Sokolnikoff [8], Art. 30)

$$\Delta\sigma_{33} = \Delta\sigma$$

$$\Delta\epsilon_{33} = \frac{\Delta\sigma}{E}, \quad \Delta\epsilon_{11} = \Delta\epsilon_{22} = -\frac{\nu\Delta\sigma}{E} \tag{12}$$

$$\Delta u_3 = \frac{x_3}{E}\Delta\sigma, \quad \Delta u_1 = -\frac{\nu x_1}{E}\Delta\sigma, \quad \Delta u_2 = -\frac{\nu x_2}{E}\Delta\sigma$$

on R. That this is the solution to the incremental problem is verified directly through substitution into Eqs. (6)–(11).

The integrated elasticity expressions for stresses and strains are obtained immediately from their incremental counterparts by evaluating the corresponding simple integrals of Eq. (5) to yield

$$\sigma_{33} = \sigma$$

$$\epsilon_{33} = \frac{\sigma}{E}, \quad \epsilon_{11} = \epsilon_{22} = -\frac{\nu\sigma}{E} \tag{13}$$

To obtain the integrated elasticity predictions for displacements, we first recall that the deformed coordinates x_i are related to their undeformed counterparts X_i by

$$x_i = X_i + u_i$$

For $i=3$, substituting this relation into the expression for Δu_3 of Eq. (12) and taking the limit as the increments tend to zero, we can write a differential expression for the longitudinal displacement increment at any load level as

$$du_3 = \frac{(X_3 + u_3)}{E} d\sigma$$

On integrating we obtain

$$u_3 = X_3(e^{\sigma/E} - 1) \tag{14}$$

Following a similar procedure, we obtain the expressions for the lateral displacements as

$$u_1 = X_1(e^{-\nu\sigma/E} - 1), \quad u_2 = X_2(e^{-\nu\sigma/E} - 1) \tag{15}$$

Equations (13)–(15) constitute the integrated elasticity solution for the uniaxial tension problem. Here deformed states are only weakly geometrically similar to their antecedents, but this still facilitates analysis sufficiently to obtain closed-form expressions. In these expressions, the absence of rotations altogether guarantees the absence of errors associated therewith.

The integrated elasticity solution has a couple of consequences worth noting. First, we observe in Eq. (13) that the accumulated strain measure is linearly proportional to the stress, and that it obeys Hooke's law. Substituting the strain for σ/E into Eq. (14) and rearranging yields the relation between ϵ_{33} and the total deflection δ, where $\delta = u_3$ at $X_3 = L_0$. This relation has

$$\epsilon_{33} = \ln\left[1 + \frac{\delta}{L_0}\right] \tag{16}$$

In Eq. (16), we recognize ϵ_{33} as the well-known natural or true strain originally proposed in Ludwik [9]. The corresponding result to Eq. (16) for σ_{33} is also consistent, up to and including $O((\delta/L_0)^2)$, with that of Green [10].

Second, we note from Eq. (15) that both the X_1 and X_2 directions are simply scaled by $e^{-\nu\sigma/E}$. Consequently, the loaded cross-sectional area, A, is related to the undeformed area, A_0, by

$$A = A_0 e^{-2\nu\sigma/E} \tag{17}$$

The companion force-stress response follows directly on multiplying Eq. (17) through by σ. Thus, on normalizing by E

$$\frac{F}{EA_0} = \frac{\sigma}{E} e^{-2\nu\sigma/E} \tag{18}$$

To obtain the associated load-deflection response, we substitute for σ/E in terms of δ/L_0 from Eq. (14). Thus

$$\frac{F}{EA_0} = \frac{\ln\left[1 + \frac{\delta}{L_0}\right]}{\left[1 + \frac{\delta}{L_0}\right]^{2\nu}} \tag{19}$$

We observe that Eqs. (18) and (19) also hold for uniaxial compression, as do their antecedents Eqs. (13)–(17).

To compare the response for integrated elasticity with that of linear elasticity, we begin by recovering the linear elasticity relations for small loads. For Eq. (18) this corresponds to taking the limit $\sigma/E \to 0$, and for Eq. (19), the limit $\delta/L_0 \to 0$. Accordingly we have

$$\frac{F}{EA_0} = \frac{\sigma^o}{E}, \quad \frac{F}{EA_0} = \frac{\delta^o}{L_0} \tag{20}$$

where the superscript o distinguishes the linear elasticity predictions. That Eqs. (20) are indeed the linear elasticity relations may be confirmed from standard texts (see, e.g., Sokolnikoff [8], Art. 30).

The means of derivation of Eq. (20) has, as an immediate consequence, that the results of the two theories must agree for small loads. To examine the differences between the two for larger loads, we sketch their stress-force responses in Fig. 3 (from Eq. (18) and the first of Eq. (20)), and their force-deflection responses in Fig. 4 (from Eq. (19) and the second of Eq. (20)). Both figures are for a force range of $|F/EA_0| \leq 1$. In both cases, the linear

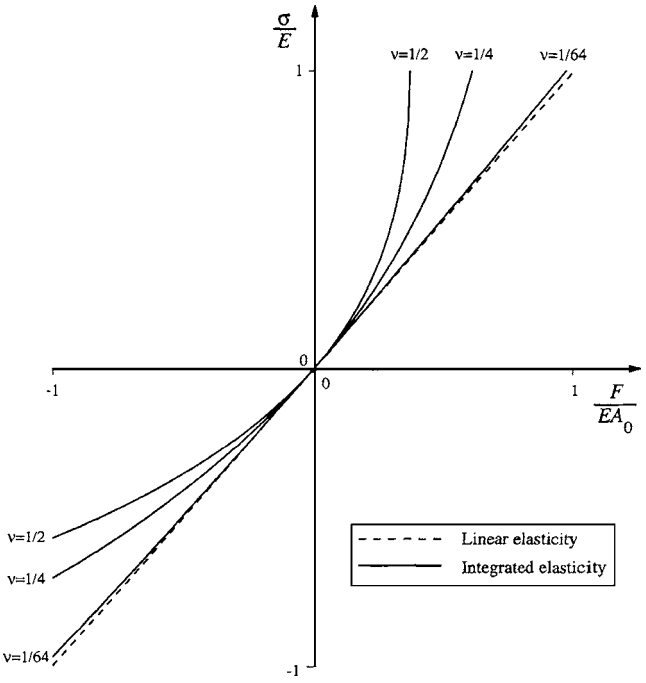

Fig. 3 Comparison of stress versus force response of linear and integrated elasticity

elasticity predictions are represented by a single broken line, as they do not depend on ν. The integrated elasticity results, on the other hand, do depend on ν. Thus we overlay several curves for each response corresponding to a representative spectrum of values of Poisson's ratio. When $\nu=0$, the material has no lateral contraction in response to stretch. The stress is, therefore, merely the quotient of the force by the original cross section, and the curve for integrated elasticity is identical to that of linear elasticity. In Fig. 3, this response together with that for $\nu \neq 0$ is shown: The stress predicted by integrated elasticity for a given tensile force is amplified by the lateral contraction, while for compression, it is reduced due to lateral expansion. In Fig. 4, the deflection predicted by integrated elasticity for $\nu=0$ for a given tensile force level is greater than that for linear elasticity (independent of ν). This is due to the progressive decrease in the body's stiffness as integrated elasticity tracks the stretch in the length direction. For nonzero values of Poisson's ratio, the increase in the predicted deflection is even more pronounced as the presence of lateral contraction reduces the body's stiffness even further. Conversely, the lengthwise contraction predicted by integrated elasticity is less for a given compressive force due to the increases in stiffness associated with the bar shortening and laterally expanding.

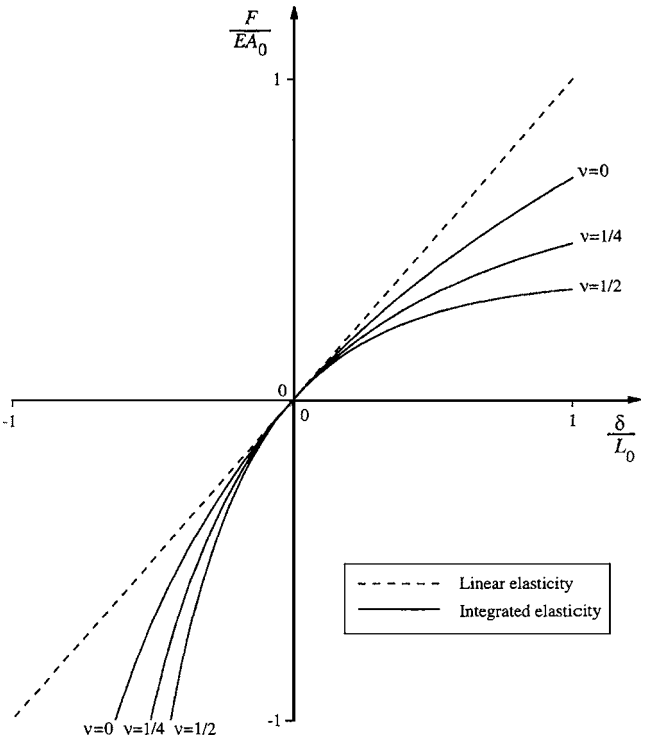

Fig. 4 Comparison of force versus deflection response of linear and integrated elasticity

To examine the physical appropriateness of the force-deflection relationship of integrated elasticity compared to that of linear elasticity, we review some experimental results obtained for rubber bands and latex tubes. These materials can be expected to deform significantly and yet recover largely elastically; consequently, they enter a regime wherein linear elasticity can be expected to depart from the physical response. The point, then, of these two sets of experiments is to see whether or not integrated elasticity can still track the physical response.

The first set of experiments entails three flat-ribbon rubber bands of the common office-supplier variety. These rubber bands are supplied by different manufacturers and consequently do not necessarily have the same composition. The objective of these experiments is to see whether or not the integrated elasticity result of Eq. (19) can capture the response of the three different rubber bands for moderate engineering strains ($\delta/L_0 \leqslant 1/2$). While there are quite a number of tension tests on rubber reported in the literature (e.g., Rivlin and Saunders [11]), the focus of these tests is typically on large strains ($\delta/L_0 \leqslant$ [12]), and not a lot of data are provided throughout the range of interest here.[3]

The simple experimental procedures for these rubber band tests are set out in Ref. [12]. Results are summarized in Fig. 5. In fitting theories to measured data in this figure, we first take Poisson's ratio to be 0.5, an accepted value for rubber materials. To determine E for linear elasticity, we use a least-squares fit to the initial slope. For integrated elasticity, however, we observe that the curvature of experimental results in Fig. 5 is similar to that in Fig. 4 for $\nu=1/2$. Thus we determine E by separately fitting the highest strain result ($\delta/L_0 \approx 0.45$) for each of the rubber bands.

In contrast to linear elasticity, the predictions of integrated elasticity and Eq. (19) are in trendwise agreement with measured data. Where scatter ranges are indicated, they intersect or touch 11 of 14 or 78% (not including the fitted points). Moreover, measured scatter here is only attributable to repeating the loading process three times for the same rubber band, so quite possibly is underestimated. All told, reasonable agreement is found between integrated elasticity and measured responses in these preliminary experiments.

Encouraged by the foregoing, the second set of experiments seeks to capture the response of latex tubes with more attention being paid to experimental scatter, and with an independent determination of Young's modulus. To assess scatter, six large hollow tubes and six small are subjected to tension. The tubes are then combined and subjected to torsion to furnish an independent determination of the shear modulus, hence E.

All of the tubes are from a single manufacturer and are described as being made of pure latex. They are sized so that they can individually be readily tested in tension, yet can be combined via an interference fit for torsion testing, the six tubes so formed

[3]For $\delta/L_0 \leqslant 1/2$, there are six reported measurements in Ref. [11]: Eq. (19) can fit these six to within 5%.

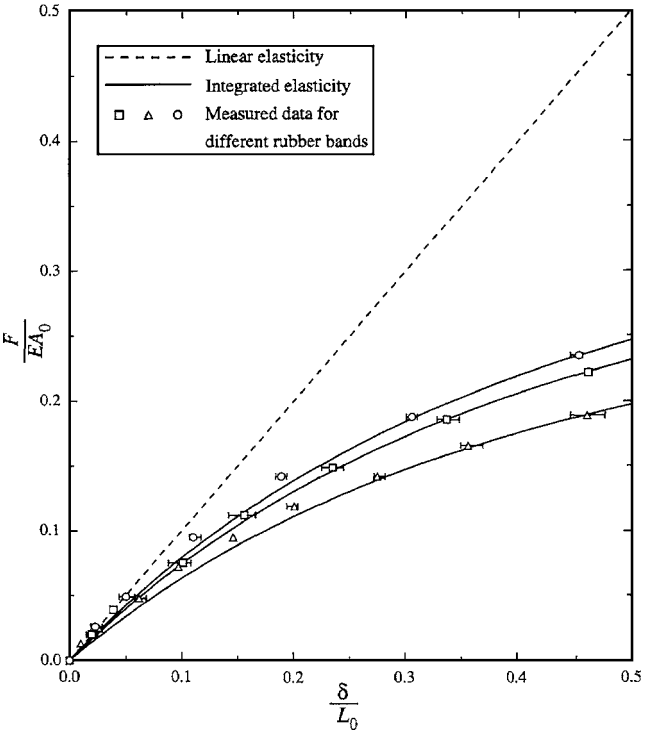

Fig. 5 Force-deflection response of rubber band specimens

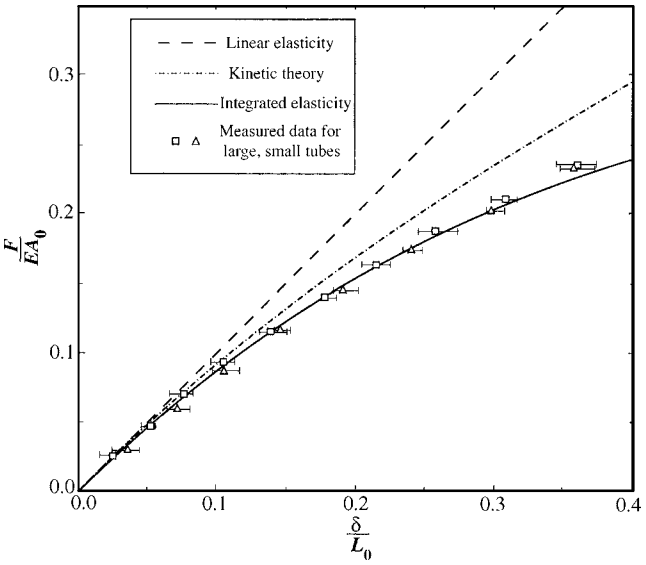

Fig. 6 Force-deflection response of latex tubes

being less susceptible to buckling. Details of the experimental procedures for these latex tube tests are set out in Ref. [12].

For torsion, a linear torque-twist response is predicted by both linear elasticity and integrated elasticity. Here experiments are found to confirm this to be the case for the mean twist up to an engineering shear strain of 0.54, corresponding to an axial engineering strain of $\delta/L_0=0.27$ (see Ref. [12] for details; like results to similar strain levels may be found in Rivlin and Saunders [11]). From the linear response, the mean shear modulus is determined, and hence on continuing to take $\nu=1/2$

$$E = 1.82 \text{ MPa} \tag{21}$$

with a range of 1.64–2.15 MPa. These results are in agreement with other reported values for rubber materials (e.g., Treloar [13], p. 96, which has a range of E from 1.17 MPa to 2.36 for seven different vulcanized rubbers).

For tension, results are presented in Fig. 6. The linear and integrated elasticity predictions included in Fig. 6 both employ E of Eq. (21); the latter also continues to use $\nu=1/2$. As expected at these levels of deformation, again linear elasticity does not track the physical response. Integrated elasticity, on the other hand, captures it quite well up to engineering strains of 30%. For scatter ranges up to this level, integrated elasticity intersects 15 of 16 or 94%.

For the latex tube data of Fig. 6, it is appropriate to compare as well with predictions of neo-Hookean constitutive laws from rubber elasticity. In essence there are two basic approaches to the development of these neo-Hookean laws: molecular network thermodynamics (Treloar [13], Chaps. 2–6), and phenomenological fits of strain energy functions (ibid., Chaps. 10, 11). We compare with kinetic theory for Gaussian chains developed via the first approach. We make this choice because kinetic theory is physically reasoned and enjoys long-standing acceptance. We also make it because it too takes $\nu=1/2$ and then has a single parameter to fit, as does integrated elasticity in Fig. 6: indeed, kinetic theory has the same parameter in effect, namely E.

For tension, kinetic theory predicts

$$\frac{F}{EA_0} = \frac{1}{3}\left[1 + \frac{\delta}{L_0} - \left(1 + \frac{\delta}{L_0}\right)^{-2}\right] \tag{22}$$

Expanding Eq. (22) for small δ/L_0 gives

$$\frac{F}{EA_0} = \frac{\delta}{L_0} - c\left(\frac{\delta}{L_0}\right)^2 + O\left(\left(\frac{\delta}{L_0}\right)^3\right) \tag{23}$$

c being a constant. As should be the case, the first term on the right hand side is that for linear elasticity (cf. Eq. (20)). The second term actually has $c=1$. Integrated elasticity has an expansion of the same form (from Eq. (19)), but with $c=3/2$. Thus integrated elasticity can be expected to be qualitatively similar to kinetic theory for small to moderate engineering strains, yet quantitatively different.

To gauge which agrees better with the physical data, Fig. 6 includes the preditions of kinetic theory with E from Eq. (21). While both kinetic theory and integrated elasticity are trendwise correct in Fig. 6, integrated elasticity appears to track this data better. This may be due to some of the additional assumptions underlying kinetic theory not being strictly adhered to by the tested material in this strain range. At higher strains, kinetic theory performs better than integrated elasticity, though ultimately it too deviates significantly from the physical data. At such large deformation levels, higher-order molecular chain theories can be expected to perform well and indeed they do (see Ward and Sweeney [14], Secs. 3.4, 3.5, for a recent review of these theories).

In closing this section we remark that states of biaxial or triaxial tension or compression of some configurations are amenable to closed-form solution within the context of integrated elasticity. It is also possible to analyze tension in combination with torsion for a right circular cylinder.

4 Pressure Within Thin-Walled Spherical and Cylindrical Vessels

Here we treat a further class of simple configurations, namely that of thin-walled vessels under internal pressure. For cases where such configurations expand considerably under pressure, we expect that significant differences could arise between integrated elasticity and linear elasticity because of the thinning that accompanies expansion. We concentrate on a thin-walled spherical vessel subjected to an applied internal pressure (Fig. 7) be-

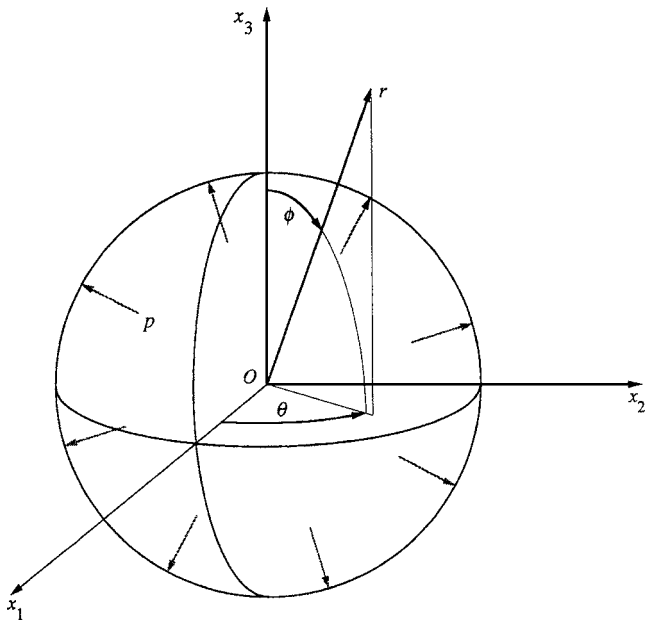

Fig. 7 Spherical vessel under internal pressure

cause it enables comparison with data from a rudimentary experiment on rubber balloons, but do include corresponding results for a cylindrical vessel.

Classical treatments of thin-walled pressure vessels in the linear elastic regime assume small deformations. As a result, they do not attempt to estimate the thinning effects, these being taken as negligible. At least, we have not been able to obtain such an estimate from a dozen or so standard texts. As a result, we derive one here.

To this end we proceed as follows. We set up our basic incremental formulation for thick-walled spherical pressure vessels. Once we have obtained the corresponding fields, we take averages through the thickness of the stresses and radial displacement, and evaluate the thinning as the difference of the displacements. Thereafter we expand all resulting expressions in terms of the thickness and take the lowest order terms as our thin-walled incremental results. In so doing, we are assuming that the thickness of the vessel is small enough relative to its radius that the stresses and displacement are well represented by their respective averages over the thickness. Last, we accumulate these increments. The formulation that follows is in accordance with the above but sets it out in reverse order.

The spherical vessel has an undeformed inner radius R_0, and relatively small thickness t_0. We use spherical coordinates r, θ, ϕ, to describe the deformed geometry (Fig. 7). These coordinates are related to their rectangular Cartesian counterparts by the following relations

$$x_1 = r\sin\phi\cos\theta, \quad x_2 = r\sin\phi\sin\theta, \quad x_3 = r\cos\phi$$

for $0 \leqslant r < \infty$, $0 \leqslant \theta < 2\pi$, $0 \leqslant \phi \leqslant \pi$. In its undeformed state the vessel occupies an open region R_0 together with its closure, where

$$R_0 = \{(r,\theta,\phi) | R_0 < r < R_0 + t_0, 0 \leqslant \theta < 2\pi, 0 \leqslant \phi \leqslant \pi\}$$

The problem at hand is spherically symmetric. Hence the deformed sphere occupies the region R such that

$$R = \{(r,\theta,\phi) | R < r < R + t, 0 \leqslant \theta < 2\pi, 0 \leqslant \phi \leqslant \pi\}$$

where R and t are the inner radius and the wall thickness after deformation.

In view of the spherical symmetry, the radial displacement u_r is the only nonzero displacement component, being also independent of both ϕ and θ. Thus we seek throughout R the average radial stress $\bar{\sigma}_{rr}$, the average hoop stresses $\bar{\sigma}_{\theta\theta} = \bar{\sigma}_{\phi\phi}$, and the average radial displacement $\bar{u}_r$. These result from the accumulation of corresponding increments, under a gradually applied internal pressure p, in accordance with

$$\bar{\sigma}_{rr} = \int_0^p \Delta\bar{\sigma}_{rr}\,dp, \quad \bar{\sigma}_{\theta\theta} = \int_0^p \Delta\bar{\sigma}_{\theta\theta}\,dp, \quad \bar{u}_r = \int_0^p \Delta\bar{u}_r\,dp$$

on R, wherein $\Delta\bar{\sigma}_{rr}$, $\Delta\bar{\sigma}_{\theta\theta}$, and $\Delta\bar{u}_r$ are the average radial stress, hoop stress, and radial displacement increments, respectively. The average increments are obtained from their corresponding unaveraged counterparts as follows

$$\Delta\bar{\sigma}_{rr} = \frac{1}{t}\int_R^{R+t} \Delta\sigma_{rr}\,dr, \quad \Delta\bar{\sigma}_{\theta\theta} = \frac{1}{t}\int_R^{R+t} \Delta\sigma_{\theta\theta}\,dr$$

$$\Delta\bar{u}_r = \frac{1}{t}\int_R^{R+t} \Delta u_r\,dr \tag{24}$$

In turn, the unaveraged, incremental field quantities satisfy the following: the stress equation of equilibrium

$$\frac{d(\Delta\sigma_{rr})}{dr} + \frac{2(\Delta\sigma_{rr} - \Delta\sigma_{\theta\theta})}{r} = 0$$

on R; the stress-displacement relations

$$\Delta\sigma_{rr} = \frac{E}{(1+\nu)(1-2\nu)}\left[(1-\nu)\frac{d(\Delta u_r)}{dr} + 2\nu\frac{\Delta u_r}{r}\right]$$
$$\Delta\sigma_{\theta\theta} = \frac{E}{(1+\nu)(1-2\nu)}\left[\frac{\Delta u_r}{r} + \nu\frac{d(\Delta u_r)}{dr}\right] \tag{25}$$

on R; and the boundary conditions applying a pressure on the inner wall while maintaining the outer stress free

$$\Delta\sigma_{rr} = -\Delta p \quad \text{at } r = R$$

$$\Delta\sigma_{rr} = 0 \quad \text{at } r = R + t$$

for $0 \leqslant \theta < 2\pi, 0 \leqslant \phi \leqslant \pi$.

The formulation for the incremental fields is identical to that of linear elasticity for a spherical container under internal pressure. Therefore, we draw on linear elasticity results in the literature to write expressions for the radial and hoop stress increments, $\Delta\sigma_{rr}$, $\Delta\sigma_{\theta\theta}$, and $\Delta\sigma_{\phi\phi}$, resulting from an increment of applied internal pressure (see, e.g., Sokolnikoff [8], Art. 94). These results yield

$$\Delta\sigma_{rr} = \Delta p\frac{R^3}{(R+t)^3 - R^3}\left[1 - \frac{(R+t)^3}{r^3}\right]$$
$$\Delta\sigma_{\theta\theta} = \Delta\sigma_{\phi\phi} = \Delta p\frac{R^3}{(R+t)^3 - R^3}\left[1 + \frac{(R+t)^3}{2r^3}\right] \tag{26}$$

The radial displacement increment Δu_r may be derived by substituting the stress results from Eq. (26) into Eq. (25) and integrating to get

$$\Delta u_r = \frac{rR^3}{(R+t)^3 - R^3}\frac{\Delta p}{E}\left[1 - 2\nu + (1+\nu)\frac{(R+t)^3}{2r^3}\right] \tag{27}$$

Upon averaging the expressions in Eqs. (26) and (27) over the thickness as in Eq. (24), we obtain the average stress increments, $\Delta\bar{\sigma}_{rr}$, $\Delta\bar{\sigma}_{\theta\theta}$, and $\Delta\bar{\sigma}_{\phi\phi}$, and the radial displacement increment $\Delta\bar{u}_r$ for a thick-walled sphere. We evaluate the increment of change in thickness, or increment of thinning, as the difference of displacement increments at the outer and inner sphere walls. We then expand the resulting expressions for small values of t to obtain the incremental expressions for a thin-walled sphere

$$\Delta\bar{\sigma}_{rr} = -\frac{\Delta p}{2}(1 + O(t)), \quad \Delta\bar{\sigma}_{\theta\theta} = \Delta\bar{\sigma}_{\phi\phi} = \frac{R\Delta p}{2t}(1 + O(t))$$

$$\Delta\bar{u}_r = \frac{(1-\nu)}{2E}\frac{R^2\Delta p}{t}(1+O(t)), \quad \Delta t = -\frac{\nu R\Delta p}{E}(1+O(t)) \tag{28}$$

as $t\to 0$, wherein O is the large order O symbol. We note, from the first of Eq. (28), that the mean pressure in the sphere's wall is the average of the boundary values. Further, from the second of Eq. (28), the hoop stresses found here are in fact consistent with those obtained from classical elementary treatments. The average displacement and thinning, for their part, are the apparently new results needed to proceed with the remainder of the integrated elasticity analysis.

The integrated elasticity solution may be obtained by using the fields in Eq. (28). The procedure starts by taking the limit $\Delta p \to dp$ and writing the expressions for change in radius and thinning in differential form in terms of the current, deformed, radius R and thickness t, and the pressure differential dp. Hence, from the last two of Eq. (28),

$$dR = \frac{(1-\nu)}{2E}\frac{R^2}{t}dp, \quad dt = -\frac{\nu R}{E}dp \tag{29}$$

Each equation in Eq. (29) involves all three variables R, t, and p. To separate and then integrate, we need expressions with just two. Consequently, we need to eliminate a variable: We choose p as it appears solely as dp. Hence

$$dR = -\frac{(1-\nu)}{2\nu}\frac{R}{t}dt$$

Now integrating, the integrated elasticity relation for R versus t is

$$\frac{R}{R_0} = \left(\frac{t}{t_0}\right)^{-(1-\nu)/2\nu} \tag{30}$$

Substituting this result into the second of Eq. (29), we can eliminate R to obtain

$$dt = -\frac{\nu R_0}{E}\left(\frac{t}{t_0}\right)^{-(1-\nu)/2\nu} dp$$

Integrating we obtain the thickness in the deformed state as function of the applied pressure. This in turn we can substitute into Eq. (30) above to obtain the radius-pressure relation. The two expressions so derived may now be used in the differential forms for the stresses which, upon integration, yield the remainder of the integrated elasticity solution. The final results take a more compact form on exchanging Young's modulus for the shear modulus G. The entire solution can be expressed as

$$\bar{\sigma}_{rr} = -\frac{p}{2}, \quad \bar{\sigma}_{\theta\theta} = -2G\ln\left[1-\frac{R_0}{nt_0}\frac{p}{G}\right]$$
$$\frac{R}{R_0} = \left[1-\frac{R_0}{nt_0}\frac{p}{G}\right]^{-n_\nu}, \quad \frac{t}{t_0} = \left[1-\frac{R_0}{nt_0}\frac{p}{G}\right]^{1-n_\nu} \tag{31}$$

where $n_\nu = 2(1-\nu)/(2-2\nu+\nu n)$, and $n=4$ with $\bar{\sigma}_{\phi\phi} = \bar{\sigma}_{\theta\theta}$ for the thin-walled, spherical, pressure vessel. In Eq. (31), we introduce the index n and related variable n_ν so as to provide the corresponding results for a thin-walled, cylindrical, pressure vessel in plane strain. These are derived in an analogous manner to the sphere, and the final results take the same form: namely, as in Eq. (31) but for $n=2$. We note that thick-walled pressure vessels are also tractable to analysis to yield closed-form solutions. Details of such an analysis and resulting expressions are given in the Appendix. For all these configurations, the weak geometric similarity of deformed geometries to their antecedents again enables closed-form solutions to be derived. Further, all of these solutions have no rotations and therefore are free of any associated errors.

To compare the integrated elasticity response for the sphere to its linear elasticity counterpart, we begin by writing $\bar{\sigma}_{\theta\theta}$ and R of Eq. (31) explicitly for the sphere. Hence

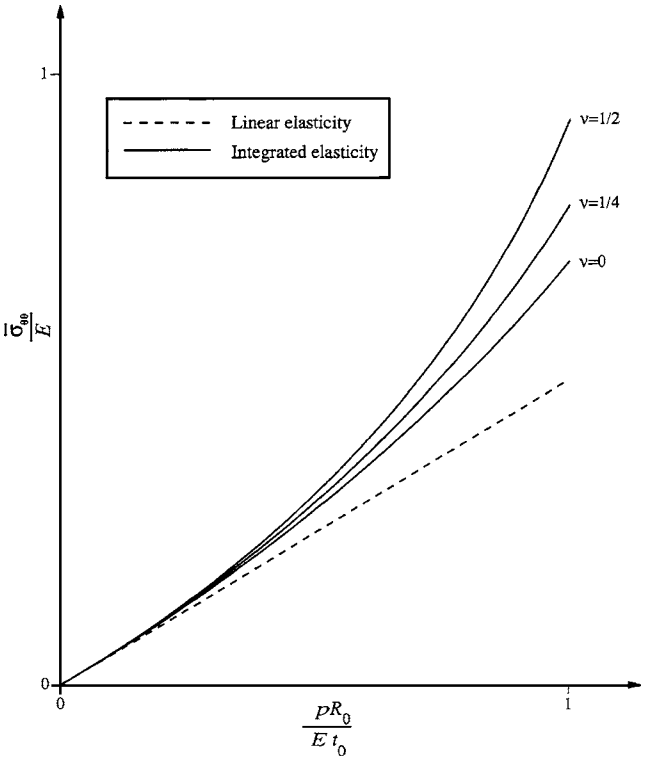

Fig. 8 Comparison of stress versus pressure response of linear and integrated elasticity

$$\bar{\sigma}_{\theta\theta} = -2G\ln\left[1-\frac{R_0}{4t_0}\frac{p}{G}\right], \quad \frac{R}{R_0} = \left[1-\frac{R_0}{4t_0}\frac{p}{G}\right]^{-(1-\nu)/(1+\nu)} \tag{32}$$

Next we expand the integrated elasticity expressions for small loads to obtain expressions valid in the linear elastic regime. Thus, on reverting to E and taking the limit as $pR_0/Et_0 \to 0$, we get

$$\bar{\sigma}^o_{\theta\theta} = \frac{pR_0}{2t_0}, \quad \frac{R^o}{R_0} = 1+\frac{1-\nu}{2}\frac{R_0}{t_0}\frac{p}{E} \tag{33}$$

where the superscript o again serves to distinguish linear elasticity predictions. These are consistent with Eq. (28): The expression for the hoop stress is also consistent with that obtained from standard treatments of thin spherical shells (see, e.g., Sokolnikoff [8], Art. 94).

In the range of small loads where both theories are linear, the fact that Eq. (33) can be obtained directly from Eq. (32) guarantees that they will agree. To examine the differences between the two for larger loads, we sketch their hoop stress responses to pressure in Fig. 8 (from the first of both Eq. (32) and Eq. (33), with the former converted to E), and their pressure-radius responses in Fig. 9 (from the second of both Eq. (32) and Eq. (33), again with the former converted to E). Both figures are for a load range $0 \leqslant pR_0/Et_0 \leqslant 1$, with a family of plots corresponding to $\nu = 0, 1/4, 1/2$. In Fig. 8, the linear elasticity prediction for stress is represented by a single straight line, as it is independent of the parameter ν. In contrast, the predictions of integrated elasticity do depend on ν. For $\nu=0$, the difference between the two theories is due solely to integrated elasticity tracking the expanding radius. That the gap increases with ν is attributable to integrated elasticity additionally tracking the thinning effect on the sphere's wall, and thus on the stress. In Fig. 9, both theories predict that the change in radius depends on ν. For linear elasticity, this is because each in-plane stress component contributes a lateral contraction in the direction of the other due to Poisson's ratio effect. Consequently,

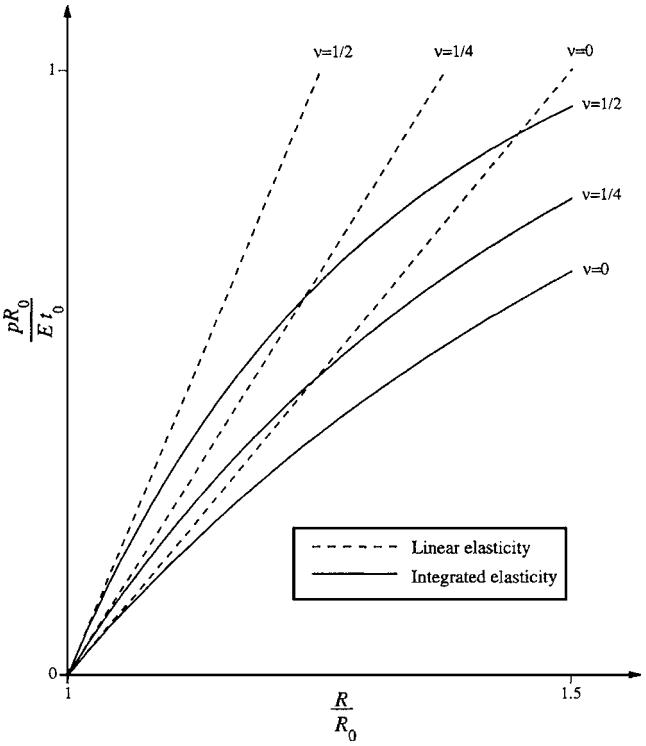

Fig. 9 Comparison of pressure versus radius response of linear and integrated elasticity

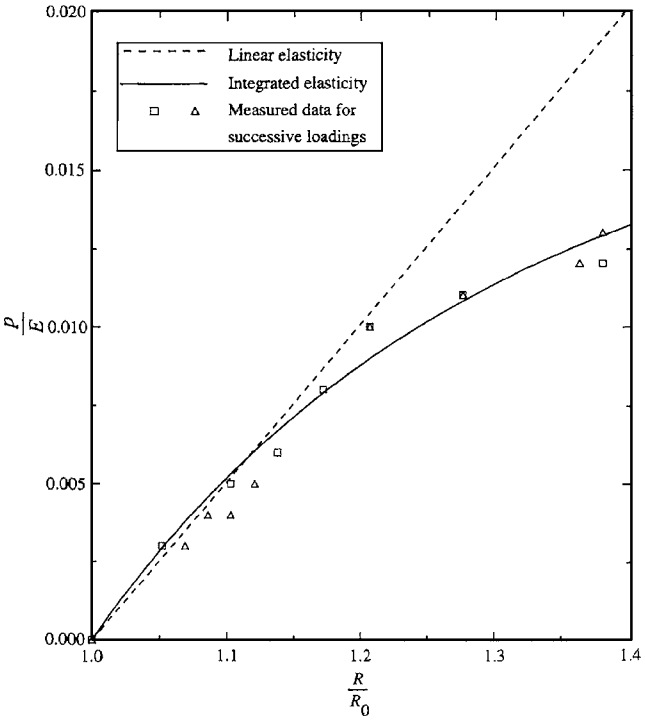

Fig. 10 Pressure-radius response of rubber balloons

net strains are reduced with increasing ν. This in turn means that, for a given pressure, the radius decreases with increasing Poisson's ratio. For integrated elasticity, this effect is offset by both the tracking of the increase in radius (for $\nu=0$) as well as the tracking of thinning ($\nu\neq 0$). In Fig. 9, this can most easily be appreciated by examining the reduction in the pressure required to produce a given radius.

To gain an appreciation for the applicability of the integrated elasticity results for a sphere and contrast them with those of classical elasticity, we compare predictions to some pressure-versus-radius measurements. There are a number of such measurements reported in the literature (e.g., Hart-Smith [15]), but typically they are for far higher levels of deformation than those of interest here. Accordingly we perform our own set of experiments with a view to providing more data in the engineering strain range 0–40 %. Here the intent is merely to assess whether the spherical vessel's response is linear or not.

With this objective in mind, we put together a simple apparatus for inflating rubber balloons. The apparatus consists of a piping system, pressurized by a bicycle pump, and fitted with a water manometer (see Ref. [16] for further details). Figure 10 shows a plot of the pressure-versus-radius data recorded during two successive inflation runs, overlaid with the predictions of integrated and linear elasticity. The modulus of elasticity values in these predictions are based on a least-squares fit to all the data for integrated elasticity, and to the initial data for linear elasticity: Poisson's ratio continues to be taken to be one half for both theories. These fits lead to a slightly lower value of E for linear elasticity, hence integrated elasticity predictions that are initially somewhat higher than those of linear elasticity, in contrast to Fig. 9. At higher radii, however, integrated elasticity predicts softening, whereas linear elasticity does not. These simple experiments confirm the softening. The same softening is found in other experiments (e.g., Ref. [15]): It can also be tracked using kinetic theory instead of integrated elasticity.

5 Far-Field Tension of a Plate with an Elliptical Hole

In this section we consider an elastic plate of infinite extent, weakened by an elliptical hole, under uniaxial tension at infinity (Fig. 11). In general, the integrals encountered in developing the integrated elasticity solution for such a configuration are not that tractable, but some key results can be readily obtained. We derive these in what follows, then comment on similar results in Griffith [2] and Mansfield [17], including a limited comparison with some physical data.

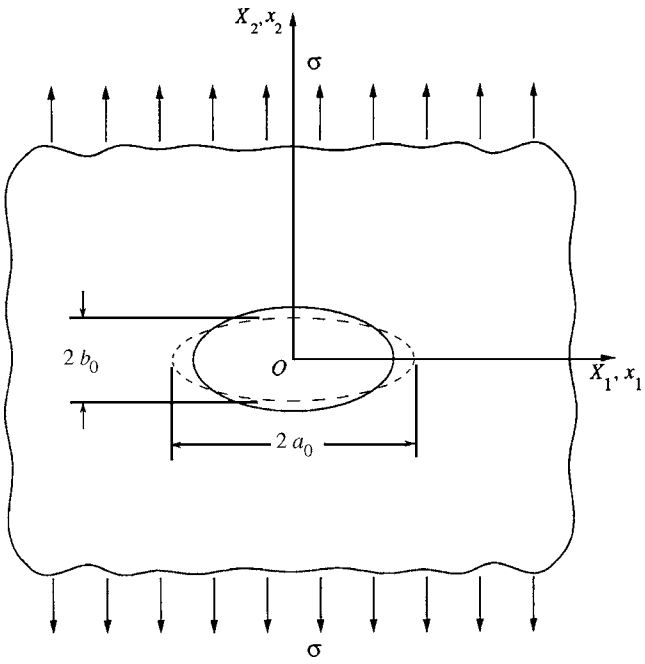

Fig. 11 Plate weakened by an elliptical hole under tension at infinity

In the undeformed state, the elliptical hole has a major axis of length $2a_0$, and minor axis of length $2b_0$ (Fig. 11). In plane rectangular Cartesian coordinates X_1, X_2, the major axis of the hole is parallel to the X_1 axis. Initially, therefore, the hole is described by

$$\left(\frac{X_1}{a_0}\right)^2+\left(\frac{X_2}{b_0}\right)^2=1 \tag{34}$$

The plate is subjected to a uniform tensile traction σ at infinity parallel to the X_2 axis.

Before we proceed to a formal statement of the associated integrated elasticity problem, we need to check whether the corresponding linear elasticity solution deforms an elliptical hole into yet another elliptical hole: Such weak geometric similarity of deformed geometries facilitates both formulation and subsequent analysis. That this geometric similarity is maintained in the earlier examples is immediately established by inspection of the simple deformation fields attending their linear elasticity solutions: Here it is not so obvious.

The linear elasticity solution for this configuration was first given in Kolossoff [18] and subsequently in Inglis [19]. While a number of contributors have since furnished alternate solution forms for the linear elastic response, in terms of complex potentials, for example, the complete stress and displacement fields are not readily available in the open literature. Accordingly we draw on an internal report that develops these fields, Kondo and Sinclair [20].

For a state of plane stress, the hole boundary displacements can be obtained from Ref. [20]. After some algebra, these components can be resolved into the X_1 and X_2 directions. This yields the following relatively simple expressions

$$u_1^b=-\frac{\sigma X_1}{E},\quad u_2^b=\frac{\sigma}{E}\left(1+2\frac{a_0}{b_0}\right)X_2 \tag{35}$$

where the superscript b distinguishes displacements on the hole boundary (here, as opposed to elsewhere, displacements are independent of ν). To investigate the deformed shape of the hole under tension we consider

$$\left(\frac{x_1}{a}\right)^2+\left(\frac{x_2}{b}\right)^2$$

where x_1, x_2 are the plane rectangular Cartesian coordinates describing the deformed shape, and a and b are the lengths of the deformed semi-major and semi-minor axes, respectively. Recognizing that, on the hole boundary, $x_1=X_1+u_1^b$, $x_2=X_2+u_2^b$, and that $a=a_0+u^b_{1|X_1=a_0}$, $b=b_0+u^b_{2|X_2=b_0}$, we obtain, from Eq. (35),

$$\left(\frac{x_1}{a}\right)^2+\left(\frac{x_2}{b}\right)^2=\left[\frac{X_1\left(1-\frac{\sigma}{E}\right)}{a_0\left(1-\frac{\sigma}{E}\right)}\right]^2+\left[\frac{X_2\left[1+\frac{\sigma}{E}\left(1+2\frac{a_0}{b_0}\right)\right]}{b_0\left[1+\frac{\sigma}{E}\left(1+2\frac{a_0}{b_0}\right)\right]}\right]^2$$

That is, from Eq. (34)

$$\left(\frac{x_1}{a}\right)^2+\left(\frac{x_2}{b}\right)^2=1 \tag{36}$$

Consequently, the elliptical hole does indeed deform into another elliptical hole. Hence we can specify the deformed region in our formulation to reflect this fact and proceed as previously to derive some integrated elasticity results.

In the undeformed state, the plate occupies an open region R_0 together with its boundary, where

$$R_0=\{(X_1,X_2)|1<(X_1/a_0)^2+(X_2/b_0)^2<\infty\}$$

In light of the foregoing, when loaded parallel to the X_2 axis, the plate deforms so as to occupy the open region R described in the x_1, x_2-coordinate system by

$$R=\{(x_1,x_2)|1<(x_1/a)^2+(x_2/b)^2<\infty\}$$

where a and b continue as the deformed counterparts of a_0 and b_0.

In general, then, we seek throughout R the stresses σ_{ij} and the displacements u_i as functions of x_i, where now the subscripts i,j only range over 1,2. These result from the accumulation of corresponding increments, under a gradually applied traction σ, in accordance with

$$\sigma_{ij}=\int_0^\sigma \Delta\sigma_{ij}d\sigma,\quad u_i=\int_0^\sigma \Delta u_i d\sigma$$

on R, wherein $\Delta\sigma_{ij}$ and Δu_i are the stress and displacement increments, respectively. At any stage of deformation, an additional increment of traction $\Delta\sigma$ engenders these increments such that they satisfy: the stress equations of equilibrium in the absence of body forces

$$\frac{\partial(\Delta\sigma_{ij})}{\partial x_j}=0$$

on R; the stress-displacement relations for a state of plane stress[4]

$$\Delta\sigma_{ij}=\frac{E}{2(1+\nu)}\left(\frac{2\nu}{1-\nu}\frac{\partial(\Delta u_k)}{\partial x_k}\delta_{ij}+\frac{\partial(\Delta u_i)}{\partial x_j}+\frac{\partial(\Delta u_j)}{\partial x_i}\right) \tag{37}$$

on R where k is summed over 1,2; the boundary conditions for the stress-free hole

$$\Delta\sigma_{\xi\xi}=\Delta\sigma_{\xi\eta}=0$$

for x_1, x_2 satisfying Eq. (36), where $\Delta\sigma_{\xi\xi}$, the normal stress component perpendicular to the boundary, and $\Delta\sigma_{\xi\eta}$, the shear stress component parallel to it, are given by

$$\Delta\sigma_{\xi\xi}=\tfrac{1}{2}(\Delta\sigma_{11}+\Delta\sigma_{22})+\alpha\gamma(\Delta\sigma_{11}-\Delta\sigma_{22})+2\beta\gamma\Delta\sigma_{12}$$

$$\Delta\sigma_{\xi\eta}=2\alpha\gamma\Delta\sigma_{12}-\beta\gamma(\Delta\sigma_{11}-\Delta\sigma_{22})$$

wherein

$$\alpha=\frac{a^2+b^2}{a^2-b^2}\left(\frac{x_1^2}{a^2}-\frac{x_2^2}{b^2}\right)-1,\quad \beta=\frac{4x_1x_2}{a^2-b^2},$$

$$\gamma=\left[\frac{a^2+b^2}{a^2-b^2}-\frac{x_1^2}{a^2}+\frac{x_2^2}{b^2}\right]/2[\alpha^2+\beta^2]$$

and the boundary conditions at infinity, prescribing the application of the traction transverse to the hole

$$\Delta\sigma_{22}=\Delta\sigma,\quad \Delta\sigma_{12}=0,\quad \text{as } x_2\to\pm\infty$$

$$\Delta\sigma_{11}=\Delta\sigma_{12}=0,\quad \text{as } x_1\to\pm\infty$$

on R.

We begin the integrated elasticity solution by seeking displacements in the deformed state. These involve integrals that are readily tractable only at the tips of the major and minor axes of the elliptical hole. Since the ellipse deforms into another ellipse, we only need expressions for the lengths of the major and minor axes to describe the hole geometry as deformation progresses. We use Eq. (35) to write the displacement increments on the hole boundary, du_i^b, in response to an incrementally applied stress, $d\sigma$. Specifically, for the major axis, we have

$$du_1^b=-\frac{x_1}{E}d\sigma$$

Introducing $da=du_1^b$ and $a=x_1$ and integrating, we obtain

[4]For plane strain, exchange E for $2(1+\nu)G$ then replace the remaining occurrences of ν with $\nu/(1-\nu)$.

$$a = a_0 e^{-\sigma/E} \tag{38}$$

Now, for the minor axis, the second of Eq. (35) has

$$du_2^b = \frac{x_2}{E}\left(1 + 2\frac{a}{b}\right)d\sigma$$

Introducing $db = du_2^b$, $x_2 = b$, and the expression for a of Eq. (38), we obtain a first order linear differential equation in b, namely

$$\frac{db}{d\sigma} - \frac{b}{E} = \frac{2a_0}{E} e^{-\sigma/E}$$

Upon integrating we get

$$b = 2a_0 \text{sh}\, \sigma/E + b_0 e^{\sigma/E} \tag{39}$$

Here and henceforth, the Russian notation for hyperbolic functions is used for compactness. Equations (38) and (39) are our integrated elasticity solution for the lengths of the ellipse semi-axes.

Turning to the stress fields, these also involve integrals that are only readily tractable at the axis tips on the hole boundary. However, these are the locations of the peak tensile and compressive stresses. Drawing on the linear elasticity solution in Inglis [19], we have, at $X_1 = \pm a_0$, $X_2 = 0$

$$\sigma_{22}^{\max} = \left(1 + 2\frac{a_0}{b_0}\right)\sigma \tag{40}$$

Here the superscript max denotes the peak tensile stress. Hence the stress differential at the tip of the major axis of the elliptical hole can be written as

$$d\sigma_{22}^{\max} = \left(1 + 2\frac{a}{b}\right)d\sigma$$

Now substituting Eqs. (38) and (39) and integrating, we obtain the peak tensile stress

$$\sigma_{22}^{\max} = E \ln\left[\left(1 + \frac{a_0}{b_0}\right)e^{2\sigma/E} - \frac{a_0}{b_0}\right] - \sigma \tag{41}$$

Again drawing on Inglis [19], we find that $\sigma_{11} = -\sigma$ at $X_1 = 0$, $X_2 = \pm b_0$. Hence $d\sigma_{11} = -d\sigma$ and the trivial integration yields

$$\sigma_{11}^{\min} = -\sigma \tag{42}$$

where the superscript min denotes the peak compressive stress. Equations (41) and (42) are our integrated elasticity solution for the stress at the semi-axes of an elliptical hole under uniform uniaxial tension in the far field.

The elliptical hole in a thin plate under all-round tension admits to a similar treatment within integrated elasticity. Such an analysis yields results consistent with some earlier ones, independently obtained in Griffith [2] and Mansfield [17]. The semi-axis lengths and maximum and minimum stresses on the hole boundary for this case are given by

$$a = a_0 \text{ch}\, \frac{2\sigma}{E} + b_0 \text{sh}\, \frac{2\sigma}{E}$$

$$b = a_0 \text{sh}\, \frac{2\sigma}{E} + b_0 \text{ch}\, \frac{2\sigma}{E} \tag{43}$$

and

$$\sigma_{22}^{\max} = E \ln\left[\text{ch}\, \frac{2\sigma}{E} + \frac{a_0}{b_0}\text{sh}\, \frac{2\sigma}{E}\right]$$

$$\sigma_{11}^{\min} = E \ln\left[\text{ch}\, \frac{2\sigma}{E} + \frac{b_0}{a_0}\text{sh}\, \frac{2\sigma}{E}\right] \tag{44}$$

for $a_0 > b_0$. Equations (43) and (44) complete our limited set of closed-form solutions for a plate with an elliptical hole.

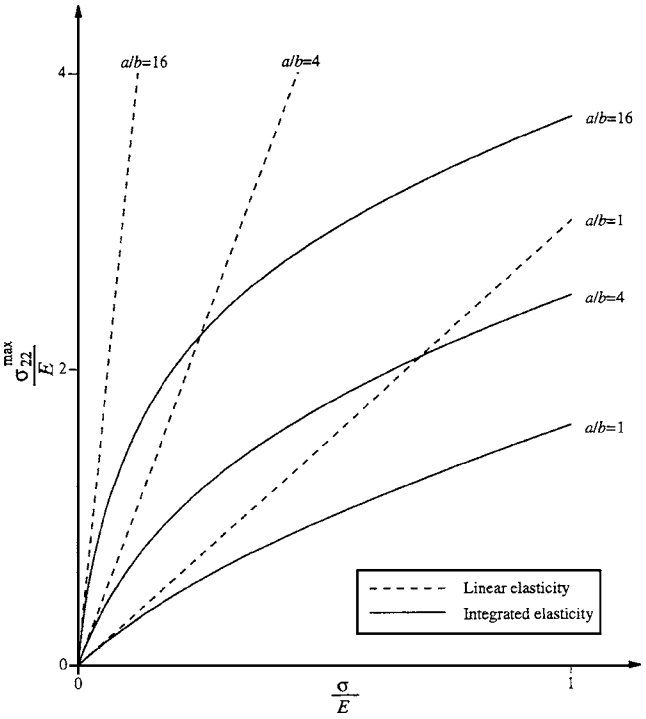

Fig. 12 Comparison of peak stress versus applied stress for linear and integrated elasticity

Some comments are in order on the integrated elasticity solutions in Eqs. (38), (39), and Eqs. (41) through (44). First, we observe that the two elliptical hole configurations treated do undergo rotations and so these solutions are approximate, as are their linear elasticity antecedents in this respect. Second, under the limit $\sigma/E \to 0$, we recover the corresponding linear elasticity solutions, as should be the case. That is, $a = a_0$, $b = b_0$ for both types of loading, and Eqs. (40) and (42) for uniaxial tension, $\sigma_{22}^{\max} = 2a_0\sigma/b_0$, $\sigma_{11}^{\min} = 2b_0\sigma/a_0$ for all-round tension. Third, under the limit $b_0 \to 0$, the elliptical hole becomes a mathematically sharp crack. For both loading configurations considered here, integrated elasticity then predicts a stress singularity at the crack tip. However, the tip stresses, $\sigma_{22}^{\max}$ of Eqs. (41) and (44), now increase only as $O(\ln(b_0))$ as $b_0 \to 0$. This is in contrast to classical elasticity which has peak stresses of $O(1/b_0)$ as $b_0 \to 0$.

The last result for the limit as $b_0 \to 0$ reflects the general reduction in peak stress that attends integrated elasticity for this configuration. This is in contrast with some earlier configurations, where tracking the deformation generally resulted in higher stresses due to thinning and other effects. To illustrate the present case we plot peak stress response for integrated elasticity for various elliptical holes under uniaxial tension. More precisely, $\sigma_{22}^{\max}$ from Eq. (41) for $a/b = 1, 4, 16$ (Fig. 12). For comparison, we include the corresponding peak stress response for linear elasticity. That is, $\sigma_{22}^{\max}$ from Eq. (40). The reduction in stress evident in Fig. 12 with integrated elasticity results from its tracking of the progressive blunting of the ellipse, something which linear elasticity does not do.

As in previous sections, we seek to ascertain whether integrated elasticity agrees better than linear elasticity with the physical response in instances of moderate deformation of elastic materials. To this end, we consider experimental data furnished by Mansfield [17]. In Ref. [17], two thin rubber sheets with a razor-sharp crack are subjected to biaxial tension, and the changes in the crack profile are recorded as it deforms. In Fig. 13, we reproduce measured data from Ref. [17] for the semi-length of the crack plotted against the normalized applied stress as load increases. This

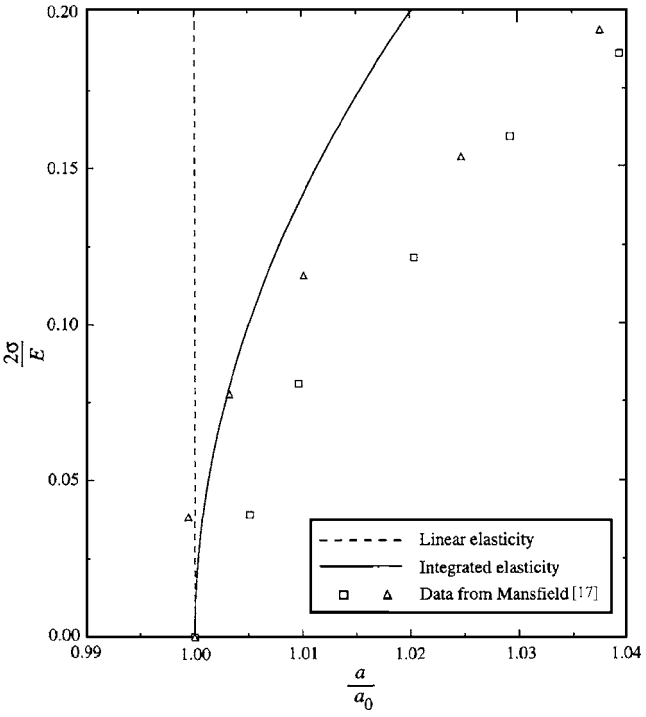

Fig. 13 Crack length response of a rubber sheet under tension (data from Mansfield [17])

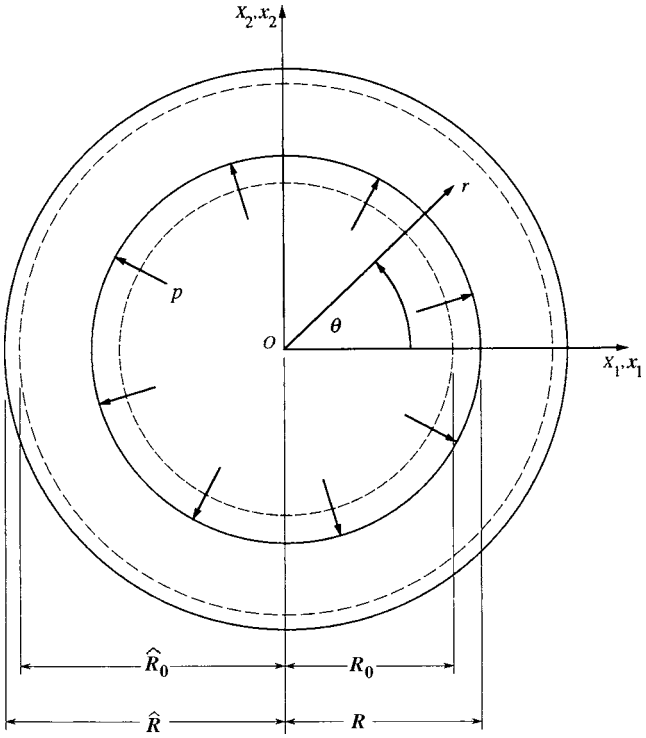

Fig. 14 Cross section of a thick-walled spherical pressure vessel

length corresponds to a under the limit $b_0 \to 0$ for the elliptical hole. Thus, for comparison, we overlay on this plot the predictions of linear elasticity, namely that $a=a_0$, and of integrated elasticity which has $a=a_0\mathrm{ch}(\sigma/E)$ (see Eq. (43) with $b_0=0$). In the latter we use the same value of E as is implicit in Mansfield [17]. The results from Ref. [17] agree fairly well qualitatively with the predictions of integrated elasticity in as much as the rubber's response is curved downwards: this is in contrast to linear elasticity which has that the major semi-axis length is constant under load. However, quantitative agreement is not good for the choice of Young's modulus in Mansfield [17].

6 Concluding Remarks

In this study, we consider some implications of relaxing the third linearization of the theory of linear elasticity which holds that the loads be applied entirely on the undeformed shape. The so relaxed theory applies load increments as deformation progresses and then integrates the result. Consequently, we term the resulting modified formulation *integrated elasticity*.

In certain instances, this integrated elasticity formulation is amenable to solution in closed form. This can be the case when classical elasticity results in a deformed shape that is either geometrically similar or weakly geometrically similar to its undeformed antecedent. This class of problems immediately admits to integral representations for its integrated elasticity solutions. On occasion such integrals may be evaluated exactly. All such solutions recover their linear elastic antecedents as the first order term when expanded in the limit as the applied loading tends to zero. It follows that integrated elasticity only differs significantly from linear elasticity when deformation levels are moderately high. Under every such circumstance as was investigated here, integrated elasticity captured the nature of the physical response better than linear elasticity, and actually agreed well with measured responses up to engineering strains of 30%. This can reasonably be expected to be the case in further like configurations.

Acknowledgment

We wish to thank J. W. Hutchinson, of Harvard University, for directing our attention to Mansfield's report, Ref. [17].

Appendix: Pressure Within Thick-Walled Spherical and Cylindrical Vessels

Here we provide the complete stress and displacement fields for the integrated elasticity solutions for spherical and cylindrical, thick-walled, pressure vessels. We outline the analysis and give results for the spherical vessel, and just report the results for the cylinder vessel which admits to a similar treatment.

The spherical pressure vessel occupies an undeformed region in space with inner radius R_0, and outer radius $\hat{R}_0$. Under internal pressure p, the radii become R and $\hat{R}$, respectively (Fig. 14). For this spherical pressure vessel, the formulation is the same as that of Sec. 4 for the thin-walled vessel, except for the absence of averaging through the thickness.

As a result of sharing common elements with its formulation, the thick-walled sphere has the same incremental fields as the unaveraged thin-walled sphere. Thus these unaveraged fields are given by Eqs. (26) and (27), with $\hat{R}$ substituted for the sum of the inner radius and the thickness. Hence Eq. (27) yields the differential expressions for both the inner and outer radii, namely

$$dR = \frac{R^4}{\hat{R}^3 - R^3}\frac{dp}{E}\left[1 - 2\nu + (1+\nu)\frac{\hat{R}^3}{2R^3}\right]$$

$$d\hat{R} = \frac{R^3\hat{R}}{\hat{R}^3 - R^3}\frac{dp}{E}\left[1 - 2\nu + \frac{1}{2}(1+\nu)\right] \tag{A1}$$

Each equation in (A1) involves all three variables, R, $\hat{R}$, and p. Now, though, integration cannot proceed as simply as in Eq. (29) et seq. via the direct elimination of a variable then separating remaining variables. However, we can proceed if we recognize

that the number of dimensions characterizing the cross section can be reduced if we scale the outer radius by the inner. That is, we take

$$\hat{R} = \lambda R$$

The differential for $\hat{R}$ is then given by

$$d\hat{R} = \lambda dR + R d\lambda$$

On substituting for $\hat{R}$ and $d\hat{R}$, we get

$$\frac{dR}{R} = \frac{1}{(\lambda^3 - 1)}\left[1 - 2\nu + \frac{1}{2}(1+\nu)\lambda^3\right]\frac{dp}{E}$$

$$\frac{d\lambda}{\lambda} = -\frac{1}{2}(1+\nu)\frac{dp}{E} \tag{A2}$$

Now the last of (A2) involves only two variables, thereby enabling integration for λ. Substituting the resulting expression for λ into the first of (A2), we obtain an expression for R. Hence we have

$$\lambda = \lambda_0 e^{-(1+\nu)p/2E}$$

$$\ln\frac{R}{R_0} = -(1-2\nu)\frac{p}{E} - \frac{1-\nu}{1+\nu}\ln\left[\frac{\lambda^3 - 1}{\lambda_0^3 - 1}\right] \tag{A3}$$

where $\lambda_0 = \hat{R}_0/R_0$. To obtain the distribution of the radial displacement across the thickness of the vessel, we start by writing the differential of the displaced radial coordinate r, from Eq. (27), as

$$dr = \frac{rR^3}{\hat{R}^3 - R^3}\left[1 - 2\nu + (1+\nu)\frac{\hat{R}^3}{2r^3}\right]\frac{dp}{E}$$

Defining the dimensionless radius $\rho = r/R$, we recast the above expression in terms of ρ, R, and λ

$$Rd\rho + \rho dR = \frac{\rho R}{\lambda^3 - 1}\left[1 - 2\nu + (1+\nu)\frac{\lambda^3}{2\rho^3}\right]\frac{dp}{E}$$

Dividing by ρR and using the first of (A2), we obtain

$$\frac{\rho^2 d\rho}{1 - \rho^3} = \frac{\lambda^3(1+\nu)}{2(\lambda^3 - 1)}\frac{dp}{E}$$

We then use the first of (A3) to substitute for λ and integrate, obtaining

$$\ln\left[\frac{\rho^3 - 1}{\rho_0^3 - 1}\right] = -\frac{3}{2}(1+\nu)\frac{p}{E} + \ln\left[\frac{\lambda_0^3 - e^{\frac{3(1+\nu)p}{2E}}}{\lambda_0^3 - 1}\right]$$

where ρ_0 is r/R in the undeformed state. The expressions for the radial and hoop stresses are obtained in similar fashion in terms of λ and ρ, starting from Eq. (26).

As with the results in Sec. 4, expressions here are more compact when expressed in terms of the shear modulus G rather than Young's modulus E. The complete integrated elasticity solution for a thick-walled spherical vessel is then given by

$$\sigma_{rr} = -p - 2(m-1)G\ln\left[\frac{\rho}{\rho_0}\right], \quad \sigma_{\theta\theta} = -p + 2G\ln\left[\frac{\rho(\rho_0^m - 1)}{\rho_0(\rho^m - 1)}\right]$$

$$\frac{R}{R_0} = e^{-(1-2\nu)p/2m_\nu G}\left[\frac{\lambda_0^m - 1}{\lambda^m - 1}\right]^{(1-\nu)/m_\nu}, \quad \frac{\lambda}{\lambda_0} = e^{-p/2(m-1)G}$$

$$\frac{\rho^m - 1}{\lambda^m - 1} = \frac{\rho_0^m - 1}{\lambda_0^m - 1} \tag{A4}$$

where $m_\nu = 1 - 2\nu + \nu m$, and $m = 3$ with $\sigma_{\phi\phi} = \sigma_{\theta\theta}$ for the thick-walled spherical pressure vessel. In (A4), we introduce the index m and related variable m_ν so as to provide the corresponding results for a thick-walled cylindrical pressure vessel in plane strain. These are derived in an analogous manner to the sphere, and the final results take the same form. That is, as in (A4) but for $m = 2$. Expanding (A4) for small p/G recovers the linear elasticity results for both the thick-walled sphere and cylinder (see, e.g., Sokolnikoff [8], Arts. 94 and 81, respectively).

References

[1] Frisch-Fay, R., 1962, *Flexible Bars*, Butterworth, Inc. Washington.
[2] Griffith, A. A., 1920, "The Phenomena of Rupture and Flow in Solids," Philos. Trans. R. Soc. London, Ser. A, **221**, pp. 163–198.
[3] Truesdell, C., 1952, "The Mechanical Foundations of Elasticity and Fluid Mechanics," J. Rational Mech. Anal, **1** pp. 125–300.
[4] Murnaghan, F. D., 1949, "The Foundations of the Theory of Elasticity," in: *Non-Linear Problems in Mechanics of Continua*, American Mathematical Society, New York, pp. 158–174.
[5] Jaumann, G., 1911, "Geschlossenes System Physikalischer und Chemischer Differentialgesetze," Akad.Wiss. Wien Sitzber. (IIa), **120**, pp. 385–530.
[6] Hencky, H., 1929, "Das Superpositionsgesetz Eines Endlich Deformierten Relaxasionsfähigen Elastischen Kontinuums und Seine Bedeutung für Eine Exakte Ableitung der Gleichungen für die Zähe Flüssigkeit in der Eulerschen Form" Ann. Phys., **5**, pp. 617–630.
[7] Fung, Y. C., 1965, *Foundations of Solid Mechanics*, Prentice–Hall, Inc. Englewood Cliffs, NJ.
[8] Sokolnikoff, I. S., 1956, *Mathematical Theory of Elasticity*, 2nd ed., McGraw–Hill, New York.
[9] Ludwik, P., 1909 *Elemente der Technologischen Mechanik*, Springer, Berlin.
[10] Green, A. E., 1956, "Simple Extension of a Hypo-Elastic Body of Grade Zero Mechanics," J. Rational Mech. Anal. **5**, pp. 637–642.
[11] Rivlin, R. S., and Saunders, D. W., 1951, "Large Elastic Deformations of Isotropic Materials VII. Experiments on the Deformation of Rubber," Philos. Trans. R. Soc. London, Ser. A, **243**, pp. 251–288.
[12] Assaad, A. T., and Sinclair, G. B., 2005, "An Experimental Study of the Applicability of Integrated Elasticity to the Tension and Torsion of Rubber Materials," Report No. ME-MA7-05, Department of Mechanical Engineering, Louisiana State University, Baton Rouge.
[13] Treloar, L. R. G., 1975, *The Physics of Rubber Elasticity*, 3rd ed., Clarendon Press, Oxford.
[14] Ward, I. M., and Sweeney, J., 2004, *The Mechanical Properties of Solid Polymers*, 2nd ed., Wiley, Sussex, UK.
[15] Hart-Smith, L. J., 1966, "Elasticity Parameters for Finite Deformations of Rubber-Like Materials," Z. Angew. Math. Phys. **17**, pp. 608–626.
[16] Assaad, A. T., and Sinclair, G. B., 2000, "Some Experiments on the Size-Versus-Pressure Response of Balloons," Report No. SM 00-2, Department of Mechanical Engineering, Carnegie Mellon University, Pittsburgh.
[17] Mansfield, E. H., 1967, "On the Stresses Near a Crack in an Elastic Sheet," Technical Report No. 67030, Royal Aircraft Establishment, Cranfield, UK.
[18] Kolossoff, G., 1910, On an Application of the Theory of Complex Variables to the Two-Dimensional Problem of Elasticity Theory," Ph.D. dissertation, St. Petersburg; See also Z. Angew. Math. Phys. **62**, pp. 384–409.
[19] Inglis, C. E., 1913, "Stresses in a Plate due to the Presence of Cracks and Sharp Corners," Trans. INA **55**, pp. 219–241.
[20] Kondo, M., and Sinclair, G. B., 1982, "Stress and Displacement Fields for an Elliptical Hole in a Thick Elastic Plate Under tension," Report No. SM 82-15, Department of Mechanical Engineering, Carnegie Mellon University, Pittsburgh.

Identification of Linear Time-Varying Dynamical Systems Using Hilbert Transform and Empirical Mode Decomposition Method

Z. Y. Shi
Postdoctoral Research Fellow
e-mail: cezyshi@polyu.edu.hk

S. S. Law
Associate Professor
e-mail: cesslaw@polyu.edu.hk

Department of Civil and Structural Engineering,
Hong Kong Polytechnic University,
Yuk Choi Road,
Hunghom Kowloon,
Hong Kong oooo,
Hong Kong

This paper addresses the identification of linear time-varying multi-degrees-of-freedom systems. The identification approach is based on the Hilbert transform and the empirical mode decomposition method with free vibration response signals. Three-different types of time-varying systems, i.e., smoothly varying, periodically varying, and abruptly varying stiffness and damping of a linear time-varying system, are studied. Numerical simulations demonstrate the effectiveness and accuracy of the proposed method with single- and multi-degrees-of-freedom dynamical systems. [DOI: 10.1115/1.2188538]

1 Introduction

Linear time-invariant (LTI) systems are appropriate to model systems that have stationary properties. Linear time-varying (LTV) systems are frequently used to model systems that have nonstationary properties and undergo low magnitude vibrations. The identification of LTV dynamical systems has received increasing attention nowadays. In electrical engineering and control engineering, various identification techniques with time-varying systems have been proposed both by using single input and output time sequence and by using multiple input and output sequence [1–4]. In civil engineering and mechanical engineering, identification of LTV systems has been attracting considerable attention in recent years because most real structures exhibit nonstationary dynamical behavior during their service life. It is generally recognized that the LTV model is more appropriate and better than the LTI model to capture the instantaneous dynamical behaviors of the system, and it could be used to assess the condition of the system or to diagnose its failure [5,6].

Many discrete-time state-space identification algorithms, such as the eigensystem realization, singular value decomposition (SVD), observability range space extraction, etc., have been employed in the modal testing community. Starting from the 1990s, some efforts have been made in extending the discrete-time state-space methods to LTV systems [2,7]. A subspace-based identification technique [8] was proposed to describe linear time-varying systems subject to initial disturbance. The concept of pseudo-modal parameters is proposed to characterize the dynamic properties of LTV systems. The essence of the new algorithm is to form a series of the general Hankel matrices using an ensemble of response sequences. Then the SVD is used to extract observability range spaces and identify the pseudo-modal parameters. Experimental verification studies on an axially moving cantilever beam were addressed in Ref. [9].

Compared with the Fourier analysis, the wavelet transform (WT) makes use of adjustable window location and size to decompose signals and thus can obtain more time-localized information. The wavelet packet decomposition (WPD) is furthermore considered to be a powerful signal processing tool due to its rich library of redundant bases with arbitrary time-frequency resolution [10]. Many authors have recently addressed the identification problem based on WT theory, and a wavelet-based identification approach for nonlinear structural dynamic systems has been proposed [11]. Hou et al. [12] have developed a structural model with multiple breakable springs subjected to a harmonic excitation. Studies show that the WT can successfully be used to identify both abrupt and cumulative damages. A WPD-based method combined with the neural network technique was proposed for the damage assessment of structures [13]. Sun and Chang [14] made use of the combination of the wavelet packet feature extraction technique and a covariance-driven preprocessing procedure to deal with the output-only signal in developing a structural health monitoring method. All the above-mentioned approaches are only for cases of LTI systems. The wavelet-based identification approach for the analysis of linear time-varying systems was presented [15,16]. The identification algorithm focuses on the estimation of the parameters associated with a differential equation model relating input and the output measurements using the Galerkin approach.

The Hilbert transform (HT) also has the capability of decomposing measured signals in the time-frequency domain to capture the time-localized information such as the instantaneous frequency at a time instance. Successful approaches of identification for a special type of single-degree-of-freedom (SDOF) time-varying and nonlinear system have been developed with the Hilbert transform [17,18]. Then, the empirical mode decomposition combined with the Hilbert transform, noted as the Hilbert-Huang transform (HHT), has been proposed [19]. This method, which is based on the EMD and Hilbert transform, has been applied to identify the modal parameters of multi-degrees-of-freedom (MDOF) including not only the natural frequencies and damping ratios, but also the mode shapes as well as the mass, stiffness, and damping matrices of the linear systems [20]. Its application for identification of natural frequencies and dampings of in situ tall buildings using ambient wind vibration data has been investigated [21]. However, these HHT-based approaches are applicable only to the time-invariant systems.

In this paper a new identification approach for linear time-varying dynamical systems based on the Hilbert transform and the empirical mode decomposition method is proposed with free vi-

Contributed by the Applied Mechanics Division of ASME for publication in the JOURNAL OF APPLIED MECHANICS. Manuscript received May 2, 2005; final manuscript received January 17, 2006. Review conducted by I. Mezic. Discussion on the paper should be addressed to the Editor, Prof. Robert M. McMeeking, Journal of Applied Mechanics, Department of Mechanical and Environmental Engineering, University of California-Santa Barbara, Santa Barbara, CA 93106-5070, and will be accepted until four months after final publication of the paper itself in the ASME JOURNAL OF APPLIED MECHANICS.

bration response signals. Three types of time-varying systems are studied to demonstrate the effectiveness and accuracy of the proposed identification algorithm. The paper is organized as follows. Section 2 introduces the basic theory of the Hilbert transform and the empirical mode decomposition. Section 3 develops the identification technique for the linear time-varying multi-degrees-of-freedom system with free vibration response data. Section 4 presents two numerical examples to illustrate the use of the proposed approach and demonstrate its effectiveness. Section 5 gives a brief conclusion.

2 Theoretical Bases

2.1 Hilbert Transform. The behavior of the dynamic response signal of a time-varying nonlinear system is generally varying both in the time and frequency domains. Many transient responses exhibit this variation in an inconspicuous way. The Fourier transform cannot show the signal's instantaneous dynamic characters even if no information of the signal has been lost during the signal processing procedure. The best and successful approach to study this varying dynamic nature is the use of the Hilbert transform.

For an arbitrary dynamic response signal $y(t)$, the Hilbert transform of $y(t)$, denoted by $\tilde{y}(t)$, is given by

$$\tilde{y}(t) = \mathrm{HT}[y(t)] = \frac{1}{\pi} P \int_{-\infty}^{+\infty} \frac{y(\tau)}{t-\tau} d\tau \tag{1}$$

where P indicates the Cauchy principal value. With this definition, $y(t)$ and $\tilde{y}(t)$ form a complex conjugate pair, and the analytical signal $Y(t)$ of $y(t)$ is expressed as

$$Y(t) = y(t) + j\tilde{y}(t) = A(t)\exp[j\psi(t)] \tag{2a}$$

in which

$$y(t) = A(t)\cos[\psi(t)] \tag{2b}$$

$$A(t) = \sqrt{y^2(t) + \tilde{y}^2(t)} \tag{2c}$$

$$\psi(t) = \arctan[\tilde{y}(t)/y(t)] \tag{2d}$$

$A(t)$ is an envelope signal (the instantaneous amplitude), $\psi(t)$ is the instantaneous phase angle, and $j=(-1)^{1/2}$. The instantaneous frequency $\omega(t)$ of the signal is the time derivative of the instantaneous phase, obtained as

$$\omega(t) = \dot{\psi}(t) = \frac{y(t)\dot{\tilde{y}}(t) - \dot{y}(t)\tilde{y}(t)}{A^2(t)} \tag{3}$$

The time derivative of the instantaneous amplitude is also important to represent the analytic signal, expressed as

$$\dot{A}(t) = \frac{y(t)\dot{y}(t) + \tilde{y}(t)\dot{\tilde{y}}(t)}{A(t)} \tag{4}$$

Equations (1)–(4) only show the instantaneous behavior of a single frequency signal at any time t if the signal $y(t)$ is processed through the Hilbert transform. However, for a general signal at any time, there is a spectrum of frequencies at that time instance rather than just a single frequency. Therefore, to obtain a meaningful decomposition of a general signal in the time-frequency domain becomes very important in order to clearly show the instantaneous behavior of the signal at any time instance.

2.2 The Empirical Mode Decomposition. The method to decompose a general signal into n intrinsic mode functions (IMFs), such as $y(t)$ in Eq. (2), is proposed by Huang et al. [19] using the empirical mode decomposition (EMD) approach.

An IMF should satisfy two conditions: (a) in the whole range of data, the number of extrema and the number of zero crossings must either be equal or differ at most by one, and (b) at any point, the mean value of the envelope defined by the local maxima and the envelope defined by the local minima is zero. Huang et al. used the sifting process to decompose a general signal and obtain its IMFs. A step in the sifting process is to identify all the local maxima and minima of the signal and to connect all these local maxima and minima with two cubic splines as the upper envelope, and lower envelope respectively. The mean of the upper and lower envelopes is then found. If this mean satisfies the above two conditions, it is an IMF. The sifting processing is repeated by subtracting this mean from the original signal to form a new curve from which cubic splines are found for the upper and lower envelopes. The process is repeated to obtain more IMFs. Suppose n intrinsic mode functions are obtained after all the sifting processes. The original signal can be expressed as

$$y(t) = \sum_{j=1}^{n} y_j(t) + r(t) \tag{5}$$

in which $y_j(t)$, $j=1,2,\ldots,n$, are the IMFs of the original signal and $r(t)$ is the residue, which is a monotonic function from which no more IMFs can be extracted. Such a process is referred to as the EMD method.

3 Identification Technique via Free Vibration Data

The equation of free vibration of a linear time-varying multi-degree-of-freedom (MDOF) system can be expressed as

$$\mathbf{M}(t)\ddot{\mathbf{y}}(t) + \mathbf{C}(t)\dot{\mathbf{y}}(t) + \mathbf{K}(t)\mathbf{y}(t) = 0 \tag{6}$$

in which $\mathbf{y}(t)=[y_1(t), y_2(t), \ldots, y_n(t)]^T$ is the displacement vector, and $\mathbf{M}(t)$, $\mathbf{C}(t)$, and $\mathbf{K}(t)$ are $(n\times n)$ time-varying mass, damping, and stiffness matrices, respectively. For the linear system, the displacement vector can be expressed as the superposition of n IMFs. The ith element of the displacement vector can be denoted as

$$y_i(t) = \sum_{j=1}^{n} y_{ij}(t) = \sum_{j=1}^{n} A_{ij}(t)\cos[\psi_{ij}(t)] \quad (j = 1,2,\ldots,n) \tag{7}$$

in which $A_{ij}(t)\cos[\psi_{ij}(t)]$ is the jth IMF extracted for the ith element (which corresponds to the ith DOF) of the displacement vector, such as the IMF shown in Eq. (2).

According to Bedrosian's theorem [22] on the Hilbert transform of the product of two signals, consider the case of nonoverlapping spectra of the signals $f(t)$ and $g(t)$, where $f(t)$ is the low-pass portion of the signal and $g(t)$ is the high-pass portion of the signal. Then $\mathrm{H}[f(t)g(t)]=f(t)\mathrm{H}[g(t)]$, and we have

$$\mathrm{H}[\mathbf{M}(t)\ddot{\mathbf{y}}(t)] = \mathbf{M}(t)\mathrm{H}[\ddot{\mathbf{y}}(t)] = \mathbf{M}(t)\ddot{\tilde{\mathbf{y}}}(t) \tag{8a}$$

$$\mathrm{H}[\mathbf{C}(t)\dot{\mathbf{y}}(t)] = \mathbf{C}(t)\mathrm{H}[\dot{\mathbf{y}}(t)] = \mathbf{C}(t)\dot{\tilde{\mathbf{y}}}(t) \tag{8b}$$

$$\mathrm{H}[\mathbf{K}(t)\mathbf{y}(t)] = \mathbf{K}(t)\mathrm{H}[\mathbf{y}(t)] = \mathbf{K}(t)\tilde{\mathbf{y}}(t) \tag{8c}$$

Equation (8) implies that the coefficients, $\mathbf{M}(t)$, $\mathbf{C}(t)$, and $\mathbf{K}(t)$, do not vary quickly over time. This means Eq. (8) is not suitable for the abrupt varying systems. This will be further discussed in the simulation studies.

Use the Hilbert transform for both sides of Eq. (6), and together with Eqs. (8*a*)–(8*c*). The Hilbert transform of Eq. (6) becomes

$$\mathbf{M}(t)\ddot{\tilde{\mathbf{y}}}(t) + \mathbf{C}(t)\dot{\tilde{\mathbf{y}}}(t) + \mathbf{K}(t)\tilde{\mathbf{y}}(t) = 0 \tag{9}$$

Multiplying each term of Eq. (9) by j and adding it to the corresponding term of Eq. (6), a differential equation on the analytic signal is obtained as

$$\mathbf{M}(t)\ddot{\mathbf{Y}}(t) + \mathbf{C}(t)\dot{\mathbf{Y}}(t) + \mathbf{K}(t)\mathbf{Y}(t) = 0 \tag{10}$$

in which $\mathbf{Y}(t)=[Y_1(t), Y_2(t), \ldots, Y_n(t)]^T$ is the analytic signal of the displacement vector, and the ith element (which corresponds to the ith DOF) of the analytic signal can be written as Eq. (2) by

$$Y_i(t) = \sum_{j=1}^{n} Y_{ij}(t) = \sum_{j=1}^{n} A_{ij} \exp[j\psi_{ij}(t)] \tag{11}$$

in which

$$y_{ij}(t) = A_{ij}(t)\cos\ \psi_{ij}(t)$$

$$A_{ij}(t) = \sqrt{y_{ij}^2(t) + \tilde{y}_{ij}^2(t)}$$

$$\psi_{ij}(t) = \arctan[\tilde{y}_{ij}(t)/y_{ij}(t)]$$

Using the analytic signal from Eq. (11), and together with Eqs. (3) and (4), we have

$$\dot{Y}_{ij}(t) = Y_{ij}(t)[\dot{A}_{ij}(t)/A_{ij}(t) + j\omega_{ij}(t)] \tag{12}$$

$$\ddot{Y}_{ij}(t) = Y_{ij}(t)[\ddot{A}_{ij}(t)/A_{ij}(t) - \omega_{ij}^2(t) + j(2\dot{A}_{ij}(t)\omega_{ij}(t)/A_{ij}(t) + \dot{\omega}_{ij}(t))] \tag{13}$$

in which

$$\omega_{ij}(t) = \dot{\psi}_{ij}(t) = \frac{y_{ij}(t)\dot{\tilde{y}}_{ij}(t) - \dot{y}_{ij}(t)\tilde{y}_{ij}(t)}{A_{ij}^2(t)} = \mathrm{Im}\left[\frac{\dot{Y}_{ij}(t)}{Y_{ij}(t)}\right] \tag{14a}$$

$$\dot{A}_{ij}(t) = \frac{y_{ij}(t)\dot{y}_{ij}(t) + \tilde{y}_{ij}(t)\dot{\tilde{y}}_{ij}(t)}{A_{ij}(t)} = A_{ij}\,\mathrm{Re}\left[\frac{\dot{Y}_{ij}(t)}{Y_{ij}(t)}\right] \tag{14b}$$

$$\dot{\omega}_{ij}(t) = \mathrm{Im}\left[\frac{\ddot{Y}_{ij}(t)}{Y_{ij}(t)}\right] - 2\frac{\dot{A}_{ij}(t)\omega_{ij}(t)}{A_{ij}(t)} \tag{14c}$$

$$\ddot{A}_{ij}(t) = A_{ij}(t)\left(\mathrm{Re}\left[\frac{\ddot{Y}_{ij}(t)}{Y_{ij}(t)}\right] + \omega_{ij}^2(t)\right) \tag{14d}$$

The free vibration of the linear time-varying MDOF system in Eq. (10) can be solved by substituting $\ddot{\mathbf{Y}}$ and $\dot{\mathbf{Y}}$ of Eqs. (12) and (13), and using Eqs. (11) and (14). Assuming the mass to be known, Eq. (10) can be simplified and written in compact matrix notation for the jth IMF of the analytic signal.

$$\mathbf{P}_j^c\boldsymbol{\beta}_j^c + \mathbf{P}_j^k\boldsymbol{\beta}_j^k = \mathbf{P}_j^m \tag{15}$$

in which $\boldsymbol{\beta}_j^c = \{c_1\ c_2\ \cdots\ c_i\ \cdots\ c_n\}^T$, $\boldsymbol{\beta}_j^k = \{k_1\ k_2\ \cdots\ k_i\ \cdots\ k_n\}^T$, and

$$\mathbf{P}_j^c = \begin{bmatrix} h_{1j}^c Y_{1j} & h_{1j}^c Y_{1j} - h_{2j}^c Y_{2j} & & & & \\ & h_{2j}^c Y_{2j} - h_{1j}^c Y_{1j} & h_{2j}^c Y_{2j} - h_{3j}^c Y_{3j} & & & \\ & & \cdots & \cdots & & \\ & & & h_{ij}^c Y_{ij} - h_{i-1j}^c Y_{i-1j} & h_{ij}^c Y_{ij} - h_{i+1j}^c Y_{i+1j} & \\ & & & & \cdots & \cdots \\ & & & & & h_{nj}^c Y_{nj} - h_{n-1j}^c Y_{n-1j} \end{bmatrix} \tag{16}$$

$$\mathbf{P}_j^k = \begin{bmatrix} Y_{1j} & Y_{1j} - Y_{2j} & & & & \\ & Y_{2j} - Y_{1j} & Y_{2j} - Y_{3j} & & & \\ & & \cdots & \cdots & & \\ & & & Y_{ij} - Y_{i-1j} & Y_{ij} - Y_{i+1j} & \\ & & & & \cdots & \cdots \\ & & & & & Y_{nj} - Y_{n-1j} \end{bmatrix} \tag{17}$$

$$\mathbf{P}_j^m = \{-m_1 h_{1j}^m Y_{1j} \quad -m_2 h_{2j}^m Y_{2j} \quad \cdots \quad -m_i h_{ij}^m Y_{ij} \quad \cdots \quad -m_n h_{nj}^m Y_{nj}\}^T \tag{18}$$

The coefficients h_{ij}^c and h_{ij}^m in Eqs. (16) and (18) are

$$h_{ij}^c = \frac{\dot{A}_{ij}(t)}{A_{ij}(t)} + j\omega_{ij}(t) \tag{19}$$

$$h_{ij}^m = \left[\frac{\ddot{A}_{ij}(t)}{A_{ij}(t)} - \omega_{ij}^2(t)\right] + j\left[\frac{2\dot{A}_{ij}(t)\omega_{ij}(t)}{A_{ij}(t)} + \dot{\omega}_{ij}(t)\right] \tag{20}$$

The complex Eq. (15) can be separated into two equations according to the real and imaginary parts, and then the two parts can be assembled in the following form,

$$\begin{bmatrix} \mathrm{Re}(\mathbf{P}_i^c) & \mathrm{Re}(\mathbf{P}_i^k) \\ \mathrm{Im}(\mathbf{P}_i^c) & \mathrm{Im}(\mathbf{P}_i^k) \end{bmatrix} \begin{Bmatrix} \boldsymbol{\beta}_i^c \\ \boldsymbol{\beta}_i^k \end{Bmatrix} = \begin{Bmatrix} \mathrm{Re}(\mathbf{P}_i^m) \\ \mathrm{Im}(\mathbf{P}_i^m) \end{Bmatrix} \tag{21}$$

For an n DOF linear time-varying system, Eq. (21) contains $2n$ time-varying unknown parameters and $2n$ time-varying equations for each IMF of the original signal. Therefore, each IMF extracted from the original signal can be used in Eq. (21) to solve for one set of identification results. This is an important advantage of the proposed method in practical system identification as only one set of IMFs is required to solving all the time-varying unknown system parameters.

For a single-degree-of-freedom system, the identified results from Eq. (21) can be simplified and written as the following explicit expressions, which are the same as presented in Ref. [17].

$$c(t) = -m\left(\frac{2\dot{A}(t)}{A(t)} + \frac{\dot{\omega}(t)}{\omega(t)}\right) \tag{22a}$$

$$k(t) = m\omega_0^2(t) \tag{22b}$$

in which

$$\omega_0^2(t) = \frac{k(t)}{m} = \omega^2(t) - \frac{\ddot{A}(t)}{A(t)} + \frac{2\dot{A}^2(t)}{A^2(t)} + \frac{\dot{A}(t)\dot{\omega}(t)}{A(t)\omega(t)} \tag{23a}$$

$$\omega(t) = \dot{\psi}(t) = \frac{y(t)\dot{\tilde{y}}(t) - \dot{y}(t)\tilde{y}(t)}{A^2(t)} = \mathrm{Im}\left[\frac{\dot{Y}(t)}{Y(t)}\right] \tag{23b}$$

$$\dot{A}(t) = \frac{y(t)\dot{y}(t) + \tilde{y}(t)\dot{\tilde{y}}(t)}{A(t)} = A(t)\mathrm{Re}\left[\frac{\dot{Y}(t)}{Y(t)}\right] \tag{23c}$$

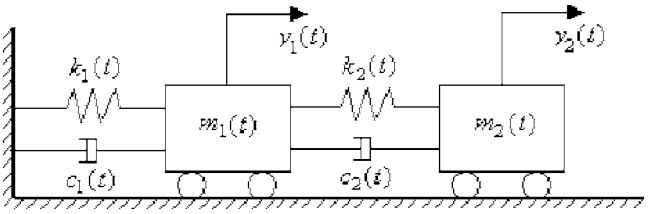

Fig. 1 2 DOF linear time-varying system

$$\dot{\omega}(t) = \mathrm{Im}\left[\frac{\ddot{Y}(t)}{Y(t)}\right] - 2\frac{\dot{A}(t)\omega(t)}{A(t)} \tag{23d}$$

$$\ddot{A}(t) = A(t)\left(\mathrm{Re}\left[\frac{\ddot{Y}(t)}{Y(t)}\right] + \omega^2(t)\right) \tag{23e}$$

4 Simulation Results

To demonstrate the effectiveness and accuracy of the proposed identification method for the linear time-varying system, two numerical examples are presented in this section. One example is a single-degree-of-freedom mass-spring-damping dynamical system. Another system with two degrees-of-freedom is shown in Fig. 1, in which the two stiffness coefficients and the two damping coefficients are assumed to be time dependent, and the mass coefficients are known. Three different types of time variation are studied, which are respectively the smoothly varying system, the periodically varying system, and the abruptly varying system. The response signals of the systems used to perform the identification can be the displacement, velocity, and acceleration time sequences, which are obtained from the numerical solutions of the free vibration differential equations using the Newton-Raphson method [23]. The time interval between two data points in the analysis is

$$\Delta t = \frac{T}{N} = \frac{10}{1024} \approx 0.01 \text{ s}$$

The identification procedure can be summarized as follows: (1) The free vibration response signals obtained from the numerical solution of the governing differential equations using the Newton-Raphson method are decomposed based with the EMD method. Each IMF is extracted from the response signals, which is suitable for analysis with the Hilbert transform. (2) Each IMF is analyzed using the Hilbert transform. Coefficients of instantaneous amplitude, instantaneous frequency, and their time derivatives are computed according to Eq. (14). All these coefficients are time dependent. (3) At each time step, each element of the matrices in Eqs. (16)–(18) is then calculated using these coefficients. Then Eq. (21) is constructed. (4) Equation (21) is solved to identify the stiffness and damping coefficients at this time step. (5) Repeat steps (3) and (4) to obtain results for the whole time history.

4.1 Identification of Smoothly Varying Systems. This section addresses the identification of the smoothly varying changes in the stiffness and/or damping of the linear time-varying systems. For a SDOF system, the stiffness and damping variations are given by

$$k(t) = 100\pi^2 - 10\pi^2 t, \quad c(t) = 0.66 + 0.15t, \quad \text{when } t < 3$$

$$k(t) = 70\pi^2, \quad c(t) = 1.11, \quad \text{when } t \geq 3$$

The mass coefficient is assumed to be known ($m=1$). The initial conditions for the free vibration analysis are $y_0=1.0$ and $\dot{y}_0=0$.

Identification results are shown in Figs. 2 and 3. Figure 2 shows the identified stiffness coefficients versus time. The identified stiffness coefficient is denoted with the dashed line and the true stiffness coefficient is denoted with the solid line. Likewise, the identified damping results are shown in Fig. 3. The identified stiffness and damping coefficients are close to the true values.

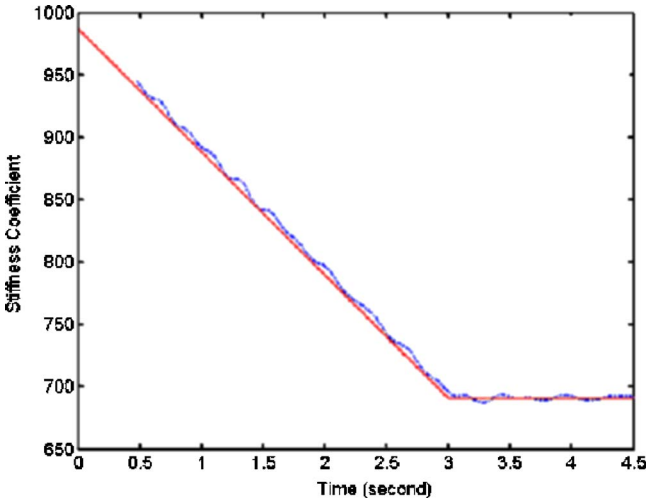

Fig. 2 Smoothly varying change of SDOF system: identified stiffness coefficient

For the 2-DOF system shown in Fig. 1, the stiffness coefficients are given by

$$k_1 = 40\,053, \quad k_2 = 87\,552 \quad \text{when } t < 1$$

$$k_1 = 40\,053, \quad k_2 = 87\,552 - 8755.2(t-1) \quad \text{when } 1 \leq t \leq 3$$

$$k_1 = 40\,053, \quad k_2 = 70\,042 \quad \text{when } t > 3$$

The damping coefficients and mass coefficients are assumed as constants: $c_1=30$, $c_2=0$, and $m_1=m_2=50$. The initial conditions for the free vibration analysis are $y_{10}=0.0$, $y_{20}=1.0$ and $\dot{y}_{10}=0$, $\dot{y}_{20}=0$.

Two IMFs are decomposed from the response signals. The stiffness coefficients are identified from each IMF and the average values of k_1 and k_2 identified from both IMFs are plotted in Figs. 4 and 5, respectively. Figure 6 shows the identified stiffness coefficient k_2 from only the second IMF. These results show the identification results are very close to the true values in the whole time period when using single IMF data or both IMFs data.

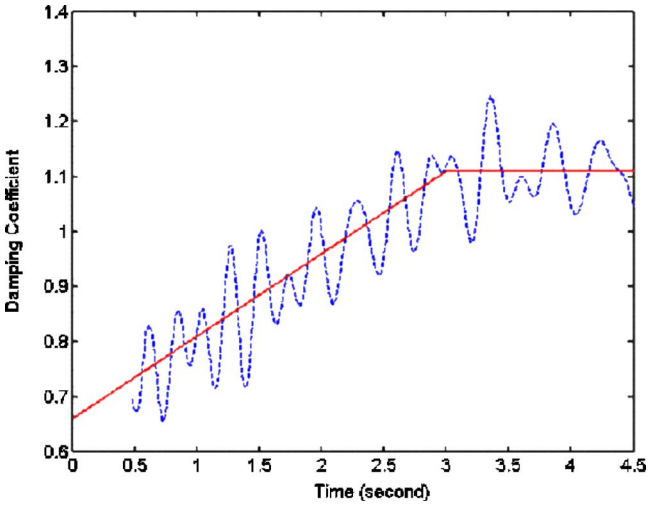

Fig. 3 Smoothly varying change of SDOF system: identified damping coefficient

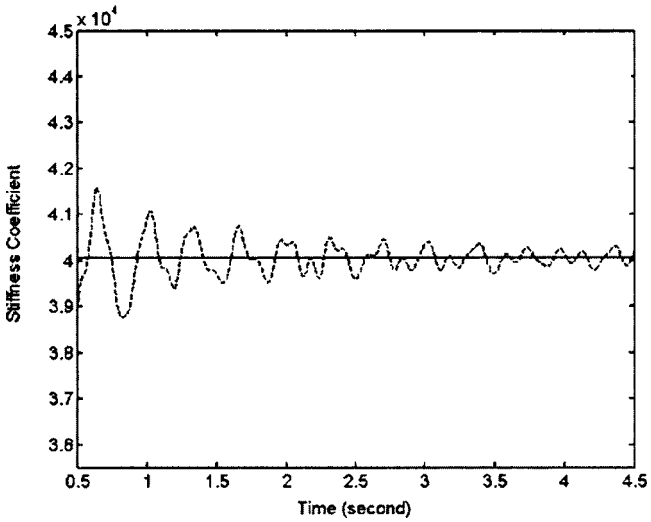

Fig. 4 Smoothly varying change of 2 DOF system: identified stiffness coefficient k_1 (from both IMFs)

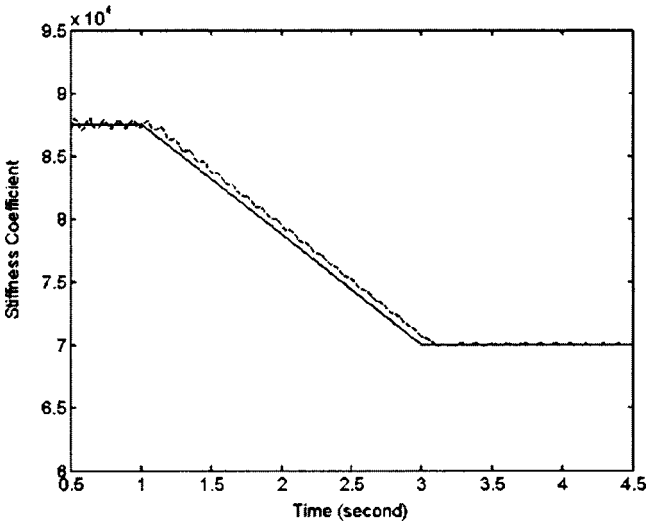

Fig. 6 Smoothly varying change of 2-MDOF system: identified stiffness coefficient k_2 (from the second IMF)

4.2 Identification of Abruptly Varying Systems. The case with abruptly varying stiffness in a linear time-varying system is discussed. In the SDOF system, the stiffness variation is given by $k(t)=100\pi^2$ for $t<1.5$, $k(t)=60\pi^2$ for $1.5\leqslant t\leqslant 3.5$, and $k(t)=80\pi^2$ for $t>3.5$. The damping coefficient is invariant at $c(t)=0.7$. The mass coefficient is assumed to be known ($m=1$). The initial conditions for the free vibration analysis are $y_0=1.0$ and $\dot{y}_0=0$.

The analysis results are shown in Figs. 7 and 8. Figure 7 shows the time-frequency distribution of the time-varying response signal. Two abrupt jumps in the instantaneous frequency at $t=1.5s$ and $t=3.5s$ are noted, suggesting that there are abrupt changes in the physical parameter of the system. The identified results in Fig. 8 with the dashed line shows the abrupt stiffness changes at $t=1.5s$ and $t=3.5s$, which accords with the observed changes in Fig. 7, and they match closely the true values which are denoted with the solid line in Fig. 8.

For the 2-DOF system, the stiffness coefficients are given by $k_1=40\,053$, $k_2=87\,552$, $c_1=30$, $c_2=0$ for $t\leqslant 3$, and $k_1=36\,048$, $k_2=70\,042$, $c_1=30$, $c_2=0$ for $t>3$. The mass coefficients are assumed to be known as $m_1=m_2=50$. The initial conditions for the free vibration analysis are $y_{10}=0.0$, $y_{20}=1.0$ and $\dot{y}_{10}=0$, $\dot{y}_{20}=0$.

The abrupt stiffness damages in k_1 and k_2 are identified using both IMFs, which are extracted from the response data based on the Hilbert transform. Results are shown in Figs. 9 and 10, respectively. The identified stiffness coefficients denoted with the dashed line are very close to the true values which are represented by the solid line.

However, it is noted from Figs. 8–10 that there exists larger identification error at the time instances when the system stiffness

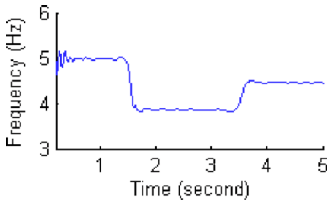

Fig. 7 Abruptly varying change of SDOF system: instantaneous frequency versus time

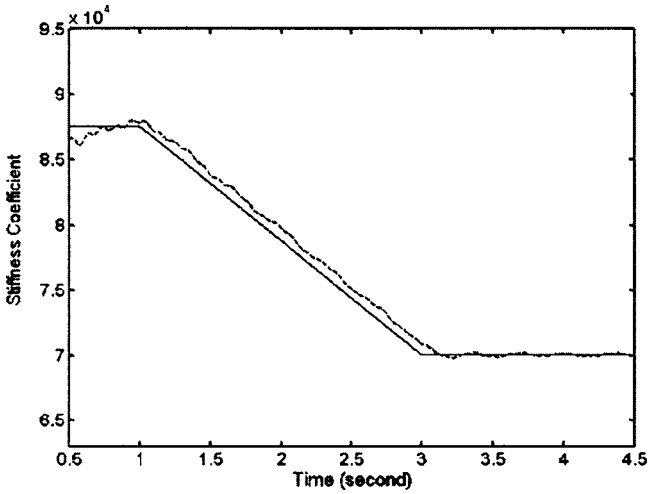

Fig. 5 Smoothly varying change of 2 DOF system: identified stiffness coefficient k_2 (from both IMFs)

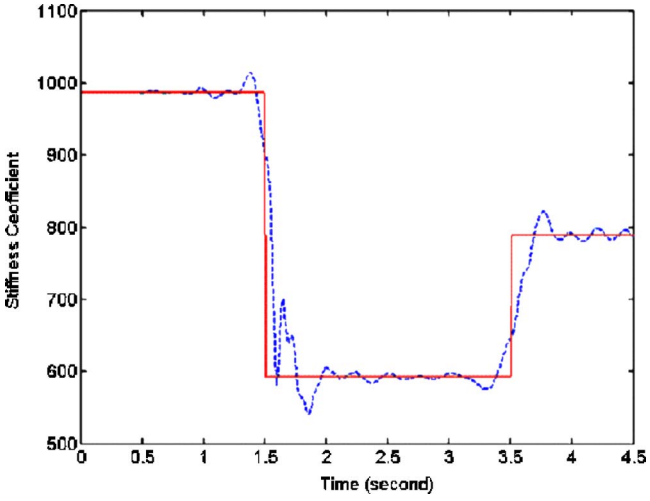

Fig. 8 Abruptly varying change of SDOF system: identified stiffness coefficient

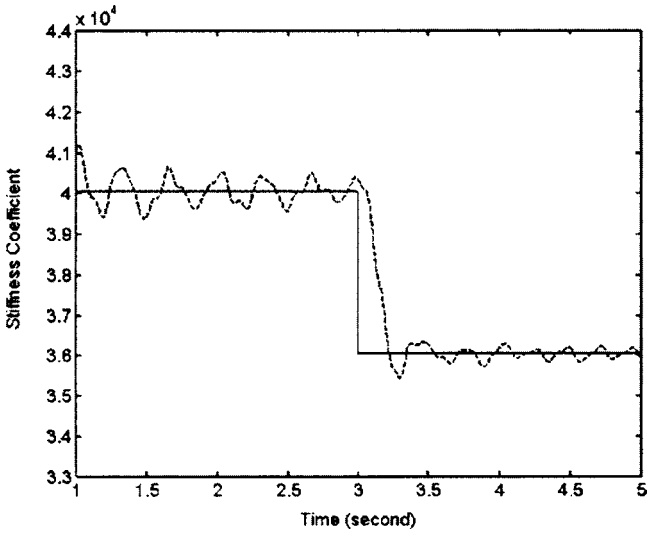

Fig. 9 Abruptly varying change of 2 DOF system: identified stiffness coefficient k_1 (from both IMFs)

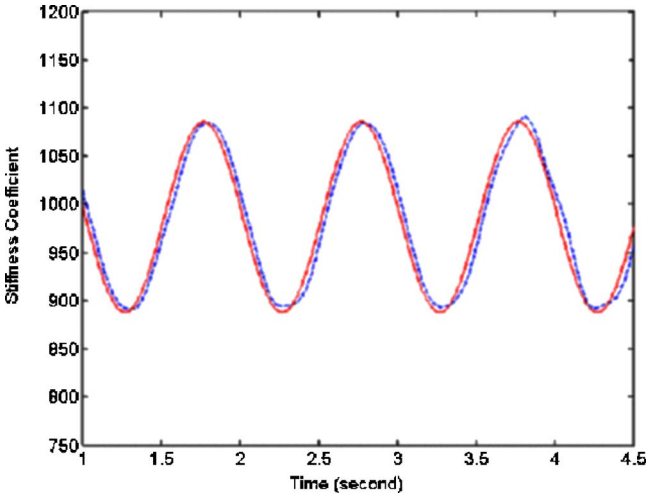

Fig. 11 Periodically varying change of SDOF system: identified stiffness coefficient

has abrupt changes. This indicates that the proposed method has poor capability in tracking the abrupt variations of the system parameters due to limitations in Eq. (8).

4.3 Identification of Periodically Varying Systems. This section addresses the identification of the periodically varying stiffness of the linear time-varying systems. For a SDOF system, the stiffness variation is given by $k(t)=100\pi^2-10\pi^2\sin(2\pi t)$, $c(t)=1.26$, and the mass coefficient is known ($m=1$). The initial conditions for the free vibration analysis are $y_0=1.0$ and $\dot{y}_0=0$.

Identification results are shown in Figs. 11 and 12. The identified stiffness and the damping results are shown varying closely around the true values.

For the 2 MDOF system shown in Fig. 2, the stiffness coefficients are given by

$$k_1 = 40\,053, \quad k_2 = 87\,552, \quad c_1 = 30, \quad c_2 = 0 \text{ for } t < 2$$

$$k_1 = 40\,053 - 4005.3\sin[\pi(t-2)], \quad k_2 = 87\,552, \quad c_1 = 30,$$

$$c_2 = 0 \text{ for } t \geqslant 2$$

The mass coefficients are assumed as constants: $m_1=m_2=50$. The initial conditions for the free vibration analysis are $y_{10}=0.0$, $y_{20}=1.0$ and $\dot{y}_{10}=0$, $\dot{y}_{20}=0$.

For the 2 MDOF system, two IMFs are decomposed from the response signals and they are used to identify the system parameters. The time-frequency distribution of the first IMF extracted from the response signal at the second DOF is shown in Fig. 13. It can be seen that there is a change in the periodical varying instantaneous frequency starting from $t=2s$. This phenomena indicates that a physical parameter change occurs at that time and this kind of change may be periodical if it is a stiffness change. The identified stiffness coefficient k_1 shown in Fig. 14 verifies the above observation. Other identified results on the coefficients k_2, c_1, and c_2 are shown in Figs. 15–17, respectively. All of them are identified using both IMFs data. The stiffness coefficient k_1 identified from using only the first IMF is shown in Fig. 18, which is similar to that obtained from both IMFs. All these results are found varying closely to the true values of the system.

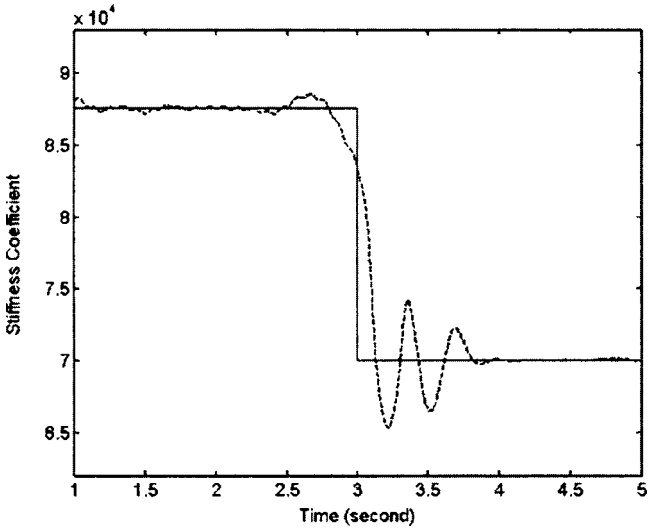

Fig. 10 Abruptly varying change of 2 DOF system: identified stiffness coefficient k_2 (from both IMFs)

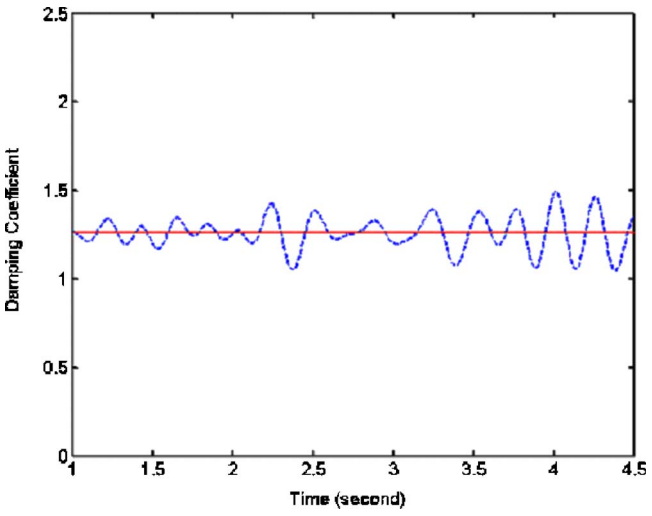

Fig. 12 Periodically varying change of SDOF system: identified damping coefficient

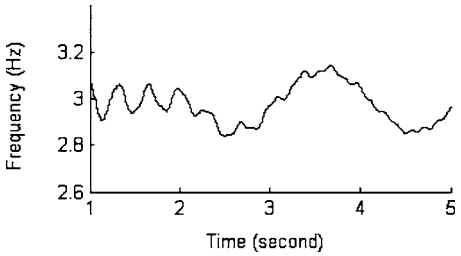

Fig. 13 Periodically varying change of 2 DOF system: instantaneous frequency versus time (from first IMF of the second DOF)

5 Conclusions

A new identification approach for a linear time-varying dynamical system is proposed based on the Hilbert transform and the empirical mode decomposition method using free vibration response time histories. A single-degree-of-freedom system and a multi-degree-of-freedom system have been studied to demonstrate

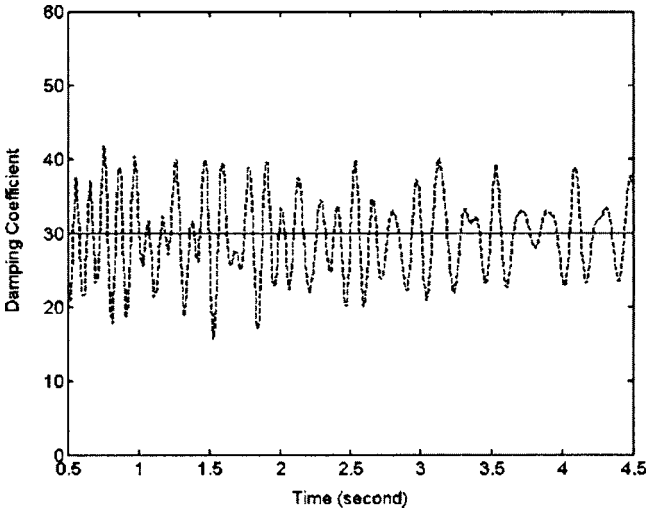

Fig. 16 Periodically varying change of 2 DOF system: identified damping coefficient c_1 (from both IMFs)

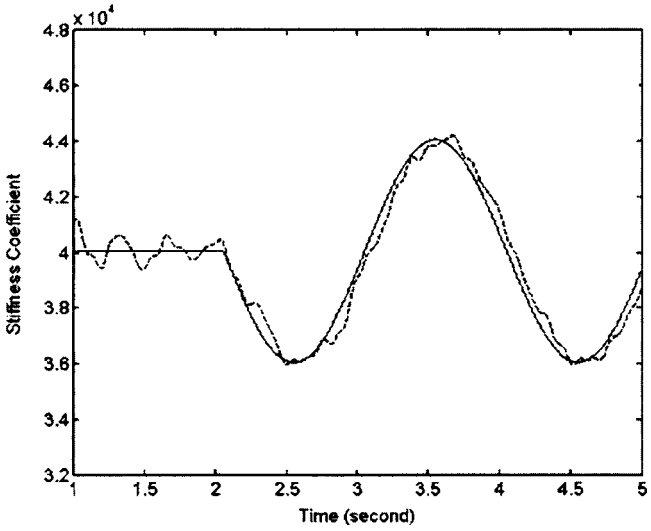

Fig. 14 Periodically varying change of 2 DOF system: identified stiffness coefficient k_1 (from both IMFs)

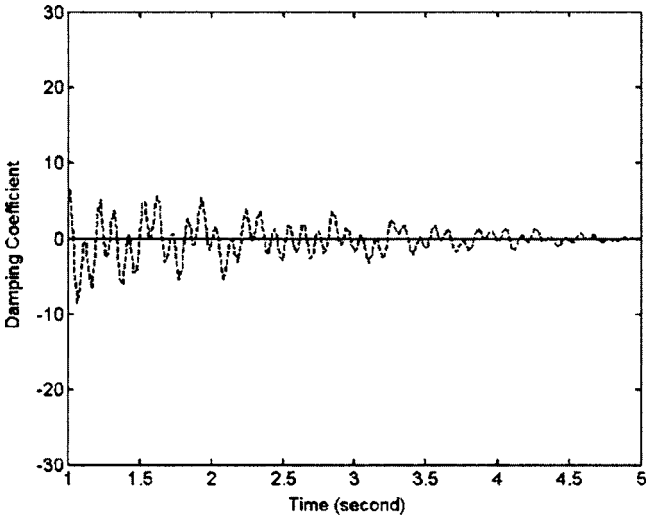

Fig. 17 Periodically varying change of 2 DOF system: identified damping coefficient c_2 (from both IMFs)

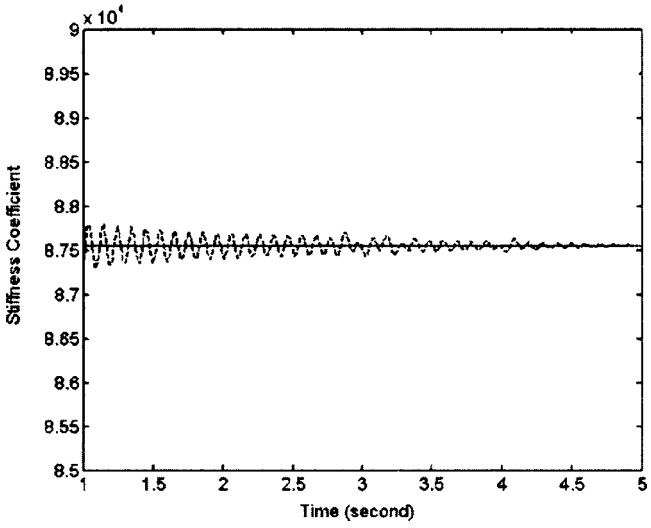

Fig. 15 Periodically varying change of 2 DOF system: identified stiffness coefficient k_2 (from both IMFs)

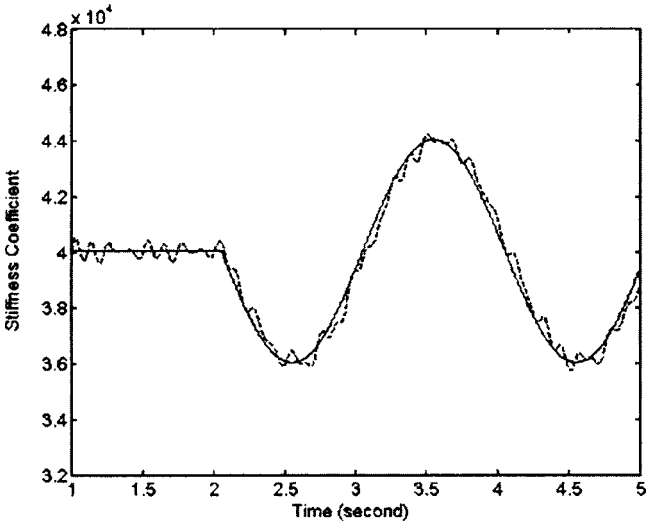

Fig. 18 Periodically varying change of 2 DOF system: identified stiffness coefficient k_1 (from the first IMF)

the effectiveness and accuracy of the proposed method. Three types of time-dependent stiffness and damping parameters, i.e., smoothly varying, periodically varying, and abruptly varying stiffness and damping of the linear time-varying system, are assumed and used in the above studies. The identification method may not be suitable for fast varying system parameters due to the assumption of nonoverlapping frequency range in the response and the system parameters, but simulation results show that the proposed approach has the capability of tracking these variations using single or more IMFs extracted from free vibration response signals. This is an important feature of the proposed system identification approach with a linear time-varying system because a single IMF can be extracted very conveniently from the vibration response signals in practice.

Acknowledgment

This research is supported by the National Natural Science Foundation of China through Grant No. 10372041 and a research grant from Hong Kong Polytechnic University Grant No. G-YX26.

References

[1] McNeil, J. B., Kearney, R. E., and Hunter, I. W., 1992, "Identification of Time-Varying Biological Systems from Ensemble Data," IEEE Trans. Biomed. Eng., **39**, pp. 1213–1225.
[2] Verhaegen, M., and Yu, X., 1995, "A Class of Subspace Model Identification Algorithms to Identify Periodically and Arbitrarily Time-Varying Systems," Automatica, **31**, pp. 201–216.
[3] Xu, X., and Agrawal, S. K., 2000, "Linear Time-Varying Dynamic Systems Optimization Via High-Order Method: A Sub-Domain Approach," ASME J. Vibr. Acoust., **122**(1), pp. 31–35.
[4] Tan, K. K., Huang, S. N., Lee, T. H., and Lim, S. Y., 2003, "A Discrete-Time Iterative Learning Algorithm for Linear Time-Varying Systems," Eng. Applic. Artif. Intell., **16**, pp. 185–190.
[5] Lin, C. C., Soong, T. T., and Natke, H. G., 1990, "Real-Time System Identification of Degrading Structures," J. Eng. Mech., **116**, pp. 2258–2274.
[6] Udwadia, F. E., and Jerath, N., 1980, "Time Variations of Structural Properties During Strong Ground Shaking," J. Eng. Mech. Div., Am. Soc. Civ. Eng., **106**, pp. 111–121.
[7] Shokoohi, S., and Silverman, L., 1987, "Identification and Model Reduction of Time-Varying Discrete-Time Systems," Automatica, **23**, pp. 509–521.
[8] Liu, K., 1997, "Identification of Linear Time-Varying Systems," J. Sound Vib., **204**, pp. 487–500.
[9] Liu, K., and Deng, L., 2004, "Experimental Verification of an Alogorithm for Identification of Linear Time-Varying Systems," J. Sound Vib., **279**, pp. 1170–1180.
[10] Learned, R. E., and Willsky, A. S., 1995, "A Wavelet Packet Approach to Transient Signal Classification," Appl. Comput. Harmon. Anal., **2**(3), pp. 265–278.
[11] Kitada, Y., 1998, "Identification of Nonlinear Structural Dynamic Systems Using Wavelets," J. Eng. Mech., **124**(10), pp. 1059–1066.
[12] Hou, Z., Noori, M., and Amand, R. S., 2000, "Wavelet-Based Approach for Structural Damage Detection," J. Eng. Mech., **124**(10), pp. 1059–1066.
[13] Sun, Z., and Chang, C. C., 2002, "Structural Damage Assessment Based on Wavelet Packet Transform," J. Eng. Mech., **128**(10), pp. 1354–1361.
[14] Sun, Z., and Chang, C. C., 2004, "Statistical Wavelet-Based Method for Structural Health Monitoring," J. Eng. Mech., **130**(7), pp. 1055–1062.
[15] Amaratunga, K., Williams, J. R., Qian, S., and Weiss, J., 1994, "Wavelet-Galerkin Solutions for One Dimensional Partial Differential Equations," Int. J. Numer. Methods Eng., **37**, pp. 2703–2716.
[16] Ghanem, R., and Romeo, F., 2000, "A Wavelet-Based Approach for the Identification of Linear Time-Varying Dynamic Systems," J. Sound Vib., **234**(4), pp. 555–576.
[17] Feldman, M., 1994, "Non-Linear System Vibration Analysis Using Hilbert Transform—I: Free Vibration Analysis Method FREEVIB," Mech. Syst. Signal Process., **8**(2), pp. 119–127.
[18] Feldman, M., 1994, "Non-Linear System Vibration Analysis Using Hilbert Transform—II: Forced Vibration Analysis Method FORCEVIB," Mech. Syst. Signal Process., **8**(3), pp. 309–318.
[19] Huang, N. E., Shen, Z., Long, S. R., Wu, M. C., Shih, H. H., Zheng, Q., Yen, N. C., Tung, C. C., and Liu, H. H., 1998, "The Empirical Mode Decomposition and Hilbert Spectrum for Nonlinear and Nonstationary Time Series Analysis," Proc. R. Soc. London, Ser. A, **454**, pp. 903–995.
[20] Yang, J. N., Lei, Y., Lin, S., and Huang, N., 2003, "System Identification of Linear Structures Based on Hilbert-Huang Spectral Analysis. Part 1: Normal Modes," Earthquake Eng. Struct. Dyn., **32**, pp. 1443–1467.
[21] Yang, J. N., Lei, Y., Lin, S., and Huang, N., 2004, "Identification of Natural Frequencies and Dampings of in Situ Tall Buildings Using Ambient Wind Vibration Data," J. Eng. Mech., **130**(5), pp. 570–577.
[22] Stefan, L. H., 1996, *Hilbert Transform in Signal Processing*, Artech House Inc., Boston.
[23] Chan, S. L., and Chui, P. P. T., 2000, *Non-Linear Static and Cyclic Analysis of Steel Frames With Semi-Rigid Connections*, Elsevier, New York.

A Discrete Quasi-Coordinate Formulation for the Dynamics of Elastic Bodies

G. M. T. D'Eleuterio
e-mail: gabriele.deleuterio@utoronto.ca

T. D. Barfoot
e-mail: tim.barfoot@utoronto.ca

Institute for Aerospace Studies,
University of Toronto,
Toronto, ON, M3H 5T6, Canada

The discretized equations of motion for elastic systems are typically displayed in second-order form. That is, the elastic displacements are represented by a set of discretized (generalized) coordinates, such as those used in a finite-element method, and the elastic rates are simply taken to be the time-derivatives of these displacements. Unfortunately, this approach leads to unpleasant and computationally intensive inertial terms when rigid rotations of a body must be taken into account, as is so often the case in multibody dynamics. An alternative approach, presented here, assumes the elastic rates to be discretized independently of the elastic displacements. The resulting dynamical equations of motion are simplified in form, and the computational cost is correspondingly lessened. However, a slightly more complex kinematical relation between the rate coordinates and the displacement coordinates is required. This tack leads to what may be described as a discrete quasi-coordinate formulation. [DOI: 10.1115/1.2189873]

1 Introduction

The dynamics of rapidly rotating elastic bodies has received considerable attention in recent years [1–7]. The principal motivation comes from robotics, where the demand for faster operation requires one to consider elasticity in the joints and links as well as a litany of other effects.

The approach normally taken in addressing this problem numerically is to discretize the elastic deformations and render the equations of motion as second-order differential equations in these coordinates. To account for fast rotational rates, it is imperative to consider quantities that tend as the square or even the cube of the elastic coordinates. Many of these make themselves present in the inertial terms as first-degree and second-degree corrections to the moments of mass of the body in question.[1]

The retention of these higher-degree terms means that the system mass matrix becomes dependent on the elastic coordinates, in essence on the shape of the body at any given time. In numerical integration, this matrix must be inverted or Gaussian elimination must be applied thereon to obtain the accelerations. These frequent operations add heavily to the computational cost.

A welcome alternative would be a choice of coordinates that would keep the system mass matrix constant. Such an alternative is afforded by the use of *quasi-coordinates*. Here, we propose to discretize the elastic displacement field and the elastic velocity field separately, which leads to a constant mass matrix. The two discretized fields are brought in accord via an appropriate kinematical relationship. The approach is, in fact, reminiscent of Euler's equations for rotational motion.

The term quasi-coordinate, or more properly *differentials or rates of quasi-coordinates* or even *quasi-velocities* as some authors prefer, alludes to the fact that the equation relating it to the configuration coordinates is not integrable. The situation calls to mind nonholonomic constraints. When quasi-coordinates are involved, a direct application of Lagrange's equations is not possible. The theory on the use of quasi-coordinates in Lagrangian dynamics was begun by Boltzmann [8] and developed by Hamel [9], and the resulting equations have become known as the Boltzmann-Hamel version of Lagrange's equations or simply the Boltzmann-Hamel equations [10].

Recently, Junkins and Schaub [11] presented a very general and most elegant approach to this problem. They have developed a formulation by which the mass matrix is diagonalized by eigendecomposition. To accomplish this, they employ quasi-velocities and take the Boltzmann-Hamel path to the equations of motion. The generality of their approach makes it applicable to the present problem as well. In our development, we take a different approach that specifically addresses the case of elastic continua and we seek only to obtain a constant mass matrix. Nevertheless, the spirit of our work is the same and, indeed, originally motivated by the same problems that motivated Junkins and Schaub, namely, multibody systems. Junkins and Schaub's method can also facilitate constraints; an issue we do not address at all here.

Now, one cannot enter this realm of inquiry without alighting on the problem of "geometric stiffening," for when considering inertial terms that involve nonlinear effects owing to deformation, it is only consistent to consider as well nonlinearity in the stiffness terms. There has been much written on this topic, and although our model will take this into account, we wish to make clear that it is not the central subject of this paper.

We shall first present a development of the second-order formulation followed by the first-order one using the Boltzmann-Hamel idea in conjunction with Hamilton's principle. In this procedure, the discretization of the elastic continuum occurs at the end. The results of a numerical example—the ever popular slender Euler-Bernoulli beam—will be reported for both formulations. It is demonstrated that the first-order development is not only analytically attractive but also, as our preliminary numerical results suggest, computationally more expedient.

2 A Typical Second-Order Formulation

Let us consider an elastic body $\mathcal{E}$, as shown in Fig. 1, and affix to this body a reference point O at which we place a reference frame $\mathcal{F}_\mathcal{E}$. The velocity of O and the angular velocity of $\mathcal{F}_\mathcal{E}$ relative to inertial space shall be given by $\mathbf{v}_0$ and $\boldsymbol{\omega}$ as expressed in $\mathcal{F}_\mathcal{E}$. All quantities in this development will be assumed to be ex-

[1]There is potentially a confusion in using the word *order* for it may refer to differential order as well as algebraic order. To avoid this, we shall restrict the use of the term *order* to the former and cmploy *degree*, which is customarily used in reference to polynomials, for the latter.

Contributed by the Applied Mechanics Divison of ASME for publication in the JOURNAL OF APPLIED MECHANICS. Manuscript received July 12, 2004; final manuscript received January 30, 2006. Review conducted by I. Mezic. Discussion on the paper should be addressed to the Editor, Prof. Robert M. McMeeking, Journal of Applied Mechanics, Department of Mechanical and Environmental Engineering, University of California—Santa Barbara, Santa Barbara, CA 93106-5070, and will be accepted until four months after final publication of the paper itself in the ASME JOURNAL OF APPLIED MECHANICS.

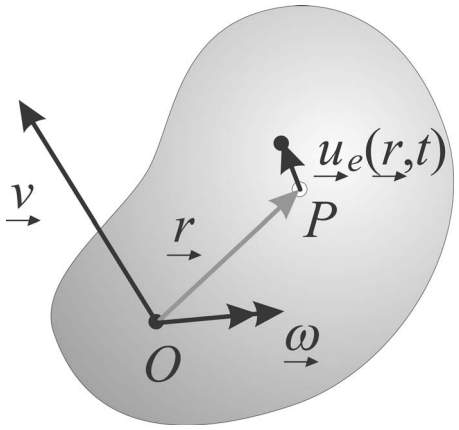

Fig. 1 An elastic body

pressed in the frame $\mathcal{F}_\mathcal{E}$ unless otherwise specified. The position of an arbitrary point P relative to O in the undeformed body shall be denoted by $\mathbf{r}$. The deformation P will be indicated by $\mathbf{u}_e(\mathbf{r},t)$.

The elastic displacement field $\mathbf{u}_e(\mathbf{r},t)$ will be discretized in the customary manner as

$$\mathbf{u}_e(\mathbf{r},t) = \sum_{\alpha=1}^{n} \boldsymbol{\psi}_\alpha(\mathbf{r}) q_\alpha(t) \tag{1}$$

where $\psi_\alpha(\mathbf{r})$ are basis functions satisfying the cantilever conditions at O. In the immediate sequel, we shall derive the second-order equations of motion for $\mathcal{E}$ using a Lagrangian approach.

2.1 Kinetic Energy. The kinetic energy of the body is given by

$$T = \frac{1}{2}\int_\mathcal{E} \mathbf{w}^T\mathbf{w}\, dm \tag{2}$$

where $dm=(\mathbf{r})dV$ is a mass element and $\sigma(\mathbf{r})$ is the mass density with dV being the volume element. The velocity field $\mathbf{w}(\mathbf{r},t)$ is

$$\mathbf{w}(\mathbf{r},t) = \mathbf{v}(t) + \dot{\mathbf{u}}_e(\mathbf{r},t) + \boldsymbol{\omega}(t)[\mathbf{r} + \mathbf{u}_e(\mathbf{r},t)] \tag{3}$$

Substituting (1) and (3) into (2) yields

$$T = \tfrac{1}{2}m\mathbf{v}^T\mathbf{v} + \tfrac{1}{2}\boldsymbol{\omega}^T\hat{\mathbf{J}}\boldsymbol{\omega} + \tfrac{1}{2}M_{\alpha\beta}\dot{q}_\alpha\dot{q}_\beta - \mathbf{v}^T\hat{\mathbf{c}}^\times\boldsymbol{\omega} + \mathbf{v}^T\mathbf{p}_\alpha\dot{q}_\alpha + \boldsymbol{\omega}^T\hat{\mathbf{h}}_\alpha\dot{q}_\alpha \tag{4}$$

To avoid a plethora of summation signs, *we shall assume the Einstein convention of implying summation on repeated indices.* The cross operator, corresponding to the vector cross product, is defined such that

$$\begin{bmatrix} x \\ y \\ z \end{bmatrix}^\times \triangleq \begin{bmatrix} 0 & -z & y \\ z & 0 & -x \\ -y & x & 0 \end{bmatrix}$$

In (4), m is the mass of the body. The first moment of mass, which is dependent on the elastic deformation of the body, is

$$\hat{\mathbf{c}} = \mathbf{c}^{(0)} + \mathbf{c}^{(1)}$$

where

$$\mathbf{c}^{(0)} \triangleq \int_\mathcal{E} \mathbf{r}\, dm, \quad \mathbf{c}^{(1)} \triangleq \mathbf{p}_\alpha q_\alpha$$

and

$$\mathbf{p}_\alpha \triangleq \int_\mathcal{E} \boldsymbol{\psi}_\alpha(\mathbf{r})\, dm$$

The second moment of mass, also dependent on elastic deformation, is

$$\hat{\mathbf{J}} = \mathbf{J}^{(0)} + \mathbf{J}^{(1)} + \mathbf{J}^{(2)}$$

where

$$\mathbf{J}^{(0)} \triangleq -\int_\mathcal{E} \mathbf{r}^\times\mathbf{r}^\times dm, \quad \mathbf{J}^{(1)} \triangleq (\boldsymbol{\Gamma}_\beta^T + \boldsymbol{\Gamma}_\beta)q_\beta, \quad \mathbf{J}^{(2)} \triangleq \boldsymbol{\Pi}_{\beta\gamma}q_\beta q_\gamma$$

where

$$\boldsymbol{\Gamma}_\beta \triangleq -\int_\mathcal{E} \boldsymbol{\psi}_\beta^\times\mathbf{r}^\times dm, \quad \boldsymbol{\Pi}_{\beta\gamma} \triangleq -\int_\mathcal{E} \boldsymbol{\psi}_\beta^\times(\mathbf{r})\boldsymbol{\psi}_\gamma^\times(\mathbf{r})dm$$

Also

$$\hat{\mathbf{h}}_\alpha = \mathbf{h}_\alpha^{(0)} + \mathbf{h}_\alpha^{(1)}$$

where

$$\mathbf{h}_\alpha^{(0)} \triangleq \int_\mathcal{E} \mathbf{r}^\times\boldsymbol{\psi}_\alpha(\mathbf{r})dm, \quad \mathbf{h}_\alpha^{(1)} \triangleq \boldsymbol{\upsilon}_{\alpha\beta}q_\beta$$

where

$$\boldsymbol{\upsilon}_{\alpha\beta} \triangleq -\int_\mathcal{E} \boldsymbol{\psi}_\alpha^\times(\mathbf{r})\boldsymbol{\psi}_\beta(\mathbf{r})dm$$

Finally,

$$M_{\alpha\beta} = \int_\mathcal{E} \boldsymbol{\psi}_\alpha^T(\mathbf{r})\boldsymbol{\psi}_\beta(\mathbf{r})dm$$

forms the mass matrix associated with the elastic coordinates.

The terms in (4) have been arranged to highlight the quadratic rate terms. Accordingly, the superscripts (0), (1), and (2) indicate zeroeth-, first-, and second-degree terms in the elastic displacement coordinates. In particular, $\mathbf{c}^{(0)}$ and $\mathbf{J}^{(0)}$ are the rigid-body first and second moments of mass. It is also worthwhile noting that the coefficients $\mathbf{p}_\alpha$ and $\mathbf{h}_\alpha^{(0)}$ correspond, respectively, to the momentum and angular momentum associated with the basis function $\boldsymbol{\psi}_\alpha(\mathbf{r})$. The augmented quantity $\hat{\mathbf{h}}_\alpha$ accounts for the deformation in the body. When the basis functions are the mode shapes, we may refer to these coefficients as *modal momentum coefficients* [12].

2.2 Potential Energy. We shall consider the potential energy in the body to be completely due to strain. Given that we are considering nonlinearities in the inertial terms, we permit a general nonlinear expression for the strain energy,

$$U = U(\mathbf{u}_e) \tag{5}$$

As such, it follows that $U=U(\boldsymbol{q}_e)$, where as a shorthand we write $\boldsymbol{q}_e=\text{col}\{q_\alpha\}$.

2.3 Equations of Motion. The equations of motion for the elastic body $\mathcal{E}$ in general translation and rotation may be obtained

from an approach *à la* Lagrange, as for example in [13],

$$\frac{d}{dt}\left(\frac{\partial L}{\partial \mathbf{v}}\right)+\boldsymbol{\omega}^{\times}\frac{\partial L}{\partial \mathbf{v}}=\mathbf{f}_r$$

$$\frac{d}{dt}\left(\frac{\partial L}{\partial \omega}\right)+\mathbf{v}^{\times}\frac{\partial L}{\partial \mathbf{v}}+\boldsymbol{\omega}^{\times}\frac{\partial L}{\partial \boldsymbol{\omega}}=\mathbf{g}_r$$

$$\frac{d}{dt}\left(\frac{\partial L}{\partial \dot{q}_\alpha}\right)-\frac{\partial L}{\partial q_\alpha}=f_\alpha \quad \alpha=1,\ldots,n \tag{6}$$

where $L\triangleq T-U\equiv L(\mathbf{v},\boldsymbol{\omega},\boldsymbol{q}_e,\dot{\boldsymbol{q}}_e)$. Also $\mathbf{f}_r(t)$ and $\mathbf{g}_r(t)$ are the total force and torque acting on the body and

$$f_\alpha(t)\triangleq\int_{\mathcal{E}}\boldsymbol{\psi}_\alpha^T(\mathbf{r})\mathbf{f}(\mathbf{r},t)dV$$

where $\mathbf{f}(\mathbf{r},t)$ is the force distribution applied to $\mathcal{E}$. The origin of (6) is, in fact, central to our development. The reader will no doubt recognize that it is not the standard form of Lagrange's equations. It is actually an example of the application of the Boltzmann-Hamel equations; however, we shall defer our discussion thereon until later.

Inserting (4) and (5) into (6) yields

$$m\dot{\mathbf{v}}-\hat{\mathbf{c}}^{\times}\dot{\boldsymbol{\omega}}+\mathbf{p}_\alpha\ddot{q}_\alpha+m\boldsymbol{\omega}^{\times}\mathbf{v}-\boldsymbol{\omega}^{\times}\hat{\mathbf{c}}^{\times}\boldsymbol{\omega}+2\boldsymbol{\omega}^{\times}\mathbf{p}_\alpha\dot{q}_\alpha=\mathbf{f}_r$$

$$\hat{\mathbf{c}}^{\times}\dot{\mathbf{v}}+\mathbf{J}\dot{\boldsymbol{\omega}}+\hat{\mathbf{h}}_\alpha\ddot{q}_\alpha+\hat{\mathbf{c}}^{\times}\boldsymbol{\omega}^{\times}\mathbf{v}+\boldsymbol{\omega}^{\times}\hat{\mathbf{J}}\boldsymbol{\omega}+2\boldsymbol{\Gamma}_\alpha^T\boldsymbol{\omega}\dot{q}_\alpha=\mathbf{g}_r$$

$$\mathbf{p}_\alpha^T\dot{\mathbf{v}}+\hat{\mathbf{h}}_\alpha^T\dot{\boldsymbol{\omega}}+M_{\alpha\beta}\ddot{q}_\alpha+\mathbf{p}_\alpha^T\boldsymbol{\omega}^{\times}\mathbf{v}-\boldsymbol{\omega}^T\hat{\boldsymbol{\Gamma}}_\alpha\boldsymbol{\omega}+2\boldsymbol{\nu}_{\alpha\beta}^T\boldsymbol{\omega}\dot{q}_\beta+K_{\alpha\beta}q_\beta=f_\alpha \quad \alpha=1,\ldots,n \tag{7}$$

where, following our practice,

$$\hat{\boldsymbol{\Gamma}}_\alpha=\boldsymbol{\Gamma}_\alpha^{(0)}+\boldsymbol{\Gamma}_\alpha^{(1)}$$

and

$$\boldsymbol{\Gamma}_\alpha^{(0)}\triangleq\boldsymbol{\Gamma}_\alpha,\quad \boldsymbol{\Gamma}_\alpha^{(1)}\triangleq\boldsymbol{\Pi}_{\alpha\beta}q_\beta$$

(Note that summation is applied over α in the first two equations of (7) but not in the third as the index is not repeated; the summation in the last equation is on β.) The stiffness matrix $K_{\alpha\beta}=K_{\alpha\beta}(q_\gamma)$ is, in general, nonlinear and may be written as

$$K_{\alpha\beta}=\frac{\partial^2 U}{\partial q_\alpha\partial q_\beta}$$

We may compress (7) into the following form:

$$\hat{\mathbf{M}}_{rr}\dot{\boldsymbol{v}}+\hat{\mathbf{M}}_{re}\ddot{\boldsymbol{q}}_e=\mathbf{f}_r+\hat{\mathbf{f}}_{I,r}$$

$$\hat{\mathbf{M}}_{re}^T\dot{\boldsymbol{v}}+\mathbf{M}_{ee}\ddot{\boldsymbol{q}}_e+\mathbf{K}_{ee}(\boldsymbol{q}_e)\boldsymbol{q}_e=\mathbf{f}_e+\hat{\mathbf{f}}_{I,e} \tag{8}$$

where

$$\boldsymbol{v}\triangleq\begin{bmatrix}\mathbf{v}\\ \boldsymbol{\omega}\end{bmatrix},\quad \mathbf{f}_r\triangleq\begin{bmatrix}\mathbf{f}_r\\ \mathbf{g}_r\end{bmatrix},\quad \hat{\mathbf{M}}_{rr}\triangleq\begin{bmatrix}m\mathbf{1} & -\hat{\mathbf{c}}^{\times}\\ \hat{\mathbf{c}}^{\times} & \hat{\mathbf{J}}\end{bmatrix},\quad \hat{\mathbf{M}}_{re}\triangleq\begin{bmatrix}\mathbf{P}\\ \mathbf{H}\end{bmatrix}$$

and $\mathbf{P}\triangleq\text{row}\{\mathbf{p}_\alpha\}$, $\hat{\mathbf{H}}\triangleq\text{row}\{\hat{\mathbf{h}}_\alpha\}$, $\mathbf{M}_{ee}\triangleq\text{matrix}\{M_{\alpha\beta}\}$, $\mathbf{f}_e\triangleq\text{col}\{f_\alpha\}$. The nonlinear inertial terms $\hat{\mathbf{f}}_{I,r}$ and $\hat{\mathbf{f}}_{I,e}$ can be inferred from (7). All of the hatted quantities above depend on the deformation of the body. (This also generally applies to the stiffness matrix, although it is governed by the specific nature of the strain energy, for which reason we choose to denote it by a functional dependence on $\boldsymbol{q}_e$.)

Equations (7), or equivalently (8), represent what we shall refer to as the *second-order formulation* for the dynamics of a free elastic body. The numerical intergration of these equations requires us to solve for the accelerations $\dot{\boldsymbol{v}}$ and $\ddot{\boldsymbol{q}}_e$ at each step. That the system mass matrix is dependent on the body's deformation would seem to bode ill because, in principle, the mass matrix must be inverted or decomposed in Gaussian fashion at each time step.

2.4 Kinematical Equations. We must not forget that there are kinematical equations that accompany the dynamical equations (7). Denote by $\boldsymbol{\rho}$ the position of O relative to some inertially fixed point as expressed in an inertial frame $\mathcal{F}_\mathfrak{I}$. The velocity $\mathbf{v}$ is related to $\boldsymbol{\rho}$ as follows:

$$\mathbf{v}=\mathbf{C}(\boldsymbol{\theta})\dot{\boldsymbol{\rho}} \tag{9}$$

where $\mathbf{C}$ is the rotation matrix from $\mathcal{F}_\mathfrak{I}$ to the body frame $\mathcal{F}_\mathcal{E}$ and $\boldsymbol{\theta}=\text{col}\{\theta_1,\theta_2,\theta_3\}$ may be regarded as an Euler set of rotation angles. The angular velocity $\boldsymbol{\omega}$ can thus be expressed as

$$\boldsymbol{\omega}=\mathbf{S}(\boldsymbol{\theta})\dot{\boldsymbol{\theta}} \tag{10}$$

where $\mathbf{S}$ depends on the sequence of rotations. These must be solved simultaneously with the dynamical equations (along with integrating $\ddot{\boldsymbol{q}}_e$ twice) to obtain the configuration of the body.

3 A First-Order Formulation

Let us now consider an alternate approach wherein we discretize the elastic *velocity* field in addition to the elastic *displacement* field. That is, we shall still employ (1) as the discretization for $\mathbf{u}_e(\mathbf{r},t)$, but rather than using (3) for the total velocity field $\mathbf{w}(\mathbf{r},t)$, we shall write

$$\mathbf{w}(\mathbf{r},t)=\mathbf{v}(t)-\mathbf{r}^{\times}\boldsymbol{\omega}(t)+\mathbf{v}_e(\mathbf{r},t) \tag{11}$$

and expand $\mathbf{v}_e(\mathbf{r},t)$ directly as

$$\mathbf{v}_e(\mathbf{r},t)=\sum_{\alpha=1}^{n}\boldsymbol{\phi}_\alpha(\mathbf{r})v_\alpha(t) \tag{12}$$

where $\boldsymbol{\phi}_\alpha(\mathbf{r})$ are appropriately chosen basis functions and v_α are generalized rate coordinates. Although $\boldsymbol{\phi}_\alpha$ can, in general, be different from $\boldsymbol{\psi}_\alpha$, we shall in this development take them to be the same. The cantilever conditions inherent in $\boldsymbol{\psi}_\alpha$ keep the velocity of O and the local angular velocity at O as $\mathbf{v}$ and $\boldsymbol{\omega}$. The choice of same basis functions, however, is more out of convenience for it requires us to keep track of only one set of functions and the discretized inertial quantities that issue therefrom.

It is our aim here to derive the equations of motion for $\mathcal{E}$ in terms of v_α in place of $\dot{q}_\alpha$. This would typically require us to use the Boltzmann-Hamel version of Lagrange's equations; however, we shall choose to take the Boltzmann-Hamel approach in conjunction with Hamilton's principle. But first we should explore the kinematical relationships.

3.1 Quasi-Coordinates. The kinematical equations (9) and (10) for the translational and rotational velocities still hold. To reconcile (1) with (12), we require that

$$\mathbf{v}_e=\dot{\mathbf{u}}_e+\boldsymbol{\omega}^{\times}\mathbf{u}_e \tag{13}$$

at all points in $\mathcal{E}$.

We have a situation here in which "quasi-coordinates," as Whittaker [14] for example refers to them, naturally arise. Equations (9), (10), and (13) can be expressed in differential form as

$$d\boldsymbol{\pi}_\rho=\mathbf{C}d\boldsymbol{\rho}$$

$$d\boldsymbol{\pi}_\theta=\mathbf{S}d\boldsymbol{\theta}$$

$$d\boldsymbol{\pi}_e=d\mathbf{u}_e-\mathbf{u}_e^{\times}\mathbf{S}d\boldsymbol{\theta} \tag{14}$$

The quantities $d\boldsymbol{\pi}_\rho$, $d\pi_\theta$, and $d\pi_e$ represent *differentials of quasi-coordinates*, so called because unlike *true coordinates* none of (14) is, in general, integrable.

3.2 Hamilton's Principle Using Quasi-Coordinates. The extended Hamilton's principle states that the motion of a system is given by

$$\delta\int_{t_1}^{t_2} L dt + \int_{t_1}^{t_2} \delta W_e dt = 0 \tag{15}$$

where $L=T-U$ as before and δW_e is the virtual work. We begin with a continuum formulation and, accordingly, shall express these quantities in terms of $\mathbf{v}$, $\boldsymbol{\omega}$, $\mathbf{v}_e$, and $\mathbf{u}_e$.

The kinetic energy is

$$T = \frac{1}{2}\int_{\mathcal{E}} (\mathbf{v} - \mathbf{r}^{\times}\boldsymbol{\omega} + \mathbf{v}_e)^T(\mathbf{v} - \mathbf{r}^{\times}\boldsymbol{\omega} + \mathbf{v}_e) dm \tag{16}$$

The first variation in the kinetic energy is

$$\delta T = \int_{\mathcal{E}} (\delta\mathbf{v} - \mathbf{r}^{\times}\delta\boldsymbol{\omega} + \delta\mathbf{v}_e)^T(\mathbf{v} - \mathbf{r}^{\times}\boldsymbol{\omega} + \mathbf{v}_e) dm \tag{17}$$

We need to transform the variational quantities $\delta\mathbf{v}$, $\delta\boldsymbol{\omega}$, $\delta\mathbf{v}_e$ into $\delta\boldsymbol{\pi}_\rho$, $\delta\boldsymbol{\pi}_\theta$, $\delta\boldsymbol{\pi}_e$. The latter set can be expressed in terms of the true coordinates using the variational form of (14)

$$\delta\boldsymbol{\pi}_\rho = \mathbf{C}\delta\boldsymbol{\rho}$$

$$\delta\boldsymbol{\pi}_\theta = \mathbf{S}\delta\boldsymbol{\theta}$$

$$\delta\boldsymbol{\pi}_e = \delta\mathbf{u}_e - \mathbf{u}_e^{\times}\mathbf{S}\delta\boldsymbol{\theta} \tag{18}$$

The strategy is thus to render (17) first in terms of $\delta\boldsymbol{\rho}$, $\delta\boldsymbol{\theta}$, $\delta\mathbf{u}_e$. This can be facilitated by noting the relations

$$\frac{\partial\mathbf{v}}{\partial\boldsymbol{\theta}} = \mathbf{v}^{\times}\mathbf{S}, \quad \frac{\partial\boldsymbol{\omega}}{\partial\boldsymbol{\theta}} = \dot{\mathbf{S}} + \boldsymbol{\omega}^{\times}\mathbf{S}$$

and taking the first variation of (9), (10), and (13), namely,

$$\delta\mathbf{v} = \frac{\partial\mathbf{v}}{\partial\boldsymbol{\theta}}\delta\theta + \frac{\partial\mathbf{v}}{\partial\dot{\boldsymbol{\rho}}}\delta\dot{\boldsymbol{\rho}} = \mathbf{v}^{\times}\mathbf{S}\delta\boldsymbol{\theta} + \mathbf{C}\delta\dot{\boldsymbol{\rho}}$$

$$\delta\boldsymbol{\omega} = \frac{\partial\boldsymbol{\omega}}{\partial\boldsymbol{\theta}}\delta\boldsymbol{\theta} + \frac{\partial\boldsymbol{\omega}}{\partial\dot{\boldsymbol{\theta}}}\delta\dot{\boldsymbol{\theta}} = (\dot{\mathbf{S}} + \boldsymbol{\omega}^{\times}\mathbf{S})\delta\boldsymbol{\theta} + \mathbf{S}\delta\dot{\boldsymbol{\theta}}$$

$$\delta\mathbf{v}_e = \delta\dot{\mathbf{u}}_e + \boldsymbol{\omega}^{\times}\delta\mathbf{u}_c - \mathbf{u}_e^{\times}\delta\boldsymbol{\omega}$$

Substituting these in (17) and integrating by parts in time where necessary yields

$$\begin{aligned}\int_{t_1}^{t_2}\delta T\, dt = -\int_{t_1}^{t_2}\int_{\mathcal{E}} \{&\delta\boldsymbol{\pi}_\rho^T[\dot{\mathbf{v}} - \mathbf{r}^{\times}\dot{\boldsymbol{\omega}} + \dot{\mathbf{v}}_e + \boldsymbol{\omega}^{\times}(\mathbf{v} - \mathbf{r}^{\times}\boldsymbol{\omega} + \mathbf{v}_e)]\\ &+ \delta\boldsymbol{\pi}_\theta^T[\mathbf{r}^{\times}(\dot{\mathbf{v}} - \mathbf{r}^{\times}\dot{\boldsymbol{\omega}} + \dot{\mathbf{v}}_e) + \mathbf{r}^{\times}\boldsymbol{\omega}^{\times}\mathbf{v} - \boldsymbol{\omega}^{\times}\mathbf{r}^{\times}\mathbf{r}^{\times}\boldsymbol{\omega}\\ &- \mathbf{r}^{\times}\mathbf{v}_e^{\times}\boldsymbol{\omega}] + \delta\boldsymbol{\pi}_e^T[\dot{\mathbf{v}} - \mathbf{r}^{\times}\dot{\boldsymbol{\omega}} + \dot{\mathbf{v}}_e + \boldsymbol{\omega}^{\times}(\mathbf{v} - \mathbf{r}^{\times}\boldsymbol{\omega}\\ &+ \mathbf{v}_e)]\}dm\, dt\end{aligned} \tag{19}$$

assuming, as usual, that the variations vanish at t_1 and t_2. It is also necessary to note Poisson's equations $\dot{\mathbf{C}} + \boldsymbol{\omega}^{\times}\mathbf{C} = \mathbf{O}$ in arriving at (19).

The expression for the potential energy, being a function of $\mathbf{u}_e$ only, remains unchanged. The first variation may be written as

$$\delta U = \int_{\mathcal{E}} \delta\mathbf{u}_e^T\mathcal{K}(\mathbf{u}_e)dV$$

where $\mathcal{K}$ is the nonlinear stiffness operator. Using the last of (18) to introduce the quasi-coordinates gives

$$\delta U = \int_{\mathcal{E}} (\delta\boldsymbol{\pi}_e + \mathbf{u}_e^{\times}\delta\boldsymbol{\pi}_\theta)^T\mathcal{K}(\mathbf{u}_e)dV \tag{20}$$

The virtual work is

$$\delta W_e = \delta\boldsymbol{\pi}_\rho^T\mathbf{f}_r + \delta\boldsymbol{\pi}_\theta^T\mathbf{g}_r + \int_{\mathcal{E}} \delta\mathbf{u}_e^T\mathbf{f}_e\, dV$$

which becomes

$$\delta W_e = \delta\boldsymbol{\pi}_\rho^T\mathbf{f}_r + \delta\boldsymbol{\pi}_\theta^T\mathbf{g}_r + \int_{\mathcal{E}} (\delta\boldsymbol{\pi}_e + \mathbf{u}_e^{\times}\delta\boldsymbol{\pi}_\theta)^T\mathbf{f}_e\, dV \tag{21}$$

using (18) again.

We need now to express $\delta\boldsymbol{\pi}_e$ in terms of the basis functions. The expansion, in fact, is the same as that for $\mathbf{v}_e$ in (12), namely,

$$\delta\boldsymbol{\pi}_e(\mathbf{r},t) = \sum_{\alpha=1}^{n} \boldsymbol{\psi}_\alpha(\mathbf{r})\,\delta\pi_{\alpha,e}(t) \tag{22}$$

(with $\boldsymbol{\phi}_\alpha = \boldsymbol{\psi}_\alpha$) for this is the variational version of (12). Upon substitution into (19)–(21) and, in turn, into (15), while recognizing the independence of $\delta\boldsymbol{\pi}_\rho$, $\delta\boldsymbol{\pi}_\theta$, and $\delta\pi_{\alpha,e}$, we have

$$\begin{aligned}
&m\dot{\mathbf{v}} - \mathbf{c}^{\times}\dot{\boldsymbol{\omega}} + \mathbf{p}_\alpha\dot{v}_\alpha + m\boldsymbol{\omega}^{\times}\mathbf{v} - \boldsymbol{\omega}^{\times}\mathbf{c}^{\times}\boldsymbol{\omega} + \boldsymbol{\omega}^{\times}\mathbf{p}_\alpha v_\alpha = \mathbf{f}_r\\
&\mathbf{c}^{\times}\dot{\mathbf{v}} + \mathbf{J}\dot{\boldsymbol{\omega}} + \mathbf{h}_\alpha\dot{v}_\alpha + \mathbf{c}^{\times}\boldsymbol{\omega}^{\times}\mathbf{v} + \boldsymbol{\omega}^{\times}\mathbf{J}\boldsymbol{\omega} + \boldsymbol{\Gamma}_\alpha^T\boldsymbol{\omega}v_\alpha + \boldsymbol{\kappa}_\alpha q_\alpha = \mathbf{g}_r + \mathbf{g}_\alpha q_\alpha\\
&\mathbf{p}_\alpha^T\dot{\mathbf{v}} + \mathbf{h}_\alpha^T\dot{\boldsymbol{\omega}} + M_{\alpha\beta}\dot{v}_\beta + \mathbf{p}_\alpha^T\boldsymbol{\omega}^{\times}\mathbf{v} - \boldsymbol{\omega}^T\boldsymbol{\Gamma}_\alpha\boldsymbol{\omega} + \boldsymbol{\omega}^T\boldsymbol{\upsilon}_{\alpha\beta}v_\beta + K_{\alpha\beta}q_\beta\\
&\qquad = f_\alpha \quad \alpha = 1, \ldots, n
\end{aligned} \tag{23}$$

where

$$\boldsymbol{\kappa}_\alpha(q_\gamma) \triangleq -\int_{\mathcal{E}} \boldsymbol{\psi}_\alpha^{\times}\mathcal{K}(\boldsymbol{\psi}_\gamma q_\gamma)dV, \quad K_{\alpha\beta}(q_\gamma)q_\beta \triangleq \int_{\mathcal{E}} \boldsymbol{\psi}_\alpha^T\mathcal{K}(\boldsymbol{\psi}_\gamma q_\gamma)\, dV$$

from which $K_{\alpha\beta}(q_\gamma)$ can be inferred; this is the same (nonlinear) stiffness matrix that appeared in the second-order formulation expressed in terms of the stiffness operator instead of the strain energy. Both types of quantity may, and in general are dependent, on deformation. Also,

$$\mathbf{g}_\alpha(t) \triangleq -\int_{\mathcal{E}} \boldsymbol{\psi}_\alpha^{\times}(\mathbf{r})\mathbf{f}_e(\mathbf{r},t)dV$$

which accounts for a first-degree correction to the net applied torque and may be directly compared to $\boldsymbol{\kappa}_\alpha$. If the only force and torque are applied at O then $\mathbf{g}_\alpha = \mathbf{0}$. (Note again that summation is applied over α in the first two equations of (23) but not in the third as the index is not repeated; the summation in the last equation is on β.)

We may as in the second-order case collect the terms of (23) in a more compact expression

$$\begin{aligned}
&\mathbf{M}_{rr}\dot{\mathbf{v}} + \mathbf{M}_{re}\dot{\mathbf{v}}_e + \mathbf{K}_{re}(\boldsymbol{q}_e)\boldsymbol{q}_e = \boldsymbol{f}_r + \boldsymbol{f}_{I,r} + \mathbf{F}_{re}\boldsymbol{q}_e\\
&\mathbf{M}_{re}^T\dot{\mathbf{v}} + \mathbf{M}_{ee}\dot{\mathbf{v}}_e + \mathbf{K}_{ee}(\boldsymbol{q}_e)\boldsymbol{q}_e = \boldsymbol{f}_e + \boldsymbol{f}_{I,e}
\end{aligned} \tag{24}$$

where the new terms are

$$\mathbf{M}_{rr} \triangleq \begin{bmatrix} m\mathbf{1} & -\mathbf{c}^{\times} \\ \mathbf{c}^{\times} & \mathbf{J} \end{bmatrix}, \quad \mathbf{M}_{re} \triangleq \begin{bmatrix} \mathbf{P} \\ \mathbf{H} \end{bmatrix}$$

$$\mathbf{K}_{re} \triangleq \begin{bmatrix} \mathbf{O} \\ \mathbf{K} \end{bmatrix}, \quad \mathbf{F}_{re} \triangleq \begin{bmatrix} \mathbf{O} \\ \mathbf{G} \end{bmatrix}$$

and $\boldsymbol{\upsilon}_e \triangleq \mathrm{col}\{v_\alpha\}$, $\mathbf{H} = \mathrm{row}\{\mathbf{h}_\alpha\}$, $\mathbf{K} \triangleq \mathrm{row}\{\boldsymbol{\kappa}_\alpha\}$, $\mathbf{G} \triangleq \mathrm{row}\{\mathbf{g}_\alpha\}$.

3.3 Kinematical Equations. Equations (9) and (10) must be solved in conjunction with (23). But, in addition, we must solve (13) or rather a discretized form of it. We choose to discretize (13) by substituting (1) and (12), then premultiplying by $\boldsymbol{\psi}_\alpha^T(\mathbf{r})$ and integrating over the mass distribution of the body. This leads to

$$M_{\alpha\beta}\upsilon_\beta = M_{\alpha\beta}\dot{q}_\beta - \boldsymbol{\omega}^T\boldsymbol{\upsilon}_{\beta\alpha}q_\beta \quad \alpha = 1, \ldots, n$$

(the summation is over β) or, in matrix form,

$$\mathbf{M}_{ee}\boldsymbol{v}_e = \mathbf{M}_{ee}\dot{\boldsymbol{q}}_e - q_\beta \boldsymbol{\Upsilon}_\beta^T \boldsymbol{\omega} \tag{25}$$

(the summation remains on β) where $\boldsymbol{\Upsilon}_\beta \triangleq \mathrm{row}_\alpha\{\boldsymbol{v}_{\beta\alpha}\}$.

We shall refer to the foregoing development as the *first-order formulation* for the dynamics of a free elastic body. The key difference is that none of the inertial parameters here depends on the deformation. The coefficient matrix—that is, the system mass matrix—is constant, and thus, solving for the accelerations in a numerical integration scheme requires the inversion of this matrix only once at the outset. There is no other procedure that is needed at each evaluation as in the second-order formulation, which, in principle, involves at least Gaussian decomposition at each step.

There is, however, a price to be paid, namely, the slightly more complex kinematical equation above which must be solved for $\dot{\boldsymbol{q}}_e$; however, this can be done easily for, again, the coefficient matrix is constant. There is in addition a new stiffness term, $\mathbf{K}_{re}(\boldsymbol{q}_e)\boldsymbol{q}_e$, in the dynamical equations as well as a new force term, $\mathbf{F}_{re}\boldsymbol{q}_e$, in general. It is not necessary though to compute anew the stiffness parameters for the former term as they can typically be inferred from those in $\mathbf{K}_{ee}(\boldsymbol{q}_e)$; the same can be said for $\mathbf{F}_{re}$.

4 Example: Free-Free Euler-Bernoulli Beam

It is customary to test theories of this kind numerically on a slender Euler-Bernoulli model of a beam, and so we shall. We will consider a uniform beam of length ℓ and total mass m rotated about one end by a prescribed torque. Both axial (u_1) and transverse (u_2 and u_3) deformation will be taken into account. The beam is assumed to possess the same bending stiffness EI in all transverse directions and an axial stiffness EA.

The expansion for the displacement field (1) may be dissembled as

$$u_1(x,t) = \sum_{\alpha=1}^{n_1} \psi_{1,\alpha}(x) q_{1,\alpha}(t)$$

$$u_2(x,t) = \sum_{\beta=1}^{n_2} \psi_{2,\beta}(x) q_{2,\beta}(t)$$

$$u_3(x,t) = \sum_{\gamma=1}^{n_3} \psi_{3,\gamma}(x) q_{3,\gamma}(t) \tag{26}$$

where $n_1+n_2+n_3=n$. The axial coordinate along the undeformed beam is x.

As we have maintained, and as is abundantly demonstrated in the literature, it is not consistent to consider higher-order inertial terms while neglecting higher-order, i.e., nonlinear, terms in the stiffness. Some authors, however, have chosen to give the appearance of a linear stiffness term by employing a "stretch" coordinate along the elastic axis of the beam. It is not our intention to wade into this issue but direct the reader to Sharf [4] for a comprehensive study of the various approaches taken.

4.1 Strain Energy. The strain energy due to Euler-Bernoulli bending and nonlinear axial strain effects is given by [2]

$$U = \frac{1}{2}\int_0^\ell \left[EAu_1'^2 + EIu_2''^2 + EIu_3''^2 + EAu_1'(u_2'^2 + u_3'^2) + \frac{1}{4}EA(u_2'^4 + 2u_2'^2 u_3'^2 + u_3'^4) \right] dx \tag{27}$$

where $(\cdot)' \triangleq d(\cdot)/dx$. This form of the strain energy, which uses Lagrangian strain, will allow us to take properly into account geometric (centrifugal) stiffening.

On substitution of (26), we may write

$$\begin{aligned} 2U = {} & K^{(0)}_{11,\alpha\alpha'} q_{1,\alpha} q_{1,\alpha'} + K^{(0)}_{22,\beta\beta'} q_{2,\beta} q_{2,\beta'} + K^{(0)}_{33,\gamma\gamma'} q_{3,\gamma} q_{3,\gamma'} \\ & + K^{(1)}_{122,\alpha\beta\beta'} q_{1,\alpha} q_{2,\beta} q_{2,\beta'} + K^{(1)}_{133,\alpha\gamma\gamma'} q_{1,\alpha} q_{3,\gamma} q_{3,\gamma'} \\ & + \tfrac{1}{4} K^{(2)}_{2222,\beta\beta'\delta\delta'} q_{2,\beta} q_{2,\beta'} q_{2,\delta} q_{2,\delta'} \\ & + \tfrac{1}{2} K^{(2)}_{2233,\beta\beta'\gamma\gamma'} q_{2,\beta} q_{2,\beta'} q_{3,\gamma} q_{3,\gamma'} + \tfrac{1}{4} K^{(2)}_{3333,\gamma\gamma'\epsilon\epsilon'} q_{3,\gamma} q_{3,\gamma'} q_{3,\epsilon} q_{3,\epsilon'} \end{aligned} \tag{28}$$

The superscripts are used for the same designation as before, and the summation convention is once again in force. For clarity we have chosen the subscripts α and α' in these parsed expressions to relate to the axial quantities and hence to range from 1 to n_1. The subscripts β and β' (and δ and δ'), associated with the transverse quantities in one direction, range from 1 to n_2; the subscripts γ and γ' (and ε and ε'), associated with the transverse quantities in the perpendicular direction, range from 1 to n_3.

The stiffness coefficients are

$$K^{(0)}_{11,\alpha\alpha'} = K^{(0)}_{11,\alpha'\alpha} = \int_0^\ell EA\psi'_{1,\alpha}\psi'_{1,\alpha'}\,dx$$

$$K^{(0)}_{22,\beta\beta'} = K^{(0)}_{22,\beta'\beta} = \int_0^\ell EI\psi''_{2,\beta}\psi''_{2,\beta'}\,dx$$

$$K^{(0)}_{33,\gamma\gamma'} = K^{(0)}_{33,\gamma'\gamma} = \int_0^\ell EI\psi''_{3,\gamma}\psi''_{3,\gamma'}\,dx$$

$$K^{(1)}_{122,\alpha\beta\beta'} = K^{(1)}_{122,\alpha\beta'\beta} = \int_0^\ell EA\psi'_{1,\alpha}\psi'_{2,\beta}\psi'_{2,\beta'}\,dx$$

$$K^{(1)}_{133,\alpha\gamma\gamma'} = K^{(1)}_{133,\alpha\gamma'\gamma} = \int_0^\ell EA\psi'_{1,\alpha}\psi'_{3,\gamma}\psi'_{3,\gamma'}\,dx$$

$$K^{(2)}_{2222,\beta\beta'\delta\delta'} = K^{(2)}_{2222,\beta'\beta\delta\delta'} = K^{(2)}_{2222,\delta\delta'\beta\beta'} = \int_0^\ell EA\psi'_{2,\beta}\psi'_{2,\beta'}\psi'_{2,\delta}\psi'_{2,\delta'}\,dx$$

$$K^{(2)}_{2233,\beta\beta'\gamma\gamma'} = K^{(2)}_{2233,\beta'\beta\gamma\gamma'} = K^{(2)}_{2233,\beta\beta'\gamma'\gamma} = \int_0^\ell EA\psi'_{2,\beta}\psi'_{2,\beta'}\psi'_{3,\gamma}\psi'_{3,\gamma'}\,dx$$

$$K^{(2)}_{3333,\gamma\gamma'\epsilon\epsilon'} = K^{(2)}_{3333,\gamma'\gamma\epsilon\epsilon'} = K^{(2)}_{3333,\epsilon\epsilon'\gamma\gamma'} = \int_0^\ell EA\psi'_{3,\gamma}\psi'_{3,\gamma'}\psi'_{3,\epsilon}\psi'_{3,\epsilon'}\,dx$$

The elastic forces corresponding to the axial and transverse generalized coordinates are accordingly

$$\frac{\partial U}{\partial q_{1,\alpha}} = K^{(0)}_{11,\alpha\beta} q_{1,\beta} + \frac{1}{2}K^{(1)}_{122,\alpha\beta\gamma} q_{2,\beta} q_{2,\gamma} + K^{(1)}_{133,\alpha\beta\gamma} q_{3,\beta} q_{3,\gamma} \tag{29}$$

$$\frac{\partial U}{\partial q_{2,\beta}} = K^{(0)}_{22,\beta\beta'} q_{2,\beta'} + K^{(1)}_{122,\alpha\beta\beta'} q_{1,\alpha} q_{2,\beta'} + \frac{1}{2}K^{(2)}_{2222,\beta\beta'\delta\delta'} q_{2,\beta'} q_{2,\delta} q_{2,\delta'} + \frac{1}{2}K^{(2)}_{2233,\alpha\beta\gamma\gamma'} q_{2,\beta'} q_{3,\gamma} q_{3,\gamma'} \tag{30}$$

$$\frac{\partial U}{\partial q_{3,\gamma}} = K^{(0)}_{33,\gamma\gamma'} q_{3,\gamma'} + K^{(1)}_{133,\alpha\gamma\gamma'} q_{1,\alpha} q_{3,\gamma'} + \frac{1}{2} K^{(2)}_{2233,\beta\beta'\gamma\gamma'} q_{2,\beta} q_{2,\beta'} q_{3,\gamma'} + \frac{1}{2} K^{(2)}_{3333,\gamma\gamma'\epsilon\epsilon'} q_{3,\gamma'} q_{3,\epsilon} q_{3,\epsilon'} \tag{31}$$

We can give this result a conventional appearance by writing

$$\frac{\partial U}{\partial \boldsymbol{q}_e} = \mathbf{K}_{ee}(\boldsymbol{q}_e)\boldsymbol{q}_e \tag{32}$$

where

$$\boldsymbol{q}_e = \begin{bmatrix} \underset{\alpha=1,n_1}{\text{col}} \{q_{1,\alpha}\} \\ \underset{\beta=1,n_2}{\text{col}} \{q_{2,\beta}\} \\ \underset{\gamma=1,n_3}{\text{col}} \{q_{3,\gamma}\} \end{bmatrix}$$

and

$$\mathbf{K}_{ee} = \begin{bmatrix} \mathbf{K}_{11} & \mathbf{K}_{22} & \mathbf{K}_{13} \\ \mathbf{K}_{12}^T & \mathbf{K}_{22} & \mathbf{K}_{23} \\ \mathbf{K}_{13}^T & \mathbf{K}_{23}^T & \mathbf{K}_{33} \end{bmatrix}$$

The components of the (nonlinear) stiffness matrix are as follows:

$$K_{11,\alpha\alpha'} = K^{(0)}_{11,\alpha\alpha'}$$

$$K_{22,\beta\beta'} = K^{(0)}_{22,\beta\beta'} + \tfrac{1}{2} K^{(1)}_{122,\alpha'\beta\beta'} q_{1,\alpha'} + \tfrac{1}{2} K^{(2)}_{2222,\beta\delta\beta'\delta'} q_{2,\delta} q_{2,\delta'}$$

$$K_{33,\gamma\gamma'} = K^{(0)}_{33,\gamma\gamma'} + \tfrac{1}{2} K^{(1)}_{133,\alpha'\gamma\gamma'} q_{1,\alpha'} + \tfrac{1}{2} K^{(2)}_{3333,\gamma\epsilon\gamma'\epsilon'} q_{3,\epsilon} q_{3,\epsilon'}$$

$$K_{12,\alpha\beta} = K_{21,\beta\alpha} = \tfrac{1}{2} K^{(1)}_{122,\alpha\beta\beta'} q_{2,\beta'}$$

$$K_{13,\alpha\gamma} = K_{31,\gamma\alpha} = \tfrac{1}{2} K^{(1)}_{133,\alpha\gamma\gamma'} q_{3,\gamma'}$$

$$K_{23,\beta\gamma} = K_{32,\gamma\beta} = \tfrac{1}{2} K^{(2)}_{2233,\beta\beta'\gamma\gamma'} q_{2,\beta'} q_{3,\gamma'} \tag{33}$$

Note that $\mathbf{K}_{ee}(\boldsymbol{q}_e)$ is symmetric.

For the first-order formulation, there are yet more stiffness coefficients to determine but in fact no new computations are required. They only need be picked out from those already calculated from the foregoing expressions. Setting $\mathbf{g}_s = \mathbf{K}_{re}(\boldsymbol{q}_e)\boldsymbol{q}_e$, the corresponding stiffness torques are

$$g_{s,1} = 0 \tag{34}$$

$$g_{s,2} = -K^{(1)}_{EA,13,\alpha\gamma} q_{1,\alpha} q_{3,\gamma} + K^{(1)}_{EI,13,\alpha\gamma} q_{1,\alpha} q_{3,\gamma} + K^{(2)}_{113,\alpha\alpha'\gamma} q_{1,\alpha} q_{1,\alpha'} q_{3,\gamma} - \tfrac{1}{2} K^{(2)}_{223,\beta\beta'\gamma} q_{2,\beta} q_{2,\beta^1} q_{3,\gamma} - \tfrac{1}{2} K^{(2)}_{333,\epsilon\epsilon'\gamma} q_{3,\epsilon} q_{3,\epsilon'} q_{3,\gamma} + \tfrac{1}{2} K^{(3)}_{1333,\alpha\epsilon\epsilon'\gamma} q_{1,\alpha} q_{3,\epsilon} q_{3,\epsilon'} q_{3,\gamma} + \tfrac{1}{2} K^{(3)}_{1223,\alpha\beta\beta'\gamma} q_{1,\alpha} q_{2,\beta} q_{2,\beta'} q_{3,\gamma} \tag{35}$$

Table 1 Run times

N_e	First-Order (s)	Second-Order (s)	Improvement in First-Order (%)
1	208.6	262.6	20.5
2	2285	2555	10.6
3	46440	70630	34.2

$$g_{s,3} = K^{(1)}_{EA,12,\alpha\beta} q_{1,\alpha} q_{2,\beta} - K^{(1)}_{EI,12,\alpha\beta} q_{1,\alpha} q_{2,\beta} - K^{(2)}_{112,\alpha\alpha'\beta} q_{1,\alpha} q_{1,\alpha'} q_{2,\beta} + \tfrac{1}{2} K^{(2)}_{222,\delta\delta'\beta} q_{2,\delta} q_{2,\delta'} q_{2,\beta} + \tfrac{1}{2} K^{(2)}_{233,\beta\epsilon\epsilon'} q_{2,\beta} q_{3,\epsilon} q_{3,\epsilon'} - \tfrac{1}{2} K^{(3)}_{1222,\alpha\beta\delta\delta'} q_{1,\alpha} q_{2,\beta} q_{2,\delta} q_{2,\delta'} - \tfrac{1}{2} K^{(3)}_{1233,\alpha\beta\gamma\gamma'} q_{1,\alpha} q_{2,\beta} q_{3,\gamma} q_{3,\gamma'} \tag{36}$$

where

$$K^{(1)}_{EA,12,\alpha\beta} = \int_0^\ell EA\,\psi'_{1,\alpha}\psi'_{2,\beta}\,dx$$

$$K^{(1)}_{EI,12,\alpha\beta} = \int_0^\ell EI\,\psi''_{1,\alpha}\psi''_{2,\beta}\,dx$$

$$K^{(2)}_{112,\alpha\alpha'\beta} = \int_0^\ell EA\,\psi'_{1,\alpha}\psi'_{1,\alpha'}\psi'_{2,\beta}\,dx$$

$$K^{(2)}_{222,\delta\delta'\beta} = \int_0^\ell EA\,\psi'_{2,\delta}\psi'_{2,\delta'}\psi'_{2,\beta}\,dx$$

$$K^{(2)}_{233,\beta\epsilon\epsilon'} = \int_0^\ell EA\,\psi'_{2,\beta}\psi'_{3,\epsilon}\psi'_{3,\epsilon'}\,dx$$

$$K^{(3)}_{1222,\alpha\beta\delta\delta'} = \int_0^\ell EA\,\psi'_{1,\alpha}\psi'_{2,\beta}\psi'_{2,\delta}\psi'_{2,\delta'}\,dx$$

$$K^{(3)}_{1233,\alpha\beta\gamma\gamma'} = \int_0^\ell EA\,\psi'_{1,\alpha}\psi'_{2,\beta}\psi'_{3,\gamma}\psi'_{3,\gamma'}\,dx$$

and similarly for the others. Clearly, if the same basis functions are used in each direction then none of these needs to be calculated. For example, $K^{(1)}_{EA,12,\alpha\beta} = K^{(0)}_{11,\alpha\beta}$ and so on. Note that the terms here bear a higher degree (as marked by the superscript) owing to the involvement of $\mathbf{u}_e^\times$ in $\mathbf{K}_{re}$. In fact, there is now another level of stiffness terms.

4.2 Numerical Results. For our numerical values, we shall take the same as those used originally by Kane et al. [1] and later used by a succession of authors [2–4,7]. That is, $m=12$ kg, $\ell=10$ m, $EI=14{,}004$ Nm^2, and $EA=31{,}724{,}000$ N.

A torque was applied only about the 3-axis and was given by

$$g_3(t) = \begin{cases} g_{\max}\left(1 - \cos\dfrac{2\pi t}{T}\right), & 0 \geqslant t \geqslant T \\ g_{\max}, & t > T \end{cases}$$

with $g_{\max}=160$ N and $T=15$ s. This is the same torque profile as used by Damaren and Sharf [3] and Sharf [7]; Hanagud and Sarkar [2] specified the angular velocity, which corresponds to the above torque applied to the beam if it were rigid.

The equations of motion were solved using MATLAB. The ordinary-differential-equation solver chosen was "ode15s" with "MaxOrder=1." An accelerator package was not implemented which accounts for some of the longer simulation times (Table 1).

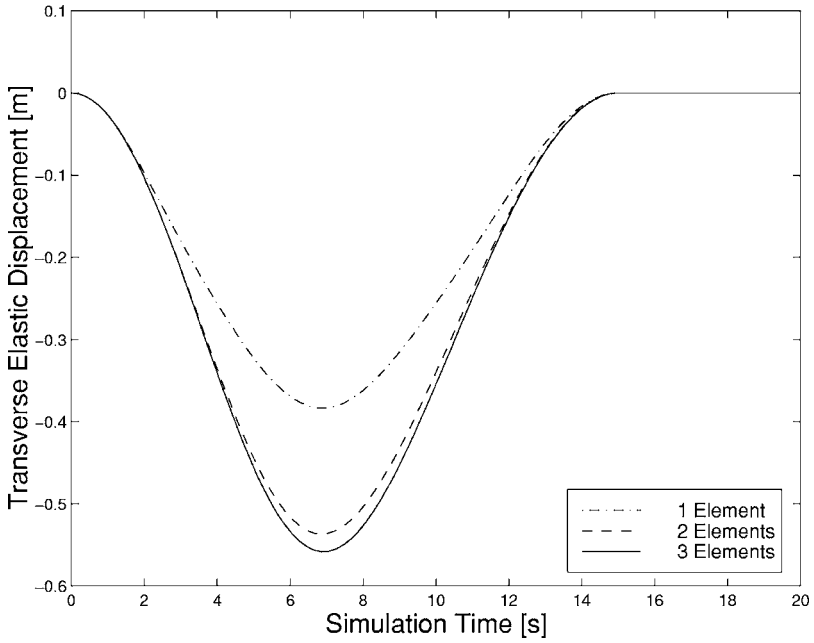

Fig. 2 Transverse deflection (full model, $Q=3$)

The basis functions in each direction were chosen to be the standard Hermite cubic functions of finite-element fame. Numerical results were obtained for elements 1, 2, and 3. The transverse tip deflection is shown in Fig. 2 and the axial tip deflection in Fig. 3. The results were the same to within one part in 10^5 for the first-order and second-order formulations. During the integration, the total energy was monitored against the work done for the applied torque. In all cases, they agreed to $\mathcal{O}(10^{-3})$ or better relative to the peak energy. Moreover, the transverse results agree with those of Sharf [7] who also uses Hermite cubic polynomials for both transverse and axial deformations. Note that the axial deflection is inward before it settles into its steady-state elongation. This is the so-called foreshortening effect arising from the bending beam.

The effect of the various levels of higher-degree terms are shown in Figs. 4 and 5 for the first-order approach. In these plots, Q refers to the highest degree of retained terms in q_α as indicated by the bracketed superscripts. The $\dot{q}_\alpha$ terms, as well as those involving $\ddot{q}_\alpha$, are always retained. The responses are similar for the second-order formulation although $Q=3$ does not apply for it. (Third-degree terms appear only with $\kappa^{(3)}_{\alpha\beta}$ in the first-order formulation.) For $Q=0$, only the linear stiffness term ($K^{(0)}_{\alpha\beta}q_\beta$) is retained as it is comparable to the elastic inertial forces ($M_{\alpha\beta}\ddot{q}_\beta$).

The numerical response quickly diverges for $Q=1$ (and hence is not shown). This is a result of the "softening" effect which enters

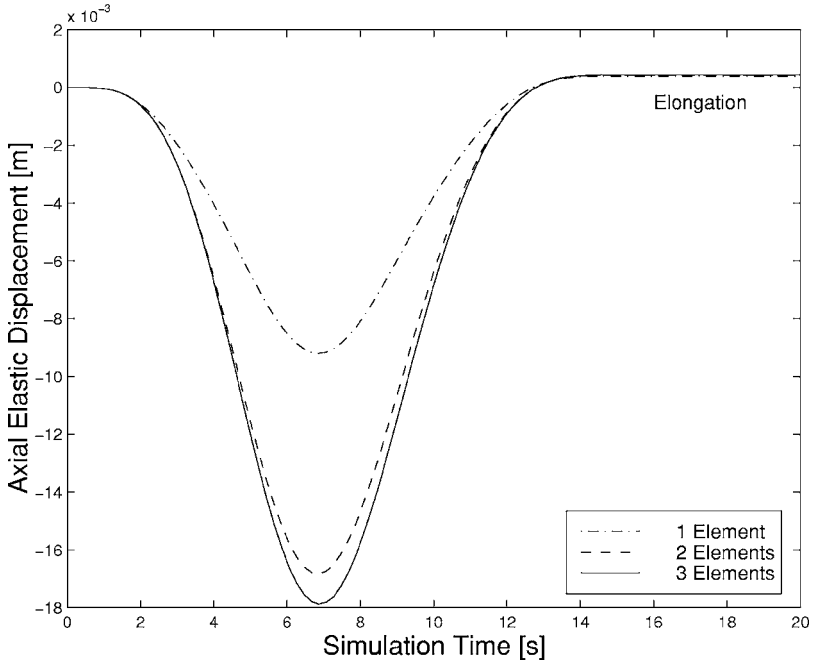

Fig. 3 Axial deflection (full model, $Q=3$)

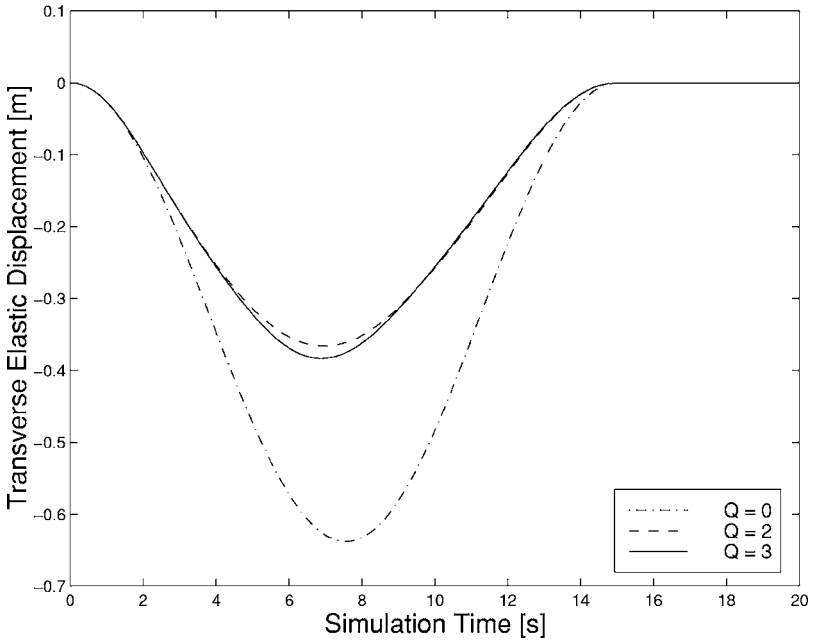

Fig. 4 Effect of higher-degree terms on transverse deflection (N_e=1)

via $\hat{\mathbf{\Gamma}}_\alpha$ in the elastic equations in the second-order formulation. The term $-\boldsymbol{\omega}^T\boldsymbol{\pi}_{\alpha\beta}\boldsymbol{\omega}q_\beta$ creates a destabilizing effect. This term is not explicit in the first-order approach, but the result, owing to the kinematical equation, is the same. Higher-degree terms are required to counteract this effect.

The first-order formulation clearly holds an edge in computational efficiency. The run times on a Pentium II 450-Hz PC computer are summarized for this example in Table 1. However, we emphasize that these limited results are not presented as evidence for a definitive statement of computational efficiency (properly done that would entail a separate study) but merely to whet the numerical appetite.

5 Concluding Remarks

We have offered a first-order formulation for the dynamics of an elastic body that may be constrained, partially constrained, or completely unconstrained. The benefit of this approach is that it dispenses with the cumbersome inertial parameters that are dependent on deformation in a second-order formulation. There is, however, a slightly more involved kinematical relation for the elastic coordinates that accompanies the first-order dynamical equations. In addition, a new stiffness and force term enter the first-order picture although, typically, their parameters can be easily gleaned from quantities that would otherwise be readily available.

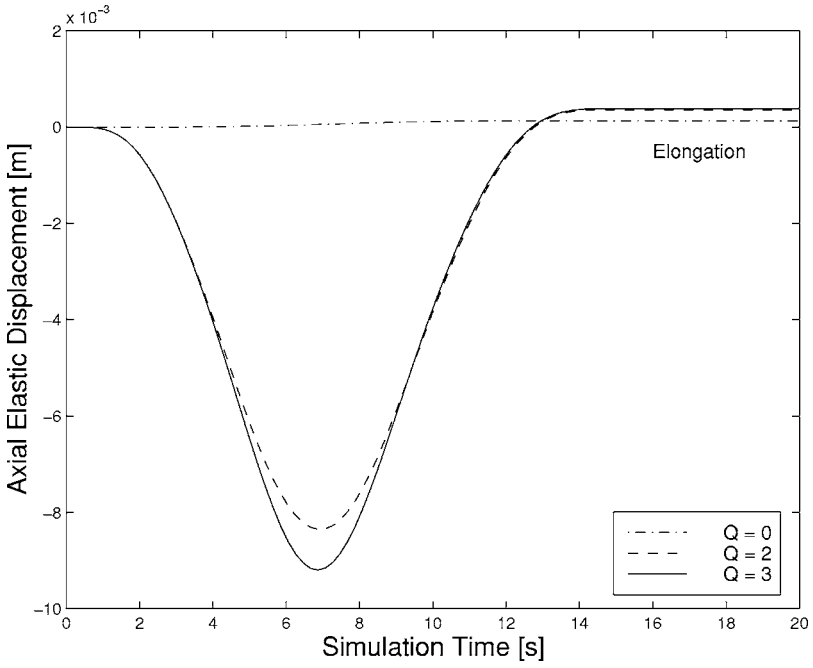

Fig. 5 Effect of higher-degree terms on axial deflection (N_e=1)

The development of the first-order formulation is, in itself, analytically interesting, which makes use of the Boltzmann-Hamel approach to quasi-coordinates—a method in dynamics that is rarely employed these days. Moreover and more important from a practical standpoint, judging by the numerical example of a rotating elastic beam, the first-order formulation computationally outperforms the second-order one as may have been anticipated by the simplification of the inertial parameters. It is hazardous, of course, to reach any sweeping conclusion regarding the relative efficiency of the two formulations. There has been no attempt here to streamline either method.

As the literature plainly shows, there is still a vigorous debate on the relative importance of various nonlinear terms, which of course depends greatly on the system and the prevailing conditions. In this paper, we have not sought to address this issue. We do, nonetheless, feel justified in asserting as a preliminary conclusion that the first-order formulation, in the analysis of elastic-body dynamics, merits serious consideration and a closer look.

References

[1] Kane, T. R., Ryan, R. R., and Banerjee, A. K., 1987, "Dynamics of a Cantilever Beam Attached to a Moving Base," J. Guid. Control Dyn., **10**(2), pp. 139–151.

[2] Hanagud, S., and Sarkar, S., 1989, "Problem of the Dynamics of a Cantilever Beam Attached to a Moving Base," J. Guid. Control Dyn., **12**(3), pp. 438–441.

[3] Damaren, C. J., and Sharf, I., 1995, "Simulation of Flexible-Link Manipulators With Inertial and Geometric Nonlinearities," ASME J. Dyn. Syst., Meas., Control, **117**, pp. 74–87.

[4] Sharf, I., 1995, "Geometric Stiffening in Multibody Dynamics Formulations," J. Guid. Control Dyn., **18**(4), pp. 882–890.

[5] White, M. W. D., and Heppler, G. R., 1995, "Vibration Modes and Frequencies of Timoshenko Beams With Attached Rigid Bodies," ASME J. Appl. Mech., **62**(1), pp. 193–199.

[6] Oguamanam, D. C. D., and Heppler, G. R., 1998, "Geometric Stiffening of Timoshenko Beams," ASME J. Appl. Mech., **65**(4), pp. 923–929.

[7] Sharf, I., 1999, "Nonlinear Strain Measures, Shape Functions and Beam Elements for Dynamics of Flexible Beams," Multibody Syst. Dyn., **3**, pp. 189–205.

[8] Boltzmann, L., 1902, "Über die Form der Lagrange'schen Gleichungen fr nichtholonome, Generalisierte Coordinaten," *Sitzungsberichte der Kaiserlichen Akademie der Wissenschaften* (Wien), CXI. Band, X. Heft, pp. 1603–1614.

[9] Hamel, G., 1904, "Die Lagrange-Eulerschen Gleichungen der Mechanik," Z. Math. Phys., **50**, pp. 1–57.

[10] Papastavridis, J. G., 1994, "On the Boltzmann-Hamel Equations of Motion: A Vectorial Treatment," ASME J. Appl. Mech., **61**(6), pp. 453–459.

[11] Junkins, J. L., and Schaub, H., 1997, "An Instantaneous Eigenstructure Quasivelocity Formulation for Nonlinear Multibody Dynamics," J. Astronaut. Sci., **45**(3), pp. 279–295.

[12] Hughes, P. C., 1980, "Modal Identities for Elastic Bodies, With Application to Vehicle Dynamics and Control," ASME J. Appl. Mech., **47**, pp. 177–184.

[13] Meirovitch, L., 1991, "Hybrid state Equations of Motion for Flexible Bodies in Terms of Quasi-Coordinates," J. Guid. Control Dyn., **14**(5), pp. 1008–1013.

[14] Whittaker, E. T., 1937, *A Treatise on the Analytical Dynamics of Particles and Rigid Bodies*, Cambrigde University Press, Cambridge, UK.

Delamination Detection-Oriented Finite Element Model for a Fiber Reinforced Polymer Bonded Concrete Plate and Its Application With Vibration Measurements

D. Wu

S. S. Law

Department of Civil and Structural Engineering,
Hong Kong Polytechnic University,
Yuk Choi Road,
Hunghom Kowloon,
Hong Kong 0000,
China

Delamination is a common type of damage in laminated fiber-reinforced polymer (FRP) composites. As FRP composites are becoming popular in upgrading and strengthening of civil concrete structures, the specific delamination damage, i.e., the FRP-concrete debonding, is considered more critical than inter-laminar delamination occurring in the FRP composites. A finite element formulation on the FRP-bonded concrete plate with this type of delamination fault is developed in the context of non-destructive evaluation from vibration measurements and compared with a two-layer solid element model. An adhesive interface where possible debonding could occur is introduced between the FRP and the concrete plates. A scalar damage parameter characterizing the delamination is incorporated into the formulation of a finite element model that is compatible with the vibration-based damage identification procedure. The formulated model is then applied to the prediction of FRP-concrete delaminations from modal test results based on the sensitivity analysis of uniform load surface curvature, which has been previously proposed by the authors. The validity of the methodology is demonstrated in two numerical examples. The first one is used to check the model accuracy, while the second one assesses the efficiency of the model-based identification method. [DOI: 10.1115/1.2190228]

1 Introduction

Over the last few decades, fiber-reinforced polymer (FRP) composite materials have been increasingly used in many engineering applications, especially in the aerospace and defense industries, due to their high ratio of stiffness and strength to self-weight. The use of FRP in upgrading and strengthening of civil concrete structures has become more popular in recent years due to the large reduction of material cost. Previous research [1,2] showed that glass fiber composites could be effectively used for concrete beam strengthening to improve the flexural load carrying capacity. Compared with conventional rehabilitation techniques with steel reinforcing patch, the technique of using FRP for tension face strengthening provides better ultimate flexural load capacity, less labor intensive implementation, and less maintenance problems with the material at the expense of a small additional self weight.

Delamination is one of the most common types of damage in laminated FRP composites due to their relatively weak interlaminar strengths. For a concrete beam or plate reinforced with the FRP bonding technique for enhancing the ultimate failure loads and the desirable failure behaviors, the connecting layer between the FRP plate and concrete host is more vulnerable to delamination damage due to the distinctly different ductility of the FRP and concrete materials. Although fracture mechanics of the FRP-concrete debonding are different to that of the interlaminar delamination which occurred inside the FRP composite, and many experimental studies show that the FRP-concrete debonding failure scenarios may be very variegated [3], their effects on the static and dynamic behaviors of the structure are similar in the design consideration. The presence of delamination may significantly affect the structural integrity, hence severely reduce the stiffness and strength of the structure statically, and in some cases lead to catastrophic failure. Therefore, the development of a reliable delamination detection or integrity evaluation system becomes very important. Fortunately the delamination also affects the structural stiffness and damping dynamically, which results in changes in the dynamic characteristics of the structure. Thus vibration measurements from a structure at two or more stages of its life span offer the possibility of detecting delamination damages.

As previously mentioned, the FRP-concrete debonding failure modes may be very variegated, and their effects on the structural dynamic characteristics vary greatly. In this paper, only delamination damage occurred in the interface between the FRP and the concrete is investigated as a typical failure mode. Delamination reduces the stiffness and increases damping of the structure in general, which in turn decreases the frequencies and increases the modal damping of the delaminated structure. Delamination involves mainly a separation of the two types of materials, and its effects on the structural mass are usually small and thus are neglected in this paper. Diaz Valdes and Soutis [4,5] studied the effect of delamination on the modal frequencies of existing laminated composite beams. Modal frequencies were obtained by applying a novel method known as resonant ultrasound spectroscopy. It was demonstrated that changes of the modal frequencies after delamination, when compared with those of an intact specimen, give a good indication on the presence and magnitude of damage. With the help of the modal strain energy distribution in a beam, Griffin and Sun [6] presented a delamination identification method based on changes of damping ratio of a delaminated structure. Luo and Hanagud [7] carried out a comparative study on the sensitivity of four quantitative indices: frequencies, mode shapes,

Contributed by the Applied Mechanics Division of ASME for publication in the JOURNAL OF APPLIED MECHANICS. Manuscript received March 29, 2004; final manuscript received February 3, 2006. Review conducted by S. Govindjee. Discussion on the paper should be addressed to the Editor, Prof. Robert M. McMeeking, Journal of Applied Mechanics, Department of Mechanical and Environmental Engineering, University of California—Santa Barbara, Santa Barbara, CA 93106-5070, and will be accepted until four months after final publication of the paper itself in the ASME JOURNAL OF APPLIED MECHANICS.

damping ratios, and delamination coefficients (defined as $D = \int_\Omega |\Delta\phi| d\Omega / \int_\Omega |\phi| d\Omega$, where ϕ is the mode shape of the composite plate and Ω is the area of the plate). The authors concluded that the frequency information alone is insufficient to provide a reliable prediction of delamination, and that the delamination coefficients give a better indication of the presence of delamination among the four indices. Ratcliffe and Bagaria [8] found that the curvature of an undamaged structure is smooth and continuous and the irregularity of the curvature could indicate the location of delamination in a composite beam. When incorporated with the "gapped-smoothing" technique, the method has an advantage of not requiring an undamaged reference of the structure.

All the above methods are experiment-driven without an analytical model to represent the delaminated structure, and therefore they do not lead to a quantitative indication of the damage. For an accurate investigation of the effects of delamination, finite element models of delaminated beams and plates were developed based on Euler beam theory [9], engineering beam theory [10], and Timoshenko beam theory and the Galerkin method [11]. A finite element model using layer-wise theory was also developed for laminated composite plates [12], which can be used to study the multi-delamination problem in the thickness of the plate. When incorporated with modern artificial intelligence (AI) computation techniques of neural network [13–15] or genetic algorithm [16], these models make the real-time non-destructive delamination detection based on vibration measurements possible.

In consideration of dynamic behavior of the delaminated beams (or plates), one may assume the delaminated members to deform independently without taking into account the mutual contact and friction effects. This kind of modeling is known as "free mode" analysis [17]. In order to take into account the possible dynamic contact between delaminated layers in an approximate way, a "constrained mode" has also been proposed, in which the delaminated layers are assumed to have the same transverse displacement but are allowed to slide over each other [9]. A more refined model may adopt contact elements or contact conditions in the finite element modeling to avoid overlapping between the upper and lower portions of a delaminated plate and the dynamic analysis must be performed by time integration techniques [18].

All the above models are not suitable for the structural damage identification that is an inverse problem mathematically. In order to study the location and magnitude of a particular delamination damage, a new finite element mesh has to be constructed for each case. Thereby, to use these models in model-based damage identification procedures, one has to construct a large number of finite element meshes and choose the one that closely reproduces the experimental data. Perel and Palazotto [19] developed a finite element model of a delaminated beam particularly for the damage identification procedure. Three parameters characterizing the location and magnitude of delamination are selected and estimated by minimizing the discrepancy between the computed and measured responses.

This paper focuses on the FRP-bonded concrete plate structures and the delaminations are confined to occur between the FRP layer and the concrete host. A scalar damage parameter characterizing the extent of delamination is introduced and a finite element model with this type of delamination is formulated. Instead of using AI-based searching techniques to minimize the discrepancy between the computed and measured dynamic characteristics, a sensitivity analysis with the uniform load surface curvature (ULSC) with respect to the delamination is applied to identify the damage parameters.

2 Finite Element Formulation

2.1 Assumptions and Governing Equations of the Interface Layer. An FRP-bonded concrete plate as shown in Fig. 1 can be modeled as a laminate comprising two plies: the concrete host and the FRP plate, between which an interface is introduced, where the delamination is likely to occur. The interface behaves as

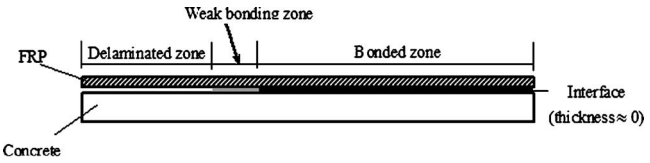

Fig. 1 Propagation of delamination from the free end of FRP-bonded concrete beams

an entity with large stiffness but negligible thickness. Its physical justification at a microscopic level is the existence of the thin resin-rich layer between the plies. When the loading level increases, or the fatigue durability of the structure decreases during its service life, delamination damage initiates and gradually develops at the interface. From the viewpoint of micro-mechanics, there is an interim state between the intact and the delaminated interface states. This damage zone containing micro-defects is called the weak bonding zone (WBZ) in this paper. Macrodelamination forms after these micro-defects grow and coalesce. To represent these micro-defects in the context of continuum damage mechanics, a damage parameter is required to describe the macroscopic effects of these distributed micro-defects.

The parameter p_b is therefore introduced to characterize the growth of the micro-cracks or the macro-bonding condition of the interface

$$p_b = \begin{cases} 0 & \text{delaminated} \\ >0 \text{ and } <1 & \text{weak bonding} \\ 1 & \text{intact} \end{cases} \tag{1}$$

The adhesive layer is assumed to carry only constant shear and peel strains over its thickness in both perfect bonding and weak bonding conditions. For the plate segment with delamination at the interface, it is assumed that there is no stress transferring between the concrete host and the FRP layer. In addition, contact and friction between the two debonded surfaces are not considered for simplicity. Based on the well-known constant shear and peel strain assumption [20], the peel and shear stress in the interface layer are given by Tong, Sun, and Atluri [21] in the form of

$$\sigma_b = \frac{p_b E_{\text{ad}}(1-\upsilon_{\text{ad}})}{(1-2\upsilon_{\text{ad}})(1+\upsilon_{\text{ad}})h_{\text{ad}}}(w_f - w_c) \tag{2}$$

$$\tau_b = \frac{p_b E_{\text{ad}}}{2(1+\upsilon_{\text{ad}})h_{\text{ad}}}\gamma \tag{3}$$

where h, E, ν, and w denote the thickness, the Young's modulus, the Poisson ratio, and the transverse deflection, respectively, and the subscripts f, ad, and c, respectively, represent the lower surface of the FRP plate, the adhesive layer and the upper surface of the concrete host. The shear strain γ_{xz} takes the form as follows:

$$\gamma_{xz} = \frac{1}{2}\left(\frac{\partial w_c}{\partial x} + \frac{\partial w_f}{\partial x}\right) + \frac{1}{2h_{\text{ad}}}\left[\left(\frac{h}{2}+h_D\right)\frac{\partial w_c}{\partial x} + \left(\frac{h}{2}-h_D\right)\frac{\partial w_f}{\partial x}\right] + \frac{u_f - u_c}{h_{\text{ad}}}, \tag{4}$$

where h denotes the thickness of the whole FRP-bonded concrete plate and h_D denotes the distance between the interface and the mid-plane of the plate, as shown in Fig. 2. u represents the longitudinal displacement along the x axis. The transverse shear strain γ_{yz} can be similarly written as Eq. (4).

2.2 Basic Equations for the Three-Dimensional Anisotropic Material. The FRP composite sheet is made of the typical anisotropic material. This section presents the basic equations on the three-dimensional anisotropic material as the basis of further formulations. These equations include the following.

The strain-displacement equations

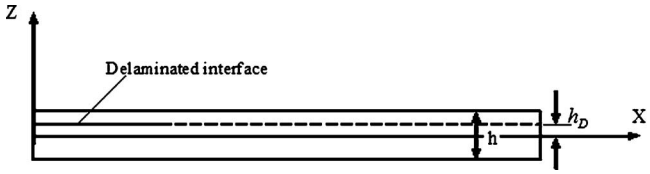

Fig. 2 Diagram of the FRP-bonded concrete beam (interface thickness=0)

$$\varepsilon_{xy}=\frac{1}{2}\left(\frac{\partial u}{\partial x}+\frac{\partial v}{\partial y}\right)\quad \varepsilon_{xz}=\frac{1}{2}\left(\frac{\partial u}{\partial z}+\frac{\partial w}{\partial x}\right)\quad \varepsilon_{yz}=\frac{1}{2}\left(\frac{\partial v}{\partial z}+\frac{\partial w}{\partial y}\right) \tag{5}$$

The equations of motion:

$$\begin{cases}\sigma_{xx,x}+\sigma_{xy,y}+\sigma_{xz,z}=\rho\ddot{u}\\ \sigma_{yy,y}+\sigma_{yx,x}+\sigma_{yz,z}=\rho\ddot{v}\\ \sigma_{zx,x}+\sigma_{zy,y}+\sigma_{zz,z}=\rho\ddot{w}\end{cases} \tag{6}$$

The constitutive relations in the principal coordinate system:

$$\begin{Bmatrix}\sigma_1\\ \sigma_2\\ \sigma_3\\ \sigma_4\\ \sigma_5\\ \sigma_6\end{Bmatrix}=\begin{bmatrix}C_{11} & C_{12} & C_{13} & 0 & 0 & 0\\ C_{12} & C_{22} & C_{23} & 0 & 0 & 0\\ C_{13} & C_{23} & C_{33} & 0 & 0 & 0\\ 0 & 0 & 0 & C_{44} & 0 & 0\\ 0 & 0 & 0 & 0 & C_{55} & 0\\ 0 & 0 & 0 & 0 & 0 & C_{66}\end{bmatrix}\begin{Bmatrix}\varepsilon_1\\ \varepsilon_2\\ \varepsilon_3\\ \varepsilon_4\\ \varepsilon_5\\ \varepsilon_6\end{Bmatrix} \tag{7}$$

where

$$\Delta=\frac{1-\nu_{12}\nu_{21}-\nu_{23}\nu_{32}-\nu_{13}\nu_{31}-2\nu_{12}\nu_{23}\nu_{31}}{E_1E_2E_3}$$

$$C_{11}=\frac{1-\nu_{23}\nu_{32}}{E_2E_3\Delta}\quad C_{12}=\frac{\nu_{21}+\nu_{23}\nu_{31}}{E_1E_3\Delta}$$

$$C_{13}=\frac{\nu_{31}+\nu_{21}\nu_{32}}{E_1E_2\Delta}\quad C_{23}=\frac{\nu_{32}+\nu_{12}\nu_{31}}{E_1E_2\Delta}$$

$$C_{22}=\frac{1-\nu_{13}\nu_{31}}{E_1E_3\Delta}\quad C_{33}=\frac{1-\nu_{12}\nu_{21}}{E_1E_2\Delta}$$

$$C_{44}=G_{23}\quad C_{55}=G_{31}\quad C_{66}=G_{12}$$

The corresponding equations of the concrete host can be similarly written except that the coefficients in Eq. (7) should be replaced by the constitutive relations of isotropic material where

$$C_{11}=C_{22}=C_{33}=\frac{E}{1-\nu^2}\quad C_{12}=C_{13}=C_{23}=\frac{\nu E}{1-\nu^2} \tag{8}$$

$$C_{44}=C_{55}=C_{66}=G$$

2.3 Strain-Stress Formulation of the Delaminated Plate. Considering the FRP-bonded plate with no externally applied loads on the upper and lower surfaces, the stress boundary conditions at the upper and lower surfaces are given as

$$\begin{cases}\sigma_{zz}=0\\ \sigma_{xz}=0\\ \sigma_{yz}=0\end{cases}\quad \text{at } z=\pm\frac{h}{2} \tag{9}$$

According to the classical plate theory, it is assumed that the thickness of the plate does not change during deformation such that

$$\varepsilon_{zz}=0 \tag{10}$$

In the case of a thin plate, the normal stress in the z axis can be assumed equal to zero

$$\sigma_{zz}=0 \tag{11}$$

and the third row of the constitutive relations in Eq. (7) can be discarded. However, in this formulation, the peel stress at the interface layer has to be taken into account, and the strain ε_{zz} could be very small but not equal to zero. Furthermore, by taking into account the boundary conditions in Eq. (9), the strains along the z axis in the concrete host and the FRP sheet take up the following forms:

$$\varepsilon_{zz}^{(1)}(x,y,z)=\phi^{(1)}(x,y)\left(1+\frac{2}{h}z\right)$$

$$\varepsilon_{zz}^{(2)}(x,y,z)=\phi^{(2)}(x,y)\left(1-\frac{2}{h}z\right) \tag{12}$$

where $\phi(x,y)$ is an unknown function that characterizes the strain distribution in the mid-plane of the plate, and the superscripts (1) and (2) represent terms in the concrete and FRP sheet respectively.

On further inspection of the stiffness coefficients in Eq. (7), the strain ε_{zz} is found to be very small due to the small dimension of the plate in z direction compared with the other two dimensions, the Poisson ratios ν_{31} and ν_{32} are also quite small compared with ν_{21}. Therefore one can assume that the coefficients C_{13} and C_{23} are negligible and the peel stress and strain in the z axis are independently related by a stiffness scalar. The resulting constitutive equations take the form as

$$\begin{Bmatrix}\sigma_1\\ \sigma_2\\ \sigma_3\\ \sigma_4\\ \sigma_5\\ \sigma_6\end{Bmatrix}=\begin{bmatrix}Q_{11} & Q_{12} & 0 & 0 & 0 & 0\\ Q_{12} & Q_{22} & 0 & 0 & 0 & 0\\ 0 & 0 & Q_{33} & 0 & 0 & 0\\ 0 & 0 & 0 & Q_{44} & 0 & 0\\ 0 & 0 & 0 & 0 & Q_{55} & 0\\ 0 & 0 & 0 & 0 & 0 & Q_{66}\end{bmatrix}\begin{Bmatrix}\varepsilon_1\\ \varepsilon_2\\ \varepsilon_3\\ \varepsilon_4\\ \varepsilon_5\\ \varepsilon_6\end{Bmatrix} \tag{13}$$

where

$$Q_{11}=\frac{E_1^2}{E_1-\nu_{12}^2E_2}\quad Q_{12}=\frac{\nu_{12}E_1E_2}{E_1-\nu_{12}^2E_2}\quad Q_{22}=\frac{E_1E_2}{E_1-\nu_{12}^2E_2}$$

$$Q_{33}=E_3\quad Q_{44}=G_{23}\quad Q_{55}=G_{13}\quad Q_{66}=G_{12}$$

The constitutive relations are expressed in another coordinate system by rotating about the z axis counterclockwise through an angle θ with respect to the principal coordinate system of the material, the relations can be rewritten as

$$\begin{Bmatrix}\sigma_{xx}\\ \sigma_{yy}\\ \sigma_{zz}\\ \sigma_{yz}\\ \sigma_{xz}\\ \sigma_{xy}\end{Bmatrix}=\begin{bmatrix}\bar{Q}_{11} & \bar{Q}_{12} & 0 & 0 & 0 & \bar{Q}_{16}\\ \bar{Q}_{12} & \bar{Q}_{22} & 0 & 0 & 0 & \bar{Q}_{26}\\ 0 & 0 & \bar{Q}_{33} & 0 & 0 & 0\\ 0 & 0 & 0 & \bar{Q}_{44} & \bar{Q}_{45} & 0\\ 0 & 0 & 0 & \bar{Q}_{45} & \bar{Q}_{55} & 0\\ \bar{Q}_{16} & \bar{Q}_{26} & 0 & 0 & 0 & \bar{Q}_{66}\end{bmatrix}\begin{Bmatrix}\varepsilon_{xx}\\ \varepsilon_{yy}\\ \varepsilon_{zz}\\ \varepsilon_{yz}\\ \varepsilon_{xz}\\ \varepsilon_{xy}\end{Bmatrix} \tag{14}$$

where

$$\bar{Q}_{11} = Q_{11}c^4 + 2(Q_{12} + 2Q_{66})s^2c^2 + Q_{22}s^4$$

$$\bar{Q}_{12} = (Q_{11} + Q_{22} - 4Q_{66})s^2c^2 + Q_{12}(s^4 + c^4)$$

$$\bar{Q}_{16} = (Q_{11} - Q_{12} - 2Q_{66})sc^3 + (Q_{12} - Q_{22} + 2Q_{66})s^3c$$

$$\bar{Q}_{26} = (Q_{11} - Q_{12} - 2Q_{66})s^3c + (Q_{12} - Q_{22} + 2Q_{66})sc^3$$

$$\bar{Q}_{22} = Q_{11}s^4 + 2(Q_{12} + 2Q_{66})s^2c^2 + Q_{22}c^4 \quad \bar{Q}_{33} = Q_{33}$$

$$\bar{Q}_{44} = Q_{44}c^2 + Q_{55}s^2, \quad \bar{Q}_{45} = (Q_{55} - Q_{44})cs \quad \bar{Q}_{55} = Q_{55}c^2 + Q_{44}s^2$$

$$\bar{Q}_{66} = (Q_{11} + Q_{22} - 2Q_{12} - 2Q_{66})s^2c^2 + Q_{66}(s^4 + c^4)$$

$$c = \cos\theta \quad s = \sin\theta$$

Considering the strain-displacement relation, $\varepsilon_{zz} = \partial w / \partial z$, the transverse displacement $w(x,y,z)$ can be obtained from Eq. (12) as

$$w^{(1)}(x,y,z) = \phi^{(1)}(x,y)\int_{-h/2}^{z}\left(1 + \frac{2}{h}z\right)dz = \phi^{(1)}(x,y)\left(\frac{z^2}{h} + z + \frac{h}{4}\right)$$

$$w^{(2)}(x,y,z) = \phi^{(2)}(x,y)\int_{z}^{h/2}\left(1 - \frac{2}{h}z\right)dz = \phi^{(2)}(x,y)\left(\frac{z^2}{h} - z + \frac{h}{4}\right) \tag{15}$$

Therefore one gets the transverse deflection at the upper surface of the concrete $w_c = w^{(1)}(x,y,h_d)$ and the deflection at the lower surface of the FRP, $w_f = w^{(2)}(x,y,h_d)$. Substituting them into Eq. (2) leads to

$$\phi^{(2)}(x,y)\left(\frac{h_D^2}{h} - h_D + \frac{h}{4}\right) - \phi^{(1)}(x,y)\left(\frac{h_D^2}{h} + h_D + \frac{h}{4}\right) = \frac{\sigma_b(1 - 2v_{ad})(1 + v_{ad})h_{ad}}{p_b E_{ad}(1 - v_{ad})} \tag{16}$$

By writing the constant peel stress at the interface layer as $\sigma_b = Q_{33}\varepsilon_{zz}^{(1)}|_{z=h_D} = Q_{33}\phi^{(1)}(x,y)(1 + 2h_D/h)$ and substituting it into Eq. (16), we can have $\phi^{(2)}$ expressed as a function of $\phi^{(1)}$

$$\phi^{(2)}(x,y) = \left[\frac{Q_{33}\left(1 + \frac{2h_D}{h}\right)(1 - 2v_{ad})(1 + v_{ad})h_{ad}}{p_b E_{ad}(1 - v_{ad})} + \frac{\frac{h_D^2}{h} + h_D + \frac{h}{4}}{\frac{h_D^2}{h} - h_D + \frac{h}{4}}\right]\phi^{(1)}(x,y) \tag{17}$$

,

Equation (17) links up the strain distributions in the two plates enabling the subsequent mathematical derivation of delamination formulation. Taking the longitudinal displacement along the x axis at the mid-plane of concrete host as $u_0^{(1)}(x,y) = u^{(1)} \times (x,y,z)|_{z=h_D/2h/4}$, the longitudinal displacement of the concrete can be written as

$$u^{(1)}(x,y,z) = u_0^{(1)}(x,y) + \int_{h_D/2-h/4}^{z}\left(2\varepsilon_{xz}^{(1)} - \frac{\partial w^{(1)}}{\partial x}\right)dz \tag{18}$$

Similarly the longitudinal displacement of the FRP sheet takes the form

$$u^{(2)}(x,y,z) = u_0^{(2)}(x,y) + \int_{h_D/2+h/4}^{z}\left(2\varepsilon_{xz}^{(2)} - \frac{\partial w^{(2)}}{\partial x}\right)dz$$

$$\text{where} \quad u_0^{(2)}(x,y) = u^{(2)}(x,y,z)|_{z=h_D/2+h/4}. \tag{19}$$

Inspecting the elements in rows 4 and 5 in the constitutive equations (14) in conjunction with the boundary conditions in Eq. (9), we can conclude that

$$\begin{cases}\varepsilon_{xz} = 0 \\ \varepsilon_{yz} = 0\end{cases} \quad \text{at } z = \pm\frac{h}{2} \tag{20}$$

Therefore the transverse shear strain $\varepsilon_{xz}^{(1)}(x,y,z)$ in the concrete host and $\varepsilon_{xz}^{(2)}(x,y,z)$ in the FRP sheet can be assumed to take the form as

$$\varepsilon_{xz}^{(1)}(x,y,z) = \varphi^{(1)}(x,y)\left(1 + \frac{2}{h}z\right)$$

$$\varepsilon_{xz}^{(2)}(x,y,z) = \varphi^{(2)}(x,y)\left(1 - \frac{2}{h}z\right) \tag{21}$$

where $\varphi(x,y)$ is an unknown function similar to $\phi(x,y)$ that characterizes the strain distribution at the mid-plane of the plate. Substituting Eqs. (21) and (15) into Eqs. (18) and (19), we have the displacement along the x axis expressed as

$$u^{(1)}(x,y,z) = u_0^{(1)}(x,y) + \int_{h_D/2-h/4}^{z}\left[2\varphi^{(1)}\left(1 + \frac{2}{h}z\right) - \frac{\partial\phi^{(1)}}{\partial x}\left(\frac{z^2}{h} + z + \frac{h}{4}\right)\right]dz = u_0^{(1)}(x,y) + 2\varphi^{(1)}\left(\frac{z^2}{h} + z + \frac{3h}{16} - \frac{h_D}{4} - \frac{h_D^2 h}{4}\right) + \frac{\partial\phi^{(1)}}{\partial x}\frac{(2h_D - h - 4z)(16z^2 + 20hz + 8h_D z + 7h^2 + 8h_D h + 4h_D^2)}{192h}$$

or in the matrix form:

$$u^{(1)}(x,y,z)=\begin{Bmatrix}1\\ z\\ z^2\\ z^3\end{Bmatrix}\begin{bmatrix}1 & \dfrac{\partial}{\partial x}\dfrac{(8h_D^3-7h^3+6h^2h_D+12h_D^2h)}{192h} & \dfrac{3h}{8}-\dfrac{h_D}{2}-\dfrac{h_D^2h}{2}\\ 0 & -\dfrac{h}{4}\dfrac{\partial}{\partial x} & 2\\ 0 & -\dfrac{h}{2}\dfrac{\partial}{\partial x} & \dfrac{2}{h}\\ 0 & -\dfrac{1}{3h}\dfrac{\partial}{\partial x} & 0\end{bmatrix}\begin{Bmatrix}u_0^{(1)}\\ \phi_{(1)}\\ \varphi_{(1)}\end{Bmatrix} \tag{22}$$

Similarly for the FRP sheet, we have

$$u^{(2)}(x,y,z)=u_0^{(2)}(x,y)+\int_{h_D/2+h/4}^{z}\left[2\varphi^{(2)}\left(1-\frac{2}{h}z\right)-\frac{\partial\phi^{(2)}}{\partial x}\left(\frac{z^2}{h}-z+\frac{h}{4}\right)\right]dz=u_0^{(2)}(x,y)+2\varphi^{(2)}\left(-\frac{z^2}{h}+z-\frac{3h}{16}-\frac{h_D}{4}+\frac{h_D^2h}{4}\right)$$
$$+\frac{\partial\phi^{(2)}}{\partial x}\frac{(4z-2h_D-h)(16z^2-20hz+8h_Dz+7h^2-8h_Dh+4h_D^2)}{192h}$$

or

$$u^{(2)}(x,y,z)=\begin{Bmatrix}1\\ z\\ z^2\\ z^3\end{Bmatrix}\begin{bmatrix}1 & \dfrac{\partial}{\partial x}\dfrac{(-8h_D^3-7h^3-6h^2h_D+12h_D^2h)}{192h} & \dfrac{h_D^2h}{2}-\dfrac{3h}{8}-\dfrac{h_D}{2}\\ 0 & \dfrac{h}{4}\dfrac{\partial}{\partial x} & 2\\ 0 & -\dfrac{h}{2}\dfrac{\partial}{\partial x} & -\dfrac{2}{h}\\ 0 & \dfrac{1}{3h}\dfrac{\partial}{\partial x} & 0\end{bmatrix}\begin{Bmatrix}u_0^{(2)}\\ \phi^{(2)}\\ \varphi^{(2)}\end{Bmatrix} \tag{23}$$

Further with the use of the strain-displacement relation, $\varepsilon_{xx}=\partial u/\partial x$, we can find the strains $\varepsilon_{xx}^{(1)}$ and $\varepsilon_{xx}^{(2)}$ in terms of the unknown characterizing functions u_0, ϕ, and φ:

$$\varepsilon_{xx}^{(1)}=\begin{Bmatrix}1\\ z\\ z^2\\ z^3\end{Bmatrix}\begin{bmatrix}\dfrac{\partial}{\partial x} & \dfrac{\partial^2}{\partial x^2}\dfrac{(8h_D^3-7h^3+6h^2h_D+12h_D^2h)}{192h} & \left(\dfrac{3h}{8}-\dfrac{h_D}{2}-\dfrac{h_D^2h}{2}\right)\dfrac{\partial}{\partial x}\\ 0 & -\dfrac{h}{4}\dfrac{\partial^2}{\partial x^2} & 2\dfrac{\partial}{\partial x}\\ 0 & -\dfrac{h}{2}\dfrac{\partial^2}{\partial x^2} & \dfrac{2}{h}\dfrac{\partial}{\partial x}\\ 0 & -\dfrac{1}{3h}\dfrac{\partial^2}{\partial x^2} & 0\end{bmatrix}\begin{Bmatrix}u_0^{(1)}\\ \phi^{(1)}\\ \varphi^{(1)}\end{Bmatrix} \tag{24}$$

and

$$\varepsilon_{xx}^{(2)}=\begin{Bmatrix}1\\ z\\ z^2\\ z^3\end{Bmatrix}\begin{bmatrix}\dfrac{\partial}{\partial x} & \dfrac{\partial^2}{\partial x^2}\dfrac{(-8h_D^3-7h^3-6h^2h_D+12h_D^2h)}{192h} & \left(\dfrac{h_D^2h}{2}-\dfrac{3h}{8}-\dfrac{h_D}{2}\right)\dfrac{\partial}{\partial x}\\ 0 & \dfrac{h}{4}\dfrac{\partial^2}{\partial x^2} & 2\dfrac{\partial}{\partial x}\\ 0 & -\dfrac{h}{2}\dfrac{\partial^2}{\partial x^2} & -\dfrac{2}{h}\dfrac{\partial}{\partial x}\\ 0 & \dfrac{1}{3h}\dfrac{\partial^2}{\partial x^2} & 0\end{bmatrix}\begin{Bmatrix}u_0^{(2)}\\ \phi^{(2)}\\ \varphi^{(2)}\end{Bmatrix} \tag{25}$$

The displacements at the delamination surfaces of the FRP and concrete sheets, u_f and u_c in Eq. (4), respectively, are written as

$$u_c=u^{(1)}(x,y,h_D)=u_0^{(1)}(x,y)+\int_{h_D/2-h/4}^{h_D}\left(2\varepsilon_{xz}^{(1)}-\frac{\partial w^{(1)}}{\partial x}\right)dz,$$

$$u_f=u^{(2)}(x,y,h_D)=u_0^{(2)}(x,y)+\int_{h_D/2+h/4}^{h_D}\left(2\varepsilon_{xz}^{(2)}-\frac{\partial w^{(2)}}{\partial x}\right)dz \tag{26}$$

One can substitute Eqs. (26), (21), and (15) into Eq. (3), and express $u_0^{(2)}(x,y)$ as a function of $u_0^{(1)}(x,y)$,

$$u_0^{(2)}(x,y) = F(\phi^{(1)}, \varphi^{(1)}, \varphi^{(2)}) \cdot u_0^{(1)}(x,y) \tag{27}$$

where $F(\phi^{(1)}, \varphi^{(1)}, \varphi^{(2)})$ is a general function of the characterizing functions $\phi^{(1)}(x,y)$, $\varphi^{(1)}(x,y)$, and $\varphi^{(2)}(x,y)$. This gives the relationship between the displacements along the x axis of the two plates which is similar to Eq. (17) which is for the out-of-plane displacements. Similar to Eqs. (18)–(27), one can obtain the formulations on the displacements along the y axis as

$$v^{(1)}(x,y,z) = v_0^{(1)}(x,y) + \int_{h_D/2-h/4}^{z} \left(2\varepsilon_{yz}^{(1)} - \frac{\partial w^{(1)}}{\partial y}\right) dz,$$

$$v^{(2)}(x,y,z) = v_0^{(2)}(x,y) + \int_{h_D/2+h/4}^{z} \left(2\varepsilon_{yz}^{(2)} - \frac{\partial w^{(2)}}{\partial y}\right) dz \tag{28}$$

and the transverse strains

$$\varepsilon_{yz}^{(1)}(x,y,z) = \psi^{(1)}(x,y)\left(1 + \frac{2}{h}z\right)$$

$$\varepsilon_{yz}^{(2)}(x,y,z) = \psi^{(2)}(x,y)\left(1 - \frac{2}{h}z\right) \tag{29}$$

It should be noted that the coefficients C_{13} and C_{23} in Eq. (7) would not be negligible in the case of a thick plate, and an inclusion of them in the above formulation is necessary.

2.4 Finite Element Formulation of the Delaminated Plate. The virtual work principle of the delaminated plate element can be written in the form as

$$\begin{aligned}
&\int\int\int_{V_{\text{Con}}} \rho^{(1)}(\ddot{u}^{(1)}\delta u^{(1)} + \ddot{v}^{(1)}\delta v^{(1)} + \ddot{w}^{(1)}\delta w^{(1)})dV \\
&+ \int\int\int_{V_{\text{FRP}}} \rho^{(2)}(\ddot{u}^{(2)}\delta u^{(2)} + \ddot{v}^{(2)}\delta v^{(2)} + \ddot{w}^{(2)}\delta w^{(2)})dV \\
&+ \int\int\int_{V_{\text{Con}}} (\sigma_{xx}^{(1)}\delta\varepsilon_{xx}^{(1)} + \sigma_{xz}^{(1)}2\delta\varepsilon_{xz}^{(1)} + \sigma_{yy}^{(1)}\delta\varepsilon_{yy}^{(1)} + \sigma_{yz}^{(1)}2\delta\varepsilon_{yz}^{(1)} \\
&+ \sigma_{zz}^{(1)}\delta\varepsilon_{zz}^{(1)} + \sigma_{xy}^{(1)}2\delta\varepsilon_{xy}^{(1)})dV + \int\int\int_{V_{\text{FRP}}} (\sigma_{xx}^{(2)}\delta\varepsilon_{xx}^{(2)} \\
&+ \sigma_{xz}^{(2)}2\delta\varepsilon_{xz}^{(2)} + \sigma_{yy}^{(2)}\delta\varepsilon_{yy}^{(2)} + \sigma_{yz}^{(2)}2\delta\varepsilon_{yz}^{(2)} + \sigma_{zz}^{(2)}\delta\varepsilon_{zz}^{(2)} \\
&+ \sigma_{xy}^{(2)}2\delta\varepsilon_{xy}^{(2)})dV = 0
\end{aligned} \tag{30}$$

in which the volume and mass of the interface layer are ignored. In order to derive the finite element formulations, the equation of motion in Eq. (6) and the constitutive relations in Eq. (14) are substituted into Eq. (30) with the unknown characterizing functions, $\phi^{(1)}(x,y)$, $u_0^{(1)}(x,y)$, $v_0^{(1)}(x,y)$, $\varphi^{(1)}(x,y)$, $\varphi^{(2)}(x,y)$, $\psi^{(1)}(x,y)$, $\psi^{(2)}(x,y)$ represented by piecewise interpolation polynomials.

Table 1 gives the maximum order of derivatives of the unknown functions required in this finite element model. If the virtual work principle contains spatial derivatives of a characterizing function with a highest order of m, then the chosen interpolation polynomial has to satisfy the following conditions: (1) it must be a complete polynomial of degree m or higher; (2) the polynomial and all its derivatives up to order $m-1$ must be continuous across the element boundaries. The Hermit polynomials of the third degree satisfying the above requirements are therefore chosen to interpolate the function $\phi^{(1)}(x,y)$ as

$$\phi^{(1)}(x,y) = [N]_{1\times 16}\{\bar{\phi}^{(1)}\}_{16\times 1}$$

where

$$N_1 = H_1(\xi)H_1(\eta) \quad N_2 = H_3(\xi)H_1(\eta) \quad N_3 = H_1(\xi)H_3(\eta)$$

Table 1 The required maximum order of the characterizing functions in the virtual work formulation

Characterizing functions	Maximum order of derivative
$\phi_{(1)}$	2
$u_0^{(1)}$	1
$v_0^{(1)}$	1
$\varphi_{(1)}$, $\varphi_{(2)}$	1
$\psi_{(1)}$, $\psi_{(2)}$	1

$$N_4 = H_3(\xi)H_3(\eta)$$

$$N_5 = H_2(\xi)H_1(\eta) \quad N_6 = H_4(\xi)H_1(\eta)$$

$$N_7 = H_2(\xi)H_3(\eta) \quad N_8 = H_4(\xi)H_3(\eta)$$

$$N_9 = H_1(\xi)H_2(\eta) \quad N_{10} = H_3(\xi)H_2(\eta)$$

$$N_{11} = H_1(\xi)H_4(\eta) \quad N_{12} = H_3(\xi)H_4(\eta)$$

$$N_{13} = H_2(\xi)H_2(\eta) \quad N_{14} = H_4(\xi)H_2(\eta)$$

$$N_{15} = H_2(\xi)H_4(\eta) \quad N_{16} = H_4(\xi)H_4(\eta)$$

$$H_1(\xi) = 1 - 3\xi^2 + 2\xi^3 \quad H_2(\xi) = 3\xi^2 - 2\xi^3$$

$$H_3(\xi) = \xi - 2\xi^2 + \xi^3 \quad H_4(\xi) = \xi^3 - \xi^2$$

and

$$\{\bar{\phi}^{(1)}\} = \{\{\bar{\phi}_1^{(1)}\}\ \{\bar{\phi}_2^{(1)}\}\ \{\bar{\phi}_3^{(1)}\}\ \{\bar{\phi}_4^{(1)}\}\}^T \tag{31}$$

where $\{\bar{\phi}_i^{(1)}\} = \{\bar{\phi}_i^{(1)}\ \partial\bar{\phi}_i^{(1)}/\partial x\ \partial\bar{\phi}_i^{(1)}/\partial y\ \partial^2\bar{\phi}_i^{(1)}/\partial x\partial y\}^T$ and i denotes the node number.

Following the same rules, the two-dimensional Lagrange polynomials of the first degree are chosen to interpolate the other six characterizing functions (take $\varphi^{(1)}(x,y)$ for example):

$$\varphi^{(1)}(x,y) = [M]_{1\times 4}\{\bar{\varphi}^{(1)}\}_{4\times 1} \tag{32a}$$

where

$$M_1 = \tfrac{1}{4}(1-\xi)(1-\eta) \quad M_2 = \tfrac{1}{4}(1+\xi)(1-\eta)$$

$$M_3 = \tfrac{1}{4}(1+\xi)(1+\eta) \quad M_4 = \tfrac{1}{4}(1-\xi)(1+\eta)$$

and

$$\text{and} \quad \{\bar{\varphi}^{(1)}\} = \{\bar{\varphi}_1^{(1)}\ \bar{\varphi}_2^{(1)}\ \bar{\varphi}_3^{(1)}\ \bar{\varphi}_4^{(1)}\}^T$$

Further we introduce a general nodal displacement vector, $\{\bar{w}\}_{10\times 1}$, the components of which are defined as

$$\bar{w}_1 = \bar{\phi}^{(1)} \quad \bar{w}_2 = \frac{\partial\bar{\phi}^{(1)}}{\partial x} \quad \bar{w}_3 = \frac{\partial\bar{\phi}^{(1)}}{\partial y} \quad \bar{w}_4 = \frac{\partial^2\bar{\phi}^{(1)}}{\partial x\partial y}$$

$$\bar{w}_5 = \bar{u}_0^{(1)} \quad \bar{w}_6 = \bar{v}_0^{(1)}$$

$$\bar{w}_7 = \bar{\varphi}^{(1)} \quad \bar{w}_8 = \bar{\varphi}^{(2)} \quad \bar{w}_9 = \bar{\psi}^{(1)} \quad \bar{w}_{10} = \bar{\psi}^{(2)} \tag{32b}$$

By substituting the polynomial approximations of the unknown functions in Eqs. (31) and (32) into the virtual work principle expression in Eq. (30), we can obtain the finite element formulation of the delaminated plate model in terms of the general nodal displacement vector:

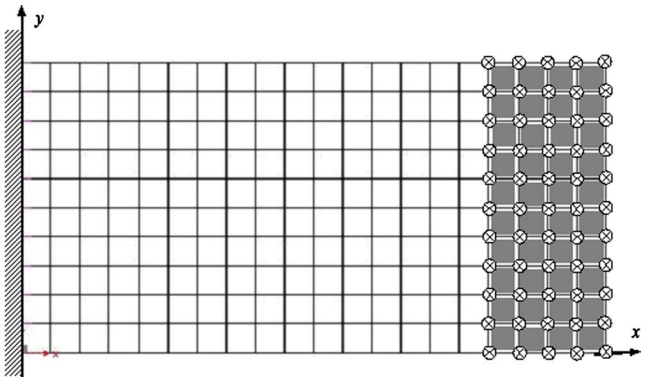

Fig. 3 Finite element model of the plate with delamination at the free end

$$\{\delta\bar{w}\}^T([m]\{\ddot{\bar{w}}\}+[k]\{\bar{w}\})=0 \tag{33}$$

where $[m]_{40\times40}$ and $[k]_{40\times40}$ are, respectively, the elemental mass and stiffness matrices of the four nodes rectangular plate element.

3 Numerical Examples for Analysis and Detection

3.1 Verification on the Finite Element Model. In order to verify the accuracy of the finite element model formulation presented above, we considered an example of a cantilever FRP-bonded plate. The plate consists of a 3-cm-thick concrete host and a bonded 0.6-cm-thick T300/5208 carbon fiber reinforced polymer (CFRP) layer, and it has the in-plane dimension of 1.6 m $\times$0.8 m. The fiber orientation of the FRP layer is parallel to the x axis which is normal to the support as shown in Fig. 3. Table 2 summarizes the material properties of the components of the structure. The cantilever plate is separately represented by two finite element models, in which one is based on the above-derived formulations with the bonding parameters $p_b=1$ for each element and the other finite element model consists of two layers of 8-nodes solid elements, with one layer for the concrete host and the other for the FRP. The two models have the same in-plane meshing of 20×10 as shown in Fig. 3. It is assumed that the delamination starts from the free end over the full width of the plate. To simulate the delamination damage with the proposed model, the bonding parameter could be set to a tiny but non-vanishing value ($p_b=1\times10^{-5}$ in this example) for the delaminated elements. For the two-layer solid element model, the delamination is simulated by un-joining the commom joints at the concrete-FRP interface. The un-joined nodes are shown as $\otimes$ in Fig. 3.

Table 2 Material properties of the cantilever plate

Properties	Concrete	T300/5208 (CFRP)
Mass density (kg/m^3)	2402	1600
Young's modulus E_1 (Pa)	2.482E10	1.81E11
Young's modulus E_2 (Pa)	--	1.03E10
Poisson ratio ν_{21}	0.2	0.28
Torsional modulus G_{12}	1.034E10	7.17E9

Modal analysis is performed separately on the two finite element models for the intact and delaminated plate. The first eight natural frequencies are listed in Table 3. The results from the proposed model are consistent with those from the two-layer solid element model for both the intact and delaminated states. Both models successfully predict the "delamination modes" without sliding and sticking (friction) between the two component plates, which are caused by the delamination and shown as the fifth and seventh modes in Fig. 4. Figure 4 shows the first eight modes of the delaminated plate.

3.2 Verification on the Delamination Detection. This section presents a method to identify the bonding parameters p_b using the uniform load surface curvatures (ULSC) of the plate that are estimated from the vibration measurements. For a linear structural system with n degrees-of-freedom, the modal-based formulation of the structural deflection vector under a set of uniform unit load was defined as Uniform Load Surface (ULS) by Zhang and Aktan [22]. The component of the deflection vector u_k is approximated as

$$u_k=\sum_{r=1}^{m}\sum_{l=1}^{n}\frac{\phi_r(k)\phi_r(l)}{\omega_r^2} \tag{34}$$

where ω_r and ϕ_r denote the rth natural frequency and the corresponding mass normalized mode shapes, and m denotes the number of the available modes from test. An approach to estimate the ULS curvature of plate structures using the Chebyshev polynomial approximation has been proposed by the authors [23]. This approach is adopted and outlined as follows.

It is assumed that the ULS values, $u(x_p,y_q)$, are obtained from Eq. (34) for all the Q measuring points on the plate. The curvature of the ULS can be obtained in terms of the second derivatives of the Chebyshev polynomials as

$$uc_{xx}=\sum_{r=1}^{N}\sum_{s=1}^{M}c_{rs}\frac{\partial^2T_r(x)}{\partial x^2}T_s(y)\quad uc_{yy}=\sum_{r=1}^{N}\sum_{s=1}^{M}c_{rs}T_r(x)\frac{\partial^2T_s(y)}{\partial y^2}$$

$$uc_{xy}=\sum_{r=1}^{N}\sum_{s=1}^{M}c_{rs}\frac{\partial T_r(x)}{\partial x}\frac{\partial T_s(y)}{\partial y} \tag{35}$$

where $T_r(x)$, $T_s(y)$ are the first kind Chebyshev polynomials and N, M are their orders. Denoting $P=N\times M$, the coefficient vector

Table 3 Natural frequencies (Hz) of the plate with delamination at the free end

	Natural frequency (Hz)				Percentage reduction (%)	
	Solid element model		Proposed model			
Mode order	Intact	Delaminated	Intact	Delaminated	Solid element model	Proposed model
1	15.087	15.078	15.135	14.833	0.06%	2.00%
2	37.135	36.074	37.576	36.668	2.86%	2.42%
3	94.397	93.264	93.318	92.563	1.20%	0.81%
4	135.71	126.89	136.18	124.96	6.50%	8.24%
5	—	163.88	—	156.76	—	—
6	185.17	170.61	186.46	173.76	7.86%	6.81%
7	—	184.95	—	180.67	—	—
8	264.33	252.39	262.31	245.05	4.52%	6.58%

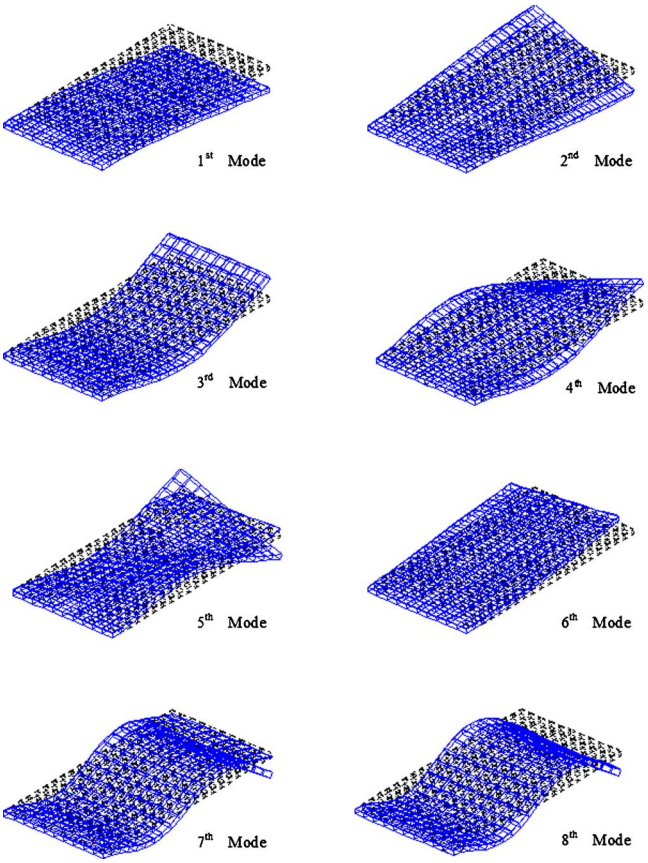

Fig. 4 Identified mode shapes of the cantilevered delaminated plate (---original plate; —deformed plate)

$\{c_{rs}\}$ can be solved by the least-squares technique as

$$\{c_{rs}\}_{P\times 1} = ([T(x_p)T(y_q)]^T_{Q\times P}[T(x_P)T(y_q)]_{Q\times P})^{-1} \times [T(x_p)T(y_q)]^T_{Q\times P}\{u(x_p,y_q)\}_{Q\times 1} \tag{36}$$

As we use the "free mode" model, in which the delaminated members deform independently without taking into account the contact and the friction effects, the delamination damage is assumed not significantly changing the linear behavior of the structure. The damage-induced changes in the ULSC of the plate can then be approximated by the first order Taylor series

$$\Delta uc_{xx}(x_p,y_q) = uc^D_{xx} - uc_{xx} = \frac{\partial uc_{xx}}{\partial p_b}\Delta p_b^{e=1} + \frac{\partial uc_{xx}}{\partial p_b}\Delta p_b^{e=2} + \cdots + \frac{\partial uc_{xx}}{\partial p_b}\Delta p_b^{e=ne} \tag{37}$$

where ne is the number of potentially damaged elements. Similar relations can be obtained for the curvature changes $\Delta uc_{yy}(x_p,y_q)$ and $\Delta uc_{xy}(x_p,y_q)$. Repeating the above relation for each measuring point and arrange them in matrix form, one gets

$$U\cdot\{\Delta p_b\} = \{\Delta uc\} \tag{38}$$

where matrix U contains all the sensitivity coefficients of the ULS curvature with respect to the bonding parameters. To calculate the sensitivity matrix, the derivative of Eq. (35) with respect to the bonding parameter p_b is obtained as

$$\frac{\partial uc_{xx}}{\partial p_b} = \sum_{r=1}^{N}\sum_{s=1}^{M}\frac{\partial c_{rs}}{\partial p_b}\frac{\partial^2 T_r(x)}{\partial x^2}T_s(y)$$

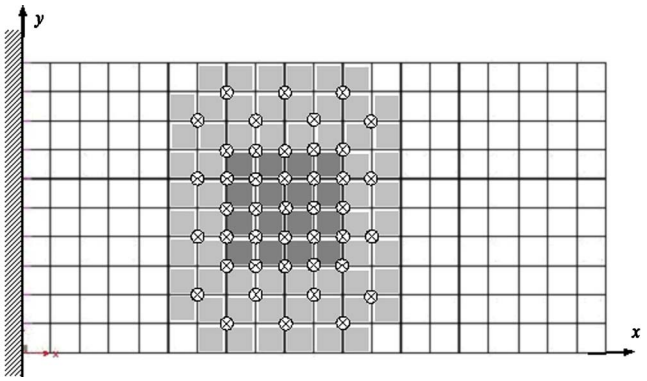

Fig. 5 Finite element model of the plate with delamination at mid-span

$$\frac{\partial uc_{yy}}{\partial p_b} = \sum_{r=1}^{N}\sum_{s=1}^{M}\frac{\partial c_{rs}}{\partial p_b}T_r(x)\frac{\partial^2 T_s(y)}{\partial y^2}$$

$$\frac{\partial uc_{xy}}{\partial p_b} = \sum_{r=1}^{N}\sum_{s=1}^{M}\frac{\partial c_{rs}}{\partial p_b}\frac{\partial T_r(x)}{\partial x}\frac{\partial T_s(y)}{\partial y}$$

where

$$\left\{\frac{\partial c_{rs}}{\partial p_b}\right\}_{P\times 1} = ([T(x_p)T(y_q)]^T_{Q\times P}[T(x_P)T(y_q)]_{Q\times P})^{-1} \times [T(x_p)T(y_q)]^T_{Q\times P}\left\{\frac{\partial u(x_p,y_q)}{\partial p_b}\right\}_{Q\times 1} \tag{39}$$

To find the derivatives of the ULS at the measuring points, Eq. (34) is differentiated with respect to p_b to have

$$\frac{\partial u(x_p,y_q)}{\partial p_b} = \frac{\partial u_k}{\partial p_b} = \sum_{r=1}^{m}\sum_{l=1}^{n}\left[\frac{1}{\omega_r^2}\left(\frac{\partial \phi_{kr}}{\partial p_b}\phi_{lr} + \frac{\partial \phi_{lr}}{\partial p_b}\phi_{kr}\right) - \frac{2}{\omega_r^3}\frac{\partial \omega_r}{\partial p_b}\phi_{kr}\phi_{lr}\right] \tag{40}$$

The derivatives of frequencies and mode shapes with respect to p_b in Eq. (40) are available if the stiffness matrix of the plate can be expressed as a function of p_b, which is a requirement of the proposed model. Therefore, iteration using Eq. (38) gives the identification results of the bonding parameters, which were all initialized as $p_b=1$ to represent perfect bonding.

To verify the proposed delamination detection method incorporating the proposed model of the plate, a new damage scenario on the previously studied cantilever plate as shown in Fig. 5 is considered. The dark-gray area represents the delaminated zone, and the surrounding grey area denotes the weak-bonding zone. The two-layer solid element model is used to simulate the real delaminated plate in test, by unjoining the interfacial joints denoted by ⊗ in the figure. All the related interfacial joints are unjoined in the delaminated zone to simulate the macro-delamination damage, while in the weak-bonding zone the interfacial nodes are unjoined at the interfacial joints at a staggered pattern to simulate the weakening effect due to the growing micro defects. It is assumed that the free vibration response of the delaminated plate is "measured" by "accelerometers" located at all nodal points along the z direction on the FRP side to extract the frequencies and mode shapes. The first eight modes from the "measurement" are used to approximately estimate the ULS curvature and its sensitivity. The above-mentioned parameter updating method is then applied to identify the bonding parameters for all potentially damaged elements in the proposed model. Table 4 lists the natural frequencies of the updated finite element model of the delaminated plate com-

Table 4 Natural frequencies (Hz) of the plate with delamination at mid-span

Mode order	Solid element model	Updated proposed model	Percentage errors (%)
1	15.04	15.18	0.91
2	37.11	36.64	1.27
3	93.89	91.68	2.36
4	135.09	129.67	4.01
5	184.89	182.73	1.17
6	256.50	257.65	0.45
7	301.89	291.91	3.31
8	323.72	315.33	2.59

pared with those from the solid element model. To denote the local delamination severity, a debonding index based on the identified bonding parameters is defined as

$$\mathrm{DI} = -\log p_b \tag{41}$$

The index would approach zero for perfectly bonded elements and tends to be a large positive scalar when the interface is completely debonded. Figure 6 shows the delamination index map of the updated plate model. It is seen that the completely debonded zone and the weak-bonding zone can be distinctly localized separately with different index values. The debonding index corresponding to the completely delaminated zone attains a value of 3.0–5.0, whereas the index for the weak-bonding zone is mostly not larger than 1.0.

4 Conclusion

A finite element formulation for the FRP-bonded concrete plate with delamination faults is developed for the non-destructive fault detection from vibration measurements. The proposed finite element model simulates the delamination effect by defining a general nodal displacement vector, which consists of a set of displacement characterizing functions on both debonded plies. To specify these unknown functions, a scalar parameter characterizing the bonding condition of the adhesive interface between the FRP and concrete plates is introduced. A gradient-based model updating method based on the sensitivity analysis of the ULSC of the plate is further presented to identify the bonding parameter for each element. An intuitive delamination index is defined based on the identified parameters to locate the damage and to scale the damage severity. Numerical examples demonstrate that the proposed model predicts the "real" delaminated plate very well and the identification methods are effective for delamination detection.

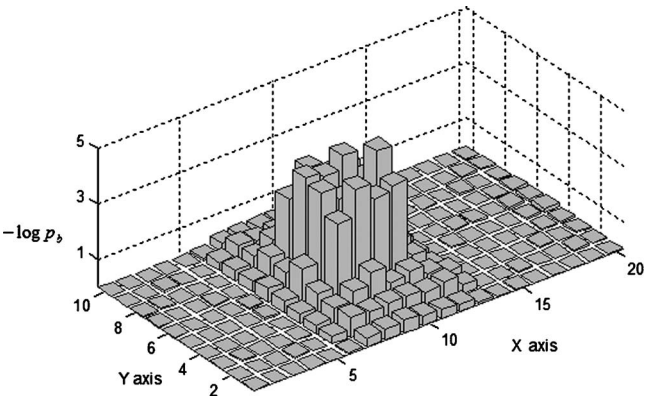

Fig. 6 Identified delamination index map of the plate with delamination at mid-span

Acknowledgment

The work described in this paper was supported by a grant from the Hong Kong Polytechnic University Research Funding Project No. G-W092.

References

[1] Varastehpour, H., and Hamelin, P., 1997. "Strengthening of Concrete Beams Using Fibre-Reinforced Plastic. Mater. Struct., **30**, pp. 160–166.

[2] Lau, K. T., and Zhou, L. M., 2001, "Mechanical Performance of Composite-Strengthened Concrete Structures," Composites, Part B, **32**(1), pp. 21–31.

[3] Teng, J. G., Chen, J. F., Smith, S. T., and Lam, L., 2002. *FRP Strengthened RC Structures*, Wiley, Chichester, UK.

[4] Diaz Valdes, S., H., and Soutis, C., 1999a. "Application of the Rapid Frequency Sweep Technique for Delamination Detection in Composite Laminates." Adv. Compos. Lett., **8**, 19–23.

[5] Diaz Valdes, S. H., and Soutis, C., 1999b. "Delamination Detection in Composite Laminates From Variations of Their Modal Characteristics," J. Sound Vib., **228**(1), 1–9.

[6] Griffin, S. F., and Sun, T. C., 1991, "Health Monitoring of Dumb and Smart Structures," *The 28th Annual Meeting of SES*, November 6–8, Gainsville, FL.

[7] Luo, H., and Hanagud, S., 1995, "Delamination Detection Using Dynamic Characteristics of Composite Plates," *Proceedings of AIAA/ASME/ASCE/AHS Structures*, Structural Dynamics & Materials Conference, 10–13, pp. 129–139.

[8] Ratcliffe, C. P., and Bagaria, W. J., 1998, "Vibration Technique for Locating Delamination in a Composite Plates," AIAA J., **36**,1074–1077.

[9] Majumdar, P. M., and Suryanarayan, S., 1988. "Flexural Vibrations of Beams With Delaminations," J. Sound Vib., **125**, pp. 441–461.

[10] Tracy, J. J., and Pardoen, G. C., 1989, "Effect of Delamination on the Natural Frequencies of Composite Laminates," J. Compos. Mater., **23**(12), pp. 1200–1215.

[11] Shen, M. H. H., and Grady, J. E., 1992, "Free Vibration of Delaminated Beams," AIAA J., **30**, pp. 1361–1370.

[12] Barbero, E. J., and Reddy, J. N., 1991, "Modelling of Delamination in Composite Laminates Using a Layerwise Plate Theory," Int. J. Solids Struct., **28**, pp. 373–388.

[13] Islam, A. S., and Cralg, K. C., 1994, "Damage Detection in Composite Structures Using Piezoelectric Materials," Smart Mater. Struct., **3**, pp. 318–328.

[14] Okafor, A. C., Chandrashekhara, K., and Jiang, Y. P., 1996, "Delamination Prediction in Composite Structures With Built-In Piezoelectric Devices Using Modal Analysis and Neutral Network," Smart Mater. Struct., **5**, pp. 338–347.

[15] Chaudhry, Z., and Ganino, A. J., 1994, "Damage Detection Using Neutral Network: An Initial Experimental Study on Debonded Beams," J. Intell. Mater. Syst. Struct., **5**, pp. 585–589.

[16] Krawczuk, M., and Ostachowicz, W., 2002, "Identification of Delamination in Composite Beams by Genetic Algorithm," Science and Engineering of Composite Materials, **10**(2), pp. 147–155.

[17] Wang, J. T. S., Liu, Y. Y., and Gibby, J. A., 1982, "Vibration of Split Beams," J. Sound Vib., **84**, pp. 491–502.

[18] Kwon, Y. W., and Aygunes, H., 1996, "Dynamic Finite Element Analysis of Laminated Beams With Delamination Cracks Using Contact-Impact Conditions," Comput. Struct., **58**(6), pp. 1160–1169.

[19] Perel, V. Y., and Palazotto, A. N., 2002, "Finite Element Formulation for Dynamics of Delaminated Composite Beams With Piezoelectric Actuators," Int. J. Solids Struct., **39**, pp. 4457–4483.

[20] Tong, L., and Steven, G. P., 1999, *Analysis and Design of Structural Bonded Joints*, Kluwer, Dordrecht.

[21] Tong, L., Sun, D. C., and Atluri, S. N., 2001, "Sensing and Actuating Behaviours of Piezoelectric Layers With Debonding in Smart Beams," Smart Mater. Struct., **10**, pp. 713–723.

[22] Zhang, Z and Aktan, A. E., 1998, "Application of Modal Flexibility and its Derivatives in Structural Identification," Research in Nondestructive Evaluation, **10**(1), pp. 43–61.

[23] Wu, D., and Law, S. S., 2005, "Sensitivity of Uls Curvature for Damage Identification in Plate Structures," J. Vibr. Acoust., **127**(1), pp. 84–92

Q. L. Ma

A. Kahraman[1]
e-mail: kahraman.1@osu.edu

Department of Mechanical Engineering,
The Ohio State University,
650 Ackerman Road,
Columbus, OH 43202

J. Perret-Liaudet

E. Rigaud

Laboratoire de Tribologie et Dynamique des Systèmes,
UMR 5513,
36 Ave. Guy de Collongue,
F-69134 Ecully Cedex,
France

An Investigation of Steady-State Dynamic Response of a Sphere-Plane Contact Interface With Contact Loss

In this study, the dynamic behavior of an elastic sphere-plane contact interface is studied analytically and experimentally. The analytical model includes both a continuous nonlinearity associated with the Hertzian contact and a clearance-type nonlinearity due to contact loss. The dimensionless governing equation is solved analytically by using multi-term harmonic balance method in conjunction with discrete Fourier transforms. The accuracy of the dynamic model and solution methods is demonstrated through comparisons with experimental data and numerical solutions for both harmonic amplitudes of the acceleration response and the phase difference between the response and the force excitation. A single-term harmonic balance approximation is used to derive a criterion for contact loss to occur. The influence of harmonic external excitation $f(\tau)$ and damping ratio ζ on the steady state response is also demonstrated. [DOI: 10.1115/1.2190230]

1 Introduction

The vibratory motions at contact interfaces of elastic solids have been of interest to several investigators. Dynamic motions at such interfaces influence fatigue and wear performance of contact surfaces. Some examples of such contact interfaces include gear meshes, rolling element bearings, and railroad wheel-rail contacts. Hertzian theory has been employed extensively to model the flexibility of the contact interfaces. One major theoretical study on contact dynamics is by Nayak [1], who proposed a single-degree-of-freedom (SDOF) dynamic model, and obtained analytical solutions by using a single-term harmonic balance method (HBM). As the theoretical predictions matched experimental results qualitatively, a heuristic approach was employed to describe the dynamic behavior further. Hess and Soom [2] studied the same problem by using the method of multiple scales, and quantified the amount of friction reduction due to contact vibrations. These earlier studies assumed that the surfaces are maintained in contact all the time. In two recent studies, Perret-Liaudet [3,4] investigated a sphere-plane contact problem that allows the separation of contacting surfaces (contact loss). The existence of subharmonic and superharmonic responses was demonstrated by using numerical methods. In a later work, Sabot et al. [5] reported the results of an extensive experimental study on the same sphere-plane contact problem. They demonstrated that the steady state response predicted by a dynamic model based on the Hertzian contact formulation agrees well with experimental data for both free and harmonically excited vibrations. Focusing on vibro-impacts, Perret-Liaudet and Sabot [6] investigated the same model of Hertzian contact by numerical methods, and confirmed the significance of clearance at the contact on super- and subharmonic resonances. In two recent studies, Rigaud and Perret-Liaudet [7], and Perret-Liaudet and Rigaud [8] solved an impacting Hertzian contact problem by using the shooting method in conjunction with parametric continuation technique.

These previous studies used either numerical or experimental methods to investigate contact vibration problems, and very little analytical treatment of this problem is available, especially when the contact loss is included. Accordingly, this paper focuses on the dynamic analysis of a flat surface in contact with a sphere by using multi-term HBM.

Variations of HBM were applied successfully in the past to oscillators having piecewise linear stiffness and linear viscous damping. Examples of such studies include papers by Singh [9–12], Natsiavas [13–17], Kahraman [18–21], Noah [22,23], and Lai and Zhang [24]. These studies demonstrated clearly that a wide range of nonlinear behavior exhibited by piecewise linear systems can be predicted by using HBM.

While there have been recent studies which expanded the use of HBM for systems having piecewise-nonlinear stiffness [e.g. Refs. [25,26]], the multi-term HBM is yet to be applied to a Hertzian contact problem having different forms of piecewise-nonlinear damping and piecewise-nonlinear stiffness. Accordingly, the multi-term HBM formulation proposed by Ma and Kahraman [26] for systems having piecewise nonlinear springs is modified here to study the dynamic behavior of a sphere-plane interface with possible contact losses. We refer to Ref. [26] for a detailed literature search of the studies that used HBM for piecewise linear systems. In order to validate the analytical predictions, the HBM solutions are compared with corresponding numerical results from the shooting method. Results of an experimental study are also presented to validate both the dynamic model and the HBM predictions. The condition for contact loss to occur is obtained by using a single-term HBM approximation. At the end, the influence of external force $f(\tau)$ and damping ratio ζ on steady-state response is quantified.

2 Multi-term HBM Formulations

2.1 Equation of Motions. A double sphere-plane Hertzian contact can be modeled as a SDOF system shown in Fig. 1 [7]. The dimensionless equation of motion is given as

[1]Author to whom correspondence should be addressed.

Contributed by the Applied Mechanics Division of ASME for publication in the JOURNAL OF APPLIED MECHANICS. Manuscript received April 12, 2005; final manuscript received February 1, 2006. Review conducted by N. Sri Namachchivaya. Discussion on the paper should be addressed to the Editor, Prof. Robert M. McMeeking, Journal of Applied Mechanics, Department of Mechanical and Environmental Engineering, University of California—Santa Barbara, Santa Barbara, CA 93106-5070, and will be accepted until four months after final publication of the paper itself in the ASME JOURNAL OF APPLIED MECHANICS.

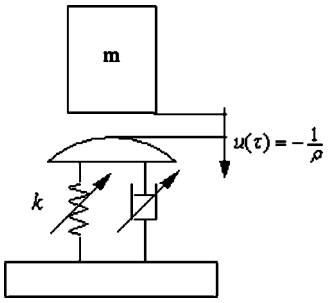

Fig. 1 The dynamic model of a single degree-of-freedom sphere-plane contact oscillator

$$\ddot{u}(\tau) + 2\zeta\{D[u(\tau)]\}^m \dot{u}(\tau) + G[u(\tau)] = 1 + f(\tau) \tag{1a}$$

where τ is the dimensionless time, an overdot denotes differentiation with respect to τ, $u(\tau)$ is the displacement of the unit mass normal to the tangent plane of the interface, ζ is the viscous damping ratio, and $f(\tau)$ is the dynamic component of external force. In Eq. (1*a*), $G[u(\tau)]$ is piecewise nonlinear restoring function defined as

$$G[u(\tau)] = \begin{cases} [1+\rho u(\tau)]^{1/\rho} & u(\tau) > -\dfrac{1}{\rho} \\ 0 & u(\tau) \leqslant -\dfrac{1}{\rho} \end{cases} \tag{1b}$$

This equation represents a Hertzian contact, allowing contact losses. Here, ρ is a constant that is $\rho=2/3$ for a sphere-plane contact of bodies made of same material. When $u(\tau) > -1/\rho$ for all τ, the contact is maintained all the time, and the model represents a typical continuously nonlinear system. However, if $u(\tau) \leqslant -1/\rho$ for certain τ, then the contact is lost, representing a piecewise-nonlinear system [11].

$D[u(\tau)]$ in Eq. (1*a*) is a damping function subject to a power index m. Here, if $m=0$, the damping force $f_d(\tau)$ is linearly proportional to $\dot{u}$. When $m=1$, $D[u(\tau)]$ includes the contact loss between the sphere and the plane, and can be defined in the following general form [7]

$$D[u(\tau)] = \begin{cases} [1+\rho u(\tau)]^{p} & u(\tau) > -\dfrac{1}{\rho} \\ 0 & u(\tau) \leqslant -\dfrac{1}{\rho} \end{cases} \tag{1c}$$

When $p=0$, $D[u(\tau)]$ reduces to a piecewise linear function:

$$D[u(\tau)] = \begin{cases} 1 & u(\tau) > -\dfrac{1}{\rho} \\ 0 & u(\tau) \leqslant -\dfrac{1}{\rho} \end{cases} \tag{1d}$$

such that the damping is a linear viscous one when there is contact, and is zero when the contact is lost. For $p \neq 0$, $f_d(\tau)$ is piecewise nonlinear function. Specifically $p=0.5$ represents a $f_d(\tau)$ that is proportional to the contact radius, $p=1$ represents a $f_d(\tau)$ that is proportional to the elastic deformation and contact area, and $p=1.5$ represents a $f_d(\tau)$ that is proportional to the elastic restoring force [7].

2.2 Multi-term HBM Solution. In previous studies, the method of multiple scales was used extensively to analyze contact vibration problems with continuous nonlinearity only [3–5]. When contact loss is considered, such perturbation methods are no longer applicable. One-term HBM was utilized by Nayak [1], and some obvious discrepancies were observed between HBM results and experiments. Multi-term HBM was used in previous studies to investigate similar discontinuous problems successfully [18,19,23,26]. The same method combined with discrete Fourier transforms (DFT) is employed here to obtain the steady-state solutions of Eq. (1). First, let $\theta=\Lambda\tau/\ \eta=\mathrm{H}\tau$ where Λ is the fundamental excitation frequency and η is a subharmonic index, and write Eq. (1*a*) as

$$H^2\frac{d^2u}{d^2\theta} + 2\zeta H\{D[u(\theta)]\}^m\frac{du}{d\theta} + G[u(\theta)] = 1 + f(\theta) \tag{2}$$

The periodic forcing function is given in the form of a Fourier series as

$$f(\theta) = \sum_{r=1}^{R}[f_{2r}\cos(r\eta\theta) + f_{2r+1}\sin(r\eta\theta)] \tag{3a}$$

and the periodic steady state response is assumed as

$$u(\theta) = u_1 + \sum_{r=1}^{R}[u_{2r}\cos(r\theta) + u_{2r+1}\sin(r\theta)] \tag{3b}$$

In order to maintain a harmonic balance, the nonlinear functions $D[u(\theta)]$ and $G[u(\theta)]$ must be periodic as well, i.e.

$$D[u(\theta)] = d_1 + \sum_{r=1}^{R}[d_{2r}\cos(r\theta) + d_{2r+1}\sin(r\theta)] \tag{3c}$$

$$G[u(\theta)] = g_1 + \sum_{r=1}^{R}[g_{2r}\cos(r\theta) + g_{2r+1}\sin(r\theta)] \tag{3d}$$

By substituting Eq. (3) into Eq. (2) and enforcing a harmonic balance with $m=1$, a vector equation $\mathbf{S}=\mathbf{0}$ is obtained as follows, where $\mathbf{S}=[S_1\ S_2\ S_3\ \ldots\ S_{2\eta R}\ S_{2\eta R+1}]^T$ and

$$S_1 = g_1 - 1 + \zeta H\eta\sum_{r=1}^{R} r(d_{2r}u_{2r\eta+1} - d_{2r+1}u_{2r\eta}) \tag{4a}$$

$$\begin{aligned} S_{2i} = &- H^2i^2u_{2i} + 2\zeta Hd_1iu_{2i+1} + g_{2i} - f_{2i/\eta} - \zeta H\sum_{r=1}^{R} d_{2r+1}[(r\eta \\ &- i)u_{2(r\eta-i)} - (i-r\eta)u_{2(i-r\eta)} + (r\eta+i)u_{2(r\eta+i)}] \\ &+ \zeta H\sum_{r=1}^{R} d_{2r}[(r\eta-i)u_{2(r\eta-i)+1} + (i-r\eta)u_{2(i-r\eta)+1} + (r\eta \\ &+ i)u_{2(r\eta+i)+1}] \quad i \in [1,R] \end{aligned} \tag{4b}$$

$$\begin{aligned} S_{2i+1} = &- H^2i^2u_{2i+1} - 2\zeta Hd_1iu_{2i} + g_{2i+1} - f_{2i/\eta+1} + \zeta H\sum_{r=1}^{R} d_{2r+1}[(r\eta \\ &- i)u_{2(r\eta-i)+1} + (i-r\eta)u_{2(i-r\eta)+1} - (r\eta+i)u_{2(r\eta+i)+1}] \\ &+ \zeta H\sum_{r=1}^{R} d_{2r}[(r\eta-i)u_{2(r\eta-i)} - (i-r\eta)u_{2(i-r\eta)} - (r\eta \\ &+ i)u_{2(r\eta+i)}] \quad i \in [1,R] \end{aligned} \tag{4c}$$

These algebraic equations can be reduced to the case of constant viscous damping ($m=0$) by letting $d_1=1$, and $d_{2r}=d_{2r+1}=0$ for $r \in [1,R]$.

Meanwhile, coefficients g_i and d_i in Eqs. (3*c*) and (3*d*) can be expressed in terms of unknown Fourier coefficients of the response $\mathbf{u}=[u_1\ u_2\ u_3\ \ldots\ u_{2R}\ u_{2R+1}]^T$ by utilizing discrete Fourier transforms (DFT) [26]. The values of $u(\theta)$ at discrete values of $\theta_n=nh$ are

$$u_n = u_1 + \sum_{r=1}^{R} \left[u_{2r} \cos\left(\frac{2\pi rn}{N}\right) + u_{2r+1} \sin\left(\frac{2\pi rn}{N}\right) \right] \quad n \in [0, N-1] \tag{5}$$

where $h=2\pi\eta/(N\Lambda)$ and $N \geqslant 2R$. Using Eq. (1*b*), nth discrete value of $G[u(\theta)]$ is given as

$$G_n = \begin{cases} (1+\rho u_n)^{1/\rho} & u_n > -\dfrac{1}{\rho} \\ 0 & u_n \leqslant -\dfrac{1}{\rho} \end{cases} \tag{6}$$

The coefficients g_i are calculated by taking the inverse DFT of Eq. (6) as

$$g_1 = \frac{1}{N}\sum_{n=0}^{N-1} G_n \quad g_{2r} = \frac{2}{N}\sum_{n=0}^{N-1} G_n \cos\frac{2\pi rn}{N}$$

$$g_{2r+1} = \frac{2}{N}\sum_{n=0}^{N-1} G_n \sin\frac{2\pi rn}{N} \tag{7}$$

For the case of a constant viscous damping model with $m=0$ in Eq. (1*a*), $D_n=1$. For a nonlinear damping model ($m=1$), nth discrete value of $D[u(\theta)]$ is given as

$$D_n = \begin{cases} [1+\rho u_n)]^p & u_n > -\dfrac{1}{\rho} \\ 0 & u_n \leqslant -\dfrac{1}{\rho} \end{cases} \tag{8}$$

and d_i are defined as

$$d_1 = \frac{1}{N}\sum_{n=0}^{N-1} D_n \quad d_{2r} = \frac{2}{N}\sum_{n=0}^{N-1} D_n \cos\frac{2\pi rn}{N}$$

$$d_{2r+1} = \frac{2}{N}\sum_{n=0}^{N-1} D_n \sin\frac{2\pi rn}{N} \tag{9}$$

Having g_i and d_i defined, the vector equation $\mathbf{S}=\mathbf{0}$ can be solved for $\mathbf{u}$ by using Newton-Raphson method as

$$\mathbf{u}^{(m)} = \mathbf{u}^{(m-1)} - [\mathbf{J}^{-1}]^{(m-1)}\mathbf{S}^{(m-1)} \tag{10}$$

where the value of $\mathbf{u}^{(m)}$ at the mth iteration is obtained from the values of $\mathbf{S}^{(m-1)}$ and $\mathbf{u}^{(m-1)}$, and $\mathbf{J}$ is the Jacobian matrix. An artificial-parameter generic homotopy method is utilized to overcome the difficulties at the turning points in the domain of control parameter Λ [27,28]. The stability of the steady-state response is determined by using the Floquet theory [29–31]. The details of the stability analysis procedure can be found in Ref. [26].

3 Experimental Setup

The experimental setup consists of a double sphere-plane contact as shown in Fig. 2. A spherical ball is preloaded between two horizontal plane surfaces. One plane is attached to a heavy rigid frame while the other plane is on a vertically moving cylinder. These two contacts can be approximated by Hertzian theory when the surface roughness of contacting surfaces is not excessive. (In this case, for the plane Ra $\leqslant$ 0.4 μm, and for the ball surface Ra $\leqslant$ 0.03 μm) In addition, other critical assumptions for Hertzian theory are met including negligible friction effects and elastic deformations. The elastic bodies in contact are made of SAE 52100 steel. The ball has a diameter of 25 mm and a mass of 0.064 kg, which is significantly lower than the weight of the moving cylinder (6.48 kg). The mass of the moving cylinder corresponds to an applied static load equal to 63.6 N. Since the ball mass is negligible in comparison with that of the moving cylinder, the experimental system acts as a single degree-of-freedom oscillator. Thus, assuming identical mechanical properties for the ball and the planes, the restoring elastic force expression can be deduced from the double sphere-plane Hertzian contact as $F=Cz^{3/2}$, where $C=E\sqrt{R}/[3\sqrt{2}(1-\nu^2)]$. Given the modulus of elasticity $E=205$ GPa, Poisson ratio $\nu=0.29$ and the radius of the ball $R=12.5$ mm mm, one finds $C=5.9(10)^9$ $Nm^{-3/2}$, $z_s=4.9$ μm, and $f_0=276$ Hz. Here, z_s corresponds to the static displacement of the moving cylinder due to its weight, and f_0 is the calculated linearized natural frequency.

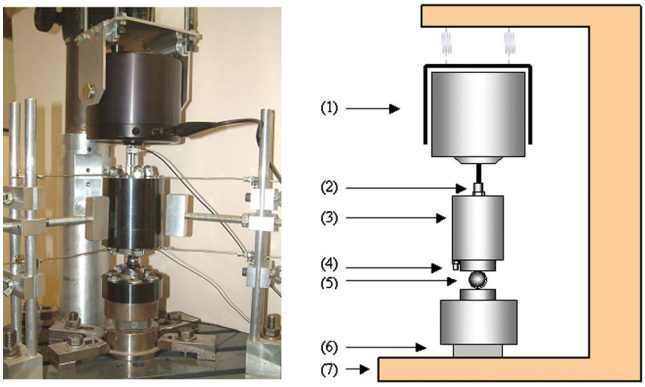

Fig. 2 The test setup: (1) vibration exciter, (2) force transducer, (3) moving cylinder, (4) accelerometer, (5) ball, (6) triaxial force transducer, and (7) rigid frame

The contact surface is excited in normal direction by a suspended vibration shaker connected to a signal generator and a power amplifier. Therefore, a harmonic normal force is applied to the moving cylinder in addition to the static load. The excitation force, the acceleration of the moving cylinder, and the normal force transmitted to the rigid frame through the contact are measured by piezoelectric transducers. Conventional charge amplifiers are used for all responses. Each harmonic component of the signal is analyzed using a lock-in amplifier. This one is based on a phase sensitive detection in order to single out the components of the signal (frequency, amplitude and phase).

The linear experimental contact natural frequency of 269 Hz and equivalent viscous damping ratio of nearly 0.7%–0.8% are measured from the resonant peaks under very small external input amplitudes. This measured natural frequency is within 3% of the calculated value of $f_0=276$ Hz. Moreover, the measured damping ratio is also in good agreement with previous studies [5]. Since the experimental data are non-dimensionalized about the measured linear contact natural frequency, any potential uncertainties on the elastic Hertzian characteristics (Young's modulus, Poisson's ratio, etc.) have no influence on the comparisons included in the paper. Meanwhile, as in any vibratory system, the value of damping ratio bears a certain amount of uncertainty. However, the model predictions do not vary drastically within this estimated measured range of damping ratio, and our experimental setup has no means to vary the damping ratio as a parameter.

4 Results and Discussion

4.1 Comparison of HBM With a Numerical Solution Method and Experiments. The predictions of multi-term HBM are compared with those of a numerical solution method to determine the accuracy of HBM solutions. The shooting method in conjunction with a continuation procedure is used as the numerical method here. Details in regards to the application of this method to contact problems can be found in Refs. [29,31]. This method employs a simple pseudo arc length continuation scheme to predict periodic solutions. The case of linear damping ($m=0$)

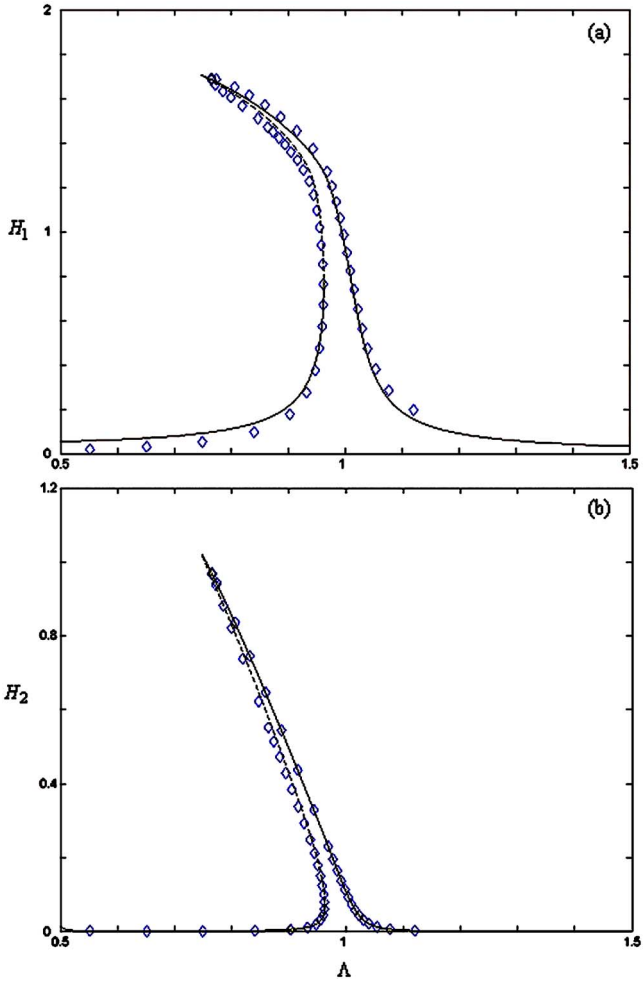

Fig. 3 Comparison of the acceleration response predicted by HBM and the shooting method for $\zeta=0.008$, $f_3=0.04$. (*a*) H_1 and (*b*) H_2; (—) stable HBM, (---) unstable HBM, and (◇) shooting method.

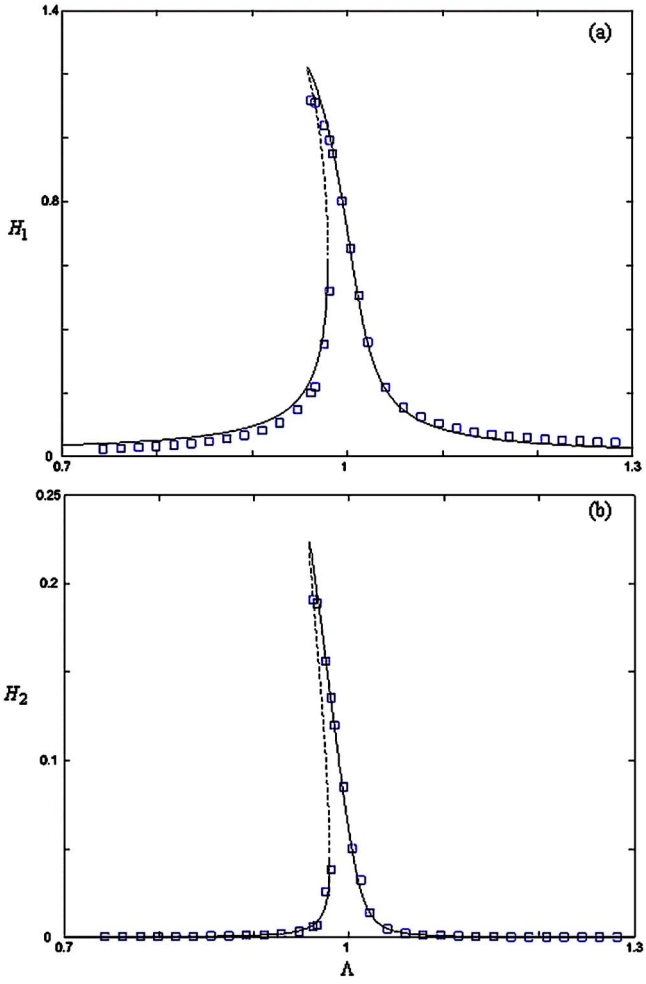

Fig. 4 Comparison of measured acceleration response to HBM prediction for $\zeta=0.007$, $f_3=0.018$. (*a*) H_1 and (*b*) H_2; (—) stable HBM, (---) unstable HBM, and (□) measurements.

with $\zeta=0.008$ is considered for this comparison. The amplitudes of the first two harmonics of $\ddot{u}(\tau)$ are defined as $H_1=\Lambda^2[u_2^2+u_3^2]^{1/2}$ and $H_2=4\Lambda^2[u_4^2+u_5^2]^{1/2}$, which are used as the parameters for the comparison. In Fig. 3, the predictions of H_1 and H_2 from HBM and the shooting method are compared for a harmonic external excitation of $f_3=0.04$ (other $f_i=0$) within the frequency range of $\Lambda\in[0.5,1.5]$. The first twelve harmonic terms are included in Eq. (3*b*) that corresponds to $R=6$. It is evident that two methods match each other well for both H_1 and H_2. The combined softening effect of continuous contact nonlinearity and contact losses results in a significant bend of the primary resonant peak to the left, forming a region of double stable motions within $\Lambda\in[0.75,0.96]$. The same level of agreement is obtained for other values of f_3 and ζ as well, which suggests that multi-term HBM is capable to solve equation (1) accurately.

Similarly, comparisons between the predictions of HBM and measured response are provided in Figs. 4 and 5 for two different excitation amplitudes in order to demonstrate the validity of Eq. (1) for representing an actual sphere-plane contact. Here, the number of harmonics for system response is chosen as 6, which is verified to be accurate enough for prediction. The damping ratio was estimated from an approximately linear case with very small external excitation [7]. Therefore, two values are trialed here for two cases, respectively. The magnitude of external excitation is decided from the input of vibration exciter. A linear damping model with $\zeta=0.007$ is used for these comparisons. In Fig. 4, the amplitudes of predicted response H_1 and H_2 are compared with measured ones for $f_3=0.007$, which are not large enough to cause any contact loss happen. Therefore, only a very slight softening type resonance peak is obtained, and the predictions of H_1 and H_2 by HBM match the measured values quite well for this continuously nonlinear case. In Fig. 5, another case is shown to represent the theoretical predictions and the measured data from the same experimental setup for $f_3=0.04$. In this case, contact loss is observed, which results in a more significant softening behavior than the previous case in Fig. 4. The values of predicted and measured H_1 and H_2 are again in good agreement, which suggests that not only HBM is suitable to investigate the problem of sphere-plane contact, but also Eq. (1) is sufficiently accurate for modeling the actual system in hand.

In Fig. 6, the phase difference between external excitation and acceleration response of the system for the first harmonic component of the motion is compared to both experimental measurements and the predictions from the shooting method for a case when $f_3=0.031$ and $\zeta=0.007$. The agreement among the phase angles predicted by multi-term HBM, numerical predictions, and the experiments is very good, further suggesting that the model and the HBM solutions are accurate.

4.2 Criterion of Contact Loss to Occur. When the amplitude of the external harmonic excitation $f_3=f_\kappa$ exceeds a threshold value, and the fundamental frequency of external excitation is

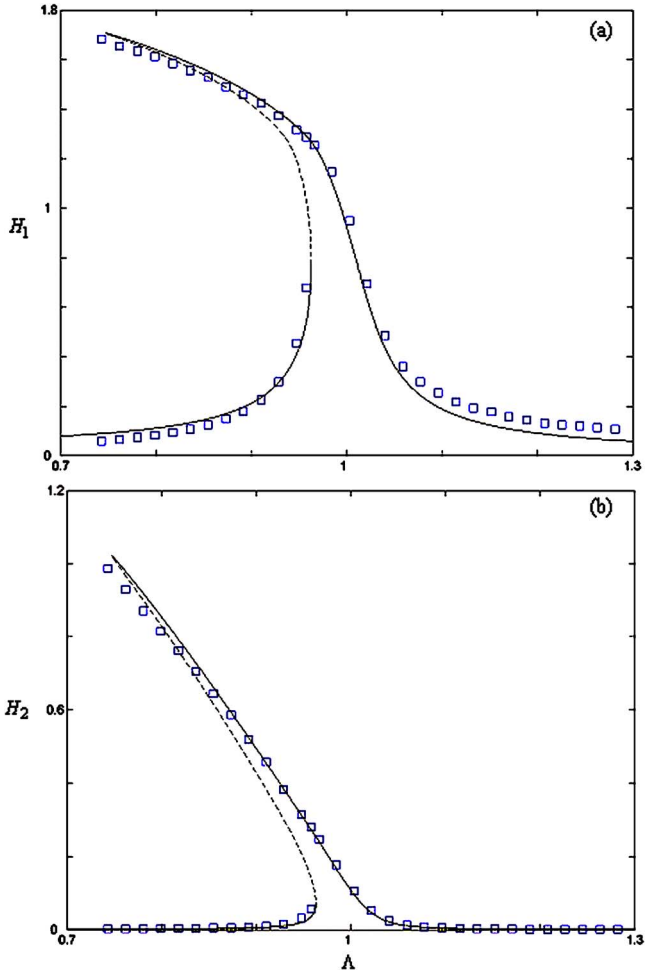

Fig. 5 Comparison of measured acceleration response to HBM prediction for $\zeta=0.008$, $f_3=0.04$. (*a*) H_1 and (*b*) H_2; (—) stable HBM, (---) unstable HBM, and (□) measurements.

near the primary resonant frequency $\Lambda=1$, the contacting surfaces of the sphere and plane might be separated during the certain portion of a vibration period [7]. The condition for contact loss to occur can be predicted approximately by using a single-term HBM formulation. Using a linear damping model ($m=0$) and expanding $G[u(\tau)]$ into a truncated Taylor series [5], one can write

$$G[u(\tau)] \cong \begin{cases} 1+\frac{3}{2}\rho u(\tau)+\frac{3}{8}[\rho u(\tau)]^2-\frac{1}{16}[\rho u(\tau)]^3 u(\tau) > -\frac{1}{\rho} \\ 0 \quad u(\tau) \leqslant -\frac{1}{\rho} \end{cases} \tag{11a}$$

This approximation of $G[u(\tau)]$ does not meet the boundary condition $G[-1/\rho]=0$ for $u(\tau)=-1/\rho$. In order to remedy this problem, the Taylor series approximation is modified slightly as

$$G[u(\tau)] \cong \begin{cases} 1+\frac{3}{2}\rho u(\tau)+\frac{3}{7}[\rho u(\tau)]^2-\frac{1}{14}[\rho u(\tau)]^3 \quad u(\tau) > -\frac{1}{\rho} \\ 0 \quad u(\tau) \leqslant -\frac{1}{\rho} \end{cases} \tag{11b}$$

In Fig. 7, the comparison of different definitions of $G[u(\tau)]$ is

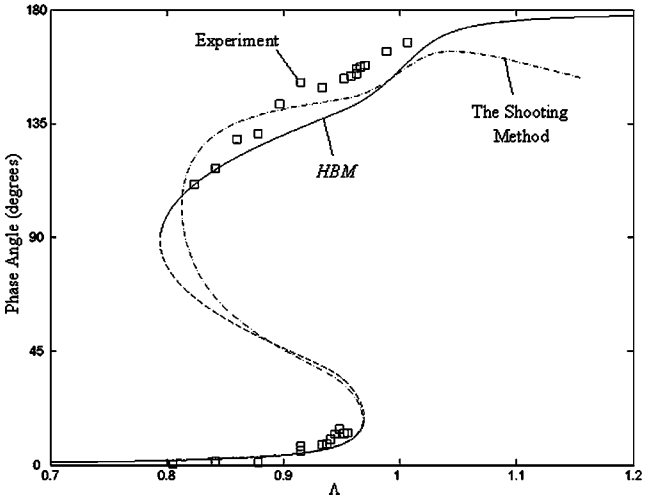

Fig. 6 Comparison of the phase angle of measured acceleration response to the prediction by HBM and the shooting method. $\zeta=0.007$ and $f_3=0.031$.

illustrated, which shows that Eq. (11*b*) is quite accurate for $u(\tau)<2$. Assume harmonic forms of $u(\tau)$ and $G[u(\tau)]$ as

$$u(\tau)=u_1+u_\kappa \sin(\kappa\Lambda\tau+\alpha_\kappa) \tag{12a}$$

$$G[u(\tau)]=\nu_1+\nu_\kappa \sin(\kappa\Lambda\tau+\alpha_\kappa) \tag{12b}$$

Here, when the sphere and the plane are in contact,

$$\nu_1=1+\frac{3}{2}\rho u_1+\frac{3}{7}\rho^2 u_1^2+\frac{3}{14}\rho^2 u_\kappa^2-\frac{1}{14}\rho^3 u_1^3 \tag{13a}$$

$$\nu_\kappa=\frac{3}{2}\rho u_\kappa+\frac{6}{7}\rho^2 u_1 u_\kappa-\frac{3}{14}\rho^3 u_1^2 u_\kappa-\frac{9}{56}\rho^3 u_\kappa^3 \tag{13b}$$

Substituting Eq. (12) into Eq. (1*a*) with $m=0$, one obtains $\nu_1-1=0$, and

$$(\nu_\kappa-\kappa^2\Lambda^2 u_\kappa)\cos\alpha_\kappa-2\zeta\kappa\Lambda u_\kappa \sin\alpha_\kappa-f_\kappa\cos\Gamma_\kappa=0 \tag{14a}$$

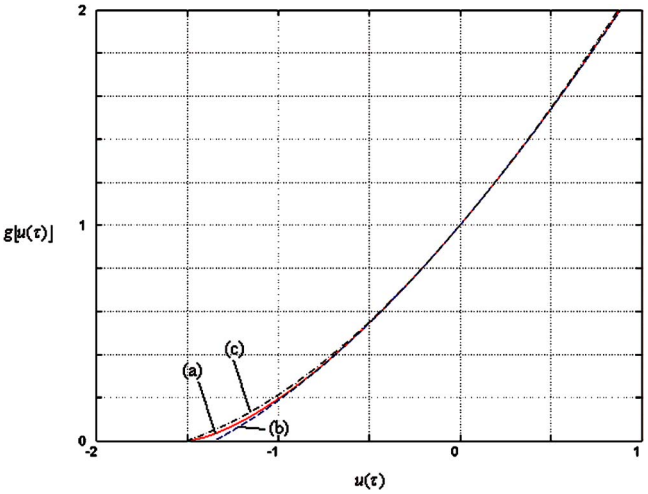

Fig. 7 Comparison of power series approximations to exact $G[u(\tau)]$, (*a*) Eq. (1*b*), (*b*) Eq. (11*a*), and (*c*) Eq. (11*b*)

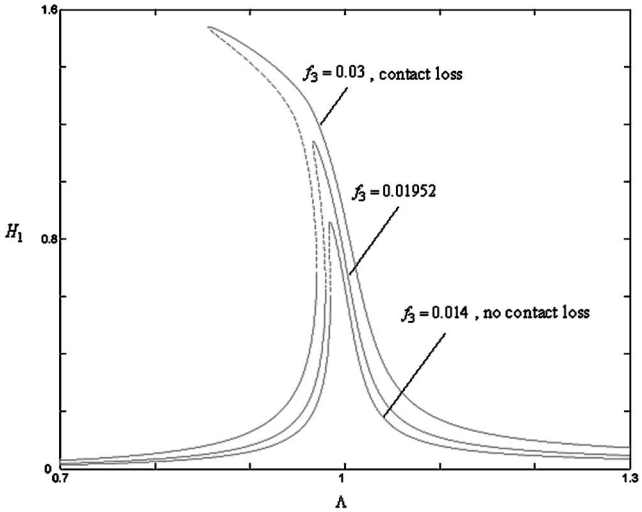

Fig. 8 H_1 **versus** Λ **for** $\zeta=0.008$ **and** $f_3=0.014$, 0.0195, **and** 0.03

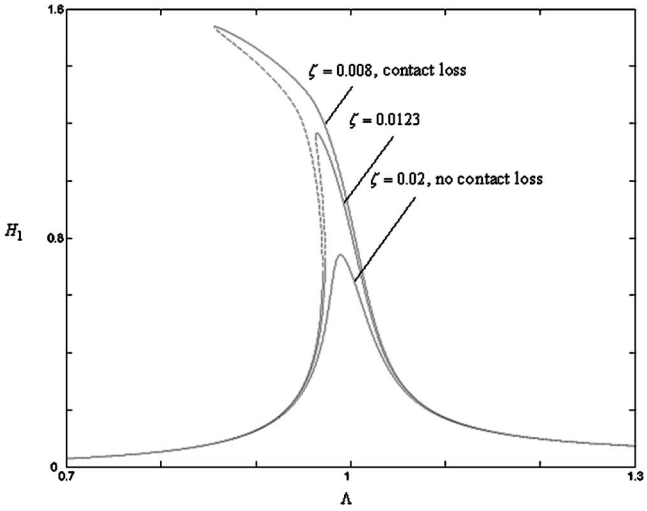

Fig. 9 H_1 **versus** Λ **for** $f_3=0.03$ **and** $\zeta=0.008$, 0.0123, **and** 0.02

$$(\nu_\kappa - \kappa^2\Lambda^2 u_\kappa)\sin\alpha_\kappa + 2\zeta\kappa\Lambda u_\kappa\cos\alpha_\kappa - f_\kappa\sin\Gamma_\kappa = 0 \quad (14b)$$

where Γ_κ is the phase angle between external excitation and the system response. By imposing the condition at the point of contact loss

$$u_1 - u_\kappa = -\frac{1}{\rho} \quad (15)$$

to Eqs. (13) and (14), a cubic polynomial in u_1 is obtained as

$$\rho^3 u_1^3 - 9\rho^2 u_1^2 - 27\rho u_1 - 3 = 0 \quad (16)$$

This equation has three real roots that can be solved numerically, and only one of them is suitable by considering the physical system at hand. With the value of u_1 known at the separation point, the magnitudes of u_κ and ν_κ can be calculated from Eqs. (15) and (13*b*). Eliminating Γ_κ and α_κ from Eqs. (14*a*) and (14*b*) yields

$$u_\kappa^2\kappa^4\Lambda^4 - 2u_\kappa(\nu_\kappa - 2\zeta^2 u_\kappa)\kappa^2\Lambda^2 + \nu_\kappa^2 - f_\kappa^2 = 0 \quad (17)$$

The transition frequencies at which the contact loss is initiated are given as

$$\Lambda_{1,2}^2 = \frac{1}{\kappa^2}\left[\frac{\nu_\kappa}{u_\kappa} - 2\zeta^2 \mp \frac{1}{u_\kappa}\sqrt{4\zeta^2 u_\kappa(\zeta^2 u_\kappa - \nu_\kappa) + f_\kappa^2}\right] \quad (18)$$

For the contact loss to happen, the discriminant of Eq. (20) should be positive. Hence, a separation criterion is obtained as

$$f_\kappa > 2\zeta\sqrt{u_\kappa(\nu_\kappa - \zeta^2 u_\kappa)} \quad (19a)$$

For a lightly damping system, $\zeta \ll 1$, Eq. (19*a*) is reduced as

$$f_\kappa > 2\zeta\sqrt{u_\kappa\nu_\kappa} \quad (19b)$$

For the experimental setup considered in this study, the values of u_κ and ν_κ at the separation point are obtained as $u_\kappa=1.3266$, and $\nu_\kappa=1.1252$, such that the condition for the contact loss to happen for this system is $f_\kappa > 2.44\zeta$. Nayak [1] used a set of heuristic arguments to arrive at a similar threshold value. He stated that the average dissipated power may be equal to the average input power at the downward jump frequency, and that the forced response is the same as the undamped free response at the same frequency. By considering the undamped free response possessing an amplitude grazing contact loss, one obtains a contact loss condition of $f_\kappa > 2.66\zeta$, which is in reasonably good agreement with the condition obtained by the single-term HBM.

In Fig. 8, the effect of harmonic excitation $f(\tau)$ on H_1 is shown for a linearly damped case of $\zeta=0.008$. Here, three response curves for the different values of f_κ are illustrated. Here, the curve for $f_t=(2.44)(0.008)=0.0195$ represents the threshold value. When $f_\kappa < f_t$, no contact loss is observed. When $f_\kappa > f_t$, such as $f_\kappa=0.03$, the contact loss takes place. Similarly, in Fig. 9, damping ratio ζ varies for constant $f_3=0.03$. The threshold value of the damping ratio is $\zeta_b=0.03/2.44=0.0123$. When ζ is as low as 0.008, contact loss is predicted. For $\zeta > 0.0123$, say $\zeta=0.02$, the softening behavior is reduced greatly since there is no contact loss.

5 Conclusion

In this paper, a sphere-plane contact problem with contact loss is investigated theoretically and experimentally. The physical system is modeled by a SDOF oscillator with piecewise nonlinear damping and stiffness. Multi-term HBM is used to obtain the steady state solution of the governing equation. The HBM solutions are confirmed by comparisons to those of the shooting method. An experimental setup is devoted to measure the steady state response of the physical system excited harmonically. A very good agreement between theoretical prediction and measurements is demonstrated for both acceleration response amplitudes and the phase difference between response and external excitation. A separation criterion, which is defined by $f(\tau)$ and ζ, is derived by using a one-term HBM formulation, and examined for different values of $f(\tau)$ and ζ.

For the contact problem at hand, a viscously linear damping model yielded results that are in good agreement with the experiments. Our current work focuses on other contact conditions that might require a nonlinear damping model. We are also in the process of expanding the HBM methodology to study multi-degree-of-freedom contact problems. Such cases exist for the experimental setup considered here when the mass of the ball is no longer negligible compared to the mass of the preload cylinder.

References

[1] Nayak, P. R., 1972, "Contact Vibrations," J. Sound Vib., **22**(3), pp. 297–322.
[2] Hess, D., and Soom, A., 1991, "Normal Vibrations and Friction Under Harmonic Loads: Part 1-Hertzian Contact," ASME J. Tribol., **113**, pp. 80–86.
[3] Perret-Liaudet, J., 1997, "Résonance Sous-Harmonique d'Ordre Deux Dans un Contact Sphère-Plan," C.R. Acad. Sci., Paris, Série IIb, **325**, pp. 443–448.
[4] Perret-Liaudet, J., 1998, "Résonance Sur-Harmonique d'ordre Deux Dans un Contact Sphère-Plan," C.R. Acad. Sci., Paris, Série IIb, **326**, pp. 787–792.
[5] Sabot, J., Krempf, P., and Janolin, C., 1998, "Non-linear Vibrations of a Sphere-plane Contact Excited by a Normal Load," J. Sound Vib., **214**(2), pp. 359–375.
[6] Perret-Liaudet, J., and Sabot, J., 1999, "Vibro-impact Induced by Nonlinear Resonances in Hertzian Contacts," in *Dynamics of Vibro-impact Systems*, V. I. Babitsky, ed., Springer, Berlin, pp. 251–260.
[7] Rigaud, E., and Perret-Liaudet, J., 2003, "Experiments and Numerical Results

on Non-linear Vibrations of an Impacting Hertzian Contact. Part 1: Harmonic Excitation," J. Sound Vib., **265**(2), pp. 289–307.
[8] Perret-Liaudet, J., and Rigaud, E., 2003, "Experiments and Numerical Results on Non-linear Vibrations of an Impacting Hertzian Contact. Part 2: Random Excitation," J. Sound Vib., **265**(2), pp. 309–327.
[9] Comparin, R. J., and Singh, R., 1989, "Nonlinear Frequency Response Characteristics of an Impact Pair," J. Sound Vib., **134**(2), pp. 259–290.
[10] Kahraman, A., and Singh, R., 1990, "Nonlinear Dynamics of a Spur Gear Pair," J. Sound Vib., **142**(1), pp. 49–75.
[11] Padmanabhan, C., and Singh, R., 1992, "Spectral Coupling Issues in a Two-Degree-Of-Freedom System With Clearance Non-Linearities," J. Sound Vib., **155**(2), pp. 209–230.
[12] Rook, T. E., and Singh, R., 1995, "Dynamic Analysis of a Reverse-Idler Gear Pair with Concurrent Clearances," J. Sound Vib., **182**(2), pp. 303–322.
[13] Natsiavas, S., 1989, "Periodic Response and Stability of Oscillators With Symmetric Trilinear Restoring Force," J. Sound Vib., **132**(2), pp. 315–331.
[14] Natsiavas, S., and Gonzalez, H., 2001, "Vibration of Harmonically Excited Oscillators With Asymmetric Constraints," J. Appl. Mech., **59**, pp. 284–290.
[15] Theodossiades, S., and Natsiavas, S., 2001, "Periodic and Chaotic Dynamics of Motor-driven Gear-Pair Systems With Backlash," Chaos, Solitons Fractals, **12**, pp. 2427–2440.
[16] Natsiavas, S., Theodossiades, S., and Goudas, I., 2000, "Dynamic Analysis of Piecewise Linear Oscillators With Time Periodic Coefficients," Int. J. Non-Linear Mech., **35**, pp. 53–68.
[17] Theodossiades, S., and Natsiavas, S., 2000, "Non-linear Dynamics of Gear-pair Systems With Periodic Stiffness and Backlash," J. Sound Vib., **229**, pp. 287–310.
[18] Blankenship, G. W., and Kahraman, A., 1995, "Steady State Forced Response of a Mechanical Oscillator With Combined Parametric Excitation and Clearance Type Non-linearity," J. Sound Vib., **185**(5), 743–765.
[19] Kahraman, A., and Blankenship, G. W., 1996, "Interactions Between Commensurate Parametric and Forcing Excitations in a System With Clearance," J. Sound Vib., **194**(3), pp. 317–336.
[20] Al-Shyyab, A., and Kahraman, A., 2005, "Non-Linear Dynamic Analysis of a Multi-Mesh Gear Train Using Multi-term Harmonic Balance Method: Period-one Motions," J. Sound Vib., **284**, pp. 151–172.
[21] Al-Shyyab, A., and Kahraman, A., 2005, "Non-Linear Dynamic Analysis of a Multi-Mesh Gear Train Using Multi-term Harmonic Balance Method: Subharmonic Resonances," J. Sound Vib., **279**, pp. 417–451.
[22] Choi, Y. S., and Noah, S. T., 1988, "Forced Periodic Vibration of Unsymmetric Piecewise-linear System," J. Sound Vib., **121**(1), pp. 117–126.
[23] Kim, Y. B., and Noah, S. T., 1991, "Stability and Bifurcation Analysis of Oscillators With Piecewise-linear Characteristics," J. Appl. Mech., **58**, pp. 545–553.
[24] Lau, S. L., and Zhang, W.-S., 1992, "Nonlinear Vibrations of Piecewise Linear Systems by Incremental Harmonic Balance Method," J. Appl. Mech., **59**, pp. 53–160.
[25] Raghothama, A., and Narayanan, S., 2000, "Bifurcation and Chaos of an Articulated Loading Platform With Piecewise Non-linear Stiffness Using the Incremental Harmonic Balance Method," Ocean Eng., **27**, pp. 1087–1107.
[26] Ma, Q. L., and Kahraman, A., 2005, "Period-One Motions of a Mechanical Oscillator With Periodically Time-Varying, PiecewiseNonlinear Stiffness," J. Sound Vib., **284**, pp. 893–914.
[27] Watson, L. T., Sosonkina, M., Melville, R. C., Morgan, A. P., and Walker, H. F., 1997, "Algorithm 777: HOMPACK90: A Suite of Fortran 90 Codes for Globally Convergent Homotopy Algorithms," ACM Trans. Math. Softw., **23**(4), pp. 514–549.
[28] Allgower, E. L., and Georg, K., 1990, *Numerical Continuation Methods: An Introduction*, Springer, New York.
[29] Nayfeh, A. H., and Balachandran, B., 1995, *Applied Nonlinear Dynamics: Analytical, Computational, and Experimental Methods*, Wiley, New York, 1995.
[30] Hsu, C. S., and Cheng, W. H., 1974, "Steady State Response of Dynamical System Under Combined Parametric and Forcing Excitations," J. Appl. Mech., **96**, pp. 371–378.
[31] Seydel, R., 1994, *Practical Bifurcation and Stability Analysis—From Equilibrium to Chaos*, Springer, New York.

The Dual Euler Basis: Constraints, Potentials, and Lagrange's Equations in Rigid-Body Dynamics

Oliver M. O'Reilly
Professor
Department of Mechanical Engineering,
University of California,
Berkeley, CA 94720-1740
e-mail: oreilly@Berkeley.edu

Given a specific set of Euler angles, it is common to ask what representations conservative moments and constraint moments possess. In this paper, we discuss the role that a non-orthogonal basis, which we call the dual Euler basis, plays in the representations. The use of the basis is illustrated with applications to potential energies, constraints, and Lagrange's equations of motion. [DOI: 10.1115/1.2190231]

1 Introduction

The Euler angle representation for a rotation consists in defining three angles $\gamma^1, \gamma^2, \gamma^3$ and their distinct axes of rotation. The unit vectors corresponding to these axes of rotation constitute the Euler basis $\{\mathbf{g}_1, \mathbf{g}_2, \mathbf{g}_3\}$. Thus, we have the following representation for the angular velocity vector $\boldsymbol{\omega}$ associated with the rotation:

$$\boldsymbol{\omega} = \dot{\gamma}^1 \mathbf{g}_1 + \dot{\gamma}^2 \mathbf{g}_2 + \dot{\gamma}^3 \mathbf{g}_3 \tag{1}$$

If we suppose that the rotation transforms a fixed set of orthogonal basis vectors $\{\mathbf{E}_1, \mathbf{E}_2, \mathbf{E}_3\}$ to a set of orthogonal basis vectors $\{\mathbf{e}_1, \mathbf{e}_2, \mathbf{e}_3\}$, then we can express any of the Euler basis vectors in terms of either of these bases.

It is well known, that, in general, $\boldsymbol{\omega} \cdot \mathbf{g}_i \neq \dot{\gamma}^i$. The question then arises as to which vectors, denoted by $\mathbf{a}$, have the property that

$$\boldsymbol{\omega} \cdot \mathbf{a} = \dot{\gamma}^i \text{ for some } i = 1,2,3 \tag{2}$$

The answer to this question provides a set of vectors, $\{\mathbf{g}^1, \mathbf{g}^2, \mathbf{g}^3\}$, which satisfy the following identities:

$$\begin{aligned} &\mathbf{g}^1 \cdot \mathbf{g}_1 = 1 \quad \mathbf{g}^1 \cdot \mathbf{g}_2 = 0 \quad \mathbf{g}^1 \cdot \mathbf{g}_3 = 0 \\ &\mathbf{g}^2 \cdot \mathbf{g}_1 = 0 \quad \mathbf{g}^2 \cdot \mathbf{g}_2 = 1 \quad \mathbf{g}^2 \cdot \mathbf{g}_3 = 0 \\ &\mathbf{g}^3 \cdot \mathbf{g}_1 = 0 \quad \mathbf{g}^3 \cdot \mathbf{g}_2 = 0 \quad \mathbf{g}^3 \cdot \mathbf{g}_3 = 1 \end{aligned} \tag{3}$$

Definition (3) provides nine equations for the nine unknown components of this basis, and the resulting vectors are such that

$$\boldsymbol{\omega} \cdot \mathbf{g}^k = \dot{\gamma}^k \quad (k = 1,2,3) \tag{4}$$

It is straightforward to show that linear independence of $\{\mathbf{g}_1, \mathbf{g}_2, \mathbf{g}_3\}$ implies that $\{\mathbf{g}^1, \mathbf{g}^2, \mathbf{g}^3\}$ is a basis which we call the dual Euler basis. The procedure for computing this basis is identical to that used in differential geometry to determine the contravariant basis vectors using the covariant basis vectors.

In the remainder of this paper, we explore the use of the dual Euler basis in determining constraint moments, conservative moments, and Lagrange's equations. After selecting a specific, and popular, choice of Euler angles, the 3-2-1 set, we then examine various applications ranging from Ziegler's example of a nonconservative constant moment to the equations of motion of a sliding rod. We wish to remark that the dual Euler basis has been used by the author for several years in courses on rigid body dynamics. They were first given a brief mention in the literature in a recent paper by O'Reilly and Srinivasa [1], and are discussed in Rao's new textbook [2]. The main purpose of the present paper is to elaborate on the results presented in Ref. [1] by examining various applications of the dual Euler basis.

2 Potential Energies, Constraints, and Lagrange's Equations of Motion

Consider a function $U = U(\gamma^1, \gamma^2, \gamma^3)$ of the Euler angles. We wish to establish a representation for the gradient of this function: ∇U. To proceed, we invoke the identity

$$\dot{U} = \nabla U \cdot \boldsymbol{\omega} \tag{5}$$

As $\dot{U} = \Sigma_{k=1}^{3} (\partial U / \partial \gamma^k) \dot{\gamma}^k$, with the help of Eqs. (1) and (4) we conclude that

$$\frac{\partial U}{\partial \gamma^k} = \nabla U \cdot \mathbf{g}_k \quad (k = 1,2,3) \tag{6}$$

Consequently, we have the following representation:

$$\nabla U = \frac{\partial U}{\partial \gamma^1} \mathbf{g}^1 + \frac{\partial U}{\partial \gamma^2} \mathbf{g}^2 + \frac{\partial U}{\partial \gamma^3} \mathbf{g}^3 \tag{7}$$

This result, which is presented in Ref. [1], enables an interesting representation for a conservative moment $\mathbf{M}$ associated with a moment potential U:

$$\mathbf{M} = -\frac{\partial U}{\partial \gamma^1} \mathbf{g}^1 - \frac{\partial U}{\partial \gamma^2} \mathbf{g}^2 - \frac{\partial U}{\partial \gamma^3} \mathbf{g}^3 \tag{8}$$

Several other treatments of a conservative moment are present in the literature, see Antman [3] and Beletskii [4]. However, they are all based on other representations of the rotation tensor.

The dual basis can also be used to calculate the constraint moment associated with a kinematic constraint. For instance, suppose a constraint is imposed on the rotational motion of a rigid body:[1]

$$\chi(\gamma^1, \gamma^2, \gamma^3, t) = 0 \tag{9}$$

This constraint can be expressed in the form

Contributed by the Applied Mechanics Division of ASME for publication in the JOURNAL OF APPLIED MECHANICS. Manuscript received September 23, 2005; final manuscript received February 3, 2006. Review conducted by R. M. McMeeking. Discussion on the paper should be addressed to the Editor, Prof. Robert M. McMeeking, Journal of Applied Mechanics, Department of Mechanical and Environmental Engineering, University of California–Santa Barbara, Santa Barbara, CA 93106-5070, and will be accepted until four months after final publication of the paper itself in the ASME JOURNAL OF APPLIED MECHANICS.

[1] We can also consider more general constraints where the translational and rotational motion of the rigid body are coupled, but this would not significantly add to the present discussion.

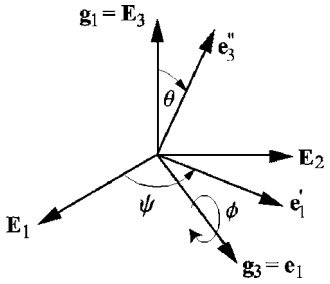

Fig. 1 Schematic of the 3-2-1 set of Euler angles: ψ, θ and ϕ. The vectors $\mathbf{e}_1' = \cos(\psi)\mathbf{E}_1 + \sin(\psi)\mathbf{E}_2$, and $\mathbf{e}_3'' = \cos(\theta)\mathbf{E}_3 + \sin(\theta)\mathbf{e}_1'$.

$$\boldsymbol{\omega} \cdot \nabla \chi + \frac{\partial \chi}{\partial t} = 0 \tag{10}$$

Using the normality prescription, we find that the constraint moment $\mathbf{M}_c$ needed to enforce this constraint is

$$\mathbf{M}_c = \mu \nabla \chi \tag{11}$$

where μ is a Lagrange mutiplier. This constraint moment does work: $\mathbf{M}_c \cdot \boldsymbol{\omega} = -\mu(\partial\chi/\partial t)$. As noted in Refs. [1,5], the prescription (11) is consistent with the Lagrange-D'Alembert principle, which states that generalized constraint forces do no virtual work.

The role that the dual Euler basis plays in constraints and potential energies naturally leads to questions concerning their role in Lagrange's equations of motion for a rigid body. To elaborate, consider a rigid body subject to a resultant external moment $\mathbf{M}$ and possessing an angular momentum relative to its center of mass $\bar{X}$ of $\mathbf{H}$. After choosing a set of Euler angles, it is known [5,6] that Lagrange's equations of motion for the attitude of the rigid body are equivalent to a balance of angular momentum $\mathbf{M} = \dot{\mathbf{H}}$:

$$\frac{d}{dt}\left(\frac{\partial T}{\partial \dot{\gamma}^k}\right) - \frac{\partial T}{\partial \gamma^k} = \mathbf{M} \cdot \mathbf{g}_k \quad (k = 1,2,3) \tag{12}$$

where T is the kinetic energy of the rigid body.

If we suppose that the sole external moment is conservative, then $\mathbf{M} = -\nabla U$, and

$$\frac{d}{dt}\left(\frac{\partial T}{\partial \dot{\gamma}^k}\right) - \frac{\partial T}{\partial \gamma^k} = -\nabla U \cdot \mathbf{g}_k = -\frac{\partial U}{\partial \gamma^k} \quad (k = 1,2,3) \tag{13}$$

from whence it is easy to establish a form of Eq. (12) featuring the Lagrangian $L = T - U$. On the other hand, if we suppose that the body is subject to a constraint, say $\gamma^3 = \text{constant}$, then, $\mathbf{M}_c = \mu \mathbf{g}^3$. Lagrange's equations in this case provide two equations to determine $\gamma^1(t)$ and $\gamma^2(t)$, while the third equation provides μ:

$$\frac{d}{dt}\left(\frac{\partial T}{\partial \dot{\gamma}^k}\right) - \frac{\partial T}{\partial \gamma^k} = \mathbf{M}_a \cdot \mathbf{g}_k \quad (k = 1,2)$$

$$\frac{d}{dt}\left(\frac{\partial T}{\partial \dot{\gamma}^3}\right) - \frac{\partial T}{\partial \gamma^3} = \mathbf{M}_a \cdot \mathbf{g}_3 + \mu \tag{14}$$

In these equations, $\mathbf{M} = \mathbf{M}_a + \mathbf{M}_c$, where $\mathbf{M}_a$ is the applied moment.

3 The 3-2-1 Set of Euler Angles

To illustrate our previous remarks, we consider the set of 3-2-1 Euler angles (see Fig. 1). For this set of angles, one starts with a rotation through ψ about $\mathbf{E}_3$, followed by a rotation θ about $\cos(\psi)\mathbf{E}_2 - \sin(\psi)\mathbf{E}_1$ and finally a rotation ϕ about $\mathbf{e}_1 = \cos(\theta)(\cos(\psi)\mathbf{E}_1 + \sin(\psi)\mathbf{E}_2) - \sin(\theta)\mathbf{E}_3$.[2]

The aforementioned sequence of rotations and the fixed basis $(\mathbf{E}_1, \mathbf{E}_2, \mathbf{E}_3)$ establishes the Euler basis. This basis is usually written in terms of the basis $(\mathbf{e}_1, \mathbf{e}_2, \mathbf{e}_3)$:

$$\begin{bmatrix} \mathbf{g}_1 \\ \mathbf{g}_2 \\ \mathbf{g}_3 \end{bmatrix} = \mathsf{A} \begin{bmatrix} \mathbf{e}_1 \\ \mathbf{e}_2 \\ \mathbf{e}_3 \end{bmatrix} \tag{15}$$

where the matrix A is

$$\mathsf{A} = \begin{bmatrix} -\sin(\theta) & \sin(\phi)\cos(\theta) & \cos(\phi)\cos(\theta) \\ 0 & \cos(\phi) & -\sin(\phi) \\ 1 & 0 & 0 \end{bmatrix} \tag{16}$$

To calculate the dual Euler basis, we note that Eq. (3) can be written in a compact form:

$$\mathsf{A}^T \mathsf{B} = \mathsf{I}, \tag{17}$$

where I is the identity matrix, T denotes transpose, and the matrix B is composed of the components of the dual basis vectors:

$$\mathsf{B} = \begin{bmatrix} \mathbf{g}^1 \cdot \mathbf{e}_1 & \mathbf{g}^1 \cdot \mathbf{e}_2 & \mathbf{g}^1 \cdot \mathbf{e}_3 \\ \mathbf{g}^2 \cdot \mathbf{e}_1 & \mathbf{g}^2 \cdot \mathbf{e}_2 & \mathbf{g}^2 \cdot \mathbf{e}_3 \\ \mathbf{g}^3 \cdot \mathbf{e}_1 & \mathbf{g}^3 \cdot \mathbf{e}_2 & \mathbf{g}^3 \cdot \mathbf{e}_3 \end{bmatrix} \tag{18}$$

Solving for the unknown components of B we find that

$$\begin{bmatrix} \mathbf{g}^1 \\ \mathbf{g}^2 \\ \mathbf{g}^3 \end{bmatrix} = \begin{bmatrix} 0 & \sin(\phi)\sec(\theta) & \cos(\phi)\sec(\theta) \\ 0 & \cos(\phi) & -\sin(\phi) \\ 1 & \sin(\phi)\tan(\theta) & \cos(\phi)\tan(\theta) \end{bmatrix} \begin{bmatrix} \mathbf{e}_1 \\ \mathbf{e}_2 \\ \mathbf{e}_3 \end{bmatrix}$$

$$= \begin{bmatrix} \sec^2(\theta) & 0 & \tan(\theta)\sec(\theta) \\ 0 & 1 & 0 \\ \tan(\theta)\sec(\theta) & 0 & \sec^2(\theta) \end{bmatrix} \begin{bmatrix} \mathbf{g}_1 \\ \mathbf{g}_2 \\ \mathbf{g}_3 \end{bmatrix} \tag{19}$$

It is easy to verify that the dual Euler basis and the Euler basis fail to be bases when this set of Euler angles have their singularities at $\theta = \pm\pi/2$. Another interesting feature is that for all sets of Euler angles $\mathbf{g}_2 = \mathbf{g}^2$. The reason for this lies in the fact that the second axis of rotation $\mathbf{g}_2$ is always normal to the other two.

4 Constant Moments are Not Necessarily Conservative

Ziegler discusses the curious example of a constant moment not being conservative in his monograph on structural stability [8]. Using an ingenious argument, he shows that the work done by the moment depends on the sequence of rotations employed, and is thus nonconservative. It is interesting to explore this example with the help of the dual Euler basis.

Consider a moment $M\mathbf{E}_3$ acting on a rigid body whose rotation tensor is parametrized using a set of 3-2-1 Euler angles. Now suppose that this moment were conservative, then we would need to find a moment potential U such that

$$M\mathbf{E}_3 = -\frac{\partial U}{\partial \psi}\mathbf{g}^1 - \frac{\partial U}{\partial \theta}\mathbf{g}^2 - \frac{\partial U}{\partial \phi}\mathbf{g}^3 \tag{20}$$

Taking the components of this equation, we find a set of partial differential equations for U:

$$\frac{\partial U}{\partial \psi} = -M \quad \frac{\partial U}{\partial \theta} = 0 \quad \frac{\partial U}{\partial \phi} = M\sin(\theta) \tag{21}$$

Clearly, $(21)_2$ and $(21)_3$ are incompatible and we conclude that no moment potential exists.

[2]This set of Euler angles is used in Refs. [2,6,7]. The term "Euler basis" first appeared in Casey.

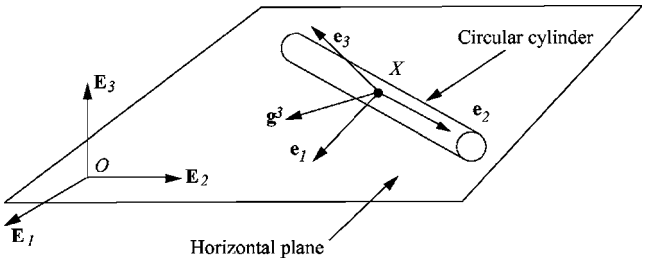

Fig. 2 A circular rod moving on a horizontal plane. The rotation of this body is an example of a situation where one of the Euler angles is constant. The basis vectors $\mathbf{e}_i$ are fixed to the rod.

5 A Sliding Rod

To further illustrate the utility of the dual Euler basis, suppose that we have a rigid body undergoing a motion where the third Euler angle is a constant ϕ_0. An example of a situation where this arises is shown in Fig. 2. There, a cylindrical rod of mass m slides on a smooth horizontal surface. A vertical gravitational force $-mg\mathbf{E}_3$ acts on the rod.

The cylinder is subject to two constraints:

$$\bar{\mathbf{x}} \cdot \mathbf{E}_3 = R \quad \phi = 0 \tag{22}$$

Here, $\bar{\mathbf{x}}$ is the position vector of the center of mass $\bar{X}$ of the rod, and the rotation of the rod is parametrized by a set of 3-2-1 Euler angles. Clearly, $(22)_2$ can be written in the form

$$\boldsymbol{\omega} \cdot \mathbf{g}^3 = 0 \tag{23}$$

The constraint force $\mathbf{F}_c$ and moment $\mathbf{M}_c$ acting on the rod can be prescribed using the normality prescription:

$$\mathbf{F}_c = N\mathbf{E}_3 \quad \mathbf{M}_c = \mu\mathbf{g}^3 \tag{24}$$

where N and μ are unknowns. It is interesting to note that the vector $\mathbf{g}^3$ for this example is normal to $\mathbf{E}_3$ and $\mathbf{e}_2$. Indeed, the moment $(24)_2$ can be realized by assuming a varying normal traction field $\mathbf{t}$ on the contacting line between the rod and the plane. The system (24) will be equipollent to the field $\mathbf{t}$.

Lagrange's equations of motion for this body are straightforward to establish once the kinetic energy has been calculated:

$$T = \frac{\lambda_t}{2}(\dot{\psi}\cos(\phi)\cos(\theta) - \dot{\theta}\sin(\phi))^2 + \frac{\lambda_2}{2}(\dot{\theta}\cos(\phi) + \dot{\psi}\cos(\theta)\sin(\phi))^2 + \frac{\lambda_t}{2}(\dot{\phi} - \dot{\psi}\sin(\theta))^2 + \frac{m}{2}(\dot{x}_1^2 + \dot{x}_2^2 + \dot{x}_3^2) \tag{25}$$

Here, λ_t and λ_2 are the principal moments of inertia, and $\bar{\mathbf{x}} = \Sigma_{i=1}^3 x_i \mathbf{E}_i$. Evaluating Lagrange's equations, imposing the constraints, introducing the constraint moment and constraint force, and the applied gravitational force $-mg\mathbf{E}_3$, we find that[3]

$$m\ddot{x}_k = 0 \quad (k = 1,2)$$

$$0 = N - mg$$

$$\lambda_t \ddot{\psi} = 0$$

$$\lambda_2 \ddot{\theta} = 0$$

$$\frac{d}{dt}(-\lambda_t \dot{\psi}\sin(\theta)) - (\lambda_2 - \lambda_t)\dot{\psi}\dot{\theta}\cos(\theta) = \mu \tag{26}$$

It follows from these equations that the center of mass of the rod moves at a constant speed, and that θ and ψ also have constant velocities. Moreover, the constraint moment acting on the rod is

$$\mathbf{M}_c = -\lambda_2 \dot{\psi}_0 \dot{\theta}_0 \cos(\theta_0 + \dot{\theta}_0 t)\mathbf{g}^3 \tag{27}$$

where $\dot{\psi}_0 = \dot{\psi}(0)$, $\dot{\theta}_0 = \dot{\theta}(0)$, and $\theta_0 = \theta(0)$ are initial conditions. It is interesting to note that the constraint moment for this elementary problem is non-trivial.

6 Closing Comments

We have presented examples from rigid body dynamics which illustrate uses of the dual Euler basis. As is hopefully evident from them, this basis enables transparent representations for constraint moments and moment potentials. These representations in turn can be easily incorporated into a treatment of Lagrange's equations for rigid bodies. The basis also has application to many areas in mechanics which feature rotations. For instance, it could be used to describe torques and torsional springs in several rod theories.

References

[1] O'Reilly, O. M., and Srinivasa, A. R., 2002, "On Potential Energies and Constraints in the Dynamics of Rigid Bodies and Particles," Math. Probl. Eng., **8**(3), pp. 169–180.
[2] Rao, A. V., 2006, *Dynamics of Particles and Rigid Bodies: A Systematic Approach*, Cambridge University Press, Cambridge.
[3] Antman, S. S., 1972, "Solution to Problem 71-24: "Angular Velocity and Moment Potentials for a Rigid Body," by J. G. Simmonds," SIAM Rev., **14**, pp. 649–652.
[4] Beletskii, V. V., 1966, *Motion of an Artificial Satellite about its Center of Mass*, (translated from the Russian by Z. Lerman), Israel Program for Scientific Translations, Jerusalem.
[5] Casey, J., and O'Reilly, O. M., 2006, "Geometrical Derivation of Lagrange's Equations for a System of Rigid Bodies," Mathematics and Mechanics of Solids, to appear.
[6] Greenwood, D. T., 1988, *Classical Dynamics*, 2nd ed., Prentice-Hall, Englewood Cliffs, NJ.
[7] Casey, J., 1983, "A Treatment of Rigid Body Dynamics," ASME J. Appl. Mech., **50**, pp. 905–907 and **51**, p. 227.
[8] Ziegler, H., 1968, *Principles of Structural Stability*, Blaisdell, Waltham, MA.

[3]To calculate the last three of these equations, we have used Eq. (12).

Gregory W. Kooistra[1]
Department of Materials Science and Engineering,
University of Virginia,
116 Engineer's Way,
Charlottesville, VA 22904
e-mail: gkooistra@watsonfurniture.com

Vikram Deshpande
Engineering Department,
Cambridge University,
Trumpington Street,
Cambridge CB2 1PZ, UK

Haydn N. G. Wadley
Department of Materials Science and Engineering,
University of Virginia,
116 Engineer's Way,
Charlottesville, VA 22904

Hierarchical Corrugated Core Sandwich Panel Concepts

The transverse compression and shear collapse mechanisms of a second order, hierarchical corrugated truss structure have been analyzed. The two competing collapse modes of a first order corrugated truss are elastic buckling or plastic yielding of the truss members. In second order trusses, elastic buckling and yielding of the larger and smaller struts, shear buckling of the larger struts, and wrinkling of the face sheets of the larger struts have been identified as the six competing modes of failure. Analytical expressions for the compressive and shear collapse strengths in each of these modes are derived and used to construct collapse mechanism maps for second order trusses. The maps are useful for selecting the geometries of second order trusses that maximize the collapse strength for a given mass. The optimization reveals that second order trusses made from structural alloys have significantly higher compressive and shear collapse strengths than their equivalent mass first order counterparts for relative densities less than about 5%. A simple sheet metal folding and dip brazing method of fabrication has been used to manufacture a prototype second order truss with a relative density of about 2%. The experimental investigation confirmed the analytical strength predictions of the second order truss, and demonstrate that its strength is about ten times greater than that of a first order truss of the same relative density. [DOI: 10.1115/1.2198243]

1 Introduction

Materials with structural hierarchy can have significantly higher stiffness or strength to weight ratios than their single-length scale microstructure counterparts. For instance, the maximum stiffness to weight ratio of an isotropic two-phase material is set by the Hashin-Shtrikman [1] (HS) upper bound. A number of two-phase composites are known to attain the HS bounds on the bulk and shear moduli. Most of these include structural hierarchy. For example, Norris [2] and Milton [3] proposed differential schemes for constructing composite structures with the extremal HS bulk and shear moduli. While Milton [3] used a laminate microstructure, Norris [2] employed coated sphere architectures. However, the procedures suggested by both authors are iterative and require an infinite number of mixing processes. On the other hand, Francfort and Murat [4] suggested a "rank" laminate approach which attained both the bulk and shear HS bounds with a finite number of layering directions. Rank laminates are obtained by a sequential process where at each stage the previous laminate is laminated again with a single lamina (always the same) in a new direction. Thus, a rank-n laminate is produced by n such successive laminations. Francfort and Murat [4] showed that while in the two-dimensional case isotropic rank-3 laminates have the extremal bulk and shear moduli, in the three-dimensional (3D) case rank-6 laminates are the optimal microstructures.

Hierarchical cellular structures consisting of self-similar structural units can also exhibit significant strength to weight improvements over comparable non-hierarchical structures. For example, Bhat et al. [5] manufactured sandwich panels with honeycomb cores; the webs of these honeycombs were in-turn made from honeycomb sandwiches resulting in a second order structure. The experimental investigation of Bhat et al. [5] indicated the second order panel had a compressive strength about six times greater than an equal mass first order honeycomb sandwich panel. A similar experimental study of hierarchical hexagonal honeycombs by Lakes [6] demonstrated that the compressive strength of a second order honeycomb was three to four times greater than a first order honeycomb of equal mass.

Lakes [6] and Murphey and Hinkle [7] presented models for the stiffness and strength of hierarchical cellular materials and truss-like structures. They assumed a "continuum" model for the material at each length scale that led to simple recursive expressions for the stiffness and strength of the hierarchical structures. In doing so, they assumed macroscopic elastic or plastic buckling of the struts to be the only operative failure modes at each length scale. Short wavelength failure modes at the higher length scales associated with the discrete nature of the hierarchical structure were neglected in these initial analyses. Nevertheless, optimizations performed using these models predict substantial strength increases with increasing structural hierarchy.

The widespread adoption of hierarchical materials has been impeded by difficulties in their manufacture and the high costs and availability of very thin sheets of material. This constraint arises because of the very large differences in the structural length scales required to achieve optimal second and higher order systems. In all but the largest macro-scale structures (e.g. the Eiffel tower) this requires the use of very thin gauge sheet materials for the webs of the structures at the smallest length scales.

Recent work in large-scale, ultralight structures that can resist dynamic loading has stimulated a renewed interest in hierarchical cellular structures as cores for sandwich panels. Prismatic sandwich core topologies (e.g., the corrugated or folded plate core) are ideal for application in sandwich beams as they provide a high in-plane stretching strength. However, low relative density two-dimensional prismatic cores collapse by elastic buckling of the webs and thus have a low strength to weight ratio. Increasing the compressive strength of such prismatic corrugated cores offers potential benefits in the design of shock resistant sandwich beams. Hierarchical construction is expected to delay the elastic buckling of the webs of these prismatic sandwich cores and is thus attractive for application in large sandwich structures (readers are referred to Deshpande and Fleck [8] for details on the relation between the bending strength of sandwich beams and the shear and compressive strengths of the core).

[1]Author to whom correspondence should be addressed.

Contributed by the Applied Mechanics Division of ASME for publication in the JOURNAL OF APPLIED MECHANICS. Manuscript received May 12, 2005; final manuscript received September 20, 2005. Review conducted by R. M. McMeeking. Discussion on the paper should be addressed to the Editor, Prof. Robert M. McMeeking, Journal of Applied Mechanics, Department of Mechanical and Environmental Engineering, University of California – Santa Barbara, Santa Barbara, CA 93106-5070, and will be accepted until four months after final publication of the paper itself in the ASME JOURNAL OF APPLIED MECHANICS.

(*a*) *Simple corrugation (1st order)*

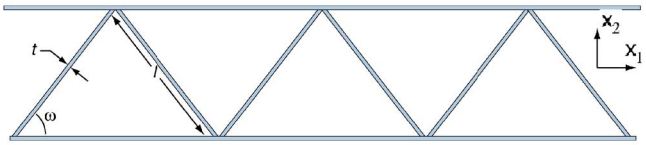

(*b*) *Hierarchical corrugation (2nd order)*

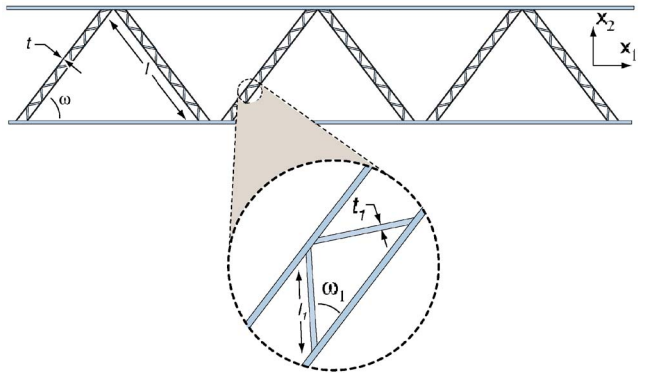

Fig. 1 Sketches of (*a*) the first and (*b*) the second order corrugated cores sandwiched between two rigid face sheets

Here, we investigate the "effective" mechanical properties of hierarchical corrugated cores. Analytical models are developed for the compressive and shear stiffness and strengths of first and second order corrugated sandwich panel cores. Expressions for the collapse strengths for six competing collapse modes are employed to generate collapse mechanism maps for a second order corrugated sandwich core and to determine optimal designs that maximize the collapse strength for a given core mass. A preliminary experimental investigation to validate the model predictions is also reported.

2 Analysis of a Corrugated Sandwich Core

Two types of prismatic corrugated sandwich cores are considered here. The first is a simple (first order) corrugated core comprising struts of thickness t, and length l, with a corrugation angle ω, as illustrated in Fig. 1(a). This type of corrugated core has no structural hierarchy and will be subsequently referred to as the first order corrugated core. A second order corrugated core then has one level of structural hierarchy, i.e., the monolithic struts of the first order core are themselves replaced by sandwich panels comprising face sheets of thickness t and a corrugated truss core comprising struts of thickness t_1 and length l_1 corrugated at an angle ω_1. These truss core sandwich panels (columns) are then corrugated at an angle ω to form the second order corrugated core, see Fig. 1(b). The sandwich columns will be referred to subsequently as the large struts of the second order core while the struts that form the core of these sandwich columns will be referred to as the smaller struts of the second order core.

Here we derive analytical expressions for the effective transverse stiffness and strength of the first and second order cores, sandwiched between two rigid face sheets. In all the subsequent analyses, we assume that the corrugated cores are made from an elastic-ideally plastic material with a Young's modulus E_s, Poisson's ratio ν, and yield strength σ_Y. The width b of the corrugated core (into the plane of the paper) is assumed to be sufficiently small for plane stress conditions to prevail in the struts.

2.1 First Order Corrugated Core. The relative density (the ratio of the volume of corrugated core material to the volume of panel) $\bar{\rho}$, of the first order corrugated structure sketched in Fig. 1(a) is, to first order in t/l, given by

$$\bar{\rho} = \frac{2}{\sin 2\omega}\left(\frac{t}{l}\right) \tag{1}$$

where ω is the angle of the corrugation. For small t/l, the contribution to the overall stiffness from the bending of the constituent struts is negligible compared to that from stretching. Thus, the struts can be assumed to be pin jointed to the face sheets and analytical expressions for the effective transverse Young's E and shear G moduli are

$$E = E_s \bar{\rho} \sin^4 \omega \tag{2}$$

and

$$G = E_s \frac{\bar{\rho}}{4} \sin^2 2\omega \tag{3}$$

respectively, where E_s is the Young's modulus of the solid material from which the corrugated core is made. As discussed above, for small t/l, it is acceptable to assume that the struts are pin jointed at the face sheets. Thus, an equilibrium analysis dictates that the effective peak transverse compressive σ_P and shear τ_P strengths are specified by

$$\sigma_p = \sigma_c \bar{\rho} \sin^2 \omega \tag{4}$$

and

$$\tau_p = \sigma_c \frac{\bar{\rho}}{2} \sin 2\omega \tag{5}$$

respectively, where σ_c is the maximum compressive strength of the struts of the first order corrugated core. For struts made from an elastic-ideally plastic material, σ_c is given by

$$\sigma_c = \begin{cases} \dfrac{k^2\pi^2 E_s}{12}\left(\dfrac{t}{l}\right)^2 & \text{if } \dfrac{t}{l} < \sqrt{\dfrac{12\sigma_Y}{\pi^2 k^2 E_s}} \\ \sigma_Y & \text{otherwise} \end{cases} \tag{6}$$

The factor k depends on the end constraints of the struts with $k=1$ or $k=2$ corresponding to pin-jointed or built-in end conditions, respectively.

2.2 Second Order Corrugated Core. The relative density of the second order corrugated core, sketched in Fig. 1(b), (to first order in t/l and t_1/l_1) is given by

$$\bar{\rho} = 4\left(\frac{t}{l}\right)\frac{1}{\sin 2\omega} + 4\left(\frac{t_1}{l}\right)\frac{\sin \omega_1}{\sin 2\omega_1 \sin 2\omega} \tag{7}$$

where the strut dimensions t, t_1, l, and l_1 along with the corrugation angles ω and ω_1 are defined in Fig. 1(b). Again, for small t/l and t_1/l_1, the contribution to the stiffness from the bending of the struts is negligible. Thus, equilibrium dictates that the effective transverse Young's and shear moduli of the second order corrugated core are

$$E = E_s \frac{\sin^3 \omega}{\cos \omega}\left(\frac{2t}{l}\right) = E_s\left[\bar{\rho} \sin^4 \omega - \left(\frac{2t_1}{l}\right)\frac{\sin \omega_1 \sin^3 \omega}{\sin 2\omega_1 \cos \omega}\right] \tag{8}$$

and

$$G = E_s \sin 2\omega\left(\frac{t}{l}\right) = E_s\left[\frac{\bar{\rho}}{4} \sin^2 2\omega - \left(\frac{t_1}{l}\right)\frac{\sin \omega_1 \sin 2\omega}{\sin 2\omega_1}\right] \tag{9}$$

respectively. Since the second level of corrugations (the miniature corrugations in Fig. 1(b)) do not contribute to the stiffness, the second order corrugated core is less efficient than the first order core from a stiffness perspective; compare Eqs. (8) and (9) with the corresponding expressions for the moduli of the first order core. This is consistent with the prediction of Lakes [6], who suggested that the stiffness to weight ratio of framework-type structures decreases with increasing structural hierarchy.

2.2.1 Failure Modes of the Second Order Corrugated Core. The second order corrugated core made from an elastic-ideally

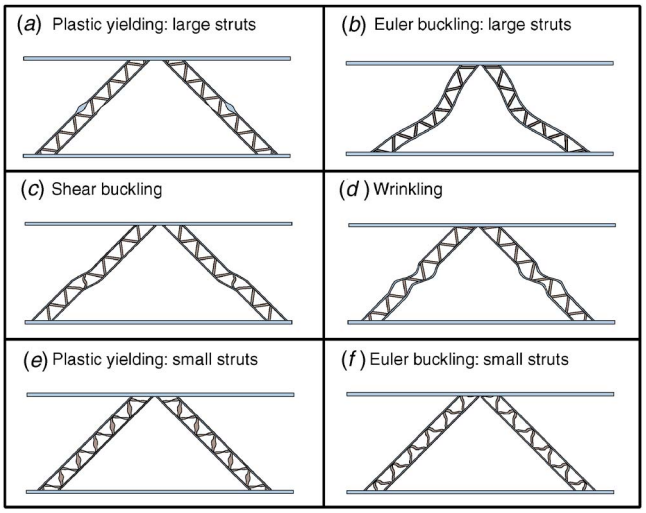

Fig. 2 Schematic drawings of the failure modes in the second order corrugated core (*a*) plastic yielding of the larger struts, (*b*) Euler buckling of the larger struts, (*c*) shear buckling of the larger struts, (*d*) elastic wrinkling of the larger strut face sheets, (*e*) yielding of the smaller struts, and (*f*) Euler buckling of the smaller struts

plastic material can fail by six competing collapse modes. We consider each of these modes in turn and derive analytical expressions for the effective transverse compressive and shear strengths, σ_p and τ_p, respectively.

2.2.1.1 Plastic yielding of the larger struts. The larger struts with face sheets of thickness t are subjected to compressive and/or tensile stresses. Thus, these struts may fail by plastic yielding of the face sheets, Fig. 2(*a*). Upon assuming all struts to be pin jointed, upper bound estimates of the compressive and shear collapse strengths in this mode are given by

$$\frac{\sigma_p}{\sigma_Y} = 2\left(\frac{t}{l}\right)\tan\omega \tag{10}$$

and

$$\frac{\tau_p}{\sigma_Y} = 2\left(\frac{t}{l}\right) \tag{11}$$

respectively.

2.2.1.2 Euler buckling of the larger struts. Under compressive loads, the larger struts can fail by Euler buckling as shown schematically in Fig. 2(*b*). Here we model these large struts as built-in Euler columns with a second moment of area

$$I = 2t\left(\frac{l_1 \sin\omega_1}{2}\right)^2 \tag{12}$$

Upon assuming this failure mode, the compressive and shear collapse strengths of the second order corrugated core are specified by

$$\frac{\sigma_p}{\sigma_Y} = \frac{2\pi^2}{\varepsilon_Y}\left(\frac{t}{l}\right)\left(\frac{l_1}{l}\right)^2 \sin^2\omega_1 \tan\omega \tag{13}$$

and

$$\frac{\tau_p}{\sigma_Y} = \frac{2\pi^2}{\varepsilon_Y}\left(\frac{t}{l}\right)\left(\frac{l_1}{l}\right)^2 \sin^2\omega_1 \tag{14}$$

respectively, where $\varepsilon_Y \equiv \sigma_Y/E_s$ is the yield strain of the solid material.

2.2.1.3 Shear buckling of the larger struts. The larger struts are sandwich columns comprising face sheets of thickness t and a corrugated core. Shear buckling (Fig. 2(*c*)) of these sandwich columns is set by the shear stiffness of the core, as discussed in Zenkert [9], and occurs at a load P_s

$$P_s = (AG)_{\text{eq}} \tag{15}$$

The equivalent shear rigidity of the core $(AG)_{\text{eq}}$ is given by

$$(AG)_{\text{eq}} = bl_1 \sin\omega_1 \frac{E}{2}\left(\frac{t_1}{l_1}\right)\sin 2\omega_1 \tag{16}$$

where b is the width of the second order corrugated core (into the plane of the paper in Fig. 1(*b*)). Thus, the compressive and shear collapse strengths in this mode are

$$\frac{\sigma_p}{\sigma_Y} = \frac{1}{\varepsilon_Y}\left(\frac{t_1}{l}\right)\sin^2\omega_1 \cos\omega_1 \tan\omega \tag{17}$$

and

$$\frac{\tau_p}{\sigma_Y} = \frac{1}{\varepsilon_Y}\left(\frac{t_1}{l}\right)\sin^2\omega_1 \cos\omega_1 \tag{18}$$

respectively.

2.2.1.4 Elastic wrinkling of the larger strut face sheets. As mentioned above, the larger struts of the second order corrugated core are sandwich columns comprising face sheets and a corrugated core. Wrinkling is short wavelength elastic buckling (Fig. 2(*d*)) of the face sheets of these sandwich columns. Sheets of thickness t can buckle as pin-ended Euler columns between the points of attachment to the smaller corrugated core. The compressive and shear collapse strengths of the second order corrugated core are then given by

$$\frac{\sigma_p}{\sigma_Y} = \frac{\pi^2}{24\varepsilon_Y}\left(\frac{t}{l}\right)^3\left(\frac{l}{l_1}\right)^2 \frac{\tan\omega}{\cos^2\omega_1} \tag{19}$$

and

$$\frac{\tau_p}{\sigma_Y} = \frac{\pi^2}{24\varepsilon_Y}\left(\frac{t}{l}\right)^3\left(\frac{l}{l_1}\right)^2 \frac{1}{\cos^2\omega_1} \tag{20}$$

respectively. It is worth emphasizing here that the above analysis neglects the stresses introduced into the face sheets by the core and thus may overestimate the wrinkling strength of the hierarchical core. A full finite element analysis may be required to investigate this effect.

2.2.1.5 Yielding of the smaller struts. The sandwich columns of length l that form the large struts of the second order corrugated core are built in at the rigid faces, see Fig. 1(*b*). Hence, shear forces develop in these sandwich columns which in turn can yield the smaller struts that form the core of the sandwich columns, see Fig. 2(*e*).

Elementary elastic beam theory dictates that the ratio of the axial force F_a to the shear force F_s in the sandwich columns of length l is

$$\frac{F_a}{F_s} = \frac{2}{3}\left(\frac{l}{l_1}\right)^2 \frac{1}{\sin 2\omega} \tag{21}$$

Note that yielding of the smaller struts implies that the maximum shear force in the larger struts is

$$F_s|_{\max} = 2b\sigma_Y t_1 \cos\omega_1 \tag{22}$$

An equilibrium analysis then gives the compressive and shear collapse strengths of the second order corrugated core as

$$\frac{\sigma_p}{\sigma_Y} = 2\left(\frac{t_1}{l}\right)\frac{\cos\omega_1}{\cos\omega}\left[\frac{1}{3\cos\omega}\left(\frac{l}{l_1}\right)^2 + \cos\omega\right] \tag{23}$$

and

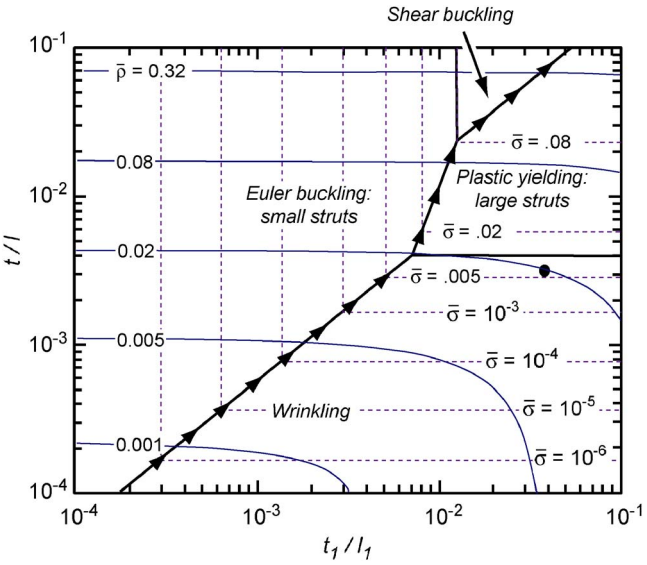

Fig. 3 Failure mechanism map for Al6061-T6 (ε_Y=0.004) second order corrugated core with l_1/l=0.04, ω_1=45 deg. The solid circle marks the geometry tested in this study. The arrows trace the path of the optimum designs that maximize the compressive strength σ_p for a given relative density $\bar{\rho}$.

$$\frac{\tau_p}{\sigma_Y} = 2\left(\frac{t_1}{l}\right)\frac{\cos\omega_1}{\cos\omega}\left[\frac{\cos^2\omega}{3\sin^3\omega}\left(\frac{l}{l_1}\right)^2 + \sin\omega\right] \tag{24}$$

respectively.

2.2.1.6 Euler buckling of the smaller struts. Elastic buckling of the smaller struts can also result in collapse of the second order corrugated core, Fig. 2(*f*). The analysis is similar to that outlined for mode (*e*) but with the maximum value of the shear force now set by elastic buckling of the smaller struts as built-in Euler columns. Thus, the maximum value of F_s is given by

$$F_s\Big|_{\max} = \frac{2}{3}b\pi^2 E_s \cos\omega_1\left(\frac{t_1}{l_1}\right)^2 t_1 \tag{25}$$

and the corresponding compressive and shear collapse strengths of the second order corrugated core are

$$\frac{\sigma_p}{\sigma_Y} = \frac{2\pi^2}{3\varepsilon_Y}\left(\frac{t_1}{l}\right)^3\left(\frac{l}{l_1}\right)^2\frac{\cos\omega_1}{\cos\omega}\left[\frac{1}{3\cos\omega}\left(\frac{l}{l_1}\right)^2 + \cos\omega\right] \tag{26}$$

and

$$\frac{\tau_p}{\sigma_Y} = \frac{2\pi^2}{3\varepsilon_Y}\left(\frac{t_1}{l}\right)^3\left(\frac{l}{l_1}\right)^2\frac{\cos\omega_1}{\cos\omega}\left[\frac{\cos^2\omega}{3\sin^3\omega}\left(\frac{l}{l_1}\right)^2 + \sin\omega\right] \tag{27}$$

respectively.

The regimes of dominance of the failure modes described above can be illustrated in a collapse mechanism map. In constructing such a map it is assumed that the operative collapse mode in compression or shear is the one associated with the lowest collapse strength. An example of such a collapse map for the compressive failure modes of a second order corrugated core with l_1/l=0.04, ω_1=45 deg and ω=60 deg, made from a solid material with a yield strain ε_Y=0.004 is shown in Fig. 3 with the nondimensional axes t/l and t_1/l_1. The regimes of dominance of the collapse modes are marked along with contours of the nondimensional collapse strength, $\bar{\sigma} \equiv \sigma_p/\sigma_Y$, and relative density, $\bar{\rho}$: wrinkling of the faces of the large struts and elastic buckling of the smaller struts are the dominant failure modes for this choice of material properties.

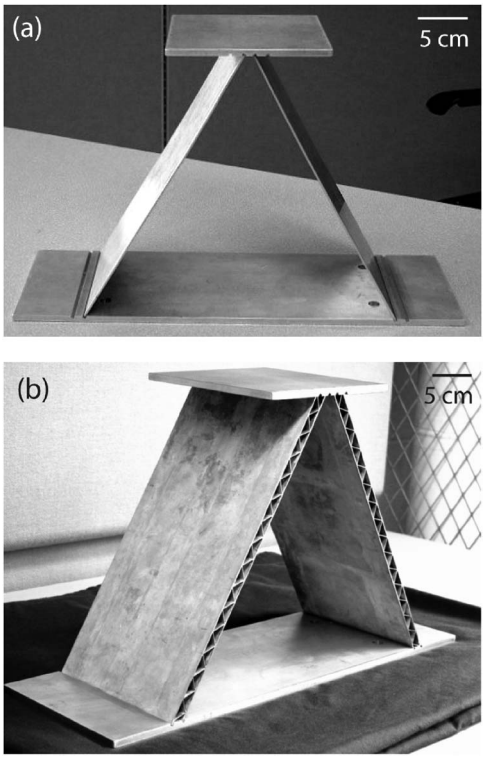

Fig. 4 Photographs of the as-manufactured (*a*) first and (*b*) second order corrugated cores. In this study the manufactured cores are comprised of a single unit cell.

3 Experimental Investigation

3.1 Sample Fabrication. Test specimens were fabricated from 6061-T6 aluminum and designed using the failure mechanism map shown in Fig. 3. The analytical predictions detailed above suggest that the second order corrugated core may outperform the first order core at relative densities where elastic buckling of the monolithic struts is the operative failure mode in the first order core. Thus, we expect the 6061-T6 aluminum second order corrugated core to only outperform the first order core at relative densities $\bar{\rho} < 0.05$ (the yield strain of 6061-T6 aluminum $\varepsilon_Y \approx 0.004$). We thus restricted the current experimental study to this range of densities. Further, the choice of sample dimensions was restricted by (i) the minimum thickness of 6061-T6 sheet that was readily available (0.51 mm in this case) and to a lesser extent (ii) by the maximum sample size that would fit within the available testing equipment. These constraints dictated a second order corrugated core marked by the filled circle in Fig. 3. We describe the manufacture and measurement of the compressive response of a first and second order corrugated core each with a relative density $\bar{\rho} \approx 0.02$.

First and second order corrugated core specimens of width b = 152 mm (into the plane of the paper in Fig. 1) were manufactured. These specimens comprised only a single unit cell as described subsequently. The first order core was manufactured from 2.3-mm-thick 6061-T6 aluminum sheets. These sheets were inclined at an angle ω=60 deg with respect to the horizontal plane and then slotted into mounting plates on the test machine, see Fig. 4(*a*). The second order corrugated core was also manufactured from 6061-T6 aluminum sheets. First 0.51-mm-thick sheets were folded to create a corrugated core with ω_1=45 deg and strut length l_1=12.7 mm. This corrugated core was then sandwiched between two 1.02-mm-thick aluminum sheets which were coated with a 0.13-mm-thick layer of a braze alloy with composition Al-12Si wt%. The assembly was then bonded by dip brazing

Table 1 Measured dimensions and relative densities of compression test samples. Both the specimens have a width b =152 mm.

Specimen type	Corrugation angle		Strut dimensions (mm)				Relative density
	ω	ω_1	t	l	t_1	l_1	$\bar{\rho}$
1st order	60 deg	⋯	2.3	311.2	⋯	⋯	0.017
2nd order	60 deg	45 deg	1.02	310	0.051	12.7	0.018

(Coleman Microwave Co., Edinburg, VA), and heat treated to the *T*6 temper. These sandwich beams of length l=310 mm were then inclined at an angle ω=60 deg with respect to the horizontal and slotted into mounting plates on the test machine to form a single unit cell of the second order corrugated core; a photograph of the as-manufactured second order corrugated unit cell is shown in Fig. 4(*b*). Table 1 gives the dimensions, and measured relative densities of the manufactured first and second order corrugated core specimens.

3.2 Measurements. Tensile specimens of dog-bone geometry were cut from a solid bar of AA6061-T6 and used to determine the tensile mechanical response of the alloy at a nominal applied strain rate of 10^{-3} s^{-1}. The measured true tensile stress versus logarithmic strain response is shown in Fig. 5 and can be adequately approximated as elastic-ideally plastic with Young's modulus E_s=69 GPa and a yield strength $\sigma_Y \approx 250$ MPa.

The first and second order samples were tested in compression at nominal applied strain rate of 10^{-3} s^{-1}. The measured load cell force was used to define the nominal applied stress while the nominal strain was obtained from a laser extensometer. The measured compressive responses of the first and second order sample are plotted in Fig. 6 using axes of nominal stress σ and nominal strain ε. The second order corrugated core achieved an initial peak stress of 1.0 MPa at an applied strain $\varepsilon \approx 0.005$. Face wrinkling of the face sheets of the large struts then set in which resulted in a sharp drop in the stress. Subsequently, the stress increased until a second wrinkle formed at approximately 0.8 MPa. The two wrinkles are clearly visible in the photograph of the deformed second order specimen ($\varepsilon \approx 0.007$) shown in Fig. 7(*a*). This oscillatory behavior continued until complete failure of the specimen at an applied strain $\varepsilon \approx 0.012$. In contrast, the peak strength of the first order core was approximately 0.08 MPa and was controlled by elastic buckling of the struts (Fig. 7(*b*)).

In line with the collapse mechanism map in Fig. 3, the second order core collapses by face wrinkling. This switch in the collapse mode from elastic buckling of the struts in the first order core to face wrinkling in the second order core results in a measured peak strength of the second order core that is about 12.5 times greater than that of a first order core of equal mass. The analytical predictions of the peak strengths of the first and second order corrugated cores are included in Fig. 6. Both the pin-ended (k=1) and built-in (k=2) elastic buckling predictions for the first order core are plotted in Fig. 6. The observed deformation mode (cf. Fig.

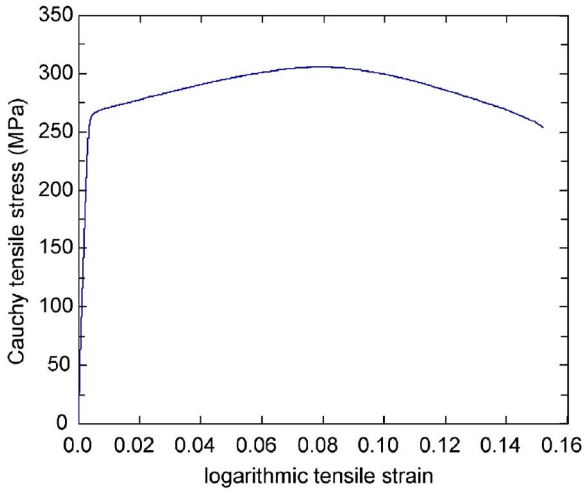

Fig. 5 Uniaxial tensile response of the Al-6061-T6

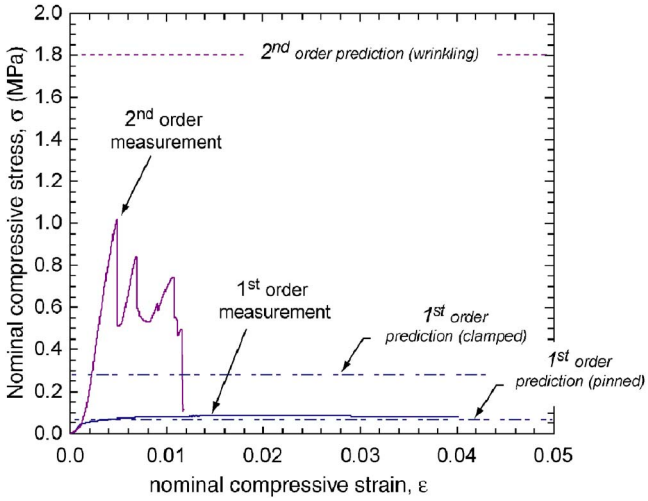

Fig. 6 Measured compressive nominal stress versus nominal strain responses of the $\bar{\rho} \approx 0.02$ first and second order corrugated cores

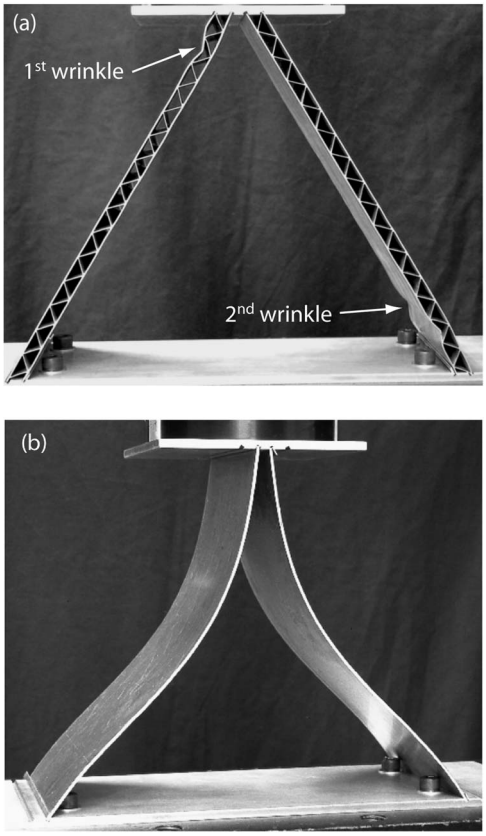

Fig. 7 Photographs showing the failure modes of (*a*) second ($\varepsilon \approx 0.007$) and (*b*) first ($\varepsilon \approx 0.20$) order corrugated cores

7(*b*)) and the measured peak strength of the first order core agree well with the pin-ended elastic buckling predictions. The analytical model overestimates the (elastic wrinkling controlled) strength of the second order core. However, the buckling strength of struts is highly sensitive to imperfections at the transition between the elastic buckling and plastic yielding modes [10]. Figure 3 clearly shows that the design of the second order core lies at the boundary between face-sheet wrinkling and the plastic yielding collapse mode. Thus, the measured strength is anticipated to be sensitive to manufacturing imperfections and be over predicted by the analytical bifurcation calculations.

4 Collapse Mechanism Maps and Optimization of the Second Order Corrugated Core

The geometry of the second order corrugated core can be optimized to maximize the shear and/or compressive collapse strengths at a given relative density. To simplify the optimization problem, we restrict attention to the case of both the smaller and larger corrugations having equal angles, i.e., $\omega=\omega_1$ (it will be seen subsequently that the choice $\omega=\omega_1=45$ deg is optimal from a practical perspective). Thus, the optimization problem under consideration can be stated as follows. Given

(i) the solid material (i.e., fixed value of yield strain, ε_Y),
(ii) the corrugation angle $\omega=\omega_1$, and
(iii) the effective relative density $\bar{\rho}$,

what are values of the non-dimensional strut aspect ratios t/l, t_1/l_1, and l_1/l that maximize the compressive or shear collapse strengths of the second order corrugated core? Unless otherwise specified, all results presented subsequently are for the choice of corrugation angles $\omega=\omega_1=45$ deg and a solid material yield strain $\varepsilon_Y=0.002$; this yield strain is representative of many structural metallic alloys.

For a prescribed length scale separation l_1/l, the optimal design is obtained by selecting a geometry $(t/l, t_1/l_1)$ that maximizes the strength for a given value of $\bar{\rho}$. To help with this optimization, collapse mechanism maps for the compressive failure of the second order corrugated core are shown in Figs. 8(*a*) and 8(*b*), for the choices $l_1/l=0.01$ and 0.03, respectively. Euler buckling of the smaller and larger struts are the dominant failure modes for the $l_1/l=0.01$ corrugated core while Euler buckling of the smaller struts and face wrinkling and plastic yielding of the larger struts dominate the collapse mechanism map of the $l_1/l=0.03$ corrugated core. To help select the optimum geometries, contours of the normalized strength $\bar{\sigma}\equiv\sigma_p/\sigma_Y$ and relative density $\bar{\rho}$ have been added to the maps. We note that the optimal designs that maximize σ_p/σ_Y for any given value of $\bar{\rho}$ lie along the boundaries of the collapse regimes. The arrows sketched in Fig. 8 designate the path of optimum designs with increasing $\bar{\rho}$.

The optimized compressive strengths of the second order corrugated cores are plotted in Fig. 9(*a*) as a function of $\bar{\rho}$, for the choices $l_1/l=0.01$, 0.03 and 0.05. The results reveal that while the choice $l_1/l=0.01$ maximizes the strength at low relative densities ($\bar{\rho}<0.004$) the choice $l_1/l=0.03$ is preferable at the higher values of $\bar{\rho}$. This suggests that the performance of the second order core may be improved by including l_1/l as an optimization variable. We shall refer to the optimal designs with l_1/l included in the optimizations as *fully optimized* while optimal designs obtained by fixing the value of l_1/l as *suboptimal*.

The fully optimized compressive strength of the second order core is plotted in Fig. 9(*a*) along with the strength versus relative density relation of the first order corrugated core [Eqns. (4) and (6)]. For the choice $\varepsilon_Y=0.002$, the first order corrugated core collapses by elastic buckling of the struts for $\bar{\rho}<0.05$ and by plastic yielding of the struts at higher values of $\bar{\rho}$. Thus, the strength of the first order core scales linearly with relative density for $\bar{\rho}>0.05$ and is proportional to $\bar{\rho}^3$ at lower relative densities. Appropriate designs of the second order corrugated cores increase the strength of the struts at low values of $\bar{\rho}$: the strength of the fully optimized second order core scales linearly with relative density for all $\bar{\rho}>0.005$. Thus, the fully optimized second order core substantially outperforms the first order core for $0.001<\bar{\rho}<0.05$. In fact, even the suboptimal second order designs outperform the first order core. For example, the suboptimal second order cores with $l_1/l=0.03$ and 0.05 have a performance approximately equal to the fully optimized design for $\bar{\rho}>0.008$ and $\bar{\rho}>0.015$, respectively, and outperform the first order core over the whole range of relative densities investigated here. However, it is worth noting that an inappropriately designed second order core can have a lower strength to weight ratio than the first order core; e.g., the strength of the $l_1/l=0.01$ suboptimal second order core is below that of the first order core for $\bar{\rho}>0.03$. In this range the suboptimal designs of the $l_1/l=0.01$ second order core collapse by a combination of elastic buckling of the larger and smaller struts or elastic buckling and shear buckling of the larger struts. On the

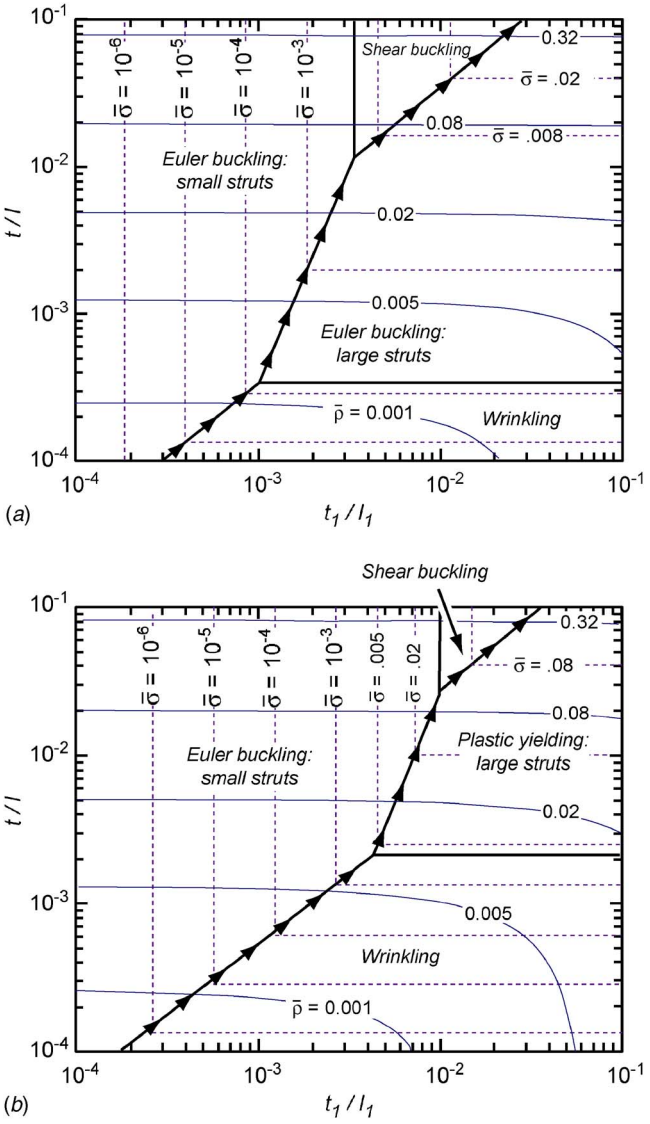

Fig. 8 Collapse mechanism maps for the compressive failure of the $\omega=\omega_1=45$ deg second order core with (*a*) $l_1/l=0.01$ and (*b*) $l_1/l=0.03$. The arrows trace the path of the optimum designs that maximize the compressive strength σ_p for a given relative density $\bar{\rho}$. The yield strain of the solid material is taken to be $\varepsilon_Y=0.002$.

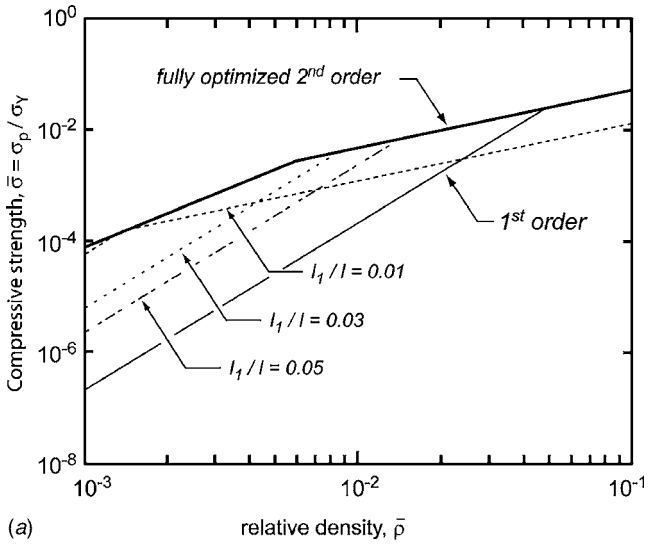

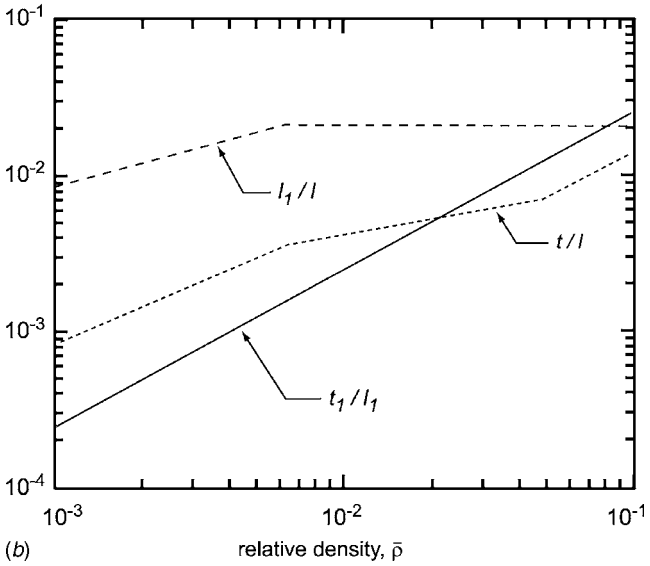

Fig. 9 (*a*) **Comparison between the normalized compressive strengths of the optimized $\omega=\omega_1=45$ deg second order corrugated cores and the $\omega=45$ deg first order core. The yield strain of the solid material is taken to be $\varepsilon_Y=0.002$.** (*b*) **The corresponding geometries of the fully optimized second order core.**

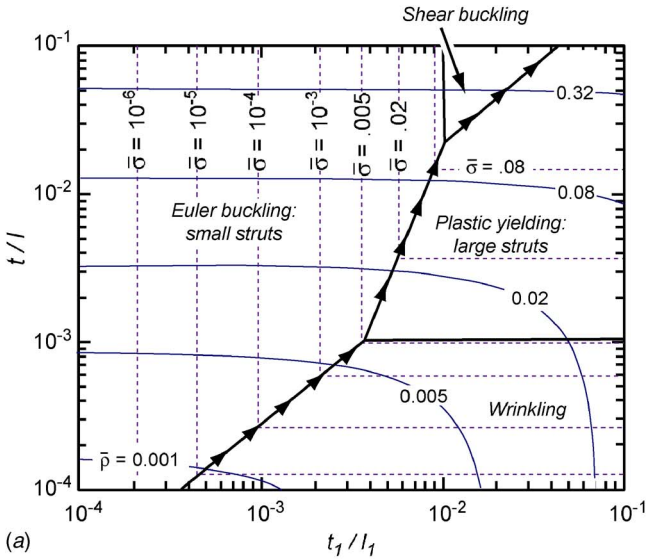

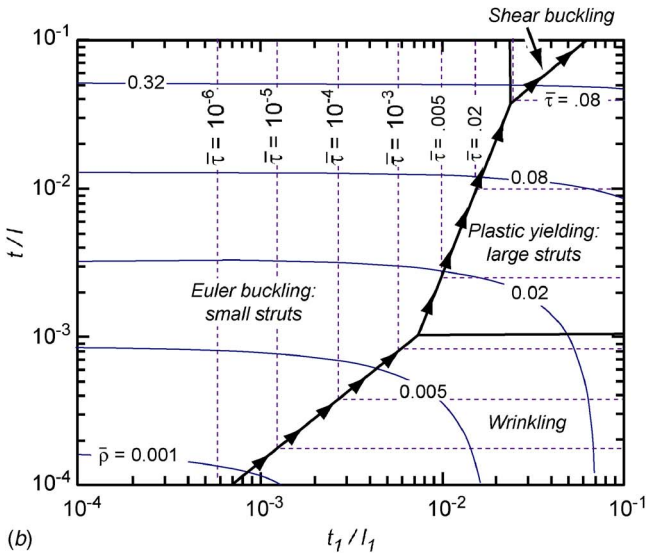

Fig. 10 (*a*) **Compressive and** (*b*) **shear failure mechanism maps for the $\omega=\omega_1=70$ deg second order corrugated core with $l_1/l=0.03$. The arrows trace the path of the optimum designs that maximize the strengths for a given relative density. The yield strain of the solid material is taken to be $\varepsilon_Y=0.002$.**

other hand, for $\bar{\rho}>0.05$, the first order core collapses by plastic yielding of the struts and thus outperforms this suboptimal design of the second order core. The geometrical parameters t/l, t_1/l_1, and l_1/l associated with the fully optimized design are plotted in Fig. 9(*b*) and clearly show that the optimal geometry is not self-similar, i.e., the relative density at each level of hierarchy is not equal as $t/l \neq t_1/l_1$.

It is worth emphasizing that the second order corrugated core can only outperform the first order corrugated core at low relative densities when elastic buckling is the collapse mechanism for the first order core. In fact, at relative densities where plastic yielding is the collapse mechanism of the first order core, the second order core will be structurally less efficient than the first order core as the smaller scale core contributes little to the strength but does increase the overall mass. In the optimal designs discussed above, the mass of the smaller scale core is very small at the higher relative densities and thus the second and first order cores have a comparable performance at the higher densities. We do not expect second order corrugated cores to find application at these high relative densities.

The corrugation angle significantly effects the competition between collapse mechanisms. Compressive and shear collapse mechanism maps for second order corrugated cores with $\omega=\omega_1=70$ deg and $l_1/l=0.03$ are plotted in Figs. 10(*a*) and 10(*b*), respectively. The compressive and shear collapse mechanism maps are quite similar with the main difference being that the elastic buckling of the smaller struts occupies a larger fraction of the shear collapse mechanism map. Contours of the normalized compressive and shear strengths are included in Figs. 10(*a*) and 10(*b*), respectively along with contours of the relative density. The arrows in these figures again trace the path of the suboptimal second order corrugated core designs that maximize the compressive and shear strengths with $l_1/l=0.03$ and $\omega=\omega_1=70$ deg.

The effect of the corrugation angle on the fully optimized compressive and shear strengths of the second order corrugated cores is illustrated in Figs. 11(*a*) and 11(*b*), respectively. Results are

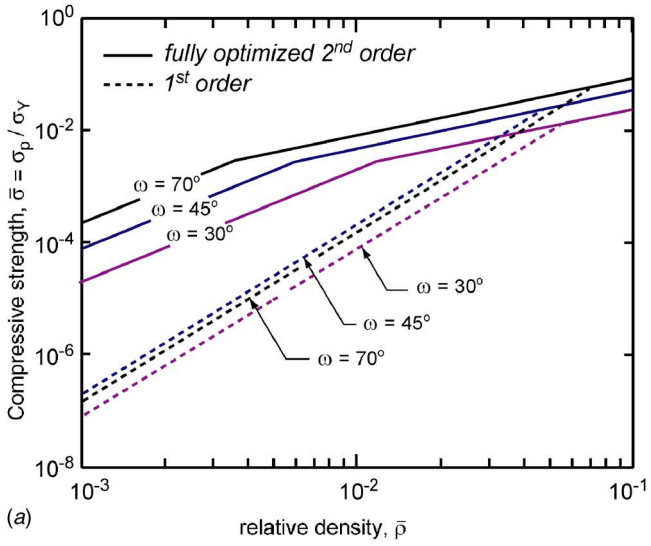

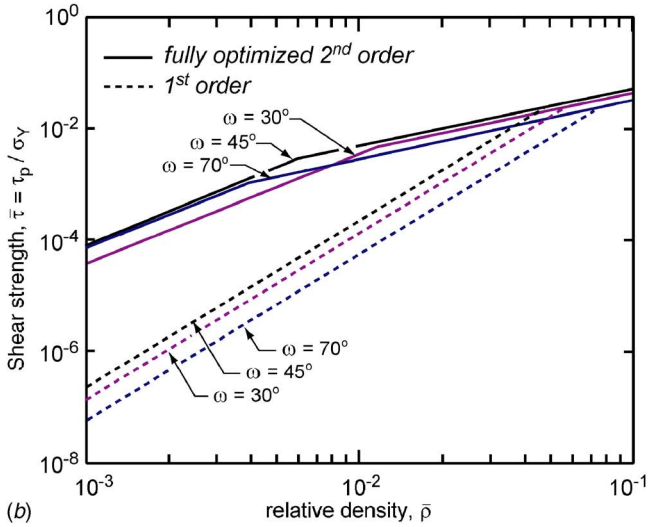

Fig. 11 Comparison between the (*a*) compressive and (*b*) shear strengths of the fully optimized second order and first order corrugated cores. Results are shown for three selected values of the corrugation angle $\omega=\omega_1$ and the yield strain of the solid material is taken to be $\varepsilon_Y=0.002$.

presented for $\omega=\omega_1=30$, 45, and 70 deg. The compressive strength increases with increasing corrugation angle, while the shear strength is a maximum for $\omega=\omega_1=45$ deg. It is worth noting that the analytical formulas for the compressive and shear-strengths are identical in all six competing collapse modes for the case $\omega=\omega_1=45$ deg. Thus, the values of the geometrical parameters plotted in Fig. 9(*b*) optimize both the compressive and shear strengths of the second order corrugated core. On the other hand, the geometrical parameters that maximize both the compressive and shear strengths of the $\omega=\omega_1=30$ and 70 deg are not identical. This is illustrated in Fig. 12 where the minimum weight designs of the $\omega=\omega_1=70$ deg second order corrugated core for both compressive (red lines) and shear (black lines) loading are plotted. While the values of l_1/l and t/l are approximately equal in the optimized compression and shear designs, t_1/l_1 is higher in the optimized shear design compared to the corresponding value in the optimized compression design. If in practice the through thickness compression and the transverse shear strengths are equally important parameters, the choice $\omega=\omega_1=45$ deg is desirable as the same design maximizes both the shear and compressive strengths.

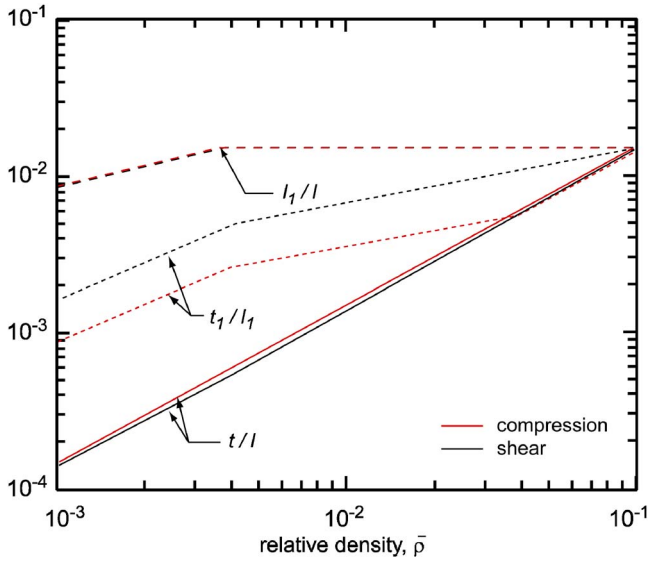

Fig. 12 The geometries of the fully optimized $\omega=\omega_1=70$ deg second order corrugated core. The geometries that maximize the compressive (red lines) and shear (black lines) strengths are included.

5 Comparison With Competing Core Topologies

It is instructive to compare the peak compressive strength σ_p of the fully optimized second order core with competing sandwich cores. In particular, we compare the performance of the second order corrugated core with (i) a square-honeycomb core, Côté et al. [11], (ii) prismatic-diamond core, Côté et al. [12], (iii) a three-dimensional pyramidal core, Wadley et al. [13] and (iv) the first order corrugated core. In all cases we assume that the sandwich cores are made from an elastic-ideally plastic solid with yield strength σ_Y and yield strain ε_Y. All these cores collapse by elastic buckling of the cell walls at low relative densities and plastic yielding at higher values of the $\bar{\rho}$. Thus, piecewise expressions for the strengths of these cores are specified below with the transition between the elastic buckling and plastic yielding modes set by both the geometry of the core and the yield strain of the solid material from which the core is made.

The normalized peak strength $\bar{\sigma}\equiv\sigma_p/\sigma_Y$ of the square-honeycomb core is given by [11]

$$\bar{\sigma}=\begin{cases}\dfrac{\pi^2}{12(1-\nu^2)\varepsilon_Y}\bar{\rho}^3 & \text{if } \bar{\rho}<\sqrt{\dfrac{12(1-\nu^2)\varepsilon_Y}{\pi^2}}\\ \bar{\rho} & \text{otherwise}\end{cases} \tag{28}$$

while the strength of the prismatic-diamond core with square cells is specified as [12]

$$\bar{\sigma}=\begin{cases}\dfrac{\pi^2}{96\varepsilon_Y}\bar{\rho}^3 & \text{if } \bar{\rho}<\sqrt{\dfrac{48\varepsilon_Y}{\pi^2}}\\ \dfrac{\bar{\rho}}{2} & \text{otherwise}\end{cases} \tag{29}$$

The three-dimensional pyramidal core with struts inclined at 45 deg to the horizontal plane is more resistant to elastic buckling compared to its two-dimensional or prismatic counterparts (for a given relative density, the struts of the 3D pyramidal core are more stocky than those in a prismatic core). An equilibrium analysis dictates that the strength of this pyramidal core is

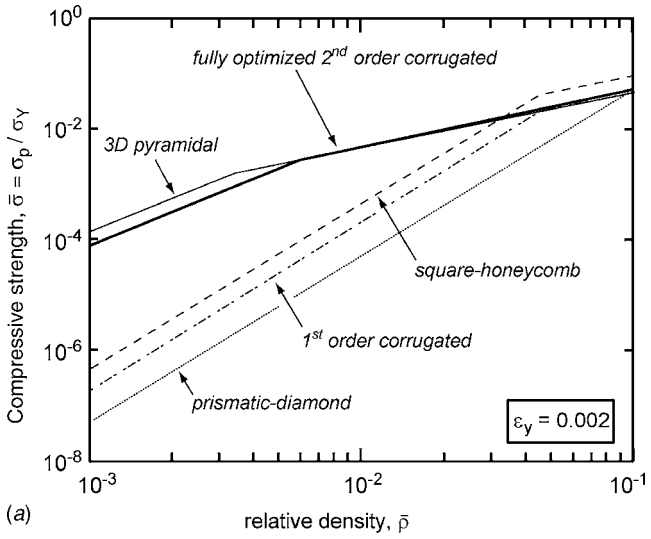

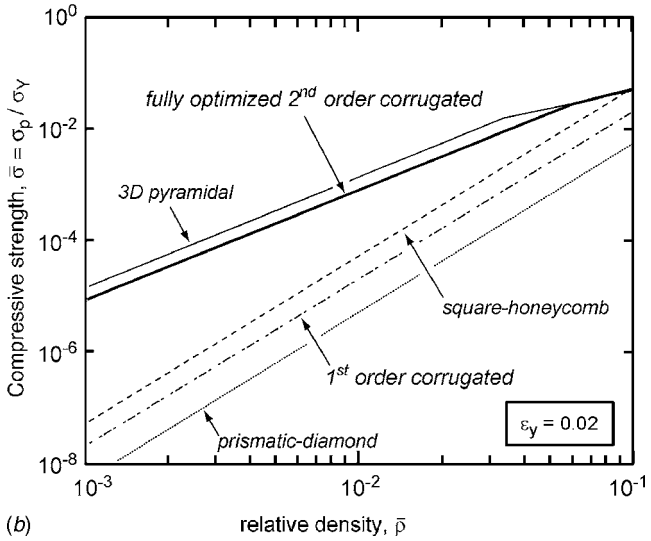

Fig. 13 Comparison between the compressive strengths of competing sandwich core topologies for the solid material yield strains (*a*) $\varepsilon_Y=0.002$ and (*b*) $\varepsilon_Y=0.02$

$$\bar{\sigma}=\begin{cases}\dfrac{\pi^2}{24\sqrt{2}\varepsilon_Y}\bar{\rho}^2 & \text{if } \bar{\rho}<\dfrac{12\sqrt{2}\varepsilon_Y}{\pi^2}\\ \dfrac{\bar{\rho}}{2} & \text{otherwise}\end{cases} \tag{30}$$

A comparison between the normalized peak compressive strengths of the competing cores is shown in Figs. 13(*a*) and 13(*b*) for the choices of solid material yield strains $\varepsilon_Y=0.002$ and 0.02, respectively. The strengths of the fully optimized $\omega=\omega_1=45$ deg second order corrugated core and the $\omega=45$ deg first order corrugated core have also been included in Fig. 13. With the choice $\varepsilon_Y=0.002$, the fully optimized second order core outperforms all other two-dimensional cores (i.e., square-honeycomb, prismatic-diamond and the first order corrugated core) for relative densities $\bar{\rho}<0.03$. However, the high elastic buckling strength of the three-dimensional pyramidal core ensures collapse by plastic yielding for $\bar{\rho}>0.003$. Thus, the second order corrugated core has no performance gain over the pyramidal core and in fact has a slightly lower collapse strength than the pyramidal core for $\bar{\rho}<0.005$. In order to make a prismatic core such as the corrugated core outperform the pyramidal core, at least three levels of structural hierarchy would be needed. It is also worth mentioning that with the choice $\varepsilon_Y=0.002$, the three-dimensional pyramidal core collapses by elastic buckling only for $\bar{\rho}<0.003$. Thus, three-dimensional hierarchical construction will only provide benefits for very low relative densities ($\bar{\rho}<0.003$). Structural hierarchy is more effective in two-dimensional or prismatic cores where such construction provides performance enhancements for relative densities $\bar{\rho}<0.05$.

The effect of increasing the yield strain to $\varepsilon_Y=0.02$ on the performance of the competing sandwich cores is illustrated in Fig. 13(*b*). Elastic buckling becomes the operative collapse mode at higher relative densities and thus hierarchical construction gives performance enhancements at even higher values of relative density. For example, with $\varepsilon_Y=0.02$, the fully optimized second order corrugated core outperforms all the competing two-dimensional cores for all $\bar{\rho}<0.10$.

The high out-of-plane strength of 3D cores such as the pyramidal truss means that 3D cores have definite advantages over their prismatic counterparts. However, unlike the pyramidal truss, prismatic topologies like a corrugated core have a high in-plane stretching resistance that is critical in applications such as clamped sandwich beams. The use of structural hierarchy to improve the out-of-plane compressive strength of such prismatic cores thus offers the attractive possibility of designing a low relative density core with high out-of-plane as well as in-plane strengths.

6 Concluding Remarks

Analytical models for the transverse stiffness and strength of second order corrugated cores have been presented. The collapse of the second order corrugated core occurs by six competing collapse modes. Analytical expressions for the collapse strengths in each of these modes have been employed to determine the optimal design of second order corrugated cores that maximize the compressive and shear strengths for a prescribed effective relative density of the core. Second order corrugated cores made from structural alloys have significantly higher collapse strengths compared to their equivalent mass first order counterparts for relative densities $\bar{\rho}<0.05$. The fully optimized second order core has a strength that scales linearly with relative density for $\bar{\rho}>0.005$ and thus it has a collapse strength about two orders of magnitude greater than its first order counterpart at $\bar{\rho}=0.005$. Increasing the order of the hierarchy to greater than two can increase the collapse strength only at relative densities $\bar{\rho}<0.005$. In contrast, increasing the level of structural hierarchy yields no enhancements in the stiffness of the corrugated core. In fact, the stiffness to weight ratio of the first order core is slightly greater than its second order counterpart suggesting that the hierarchical corrugated construction has applications in strength limited applications.

Representative first and second order corrugated core structures have been fabricated from a high strength 6061-T6 aluminum alloy using a simple sheet folding and dip brazing process. The non-optimal second order panel with a relative density of 1.7% is found to have a measured compressive strength about 12.5 times higher than that of a first order structure with a similar relative density. These results are consistent with analytical predictions and suggest that hierarchical corrugated cores have a high potential in strength limited sandwich panel applications.

Acknowledgment

We are grateful to the Office of Naval Research for support of the work reported here under Grant No. N00014-01-1-1051 (program manager, Steve Fishman). The authors would also like to thank one of the reviewers for insightful comments that have helped to improve the paper.

References

[1] Hashin, Z., and Shtrikman, S., 1963, "A Variational Approach to the Theory of the Elastic Behavior of Multi-Phase Materials," J. Mech. Phys. Solids, **11**, p. 127.

[2] Norris, A. N., 1985, "A Differential Scheme for the Effective Moduli of Composites," Mech. Mater., **4**, p. 1.

[3] Milton, G. W., 1986, "Modeling the Properties of Composites by Laminates," in *Homogenization and Effective Moduli of Materials and Media*, J. L. Ericksen, D. Kinderlehrer, R. Kohn, and J.-L. Lions, eds., Springer, New York, p. 150.

[4] Francfort, G., and Murat, F., 1986, "Homogenization and Optimal Bounds in Linear Elasticity," Arch. Ration. Mech. Anal., **94**, p. 307.

[5] Bhat, T., Wang, T. G., and Gibson, L. J., 1989, "Micro-Sandwich Honeycomb," SAMPE J., **25**(3), p. 43.

[6] Lakes, R., 1993, "Materials With Structural Hierarchy," Nature (London), **361**(11), p. 511.

[7] Murphey, T., and Hinkle, J., 2003, "Some Performance Trends in Hierarchical Truss Structures," *44th AIAA/ASME/ASCE/AHS/ASC Conference*, Norfolk, VA, Apr. 7–10, 1903.

[8] Deshpande, V. S., and Fleck, N. A., 2001, "Collapse of Truss-Core Sandwich Beams in 3-Point Bending," Int. J. Solids Struct., **38**, p. 6275.

[9] Zenkert, D., 1995, *An Introduction to Sandwich Construction*, Engineering Materials Advisory Service, Sheffield, UK, pp. 30–60.

[10] Hutchinson, J. W., 1974, "Plastic Buckling," in *Advances in Applied Mechanics*, C.-S. Yih, ed., Academic, New York, vol. 14, p. 67.

[11] Côté, F., Deshpande, V. S., Fleck, N. A., and Evans, A. G., 2004, "The Out-of-Plane Compressive Behavior of Metallic Honeycombs, Mater. Sci. Eng., A, **380**, p. 272.

[12] Côté, F., Deshpande, V. S., Fleck, N. A., and Evans, A. G., 2006, "The Compressive and Shear Responses of Corrugated and Diamond Lattice Materials," Int. J. Solids Struct., **43**, pp. 6220–6242.

[13] Wadley, H. N. G., Fleck, N. A., and Evans, A. G., 2003, "Fabrication and Structural Performance of Periodic Cellular Metal Sandwich Structures," Compos. Sci. Technol., **63**, p. 2331.

Utilization of Synchronous Averaging for Inspection of Tooth Surface Undulations on Gears (Localization of Nonmesh Harmonic Components to Individual Gear)

Haruo Houjoh
Professor
Precision and Intelligence Laboratory,
Tokyo Institute of Technology,
4259 Nagatsuta,
Midori-ku, Yokohama,
Japan
e-mail: hhoujoh@pi.titech.ac.jp

Chanat Ratanasumawong
Graduate Student
Department of Precision Machinery Systems,
Tokyo Institute of Technology,
Tokyo, Japan
e-mail: chanat@ds.pi.titech.ac.jp

Shigeki Matsumura
Associate Professor
Precision and Intelligence Laboratory,
Tokyo Institute of Technology,
Tokyo, Japan
e-mail: smatsumu@pi.titech.ac.jp

Cyclic undulation of the gear tooth surface is one of the important sources of gear noise and vibration. It has been known that vibration caused by this source can appear at the nonmesh harmonic frequency components (ghost components). As there are no relationships between the frequency of this vibration and any gear specifications, the gear noise source is hard to detect. This paper proposes the utilization of the synchronous averaging technique for diagnosis of the source of nonmesh harmonic vibration components on a gear pair, and shows the possibility of using this technique for inspection of tooth surface undulation. The method for practically applying this technique is discussed in detail. Results demonstrated in the form of spectrum showed good agreement with the undulation assessed from precise tooth surface measurement over the whole surface of every tooth. The effect of the direction of the arrangement of cyclic undulation on tooth surface and gear vibration is also discussed in this paper. Finally the limitation to the synchronous averaging technique was discussed with respect to gear ratio.
[DOI: 10.1115/1.2198248]

1 Introduction

To ensure vibration quality and quiet operation, gears are manufactured so that their geometry is as close as possible to their design. In practice, however, there are always irregularities during the manufacturing process that lead to various kinds of gear errors and resultant vibration and noise problems.

Usually gear vibration is mainly observed at the fundamental tooth meshing frequency and its harmonics. However, it is known that when gear errors exist, many other frequency components are also observed at the same time. Common errors of every gear tooth lead to vibration at meshing frequencies as well as the variation of tooth stiffness during meshing. Pitch error and the other fluctuations from common tooth shape bring about vibrations at low frequency bands and sidebands surrounding meshing components. Vibration attributed to gear local defects such as crack or nick is observed as the occurrence of an impulsive wave in time domain or a lot of comb spectra in wide frequency range.

In addition to gear error described above there are also some kinds of gear error that cause peculiar vibrations at the noninteger orders of meshing frequency. This kind of gear error and its corresponding vibration is focused in this paper. As this vibration component does not relate to any specified geometries of the gear pair, the vibration source cannot be detected by ordinary tooth profile measurement equipment, and for this reason, this peculiar vibration component is usually called ghost noise.

Contributed by the Applied Mechanics Division of ASME for publication in the JOURNAL OF APPLIED MECHANICS. Manuscript received November 12, 2004; final manuscript received February 8, 2006. Review conducted by M. P. Mignolet. Discussion on the paper should be addressed to the Editor, Prof. Robert M. McMeeking, Journal of Applied Mechanics, Department of Mechanical and Environmental Engineering, University of California – Santa Barbara, Santa Barbara, CA 93106-5070, and will be accepted until four months after final publication of the paper itself in the ASME JOURNAL OF APPLIED MECHANICS.

It is known that ghost noise is created by a periodic waviness, or cyclic undulation, on the surface of a gear tooth continuing from one tooth to the next. The source of this waviness can be traced to the irregularity in the process of generation such as the periodic error in the master worm or work spindle [1]. Mark [2] showed how periodic undulations on tooth running surfaces can generate ghost noise. Matson and Houser [3] showed experimentally that cyclic waviness on the gear surface acted as an exciter to generate ghost noise.

Matsumura et al. [4,5] introduced the use of maximum entropy method (MEM) and discrete Fourier transform (DFT) along with tooth surface measurement to verify the occurrence of periodic waviness that is the cause of ghost noise. Although MEM and DFT are very useful for detection of cyclic undulation on tooth surface, these methods require two-dimensional and multiteeth measurement, requiring significant time and cost. With this in mind, another method for inspection of the cyclic undulation is required. From Matsumura's study, it has also been known that the frequency of ghost noise generated by the cyclic undulation is synchronous to the frequency of shaft rotation but asynchronous to the meshing frequency. It should therefore be possible to apply the method of synchronous averaging of the gear vibration to diagnose the ghost noise source.

The synchronous averaging method is a time domain averaging technique. In the past, this technique has been used to reduce noise and improve the quality of the measured gear vibration signal, as shown by Smith and Wowk [6–8]. The synchronous averaging method can eliminate vibration signal components having frequency asynchronous with the signal of interest. It has been successfully applied in the area of diagnosis of failure and early defect detection in gears and bearings [9–16].

Although the synchronous averaging method has been used for diagnosis of defect in gears for a long time, there has only been recent interest for the utilization of this method for tooth surface

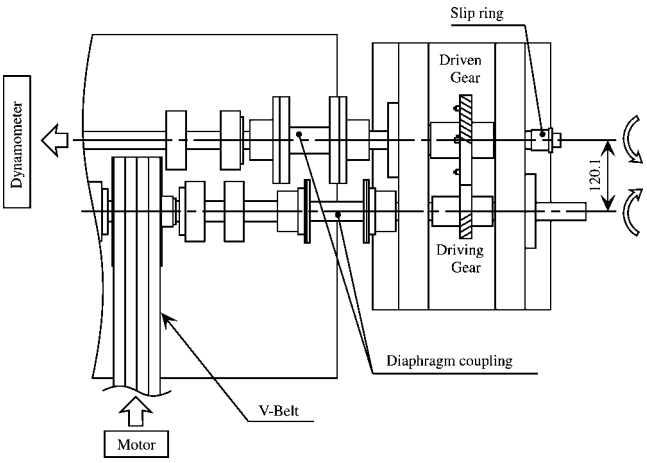

Fig. 1 Test stand

inspection. In this paper, the utilization of synchronous averaging methods for diagnosing the source of ghost noise and inspection of cyclic undulation of gear tooth surface is introduced. The method for applying this method is discussed in detail. The effectiveness of this proposed method is verified by precise tooth surface measurement.

2 Test Stand and Experimental Gear

To clarify ghost noise behavior of a gear pair, the experiments were performed with a test stand shown in Fig. 1.

A test gear pair was driven by a variable speed ac motor via V belts. A dynamometer connected to a driven shaft was used to apply the torque. Two diaphragm couplings mounted between gear shafts, the motor, and the dynamometer were used to isolate vibration attributed to the other parts of the test stand from the gearbox.

The vibration of a gear pair was measured by a pair of accelerometers attached tangentially at the driven gear to extract only torsional vibration. Then the vibration signal was sent via a slip ring to a vibration analyzer. One pulse per revolution signal was obtained from each of the driving and driven shafts by a magnetic pickup placed near the shaft surface. Each signal was used as a trigger for the synchronous averaging.

The driving gear used in this experiment had 30 teeth, while the driven gear had 53 teeth, to give a prime gear ratio. The tooth width was 20 mm, with a module of 2.5. Other parameters of the test gears are shown in Table 1.

All experiments were done by using one driven gear, finished by the indexed generation method, and which is called as the "master gear." On the other hand, the driving gear was changed to use five gears with different finishing methods to give various tooth surface conditions and various characteristics of ghost noise. All gears were finished to have reasonable production accuracy using typical production intended manufacturing tool and machines. The finishing methods of the test gears are shown in Table 2.

Table 1 Gear parameters

		Driving	Driven
Module		2.5	
Number of teeth		30	53
Pressure angle	[deg.]	20	
Helix angle	[deg.]	30 LH	30 RH
Face width	[mm]	20	
Center distance	[mm]	120.1	
Total contact ratio		2.65	

Table 2 Gear finishing method

Driven gear	Master	Finishing method Indexed generation
Driving gear	GTM2, 4	Indexed generation
	GTR2, 4	Continuous generation
	GTO1, 2	Form grinding
	SV1, 4	Shaving
	THO1, 2	Honing

Tooth profile form inspections of experimental gears are drawn in Fig. 2. The abscissa is the roll angle that was normalized with normal pitch. The ordinate is the tooth surface deviation. From these profiles, it is obvious, except for the gear SV1, that all profiles are almost the same. Moreover, it is impossible to depict the difference of cyclic surface undulation by viewing these tooth profile forms.

3 Results of Dynamic Load Test

Vibration characteristics of a gear pair covering a wide range of loads or speeds can be determined by a dynamic load test. Results are shown in Fig. 3 in the form of waterfall plots of instantaneous spectrum. These waterfall plots were obtained when the gear pair was operated under driven shaft speed ranging from 550 to

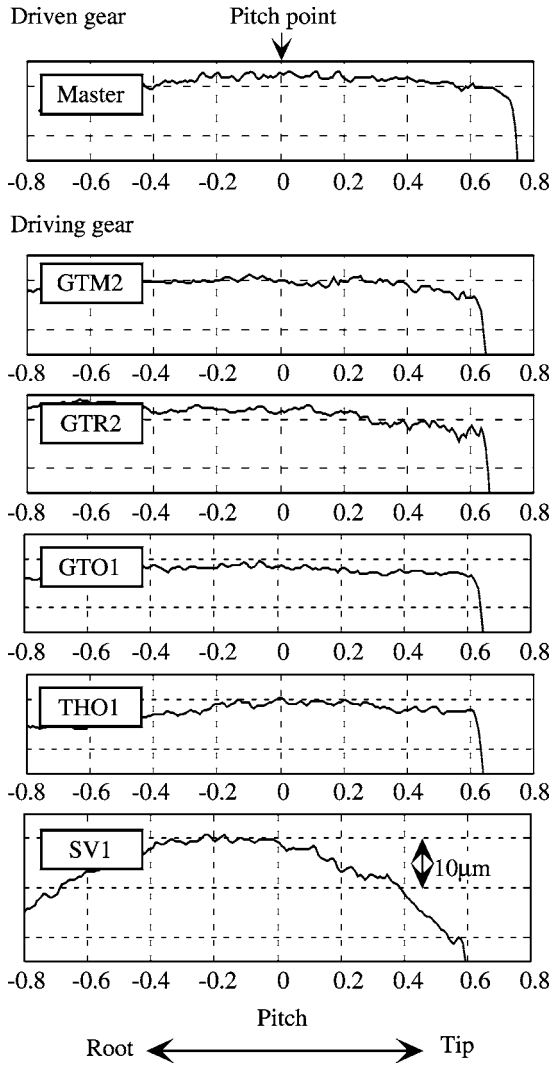

Fig. 2 Tooth profile forms

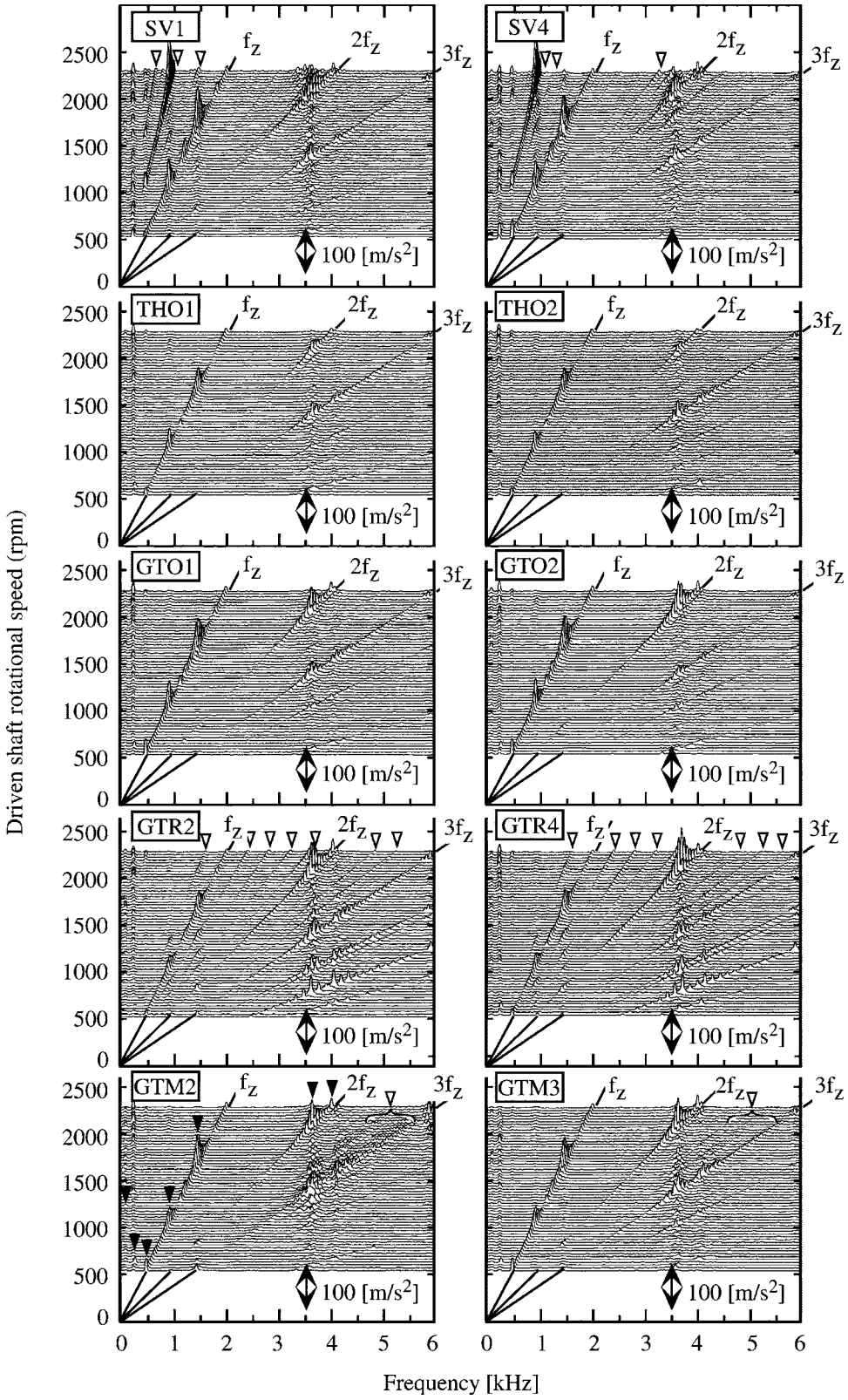

Fig. 3 Waterfall spectra of a gear pair

2300 rpm, with applied torque equal to 245 Nm (25 kgf) at the driven shaft. Spectra of the rotational acceleration at various speeds are arranged along the ordinate. The height of the spectrum is the amplitude of the tangential vibration (acceleration) at the base circle. The abscissa is the frequency of the vibration in the range 0–6 kHz.

Tooth meshing frequency component (f_z) and its harmonics ($2f_z$ and $3f_z$) (which conform to 30th, 60th, and 90th order of driving shaft rotation) are shown as the oblique solid lines. Frequencies that correspond with the peaks of the spectra are natural frequencies of this gear system and are marked by the black triangle marks (in the case of gear GTM2). In this experiment, natu-

ral frequencies are found to occur at about 90, 240, 490, 900, 1480, 3640, and 4100 Hz. These natural frequencies may shift a little from these values as the gear pair operates with the different loads. In this experiment, modes of those frequencies were not decided since only rotational vibration was measured. However, the natural frequencies at about 3640 and at 4100 Hz are strongly related to meshing stiffness. Prominent noninteger orders of meshing frequencies, or ghost noises, are observed in almost every chart with prominent ones marked by the blank triangle marks.

From the waterfall plots, it is clear that gears finished by the same method have similar patterns of ghost noise. On the other hand, gears finished by the different methods were found to have different patterns of ghost noise. For instance, gears GTM2 and GTM3 have small peaks of ghost noise between the second and third harmonic of meshing frequency. Gears GTR2 and GTR4 have a series of ghost noises every six orders of driving shaft rotation between the fundamental mesh frequency and its third harmonic.

Gears SV1 and SV4 have very high amplitude of ghost noise at the 15th order of driving shaft rotation, or half of the fundamental meshing frequency. This was known to be due to the incompleteness of the hob, which had two start screws. However, in the case of gears GTO and THO, ghost noise does not appear in the spectrum; only meshing components can be inspected in the waterfall plots.

It should be noted that these characteristics have come from individual machines used for this investigation and not from the fabrication principle itself.

Although dynamic load tests can be used to verify the occurrences of ghost noises and can also give the information about the natural frequencies of the gear system, it is impossible to detect which gear is faulty, because the gear vibration is affected from both the driving and driven gear.

4 Synchronous Averaging

4.1 Principle of Synchronous Averaging. The effect of vibration caused by the driving and driven gear can be distinguished from each other by using the synchronous averaging method. Synchronous averaging is a well-known time domain averaging technique. The schematic diagram that shows how to utilize synchronous averaging in this study is shown in Fig. 4.

First, a vibration signal and a trigger signal, one pulse per revolution of either driving or driven gear, were measured and recorded by a data recorder as shown in Fig. 4(*a*). Because the gear vibration is the combinative vibration caused by both driving and driven gear, accelerometers used to measure the gear vibration can be placed at one of either driving or driven gears. In this experiment, accelerometers were placed at the driven gear. After all signals were recorded, they were post-processed such that blocks of vibration signal beginning with the trigger where averaged. The process was done by using trigger signals from the driving and/or driven shaft as shown in Fig. 4(*b*).

By this method, the signals repeating with the shaft revolution will remain, and the signals not associated with each shaft revolution, including random noise, will be eliminated.

When using the trigger signal from the driving shaft, the vibration signal related to the driving gear, synchronized with the rotation of driving gear, will remain and others will be eliminated. On the other hand, when using the trigger signal from the driven shaft for the same vibration signal, only the signal related to driven gear will be extracted from the others.

The signal that synchronizes with both driving and driven shaft rotation such as meshing components still remains after averaging with either driving shaft trigger or driven shaft trigger. The samples of time-averaged wave form are shown in Fig. 4(*c*). With the frequency analysis (Fourier transform) synchronous averaging spectra as shown in Fig. 4(*d*) are obtained.

4.2 Effect of the Number of Averages. The number of averages is one of the important parameters that affect the accuracy of the averaged signal. Enough averaging is required for complete extraction of the vibration signal attributed to the gear of interest apart from the other gears. Although the larger number of averages normally brings higher accuracy, the measurement and calculation time is also increased. The selection of the optimum number of averages will bring accurate results together with short calculation time.

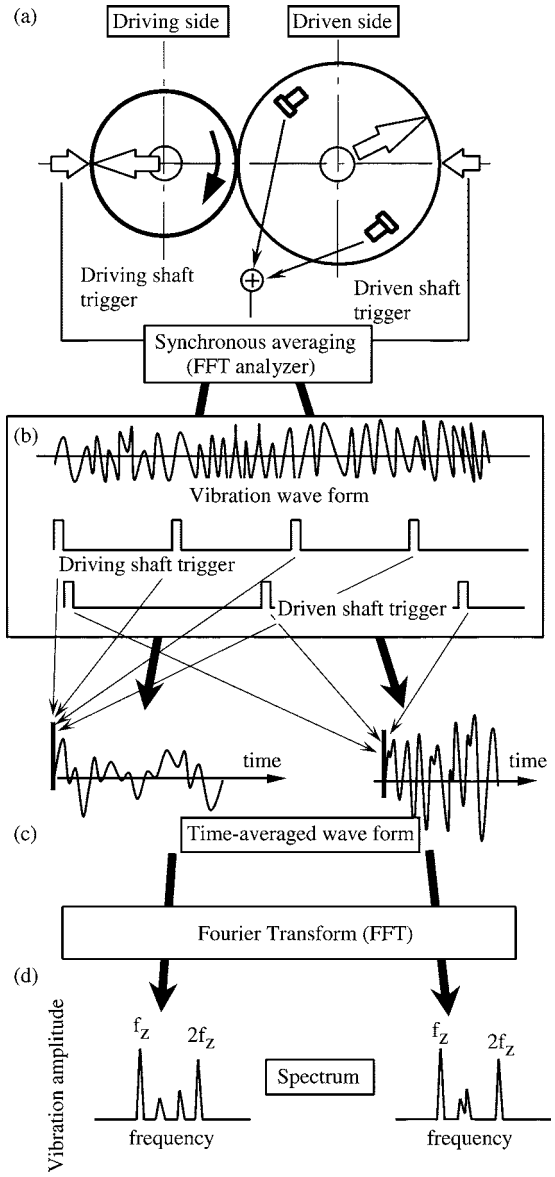

Fig. 4 Principle of synchronous averaging technique

The effect of the number of averages can be categorized according to the type of signal to be eliminated: One is a signal asynchronous with any shaft revolution (random noise), while another is a signal synchronous with a shaft revolution other than the shaft of interest.

4.2.1 Signal Asynchronous With Any Shaft Revolution or Random Noise. It is well known that the reduction of the root mean square amplitude of the random noise relates to the number of averages N [17] as shown in Eq. (1) and Fig. 5.

$$\langle n(t)\rangle_{\text{rms}} = \frac{1}{\sqrt{N}} n(t)_{\text{rms}} \tag{1}$$

where $\langle n(t)\rangle_{\text{rms}}$ is rms amplitude of the averaged random noise; $n(t)_{\text{rms}}$ is rms amplitude of random noise without averaging.

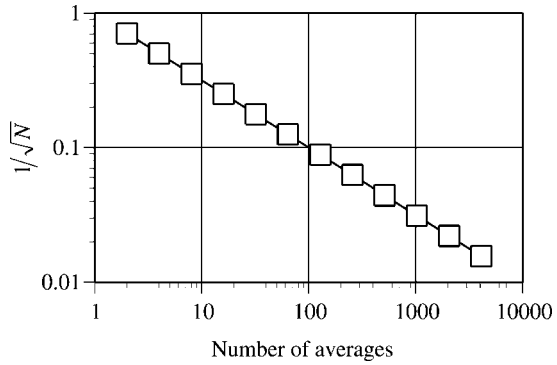

Fig. 5 The effect of the averaging times to the amplitude reduction of random noise

Therefore, after N averages, the amplitude of random noise is reduced by a factor $1/\sqrt{N}$ from the amplitude of the unaveraged random noise.

In the case of vibration produced by a rolling bearing, the revolution of the rolling bearing does not repeat exactly with the shaft revolution, since the cage does not revolve at an exact integral speed ratio of the inner rotational speed [6]. The vibration signal attributed to the rolling bearing is, therefore, considered to be asynchronous with the shaft revolution and can be categorized in this signal type.

4.2.2 Signal Synchronous With the Other Shaft Revolution. Synchronous averaging of the signals that are synchronous with the other shaft revolution but asynchronous with the revolution of gear of interest is schematically shown in Figs. 6(*a*) and 6(*b*) as a rotating vector. To simplify the analysis, the signal S that will be averaged is assumed to be a unit sinusoidal signal having frequency mf_s, when f_s is the shaft rotation frequency (asynchronous with gear of interest), and m is the harmonic order of f_s. Signal S can be written as Eq. (2)

$$S(t) = e^{j2\pi mf_s t} \tag{2}$$

Each block of signal S that will be averaged is selected synchronously with the trigger signal having frequency f_t that is different from frequency mf_s of the signal S. Because of the frequency difference between both signals, the phase angle difference φ must occur at the beginning point of the adjacent blocks of the signal S. The phase angle φ is first defined as elapsed time, which is equal to the period of trigger signal divided by the period of the signal to be eliminated. From this definition, the phase angle φ can be written as shown in Eq. (3)

$$\varphi = \frac{T_t}{T_s/m} \times 2\pi \tag{3}$$

where T_t is the period of the trigger signal and T_s is the period of the shaft revolution.

Because φ in Eq. (3) may be larger than $2k\pi$, to represent φ in the range $0-2\pi$, the phase difference φ can be rewritten in the form of φ' as shown in Eq. (4) and in Fig. 6(*b*)

$$\varphi' = \left[\left(\frac{T_t}{T_s/m}\right)\mathrm{mod}(1)\right] \times 2\pi \tag{4}$$

Usually, it is more convenient to write Eqs. (3) and (4) in terms of frequency as shown in Eqs. (5) and (6)

$$\varphi = \frac{mf_s}{f_t} \times 2\pi \tag{5}$$

$$\varphi' = \left[\left(\frac{mf_s}{f_t}\right)\mathrm{mod}(1)\right] \times 2\pi \tag{6}$$

Because the phase angle difference φ must occur between the beginning points of the adjacent blocks of the signal S, the phase differences of consecutive blocks of signal when referenced to the first block are $\varphi, 2\varphi, 3\varphi, \ldots$. Thus, because the initial phase angle of each block is different, averaging these blocks of signal makes the amplitude of the averaged signal S reduce to zero after enough averages. The amplitude of the averaged signal after N averages can be written as the following equations

$$\begin{aligned} S_{avg} &= \frac{1}{N}[e^{j2\pi mf_s t} + e^{j(2\pi mf_s t+\varphi)} + e^{j(2\pi mf_s t+2\varphi)} + \cdots \\ &\quad + e^{j(2\pi mf_s t+(N-1)\varphi)}] \\ &= \frac{1}{N}[e^{j2\pi mf_s t} + e^{j2\pi mf_s t}\cdot e^{j\varphi} + e^{j2\pi mf_s t}\cdot e^{j2\varphi} + \cdots \\ &\quad + e^{j2\pi mf_s t}\cdot e^{j(N-1)\varphi}] \\ &= \frac{e^{j2\pi mf_s t}}{N}[1 + e^{j\varphi} + e^{j2\varphi} + \cdots + e^{j(N-1)\varphi}] \end{aligned} \tag{7}$$

which becomes

$$= \frac{e^{j2\pi mf_s t}}{N}\left[\frac{1-e^{jN\varphi}}{1-e^{j\varphi}}\right] = Ae^{j2\pi mf_s t} \tag{8}$$

Here, A is the coefficient of magnitude reduction of signal S. The magnitude of A can be found by the following equation

$$|A| = \frac{1}{N}\left|\frac{1-e^{jN\varphi}}{1-e^{j\varphi}}\right| \tag{9}$$

The relation of $|A|$ and the number of averages N at various phase conditions are shown in Fig. 7.

From Fig. 7, it is found that if the proper number of averages is applied, it is possible to completely eliminate asynchronous sig-

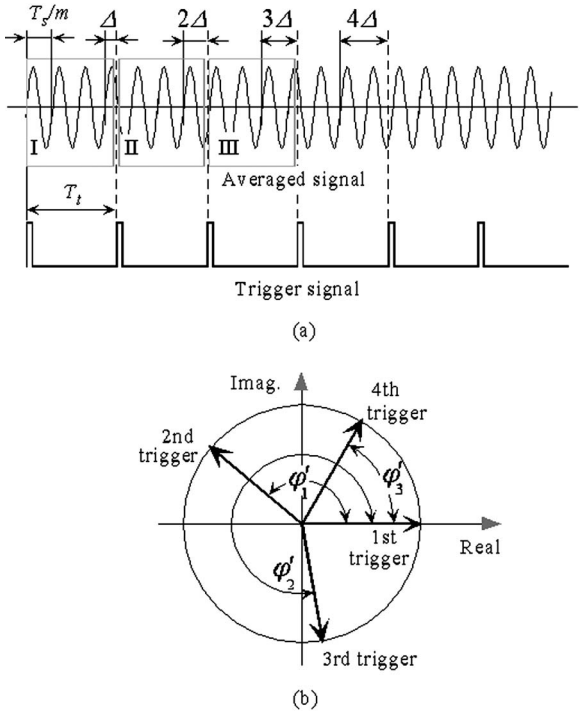

Fig. 6 Synchronous averaging of signal that is asynchronous with trigger signal

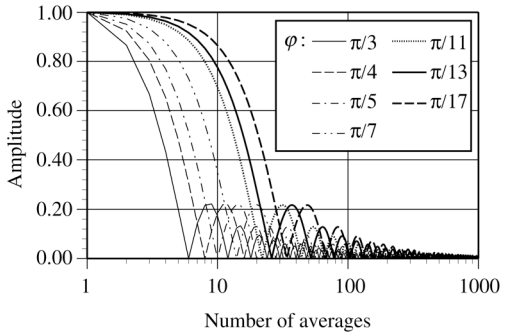

Fig. 7 The effect of the times of averaging to the amplitude reduction of asynchronous signal at various phase angles

nals from the signal of interest. From Eq. (9), asynchronous signal will be completely eliminated when $|A|=0$, or $1-e^{jN\varphi}=0$, hence

$$N\varphi = 2k\pi \tag{10}$$

The condition for complete elimination of asynchronous signals can also be considered from the rotating vector diagram shown in Fig. 6(*b*). It is found that the amplitude of the sum of the rotating vector must be exactly canceled when the *N*th vector rotates around the origin point to the position just before returning back to the same position of the first vector. In the time domain shown in Fig. (8), this condition shows that at $(N+1)$th trigger, there are no phase differences between the beginning point of the block of signal and the first block of signal *S*. From Fig. 8, it is found that

$$NT_t = a\frac{T_s}{m}$$

In the case of a gear pair, having common meshing frequencies, the trigger signal is obtained from one of the gear shafts, therefore the period of the trigger signal and signal *S* to related with the number of teeth of the gear pair, hence

$$\frac{Nm}{a} = \frac{T_s}{T_t} = \frac{Z_s}{Z_t}$$

$$(Nm)Z_t = (a)Z_s = L\,.\,C\,.\,M\,.\,(Z_tZ_s) \times p$$

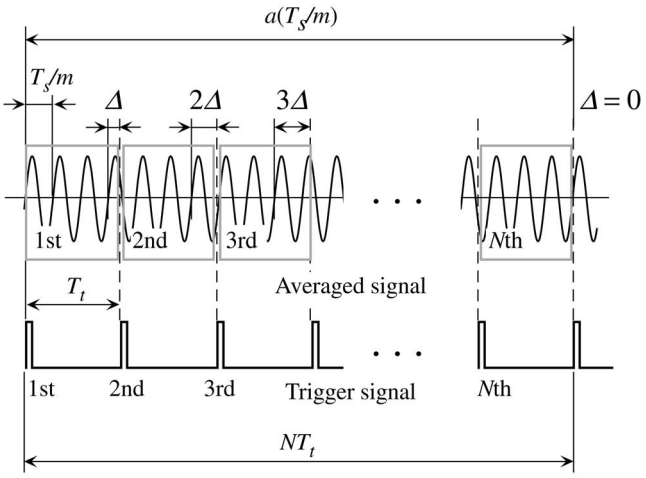

Fig. 8 Synchronous averaging of signal that is asynchronous with trigger signal (completely eliminated asynchronous signal)

$$N = \frac{\text{L.C.M.}(Z_t,Z_s) \times p}{m \times Z_t} \tag{11}$$

where Z_t is the number of teeth of the gear that its rotation is used as the trigger signal (gear of interest), Z_s is the number of teeth of another gear in the gear pair, and $L.C.M.(Z_tZ_s)$ is the least common multiplier between Z_t and Z_s. From Eq. (11), for all values of harmonic order *m*, if $p=q\cdot m$, where *q* is any arbitrary integer, *N* will be an integer. Therefore, the proper number of averages *N* that eliminates asynchronous signals attributed to another gear in the gear pair completely can be written as shown in Eq. (12)

$$N = q \times \frac{\text{L.C.M.}(Z_t,Z_s)}{Z_t} \tag{12}$$

In the case of a gear pair used in this experiment, the proper number of averaging can be calculated as follows.

1. Driving Shaft Trigger

In this case, the signal asynchronous with driving shaft rotation will be eliminated with $Z_t=30$, hence

$$N = q \times \frac{\text{L.C.M.}\,.\,(30,53)}{30} = 53q$$

Therefore in the case when the driving trigger is used, averaging with integer multiples of 53 will eliminate the asynchronous signal completely.

2. Driven Shaft Trigger

In this case, the signal asynchronous with driven shaft rotation will be eliminated. For $Z_t=53$, hence

$$N = q \times \frac{\text{L.C.M.}(30,53)}{53} = 30q$$

Therefore, in the case when the driven trigger is used, averaging with integer multiples of 30 will eliminate the asynchronous signal completely.

The relation between the number of averages and the amplitude of the averaged signal in the case of the driving and driven shaft trigger is shown in Figs. 9(*a*) and 9(*b*).

Although the proper number of averages can always be selected for any gear pair, because of the restriction of instruments (fast Fourier transform analyzer), or because of multi stage gear arrangements, it is frequently impossible to completely eliminate unrelated signals attributed to the other gears apart from the gear of interest. For this reason, a large number of averages is still essential for obtaining high accuracy results.

From Eq. (9) and Fig. 6(*b*), it is clear that the rate of the reduction of the amplitude of signals to be eliminated is also affected highly by the phase difference φ or φ'. If the phase difference φ' is very close to 0 or 2π, the amplitude of the signal is reduced slowly. Therefore, large numbers of averages will be required for elimination of this signal. The values of phase difference φ' at various harmonic order of the shaft *m* in the case of the gear pair used in this experiment are shown in the Figs. 10(*a*) and 10(*b*) for the driving and driven shaft triggers, respectively.

From Figs. 10(*a*) and 10(*b*), it is found that in the case of the driving trigger, the phase difference φ' at the 23rd and 30th harmonic of the driven shaft rotation are the closest to 2π and 0, therefore the amplitude reduction rate at these orders is very low ($53i$th harmonic are meshing components, $(23+53i)$th and $(30+53i)$th harmonic give the same phase angle with 23rd and 30th harmonic, where *i* is an integer).

In the case of the driven trigger, it is found that at 13th and 17th harmonic of driving shaft rotation, the phase differences are the closest to 0 or 2π ($30i$th harmonic are meshing components, $(13+30i)$th and $(17+30i)$th harmonic give the same phase angle with 13th and 17th harmonic, where *i* is an integer). At these orders, the amplitudes of the signal reduce slowly with the number of averages, therefore large numbers of averages will be re-

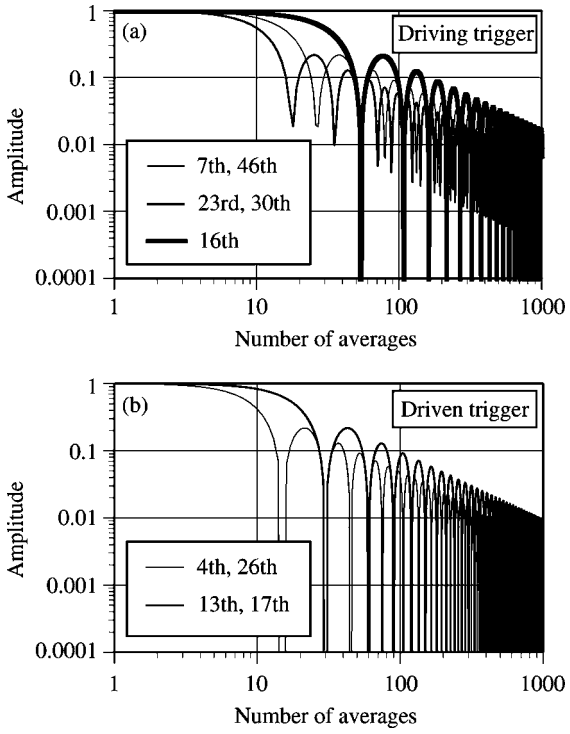

Fig. 9 The effect of the number of averages on the amplitude reduction of the asynchronous signal, (*a*) driving trigger, (*b*) driven trigger

quired for elimination of these signals. The relation between amplitude $|A|$ and number of times for averaging at these orders is shown in Figs. 9(*a*) and 9(*b*).

From Figs. 9(*a*) and 9(*b*), it is clear that averaging more than 100 times reduces the amplitudes of these signals to be less than about 10% of unaveraged signals regardless of harmonic orders. Amplitudes of these averaged signals will be reduced to less than 2% after averaging more than 1000 times.

In this experiment, the number of averages was set at 1024. With this setting, the amplitudes of the signal not related to the gear of interest will be reduced to less than 2%. The effect of random noise shown in Fig. 5 is also reduced to less than 5% of the random noise in the case of unaveraged signal. This reduction rate seems satisfactory for the analysis.

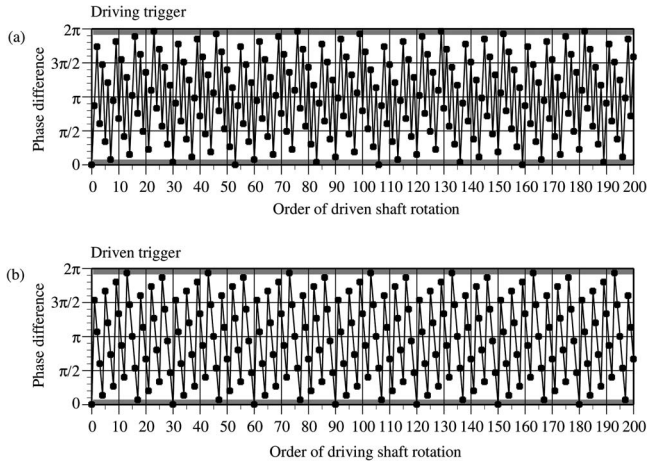

Fig. 10 Phase differences at various shaft orders; (*a*) driving trigger, (*b*) driven trigger

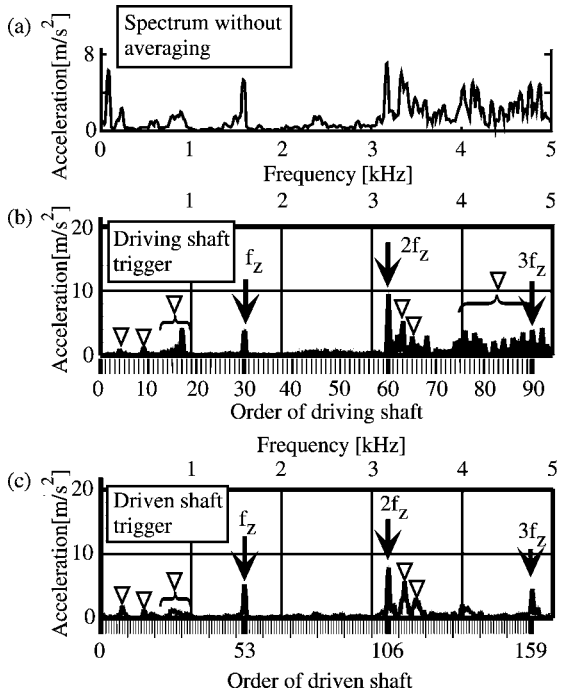

Fig. 11 Conventional spectral representation and synchronous averaged spectra of vibration at driven gear GTM2

5 Synchronous Averaging Result

The result of synchronous averaging for gear GTM2 is shown in Fig. 11. Figure 11(*a*) is a spectrum of the vibration of gear GTM2 operated at 1800 rpm, torque 98 Nm at the driven shaft, without averaging. This spectrum still consists of the contribution of both driving and driven gear. In this case the fundamental meshing frequency and its harmonics occurred at 1590, 3180, and 4770 Hz. Non-integer order of mesh vibration components can be seen in the region less than 1 kHz and greater than 3 kHz.

The synchronous averaging results with the driving and driven trigger in the range 0–5 kHz are shown in Figs. 11(*b*) and 11(*c*). It can be seen that the cluster of peaks existing between 4 and 5 kHz in the spectrum without averaging still remains after averaging with the driving trigger (this frequency band conforms to the order of driving shaft rotation in the range 75th–94th order). However, these peaks disappeared when the driven trigger was used. This result indicates that the peaks of noninteger order of meshing frequency occurring in this frequency band were generated by the driving gear. It can also be expected from this result that there are cyclic undulations between 75th order and 94th order of driving shaft rotation on the tooth surface of the driving gear.

With regard to the peaks of noninteger order of mesh frequency occurring in the region less than 1 kHz and between 3.3 and 3.7 kHz, it was found that these peaks still remained after averaging with both driving and driven trigger. Therefore, it is supposed that these are due to small cyclic undulations at the orders corresponding with these frequencies on both driving and driven gear teeth. Although these undulations are very small, they excite the gear system to vibrate at the same frequencies as the natural frequencies of the gear system, and due to the resonance effect, the amplitudes of the vibration at these frequencies were amplified to a considerable level.

It is also noticeable that in the spectrum without averaging in Fig. 11(*a*), there is a high vibration peak at frequency about 90 Hz, however this peak does not occur in synchronous averag-

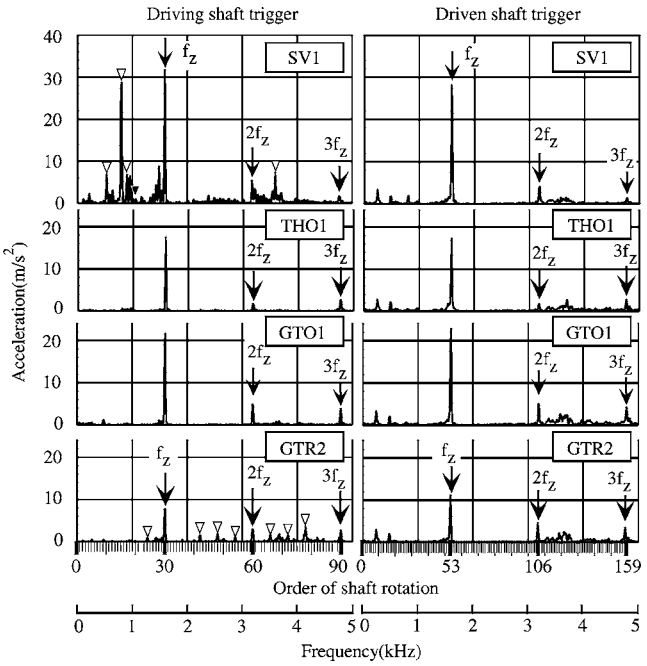

Fig. 12 Synchronously averaged spectra of vibration at driven gear

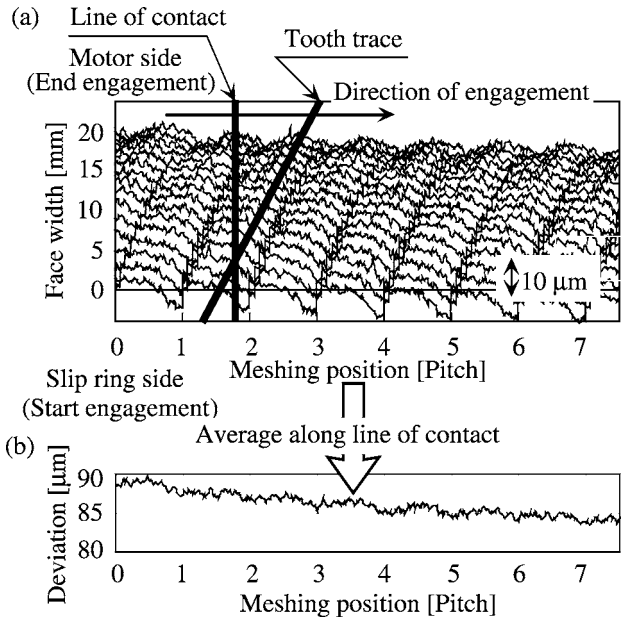

Fig. 13 Two-dimensional tooth surface forms

ing spectra in both Figs. 11(*b*) and 11(*c*). This result shows that the cyclic undulation at this order does not exist on either the driving or driven gear. However, because this frequency corresponds with one of the natural frequencies of the gear pair, the vibration at this frequency was amplified to the abnormally high level.

Figure 12 shows the results of synchronous averaging of other gears operated at the same condition as the gear GTM2. In this study, the master gear was unchanged in all experiments, and hence synchronous averaging results with driven shaft trigger, which show the vibration characteristics of the master gear, are almost the same as expected. When the driving shaft trigger was used, ghost noise components differed from each other according to gear finishing methods. Gear GTR2 has a small series of ghost noise at every sixth order of driving shaft rotation from 24th to 78th order (1272–4134 Hz). Gear SV1 has very high amplitudes of components at the 10th, 15th, and 17th order of the driving shaft rotation. On the other hand, in the case of GTO1 and THO1, the peaks of noninteger order of meshing frequency are rarely seen, and only meshing components are observed. From these results, it is summarized that there are a series of cyclic undulations occurring at every sixth order of driving shaft rotation on the tooth surface of gear GTR2, and the cyclic undulation also occurs at the 15th order of the driving shaft rotation in the case of gear SV1. Since the objective of this paper is to propose the method, causes of these undulations are not discussed further. These results also indicate that there was negligible periodic waviness on the tooth surface of gear GTO1 and THO1.

It is concluded that utilization of synchronous averaging along with considering gear vibration characteristics from waterfall plot make it possible to examine the source of extraneous ghost noises and their corresponding frequency orders, and with these results the characteristics of tooth surface undulation can be estimated.

Because the synchronous averaging shows only the existence of the order of shaft rotation when the noise occurs at each operating speed, experiments done at other operating speeds will give different amplitudes and positions of peaks from this experiment, since the amplitude of vibration is affected by other parameters such as operating speed and natural frequency of the system.

6 Spectrum Analysis of Tooth Profiles

To verify the correctness of the order of tooth surface undulation estimated from the synchronous averaging method, tooth surface geometries of gears were precisely measured. Because cyclic undulation cannot be detected by inspection of profiles of only a few teeth, tooth profile forms were measured at every tooth. Furthermore, measurements were done on 16 transverse sections on each tooth. Analysis methods for detection of tooth surface undulation were done by arranging all tooth profiles to form two-dimensional presentation of tooth surface. Profiles of each tooth were placed 1 pitch apart from each other, and profiles of each section were aligned vertically slanted after the base helix angle. With this arrangement the tooth surface condition for the two dimensions of a gear can be known. The line of contact of this tooth surface aligns vertically and the direction of meshing moves from left to right. Each tooth profile was represented with one base pitch.

A sample figure of two-dimensional tooth surface form is shown in Fig. 13(*a*). This figure shows the tooth surface of only seven teeth, however all 30 teeth were measured and taken into analysis. Because both amplitude and direction of the tooth surface undulation of all teeth and all sections affect the gear vibration, to construct representative curves including all of these effects, the deviation of gear tooth surface of all sections was averaged either along the line of contact or along the tooth trace at each meshing position. A sample representative curve of surface deviation averaged along the line of contact is shown in Fig. 13(*b*). Adopting spectral analysis on these representative curves, the spectra of tooth surface deviation averaged along the line of contact and along the tooth trace can be known and cyclic undulation of the tooth surface can be detected.

Spectra of tooth surface deviation of test gear (driving gear) averaged both along the line of contact and along tooth trace are shown in Figs. 14(*a*) and 14(*b*), respectively. By comparing these spectra with synchronous averaging results in Figs. 11 and 12 in the case of driving shaft trigger, which shows the vibration characteristics of the driving gear, it is obvious that the positions of peaks obtained from the synchronous averaging method coincide with the positions of peak of the spectra of the tooth surface deviation averaged along the line of contact. The evident example is for gear GTR2. From the spectrum of tooth surface deviation, it is recognized that on the tooth surface of gear GTR2 there are

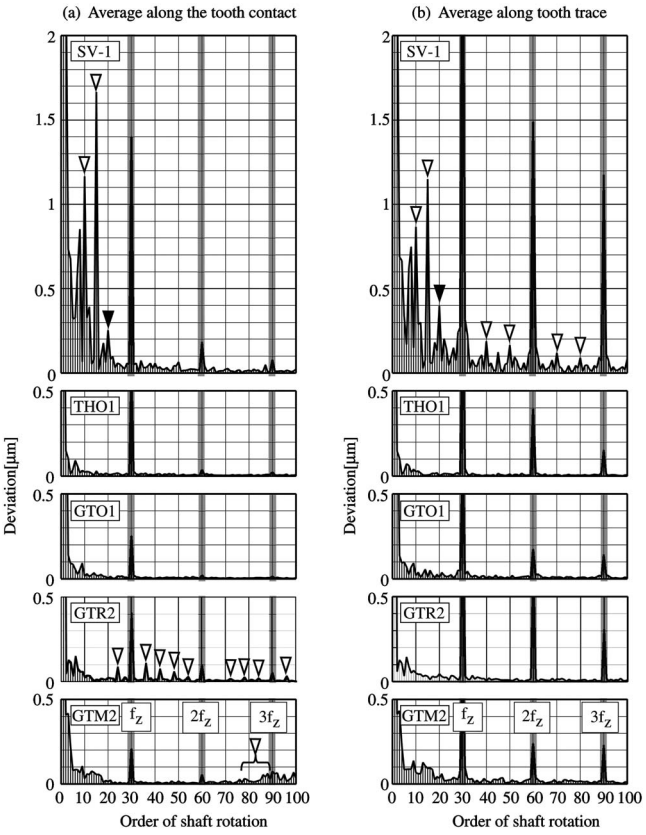

Fig. 14 Spectra of tooth surface geometry

cyclic undulations aligned synchronously with the line of contact at every sixth order of driving shaft rotation. These undulations act as exciters to the gear pair to vibrate at the same frequencies with their orders. Consequently, the peaks of the vibration at every sixth order of driving shaft rotation occur. It should be noted that, because of the difference of the motion, quantities that are displacement from the spectrum of tooth surface deviation and acceleration from synchronous averaging result, therefore the amplitude in the low frequency region from both results is different.

Although the existence of surface deviation that is synchronous with the line of contact directly affects the occurrence of gear vibration, it is found that deviation in phase with the tooth trace but not with the line of contact has little affect on the gear vibration. In the case of gear SV1, there were peaks of undulation synchronous with the tooth trace at the 40th, 50th, 70th, and 80th order of driving shaft rotation. These undulations are in phase with the tooth trace direction, therefore there are no peaks at these orders on the spectrum of tooth surface deviation collected along the line of contact. By considering vibration measurement results, the vibration at these orders also did not occur.

It is also noticeable in the case of gear SV1 that, although there is a relatively high amplitude of cyclic undulation at the 20th order of driving shaft rotation (black triangle mark) in the spectrum of tooth surface deviation averaged along the line of contact and along the tooth trace, the vibration at this order from the synchronous averaging result (black triangle mark) is very low. To understand the reason for these findings, the detail of the change of phase of surface deviation along the line of contact is considered.

Figure 15 shows the change of phase of the surface deviation along the line of contact. The abscissa is the position along face width. The ordinate is the phase angle of surface deviation measured at the individual transverse section. If the phase angle synchronizes with the line of contact, the variation of phase along the

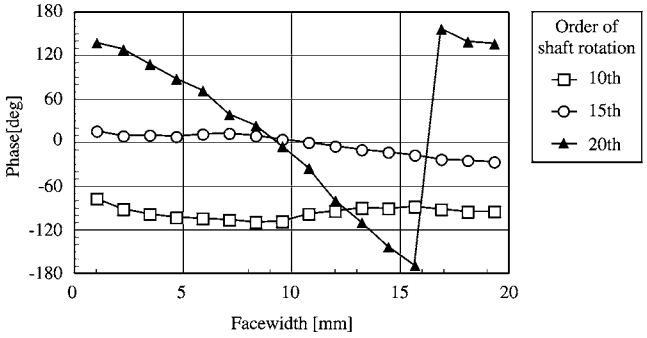

Fig. 15 The change of phase of surface undulation averaged along the line of contact

line of contact will be insignificant. This can be shown by a line lying horizontally parallel with the abscissa. From Fig. 15, it can be seen that the phase angles of cyclic undulations at the 10th and 15th order of driving shaft rotation are in phase with the line of contact and vibration at these orders is high. On the other hand, the phase angle at the 20th order does not synchronize with the line of contact, therefore the vibration level at this order is low and does not appear in the synchronous averaging result.

From the discussion above, it is obvious that the occurrence of ghost noise is not only affected by the existence of cyclic undulation on the tooth surface, but it is also affected by the phase arrangement of cyclic undulation along the tooth-width direction comparatively. Only the cyclic undulation, which is synchronous with the line of contact, affects the vibration of a gear pair.

From the results shown here, it has become clear that synchronous averaging of the gear vibration can be used effectively to detect the existence of tooth surface undulation even when the undulation is very small at the level of 0.1 μm. However, it must be remarked here that the relation between the amplitude of each cyclic undulation and the amplitude of vibration is still not known because the amplitude of vibration is also affected by the operating conditions such as the operating speed, torque, and natural frequency of the system.

7 Restrictions of Synchronous Averaging

It has been shown that the synchronous averaging method can be applied to distinguish vibration signals attributed to driving and driven gears from each other effectively as shown by the experimental results. It is, however, necessary to discuss its restrictions. It is essential that the numbers of teeth of a gear pair are relatively prime (for instance, 30:53 as used in this experiment) before the signals attributed to the driving and the driven gear can be separated from each other completely. In the case of the numbers of teeth of a gear pair being related to each other, there are also components besides meshing components that synchronize with both driving and driven shaft, and cannot be eliminated by synchronous averaging. In this case, the orders that cannot be eliminated can be determined by the following consideration.

Let the driving gear have Z_1 teeth and rotate at shaft frequency f_{s1}, and the driven gear have Z_2 teeth and rotate at shaft frequency f_{s2}. The fundamental mesh component f_z can be written as Eq. (13)

$$f_z = Z_1 f_{s1} = Z_2 f_{s2} \tag{13}$$

Where a common factor exists between Z_1 and Z_2, there is a maximum integer a, which is not equal to 1 that makes $Z_1 = am$ and $Z_2 = an$, when m and n are integers.

Substitute Z_1 and Z_2 into Eq. (13), then

$$f_z = amf_{s1} = anf_{s2}$$

and

$$f_z/a = mf_{s1} = nf_{s2} \quad (14)$$

From Eq. (14), it is clear that the frequency at the mth order of driving shaft rotation is equal to the frequency at the nth order of driven shaft rotation. Therefore the vibration component at this frequency (mth order of driving shaft rotation or nth order of driven shaft rotation) cannot be distinguished into which gear is the vibration source. Because this matter also occurs in the case of any harmonics of this frequency, the following principles can be developed about the order that can or cannot be eliminated by synchronous averaging:

1. The frequency that cannot be eliminated$=if_z/a$
2. Driving shaft order that cannot be eliminated$=im=iZ_1/a$
3. Driven shaft order that cannot be eliminated$=in=iZ_2/a$

Where a is the greatest common divisor of Z_1 and Z_2 i is an arbitrary integer $(1,2,3\ldots)$.

In the case of small a, there are only few orders where synchronous averaging cannot specify the source of the signals, therefore synchronous averaging can still be used. However, if the value of a becomes large, there are many orders that cannot be used to specify the vibration source, and synchronous averaging method is improper to use in this case.

8 Conclusions

This paper proposed the utilization of synchronous averaging method for diagnosis of ghost noise sources and inspection of the cyclic undulation on the tooth surface. First, the principle of synchronous averaging method has been reviewed and the effect of the number of averages was discussed. In this experiment, 1024 averages were used to ensure that the amplitude of asynchronous signal and random noise were reduced into negligible level.

The experimental results confirmed the effectiveness of this method; ghost noise components attributed to driving and driven gear can be distinguished from each other and from the other components obviously, and hence the ghost noise source can be precisely localized to one of the gears. Because the orders of ghost noise are conformable to the orders of the cyclic undulation on the tooth surface, with synchronous averaging method cyclic undulation on tooth surface can also be detected. From the results, a lot of ghost noise components were observed at many frequencies, especially in the case of gear GTM, GTR and SV. This means there are cyclic undulations on the teeth of these gears at various shaft orders that may excite a gear pair to vibrate at a resonance frequency at various rotational speeds.

It is also confirmed by the results shown here that the proposed method can be applied to detect surface undulation despite the amplitude of deviation being very small in the level of 0.1 μm. On the contrary, at this amplitude level, it is difficult to detect surface undulation by ordinary tooth surface measurement directly. This concludes that the synchronous averaging method has a higher ability than the use of the surface measurement method and has strong potential for tooth surface inspection.

This paper also discussed the effect of the phase angle arrangement of the cyclic undulation along the tooth width direction to the vibration of a gear pair. The results show that only the cyclic undulations synchronizing with the line of contact will affect the gear vibration.

Finally, several restrictions of the synchronous averaging method were discussed. Only in the case of a gear pair having the numbers of teeth equal to relatively prime can this technique be used to separate vibration signals attributed to driving and driven gear from each other completely.

Acknowledgment

This work is part of the activities of the research committee for gear future technology (RC-184) founded by the Japan Society of Mechanical Engineers. The authors also wish to thank Yasushi Ueda from Toyota Motor Corp., and Dr. Shogo Kato for measurement and manufacturing support.

References

[1] Merritt, H. E., 1971, *Gear Engineering*, Pitman, New York, pp. 82–83.
[2] Mark, W. D., 1992, "Contributions to the Vibratory Excitation of Gear Systems from Periodic Undulations on Tooth Running Surfaces," J. Acoust. Soc. Am., **91**(1), pp. 166–186.
[3] Matson, G. A., and Houser, D. R., 1996, "The Use of Ghost Noise as an Exciter for High Frequency Gear System Dynamics," *International Conference on Gears*, VDI, Dresden, Germany, Apr. 22–24, pp. 739–750.
[4] Matsumura, S., Houjoh, H., Ohshima, S., and Nagoya, H., 2000, "Observation of Ghost Noise on Ground Gears With Vibration Measurement and Detection of Surface Undulation," *Proceedings of the 8th International Power Transmission and Gearing Conference*, Baltimore, MD, Sep. 10–13, pp. 547–552.
[5] Matsumura, S., Kitahara, A., and Houjoh, H., 2001, "Prediction of Ghost Noise Occurrence on Ground Helical Gears with Detailed Surface Measurement," *The JSME Int. Conference on Motion and Power Transmission*, Fukuoka, Japan, Nov. 15–17, pp. 79–83.
[6] Smith, J. D., 1989, *Vibration Measurement & Analysis*, Butterworths, London, pp. 109–110.
[7] Smith, J. D., 1999, *Gear Noise and Vibration*, Dekker, New York, pp. 152–157.
[8] Wowk, V., 1991, *Machinery Vibration Measurement and Analysis*, McGraw–Hill, New York, pp. 103–105.
[9] McFadden, P. D., and Smith, J. D., 1985, "A Signal Processing Technique for Detecting Local Defects in a Gear from the Signal Average of the Vibration," Proc. Inst. Mech. Eng., Part C: Mech. Eng. Sci., **199**(C4), pp. 287–292.
[10] McFadden, P. D., and Smith, J. D., 1985, "An Explanation for the Asymmetry of the Modulation Sidebands about the Tooth Meshing Frequency in Epicyclic Gear Vibration," Proc. Inst. Mech. Eng., Part C: Mech. Eng. Sci., **199**(C1), pp. 65–70.
[11] McFadden, P. D., 1987, "Examination of a Technique for the Early Detection of Failure in Gears by Signal Processing of the Time Domain Average of the Meshing Vibration," Mech. Syst. Signal Process., **1**(2), pp. 173–183.
[12] McFadden, P. D., 1987, "A Revised Model for the Extraction of Periodic Waveforms by Time Domain Averaging," Mech. Syst. Signal Process., **1**(1), pp. 83–95.
[13] McFadden, P. D., 1991, "A Technique for Calculating the Time Domain Averages of the Vibration of the Individual Planet Gears and the Sun Gear in an Epicyclic Gearbox," J. Sov. Laser Res., **144**(1), pp. 163–172.
[14] Wang, W. J., and McFadden, P. D., 1995, "Decomposition of Gear Motion Signals and Its Application to Gearbox Diagnostics," J. Vibr. Acoust., **117**, pp. 363–369.
[15] McFadden, P. D., 2000, "Detection of Gear Faults by Decomposition of Matched Differences of Vibration Signals," Mech. Syst. Signal Process., **14**(5), pp. 805–817.
[16] McFadden, P. D., and Toozhy, M. M., 2000, "Application of Synchronous Averaging to Vibration Monitoring of Rolling Element Bearing," Mech. Syst. Signal Process., **14**(6), pp. 891–906.
[17] Loewenstein, E. B., 2000, "Reducing the Effects of Noise in a Data Acquisition System by Averaging," Application note, National Instruments.

Nonlinear Stability of the Classical Nusselt Problem of Film Condensation and Wave Effects

L. Phan

A. Narain
e-mail: narain@mtu.edu

Department of Mechanical Engineering—
Engineering Mechanics,
Michigan Technological University,
Houghton, MI 49931

Accurate steady and unsteady numerical solutions of the full two-dimensional (2D) governing equations for the Nusselt problem (film condensation of quiescent saturated vapor on a vertical wall) are presented and related to known results. The problem, solved accurately up to film Reynolds number of 60 ($\mathrm{Re}_\delta \leqslant 60$)*, establishes various features of the well-known steady solution and reveals the interesting phenomena of stability, instability, and nonlinear wave effects. It is shown that intrinsic flow instabilities cause the wave effects to grow over the well-known experiments-based range of* $\mathrm{Re}_\delta \geqslant 30$*. The wave effects due to film flow's sensitivity to ever-present minuscule transverse vibrations of the condensing surface are also described. The results suggest some ways of choosing wall noise—through suitable actuators—that can enhance or dampen wave fluctuations and thus increase or decrease heat transfer rates over the laminar-to-turbulent transition zone.* [DOI: 10.1115/1.2198249]

1 Introduction

The Nusselt problem [1] of film condensation of quiescent saturated vapor on a vertical wall has been extensively studied—analytically, computationally, and experimentally. For this problem, the state of empirical knowledge with regard to typical wave effects on the heat transfer rates is quite good (see [2]). Despite this, a good understanding of noise effects and instability mechanisms for the flow has been lacking. With the help of first-principles-based computational simulations, this paper explores these issues and presents new results and understanding. Furthermore, compatibility with the well-known results for this problem provides a test of the efficacy of the first-principles-based simulation methodology employed here. This benchmark study, along with some experimental results, also strengthens the confidence in other convergent computational solutions obtained by essentially the same simulation methodology for *internal* condensing flows studied elsewhere [3–5].

The well-known analytical solution [1] of the Nusselt problem was improvised by Rohsenow [6] to account for the effects of the energy convection term. Subsequently, Sparrow and Gregg [7] provided a similarity solution under the assumption of zero interfacial shears. Vapor shear effects were accounted for, by an integral method, in the work of Chen [8], and, by a similarity solution technique, in the work of Koh et al. [9]. Dhir and Lienhard [10] applied/generalized the solution for situations involving varying gravitational inclinations. The computational solution of the steady problem that has been presented in this paper is consistent with the well-known Nusselt solution and its improvements. A good review of the criteria for the range of applicability of the Nusselt solution and its modifications is available in Arnas et al. [11]. More specifically, this paper solves the steady Nusselt problem without making any of the usual approximations for the governing equations and yet yields the solutions which are in a good agreement with the Nusselt solution [1]. The paper also shows that, for steady solutions, it is only the near-interface vapor pressure field (p_2-p_0) that is significantly affected by the presence or absence of surface tension.

The unsteady solution for this problem—after ignoring the restriction based on the continuity of tangential velocities at the interface—has been attempted by Miyara [12]. This work has tried to improvise upon earlier related computational efforts [13] for this problem. But these computational results suffer from the fact that the three different ways of computing interfacial mass flux values (from considerations of the relative velocity of vapor at the interface, the relative velocity of liquid at the interface, and the heat transfer rates across the interface) are not equal to one another. In this regard, the simulation results presented here are accurate and are shown to satisfy this and all the remaining interface conditions.

Wave initiation mechanisms can, in principle, also be understood by linear or nonlinear stability analyses. The linearized stability analyses of Unsal and Thomas [14] and Spindler [15] yield results that are mutually consistent but do not satisfy the well-known experimental results that are associated with laminar-to-turbulence transition over $\mathrm{Re}_\delta \geqslant \mathrm{Re}_\delta|_{\mathrm{Cr}}$ with $\mathrm{Re}_\delta|_{\mathrm{Cr}} \approx 30$. The experimental observance of this laminar-to-turbulent transition is believed to be related to Tollmien-Schlichting-type instability waves [16] that are suitably modified by free surface phenomena and mass transfer across the interface. The paper shows that the instability mechanism for this problem is necessarily a nonlinear phenomenon in time (as opposed to nonlinearities due to the size of the amplitudes alone) and, therefore, cannot be identified by either the linearized stability analyses assumption ([14,15]) or partial nonlinear analyses ([17]) that employ two term expansions in wave number and wave amplitude. This full nonlinear stability analysis presented here does achieve agreement with the reported values of $\mathrm{Re}_\delta|_{\mathrm{Cr}} \approx 30$.

Our results are in basic agreement with the known experimental result that laminar wavy flows occur over a zone for which, approximately, $\mathrm{Re}_\delta \geqslant 30$ (see Re_δ definition in the Nomenclature and Incropera et al. [2]) and that the waves are typically small to nonexistent over a zone for which, approximately, $\mathrm{Re}_\delta \leqslant 30$. Experimentally obtained local heat transfer coefficients for the wavy regime have been proposed by Kutateladze [18], Chun and Seban [19], etc., and are also given in Incropera et al. [2]. The results given here are consistent with the range of heat transfer enhancements that are expected under typical wavy conditions.

Contributed by the Applied Mechanics Division of ASME for publication in the JOURNAL OF APPLIED MECHANICS. Manuscript received October 16, 2005; final manuscript received January 26, 2006. Review conducted by T. E. Tezduyar. Discussion on the paper should be addressed to the Editor, Prof. Robert M. McMeeking, Journal of Applied Mechanics, Department of Mechanical and Environmental Engineering, University of California—Santa Barbara, Santa Barbara, CA 93106-5070, and will be accepted until four months after final publication of the paper itself in the ASME JOURNAL OF APPLIED MECHANICS.

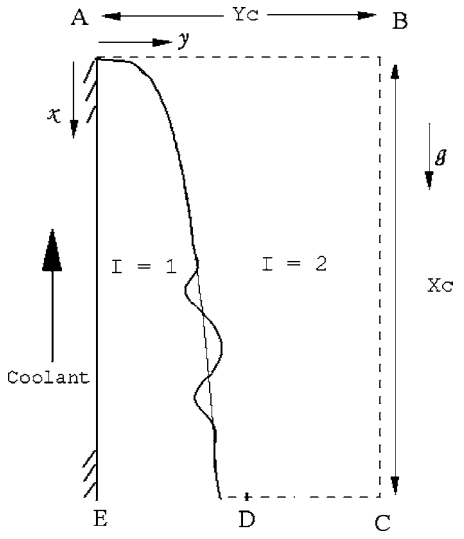

Fig. 1 Cooled vertical plate in a quiescent (far field) vapor flow—geometry used for simulations

Unlike the linearized stability analyses, the accurate simulations reported here also suggest an insignificant role of surface tension on the value of $\mathrm{Re}_{\delta}|_{\mathrm{cr}} \cong 30$. This is in agreement with experiments for this gravity driven flow but not in agreement with the results based on the linearized stability analyses given in [14,15].

This paper also clearly identifies how significantly wall noise interacts with Tollmien-Schlichting-type growing waves in the wavy laminar regime (i.e., transition to turbulence regime, which is typically characterized by $30 \leqslant \mathrm{Re}_{\delta} \leqslant 1800$). It is shown that wall noise—modeled as a linear superposition of transverse displacement standing waves of different amplitude, frequency, and wavelength—can either diminish or accentuate the wave effects. The enhancement of wave effects can be ensured if one can place suitably chosen noise sources (e.g., actuators) that satisfy a certain resonance condition. This result highlights the fact that knowledge and control of wall noise are important issues in ensuring repeatability of wave effects in the transition-to-turbulence regime.

2 Governing Equations

The liquid and vapor phases in the flow (e.g., see Fig. 1) are denoted by a subscript I: $I=1$ for liquid and $I=2$ for vapor. The fluid properties (density ρ, viscosity μ, specific heat C_p, and thermal conductivity k) with subscript "I" are assumed to take their representative constant values for each phase ($I=1$ or 2). Let $\mathcal{T}_I$ be the temperature fields, p_I be the pressure fields, $\mathcal{T}_s(p)$ be the saturation temperature of the vapor as a function of local pressure p, Δ be the film thickness, $\dot{m}$ be the local interfacial mass flux, $\mathcal{T}_w(x)$ $[<\mathcal{T}_s(p)]$ be a *known* temperature variation [here $\mathcal{T}_w(x) = \text{constant} = \mathcal{T}_w(0)$] of the cooled bottom plate, and $\mathbf{v}_I = u_I\hat{\mathbf{e}}_x + v_I\hat{\mathbf{e}}_y$ be the velocity fields. As shown in Fig. 1, instead of the original infinite domain ($x \geqslant 0$ and $y \geqslant 0$), solutions are only to be obtained over a finite subdomain ($0 \leqslant x \leqslant X_c$ and $0 \leqslant y \leqslant Y_c$). For convenience, the characteristic length for this problem is chosen to be Y_c, where Y_c is a known numerical multiple of the well known ([1]) physical value of the steady Nusselt film thickness $\Delta_N(x)$ at $x=X_c$. That is, $Y_c \equiv c \cdot \Delta_N(X_c)$, where c is a known number (e.g., $c=47$ for all cases shown here). This makes Y_c a priori known and sufficiently large to capture all the relevant vapor flow. While other choices of characteristic length Y_c are possible [e.g., $Y_c \equiv \Delta_N(X_c)$], this choice is convenient for implementing the computational approach employed here. Furthermore, let the characteristic speed U be the *average* value, at $x=X_c$, of the x component of the liquid speed obtained from the well-known [1] Nusselt solution. That is, $U \equiv g(\rho_1-\rho_2)\cdot\Delta_N(X_c)^2/3\mu_1$. The above choices of characteristic length and speed are used for defining the nondimensional variables whose computationally obtained values are reported in this paper. As needed, this choice is related to other results obtained from other commonly used choices of characteristic length and speed. Let g_x and g_y be the components of gravity along x and y axes, p_0 be the pressure of the far-field quiescent vapor, $\Delta\mathcal{T} \equiv \mathcal{T}_s(p_0) - \mathcal{T}_w(0)$ be the representative controlling temperature difference between the vapor and the bottom plate, and h_{fg} be the heat of vaporization at saturation temperature $\mathcal{T}_s(p)$. With t representing the physical time, we introduce a new list of fundamental nondimensional variables through the following definitions:

$$\{x, y, \delta, u_I, \dot{m}\} \equiv \left\{ \frac{x}{Y_c}, \frac{y}{Y_c}, \frac{\Delta}{Y_c}, \frac{u_I}{U}, \frac{\dot{m}}{\rho_1 U} \right\}$$

$$\{v_I, \theta_I, \pi_I, t\} \equiv \left\{ \frac{v_I}{U}, \frac{\mathcal{T}_I}{\Delta\mathcal{T}}, \frac{p_I - p_0}{\rho_1 U^2}, \frac{t}{(Y_c/U)} \right\} \tag{1}$$

2.1 Interior Equations. The nondimensional differential forms of mass, momentum (x and y components) and energy equations for flow in the interior of either of the phases are well-known and are given in (A1)–(A4) of the Appendix. The simplified forms that are used in obtaining the Nusselt ([1]) solution are given by (A1) and (A5) of the Appendix.

2.2 Interface Conditions. The nearly exact interface conditions (Delhaye [20]) for condensing flows, with some approximations, are given in Narain et al. [3]—see their Appendix Eqs. (A1)–(A9). Utilizing a superscript "i" for values of the flow variables at the interface given by $\mathcal{H} \equiv y - \Delta(x,t) = 0$, the nondimensionalized forms of the interface conditions are given below.

- The nondimensional form of the requirement of continuity of tangential component of velocities (Eq. (A2) of [3]) becomes:

$$u_2^i = u_1^i - \delta_x(v_2^i - v_1^i) \tag{2}$$

  where $\delta_x \equiv \partial\delta/\partial x$.
- The nondimensional form of the normal component of momentum balance at the interface (Eq. (A3) of [3]) becomes:

$$\pi_1^i = \frac{\rho_2}{\rho_1}\pi_2^i - \frac{1}{\mathrm{We}}\left(\frac{\delta_{xx}}{[1+\delta_x^2]^{3/2}}\right) + \dot{m}^2\left(\frac{\rho_1}{\rho_2} - 1\right) \tag{3}$$

  where $\mathrm{We}^{-1} \equiv \sigma/\rho_1 U^2 Y_c$ and surface tension $\sigma = \sigma(\mathcal{T})$ with $\mathcal{T}$ being the interfacial temperature.
- The tangential component of momentum balance at the interface (Eq. (A4) of [3]) becomes:

$$\left.\frac{\partial u_1}{\partial y}\right|^i = \left.\frac{\mu_2}{\mu_1}\frac{\partial u_2}{\partial y}\right|^i + [t] \tag{4}$$

  The term $[t]$ used here is defined by Eq. (A6) of the Appendix.
- The nondimensional forms of non-zero interfacial mass fluxes $\dot{m}_{LK}$ and $\dot{m}_{VK}$ (defined in Eq. (A5) of [3]) impose kinematic constraints on the interfacial values of the liquid and vapor velocity fields and are given by:

$$\dot{m}_{LK} \equiv [u_1^i(\partial\delta/\partial x) - (v_1^i - \partial\delta/\partial t)]/\sqrt{1+(\partial\delta/\partial x)^2} \text{ and}$$

$$\dot{m}_{VK} \equiv (\rho_2/\rho_1)[u_2^i(\partial\delta/\partial x) - (v_2^i - \partial\delta/\partial t)]/\sqrt{1+(\partial\delta/\partial x)^2} \tag{5}$$

- The nondimensional form of nonzero-interfacial mass flux $\dot{m}_{\mathrm{Energy}}$ (as given by Eq. (A6) of [3]) represents the constraint imposed on mass flux by the balance equation for the net energy transfer across the interface, and is given by:

$$\dot{m}_{\text{Energy}} \equiv \text{Ja}/(\text{Re}_1\,\text{Pr}_1)\{\,\partial\theta_1/\partial n|^i - (k_2/k_1)\,\partial\theta_2/\partial n|^i\} \quad (6)$$

where $\text{Ja} \equiv C_{p1}\Delta\mathcal{T}/h^0_{fg}$ and $h^0_{fg} \equiv h_{fg}[\mathcal{T}_s(p_o)] \cong h_{fg}[\mathcal{T}_s(p^i_2)]$.

- The interfacial mass balance requires that the net mass flux (in $\text{kg}/\text{m}^2/s$) at a point on the interface, as given by Eq. (A7) of [3], be single valued regardless of which physical process is used to obtain it. The nondimensional form of this requirement becomes:

$$\dot{m}_{LK} = \dot{m}_{VK} = \dot{m}_{\text{Energy}} \equiv \dot{m} \quad (7)$$

It should be noted that negligible interfacial thermal resistance and equilibrium thermodynamics on either side of the interface are assumed to hold for x values downstream of the origin (i.e., second or third computational cell onward). And hence, as in Nusselt [1] solution and as per discussions leading to Eq. (A8) in [3], no nonequilibrium thermodynamic model for the interfacial mass-flux $\dot{m}$ is needed to obtain a solution.

- The nondimensional thermodynamic restriction on interfacial temperatures (as given by Eq. (A8) in [3]) becomes:

$$\theta^i_1 \cong \theta^i_2 = \mathcal{T}_s(p^i_2)/\Delta\mathcal{T} \equiv \theta_s(\pi^i_2) \quad (8)$$

Within the vapor domain, for any of the typical refrigerants (such as R113 considered here) changes in absolute pressure relative to the inlet pressure are sufficient to affect vapor motion, but, at the same time, they are too small to affect saturation temperatures. This allows the approximation: $\theta_s(\pi^i_2) \cong \theta_s(0)$.

2.3 Boundary Conditions. Since the vapor is stationary at locations far away from the condensate, the appropriate far field vapor boundary conditions are prescribed along lines AB ($x=0$), BC ($y=Y_c$), and CD ($x=X_c$ or $x=x_c=X_c/Y_c$) in Fig. 1. These are:

$$\bullet\ \pi_2(0,y,t) = 0 \text{ and } \left.\frac{\partial u_2}{\partial x}\right|_{(0,y,t)} = 0$$

$$\bullet\ \pi_2(x,1,t) = 0 \text{ and } \left.\frac{\partial v_2}{\partial y}\right|_{(x,1,t)} = 0$$

$$\bullet\ \pi_2(x_c,y,t) = 0 \text{ and } \left.\frac{\partial u_2}{\partial x}\right|_{(x_c,y,t)} = 0 \quad (9)$$

At the condensing surface ($y=0$), we have:

$$u_1(x,0,t) = v_1(x,0,t) = 0 \text{ and } \theta_1(x,0,t) = \theta_w \equiv \mathcal{T}_w/\Delta\mathcal{T} \quad (10)$$

Furthermore, vapor can be assumed to be at uniform saturation temperature—i.e., $\theta_2(x,y,t) \cong \theta_s(0)$ at all locations in the vapor domain. This is reasonable because effects of superheat $\Delta\mathcal{T}_{\text{sup}}$ (in the typical 5–10°C range) are verifiably negligible for the typically small values of vapor Jacob number ($\text{Ja}_v \equiv Cp_2 \cdot \Delta\mathcal{T}_{\text{sup}}/h^o_{fg}$) encountered for most vapor flow conditions studied here. The point D at $x=X_c$ is considered to be slightly but sufficiently above the interface and no exit condition is imposed along ED. However the mass flow over ED—which specifically includes the liquid portion $0 \leqslant y \leqslant \delta(x_c)$—is required to satisfy the overall mass balance for a control volume formed by the bounding surfaces $x=0$, $x=X_c$, $y=0$, and $y=Y_c$.

2.4 Initial Conditions. The above described *continuum* equations do not model and incorporate various intermolecular forces that are important in determining the time evolution of very thin (10–100 nm) condensate film thickness $\delta(x,t)$. As a result, $t=0$ cannot be chosen to be the time when saturated vapor first comes in contact with and condenses on the dry subcooled $[\mathcal{T}_w(x) < \mathcal{T}_s(p_0)]$ vertical/inclined wall. With the above modeling limitations, the strategy here is to start at a time ($t=0$) for which one has a sufficiently thick *steady* solution of the *continuum* equations (where all of the governing equations clearly apply) and then, from there, one can obtain the natural large time ($t \to \infty$) smooth or wavy (steady/quasi-steady) solutions with the help of the unsteady equations. That is, if $\phi(x,y,t)$ is any variable (such as, u_I, v_I, π_I, θ_I, etc.), the initial values of ϕ and film thickness $\delta(x,t)$ are given as:

$$\phi(x,y,0) = \phi_{\text{steady}}(x,y) \text{ and } \delta(x,0) = \delta_{\text{steady}}(x) \quad (11)$$

where ϕ_{steady} and δ_{steady} are the solutions of the governing equations obtained by dropping all time dependencies in Eqs. (2)–(11).

An inspection of all the non-dimensional governing equations, interface conditions, and boundary conditions reveals the fact that the flows considered here are affected by the following set of eight independent non-dimensional parameters:

$$\left\{\text{Re}_1, \text{Ja}, \text{Fr}_x^{-1}, \text{Fr}_y^{-1}, \frac{\rho_2}{\rho_1}, \frac{\mu_2}{\mu_1}, \text{Pr}_1, \text{We}\right\} \quad (12)$$

where $\text{Re}_1 \equiv \rho_1 U Y_c/\mu_1$ indirectly depends on the physical value of $x=X_c$.

2.5 Nusselt Formulation/Solution. Besides the assumptions and approximations that lead to the interior equations given in the Appendix—namely (A1) with $I=1$ and (A5), this Nusselt ([1]) formulation for the underlying steady problem assumes: a small slope approximation ($\delta'^2 \ll 1$), negligible surface tension ($\text{We}^{-1} \cong 0$) as well as negligible momentum transfer effects on the right side of Eq. (3), and zero to negligible vapor viscosity. The assumption of negligible vapor viscosity makes continuity of tangential velocity condition in Eq. (2) to become irrelevant. This means that condensate motion is not affected by the equations governing the vapor motion and any constraints arising from the interfacial mass flux $\dot{m}_{VK}$ defined in Eq. (5). As a result, the steady Nusselt formulation requires that (A1) for $I=1$ and (A5) in the Appendix be solved subject to Eqs. (9) and (10) and the following simplified interface conditions:

- $\pi^i_2 = 0$ and $\pi^i_1 = 0$ as a replacement of Eq. (3)
- $\left.\dfrac{\partial u_1}{\partial y}\right|^i = 0$ as a replacement of Eq. (4)
- $\dot{m}_{LK} = \left[u^i_1 \dfrac{d\delta}{dx} - v^i_1\right] = \dfrac{d}{dx}\left[\displaystyle\int_0^{\delta(x)} u_1(x,y)\cdot dy\right]$ as a replacement of Eq. (5)
- $\dot{m}_{\text{Energy}} \equiv \text{Ja}/(\text{Re}_1\,\text{Pr}_1)\cdot\ \partial\theta_1/\partial y|^i$ as a replacement of Eq. (6)
- $\dot{m}_{LK} = \dot{m}_{\text{Energy}}$ as a replacement of Eqs. (2) and (7)
- $\theta^i_1 = \theta^i_2 = \theta_s(\pi^i_2)$, i.e., Eq. (8) remains the same (13)

The analytical solution of the above Nusselt formulation is known as the Nusselt ([1]) solution and is well known ([2]). This classical solution (see, e.g., [2]) and its principle results are:

$$\Delta(x) \equiv \Delta_N(x) \equiv Y_c\delta_N = \left[\frac{4k_1\mu_1\Delta\mathcal{T}x}{g\rho_1(\rho_1-\rho_2)h_{fg}}\right]^{1/4}$$

$$u_1(x,y) \equiv Uu_1(x,y) = \frac{g(\rho_1-\rho_2)\Delta_N^2}{\mu_1}\left[\frac{y}{\Delta_N} - \frac{1}{2}\left(\frac{y}{\Delta_N}\right)^2\right]$$

$$\theta_1(x,y) = \theta_w + \frac{\theta_s-\theta_w}{\delta}y$$

$$\bar{\omega}_1(x) \equiv \frac{1}{\Delta}\int_0^{\Delta} \omega_1 \, dy = \frac{g(\rho_1-\rho_2)[\Delta_N(x)]^2}{3\mu_1}$$

$$\mathrm{Re}_1(x) \equiv \frac{\rho_1 g(\rho_1-\rho_2)[\Delta_N(x)]^2 x}{3\mu_1} \text{ and}$$

$$\mathrm{Re}_\delta(x) \equiv \frac{4\rho_1 U \Delta_N(x)}{\mu_1} \tag{14}$$

3 Computational Approach

Most of the details of the 2D steady/unsteady approach are the same as described in Narain et al. [3], Liang et al. [4], and Liang [5]. However, unlike the internal condensing flows considered in the earlier papers, the external condensing flow of this paper employs a different computational approach for the implementation of the pressure boundary condition described in Eq. (9). Since the boundary conditions that need to be imposed along lines AB, BC, and CD in Fig. 1 are much like prescribing the shear and pressure on the interface, the "tau-p" approach for the interface (see "tau-p" method described in Liang [5], Narain et al. [3], and Yu [21])—instead of other available approaches [22]—was adapted to satisfy the boundary conditions in Eq. (9).

The solutions' convergence in the interior of each phase, grid independence, and satisfaction of interface and boundary conditions are better (i.e., within 5%—see a representative case in Table 2) than what were reported (within 7% on average) in [3–5]. On any interface with propagating waves, the critical and difficult to satisfy requirement is Eq. (7)—the requirement of the equality of three differently computed/obtained values of interfacial mass flux (this is known to be difficult for the more general interface capturing techniques such as level set [23] or Volume of Fluid [24]). However, this requirement is met by the interface tracking approach employed in this paper (see Table 2). As shown in [3,4], one of the interface conditions [viz. $\dot{m}_{LK}=\dot{m}_{\mathrm{Energy}}$ in Eq. (7)] yields the interface tracking equation that is used in this paper. This equation is of the hyperbolic form:

$$\frac{\partial \delta}{\partial t} + \bar{u}(x,t)\frac{\partial \delta}{\partial x} = \bar{v}(x,t) \tag{15}$$

where the characteristic speed is $\bar{u} \equiv u_1^i + \{\mathrm{Ja}/(\mathrm{Re}_1\,\mathrm{Pr}_1)\}\partial\theta_1/\partial x|^i$ and the forcing function is $\bar{v} \equiv v_1^i + \{\mathrm{Ja}/(\mathrm{Re}_1\,\mathrm{Pr}_1)\}\partial\theta_1/\partial y|^i$. The spatial and temporal grid spacings and total lengths impose a restriction on wavelength λ and frequency f that can be adequately resolved. If the maximum spacing of the grid in the x direction is Δx_m and its total length is x_e while the total time duration is t_e and is divided in equal intervals of duration Δt; the restrictions imposed by Nyquist criteria [25] are well satisfied for $\lambda \geqslant 4\Delta x_m$ and $f \leqslant (4\Delta t)^{-1}$ and the restrictions imposed by the domain lengths are well satisfied for $\lambda \leqslant x_e/2$ and $f \geqslant 2/t_e$. The initial ($t=0$) spatial and temporal grids are defined by ($n_i \times n_j \times n_t$), where n_i is the total number of initial grid points along x, n_j is the total number of initial grid points along y (0 to 1), and n_t is number of time steps with equal intervals (Δt). Typical values of n_i (and n_j) used were 30–40 (and 50–70) for typical maximum values of x (and y) of 50 (and 1). Attainable values of n_t depend on n_i, n_j, Δt, and the available computer memory for the storage of flow variables. For the cases reported here, typical maximum $n_t \times \Delta t$ ($=t$) values are in the range from 30×5 (=150) to 36×7.5 (=270).

Table 1 Specification of a flow situation involving saturated R-113 (ASHRAE [26])

p_o (kPa)	$\mathcal{T}_s(p_o)$ (°C)	$\Delta\mathcal{T}$ (°C)	ρ_2/ρ_1	μ_2/μ_1	We	Pr_1
108.85	49.5	5	0.005	0.020	67.9	7.3

4 Computational Results

4.1 Simulation Results for the Steady Problem. The classical Nusselt solution [1] was improvised by Rohsenow et al. [6] to account for the effects of the neglected convection term in the energy equation. Subsequently, Sparrow and Gregg [7] and Koh et al. [9] accounted for the effects of convection and inertia terms within the framework of the boundary layer and small slope approximations ($\partial/\partial x \ll \partial/\partial y$ and $\delta'^2 \ll 1$) of the governing equations.

For a specific case (see Table 1 and [26]), Figure 2(a) demonstrates not only the ability of our computational approach to solve the problem as posed by the Nusselt formulation [1] but, also, to solve the full steady problem without the Nusselt approximations. Since a significant amount of parametric study has already been done (see [7,9], etc.) for this problem, no parametric study has been done here. This is because this paper limits itself to a qualitative understanding of the steady base flow and has a greater focus on an understanding of the superimposed wave effects.

In Fig. 2(a) and its inset, for the conditions described in Table 1, "Curve 1" represents the classical analytical solution of Nusselt plotted as $\delta \equiv \Delta_N/Y_c$ against $x \equiv x/Y_c$, where Δ_N is defined in Eq. (14). "Curve 2" represents the solution under all Nusselt approximations except one—namely, in the interior equations, "$\partial/\partial x$" terms have been retained. "Curve 3" is for the case which retains the negligible vapor viscosity and negligible vapor motion assumptions (resulting in $\partial u_1/\partial y|^i = 0$ and $\pi_2^i = 0$) but does not neglect liquid inertia and convection. "Curve 4" is for the full problem—discussed below for "Curve 5"—except that the surface tension term on the right side of Eq. (3) has been dropped. Curve 5 is for the full steady problem posed by Eqs. (A1)–(A4) under interface conditions (2)–(8) and boundary conditions (9) and (10). The effects of the presence or absence of surface tension, as shown in Figs. 2(c) and 2(e), are negligible on the motion of the vapor but are noticeable on the interfacial values of the pressures

Table 2 Representative interfacial values of nondimensional variables show satisfaction of *all* interface conditions (for flow exposed to initial disturbance with $\varepsilon=0.7$ and $\lambda_o=15$) because appropriate contiguous columns are nearly equal to one another—as required by Eqs. (2)–(4), (7), and (8)

x	$\dot{m}_{LK}$	$\dot{m}_{VK}$	$\dot{m}_{\mathrm{Energy}}$	π_1^i	$\rho_2/\rho_1\pi_2^i$+terms	u_1^i	u_2^i	τ_1^i	τ_2^i	θ_1^i	θ_2^i
4	5.37E−05	5.33E−05	5.34E−05	1.86E−04	1.86E−04	1.15E−02	1.15E−02	0.009621	0.009621	64.53	64.53
8	3.55E−05	3.52E−05	3.53E−05	−2.22E−06	−2.22E−06	2.96E−02	2.96E−02	0.013676	0.013676	64.53	64.53
12	3.09E−05	3.07E−05	3.05E−05	−2.00E−06	−2.00E−06	4.29E−02	4.29E−02	0.005415	0.005415	64.53	64.53
16	2.77E−05	2.73E−05	2.74E−05	9.88E−07	9.88E−07	5.36E−02	5.36E−02	0.030117	0.030117	64.53	64.53
20	2.33E−05	2.31E−05	2.35E−05	−1.64E−06	−1.64E−06	6.76E−02	6.76E−02	0.004087	0.004087	64.53	64.42
24	2.41E−05	2.41E−05	2.46E−05	5.57E−07	5.57E−07	6.34E−02	6.34E−02	0.011717	0.011717	64.53	64.53

Note: terms $= -\frac{1}{\mathrm{We}}\left(\frac{\delta_{xx}}{[1+\delta_x^2]^{3/2}}\right) + \dot{m}^2\left(\frac{\rho_1}{\rho_2}-1\right)$.

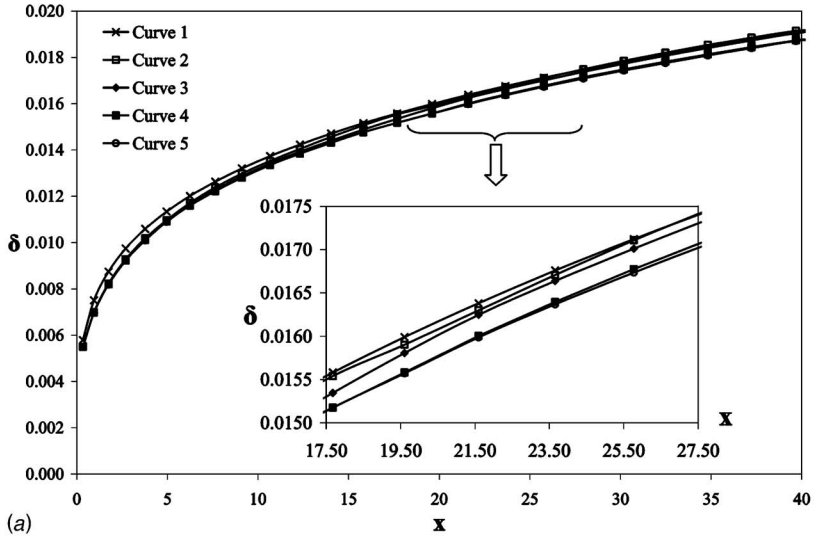

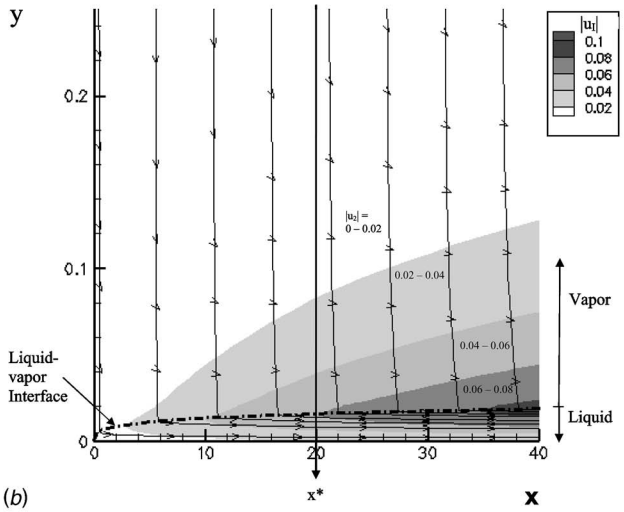

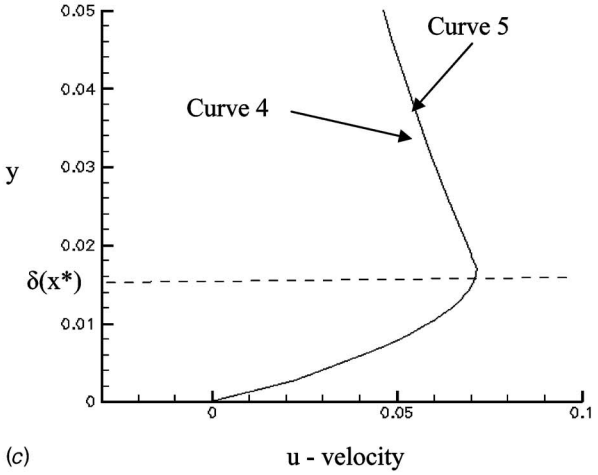

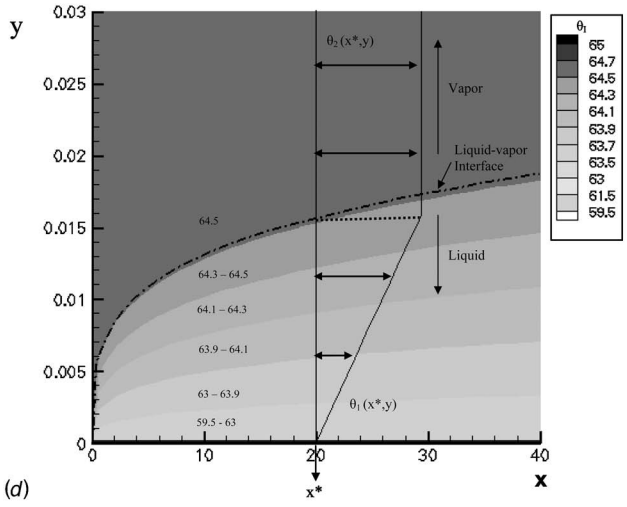

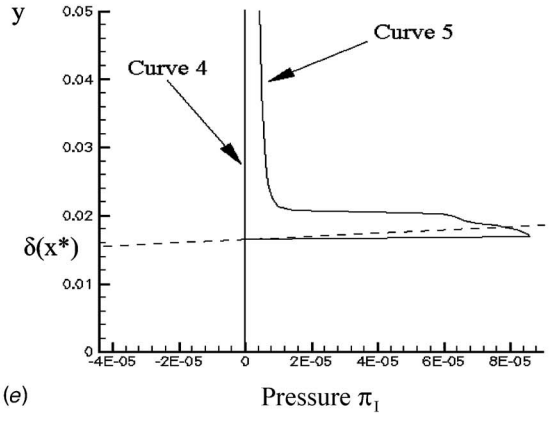

Fig. 2 (*a*) **For the case of R-113 (see Table 1) experiencing film condensation on a vertical plate, the figure above shows steady film thickness values under different approximations. Here,** $x_c = X_c / Y_c = 50$ **and** $c = Y_c / \Delta_N(X_c) = 47$**.** (*b*) **For the case of R-113 (see Table 1) experiencing film condensation on a vertical plate, the figure above shows the streamline pattern and contour zones depicting a range of** $|u_l|$ **values.** (*c*) **For Curves 4 and 5 of the base flow in** (*a*)**, the figure above shows the** $u(x^*, y)$ **versus** y **for** $x^* = 20$**.** (*d*) **For the case of R-113 (see Table 1) experiencing film condensation on a vertical plate, the figure above shows the contour zones for temperature and a representative plot of** $\theta_l(x^*, y)$ **for** $x^* = 20$**.** (*e*) **For Curves 4 and 5 of the base flow in** (*a*)**, the figure above shows the** $\pi_l(x^*, y)$ **versus** y **for** $x^* = 20$**.**

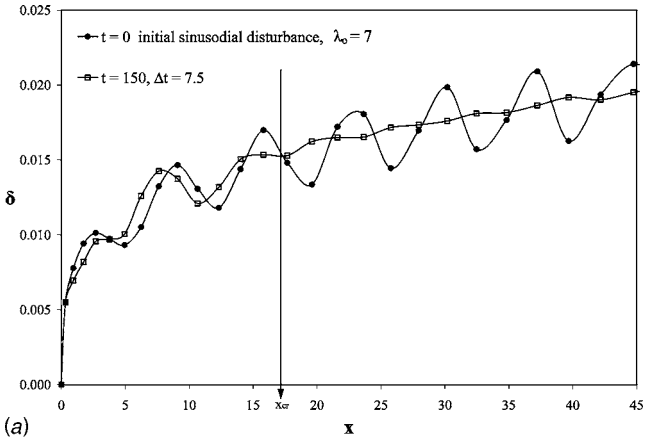

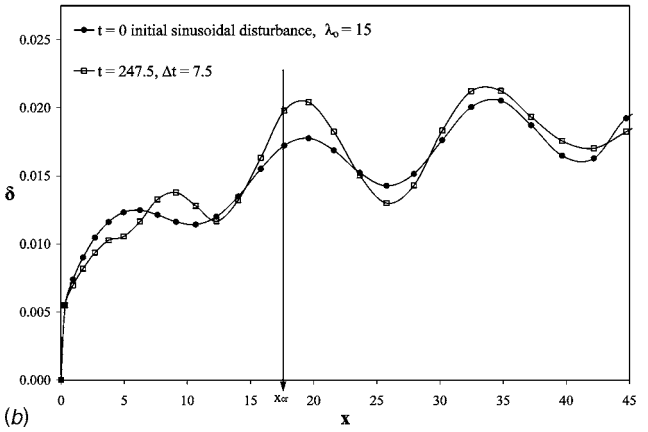

Fig. 3 (*a*) For the base flow in Fig. 2(*a*), the figure above shows the stable response (Δt=7.5, t=150) of the film thickness $\delta(x,t)$ as a result of an initial disturbance $\delta(x,0) = \delta_{steady}(x)\ [1+\varepsilon\delta'(x,0)]$, where $\delta'(x,0) \equiv \sin(2\pi x/\lambda_o)$, ε=0.15 and λ_o=7. (*b*) For the base flow in Fig. 2(*a*), the figure above shows the unstable response (Δt=7.5, t=247.5) of the film thickness $\delta(x,t)$ as a result of an initial disturbance $\delta(x,0) = \delta_{steady}(x)\ [1+\varepsilon\delta'(x,0)]$, where $\delta'(x,0) \equiv \sin(2\pi x/\lambda_o)$, ε=0.15 and λ_o=15.

π_2^j.

Generally, for all the cases considered here, the Jacob number (Ja) is small and hence all predictions of $\delta(x)$ are within 2.5% of the Nusselt solution.

4.2 Simulation Results for the Unsteady Problem.

4.2.1 Nonlinear Stability and the Effects of Initial Disturbances. The stable response of the flow in Fig. 2(*a*) to an initial sinusoidal disturbance of wavelength λ=7 is shown in Fig. 3(*a*). Here, by stability, it is meant that as waves travel forward to downstream locations, the amplitudes of the waves diminish—with respect to the initial amplitude. Similarly, by instability, it is meant that as waves travel forward to downstream locations, the amplitudes of the waves increase and become significantly larger than the initial amplitudes. Figure 3(*b*) shows an unstable response of the flow in Fig. 2(*a*) to an initial sinusoidal disturbance of wavelength λ=15. Clearly, in Figs. 3(*a*) and 3(*b*), the stability/instability phenomena manifests only after a certain downstream distance marked by $x=x_{cr}$. As indicated by the dual labeling of the x axis in Fig. 4, for any given flow, there is a one to one correspondence between $\mathrm{Re}_\delta(x)$ and $\mathrm{Re}_1(x)$, and, therefore, between $\mathrm{Re}_\delta|_{cr}$ and $\mathrm{Re}_1|_{cr}$ where $\mathrm{Re}_\delta|_{cr} \equiv \mathrm{Re}_\delta(x=x_{cr})$.

Figure 4 shows the general response, at t=247.5 of the flow in Fig. 2(*a*) to initial disturbances of various wavelengths—viz. λ=5, 9, 15, and 23. Generally, for $\lambda < \lambda_{cr}$ (here, $\lambda_{cr} \cong 11.5$), the response is stable and for $\lambda > \lambda_{cr}$, the response is unstable. The larger wavelength waves are clearly manifested for $x > x_{cr} \approx 18$ (i.e., $\mathrm{Re}_1(x) > \mathrm{Re}_1|_{cr}=7$ or, equivalently, $\mathrm{Re}_\delta > \mathrm{Re}_\delta|_{cr} \approx 28$).

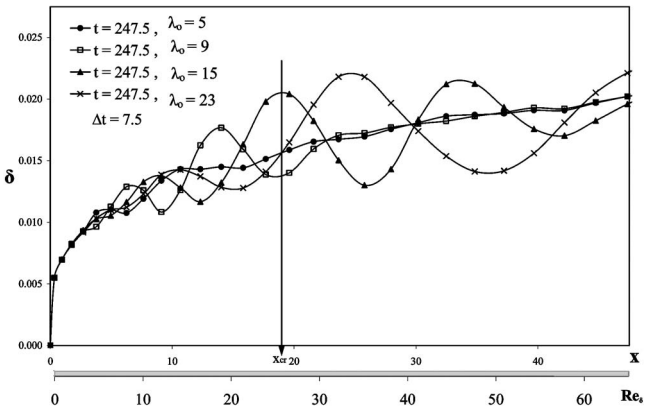

Fig. 4 For the base flow in Fig. 2(*a*), the figure above shows the stable and unstable response (Δt=7.5, t=247.5) of the film thickness $\delta(x,t)$ as a result of an initial disturbance $\delta(x,0) = \delta_{steady}(x)\ [1+\varepsilon\delta'(x,0)]$, where $\delta'(x,0) \equiv \sin(2\pi x/\lambda_o)$, ε=0.15 and λ_o=5, 9, 15, and 23

4.2.2 Effects of Surface Tension. The above described instability mechanisms—of the Tollmien-Schlichting [16] type—are only mildly affected by surface tension. Figure 5 shows that the waves are gravity dominated and surface tension effects are negligible. For the flow considered in Fig. 5, cases $\sigma=\sigma^*$ and $\sigma=2.5\sigma^*$, when compared to the σ=0 case, indicate that surface tension only slightly assists in steepening the front of the wave.

4.2.3 Computed Values of $\mathrm{Re}_\delta|_{cr}$. A compilation of various experimental results (see Incropera and DeWitt [2] and Kutateladze [18]) for steam and common refrigerants have led to the commonly used estimate of $\mathrm{Re}_\delta|_{cr} \approx 30$ and a subsequent laminar-to-turbulence transition regime that is characterized by $30 \leqslant \mathrm{Re}_\delta|_{cr} \leqslant 1800$. It is found that in the parameter set in Eq. (12), ρ_1 and μ_1, are important parameters affecting the value of $\mathrm{Re}_\delta|_{cr}$ because of their appearance in the definition of Re_1 and in the nondimensionalization process itself (e.g., $\dot{m} \equiv \dot{m}/\rho_1 U$). However, the remaining nondimensional parameters such as ρ_2/ρ_1, μ_2/μ_1, etc., are unimportant because, as shown later in Fig. 8,

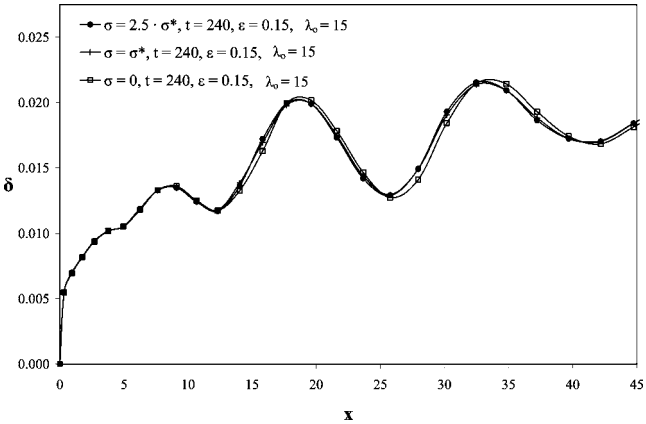

Fig. 5 For the base flow in Fig. 2(*a*), the figure above shows the effect of surface tension at the interface (Δt=7.5) on the flow exposed to initial disturbance $\delta(x,0) = \delta_{steady}(x)\ [1+\varepsilon\delta'(x,0)]$, where $\delta'(x,0) \equiv \sin(2\pi x/\lambda_o)$, ε=0.15 and λ_o=15

Table 3 Effects of changes in $\Delta\mathcal{T}$

$\Delta\mathcal{T}$	x_{cr}	Re_δ
5	19.6	27.72
10	10.7	29.54
15	7.64	31.15
20	6.25	33.27

Note: All fluids considered here have $\rho_2/\rho_1=0.00525$, $\mu_2/\mu_1=0.0289$, We $=402.133$, and $\mathrm{Pr}_1=7.223$.

vapor motion does not significantly influence the wave phenomena. In addition, Table 3 shows that effects of changes in $\Delta\mathcal{T}$ are small on the values of $\mathrm{Re}_\delta|_{cr}$ but not on x_{cr}.

Since, for common fluids, an increase in ρ_1 typically accompanies an increase in μ_1, typical changes in the kinematic viscosity ν_1 $(\equiv\mu_1/\rho_1)$ values for nonmetallic vapors are limited. For this reason, as shown in Table 4, the changes in $\mathrm{Re}_\delta|_{cr}$ with the changes in the fluid are not much and $\mathrm{Re}_\delta|_{cr}$ remains in the 27–35 range. This justifies the continued use of the estimate $\mathrm{Re}_\delta|_{cr}\approx 30$. However, for uncommon or specially designed fluids, one may be able to change ρ_1 without significantly changing μ_1 (Table 5) or change μ_1 without significantly changing ρ_1 (see Table 6). Under these special conditions, one can expect a more significant departure from "30" in the estimated value of $\mathrm{Re}_\delta|_{cr}$ (e.g., in Table 6, one finds a case for which $\mathrm{Re}_\delta|_{cr}\approx 9$).

4.2.4 Comparison of Exact Nonlinear Stability Analyses Results Presented Here With the Known Linearized Stability Results. Linearized stability analyses and associated results by Unsal and Thomas [14] and Spindler [15] for the Nusselt solution are available in the literature. However their results, though mutually compatible, are not compatible with the above described experimental estimates of $\mathrm{Re}_\delta|_{cr}\approx 30$. Subsequent attempts at nonlinear analysis for this problem (see, e.g., Unsal and Thomas [17]) indicate the partially correct view that the instabilities predicted by linear analyses are not going to work and the problem needs some sort of non-linear analysis.

To facilitate a comparison with the known results, we present here, for the first time, the nearly exact nonlinear stability analyses and associated results. It should be noted that the predictions of the time dependent disturbances $\delta'(x,\tau)=\delta(x,t)-\delta_{\mathrm{steady}}(x)$ in Figs. 3 and 4, associated with an initial nonzero disturbance $\delta'(x,0)$, are obtained by nearly exact nonlinear simulations (see Table 2 for representative satisfaction of all the interface conditions) and, therefore, these simulations are capable of providing good results from the point of view of both linear and nonlinear stability analyses. The initial disturbances in Figs. 3 and 4 are sinusoidal in nature and are given by the relation:

$$\delta'(x,0)=\varepsilon\cos\theta(x,0)\equiv\varepsilon\cos\left\{\frac{2\pi}{\lambda_o}(x-x_o^*)\right\},\qquad(16)$$

over a suitable range of x values with $\varepsilon>0$ and $x=x_o^*$ being a location where the phase angle $\theta(x,0)$ corresponds to a positive peak and is defined to be zero.

The time evolution $\delta'(x,t)$ of the initial disturbance in Eq. (16)

Table 4 Effects of changes in viscosity ($\nu_1=\mu_1/\rho_1$)

ρ_1	μ_1	$\nu_1=\mu_1/\rho_1$	Fluid name for same ν_1	x_{cr}	Re_δ
1225	0.000199	1.62204E−07	R 12	5	31.93
989.4	0.000577	5.83485E−07	Water	20	25.2
1508.8	0.000519	3.44168E−07	R 113	19.6	27.72

Note: All fluids considered here have $\rho_2/\rho_1=0.00525$, $\mu_2/\mu_1=0.0289$, We $=402.133$, and $\mathrm{Pr}_1=7.223$.

Table 5 Effects of changing ρ_1 without significantly changing μ_1

ρ_1	μ_1	x_{cr}	Re_δ
2262	5.19E−03	15.8	28.91
1885	5.19E−03	17.4	28.35
1508	5.19E−03	19.6	27.72
1206.4	5.19E−03	19.6	24.77
1005.3	5.19E−03	17.77	22.6

Note: All fluids considered here have $\rho_2/\rho_1=0.00525$, $\mu_2/\mu_1=0.0289$, We $=402.133$, and $\mathrm{Pr}_1=7.223$.

can be characterized by a sinusoidal Fourier component—associated with the disturbance in Eq. (16)—and is given as:

$$\delta'(\mathbf{x},t)=a(t)\cdot\cos\theta(x,t)\qquad(17)$$

However the linear and nonlinear stability analyses of condensing flow in the literature [14–17] and other air-water free-surface flows (see [27]) make the common, but restrictive, assumption that Eq. (17) can have a special simplified form, viz.

$$\delta'(x,t)=\mathrm{Re}\{\varepsilon\exp[\mathbf{i}\alpha\cdot(x-Ct)]\}\qquad(18)$$

where $\alpha\equiv 2\pi/\lambda_0$ is a wave number (with λ_0 being the constant wavelength) independent of x, "$\mathbf{i}$" is the complex number $\sqrt{-1}$, and $C\equiv C_r+\mathbf{i}\cdot C_i$ is a complex number dependent only on wavelength λ_0 (or wave number α). This means that the popular analyses restrict the amplitude and phase-angle variations in Eq. (17) to:

$$a(t)=\varepsilon\exp(\alpha C_i t)\ \text{and}$$

$$\theta(x,t)\equiv\alpha(x-C_r t)\qquad(19)$$

The restriction in Eq. (19) is particularly severe for free surface problems (such as this problem and other air/water and evaporating flow free-surface problems) because, as shown in Eq. (27) of Narain et al. [3], the equation governing $\delta'(x,t)$ is given by:

$$\frac{\partial\delta'}{\partial t}+\bar{u}\frac{\partial\delta'}{\partial x}=\bar{\bar{v}}\qquad(20)$$

where $\bar{\bar{v}}(x,t)\equiv\bar{v}(x,t)-\bar{v}_{\mathrm{steady}}(x)-\{\bar{u}-\bar{u}_{\mathrm{steady}}(x)\}d\delta_{\mathrm{steady}}/dx$, $\bar{v}(x,t)\equiv v_1^i+\mathrm{Ja}/\mathrm{Re}_1\mathrm{Pr}_1(\partial\theta_1/\partial y|^i)$, as per its definition in Eq. 27 of [3].

As a result of the above, it is easy to see that waves travel along a family of characteristics curves $x=x_c(t)$, where $x_c(t)$ satisfies Eq. (25) of [3]. That is:

$$\frac{dx_c}{dt}=\bar{u}[x_c(t),t]$$

$$x_c(0)=x^*\ \text{or}\ x_c(t^*)=0\qquad(21)$$

where x^* is any given value of $x^*>0$ and t^* is any given time $t>0$. For the no disturbance $[\bar{u}(x,t)\cong\bar{u}_{\mathrm{steady}}]$ and large disturbance

Table 6 Effects of changing μ_1 without significantly changing ρ_1

ρ_1	μ_1	x_{cr}	Re_δ
1508.8	1.04E−02	14	9.06
1508.8	7.79E−03	15.8	14.22
1508.8	5.19E−03	19.6	27.72
1508.8	3.46E−03	12.3	32.5
1508.8	2.60E−03	8.5	35.22

Note: All fluids considered here have $\rho_2/\rho_1=0.00525$, $\mu_2/\mu_1=0.0289$, We $=402.133$, and $\mathrm{Pr}_1=7.223$.

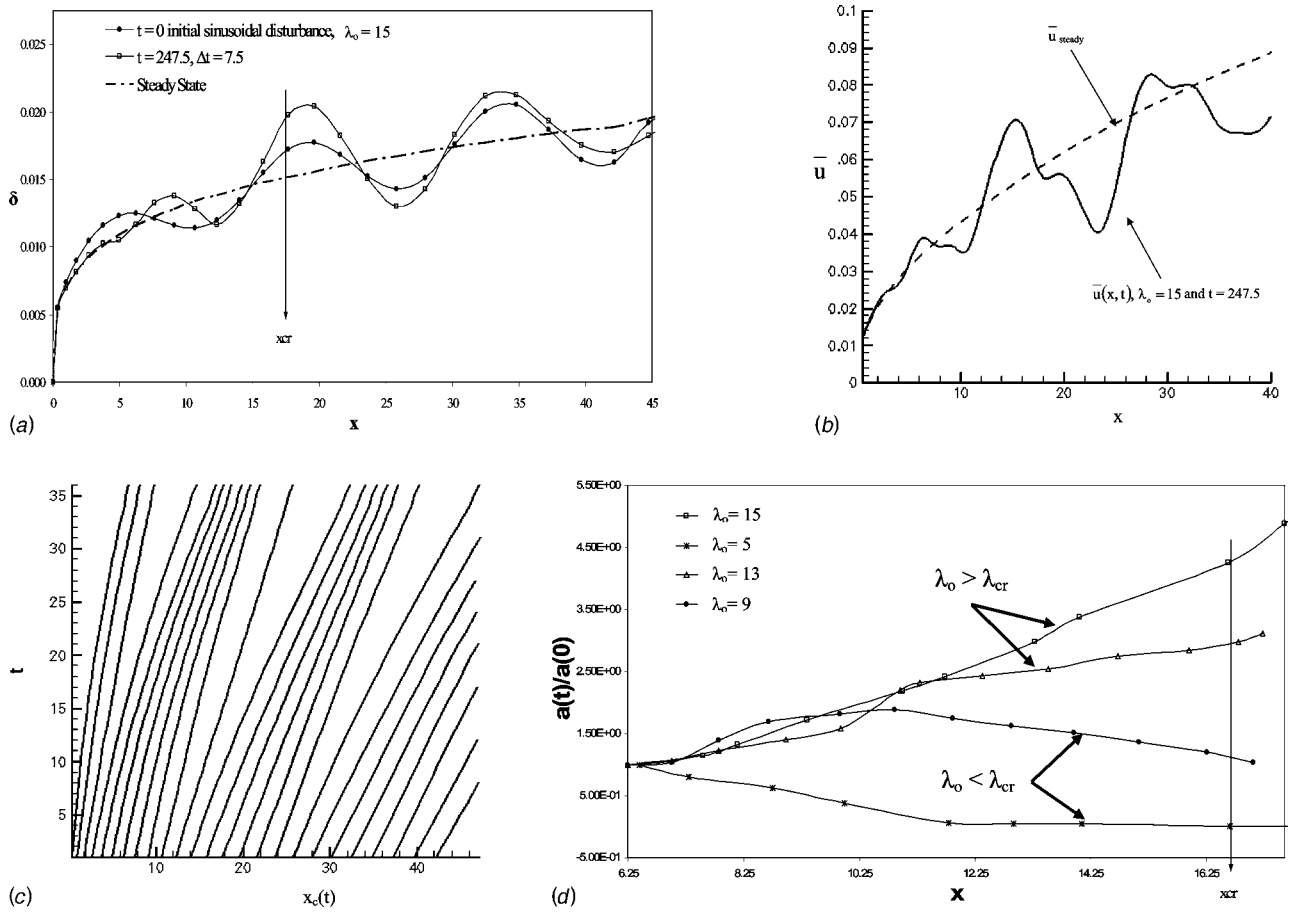

Fig. 6 (*a*) **For the base flow in Fig. 2(*a*) and initial disturbances defined in Fig. 3, the figure above shows the unstable response (Δt=7.5, t=247.5), for $\lambda_o > \lambda_{cr}$, of the film thickness $\delta(x,t)$ as a result of an initial disturbance $\delta(x,0)=\delta_{steady}(x)\,[1+\varepsilon\delta'(x,0)]$, where ε=0.15 and λ_o=15. (*b*) For the case shown in (*a*), the figure above shows the values of characteristic speed $\bar{u}$ (steady value at t=0 and disturbed value at t=247.5) as function of x. (*c*) For the case shown in (*a*), the figure above shows the characteristic curves found by solving Eq. (21) through a fourth-order Runge-Kutta method. (*d*) For the cases shown in (*a*)–(*c*), the figure above shows values of $a(t)/a(0)$ for different values of initial disturbance wavelength λ_o for $x_c(t)$=6.65.**

cases shown in Fig. 6(*a*), representative plots of $\bar{u}(x,t)$ are shown in Fig. 6(*b*). The linearized stability analyses assumption leading to Eq. (19) is $\bar{u}(x,t)=C_r(\lambda_0)$, where λ_0 is independent of x. The plots in Fig. 6(*b*) clearly indicate that $\bar{u}(x,t)\neq C_r(\lambda_0)$ and hence this linearized stability assumption is not appropriate. Furthermore, this assumption implies that the characteristics governing the problem are a set of *parallel* straight lines $[x_c=x_c(0)+C_r(\lambda_0)t]$. However, a fourth-order Runge-Kutta solution of Eq. (21) for $\bar{u}=\bar{u}_{steady}$ or $\bar{u}(x,t)$ leads to a set of characteristics whose slopes either change gradually with x (this is the case when $\bar{u}=\bar{u}_{steady}$) or have some superimposed oscillations on these gradually varying slopes [as shown for, $\bar{u}=\bar{u}(x,t)$, in Fig. 6(*b*)]. The characteristics associated with $\bar{u}=\bar{u}(x,t)$ in Fig. 6(*b*) are shown in Fig. 6(*c*). Clearly, the actual characteristics do not agree with the linearized stability assumption of them being a set of parallel straight lines.

In fact, with $\delta'(x,0)$ given by Eq. (16), it is easily seen that the characteristics speed $\bar{u}$ in Eq. (21) is also the phase-speed and waves traveling along the characteristics have a constant phase-angle $\theta(x,t)$, provided $\theta(x,t)$ is given by:

$$\theta(x,t)=\frac{2\pi}{\lambda_o}\left\{x-x_o^*-\int_0^t \bar{u}[x_c(\tau),\tau]\cdot d\tau\right\} \tag{22}$$

where $x_c(\tau)$ is the characteristic $(0\leqslant\tau\leqslant t)$ which, at time t, passes through the point x and thus satisfies $d\theta/dt=0$ along a characteristic $x=x_c(t)$. Also, Eq. (22) is compatible with the correct phase angle associated with the initial (at t=0) disturbance in Eq. (16). Therefore, all along $x_c(\tau)$ $(0\leqslant\tau\leqslant 0)$, we have $\theta(x,t)=\theta[x_c(\tau),\tau]=\theta[x_c(0),0]=2\pi/\lambda_o[x_c(0)-x_o^*]$=constant.

Substitution of Eq. (22) in the definition of local wavelength $\lambda(x,t)\equiv 2\pi[\partial\theta/\partial x]^{-1}$ and local time-period $T(x,t)\equiv -2\pi[\partial\theta/\partial t]^{-1}$ (see Eq. 1.28 in [28]) imply nonconstant wavelengths (unlike the assumption in linear stability analyses) and frequencies (or time periods T) given by:

$$\lambda(x,t)=\lambda_o\left[1-\int_0^t \frac{\partial\bar{u}}{\partial x}[x_c(\tau),\tau]d\tau\right]^{-1}$$

$$\text{and } T(x,t)=\lambda(x,t)/\bar{u}(x,t) \tag{23}$$

Also, substitution of Eq. (17) [with $\theta(x,t)$ given by Eq. (22)] in to the governing equations [Eqs. (20) and (21)] imply that, along the characteristics, the amplitude $a(t)$ grows according to the equation:

$$\frac{da}{dt}=\frac{1}{\cos\{\theta[x_c(0),0]\}}\hat{\bar{v}} \tag{24}$$

where $\hat{\bar{v}}\equiv\bar{v}[x_c(t),t]$ is the value of $\bar{v}$ in Eq. (20) along a characteristic curve. An integration of Eq. (24) along a characteristic yields:

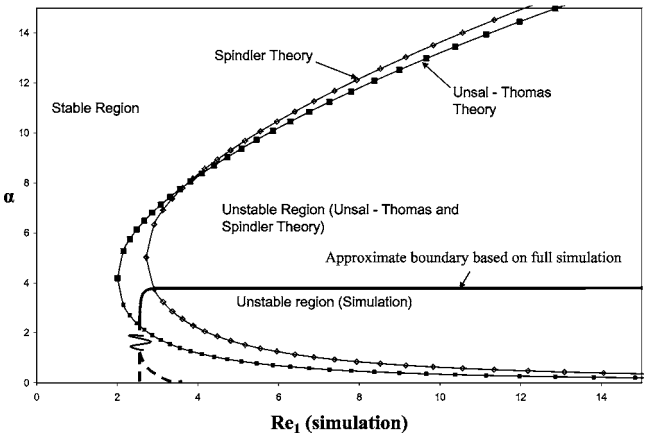

Fig. 7 Stability boundaries as obtained by Unsal and Thomas [14] and Spindler [15], and this work

$$\frac{a(t)}{a(0)} = 1 + \frac{1}{a(0)\cos\{\theta[x_c(0),0]\}} \cdot \int_0^t \hat{\bar{v}}(\tau) \cdot d\tau \qquad (25)$$

For the flow cases considered in Figs. 6(*a*)–6(*c*), a plot of "$a(t)/a(0)$" for different values of initial disturbance wavelength λ_o [see Eq. (16)], with $x_c(0)=6.65$, is shown in Fig. 6(*d*).

From Fig. 6(*d*), it is clear that the long time growth of $a(t)$ requires the full nonlinear analysis result in Eq. (25) and cannot be captured by the linearized stability assumption [14,15] of $a(t)$ being given by the exponential function in Eq. (19).

For the above reasons, for the flow considered in Figs. 6(*a*)–6(*d*), the simulation-based approximate stability boundary depicted in Fig. 7 is far more trustworthy (it is compatible with the experimental estimate on $\mathrm{Re}_\delta|_{cr} \cong 30$) than the Unsal [14] and Spindler [15] results, based on the inappropriate assumptions in Eqs. (18) and (19).

It should be further noted that the nonlinear instability mechanisms illustrated by the full nonlinear solutions in Fig. 4—besides being in agreement with experiments regarding $\mathrm{Re}_\delta|_{cr} \approx 30$—also show two other regularities. These regularities are: (i) As shown in Fig. 8 and its caption, the vapor motion or its fluctuations do not play a significant role in the evolution of gravity dominated waves, and (ii) the results in Fig. 5 indicate negligible impact of surface tension and this is consistent with experimental results but

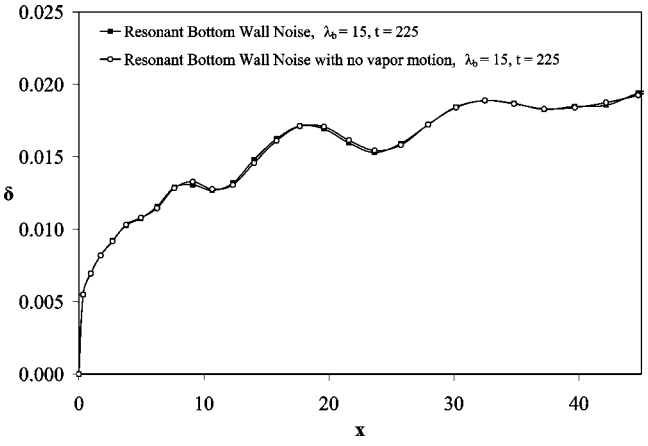

Fig. 8 Result showing waves while accounting for vapor motion and its fluctuations and, also, while neglecting vapor motion and its fluctuations (by not incorporating vapor domain calculations in the simulations). Here, Δt=7.5 and ε_b=0.15 *E*-05.

not with the linearized stability theory's result of a strong dependence of x_{cr} on the presence or absence of surface tension ⟨see Eq. (32) in [14] that states $x_{cr} \sim \sigma^{4/11}$⟩.

4.2.5 Different Wave Mechanisms in Different Zones. As marked in Fig. 4, for $x < x_{cr}$, the initial disturbances may persist but the zone is considered stable because the growth of the waves is considered small. However, at longer lengths in Fig. 6(*d*), there is a loss of stability, that is, amplitudes for $\lambda_o > \lambda_{cr}$ are eventually sufficiently large. The largeness of amplitude $a(t)$ is defined here to mean that, for $x > x_{cr}$, $a(t)/a(0) \geqslant 2.5$ at large t and, at the same time, the peaks of the resulting disturbances are off by more than 15% of the initial undisturbed film thickness values at the current locations of the waves (see Fig. 4). In the above definition of x_{cr}, the large amplitude waves at $x > x_{cr}$ (see Fig. 4) arise from initial disturbances at $x \sim 0$, where their amplitudes are sufficiently small (less than 10% of the small steady film thickness at $x \sim 0$). Another feature of x_{cr} being defined this way is that for $\lambda_o < \lambda_{cr}$, the amplitude ratio $a(t)/a(0)$ is eventually less than 1,0 [i.e., $a(t)/a(0) < 1$] at large t. Under the above definition, the longer length flows lose stability for $\mathrm{Re}_\delta \geqslant \mathrm{Re}_\delta|_{cr} \approx 30$.

The wall noise is assumed to be a superposition of standing waves of the form given by:

$$v_1(x,0,t) = \varepsilon_b \sin(2\pi x/\lambda_b)\sin(2\pi t/T_b) \qquad (26)$$

As shown in [3], one expects a resonance condition to hold if the time period of oscillations T_b in the wall noise of Eq. (26) is such that the forward travelling component of the standing noise has approximately the same phase-speed as $\bar{u}(x,t)$ (which is nearly equal to $\bar{u}_{steady}$ for small amplitude interfacial waves). This means, for resonance with large amplitude waves, $T_b = T_b(x,t)$ must satisfy:

$$\frac{\lambda_b}{T_b(x,t)} = \bar{u}(x,t) \cong \bar{u}(x,t-\Delta t) \qquad (27)$$

or $T_b = T_b(x)$ must satisfy:

$$\frac{\lambda_b}{T_b(x)} = \bar{u}_{steady}(x) \qquad (28)$$

For nonresonant single frequency (T_b=constant) wall noise, as shown in Figs. 9(*a*) and 9(*b*), depending on the value of T_b, one may have either a negligible (if T_b is nowhere in the resonant range) or a constructive (if T_b is somewhere in the resonant range) interference between wall noise and intrinsic waves. As shown in Fig. 10(*a*), for the unstable $\lambda_b = 15 > \lambda_{cr}$ case (where λ_{cr} is same as the one obtained from the earlier initial disturbance analysis), the resonant wall noise [in the sense of Eqs. (27) and (28)] interacts with the intrinsic waves and sustains a large amplitude travelling wave. Differently, but interestingly, as shown in Fig. 10(*b*), for the damped or stable $\lambda_b = 5 < \lambda_{cr}$ case, the resonant bottom wall noise governed by Eq. (28) interacts with the intrinsic waves and sustains a travelling wave which "beats" in the sense that the noises are alternately damped over a period of time and then regained over a subsequent period of time.

The above shows that wave effects will, in general, be present. They may be intrinsic in the absence of wall noise (i.e., due to initial disturbances alone) or they may be interactive in the presence of wall noise. Furthermore, the extent of the wave effects on heat transfer rates and interfacial shear will, in general, remain nondeterministic unless, experimentally, one can use wall noise actuation to have a well-defined, enhanced, or diminished form of wave effects.

4.2.6 Impact on the Heat Transfer Rates and Shear Stress. Effect of waves on the wall heat transfer rate and wall shear stress, for the $\lambda > \lambda_{cr}$ initial disturbance case of Fig. 4, is shown in Figs. 11(*a*) and 11(*b*). This confirms the well known [2] fact that, in the presence of gravity-assisted drainage, intrinsic waves enhance

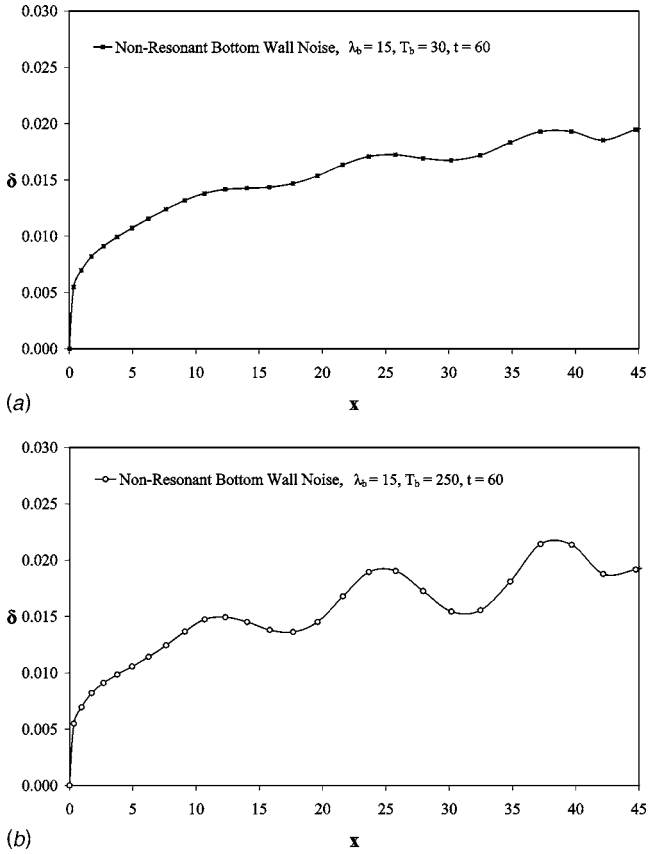

Fig. 9 (*a*) Nonresonance bottom wall noise that do not lead to growing waves. Here, Δt=7.5, ε_b=0.15 *E*-05, and T_b=30. (*b*) Nonresonance bottom wall noise that lead to growing waves. Here, Δt=7.5, ε_b=0.5 *E*-05 and T_b=250.

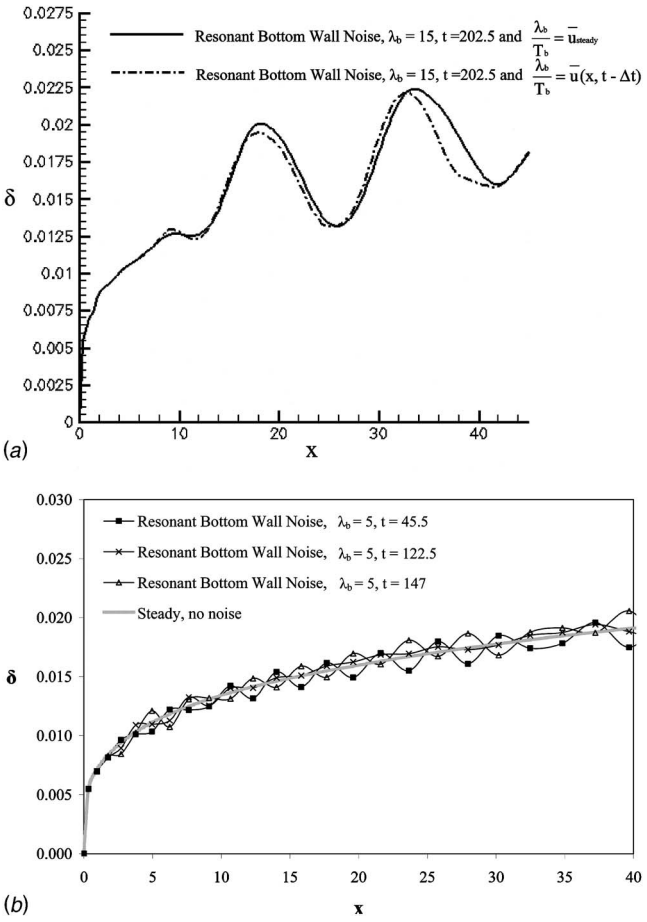

Fig. 10 (*a*) Effects of resonant noise for λ_b=15>λ_{cr} and with Δt=7.5 and ε_b=0.35 *E*-05. (*b*) Effects of resonant noise for λ_b =5<λ_{cr} and with Δt=7.5 and ε_b=0.5 *E*-05.

both of these important parameters. The extent of the heat transfer enhancements is typically found to be within the range (i.e. 1.2 times the values associated with smooth-interface heat transfer rates) suggested by empirical correlations (see [2,18]). This enhancement can be actively increased or reduced with the help of resonant or nonresonant wall noises.

5 Conclusions

- The computational approach presented here accurately solves the steady Nusselt problem and produces results in agreement with the Nusselt solution.
- The results considered thus far affirm the experimental result that instability mechanisms associated with laminar to turbulence transitions can typically be estimated to occur around $\mathrm{Re}_\delta|_{\mathrm{cr}} \approx 30$.
- The waves and the wave effects are quite sensitive to the presence or absence of the wall noise. This sensitivity to the frequency and wavelength spectrum of the wall noise can be exploited either to suppress or enhance the wave effects.
- As is well known for this problem, the results affirm that heat transfer rates and shear rates are significantly enhanced by the presence of waves.

Acknowledgment

This work was supported by NSF Grant No. CTS-0086988 and NASA Grant No. NNC04GB52G.

Nomenclature

X_c = distance from leading edge (BC in Fig. 1), m
Y_c = characteristics length (AB in Fig. 1), m
U = average liquid speed (Nusselt) at $x=X_c$, $g(\rho_1-\rho_2)\Delta_N^2(X_c)/3\mu_1$, m/s
(x,y,t) = physical distances (see Fig. 1) and physical time, (m, m, s)
(x,y,t) = nondimensional values of (x,y,t)
k = thermal conductivity, W/(m K)
C_p = specific heat, J/(kg K)
p = pressure, $\mathrm{N/m^2}$
p_o = pressure at the inlet, $\mathrm{N/m^2}$
(u,v) = values of x and y components of velocity, m/s
(u,v) = nondimensional values of u and v
$\mathcal{T}$ = temperature, K
$\Delta\mathcal{T}$ = temperature difference between the vapor and the wall, K
h_{fg} = latent heat (h_g-h_f), J/kg
Ja = Jacob number, $C_{p1}\Delta\mathcal{T}/h_{fg}$
$\mathrm{Re_I}$ = Reynolds number $\rho_1 U X_c/\mu_1$
$\mathrm{Re}_1(x)$ = Reynolds number $\rho_1 U x/\mu_1$
$\mathrm{Re}_\delta(x)$ = film Reynolds number $4\rho_1 U\Delta_N(x)/\mu_1$
$\mathrm{Pr_I}$ = Prandtl number $\mu_1 Cp_1/k_1$
Fr = Froude number U^2/gY_c
We = Weber number $\rho_1 U^2 Y_c/\sigma$
q''_w = bottom wall heat flux at any point and time, $\mathrm{W/m^2}$

Greek Symbols

π = nondimensional pressure
θ = nondimensional temperature

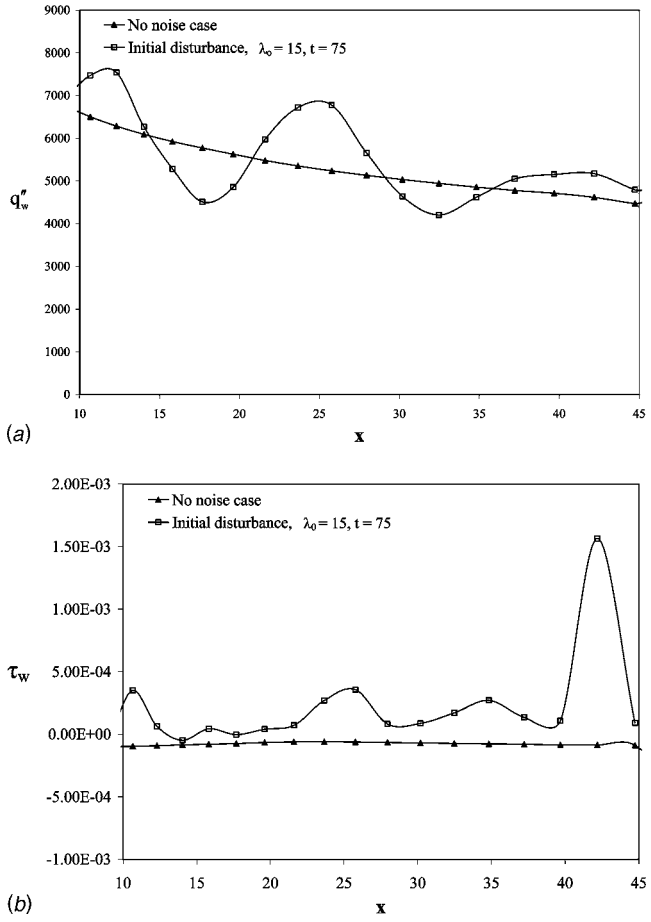

Fig. 11 (*a*) **For the base flow in Fig. 2(*a*), the figure above shows the wall heat flux (W/m^2) for cases with and without initial disturbance $\delta(x,0)=\delta_{steady}(x)\ [1+\varepsilon\delta'(x,0)]$, where $\delta'(x,0)\equiv\sin(2\pi x/\lambda_o)$, $\varepsilon=0.15$, $\lambda_o=15$, and $\Delta t=7.5$. (*b*) For the base flow in Fig. 2(*a*), the figure above shows the wall shear stress for cases with and without initial disturbance $\delta(x,0)=\delta_{steady}(x)\ [1+\varepsilon\delta'(x,0)]$, where $\delta'(x,0)\equiv\sin(2\pi x/\lambda_o)$, $\varepsilon=0.15$, $\lambda_o=15$, and $\Delta t=7.5$.**

ρ = density, kg/m^3
μ = viscosity, Pa s
Δ = physical value of condensate thickness, m
Δ_N = physical value of Nusselt film thickness at x, $[(4k_1\Delta T\mu_{1,x})/(h_{fg}\rho_1(\rho_1\text{-}\rho_2)g)]^{1/4}$, m
δ = nondimensional value of condensate thickness
ν = kinematic viscosity μ/ρ, m$^2/s$
σ = surface tension, N/m
ε = amplitude of nondimensional disturbances representing values of $\delta'(x,0)$
ε_b = amplitude of nondimensional bottom wall vibrations sensed through $v_1(x,0,t)$
λ = nondimensional wavelength
λ_o = nondimensional wavelength for the initial disturbance $\delta'(x,0)$
α = wave number, $2\pi/\lambda$

Subscripts

I = it takes a value of 1 for liquid phase and 2 for vapor phase
s = saturation condition
w = wall
b = bottom wall

Superscripts

i = value of a variable at an interface location

Appendix

The differential forms of mass, momentum (x and y components), and energy equations in terms of nondimensional variables for flows in the interior of either of the phases ($I=1$ or 2) for this external flow are given as

$$\frac{\partial u_I}{\partial x}+\frac{\partial v_I}{\partial y}=0 \tag{A1}$$

$$\frac{\partial u_I}{\partial t}+u_I\frac{\partial u_I}{\partial x}+v_I\frac{\partial u_I}{\partial y}=-\left(\frac{\partial \pi_I}{\partial x}\right)+\mathrm{Fr}_x^{-1}+\frac{1}{\mathrm{Re}_I}\left(\frac{\partial^2 u_I}{\partial x^2}+\frac{\partial^2 u_I}{\partial y^2}\right) \tag{A2}$$

$$\frac{\partial v_I}{\partial t}+u_I\frac{\partial v_I}{\partial x}+v_I\frac{\partial v_I}{\partial y}=-\left(\frac{\partial \pi_I}{\partial y}\right)+\mathrm{Fr}_y^{-1}+\frac{1}{\mathrm{Re}_I}\left(\frac{\partial^2 v_I}{\partial x^2}+\frac{\partial^2 v_I}{\partial y^2}\right) \tag{A3}$$

$$\frac{\partial \theta_I}{\partial t}+u_I\frac{\partial \theta_I}{\partial x}+v_I\frac{\partial \theta_I}{\partial y}\approx\frac{1}{\mathrm{Re}_I\,\mathrm{Pr}_I}\left(\frac{\partial^2 \theta_I}{\partial x^2}+\frac{\partial^2 \theta_I}{\partial y^2}\right), \tag{A4}$$

where $\mathrm{Re}_1\equiv\rho_1 U Y_c/\mu_1$, $\mathrm{Pr}_1\equiv\mu_1 Cp_1/k_1$, $\mathrm{Fr}_x^{-1}\equiv g_x Y_c/U^2$, and $\mathrm{Fr}_y^{-1}\equiv g_y Y_c/U^2$.

Under negligible inertia, negligible convection, and boundary layer ($\partial/\partial x \ll \partial/\partial y$) approximations for thin condensate, Nusselt formulation [1] effectively replaces, for $I=1$, (A2)–(A4) above by:

$$0\cong-\frac{\partial \pi_I}{\partial x}+\mathrm{Fr}_x^{-1}+\frac{1}{\mathrm{Re}_I}\frac{\partial^2 u_I}{\partial y^2}$$

$$0\cong-\frac{\partial \pi_I}{\partial y}+\mathrm{Fr}_y^{-1}$$

$$0\cong\frac{1}{\mathrm{Re}_I\,\mathrm{Pr}_I}\cdot\frac{\partial^2 \theta_I}{\partial y^2} \tag{A5}$$

For $I=2$, the additional Nusselt [1] approximation of negligible vapor viscosity and saturated vapor eliminates any consideration of vapor motion and vapor temperature variation for obtaining the steady liquid condensate solution. Therefore, one does not need to consider the vapor ($I=2$) Eqs. (A1)–(A4) in order to obtain the Nusselt ([1]) solution.

The term $[t]$ on the right side of Eq. (4) is given by:

$$[t]=\left\{\frac{\mu_2}{\mu_1}\frac{\partial v_2}{\partial x}\bigg|^i-\frac{\partial v_1}{\partial x}\bigg|^i\right\}+\frac{2\delta_x}{[1-\delta_x^2]}\left\{\frac{\partial u_1}{\partial x}\bigg|^i-\frac{\partial v_1}{\partial x}\bigg|^i\right\}-\frac{2\delta_x}{[1-\delta_x^2]}\frac{\mu_2}{\mu_1}\left\{\frac{\partial u_2}{\partial x}\bigg|^i-\frac{\partial v_2}{\partial y}\bigg|^i\right\} \tag{A6}$$

References

[1] Nusselt, W., 1916, Die Oberflächenkondesation des Wasserdampfes, Z. Ver. Dt. Ing., **60**(27), pp. 541–546.
[2] Incropera, F. P., and DeWitt, D. P., 1996, *Fundamentals of Heat and Mass Transfer*, 4th ed., Wiley, New York.
[3] Narain, A., Liang, Q., Yu, G., and Wang, X., 2004, "Direct Computational Simulations for Internal Condensing Flows and Results on Attainability/Stability of Steady Solutions, their Intrinsic Waviness and their Noise Sensitivity," ASME J. Appl. Mech., **71**, pp. 69–88.
[4] Liang, Q., Wang, X., and Narain, A., 2004, "Effect of Gravity, Shear, and Surface Tension in Internal Condensing Flows—Results From Direct Computational Simulations," ASME J. Heat Transfer, **126**(5), pp. 676–686.
[5] Liang, Q., 2003, "Unsteady Computational Simulations and Code Developments for a Study of Internal Film Condensation Flows Stability, Noise Sensitivity and Wavyness," Ph.D. thesis, Michigan Technological University.
[6] Rohsenow, W. M., 1956, "Heat Transfer and Temperature Distribution in Laminar Film Condensation," Trans. ASME, **78**, pp. 1645–1648.
[7] Sparrow, E. M., and Gregg, J. L., 1959, "A Boundary Layer Treatment of

Laminar Film Condensation," ASME J. Heat Transfer, **81**, pp. 13–18.
[8] Chen, M. M., 1961, "An Analytical Study of Laminar Film Condensation: Part 1—Flat Plates," ASME J. Heat Transfer, **83**, pp. 48–54.
[9] Koh, J. C. Y., Sparrow, E. M., and Hartnett, J. P., 1961, "The Tow-Phase Boundary Layer in Laminar Film Condensation," Int. J. Heat Mass Transfer, **2**, pp. 69–82.
[10] Dhir, V. K., and Lienhard, J. H., 1971, "Laminar Film Condensation on Plane and Axisymentric Bodies in Nonuniform Gravity," ASME J. Heat Transfer, **93**, pp. 97–100.
[11] Arnas, A. O., Boettner, D. D., Benson, M. J., and Van Poppel, B. P., 2004, "On the Teaching Of Condensation Heat Transfer," Proceedings of ASME-IMECE 2004, Paper No.: IMECE2004-59277, 15–19 Nov., Anaheim, CA.
[12] Miyara, A., 2001, "Flow Dynamics and Heat Transfer of Wavy Condensate Film," ASME J. Heat Transfer, **123**, pp. 492–500.
[13] Stuhlträger, E., Naridami, Y., Miyara, A., and Uehara, H., 1993, "Flow Dynamics and Heat Transfer of a Condensate Film on a Vertical Wall—I. Numerical Analysis and Flow Dynamics," Int. J. Heat Mass Transfer, **36**, pp. 1677–1686.
[14] Unsal, M., and Thomas, W. C., 1978, "Linearized Stability Analysis of Film Condensation," ASME J. Heat Transfer, **100**, pp. 629–634.
[15] Spindler, B., 1982, "Linear Stability of Liquid Films With Interfacial Phase Change," Int. J. Heat Mass Transfer, **25**, pp. 161–173.
[16] Kundu, P. K., 1990, *Fluid Mechanics*, Academic Press, New York.
[17] Unsal, M., and Thomas, W. C., 1980, "Nonlinear Stability of Film Condensation," ASME J. Heat Transfer, **102**, pp. 483–488.
[18] Kutateladze, S. S., 1963, *Fundamentals of Heat Transfer*, Academic Press, New York.
[19] Chun, K. R., and Seban, R. A., 1971, "Heat Transfer to Evaporating Liquid Films," ASME J. Heat Transfer, **93**, pp. 391–396.
[20] Delhaye, J. M., 1974, "Jump Conditions and Entropy Sources in Two-phase Systems; Local Instant Formulation," Int. J. Multiphase Flow, **1**, pp. 395–409.
[21] Yu, G., 1999, "Development of a CFD Code for Computational Simulations and Flow Physics of Annular/Stratified Film Condensation Flows," Ph.D. thesis, Michigan Technological University.
[22] *COMPACT-2D User Manual (Version 3.1)*, 1994, Innovative Research, Inc., Computational Fluid Dynamic Company, Minneapolis, MN.
[23] Sussman, M., Smereka, P., and Osher, S., 1994, "A Level Set Approach for Computing Solutions to Incompressible Two-Phase Flow," J. Comput. Phys., **114**, pp. 146–159.
[24] Hirt, C. W., and Nichols, B. D., 1981, "Volume of Fluid (VOF) Method for the Dynamics of Free Boundaries," J. Comput. Phys., **39**, pp. 201–255.
[25] Abbott, M. B., and Basco, D. R., 1997, *Computational Fluid Dynamics: An Introduction for Engineers*, Longman Science and Technol., Harlow, Essex, England.
[26] *ASHRAE Handbook*, 1985, Fundamentals SI ed., American Society of Heating, Refrigeration and Air-Conditioning Engineers, Inc., Atlanta, GA.
[27] Pierson, F. W., and Whitaker, S., 1977, "Some Theoretical and Experimental Observations of the Wave Structure of Falling Liquid Films," Ind. Eng. Chem. Fundam., **16**(4), pp. 401–408.
[28] Whitham, G. B., 1974, *Linear and Nonlinear Waves*, Wiley, New York.

Analytical Modeling for Stress-Strain Curve of a Porous NiTi

Ying Zhao

Minoru Taya
e-mail: tayam@u.washington.edu

Department of Mechanical Engineering,
University of Washington,
Box 352600,
Seattle, WA 98195-2600

Two models for predicting the stress-strain curve of porous NiTi under compressive loading are presented in this paper. Porous NiTi shape memory alloy is considered as a composite composed of solid NiTi as matrix and pores as inclusions. Eshelby's equivalent inclusion method and Mori-Tanaka's mean-field theory are employed in both models. Two types of pore connectivity are investigated. One is closed cells (model 1); the other is where the pores are interconnected to each other forming an open-cell microstructure (model 2). We also consider two different shapes of pores, spherical and ellipsoidal. The stress-strain curves of porous shape memory alloy with spherical pores and ellipsoidal pores are compared. It is found that the ellipsoidal shape assumption is more reasonable than the assumption of spherical pores. Comparison of the stress-strain curves of the two models shows that use of open-cell microstructure (model-2) makes the predictions more agreeable to the experimental results of porous NiTi whose microstructure exhibits open-cell microstructure. [DOI: 10.1115/1.2198250]

1 Introduction

Over the last two decades shape memory alloys (SMAs) have attracted great interests in various applications ranging from aerospace [1] and naval structures [2] to surgical instruments, medical implants and fixtures [3,4]. The use of SMAs has promoted extensive researches on developing SMA constitutive models.

Among SMAs, NiTi alloy has been used most extensively due to its large flow stress and shape memory effect (SME). Most recently, porous NiTi attracted an increasing attention as a possible application to medical implant devices and high energy absorption structural material and potential material for surface cooling. The progress in both manufacturing and characterization of the porous NiTi SMA has been reported by a number of researchers. A short review of the existed processing methods is presented here. Li et al. [5,6] fabricated porous NiTi SMA by combustion synthesis method, the stress-strain curves in their work exhibit brittle behavior. Li et al. [7] also fabricated the porous NiTi by powder sintering; it shows that the there is no stress plateau in the stress-strain curve and the material is still brittle. Some studies [8,9] report superelastic behavior of the foams in compression, but stresses are low due to the high porosity. Lagoudas et al. [10] used the HIP (hot isostatic press) method and the stress-strain curve in their work showing brittle behavior. Recently, we processed the porous NiTi by the spark plasma sintering (SPS) method, and the specimens exhibit large superelastic loop with high stress flow and high ductility [11].

In order to make an optimum design of the microstructure of the porous SMAs, it is important to construct a simple, yet accurate model to describe its microstructure-mechanical behavior relation. Thus far, there are few analytical studies focused on the porous SMA, particularly no analytical model for the porous SMA with open porosity. Therefore, in this paper two models are introduced. The porous NiTi is treated as a composite with solid NiTi as its matrix and pores as the inclusions. If a porous NiTi can be viewed as a special or ellipsoidal inclusion case of a particular reinforced composite, then one can construct a micromechanical model based on Eshelby's equivalent inclusion method [12] with Mori-Tanaka mean-field theory [13]. In the first model (model 1), the pores in the porous NiTi are closed, i.e., pores are not connected to each other. In the second model (model 2), pores are assumed to be connected to each other, i.e., open porosity microstructure. Effects of pores with different geometries (spherical and ellipsoidal) are also studied in both models.

There are two advantages of these models. First, it is a simpler model. We need less input data, and the input data for our model are taken from the experimental stress-strain curve of the solid NiTi, i.e., no need to manipulate types of matensite variants, their orientations, etc., often used by other models. Second, in the literature, there exists no model that treated porous NiTi with the open-cell structure. The model proposed in this paper is the first in treating the open-cell structure within the framework of Eshelby's model.

In the following, we shall state first two constitutive models, model 1 (Sec. 2) and model 2 (Sec. 3) and discuss the resulting stress-strain curves they predict. This response will be compared to previous experimental results, [11], and conclusions will be presented.

2 Model-1: Stress-Strain Curve of Porous NiTi With Closed Pores

The stress-strain curve of a SMA with superelastic grade is assumed to be composed of four stages; see Fig. 1. The first stage (I) is a linear elastic stage, with the matrix of 100% austenite. The second stage (II) is a stress-induced matensitic transformation stage; in this stage, a volume fraction of the austenite decreases from 100% to 0% while that of the martensite increases from 0% to 100%, continuously. The third stage (III) is a stage with the matrix of 100% matensite. Therefore, the third stage is an linear elastic stage. The fourth stage (VI) is the austenite transformation stage, in which the volume fraction of martensite changes from 100% to 0% while that of the austenite in the matrix increases from 0% to 100%. $\sigma^P_{M_s}$, $\sigma^P_{M_f}$, $\sigma^P_{A_s}$, and $\sigma^P_{A_f}$ are the critical stresses between the above four stages, the superscript P denotes porous and subscripts M_s, M_f, A_s, and A_f denote martensite start, martensite finish, austenite start, and austenite finish, respectively. E_{M_s} and E_{M_f} are the moduli of the first and third stages and E_T is the

Contributed by the Applied Mechanics Division of ASME for publication in the JOURNAL OF APPLIED MECHANICS. Manuscript received April 7, 2005; final manuscript received January 17, 2006. Review conducted by M. R. Begley. Discussion on the paper should be addressed to the Editor, Prof. Robert M. McMeeking, Journal of Applied Mechanics, Department of Mechanical and Environmental Engineering, University of California-Santa Barbara, Santa Barbara, CA 93106-5070, and will be accepted until four months after final publication of the paper itself in the ASME JOURNAL OF APPLIED MECHANICS.

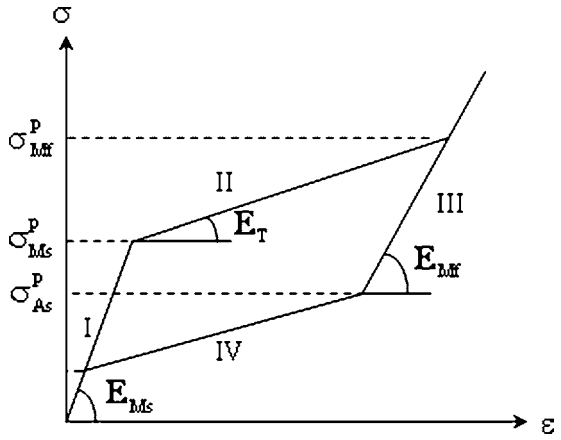

Fig. 1 Linearized four-stage stress-strain curve of porous NiTi

tangent modulus of the second and fourth stages. It is noted that the slope of the forth stage is the same as that of the second stage. In this paper, we use the stress-strain curve of the solid NiTi (i.e., without pores) as a reference.

2.1 Eshelby Model for a Porous SMA With Closed Pores. Consider an Eshelby model for a porous NiTi with closed pores subjected to applied stress σ^0_{ij} where the matrix is solid with uniform martensite transformation strain ε^T_{ij} (Fig. 2(*a*)). The uniform transformation strain ε^T_{ij} is assumed only for the second and fourth stages, while for the first and third stages, $\varepsilon^T_{ij}=0$. In the Eshebly's model, an infinite elastic body (D), which contains spherical or ellipsoidal pores (Ω_p), is subjected to a uniform stress σ^0_{33} as shown in Fig. 2. As far as the stress field is concerned, the model of Fig. 2(*a*) is equivalent to that of Fig. 2(*b*) where the uniform transformation strain in the matrix is removed from and added with minus sign to the pore domain. Thus, the present problem is reduced to the inhomogeneous inclusion problem where the elastic stiffness tensor C^m_{ijkl} is homogeneous in the entire domain D, Fig. 2(*b*) [14].

The Eshelby's inhomogeneous inclusion problem with Mori-Tanaka's mean field theory provides the total stress field given by

$$\sigma^0_{ij}+\sigma_{ij}=\mathbf{C}^m_{ijkl}[e^0_{kl}+\bar{\varepsilon}_{kl}+\varepsilon_{kl}-(\varepsilon^*_{kl}-\varepsilon^T_{kl})]$$
$$=\mathbf{C}^m_{ijkl}(\varepsilon^0_{kl}+\bar{\varepsilon}_{kl}+\varepsilon_{kl}-\varepsilon^{**}_{kl})=\mathbf{C}^p_{ijkl}(\varepsilon^0_{kl}+\bar{\varepsilon}_{kl}+\varepsilon_{kl}) \quad (1)$$

where $\mathbf{C}^m_{ijkl}$ and $\mathbf{C}^P_{ijkl}$ are the elastic stiffness tensor of matrix and pores, respectively. σ_{ij} and ε_{kl} are stress and strain disturbance due to existence of pores, respectively. $\bar{\varepsilon}_{kl}$ is the average strain disturbance in the matrix due to the pores (Ω_p). ε^*_{ij} is the fictitious eigenstrain, which has nonvanishing components in the domain Ω_p. Here, we introduce

$$\varepsilon^{**}_{kl}\equiv\varepsilon^*_{kl}-\varepsilon^T_{kl} \quad (2)$$

For the entire domain D, the following relation always holds:

$$\sigma^0_{ij}=\mathbf{C}^m_{ijkl}\varepsilon^0_{kl} \quad (3)$$

Following the Mori-Tanaka mean filed theory, the average stress disturbance in the matrix, $\langle\sigma_{ij}\rangle_m$ is given by

$$\langle\sigma_{ij}\rangle_m=\mathbf{C}^m_{ijkl}\bar{\varepsilon}_{kl} \quad (4)$$

The strain disturbance is related to ε^{**}_{mn} as

$$\varepsilon_{kl}=\mathbf{S}_{klmn}\varepsilon^{**}_{mn} \quad (5)$$

The requirement that integration of the stress disturbance over the entire body (D) vanishes, leading to

$$\bar{\varepsilon}_{kl}=-f_P(\mathbf{S}_{klmn}\varepsilon^{**}_{mn}-\varepsilon^{**}_{kl}) \quad (6)$$

where $\mathbf{S}_{klmn}$ is Eshelby's tensor for pore inclusion and its exact values are given in Appendix and f_p is the volume fraction of pore, i.e., porosity of the SMA. A substitution of Eq. (3)–(6) into (1) provides a solution for ε^{**}_{kl}

$$\varepsilon^{**}_{ij}=\{(1-f_P)\mathbf{C}^m_{ijkl}(\mathbf{S}_{klmn}-\mathbf{I}_{klmn})+\mathbf{C}^P_{ijkl}[(1-f_P)\mathbf{S}_{klmn}+f_P]\}^{-1}(\mathbf{C}^P_{mnst}\mathbf{C}^{m-1}_{stpq}-\mathbf{I}_{mnpq})\sigma^0_{pq} \quad (7)$$

where $\mathbf{I}$ is identity matrix of 6×6. In this paper boldface symbols ($\mathbf{S},\mathbf{C},\mathbf{I}$), are fourth-order tensor, and they are converted to 6×6 matrix form for facilitation of calculation. These boldface symbols with subscripts should be written as not boldface with subscript when they are scalar components. However, to avoid confusion, we keep boldface symbols.

As the stiffness of the pores is zero, $\mathbf{C}^P_{ijkl}=0$; thus, Eq. (7) is given as

$$\varepsilon^{**}_{mn}=-\frac{1}{1-f_P}(\mathbf{S}_{klmn}-\mathbf{I}_{klmn})^{-1}C^{m-1}_{ijkl}\sigma^0_{ij} \quad (8)$$

By setting $\mathbf{C}^P_{ijkl}=0$, Eq. (1) becomes

$$\sigma^0_{ij}=-\sigma_{ij} \quad (9)$$

Next, we shall consider the strain energy density of the inhomogeneous inclusion problem of Fig. 2(*b*), which is given by [15]

$$W_{mi}=\frac{1}{2}\sigma^0_{ij}\varepsilon^0_{ij}+\frac{1}{2}f_P\sigma^0_{ij}\varepsilon^*_{ij}-\frac{1}{2}f_P\sigma_{ij}\varepsilon^T_{ij} \quad (10)$$

Let us call W_{mi} as microscopic strain energy density. It is noted in Eq. (10) that W_{mi} is valid for all three stages, i.e., for the first and third stages $\varepsilon^T_{ij}=0$, whereas for the second stage, all three terms on the right-hand side of Eq. (10) are nonvanishing.

2.1.1 Stiffness of First and Third Stages. The equivalency of strain energy density of porous SMA for the first and third stages can be derived from Eq. (10) with $\varepsilon^T_{ij}=0$, which is set equal to the strain energy density of a porous SMA with its elastic stiffness tensor $\mathbf{C}^c_{ijkl}$, where c refers to "composite," as porosity is a special case of composite.

$$\frac{1}{2}\mathbf{C}^{c-1}_{ijkl}\sigma^0_{ij}\sigma^0_{kl}=\frac{1}{2}\mathbf{C}^{m-1}_{ijkl}\sigma^0_{ij}\sigma^0_{kl}+\frac{1}{2}f_P\sigma^0_{ij}\varepsilon^*_{ij} \quad (11)$$

where $\mathbf{C}^{c-1}_{ijkl}$ and $\mathbf{C}^{m-1}_{ijkl}$ are the elastic compliances of the composite and the matrix material (solid NiTi), respectively. Since only the nonvanishing component of σ^0_{ij} is $\sigma^0_{33}=\sigma_0$ (Fig. 2), Eq. (11) is reduced to

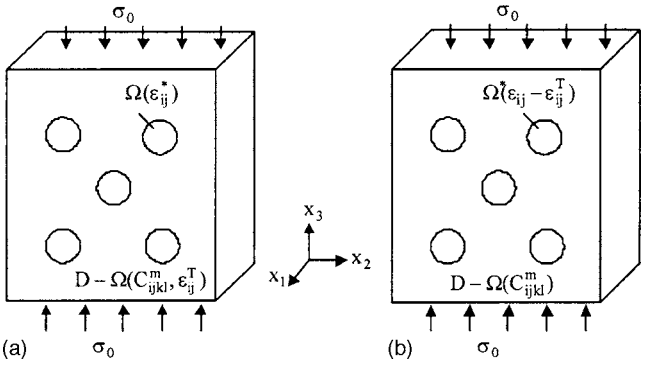

Fig. 2 The Eshelby's model for a porous SMA: (*a*) the problem of pores embedded in the NiTi matrix with stiffness C^m_{ijkl} and transformation strain ε^T_{ij}, which can be converted to equivalent inclusion problem (*b*), where ε^*_{ij} is the fictitious eigenstrain, which is unknown.

$$\frac{\sigma_0^2}{2E_c} = \frac{\sigma_0^2}{2E_m} + \frac{f_P}{2}\sigma_0\varepsilon_{33}^* \tag{12}$$

where E_c and E_m are the Young's moduli of the composite and the matrix, respectively. In the first stage, E_c is E_{M_s}, and E_m is the Young's modulus of austenite E_A. Combining Eq. (12) with Eq. (2) and (8) with $\varepsilon_{ij}^T=0$, the Young's modulus of the porous NiTi in the first stage, E_{M_s} normalized by E_A is given as

$$\frac{E_{M_s}}{E_A} = \frac{1}{1+\eta f_P} \tag{13}$$

where η is a parameter, a function of porosity f_P and shape of the porous inclusion

$$\eta = \frac{-(\mathbf{H}_{1133}+\mathbf{H}_{2233}+\mathbf{H}_{3333})}{(1-f_p)} \tag{14a}$$

$\mathbf{H}$ is a (6×6) matrix, which is given as

$$\mathbf{H}_{ijmn} = (\mathbf{S}_{ijkl}-\mathbf{I}_{ijkl})^{-1}\mathbf{C}_{klmn}^{-1} \tag{14b}$$

Young's modulus of the porous NiTi at the third stage, E_{M_f} can be obtained in the same manner as the above,

$$\frac{E_{M_f}}{E_M} = \frac{1}{1+\eta f_P} \tag{14c}$$

2.1.2 Critical Stresses $\sigma_{M_s}^P$ and $\sigma_{M_f}^P$. Under the uniaxial stress along the x_3-axis (σ_0), the transformation strain ε_{ij}^T is assumed to be uniform with the following components:

$$\varepsilon_{ij}^T = \{\nu\varepsilon^T \ \nu\varepsilon^T \ -\varepsilon^T \ 0 \ 0 \ 0\}^T \tag{15}$$

where ε^T is the transformation strain along x_3-axis.

The stress disturbance σ_{ij} is obtained from Eq. (9). The change of the total potential energy of the inhomogeneous inclusion of the problem of Fig. 2(*b*), δU, due to the change in transformation strain $\delta\varepsilon_{ij}^T$ is given by [16]

$$\delta U = -\delta\varepsilon_{ij}^T](1-f_P)\sigma_{ij}^0 - f_P\sigma_{ij}] \tag{16}$$

The work done by the applied stress δQ causing infinitesimal transformation strain $\delta\varepsilon_T$ is

$$\delta Q = (1-f_P)\sigma_{M_s}^S\delta\varepsilon_T \tag{17}$$

where $\sigma_{M_s}^S$ is the stress of the matrix at the onset of stress-induced martensite transformation, at the beginning of the second stage of the solid NiTi, the superscript S denotes solid material, and the subscript M_s denotes matensitic start transformation. Since $\delta U + \delta Q = 0$, we obtain

$$\sigma_0 = \sigma_{M_s}^S + \frac{f_P}{1-f_P}(\sigma_{33}-\sigma_{11}) \tag{18}$$

substituting $\sigma_{33}=-\sigma_0$ and $\sigma_{11}=0$ from Eq. (9) into Eq. (18), we obtain

$$\sigma_{M_s}^P = (1-f_P)\sigma_{M_s}^S \tag{19a}$$

The martensitic transformation finish critical stress $\sigma_{M_f}^P$ can be obtained in the same manner

$$\sigma_{M_f}^P = (1-f_P)\sigma_{M_f}^S \tag{19b}$$

2.1.3 Stiffness of Second Stage. Refer to Fig. 3(*a*), Young's modulus (E) of a SMA with transformation ε_T is estimated by

$$E(\varepsilon_T) = E_A + \frac{\varepsilon_T}{\varepsilon_{M_f}^T}(E_M - E_A) \tag{20}$$

where E_A, E_M are the Young's modulus of 100% austenite and 100% martensite phase, respectively, Fig. 3(*a*), and $\varepsilon_{M_f}^T$ is the maximum transformation strain, and it is given by

$$\varepsilon_{M_f}^T = \varepsilon_{M_f} - \frac{\sigma_{M_f}}{E_M} \tag{21}$$

Equation (20) is valid for both dense and porous SMA; thus, we can rewrite Eq. (20) using Eq. (21) as

$$E^i = E_A^i - \frac{E_A^i - E_M^i}{\varepsilon_{M_f}^i - \sigma_{M_f}^i/E_M^i}\varepsilon_T \tag{22}$$

where the superscript i denotes $i=S$ (solid) or P (porous). In order to obtain the slope of the linearized second stage of compressive stress-strain curve of a porous NiTi, we consider the equivalency of strain energy density. In addition, in the case of the second stage, we evaluate the macroscopic strain energy density of a porous NiTi graphically from Fig. 3(*a*), i.e., area enclosed by the curve. W_{ma} is given by

$$W_{ma} = \frac{1}{2}(\sigma_{M_s}^P + \sigma_0^P)\left(\varepsilon_T^P + \frac{\sigma_0^P}{E_{AM}} - \frac{\sigma_{M_s}^P}{E_{M_s}}\right) \tag{23}$$

where $\sigma_{M_s}^P$ is the martensitic start transformation stress of porous SMA, σ_0^P is an applied stress, ε_T^P is the strain corresponding to σ_0^P. Since there is no transformation strain in pores, the transformation

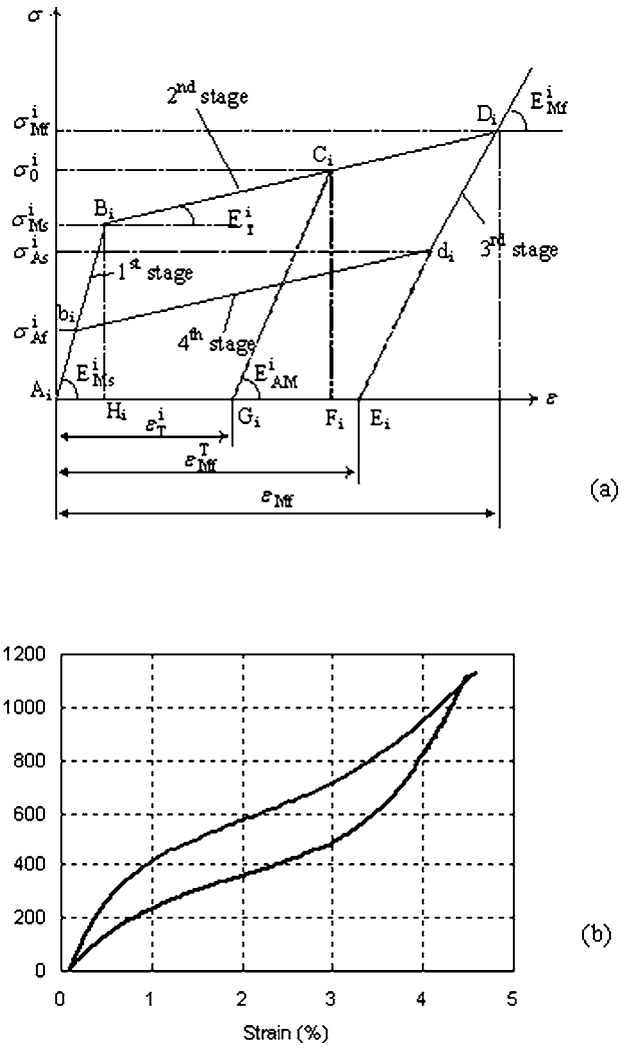

Fig. 3 (*a*) Stress-strain curve of porous or solid sample (*i=P* or *S*), (*b*) stress-strain curve of solid NiTi

strain for porous SMA ε_T^P is the uniform transformation strain in the matrix, i.e., solid NiTi,

$$\varepsilon_T^P = \varepsilon_T^S \equiv \varepsilon_T \tag{24}$$

The above macroscopic strain energy density is set equal to the microscopic stain energy density W_{mi} defined by Eq. (10), where the solution for ε_{ij}^* is obtained from Eqs. (1)–(7) as

$$\varepsilon_{kl}^* = \varepsilon_{kl}^T - \frac{1}{1-f_P}(\mathbf{S}_{klmn} - \mathbf{I}_{klmn})^{-1}\mathbf{C}_{mnij}^{m-1}\sigma_{ij}^0 \tag{25}$$

In Eq. (25), the first term on the right represents the transformation in the solid NiTi matrix; the second term comes from the interactions between pores and applied stress.

Substituting Eq. (25) into Eq. (10), the microscopic strain energy density, W_{mi} is given by

$$W_{mi} = \frac{1}{2}\sigma_{ij}^0\varepsilon_{ij}^0 + \frac{1}{2}f_P\sigma_{ij}^0\left[2\varepsilon_{ij}^T - \frac{1}{1-f_P}(\mathbf{S}_{ijkl} - \mathbf{I}_{ijkl})^{-1}\varepsilon_{kl}^0\right] \tag{26}$$

Since the porous NiTi is subjected to uniaxile load, i.e., $\sigma_{ij}^0 = \{0\ 0\ \sigma_0^P\ 0\ 0\ 0\}^T$, and transformation strain given by $\varepsilon_{ij}^T = \{\nu\varepsilon_T\ \nu\varepsilon_T\ -\varepsilon_T\ 0\ 0\ 0\}^T$, and the pores are assumed to be spherical; thus, Eq. (26) can be reduced to

$$W_{mi} = \frac{1}{2}\sigma_0^P\varepsilon_0 + \frac{1}{2}f_P\sigma_0^P\left[2\varepsilon_T - \frac{1}{1-f_P}\mathbf{Z}_{3333}\varepsilon_0\right] \tag{27}$$

where $\mathbf{Z}_{3333}$ is a component of a 6×6 matrix, $\mathbf{Z}=(\mathbf{S}_{ijkl}-\mathbf{I}_{ijkl})^{-1}$. $\mathbf{S}$ is Eshelby tensor for spherical and ellipsoidal inclusions, respectively. ε_0 is the macroscopic strain of the porous SMA, and it is related to applied stress σ_0^P as

$$\varepsilon_0 = \frac{\sigma_0^P}{E_{AM}} \tag{28}$$

Substituting Eq. (28) into Eq. (27), the microscopic strain energy density W_{mi} of porous NiTi is finally reduced to

$$W_{mi} = \frac{1}{2}\frac{(\sigma_0^P)^2}{E_{AM}} + \frac{1}{2}f_P\sigma_0^P\left(2\varepsilon_T^P - \mathbf{Z}_{3333}\frac{\sigma_0^P}{E_{AM}}\right) \tag{29}$$

where E_{AM} is the Young's modulus of solid (matrix) SMA with ε_T.

By equating the macroscopic strain energy density W_{ma} of Eq. (23) W_{mi} of Eq. (29), and using Eq. (22) with $i=P$, we obtained the following algebraic equation of second-order ε_T as:

$$F(\varepsilon_T)^2 + G\varepsilon_T + H = 0 \tag{30}$$

$$F = \frac{(\gamma\sigma_0^P + \sigma_{M_s}^P)(1-\beta)}{\varepsilon_{M_s}}, \quad G = \gamma\sigma_0^P + \sigma_{M_s}^P + \frac{\sigma_{M_s}^P(1-\beta)(\sigma_{M_s}^P + \sigma_0^P)}{E_{M_s}\varepsilon_{M_f}},$$

$$H = \frac{(1-\alpha)(\sigma_0^P)^2 - (\sigma_{M_s}^P)^2}{E_{M_s}}, \quad \alpha = 1 - \frac{f_P}{1-f_P}\mathbf{Z}_{3333},$$

$$\beta = \frac{E_{M_f}}{E_{M_s}}, \quad \gamma = 1 - 2f_P \tag{31}$$

The solution of ε_T^P, which corresponds to the second kink point D_P in Fig. 3(*a*), is given by

$$\varepsilon_T = \frac{-G + \sqrt{G^2 - 4FH}}{2F} \tag{32}$$

The tangent modulus of the porous SMA is the slope of the second stage of the stress-strain curve shown in Fig. 1, thus, E_T can be expressed in terms of transformation strain ε_T and the stresses, σ_0^P and $\sigma_{M_s}^P$ as

$$E_T = \frac{\sigma_0^P - \sigma_{M_s}^P}{\varepsilon_T} \tag{33}$$

2.2 Unloading Curve. During unloading, the porous SMA material undergoes reverse transformation (martensite phase to austenite phase). Before the applied stress reaches to a critical value σ_{As}^P, the matrix SMA remains 100% martensite phase (first stage of the unloading stress-strain curve in the modeling curve). When the applied stress is decreased to σ_{As}^P, reverse transformation starts and it finishes when the stress reaches another critical value σ_{Af}^P; thereafter, the porous SMA material remains 100% austenite. Therefore, the slope of the first and third stages of the unloading curve is the Young's modulus of the 100% martensite and 100% austenite phase, respectively. The slope of the fourth stage is the same as that of the loading curve in the second stage. Therefore, the Young's moduli of the unloading curve are related to those of the loading curve as

$$E_{As} = E_{M_f} \tag{34a}$$

$$E_T^u = E_T \tag{34b}$$

$$E_{Af} = E_{Ms} \tag{34c}$$

where E_T^u is the slope of the second stage of the unloading curve. The superscript u denotes unloading, whereas those without superscript are the slopes of loading curve.

The austenite start and finish transformation stresses of porous SMA, σ_{As}^P and σ_{Af}^P are related to the corresponding stresses of the solid NiTi by

$$\sigma_{As}^P = (1-f_P)\sigma_{As}^S \tag{35a}$$

$$\sigma_{Af}^P = (1-f_P)\sigma_{Af}^S \tag{35b}$$

where σ_{As}^S and σ_{Af}^S are austenite start and finish transformation stresses of the solid NiTi, respectively. First, we assume that the solid NiTi matrix is isotropic with Poisson's ratio $\nu^A = \nu^M = 0.33$.

3 Model 2: Stress-Strain Curve of Porous NiTi With Open Pores

Here we shall discuss the Eshelby model for a porous SMA with open pores where pores are interconnected (Fig. 4), where unknown fictitious eigenstrain is in pore 1 (ε_{ij}^{*1}) and in pore 2 (ε_{ij}^{*2}) will be determined by Eshelby method. Initially, we distinguish the elastic constant ($\mathbf{C}_{ijkl}$) and eigenstrain (ε^*) associated with pores 1 and those with pores 2, but later we will set those identical to each other as two adjacent pores of the same shape, and orientation should have the same $\mathbf{C}_{ijkl}$ and ε_{ij}^*. There are two steps to obtain the eigenstrains. The first step is to find the eigenstrain ε_{ij}^{*1} and the disturbed stress σ_{ij}^1 in Ω_1 for an infinite body containing ellipsoidal or spherical pores and subjected to uniaxial applied stress σ_0. In the first problem, the other pore Ω_2 is not considered for obtaining ε_{ij}^{*1}, but the interaction between the pores is taken into account by Mori-Tanaka mean field theory. The second step is to find the eigenstrain ε_{ij}^{*2} and disturbed stress σ_{ij}^2 in Ω_2, where the interactions between Ω_1 and Ω_2 is taken into account. After obtaining ε_{ij}^{*1} and ε_{ij}^{*2}, we take the average of these eigenstrains to represent the eigenstrain for the two interconnected pores. The transformation strain ε_T is zero in the first and third stages, since there is no transformation occurring in these two stages, whereas it is not zero in the second and fourth stage. That is the same as in Sec. 2.

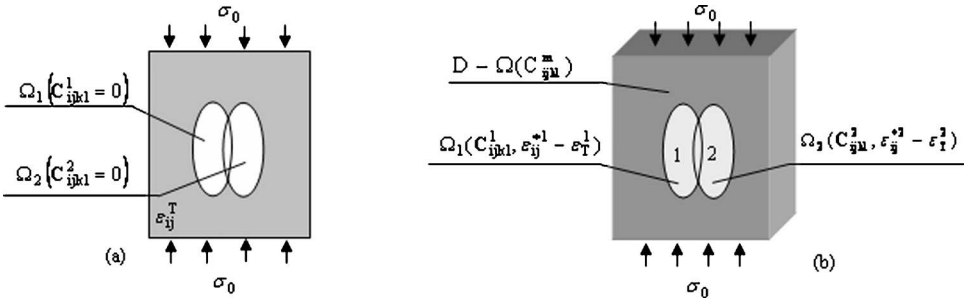

Fig. 4 (*a*) Eshelby's model for interconnected pores in NiTi matrix, which is converted to equivalent inclusion problem (*b*)

3.1 Computation of Average Eigenstrain in Open Pores. In this model, we will simulate the stress-strain curve of a porous SMA with open porosity where two kinds of pore shapes—spherical and ellipsoidal—are used.

3.1.1 Solution of Eigenstrain in Ω_1 Without Ω_2, ε^{**1}_{ij}. The Eshelby model for finding ε^{**1}_{ij} is the same as the in model 1; therefore, we list only the final solutions

$$\varepsilon^{**1}_{kl} = -\frac{1}{1-f_P}(\mathbf{S}_{klmn}-\mathbf{I}_{klmn})^{-1}\mathbf{C}^{m-1}_{mnij}\sigma^0_{ij} \tag{36}$$

3.1.2 Solution of Eigenstrain in Ω_2 by Accounting Interactions Between Ω_1 and Ω_2, ε^{**2}_{ij}. In this step, the disturbed stress in Ω_2 is obtained in terms of ε^{**2}_{ij}, which is unknown thus far. In the first problem, disturbed stress outside the end of the Ω_1, σ^{-1}_{ij} is expressed in terms of σ^1_{ij}. Then the total stress σ^t_{ij} in Ω_2 vanishes

$$\sigma^t_{ij} = \sigma^0_{ij} + \sigma^2_{ij}(\varepsilon^{**2}_{ij}) + \sigma^{-1}_{ij} = 0 \tag{37}$$

where $\sigma^2_{ij}(\varepsilon^{**2}_{ij})$ is the self-stress in Ω_2 induced by eigenstrain ε^{**2}_{ij} The disturbed stress σ^{-1}_{ij} is given by the formula of Hill-Walpole-Mura jump condition [17]

$$\sigma^{-1}_{ij} - \sigma^1_{ij} = \mathbf{C}_{ijkl}(-\mathbf{C}_{pqmn}\varepsilon^{**1}_{mn}M_{kp}n_q n_l + \varepsilon^{**1}_{kl}) \tag{38a}$$

where

$$M_{kp} = \frac{\left\lfloor \frac{\delta_{kp}-n_k n_p}{2(1-\nu)} \right\rfloor}{\mu} \tag{38b}$$

and where n_i is the ith component of an unit vector outer normal to the inclusion and is given by

$$n = (1\ 0\ 0) \tag{38c}$$

It is noted in Fig. 4 that the interconnection between Ω_1 and Ω_2 is at the equator region with its normal base vector pointing to x_1-axis. With Eq. (38*c*), Eq. (38*a*) yields

$$\sigma^{-1}_{ij} = \sigma^1_{ij} + \mathbf{C}_{ij11}(-\mathbf{C}_{11mn}\varepsilon^{**1}_{mn}M_{11} + \varepsilon^{**1}_{11}) \tag{39}$$

$$\text{where } M_{11} = \frac{(1+\nu)(1-2\nu)}{E(1-\nu)} \tag{40}$$

The applied stress is given as

$$\sigma^0_{ij} = (0\ 0\ \sigma^0\ 0\ 0\ 0) \tag{41}$$

Stress in Ω_2 in terms of eigensrain ε^{**2}_{ij} is given by

$$\sigma^2_{ij} = (1-f_P)\mathbf{C}^m_{ijkl}(\mathbf{S}_{klmn}-\mathbf{I}_{klmn})\varepsilon^{**2}_{mn} \tag{42}$$

By substituting Eq. (39), (41), and (42) into Eq. (37), we obtain eigenstrain in Ω_2 ε^{**2}_{ij} as

$$\varepsilon^{**2}_{mn} = \mathbf{\Pi}_{mnrs}\varepsilon^{**1}_{rs} \tag{43a}$$

$$\text{where } \mathbf{\Pi}_{mnrs} = -(\mathbf{S}_{mnpq}-\mathbf{I}_{mnpq})^{-1}(-\mathbf{C}_{pqrs}M_{11}+\mathbf{I}_{pqrs})/(1-f_P) \tag{43b}$$

We take average of the eigenstrains in Ω_1 and Ω_2 to represent the eigenstrain of all interconnected pores

$$\varepsilon^{**}_{mn} = \frac{1}{2}(\varepsilon^{**1}_{mn}+\varepsilon^{**2}_{mn}) = \frac{1}{2}(\mathbf{\Pi}_{mnrs}+\mathbf{I}_{mnrs})\varepsilon^{**1}_{rs} \tag{44}$$

Once the average eigenstrain ε^{**}_{mn} is obtained, we can use the first model to calculate the moduli and critical stresses. Therefore, we list only the final useful for the moduli and critical stresses in the following.

3.2 Elastic Moduli at Stage I and III. Since there is no transformation at stage I and III, the Young's modulus of each stage can be obtained by equivalency of energy density as in model 1 from Eq. (11). Therefore, the Young's modulus of stage I is given as

$$\frac{E_{M_s}}{E_A} = \frac{1}{1+\mathbf{D}_{3333}f_P} \tag{45a}$$

and that of stage III is

$$\frac{E_{M_f}}{E_M} = \frac{1}{1+\mathbf{D}_{3333}f_P} \tag{45b}$$

where $\mathbf{D}_{3333}$ is a component of a 6×6 matrix $\mathbf{D}_{klrs}$, which is given as

$$\mathbf{D}_{klrs} = -\frac{\mathbf{A}_{klmn}\cdot\mathbf{B}_{mnpq}\cdot\mathbf{C}_{pqrs}}{2(1-f_P)} \tag{46}$$

where $\mathbf{A}_{klmn}=\mathbf{I}_{klmn}+\mathbf{\Pi}_{klmn}$, $\mathbf{B}_{mnpq}=(\mathbf{S}_{mnpq}-\mathbf{I}_{mnpq})^{-1}$, $\mathbf{C}_{pqrs}=\mathbf{C}^{-1}_{pqrs}$.

3.3 Tangent Stiffness of Stage II and IV. To obtain E_T, first we have to obtain the transformation strain ε_T. The transformation strain is obtained in the same manner as that in model 1

$$\varepsilon_T = \frac{(-G_2+\sqrt{G_2^2-4G_1G_3})}{2G_1} \tag{47}$$

where

$$G_1 = [\sigma^p_{M_s}+(1-f_P)\sigma^p_0]\xi_1 \tag{48a}$$

$$G_2 = f_P\sigma^p_0E_A - f_PD_{3333}(\sigma^p_0)^2\xi_1 - (\sigma^p_{M_s}+\sigma^p_0)E_A - \xi_1\xi_2 \tag{48b}$$

Table 1 Input data given by solid NiTi reference curve

σ^s_{Ms}	σ^s_{Mf}	σ^s_{Af}	E_A	E_M	ε_{Ms}	ε_{Mf}
420 MPa	780 MPa	450 MPa	75 GPa	31 GPa	0.0053	0.04

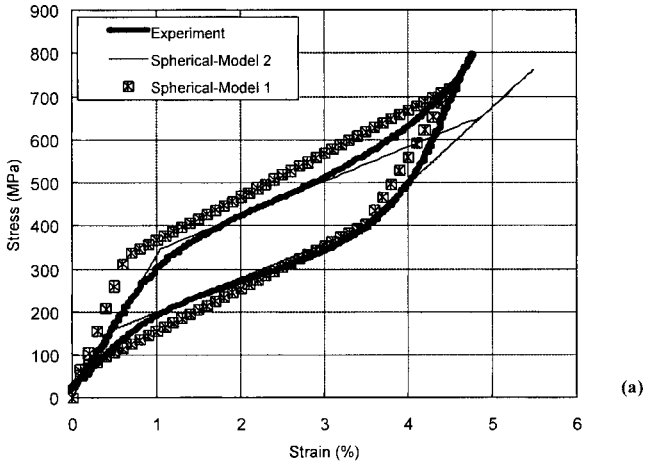

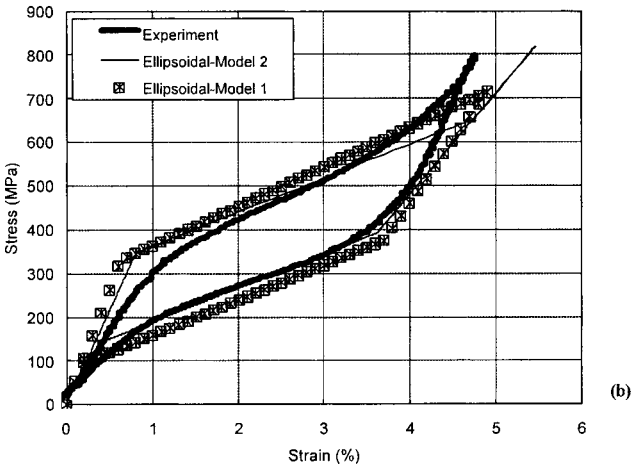

Fig. 5 Comparison of the experimental data to predictions by the present two models

$$G_3 = \xi_2 E_A - \sigma^p_{M_s}\sigma^p_0 + f_p D_{3333}(\sigma^p_0)^2 E_A \tag{48c}$$

and

$$\xi_1 = \frac{(E_A - E_M)}{(\varepsilon_{M_f} - \sigma^p_{M_s}/E_M)} \tag{49a}$$

$$\xi_2 = \frac{(\sigma^p_{M_s} + \sigma^p_0)\sigma^p_{M_s}}{E_{M_s}} \tag{49b}$$

Therefore, the tangent modulus, E_T is given in terms of transformation strain as

$$E_T = \frac{\sigma^P_0 - \sigma^P_{M_s}}{\varepsilon_T} \tag{50}$$

Table 2 Comparison of the critical stresses and Young's moduli of experimental data and predictions by two models

	E_{Ms} (GPa)	E_T (GPa)	E_{Mf} (GPa)
Experimental	41.0	8.0	27.0
Ellipsoidal pore—Model 1	52.6	9.2	23.7
Spherical pores—Model 1	52.6	10.1	22.7
Ellipsoidal pore—Model 2	43.2	7.7	23.2
Spherical pores—Model 2	33.2	7.9	17.9

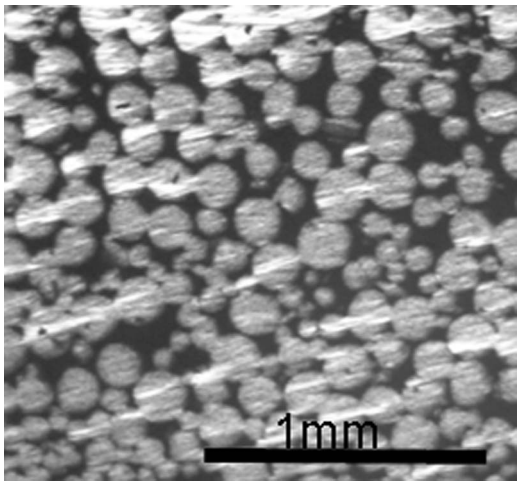

Fig. 6 Microstructure of 13% porosity specimen

3.4 Critical Stress. The four critical stresses are obtained in the same manner as that in model 1. They are given by

$$\sigma^P_{M_s} = (1 - f_P)\sigma^S_{M_s} \tag{51a}$$

$$\sigma^P_{M_f} = (1 - f_P)\sigma^S_{M_f} \tag{51b}$$

$$\sigma^P_{As} = (1 - f_P)\sigma^S_{As} \tag{51c}$$

$$\sigma^P_{Af} = (1 - f_P)\sigma^S_{Af} \tag{51d}$$

It is noted here that superscripts S and P denote solid and porous SMA, respectively.

4 Discussion

We use Ti-50.9 at. %Ni as SMA, and the experimental data of the stress-strain curve of solid NiTi under compressive loading is made into piecewise linear wire four stages, Fig. 3(*a*). Table 1 shows the input data of the piecewise linearized stress-strain curve of solid NiTi to simulate the stress-strain curve of 13% porosity NiTi specimen [11].

Figure 5 shows the stress-strain curves predicted by models 1 and 2. Table 2 lists the values of the critical stresses and Young's

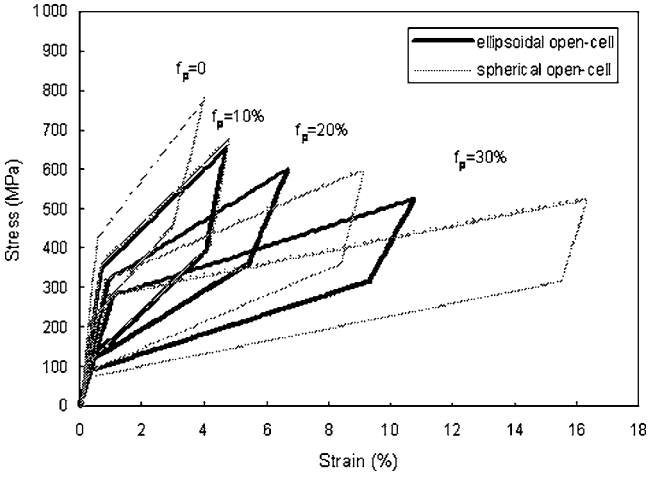

Fig. 7 Stress-strain curves predicted by ellipsoidal and spherical open-cell model

moduli predicted by two models, as well as the experiment [11]. The comparison shows that the simulations have reasonable good agreement with the experimental data.

It is noted that the stress-strain curve of the ellipsoidal pore-shape assumption is closer to the experimental curve than that of the spherical pore-shape assumption. This indicates that the ellipsoidal pore shape is more likely the realistic pore shape in the specimen used for the experiment. Figure 6 shows the microstructure of the porous NiTi specimen. Although, from this figure we can see that the realistic pore shape is not ellipsoidal, but the ellipsoidal is closer than the spherical to the realistic shape. Therefore, the model with ellipsoidal pore shape predicts more accurately.

Comparing the stress-strain curves predicted by Models 1 and 2, we can see that model 2 is more accurate than model 1. This is because model 2 takes into account the interactions between two adjacent pores by assuming they are interconnecting to each other. Figure 6 supports this assumption that pores are indeed interconnected. Model 2 can take account for the interaction between the interconnected pores; therefore, the predictions by model 2 give rise to closer agreement with the experiment.

Figure 7 shows how the porosity f_P influents stress-strain curve predicted by model 2, the open-cell model. It is found in Fig. 7 that when the porosity is $<10\%$, the ellipsoidal and spherical shapes have almost same prediction; but once when the porosity gets larger and larger, the difference between the two shapes increases dramatically.

5 Conclusion

Two models predicting the stress-strain curve of porous SMA subjected to compressive load are presented. Pores are treated as separate individuals in model 1, whereas they are interconnected to each other in model 2. Both models explain the experimental data reasonably well. Model 2, which can take account for the interactions among interconnected pores, provides better predictions than model 1 in predicting the experimental data of the Young's moduli of porous NiTi.

Acknowledgment

The present work was supported by a grant from ONR-MURI project (N-000140210666) via University of California at San Diego, where PI is Professor S. Nemat-Nasser. The program monitor at ONR is Dr. R. Barsoum.

References

[1] Lagoudas, D. C., Strelec, J. K., Yen, J., and Khan, M. A., 2001, "Intelligent Design Optimization of a Shape-Memory-Alloy-Actuated Reconfigurable Wing," Proc. SPIE, **3984**, pp. 338–348.
[2] Garner, L. N., Wilson, L. J., Lagoudas, D. C., and Rediniotis, O. K., 2000, "Development of a Shape Memory Alloy Actuated Biomimetic Vehicle," Smart Mater. Struct., **9**, pp. 673–683.
[3] Martynova, I., Skorohod, V., and Solonin, S., 1991, "Shape Memory and Superelasticity Behavior of Porous Ti-Ni Material," J. Phys. IV, **1991**, pp. C4/421–C4/426.
[4] Goncharuk, N. V., Martynova, I., Naidenova, I. F., and Skorokhod, O. R., 1992, "Superelaticity and Shape Memory of Sintered Porous Titanium Nickelide," Poroshk. Metall. (Kiev), **4**, pp. 56–60.
[5] Li, Y. H., Rong, L. J., and Li, Y. Y., 1998, "Porous NiTi Alloy Prepared From Elemental Powder Sintering," J. Mater. Res., **13**, pp. 2847–2851.
[6] Li, Y. H., Rong, L. J., Luo, X. H., and Li, Y. Y., 2000, "Microstructure and Superelaticity of Porous NiTi Alloy," Sci. China, Ser. E: Technol. Sci., **E-42**, pp. 94–101.
[7] Li, B. Y., Rong, L. J., and Li, Y. Y., 1998, "Transformation Behavior of Sintered Porous NiTi Alloys," Metall. Mater. Trans. A, **30A**, pp. 2753–2756.
[8] Yuan, B., Chung, C. Y., and Zhu, M., 2004, "Microstructure and Martensitic Transformation Behavior of Porous NiTi Shape Memory Alloy Prepared by Hot Isostaic Pressing Processing," Mater. Sci. Eng., A, **382**, pp. 181–187.
[9] Li, B. Y., Rong, L. J., Gjuanter, V. E., and Li, Y. Y., 2000, "Porous NiTI Shape Memory Alloys Produced by Two Different Methods," Z. Metallkd., **91**, pp. 291–295.
[10] Lagoudas, D. C., Entchev, P. B., and Vandygriff, E. C., 2000, "Modeling of Thermomehcanical Response of Porous Shape Memory Alloys," Proc. SPIE, **3992**, pp. 141–153.
[11] Zhao, Y., Taya, M., Kang, Y. S., and Kawasaki, A., 2005, "Compressive Behavior of Porous NiTi Shape Memory Alloy," Acta Mater., **53**(2), pp. 337–343.
[12] Eshelby, J. D., 1957, "The Determination of the Elastic Field of an Ellipsoidal Inclusion, and Related Problems," Proc. R. Soc. London, Ser. A, **3**, pp. 376–396.
[13] Tanaka, K., and Mori, T., 1973, "Average Stress in Matrix and Average Elastic Energy of Materials With Misfitting Inclusions," Acta Metall., **21**, pp. 571–574.
[14] Mura, T., 1987, *Micromechanics of Defects in Solids*, 2nd ed., Martinus Nijhoff, Dordrecht, pp. 168–170.
[15] Taya, M., and Chou, T. W., 1981, "On Two Kinds of Ellipsoidal Inhomogeneities in an Infinite Elastic Body: An Application to a Hybrid Composite," Int. J. Solids Struct., **136**, pp. 553–563.
[16] Taya, M., and Mura, T., 1981, "On Stiffness and Strength of an Aligned Short-Fiber Reinforced Composite Containing Fiber-End Cracks Under Uniaxial Applied Stress," ASME J. Appl. Mech., **48**, pp. 361–367.
[17] Arsenault, R. J., and Taya, M., 1987, "Thermal Residual Stress in Metal Matrix Composite," Acta Metall., **35**, pp. 651–659.

Application of Minature Ring-Core and Interferometric Strain/Slope Rosette to Determine Residual Stress Distribution With Depth—Part I: Theories

Keyu Li
e-mail: kli@oakland.edu

Wei Ren
e-mail: weiren74@hotmail.com

Department of Mechanical Engineering,
Oakland University,
Rochester, MI 48309

The principle of an interferometric strain/slope rosette (ISSR) is based on interference of laser beams reflected from three microindentations on a specimen surface. The ISSR can simultaneously measure the in-plane strains and the out-of-plane slopes. Ring-core cutting is a mechanical stress relief method. When used with the ISSR technique for residual stress measurement, the ring core can be made much smaller than used with the resistance strain rosette. Thus, more localized residual stresses can be measured. The theories of the ISSR/ring-core cutting method are described in this paper. Both mechanical and finite element models are developed for the incremental ring-core cutting process with the application of the ISSR technique. The stress-strain coefficients of the ISSR/ring-core method are calculated and nondimensionalized for general applications. A test example is given to demonstrate how residual stress distribution is determined by using the stress-strain coefficients and the ISSR data. [DOI: 10.1115/1.2198251]

1 Introduction

Ring-core cutting combined with a resistance strain rosette (RSR) was used to measure residual stresses. Ring-core cutting method mills an annular groove to relieve residual stresses around a resistance strain-gage rosette. The resistance strain rosette is bonded on the surface for strain measurement during the ring-core cutting [1]. Because of connecting electrical wires of the RSR and the complicated measurement system, the RSR/ring-core method is far less used than the RSR/hole-drilling method. Since disconnecting and reconnecting the RSR wires for each incremental cutting step would possibly cause circuit instability and lead to significant errors, the wires have to be led vertically upward through the hollow drive spindle [1]. Thus, the cutting and measurement equipment is very complicated. Besides mechanical milling methods, some researchers use electron discharge machining (EDM) apparatus to burn the material and create a ring-core groove [2]. Exact ring-core shape and accurate depth measurement are required for each cutting step. Hence, the operation of material removal with EDM is very technique demanding. The EDM process could also induce large errors on the residual stresses.

The ring-core cutting has several advantages over the hole-drilling release residual stresses: (i) the relieved strains are one order of magnitude larger than in the hole-drilling so that it offers greater measurement sensitivity; (ii) the ring-core cutting causes no stress concentration on the gage grid and can be used to quantify the stress larger than half of yield strength; (iii) the ring-core method is less sensitive to the location of the drilling when used with a strain rosette [3]. On the theoretical development, similar to the application in the hole-drilling method, the integral method was applied in the incremental ring-core cutting problem to include the change of the groove geometry [4]. Various cutting increment distributions were investigated, and an optimized increment distribution was proposed [5]. The assumption of uniform stress distribution is normally made within each removed layer where the measured strains are averaged strains over the gage grids of the rosette. Therefore, the size of the rosette is a critical factor in improving the resolution and accuracy of strain measurement. The magnitude of the inner diameter is limited by the size of the rosette. The commonly used resistance rosette for the ring-core cutting has a 12 mm diameter (measuring grid with carrier) and the length of measuring grid is about half of the diameter. The corresponding core diameter is about 14 mm for this type of RSR. If a smaller ring-core could be cut, more localized residual stresses can be measured. This can improve the resolution and accuracy of strain measurement, especially at the locations with high stress gradients.

To overcome the difficulties of the RSR/ring-core method, optical methods may be considered due to their noncontacting nature. Different optical methods, such as Morié, holography, and speckle methods have been used with the hole drilling to measure residual stresses [6,7]. However, when any of the above methods would be utilized in conjunction with the ring-core method to measure residual stresses, it would be difficult to acquire reliable fringe patterns in a small core area. According to our literature review, there has been no published paper about optical method applied with the ring-core cutting for residual stress measurement.

Optical gages have been developed to measure strains, such as the grating diffraction strain gage [7], diffractographic strain gage [8], and the interferometric strain/displacement gage (ISDG) [9]. The ISDG is based on interference of laser reflected from two grooves, and a biaxial ISDG developed later can be used to measure two orthogonal strains [10]. The interferometric strain/slope rosette (ISSR) technique [11] is extended from the ISDG. The

Contributed by the Applied Mechanics Division of ASME for publication in the JOURNAL OF APPLIED MECHANICS. Manuscript received May 6, 2004; final manuscript received February 5, 2006. Review conducted by H. D. Espinsoa. Discussion on the paper should be addressed to the Editor, Prof. Robert M. McMeeking, Journal of Applied Mechanics, Department of Mechanical and Environmental Engineering, University of California-Santa Barbara, Santa Barbara, CA 93106-5070, and will be accepted until four months after final publication of the paper itself in the ASME JOURNAL OF APPLIED MECHANICS.

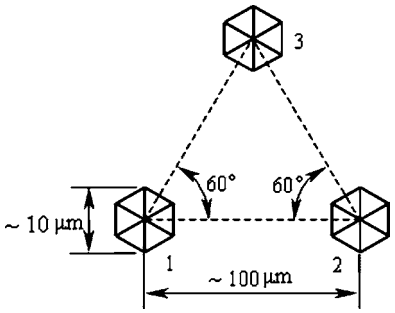

Fig. 1 60 deg ISSR with three hexagonal pyramidal indentations

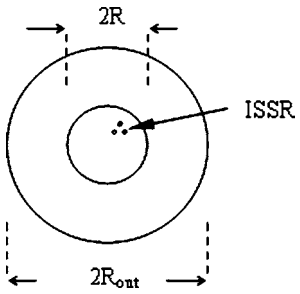

Fig. 2 Schematic diagram of ring core and ISSR

ISSR has high accuracy for measurements of three strain components and three out-of-plane slopes [12]. Besides its noncontacting nature, the ISSR has extremely short gage length (50–250 μm). When the ISSR is applied to specimens with complex geometry, its miniature size makes strain measurement effective in the areas with steep stress gradients. The ISSR method has been tested through various calibration experiments, such as measurements in a uniaxially stressed field on a thin-walled tube [13] and near a through-hole on a loaded thin bar [14]. The test results have shown good agreement with the theoretical solutions. The ISSR in conjunction with the hole-drilling method has been developed as means of residual stress measurement [14].

In this paper, the ISSR is used with the ring-core method for residual stress measurement. The diameter of central core used with the ISSR is about 2 mm, only 1/7 of that used with the RSR. Ring-core cutting and data acquisition are more convenient due to the noncontacting nature of the ISSR. The purpose of this paper is to develop the principles of the ISSR/ring-core cutting method. A new mechanical model of incremental ring-core cutting must be created to simulate the response of the ISSR. Furthermore, the numerical methods, such as finite element analysis (FEA), must be implemented to set up the relationship between the residual stresses and the ISSR strain measurements.

2 Theoretical Development of ISSR/Ring-Core Method

2.1 Application of ISSR With Ring-Core Method. An ISSR normally consists of three microindentations and can have a configuration of delta or rectangular rosette. The δ rosette contains three six-faced indentations and these indentations form an equilateral triangle as shown in Fig. 1. The size of indentations is in the order of 10 μm, and the separation between a pair of indentations or gage length is in the order of 100 μm. Under illumination by an incident laser beam, the six faces of each indentation in a δ rosette reflect and diffract the light in six directions, which are 60 deg apart from one another, and there exists an interference fringe pattern in every 60 deg direction. Both in-plane and out-of-plane displacements between the indentations cause the change of the optical path length and, hence, the phase change between two interfering laser beams. The strains and slopes are measured according to the movement of the interference fringes. The governing equations [11] are

$$\frac{\delta d_1}{d_1}=\frac{\lambda}{2d_1\sin\alpha}(\delta m_1+\delta m_4)\quad \frac{\delta w_1}{d_1}=\frac{\lambda}{2d_1(1+\cos\alpha)}(\delta m_1-\delta m_4)$$

$$\frac{\delta d_2}{d_2}=\frac{\lambda}{2d_2\sin\alpha}(\delta m_3+\delta m_6)\quad \frac{\delta w_2}{d_2}=\frac{\lambda}{2d_2(1+\cos\alpha)}(\delta m_3-\delta m_6)$$

$$\frac{\delta d_3}{d_3}=\frac{\lambda}{2d_3\sin\alpha}(\delta m_2+\delta m_5)\quad \frac{\delta w_3}{d_3}=\frac{\lambda}{2d_3(1+\cos\alpha)}(\delta m_5-\delta m_2) \tag{1}$$

where λ is the wavelength of the laser, α is the angle between the incident laser beam and the reflected laser beams, d_i ($i=1$, 2, and 3) is the separation between each pair of the indentations or gage length, δd_i is the relative in-plane displacement, δw_i is the relative out-of-plane displacement, δm_j ($j=1,2,\ldots 6$) is the change of the fringe order in the interference pattern j, which is measured by a six-channel linear-array system, and $\delta d_i/d_i$ and $\delta w_i/d_i$ are strains and slopes with respect to the direction of corresponding indentation separation, respectively.

For a thin plate in the plane stress state, if the material is isotropic and linear elastic, and strains are small, the stresses are uniformly distributed through the thickness of the plate. For a ring-core cutting, Fig. 2 illustrates the relative positions of the ring core and the ISSR, where R is the radius of central core and R_{out} is the outer radius of the ring core. The rectangular and polar coordinate systems are shown in Fig. 3, where σ_1 and σ_2 are the maximum and minimum principal stresses, respectively, $\boldsymbol{r}$ is the vector from the core center to the ISSR center, θ is the angle from the x-axis to the vector $\boldsymbol{r}$, and φ is the angle from the x-axis to the direction of σ_1. Both θ and φ are defined to be positive in counterclockwise direction. If the ring-core cutting is through the plate thickness, the stresses around the central core are completely relieved and only the strain relaxation on the central core needs to be analyzed. As the relieved in-plane strains in polar coordinates, ε_r, ε_θ, and $\gamma_{r\theta}$ can be derived in terms of the original stresses in Eq. (2), where E is Young's modulus and ν is Poisson's ratio.

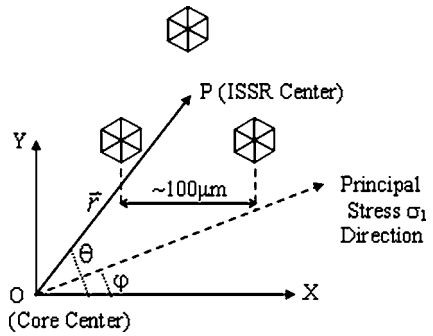

Fig. 3 Schematic diagram of rectangular and polar coordinates for the ISSR/ring-core method

$$\begin{bmatrix} \varepsilon_r \\ \varepsilon_\theta \\ \gamma_{r\theta} \end{bmatrix} = \frac{1}{E} \begin{bmatrix} 1-\nu & (1+\nu)\cos 2\theta & -(1+\nu)\sin 2\theta \\ 1-\nu & -(1+\nu)\cos 2\theta & (1+\nu)\sin 2\theta \\ 0 & -2(1+\nu)\sin 2\theta & -2(1+\nu)\cos 2\theta \end{bmatrix} \times \begin{bmatrix} -\dfrac{\sigma_1+\sigma_2}{2} \\ -\dfrac{\sigma_1-\sigma_2}{2}\cos 2\varphi \\ \dfrac{\sigma_1-\sigma_2}{2}\sin 2\varphi \end{bmatrix} \quad (2)$$

2.2 Incremental Ring-Core Cutting/ISSR Method. Incremental ring-core cutting must be conducted to obtain the distribution of residual stresses with respect to depth of cutting into the material surface. The ring-core is cut around the ISSR layer by layer. After the relieved strains are measured on the surface of the specimen, residual stresses in the first layer of cutting can be approximately calculated using the equation of the through-ring-core case, e.g., Eq. (2). To obtain more accurate solutions, the geometry of the blind ring-core cut has to be taken into account and numerical methods such as finite element analysis (FEA) need to be adopted to calibrate the stress-strain relationship.

To simulate the removed ring of material during the first step of cutting, normal and shear tractions with same depth are applied to the inner and outer walls of the ring core. At any arbitrary angle, the tractions applied to the inner and outer walls have same magnitudes but opposite directions. A uniform plane-stress state is assumed for the first layer of cutting. The tractions on a unit area can be expressed in terms of the stress field as

$$T_r^{\text{in}} = \left(\frac{\sigma_1+\sigma_2}{2}\right) + \left(\frac{\sigma_1-\sigma_2}{2}\right)\cos[2(\theta-\varphi)] = -T_r^{\text{out}} \quad (3a)$$

$$T_{r\theta}^{\text{in}} = -\frac{\sigma_1-\sigma_2}{2}\sin[2(\theta-\varphi)] = -T_{r\theta}^{\text{out}} \quad (3b)$$

where T_r^{in} is the normal traction acting on the inner wall, T_r^{out} is the normal traction acting on the outer wall, $T_{r\theta}^{\text{in}}$ and $T_{r\theta}^{\text{out}}$ are circumferential tractions acting on the inner wall and the outer wall, respectively, σ_1 and σ_2 are the maximum and minimum principal residual stresses at the first depth increment of cutting respectively, and θ and φ are defined in Sec. 2.1 and are shown in Fig. 3. The superposition of the original stress state and the stress change due to cutting results in a final zero stress state [15].

Let $P=-[(\sigma_1+\sigma_2)/2]$, $Q=-[(\sigma_1-\sigma_2)/2]\cos[2(\theta-\varphi)]$ and $R=(\sigma_1-\sigma_2)/2\sin[2(\theta-\varphi)]$, where P is called the hydrostatic radial stress, Q is called the second-order harmonic radial stress and R is called the second-order harmonic circumferential stress. If the geometry of the problem is axisymmetric, the displacements must also show the same harmonics and symmetry as the tractions [16]. P and Q are symmetric functions while R is anti-symmetric function. Since P and Q represent normal stresses, and R represents shear stress; P, Q, and R are all symmetrical with respect to the principal direction of σ_1. A symmetric and harmonic displacement field would be resulted as

$$u_r = A(r)P + B(r)Q \quad u_\theta = C(r)R \quad u_z = D(r)P + F(r)Q \quad (4)$$

where r is the norm of the vector $\mathbf{r}$ as shown in Fig. 3, u_r, u_θ, and u_z are displacement components in polar coordinates and expressed in terms of σ_1, σ_2, and φ; A, B, C, D, and F are coefficients, which are functions of the ISSR position parameter r, core radius R, outer radius R_{out}, Young's modulus E, and Poisson's ratio ν. All these parameters are taken into account in the FEA. For the model with $R_{\text{out}} > 2R$, the coefficients $A-F$ show little dependence on the change of outer radius. Therefore, owing to the usage of R_{out} larger than $2R$, the variation of R_{out} would not be taken into account when the coefficients are developed. The displacement components are differentiated to calculate strains and slopes. The relieved strains during the blind ring-core cutting are derived to relate to the residual stresses in Eq. (5*a*) or Eq. (5*b*). When $A(r)=(1-\nu)r/E$, $B(r)=(1+\nu)r/E$, and $C(r)=(1+\nu)r/E$, Eq. (5*a*) can be simplified to Eq. (2), indicating the through-ring-core cutting case

$$\begin{bmatrix} \varepsilon_r \\ \varepsilon_\theta \\ \gamma_{r\theta} \\ \dfrac{\partial u_z}{\partial r} \\ \dfrac{1}{r}\dfrac{\partial u_z}{\partial \theta} \end{bmatrix}_1 = \begin{bmatrix} \dfrac{\partial A(r)}{\partial r} & \dfrac{\partial B(r)}{\partial r}\cos 2\theta & -\dfrac{\partial B(r)}{\partial r}\sin 2\theta \\ \dfrac{A(r)}{r} & \dfrac{B(r)}{r}\cos 2\theta - \dfrac{2C(r)}{r}\cos 2\theta & -\dfrac{B(r)}{r}\sin 2\theta + \dfrac{2C(r)}{r}\sin 2\theta \\ 0 & -\dfrac{2B(r)}{r}\sin 2\theta - \dfrac{\partial C(r)}{\partial r}\sin 2\theta + \dfrac{C(r)}{r}\sin 2\theta & -\dfrac{2B(r)}{r}\cos 2\theta - \dfrac{\partial C(r)}{\partial r}\cos 2\theta + \dfrac{C(r)}{r}\cos 2\theta \\ \dfrac{\partial D(r)}{\partial r} & \dfrac{\partial F(r)}{\partial r}\cos 2\theta & -\dfrac{\partial F(r)}{\partial r}\sin 2\theta \\ 0 & -\dfrac{2F(r)}{r}\sin 2\theta & -\dfrac{2F(r)}{r}\cos 2\theta \end{bmatrix}_{11} \begin{bmatrix} -\dfrac{\sigma_1+\sigma_2}{2} \\ -\dfrac{\sigma_1-\sigma_2}{2}\cos 2\varphi \\ \dfrac{\sigma_1-\sigma_2}{2}\sin 2\varphi \end{bmatrix}_1 \quad (5a)$$

or

$$\boldsymbol{L}_1 = \boldsymbol{U}_{11}\boldsymbol{I}_1 \tag{5b}$$

In Eq. (5*b*), $\boldsymbol{I}_1$ is the 3×1 vector of unknown stresses, $\boldsymbol{U}_{11}$ is the 5×3 matrix of relaxation coefficients, and $\boldsymbol{L}_1$ is the 5×1 vector of displacement derivatives including strains and slopes. The components of strains and slopes are measured by the ISSR during the ring-core cutting. There are five equations to be solved for the three unknown stress components in Eq. (5*a*) or (5*b*). The least-squares method can be applied to solve this overdetermined problem and the solution can be obtained through the pseudoinversion. The last two elements of the vector $\boldsymbol{L}_1$ represent the out-of-plane slopes. If $\boldsymbol{\psi}_1$ is taken as a 3×1 vector with the first three elements of the vector $\boldsymbol{L}_1$ and the upper 3×3 submatrix of the matrix $\boldsymbol{U}_{11}$ is designated as the matrix $\boldsymbol{K}_{11}$, the residual stresses can be calculated by direct inversion as

$$\boldsymbol{I}_1 = \mathbf{K}_{11}^{-1}\cdot\boldsymbol{\psi}_1 \tag{6}$$

The stress vector $\boldsymbol{I}_1$ can be solved if the coefficients in matrix $\boldsymbol{U}_{11}$ or $\boldsymbol{K}_{11}$ are provided. The determination of $\boldsymbol{U}_{11}$ and $\boldsymbol{K}_{11}$ relies on the FEA and will be discussed in Sec. 3.1.

2.3 Application of Integral Method. The applied tractions and the matrix formulation in the first step of ring-core cutting can be generalized to the subsequent cutting steps. The isotropic material and plane-stress assumptions are still valid in each removed layer. The in-plane residual stresses are uniform for each depth increment, but may vary with respect to the depths of increments. Integral method was used for the resistance strain rosette and ring-core method. Two sets of the relaxation coefficients were determined numerically through a boundary element method [4]. For the ISSR/ring-core method, more relaxation coefficients are involved in the mechanical model. Thus, a new scheme needs to be developed for the stress calculation by using the integral method. The relaxed strains in the various layers are expressed as

$$\begin{bmatrix}\boldsymbol{L}_1\\ \boldsymbol{L}_2\\ \vdots\\ \boldsymbol{L}_n\end{bmatrix} = \begin{bmatrix}\boldsymbol{U}_{11} & 0 & \cdots & 0\\ \boldsymbol{U}_{21} & \boldsymbol{U}_{22} & \cdots & 0\\ \vdots & \vdots & \ddots & \vdots\\ \boldsymbol{U}_{n1} & \boldsymbol{U}_{n2} & \cdots & \boldsymbol{U}_{nn}\end{bmatrix}\cdot\begin{bmatrix}\boldsymbol{I}_1\\ \boldsymbol{I}_2\\ \vdots\\ \boldsymbol{I}_n\end{bmatrix} \Leftrightarrow \boldsymbol{L} = \boldsymbol{U}\cdot\boldsymbol{I} \tag{7}$$

If the form of direct inversion in Eq. (6) is used, the in-plane strains can be expressed as

$$\begin{bmatrix}\boldsymbol{\psi}_1\\ \boldsymbol{\psi}_2\\ \vdots\\ \boldsymbol{\psi}_n\end{bmatrix} = \begin{bmatrix}\boldsymbol{K}_{11} & 0 & \cdots & 0\\ \boldsymbol{K}_{21} & \boldsymbol{K}_{22} & \cdots & 0\\ \vdots & \vdots & \ddots & \vdots\\ \boldsymbol{K}_{n1} & \boldsymbol{K}_{n2} & \cdots & \boldsymbol{K}_{nn}\end{bmatrix}\cdot\begin{bmatrix}\boldsymbol{I}_1\\ \boldsymbol{I}_2\\ \vdots\\ \boldsymbol{I}_n\end{bmatrix} \Leftrightarrow \boldsymbol{\psi} = \boldsymbol{K}\cdot\boldsymbol{I} \tag{8}$$

In Eq. (7), each of $\boldsymbol{L}_i$, $\boldsymbol{I}_i$, and $\boldsymbol{U}_{ij}$ $(1\leqslant j\leqslant i\leqslant n)$ takes the same form as $\boldsymbol{L}_1$, $\boldsymbol{I}_1$, and $\boldsymbol{U}_{11}$ in Eq. (5*a*). $\boldsymbol{L}_i$ represents the vector of cumulative strains and slopes till the completion of the ith step of cutting while $\boldsymbol{\psi}_i$ in Eq. (8) only consists of the strain elements of $\boldsymbol{L}_i$, $\boldsymbol{I}_i$ is the vector of residual stresses in the ith removed layer. $\boldsymbol{U}_{ij}$ is the matrix with incremental strain/slope relaxation coefficients when the current cutting step is i and tractions are only applied to the jth layer. $\boldsymbol{K}_{ij}$ in Eq. (8) is the upper 3×3 submatrix of $\boldsymbol{U}_{ij}$. After the ith cutting step is finished, the cumulative relaxed strains are related to residual stresses in all the 1st–ith layers. The physical meanings of $\boldsymbol{K}_{ij}$ matrices are illustrated by a three-step ring-core cutting example shown in Fig. 4, where only the normal tractions are plotted. In Fig. 4, it can be found that the variation of ring-core geometry is taken into account for each step of cutting. The stress components for each layer can be solved through the inversion form of Eq. (7) or (8).

3 Numerical Calibrations of Relaxation Coefficients

In this section, a finite element model is developed to simulate the process of ring-core cutting around the ISSR. The relaxation coefficients in $\boldsymbol{U}_{ij}$ and $\boldsymbol{K}_{ij}$ are numerically calibrated by applying the loads on the boundary of the model. The coefficients are also nondimensionalized for general applications.

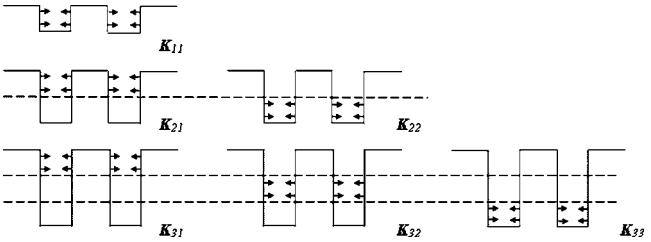

Fig. 4 Mechanical model used to calculate the relaxation matrices $K_{11}-K_{33}$

3.1 Finite Element Analysis of the Problem. A three-dimensional problem with axisymmetric geometry can be reduced to a two-dimensional problem by means of Fourier expansion [17]. The axisymmetric element ANSYS PLANE83, is used in the finite element modeling. Each node has three degrees of freedom, which are translations in x, y, and z directions. The geometry of this thick plate model is shown in Fig. 5. The model width and height are chosen sufficiently large with respect to the ring-core dimensions to minimize the influence caused by constraints. Selection of a suitable constraint is based on the clamping and supporting conditions in the test. The model is originally built in a rectangular shape, and the elements in GEFH zone in Fig. 5 are gradually removed to simulate the layer-by-layer ring-core cutting. The finite element mesh in the ring-core area is shown in Fig. 6, where the elements in several layers have been "killed." The zeroth and second-order harmonic loads are applied to the inner and outer walls. With given magnitudes of loads, the displacement response at the ISSR on the core surface can be obtained.

For an equibiaxial stress case ($\sigma_1=1$ MPa and $\sigma_2=1$ MPa), Eq. (4) yields

$$u_z = -D(r)$$

$$u_r = -A(r) \tag{9}$$

For a pure shear stress case ($\sigma_1=1$ MPa and $\sigma_2=-1$ MPa), Eq. (4) results in the following displacement field:

$$u_r = -B(r)\cos 2(\theta-\varphi)$$

$$u_\theta = C(r)\sin 2(\theta-\varphi)$$

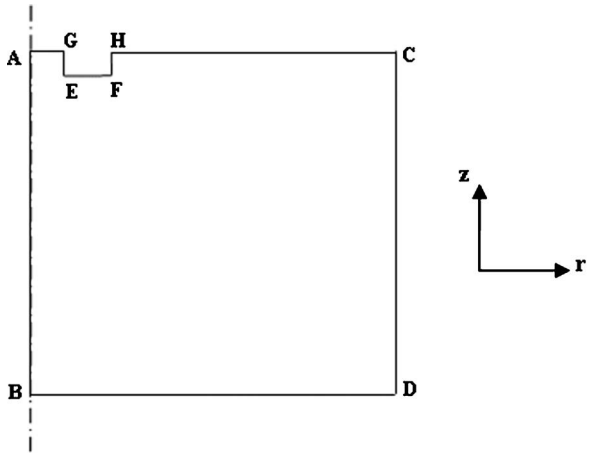

Fig. 5 Geometry of finite element model

$$u_z = -F(r)\cos 2(\theta - \varphi) \tag{10}$$

B, C, and F are related to the displacements caused by the second-order harmonic tractions. Hence, all the u_r, u_θ, and u_z in Eq. (10) consist of displacements caused by both radial and circumferential tractions.

By setting different loading cases and angles in Eqs. (9) and (10), A, B, C, D, and F can be determined. In practice, the cumulative displacement coefficients $\bar{A}$, $\bar{B}$, $\bar{C}$, $\bar{D}$, and $\bar{F}$ are obtained when the applied loads are cumulative tractions. For different cutting depths and loading depths, the finite element model can always generate $\bar{A}$–$\bar{F}$ values at all the mesh points on the core surface. If H represents the current cutting depth, and the tractions are applied from the surface down to a cutting depth h ($0 \leqslant h \leqslant H$), $\bar{A}$ is a function of H, h, and r. For a given H and h, a series of $\bar{A}$ values are obtained when r ranges from the core center to the core edge, and these values can be fitted by a continuous function as

$$\bar{A} = a_1 + a_2 r + a_3 r^2 + a_4 r^3 + a_5 r^4 + a_6 r^5 + a_7 r^6 + a_8 r^7 \tag{11}$$

where $a_1, a_2, \ldots, a_8$ are constants of fit. Similarly, $\bar{B}$, $\bar{C}$, $\bar{D}$, and $\bar{F}$ can also be calculated. When the current cutting step is i with the cutting depth of H and tractions are applied from surface down to each cutting depth h with the jth step ($0 \leqslant j \leqslant i$), the cumulative displacement coefficients can be denoted as $\bar{A}_{ij}$, $\bar{B}_{ij}$, $\bar{C}_{ij}$, $\bar{D}_{ij}$, and $\bar{F}_{ij}$.

3.2 Nondimensionalized Strain/Slope Coefficients. The matrix $\boldsymbol{U}_{ij}$ with cumulative relaxation coefficients is denoted as $\hat{\boldsymbol{U}}_{ij}$. To simplify the problem, the angle θ is set to zero in the matrix $\hat{\boldsymbol{U}}_{ij}$. Hence, the x-axis is in the direction of vector $\boldsymbol{r}$ and through the ISSR center. Several coefficients in $\hat{\boldsymbol{U}}_{ij}$ are zeros as shown in

$$\hat{\boldsymbol{U}}_{ij} = \begin{bmatrix} \dfrac{\partial \bar{A}_{ij}(r)}{\partial r} & \dfrac{\partial \bar{B}_{ij}(r)}{\partial r} & 0 \\ \dfrac{\bar{A}_{ij}(r)}{r} & \dfrac{\bar{B}_{ij}(r)}{r} - \dfrac{2\bar{C}_{ij}(r)}{r} & 0 \\ 0 & 0 & -\dfrac{2\bar{B}_{ij}(r)}{r} - \dfrac{\partial \bar{C}_{ij}(r)}{\partial r} + \dfrac{\bar{C}_{ij}(r)}{r} \\ \dfrac{\partial \bar{D}_{ij}(r)}{\partial r} & \dfrac{\partial \bar{F}_{ij}(r)}{\partial r} & 0 \\ 0 & 0 & -\dfrac{2\bar{F}_{ij}(r)}{r} \end{bmatrix}$$

$$= \begin{bmatrix} \hat{A}_{ij} & \hat{B}_{ij} & 0 \\ \hat{C}_{ij} & \hat{D}_{ij} & 0 \\ 0 & 0 & \hat{F}_{ij} \\ \hat{G}_{ij} & \hat{J}_{ij} & 0 \\ 0 & 0 & \hat{T}_{ij} \end{bmatrix} \tag{12}$$

The strain/slope relaxation coefficients $\hat{A}_{ij}$, $\hat{B}_{ij}$, $\hat{C}_{ij}$, $\hat{D}_{ij}$, $\hat{F}_{ij}$, $\hat{G}_{ij}$, $\hat{J}_{ij}$, and $\hat{T}_{ij}$ are calculated from the cumulative displacement coefficients $\bar{A}_{ij}$–$\bar{F}_{ij}$. The coefficients $\hat{A}_{ij}$–$\hat{T}_{ij}$ are not only functions of the dimension ratios H/R, h/R, and r/R, but also functions of the elastic properties (E and ν). To apply the coefficients to different engineering materials, $\hat{A}_{ij}$–$\hat{T}_{ij}$ are transformed to be independent of material constants. Based on the aluminum material (E = 70 GPa and ν=0.33) and the thick plate model shown in Fig. 5, the cumulative coefficients in $\hat{\boldsymbol{U}}_{ij}$ are nondimensionalized with respect to E and ν as

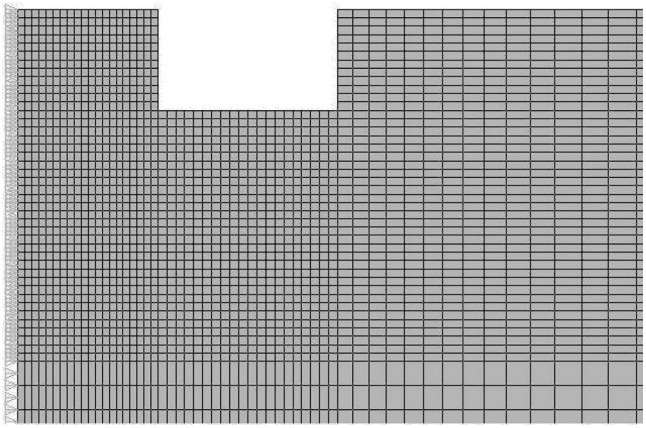

Fig. 6 Finite element mesh of local ring-core area

$$\hat{A}'_{ij} = \frac{E}{1-\nu}\hat{A}_{ij} \quad \hat{B}'_{ij} = E\hat{B}_{ij} \quad \hat{C}'_{ij} = \frac{E}{1-\nu}\hat{C}_{ij} \quad \hat{D}'_{ij} = E\hat{D}_{ij}$$

$$\hat{F}'_{ij} = E\hat{F}_{ij} \quad \hat{G}'_{ij} = E(1+\nu)\hat{G}_{ij} \quad \hat{J}'_{ij} = E(1+\nu)\hat{J}_{ij} \quad \hat{T}'_{ij} = E(1+\nu)\hat{T}_{ij} \tag{13}$$

The cumulative strain/slope relaxation coefficients $\hat{A}'_{ij}$–$\hat{T}'_{ij}$ are independent of the material properties. For the given ratios of r/R, H/R, and h/R ($0 \leqslant h \leqslant H$), the coefficients $\hat{A}'_{ij}$–$\hat{T}'_{ij}$ ($0 \leqslant j \leqslant i$) are calculated using Eqs. (9)–(13) and recorded in Table 1.

Within elastic range, the nondimensionalized coefficients in Table 1 can be applied to many isotropic and linear elastic engineering materials, and the coefficients are suitable for various ring-core geometry. Most of engineering materials have close Poisson's ratios. Some metal materials with ν ranging from 0.28 to 0.33 are examined. After nondimensionalization, using Eq. (13), $\hat{A}'$, $\hat{B}'$, $\hat{C}'$, $\hat{D}'$, and $\hat{F}'$ have shown little dependence on ν. These coefficients represent in-plane strain relaxation. For out-of-plane slope coefficients $\hat{G}'$, $\hat{J}'$, and $\hat{T}'$, although the dependence on ν is reduced through the nondimensionalization, they are still related to the ratio ν. For example, most values of $\hat{G}'$, $\hat{J}'$ and $\hat{T}'$ at r/R=0.4 have $<7\%$ differences between the values calculated with ν=0.28 and ν=0.33. But for some cutting depths, the differences can be $>10\%$.

In Table 1, the nondimensionalized coefficients for the through ring-core cutting are calculated using Eqs. (2) and (13). Ideally, the coefficients of a blind ring core should be smaller in magnitude than those from a through ring core. However, when the ISSR position is near the core edge and the cutting depth is large, e.g., r/R=0.8 and H/R=h/R=0.6, $\hat{A}'$, $\hat{B}'$, $\hat{C}'$, and $\hat{F}'$ show values greater than the through-ring-core coefficients. The constraints of type I in Fig. 5 are used as the constraint conditions in the calculation of Table 1. Only slight differences are observed between the two sets of coefficients calculated by using type I and type II constraints. For a thick plate model with length and thickness beyond certain values, the constraints on the sides of the model show little influence on the surface area of the ring core.

4 Determination of Residual Stresses

4.1 Residual Stress Calculation. In the ring core cutting test, if the cutting depth ratios are the same as listed in Table 1, the

Table 1 Nondimensionalized cumulative coefficients in matrix $\hat{U}'$

r/R	H/R Through ring	h/R core	$\hat{A}'$ 1	$\hat{B}'$ 1.33	$\hat{C}'$ 1	$\hat{D}'$ −1.33	$\hat{F}'$ −2.66	$\hat{G}'$	$\hat{J}'$	$\hat{T}'$
0.2	0.05	0.05	0.0634	0.0474	0.0592	−0.0373	−0.1028	−0.0098	−0.0098	−0.0046
	0.1	0.05	0.0804	0.0570	0.0820	−0.0500	−0.1284	−0.0092	−0.0092	−0.0012
		0.1	0.1465	0.1049	0.1489	−0.1018	−0.2215	−0.0070	−0.0065	0.0063
	0.2	0.05	0.1150	0.0835	0.1147	−0.0755	−0.1783	−0.0103	−0.0092	0.0037
		0.1	0.2182	0.1571	0.2167	−0.1523	−0.3194	−0.0094	−0.0069	0.0158
		0.2	0.3835	0.2774	0.3694	−0.2698	−0.5460	−0.0249	−0.0166	0.0260
	0.4	0.05	0.1565	0.1374	0.1538	−0.1246	−0.2799	−0.0188	−0.0216	0.0144
		0.1	0.3008	0.2599	0.2945	−0.2465	−0.5140	−0.0261	−0.0303	0.0360
		0.2	0.5578	0.4708	0.5342	−0.4486	−0.9140	−0.0599	−0.0594	0.0628
		0.4	0.8476	0.7180	0.8223	−0.6941	−1.4084	−0.1167	−0.0954	0.0918
	0.6	0.05	0.1709	0.1763	0.1684	−0.1623	−0.3567	−0.0232	−0.0359	0.0282
		0.1	0.3295	0.3343	0.3237	−0.3187	−0.6609	−0.0348	−0.0573	0.0619
		0.2	0.6158	0.6078	0.5933	−0.5818	−1.1848	−0.0770	−0.1075	0.1091
		0.4	0.9854	0.9644	0.9636	−0.9358	−1.8977	−0.1562	−0.1744	0.1678
		0.6	1.1143	1.1103	1.1037	−1.0900	−2.1992	−0.1799	−0.1816	0.1762
0.4	0.05	0.05	0.0767	0.0557	0.0636	−0.0516	−0.0937	0.0072	0.0071	0.0049
	0.1	0.05	0.1123	0.0783	0.0858	−0.0652	−0.1271	0.0013	0.0017	0.0062
		0.1	0.2018	0.1430	0.1569	−0.1185	−0.2505	−0.0168	−0.0133	0.0110
	0.2	0.05	0.1576	0.1146	0.1220	−0.0905	−0.1898	−0.0122	−0.0114	0.0127
		0.1	0.2947	0.2138	0.2318	−0.1695	−0.3752	−0.0442	−0.0388	0.0241
		0.2	0.4766	0.3518	0.3963	−0.2970	−0.6503	−0.0885	−0.0688	0.0489
	0.4	0.05	0.2039	0.1768	0.1635	−0.1371	−0.2993	−0.0324	−0.0429	0.0395
		0.1	0.3863	0.3325	0.3144	−0.2596	−0.5852	−0.0838	−0.0978	0.0746
		0.2	0.6684	0.5749	0.5704	−0.4722	−1.0509	−0.1699	−0.1755	0.1406
		0.4	0.9484	0.8358	0.8577	−0.7387	−1.5793	−0.2781	−0.2444	0.2089
	0.6	0.05	0.2171	0.2150	0.1778	−0.1715	−0.3721	−0.0415	−0.0740	0.0687
		0.1	0.4124	0.4053	0.3428	−0.3256	−0.7245	−0.1016	−0.1563	0.1298
		0.2	0.7200	0.7085	0.6277	−0.5950	−1.3083	−0.2046	−0.2794	0.2390
		0.4	1.0683	1.0764	0.9935	−0.9676	−2.0498	−0.3563	−0.4138	0.3699
		0.6	1.1484	1.2020	1.1174	−1.1289	−2.3354	−0.3845	−0.4146	0.3800
0.6	0.05	0.05	0.1235	0.0908	0.0750	−0.0586	−0.1665	−0.0233	−0.0219	0.0044
	0.1	0.05	0.1651	0.1177	0.1033	−0.0754	−0.2118	−0.0302	−0.0275	0.0104
		0.1	0.2864	0.2067	0.1850	−0.1438	−0.3660	−0.0462	−0.0373	0.0242
	0.2	0.05	0.2375	0.1783	0.1460	−0.1027	−0.2939	−0.0556	−0.0526	0.0271
		0.1	0.4341	0.3247	0.2729	−0.2010	−0.5307	−0.0978	−0.0857	0.0567
		0.2	0.6824	0.5195	0.4523	−0.3571	−0.8794	−0.1959	−0.1546	0.1029
	0.4	0.05	0.2937	0.2572	0.1908	−0.1447	−0.4135	−0.1022	−0.1302	0.0789
		0.1	0.5434	0.4740	0.3616	−0.2837	−0.7608	−0.1883	−0.2307	0.1538
		0.2	0.9063	0.7988	0.6380	−0.5261	−1.3262	−0.3799	−0.4154	0.2785
		0.4	1.1126	1.0533	0.9145	−0.8267	−1.8969	−0.5550	−0.5389	0.3882
	0.6	0.05	0.3014	0.2873	0.2040	−0.1735	−0.4749	−0.1155	−0.1803	0.1256
		0.1	0.5581	0.5313	0.3877	−0.3393	−0.8784	−0.2139	−0.3245	0.2418
		0.2	0.9340	0.9037	0.6902	−0.6309	−1.5440	−0.4277	−0.5806	0.4346
		0.4	1.1712	1.2427	1.0364	−1.0320	−2.3035	−0.6563	−0.8023	0.6417
		0.6	1.1538	1.3204	1.1305	−1.1989	−2.5404	−0.6225	−0.7460	0.6344
0.8	0.05	0.05	0.2862	0.2026	0.1008	−0.0865	−0.2676	−0.0133	−0.0066	0.0121
	0.1	0.05	0.4486	0.3168	0.1428	−0.1082	−0.3825	−0.0862	−0.0758	0.0269
		0.1	0.6862	0.4957	0.2475	−0.2047	−0.6979	−0.2111	−0.1781	0.0566
	0.2	0.05	0.5733	0.4304	0.2000	−0.1372	−0.5199	−0.2108	−0.2187	0.0735
		0.1	0.9343	0.7141	0.3641	−0.2704	−0.9807	−0.4582	−0.4475	0.1460
		0.2	1.1289	0.9225	0.5614	−0.4816	−1.4837	−0.6683	−0.6097	0.2399
	0.4	0.05	0.6020	0.4881	0.2457	−0.1722	−0.6277	−0.2894	−0.3622	0.1688
		0.1	0.9874	0.8226	0.4538	−0.3417	−1.1889	−0.6065	−0.7114	0.3235
		0.2	1.2302	1.1272	0.7473	−0.6408	−1.8991	−0.9567	−1.0731	0.5580
		0.4	1.1693	1.2656	0.9765	−0.9816	−2.3758	−0.9609	−1.0701	0.6858
	0.6	0.05	0.5993	0.4990	0.2562	−0.1929	−0.6636	−0.2977	−0.4129	0.2304
		0.1	0.9817	0.8435	0.4746	−0.3820	−1.2574	−0.6211	−0.8052	0.4389
		0.2	1.2173	1.1661	0.7882	−0.7186	−2.0263	−0.9794	−1.2336	0.7611
		0.4	1.1337	1.3415	1.0705	−1.1462	−2.6187	−0.9911	−1.3066	1.0090
		0.6	1.0534	1.3756	1.1263	−1.3012	−2.7410	−0.7875	−1.1101	0.9428

nondimensional coefficients $\hat{A}'_{ij}-\hat{T}'_{ij}$ are directly looked up from Table 1. Otherwise, the coefficients in Table 1 need to be interpolated in terms of the depth increments in the test. The coefficients $\hat{A}_{ij}-\hat{T}_{ij}$ $(0\leqslant j\leqslant i)$ can then be back-calculated through Eq. (13). With the calculated coefficients $\hat{A}_{ij}-\hat{T}_{ij}$, the matrix $\hat{\boldsymbol{U}}_{ij}$ can be obtained and the matrix with incremental coefficients can be calculated through subtractions between two adjacent $\hat{\boldsymbol{U}}_{ij}$ matrices, e.g.,

Fig. 7 Top surface of spot-weld coupon

Fig. 8 Bottom surface of spot-weld coupon after the ring-core cutting

$$\boldsymbol{U}_{ij} = \hat{\boldsymbol{U}}_{ij} - \hat{\boldsymbol{U}}_{i,j-1} \tag{14}$$

Since $\boldsymbol{U}_{ij}$ is the submatrix of $\boldsymbol{U}$ at the ith row and jth column, the matrix $\boldsymbol{U}$ can be constructed. The matrix $\boldsymbol{K}$ can be obtained as well.

The strains and slopes at the location of the ISSR are measured for each depth increment of ring-core cutting. Therefore, the strain/slope vectors ($\boldsymbol{L}$ and $\boldsymbol{\psi}$) are experimentally determined with the accumulation of the strains and slopes. The stress vector I is calculated using the inversion form of Eq. (7) or (8). If the three elements of the stress vector $\boldsymbol{I}_j$ for the jth depth increment can be recorded as $\boldsymbol{I}_j(1)$, $\boldsymbol{I}_j(2)$, and $\boldsymbol{I}_j(3)$, the uniform principal stresses and principal angle can be calculated as

$$\sigma_{1j}, \sigma_{2j} = -\boldsymbol{I}_j(1) \pm \sqrt{\boldsymbol{I}_j^2(2) + \boldsymbol{I}_j^2(3)} \quad \varphi_j = \frac{1}{2}\arctan\left[-\frac{\boldsymbol{I}_j(3)}{\boldsymbol{I}_j(2)}\right] \tag{15}$$

The stresses in the original coordinate system can be obtained through transformation as

$$\begin{bmatrix} \sigma_{xx,j} & \tau_{xy,j} \\ \tau_{xy,j} & \sigma_{yy,j} \end{bmatrix} = \begin{bmatrix} \cos\varphi_j & -\sin\varphi_j \\ \sin\varphi_j & \cos\varphi_j \end{bmatrix} \begin{bmatrix} \sigma_{1j} & 0 \\ 0 & \sigma_{2j} \end{bmatrix} \begin{bmatrix} \cos\varphi_j & \sin\varphi_j \\ -\sin\varphi_j & \cos\varphi_j \end{bmatrix} \tag{16}$$

Therefore, the stress distribution can be determined with the application of Eq. (16) to each depth increment.

4.2 Discussion of Experimental Parameters. The test parameters that can have influences on the measurement sensitivity are the ISSR position on the core surface, the ISSR gage length, the radius of the central core, the total depth of the blind ring-core cutting, and the depth of each cutting increment. These parameters are experimentally determined in the ring-core cutting test and the measurement of the parameters will be discussed in Part II [18]. These parameters are also numerically examined for the best sensitivity and measurement accuracy. On the core surface, the core radius r can be chosen within the range $0.25 \leqslant r/R \leqslant 0.65$, which not only avoids the plasticity effect near the core edge but also ensures enough sensitive response. Cutting depth $H/R \leqslant 0.7$ is a suitable range to perform the test. For $H/R > 0.7$, the core surface is no longer sensitive to the release of residual stresses in the deep layers and the errors in the calculation increase considerably. Some other researchers also suggest the similar maximum cutting depth [4].

4.3 Residual Stress Determination for Ultrasonic Spot Weld. In this section, a test on the ultrasonic spot weld is described to demonstrate the calculation procedure of the ISSR/ring-core method [19]. As a newly developed joining process, ultrasonic spot welding is conducted through the mechanical vibration at very high frequency. The upper sheet for joining is in contact with the vibrating sonotrode, and the vibration energy and clamping pressure act on the upper spot face. The lower sheet is supported by a stationary anvil. Because of depressing and clamping, a concave occurs on the top surface of the spot weld and a bulge is found on the bottom surface of the spot weld. The temperature gradients cause the inhomogeneous deformations in the material during the mass transportation. The residual stresses in the ultrasonic spot weld are valuable for the failure analysis and need to be determined.

The top view of the test coupon is shown in Fig. 7. Both top and bottom sheets are ~0.9 mm in thickness. The spot weld is small with a diameter of 6 mm. The conventional residual stress measurement methods such as resistance strain rosette, are difficult to be applied to the tiny weld. A ring-core cutting test with the ISSR method was conducted at the center of the spot weld on the bottom surface. The bottom side of the coupon after the ring core cutting is shown in Fig. 8. The dimension parameters of the ring core are measured under the microscope and recorded in Table 2.

Eight steps of cutting were conducted on the spot weld. The strain data of eight-step cutting are plotted at the end of each cutting increment in Fig. 9 as marked symbols. The strains are also fitted by the fourth-order polynomials and shown in Fig. 9. The fitted strains are used to calculate the residual stresses. For the convenience of the calculation, the rectangular coordinate system needs to be rotated 110.8 deg in the counterclockwise direction to the new polar coordinate system, where θ equals to zero. Correspondingly, strain components, ε_{xx}, ε_{yy}, and γ_{xy} are transformed into ε_{rr}, $\varepsilon_{\theta\theta}$, and $\gamma_{r\theta}$.

Each of the first three cutting increments is 0.025 mm, and the subsequent cutting increment is 0.1 mm. The nondimensionalized cumulative relaxation coefficients are listed in Table 3. (Only the coefficients of the first five cutting steps are listed.) To obtain the results with higher accuracy, the interpolation is based on a table similar to the Table 1 but with finer depth increments. $\hat{\boldsymbol{K}}'_{ij}$, the upper 3×3 submatrix of matrix $\hat{\boldsymbol{U}}'_{ij}$, is obtained from Table 3. Then each $\hat{\boldsymbol{K}}'_{ij}$ is transformed back to $\hat{\boldsymbol{K}}_{ij}$ through Eq. (13). After the subtractions are conducted to calculate the incremental coefficients, all the $\boldsymbol{K}_{ij}$ matrices can be obtained. The residual stresses are calculated through the iteration form of Eq. (8) as

Table 2 Parameters of the ring-core on the spot weld

Ring-core outer radius	Central core radius
$R_{out}=2.506\pm0.002$ mm	$R=0.955\pm0.002$ mm
ISSR position in polar coordinates	
$r=0.413\pm0.002$ mm	$\theta=110.8\pm0.2$ deg

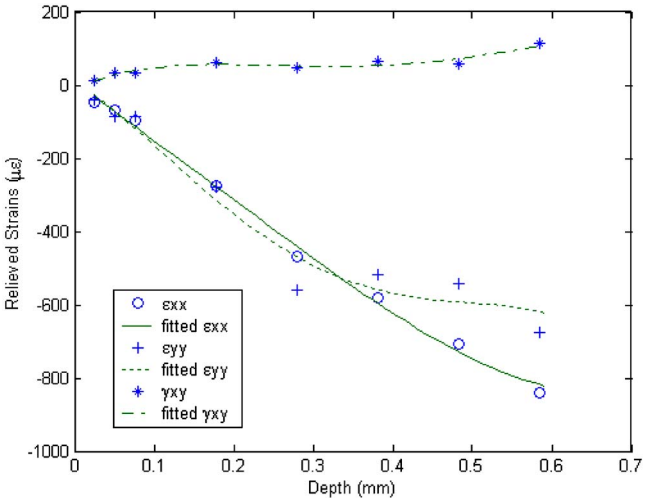

Fig. 9 Cumulative relieved strains of ultrasonic spot weld

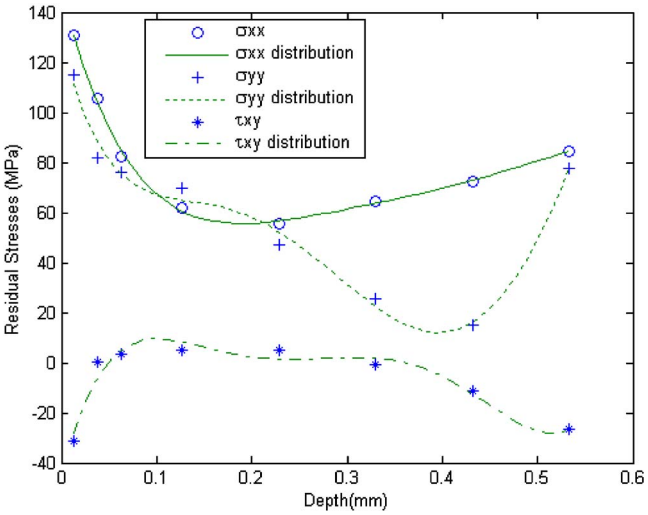

Fig. 10 Residual stress distribution of ultrasonic spot weld

$$\boldsymbol{I}_i = \boldsymbol{K}_{ii}^{-1}\boldsymbol{\psi}_i - \boldsymbol{K}_{ii}^{-1}\left(\sum_{j=1}^{i-1}\boldsymbol{K}_{ij}\boldsymbol{I}_j\right) \tag{17}$$

where $1 \leqslant j \leqslant i \leqslant 8$ for this test. The results of residual stresses are in polar coordinates and can be transformed into the original rectangular coordinates. The residual stress results are plotted at the middle of each depth increment in Fig. 10. The calculated residual stresses are fitted by the fifth-order polynomials and shown as stress distributions in Fig. 10. σ_{xx} (stress in the longitudinal direction of the coupon) and σ_{yy} (stress in the transverse direction of the coupon) are both in tension and reach the maximum values near the bottom surface. The material in the weld of bottom sheet was forced by the mass squeeze to bulge out. This expanding effect is the source to generate the internal tension stress in the weld of the bottom sheet. Being tiny and localized, the ISSR has demonstrated its advantages through the application on the ultrasonic spot weld.

Table 3 Nondimensionalized cumulative relaxation coefficients

r/R	H/R	h/R	$\hat{A}'$	$\hat{B}'$	$\hat{C}'$	$\hat{D}'$	$\hat{F}'$
0.43	0.03	0.03	0.0227	0.0180	0.0280	−0.0235	−0.0298
	0.05	0.03	0.0352	0.0254	0.0343	−0.0273	−0.0391
		0.05	0.0811	0.0586	0.0645	−0.0510	−0.0957
	0.08	0.03	0.0455	0.0320	0.0400	−0.0307	−0.0479
		0.05	0.1029	0.0722	0.0768	−0.0583	−0.1144
		0.08	0.1453	0.1033	0.1091	−0.0834	−0.1731
	0.19	0.03	0.0730	0.0528	0.0599	−0.0439	−0.0818
		0.05	0.1572	0.1124	0.1164	−0.0844	−0.1810
		0.08	0.2286	0.1633	0.1701	−0.1231	−0.2739
		0.19	0.4231	0.3083	0.3383	−0.2528	−0.5613
	0.29	0.03	0.0900	0.0710	0.0742	−0.0564	−0.1129
		0.05	0.1908	0.1479	0.1448	−0.1090	−0.2418
		0.08	0.2786	0.2152	0.2125	−0.1595	−0.3633
		0.19	0.5465	0.4237	0.4439	−0.3381	−0.7646
		0.29	0.7017	0.5530	0.5918	−0.4651	−1.0232
	0.40	0.03	0.1002	0.0869	0.0834	−0.0680	−0.1404
		0.05	0.2110	0.1789	0.1632	−0.1317	−0.2955
		0.08	0.3087	0.2606	0.2399	−0.1930	−0.4420
		0.19	0.6163	0.5206	0.5081	−0.4118	−0.9351
		0.29	0.8228	0.7005	0.7043	−0.5818	−1.2874
		0.40	0.9243	0.8011	0.8162	−0.6922	−1.4986

5 Conclusion

The interferometric strain/slope rosette technique combined with ring-core cutting method is successfully developed in order to measure residual stress distributions with depths into material surface. A mechanical model is established to simulate the incremental ring-core cutting process around the ISSR. The strain response of the ISSR is derived to relate to the residual stresses. Using the integral method, the analyses and equations in the first step of ring-core cutting are generalized to the subsequent cutting steps. By employing the FEA and solving the ring-core model, the strain/slope relaxation coefficients are determined. To measure uniform residual stresses, a through-thickness ring-core cutting case is analyzed and the corresponding relaxation coefficients are recorded in the first row of Table 1. Nonuniform residual stresses can be determined as a distribution with depth by conducting the incremental ring-core cutting test and applying the interpolation of the strain/slope relaxation coefficients recorded in Table 1. The procedures are developed to determine residual stress distribution with depth. Residual stress determination on an ultrasonic spot weld demonstrates the unique applicability of the method and the calculation procedures of residual stresses from the measured ISSR data.

Acknowledgment

Financial support for this work provided by the NSF career award Grant No. CMS-9734522 is gratefully acknowledged. A representative sample with ultrasonic spot weld was made at Oak Ridge National Laboratory. The authors also appreciate Dr. Zhili Feng for providing basic information of the ultrasonic welding.

References

[1] Keil, S., 1992, "Experimental Determination of Residual Stresses With the Ring-Core Method and an On-line Measuring System," Exp. Tech., **16**(5), pp. 17–24.
[2] Siiriäinen, J., Gripenberg, H., and Hänninen, H., 2000, "Design and Implementation of Ring-Core Method for Residual Stress Measurement," The Sixth International Conference on Residual Stresses ICRS-6, Oxford, UK, pp. 996–1003.
[3] Hornbach, D., and Prevéy, P., 1998, "Development of Machining Procedures to Minimize Distortion During Manufacture," *ASM Proceedings of 17th Heat Treating Society Conference and Exposition: Heat Treating*, ASM International, Metals Park, OH, pp. 13–18.
[4] Ajovalasit, A., Petrucci, G., and Zuccarello, B., 1996, "Determination of Nonuniform Residual Stresses Using the Ring-Core Method," ASME J. Eng. Mater. Technol., **118**(2), pp. 224–228.
[5] Zuccarello, B., 1996, "Optimization of Depth Increment Distribution in the Ring-Core Method," J. Strain Anal. Eng. Des., **31**(4), pp. 251–258.
[6] Shankar, K., Xie, H. M., Wei, R. Y., Asundi, A., and Boay, C. G., 2004, "A Study on Residual Stresses in Polymer Composites Using Morié Interferom-

etry," Adv. Comput. Math., **13**(3–4), pp. 237–253.
[7] Tjhung, T., and Li, K., 2003, "Measurement of In-Plane Residual Stresses Varying With Depth by the Interferometric Strain/Slope Rosette and Incremental Hole-Drilling," ASME J. Eng. Mater. Technol., **125**(2), pp. 153–162.
[8] Bell, J. F., 1956, "Determination of Dynamic Plastic Strain Through the Use of Diffraction Grating," J. Appl. Phys., **27**(10), pp. 1109–1113.
[9] Pryor, T. R., and North, W. P. T., 1971, "The Diffractographic Strain Gage," Exp. Tech., **1**(12), pp. 565–568.
[10] Sharpe, Jr., W. N., 1968, "The Interferometric Strain Gage," Exp. Tech., **8**(4), pp. 164–170.
[11] Sharpe, Jr., W. N., 1982, "Applications of the Interferometric Strain/Displacement Gauge," Opt. Eng., **21**, pp. 483–488.
[12] Li, K., 1996, "Out-of-plane Displacement Derivative Measurements Using Interferometric Strain/Slope Gage," ASME J. Appl. Mech., **63**(4), pp. 1033–1038.
[13] Li, K., 1997, "Interferometric Strain/Slope Rosette for Static and Dynamic Measurements," Exp. Tech., **37**(2), pp. 111–118.
[14] Li, K., 1997, "Application of Interferometric Strain Rosette to Residual Stress Measurements," Opt. Laser Technol., **27**(1), pp. 125–136.
[15] Schajer, G. S., 1981, "Application of Finite Element Calculations to Residual Stress Measurements," ASME J. Eng. Mater. Technol., **103**(2), 157–163.
[16] Cook, R. D., Malkus, D. S., and Plesha, M. E., 1989, *Concepts and Applications of Finite Element Analysis*, 3rd ed., Wiley, New York, Chap. 10.
[17] Zienkiewicz, O. C., 1977, *The Finite Element Method*, 3rd. ed., McGraw-Hill, New York, Ch 15.
[18] Ren, W., and Li, K., 2007, "Application of Minature Ring-Core and Interferometric Strain/Slope Rosette to Determine Residual Stress Distribution with Depth—Part II: Experiments," ASME J. Appl. Mech., **74**, pp. 307–314.
[19] Ren, W., Li, K., and Feng, Z., 2005, "Ultrasonic Welding Stress Distribution Measured With Optical Rosette/Ring-Core Method," SAE Congress, Apr., SP-1957, Experiments in Automotive Engineering - Optical Techniques, pp. 141–144.

Application of Miniature Ring-Core and Interferometric Strain/Slope Rosette to Determine Residual Stress Distribution With Depth—Part II: Experiments

Wei Ren
e-mail: weiren74@hotmail.com

Keyu Li
e-mail: kli@oakland.edu

Department of Mechanical Engineering,
Oakland University,
Rochester, MI 48309

*The theoretical development of the interferometric strain/slope rosette (ISSR) and ring-core cutting method is described in Part I of the paper [K. Li and W. Ren, ASME J. Appl. Mech. **74**(2), 298–306 (2007)]. In Part II, experiments are presented to demonstrate the applicability of the method. The procedures of experimentation are developed. An ISSR/ring-core cutting system was established and its measurement stability and accuracy were examined in a two-step measurement program. By repeating the two-step measurement procedures, several incremental ring-core cutting experiments were conducted. Residual stress distribution is calculated from the measured ISSR data by using the relaxation coefficients calibrated in Part I of the paper. Measurement resolution, accuracy, and sensitivity of the ISSR/ring-core method are evaluated. Tests on a titanium block show the reliability of the method in comparison with the results obtained by using other measurement methods. The new method is also applied on a laser weld which demonstrates its uniqueness to measure residual stresses in small areas with high stress gradients. The experiments show advantages of the ISSR/ring-core method, such as miniature size, noncontacting nature, and high sensitivity. The method can be effectively used to measure residual stress distributions with depth on various manufactured components.*
[DOI: 10.1115/1.2198252]

1 Introduction

The ring-core method was introduced in a companion paper [1]. The ring-core cutting has not been widely used with the resistance strain rosette (RSR) due to the drawbacks, including the inaccuracy caused by the large size of the RSR and instability due to the wire connection of the RSR. In Part II, the optical strain measurement method—interferometric strain/slope rosette (ISSR) is used with the ring-core cutting for residual stress measurement. The ISSR is tiny and its commonly used gauge length is between 50 μm and 250 μm. The diameter of the ring-core with the ISSR is only one-seventh of that with a RSR. Thus, more localized residual stresses can be measured. The ISSR is a laser-based technique and the measurement system is noncontacting. Only three tiny indentations need to be made on the core surface and they constitute an optical rosette. Bonding and wiring are not necessary for the ISSR which makes it convenient to perform ring-core cutting. According to a previous study of the ISSR technique [2], the in-plane strain measurements are not influenced by the in-plane rigid-body motion, and the out-of-plane displacement derivative measurements are not influenced by the out-of-plane rigid-body motion. Influences of in-plane rigid-body motion on out-of-plane displacement derivative measurements and out-of-plane rigid-body motion on in-plane strain measurements can be compensated [2]. In comparison with other interferometric methods, such as holography and Moiré methods, the ISSR method is less sensitive to the rigid-body motion and vibrations from the environment. The small gauge length, high accuracy, and insensitivity to vibrations make the ISSR feasible to be used with the ring-core cutting method. Although the mechanical model and finite element model have been developed in Part I [1], the feasibility of the method must be experimentally validated. The test system and procedures must be established. The accuracy and resolution of the measurement technique need to be evaluated. In the following sections, the ISSR test system and procedures are described. The reliability of the method is tested through experiments.

2 Setup and Evaluation of Test System

An ISSR/ring-core system was established to conduct tests and data acquisition. In this section, the construction of the system is explained thoroughly. Its measurement stability and accuracy are studied through a two-step test program.

2.1 Construction of the ISSR Test System. An ISSR system was constructed for use with a delta rosette. The system can be set up horizontally or vertically. The vertical setup can be located in front of any machine. The ISSR system is normally used for real-time measurements. When several loading steps are continuously applied to the specimen, the ISSR keeps recording the strain increments in real time for each loading step.

Figure 1 shows a horizontal setup of the ISSR measurement system. The light source is an 8 mW He–Ne laser (wavelength $\lambda=0.6328$ μm). The reflection angle of a mirror can be adjusted to ensure that the incident laser beam is vertically downward,

Contributed by the Applied Mechanics Division of ASME for publication in the JOURNAL OF APPLIED MECHANICS. Manuscript received May 6, 2004; final manuscript received February 5, 2006. Review conducted by H. D. Espinsoa. Discussion on the paper should be addressed to the Editor, Prof. Robert M. McMeeking, Journal of Applied Mechanics, Department of Mechanical and Environmental Engineering, University of California—Santa Barbara, Santa Barbara, CA 93106-5070, and will be accepted until four months after final publication of the paper itself in the ASME JOURNAL OF APPLIED MECHANICS.

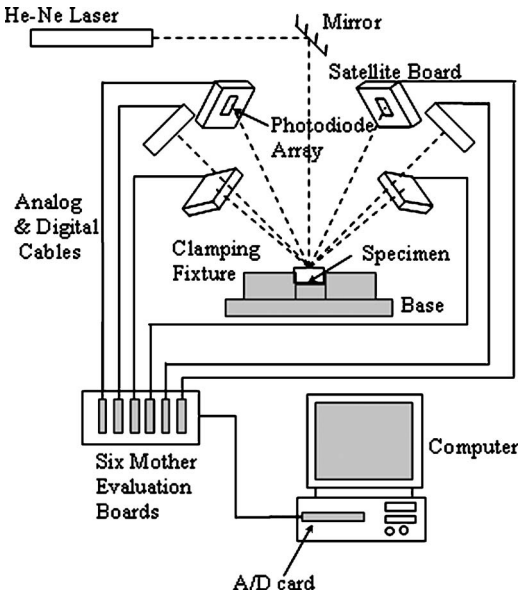

Fig. 1 Schematic diagram of ISSR measurement system

which is in the normal direction of the horizontal specimen surface. The clamping fixture is mounted on the base and the specimen can be translated and locked in the fixture. After a delta ISSR is indented on the specimen surface and the ISSR area is illuminated by an incident laser beam, six interferometric fringe patterns would appear in the directions of reflection, which are separated 60 deg apart from each other. Six linear photodiode arrays are used to record the six interferometric fringe patterns. The linear photodiode arrays convert the optical intensity signals into the voltage signals [2]. Each photodiode array is installed in the satellite board. Six satellite boards are mounted on the supporting frames of the system structure and can be translated in all three directions and rotated by two angles. Each satellite board is connected to a mother evaluation board by the extended analog and digital cables, which allow the satellite boards to be remotely located. The mother boards and the satellite boards work together as circuitry support to power and control the linear photodiode arrays. Data acquisition proceeds simultaneously for all six channels.

A computer equipped with an acquisition board can perform A/D conversion at a sampling rate of 250 kHz. Differential analog inputs are used to reduce the common mode noise. The voltage signals from the photodiodes and mother boards are digitized by the A/D conversion process. Several programs were developed to operate the A/D board, digitize the analog signals, and record the data [2]. The digitized optical intensity of the interference patterns would show a sinusoidal shape. The peaks and valleys of the sinusoidal curves represent the light and dark interferometric fringes. For a two-step measurement with a loading increment, the program was developed to record the fringe patterns before and after loading, obtain the fringe shifts according to the differences of the dark fringes (valley points) between two patterns, and calculate the strains and slopes. The data acquisition and strain/slope calculation are on a real-time basis because only little time is required for instant processing.

2.2 Evaluation of Test System. With the deformations measured by the ISSR in real time, the program for the two-step measurement acquires two sets of data separately. To evaluate the measurement procedure and the computer program, various tensile/compressive tests are conducted on a bar specimen. The dimensions of the specimen are: Thickness—3.18 mm, width—51.20 mm, and length—300 mm. The material properties of the specimen are: Young's modulus $E=70$ GPa, Poisson's ratio $\nu=0.33$, yielding stress $\sigma_y=270$ MPa, and ultimate stress $\sigma_u=310$ MPa.

Table 1 Strains measured by the ISSR in "zero-shift" experiments

Test No.	Axial strain ($\mu\varepsilon$)	Transverse strain ($\mu\varepsilon$)	Shear strain ($\mu\varepsilon$)
1	−1.66	−0.31	3.56
2	4.08	1.47	−5.38
3	−0.33	−1.34	1.56
4	4.28	−0.10	−0.52
5	2.42	1.51	1.61
Maximum difference	4.28	1.51	5.38

The first group of tests is so-called "zero-shift" experiments to test the stability of the system. A vertical ISSR system is set up at a distance of 44 cm from the specimen. The gauge length of the ISSR is 250 μm. Two-step measurements are performed within a few minutes. There is a constant load applied to hold the specimen. Ideally, the strain differences between the two steps should be zero due to constant load, and the program should output zero differences. But in real experiments, nonzero strains are recorded. The strain differences in the transverse and axial directions of the bar are measured by the ISSR and listed in Table 1. The maximum difference of strain readings between the two measurements is about 5 $\mu\varepsilon$ (microstrain), which is a shear strain. The maximum axial strain difference is about 4 $\mu\varepsilon$. The nonzero results indicate a sensitive response of the electrical-optical system to its environment.

The second group of tests is to test the two-step measurement program when loads are gradually applied. The test procedure is similar to the above test except that the loading increments are no longer zeros. In the axial direction, a RSG was bonded beside the ISSR. The theoretical strains in both axial and transverse directions are calculated according to the elastic theory. The experimental and theoretical results are listed in Table 2 and plotted in Fig. 2. In the axial direction, the results of the ISSR are compared with the theoretical calculation values and the experimental results of the RSG. In the transverse direction, only theoretical results are available for comparison with the results of the ISSR. For most of loading steps, the measured strains by the ISSR agree well with the results of theoretical calculation and those measured by the RSG. The comparison shows that the developed ISSR system and the two-step measurement program are reliable.

3 Incremental Ring-Core Cutting Experiments and Analyses

A ring-core cut on an aluminum specimen is shown in Fig. 3. An ISSR is on the surface of the core island. In comparison with a U.S. penny, the size of the ring-core is very small. With a small gauge length and noncontacting feature, the ISSR can be successfully used with the ring-core method to measure residual stresses in local areas with high stress concentrations. An application example of ISSR/ring-core on a small ultrasonic spot weld was presented in Part I of the paper [1]. In this section, the ISSR/ring-core test procedure is first introduced. Then, two samples are used to test the applicability of the method. The samples are a titanium block after a shot-peening process and a steel tube cut from truck frame after hydroforming and laser-welding processes. The processes induced residual stresses. The relieved strains are measured using the ISSR during the incremental ring-core cutting. The residual stresses are calculated from the measured strains according to the theories developed in Part I of the paper [1]. The accuracy

Table 2 Comparison of the results of the ISSR measurements, the resistance-strain-gauge (RSG) measurements, and the theoretical calculations

		Axial strains ($\mu\varepsilon$)				Transverse strains ($\mu\varepsilon$)		
Test No.	Tensile stress (MPa)	Calculation	ISSR	(RSG)	Difference between ISSR and RSG	Calculation	ISSR	Difference between calculation and ISSR
1	27.6	395	385	394	−9	−130	−134	4
2	27.4	391	383	409	−26	−129	−144	15
3	−14.0	−199	−202	−213	11	66	82	−16
4	−16.4	−235	−251	−249	−2	77	100	−23
5	−24.9	−356	−358	−376	18	117	126	−9
6	−27.4	−391	−382	−408	26	129	137	−8
7	−35.3	−504	−524	−529	5	166	208	−42
8	−41.1	−586	−567	−592	25	194	200	−6

of the ISSR/ring-core method is evaluated. Results of residual stresses are discussed and compared with the results obtained through other methods.

3.1 Ring-Core Cutting and ISSR Measurement System. The photograph of experimental setup for the ISSR/ring-core cutting method is shown in Fig. 4. The ISSR measurement system is constructed according to the schematic diagram illustrated in Fig. 1. The ring-core cutting system is installed underneath the laser and satellite boards. As part of the ring-core cutting system, the milling guide assembly is mounted above the clamping fixture. The supports of the guide are screwed on the base. The milling guide is similar to the drilling guide used in a standard hole-drilling test.

Before each cutting is conducted, a drill is inserted into the journal hole at the center of the guide. Each depth increment can be well controlled through a micrometer with the smallest division equal to 10^{-3} inches or 0.0254 mm and the stop collar of the drilling guide. The drill with a central hole is specially designed and manufactured, which can cut an annular groove and leave a cylindrical central core on the surface of specimen. To shine the laser on the ISSR area and to receive the corresponding fringe patterns, the milling guide and drill are removed after the cutting. The guide can be relocated precisely at the same position to ensure that each incremental cutting is conducted at the same ring-core location. The testing system is mounted on a separate table which isolates the optical sensors from the cutting system to minimize the vibrations. Therefore, the influences from the environment are well controlled through the experimental design.

3.2 Test Procedures. An ISSR/ring-core cutting experiment requires three major procedures: Test preparation, experiment operation, and data processing. Test preparation includes specimen preparation and test system adjustment. Normally, the surface of test specimens is slightly polished with diamond paste. Under a microhardness tester, the ISSR indentations are created on the specimen surface with suitable sizes by adjusting the indenting force and time. The specimen is clamped in a precision vise, and the whole vise assembly is translated to the position where the indentation is to be made. After three small indentations are created, the specimen is installed in the fixture of cutting system. Precaution must be taken to avoid extra stresses induced due to the clamping. Under illumination of a laser, the reflection mirror is adjusted to direct the incident laser beam to be perpendicular to the sample surface. The ISSR is translated to appear in the area of the illumination. Each satellite board is adjusted to be perpendicular to the reflected beam and locked at proper position where the fringe pattern is intercepted with the best quality.

The reference fringe patterns are first recorded before a cutting step. Then, the milling guide is mounted above the specimen and a required depth increment is milled. After the cutting, the milling guide is removed and the perturbed fringe patterns are recorded. The strains and slopes due to the stress relief at the depth increment are calculated using the two-step measurement programs. For incremental ring-core cutting, this two-step measurement procedure needs to be repeated for each incremental cutting step. The fringe shift is measured through comparison of two sets of the patterns before and after each cutting step. Since the shifts are normally much less than the one-quarter wavelength of the fringes, the fringe movements can easily be traced. For example, if four dark fringes are captured within a linear photodiode con-

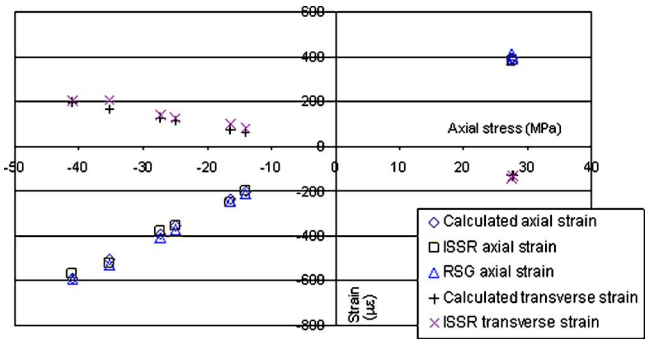

Fig. 2 Results of two-step ISSR measurements compared with those obtained by RSG measurements and theoretical calculations

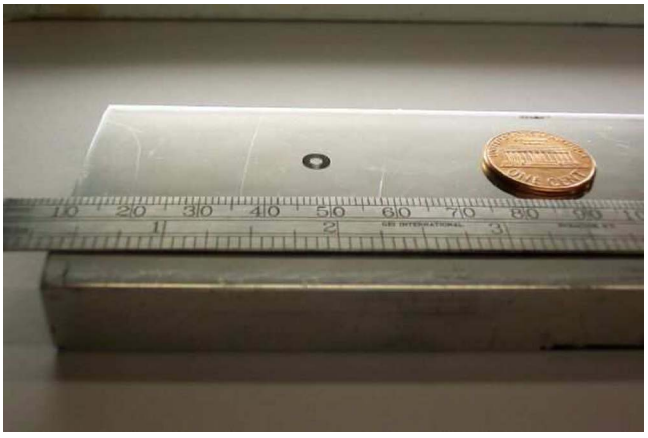

Fig. 3 Ring-core cut on the surface of aluminum bar

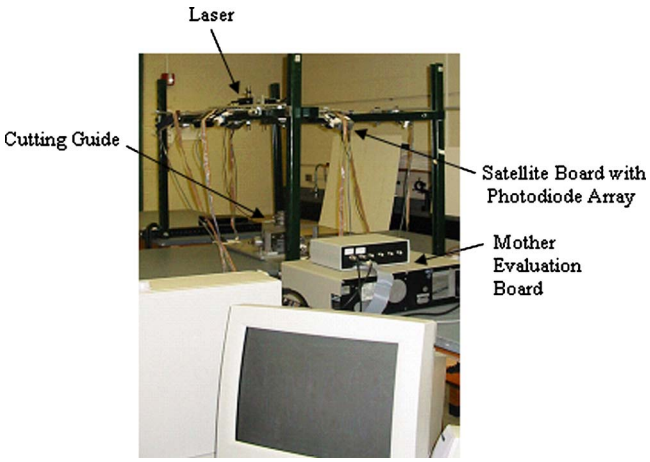

Fig. 4 Setup of the ISSR system for incremental ring-core cutting experiments

sisting of 512 pixels, the averaged fringe shift of one-quarter wavelength would correspond to 1000 $\mu\varepsilon$ of deformation, which is much greater than the normal strain relaxation at a depth increment.

After all the cutting steps are finished, the parameters, such as the core radius and the ISSR position, are measured under the microscope. The residual stresses are calculated according to Sec. 4.1 in Part I of the paper, and the results are saved in files and displayed in figures.

3.3 Incremental Ring-Core Cutting on a Titanium Block. To examine the reliability of the ISSR/ring-core cutting method, a shot-peened titanium block was tested. Shot peening is a cold working process to induce compressive residual stresses and improve fatigue life. During the shot-peening process, the surface of the titanium-alloy (TA6V) block (size $56\times49\times23$ mm) is bombarded with small spherical media called shot [3] and large compressive residual stresses are induced on the block surface. The material properties of the titanium alloy are: Young's modulus $E=110$ GPa, Poisson's ratio $\nu=0.33$, yield strength $\sigma_y=830$ MPa, and ultimate strength $\sigma_u=900-970$ MPa.

Two ring-core cutting tests were conducted on the titanium alloy block and ten steps of cutting were performed for each test. Each cutting increment was 0.0254 mm. The relieved strains at each depth increment were measured by the ISSR. The x and y axes are set along the longitudinal direction and widthwise direction of the block, respectively. The position parameters of the ring-core cutting are defined and illustrated in Fig. 3 of Part I [1], and measured and recorded in Table 3 of this paper. The incrementally relieved strains for Tests 1 and 2 are measured by the ISSR and recorded in Tables 4 and 5, respectively. The measured strains at each depth increment are added up until the completion of each depth increment to obtain the cumulative strains. The cumulative strains of the two tests are plotted in Figs. 5(a) and 6(a). The strains are fitted by the second-order polynomial functions.

The marked symbols in Figs. 5(b) and 6(b) are the calculated residual stresses for the two tests using the fitted strain curves. Stress distributions are obtained after the calculated residual stresses are fitted by high-order polynomials. For most of depth increments, the normal stresses σ_{xx} and σ_{yy} are approximately equal and the shear stress τ_{xy} is close to zero, which indicates an equibiaxial stress state. The peak compressive stress is between −700 MPa and −800 MPa for both tests. The stress distributions of the two ISSR/ring-core tests compare closely with each other.

The random errors of fringe patterns measured in the zero-shift tests are due to noise and influences from the environment. Through the experiments and tests on the titanium block, the estimated random errors based on the ISSR/ring-core cutting setup is ±4 $\mu\varepsilon$ for ε_{xx} and ε_{yy}, and ±3 $\mu\varepsilon$ for γ_{xy}. On the other hand, the systematic errors are caused by the inaccurate measurement of the experimental data and the parameters. Either the limited measurement resolution or personal error during the test could lead to the inaccurate measurement. The systematic errors can be divided into two types. The first-type errors include the error of gauge-length measurement and the inaccuracy of fringe-order counting. The second-type systematic errors are mainly caused by the inaccurate measurements of the core radius and the ISSR position. The random errors and the first-type of systematic errors cause the perturbations of the measured strains, while the second-type errors induce the perturbations into the coefficient matrix.

The errors of the gauge-length measurement and the fringe-order determination are the main concerns in the first-type systematic errors and can be analyzed by the governing equation. In both tests on the titanium block, the indentations are made with a 200 μm gauge length. According to the precision of micrometer, the error range for each gauge length is ±2 μm. Using the governing equation [Eq. (1)] in Part I of the paper [1], the error ranges in terms of the gauge-length measurement are estimated as ±1% of the measured strains ε_{xx}, ε_{yy}, and γ_{xy}. Each photodiode has 512 pixels. The measurement resolution is 1 pixel. Hence, the error range of the measurement is ±0.5 pixel. The δm_j ($j=1,2,\ldots,6$) in the governing equation is the relative fringe shift, which is obtained by dividing the absolute fringe shift with the spacing (distance between two adjacent intensity minimums). Normally, by adjusting the distance between the photodiode and

Table 3 Position parameters of the ring-core cutting on the titanium block

Test No.	Central core radius	ISSR position in polar coordinates	
1	$R=1.048\pm0.002$ mm	$r=0.332\pm0.002$ mm	$\theta=87.5\pm0.2°$
2	$R=1.041\pm0.002$ mm	$r=0.422\pm0.002$ mm	$\theta=93.6\pm0.2°$

Table 4 Measured incremental relieved strains for Test No. 1 on the titanium block

Depth (mm)	ε_{xx} ($\mu\varepsilon$)	ε_{yy} ($\mu\varepsilon$)	γ_{xy} ($\mu\varepsilon$)
0.0254	127.2	165.7	6.2
0.0508	102.3	130.7	−32.4
0.0762	149.9	168.7	−29.0
0.1016	94.6	82.7	13.1
0.127	180.0	200.5	−17.9
0.1524	78.2	117.1	−9.1
0.1778	51.3	73.3	18.0
0.2032	116.7	137.4	6.3
0.2286	124.4	160.3	−19.6
0.254	102.8	76.5	−4.9

Table 5 Measured incremental relieved strains for Test No. 2 on the titanium block

Depth (mm)	ε_{xx} ($\mu\varepsilon$)	ε_{yy} ($\mu\varepsilon$)	γ_{xy} ($\mu\varepsilon$)
0.0254	88.8	91.1	4.6
0.0508	180.8	207.8	23.7
0.0762	176.7	200.2	20.8
0.1016	90.8	202.4	−28.4
0.127	37.7	139.2	9.5
0.1524	125.5	94.9	−36.2
0.1778	150.6	166.3	8.9
0.2032	138.9	181.6	−19.6
0.2286	81.9	104.5	9.7
0.254	77.6	131.8	−9.8

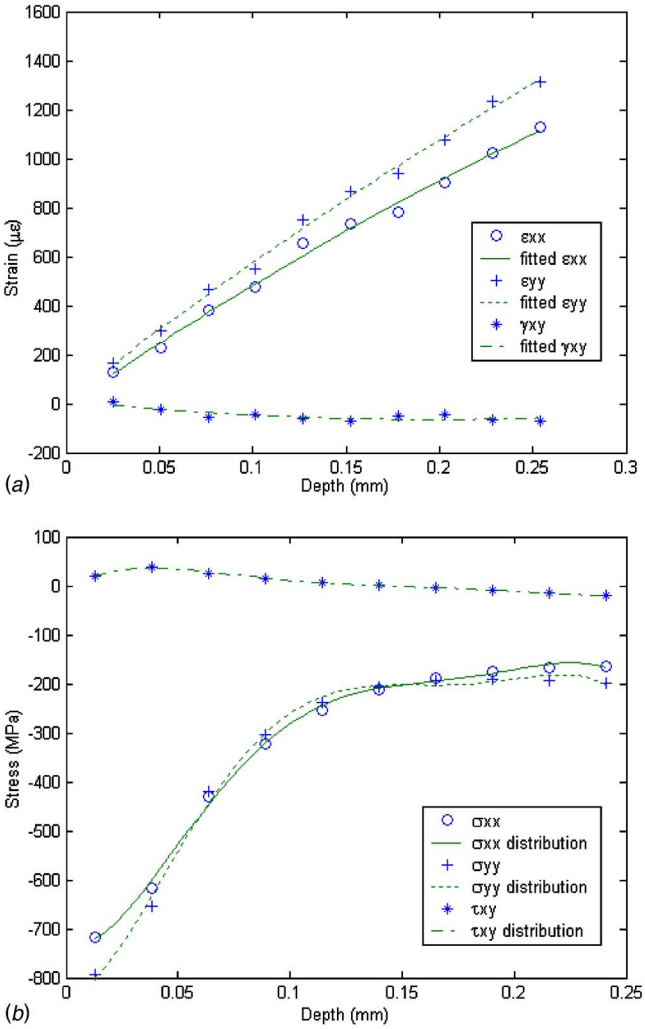

Fig. 5 Cumulative relieved strains and residual stresses for Test No. 1 on the Ti-alloy block

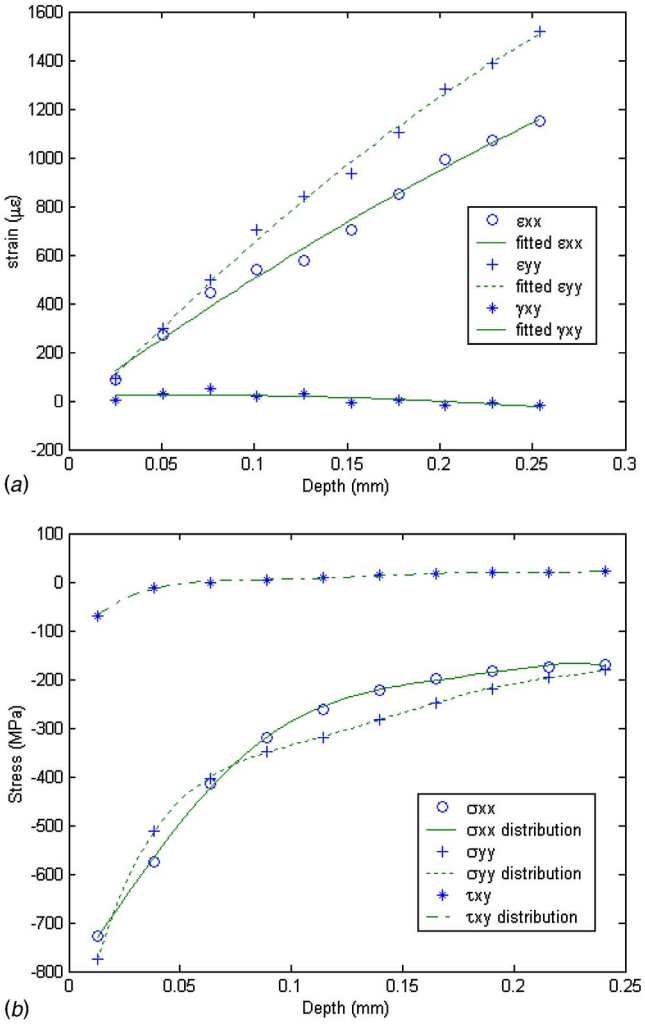

Fig. 6 Cumulative relieved strains and residual stresses for Test No. 2 on the Ti-alloy block

the sample for each channel, four to six periods of signal are captured within the photodiode length. In this case, the errors due to the resolution of fringe-shift measurement are estimated as ±0.6% of the measured strains ε_{xx}, ε_{yy}, and γ_{xy} for a 60° ISSR.

The errors induced from the strain measurement can propagate during the stress backcalculation process and cause errors in the residual stress results. In the ISSR/ring-core cutting experiment, good accuracy can still be achieved when the residual stresses are backcalculated with relatively small strain perturbations. As discussed above, the strain errors include the random errors and the first-type systematic errors. The two types of errors are added and substituted into the backcalculation scheme to examine the influences on the stress results. With the maximum error ranges of $4\ \mu\varepsilon+1.6\%|\varepsilon_{xx}|$, $4\ \mu\varepsilon+1.6\%|\varepsilon_{yy}|$ and $3\ \mu\varepsilon+1.6\%|\gamma_{xy}|$ added to the fitted strains of the first-step cutting in Test No. 1 on the Ti block, the root-mean-square values are calculated as the total strain errors and substituted into the backcalculation scheme. The estimated errors for the resultant principal stresses σ_1, σ_2, and principal angle φ are found to be 3.9%, 2.7%, and 1.7°, respectively.

For the second-type of systematic errors, the measurement errors of the core radius and ISSR position can affect the stress-strain coefficient matrix and hence the stress results. The error ranges of these parameters are recorded in Table 3. Numerical analysis is conducted according to these error ranges. With current measurement precision, it has been found that the error in the core radius is negligible. The error in the radial coordinate of the ISSR causes ±1.5%, ±1.5%, and ±3.0° errors on the principal stresses σ_1, σ_2, and principal angle φ, respectively. For most cutting steps, the error of the angular coordinate of the ISSR causes ±1.5° error on the principal angle φ, but the influence on the σ_1 and σ_2 is negligible. As an example, with both random and systematic errors considered, the total stress errors are estimated as ±5% for both σ_1 and σ_2 for the first depth increment of Test No. 1. In comparison with the stress errors of the hole-drilling method [4], the ISSR/ring-core method has a smaller error range. With efforts of accurate strain measurement and precise parameter determination, higher accuracy can be achieved in the residual stress measurement with the ISSR/ring-core method.

The same shot-peened block was tested by using the ISSR/hole-drilling method [4]. The residual stress results obtained by the ring-core method in this work compare reasonably well with the results in Ref. [4]. Both the ISSR/ring-core method and the ISSR/hole-drilling method obtain approximately −800 MPa maximum compressive residual stress near the surface. The trend of the stress distribution is also similar, showing the decrease of the stress magnitude with depth. The equibiaxial stress states are measured by both methods. The magnitude of the normal residual stresses measured by the ring-core method quickly decreases to the 200 MPa level at the depth of 0.13 mm, and thereafter the stress magnitude decreases slowly until the depth of 0.25 mm. But the magnitude of the normal stresses obtained by the hole-drilling

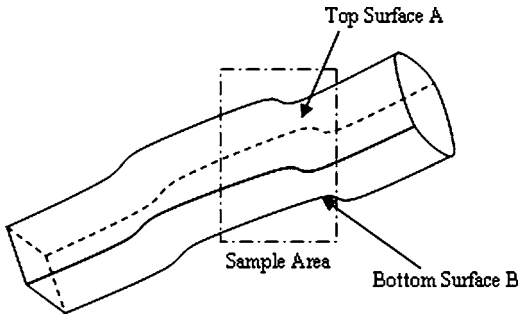

Fig. 7 Test sample cut from a hydroformed frame

method decreases almost linearly to 350 MPa from the surface to 0.25 mm. A close examination indicates that only four drilling steps were taken between 0 and 0.25 mm in the hole-drilling test. The large increments did not provide as many data points as the ring-core method provided to fit a curve. In addition, a regularization scheme used to stabilize the solutions of stresses at a deep depth in the hole-drilling method could distort the distribution of stresses over the initial depths of increments between 0 and 0.25 mm.

In summary, equibiaxial stress state is found in the sample with a peak compression residual stress of −800 MPa. The measured results of the two ring-core experiments show good agreement with the previously published results of other research [4]. The two ring-core tests have demonstrated excellent repeatability.

3.4 Incremental Ring-Core Cutting on Weld of Hydroformed Frame. In this section, an application of the ISSR/ring-core method is introduced. As shown in Fig. 7, a test sample was cut from a hydroformed frame. The sample is provided by an automotive company. The material is AISI 1010 steel and the properties are: $E=205$ GPa, and $\nu=0.30$. The sample dimensions are illustrated in Fig. 8. The width of the laser weld is about 5 mm.

Since the laser weld is narrow, it is difficult to mount RSRs to measure the residual stresses on the weld. The ISSR, being tiny, was indented at the center of the laser weld. Then, a ring-core cutting test was conducted. Ring-core geometry and ISSR position parameters in the test were measured and are recorded in Table 6. These parameters were measured under a microscope upon the completion of the ring-core cutting. The parameters are defined and illustrated in Fig. 3 of Part I [1]. Since the residual stresses

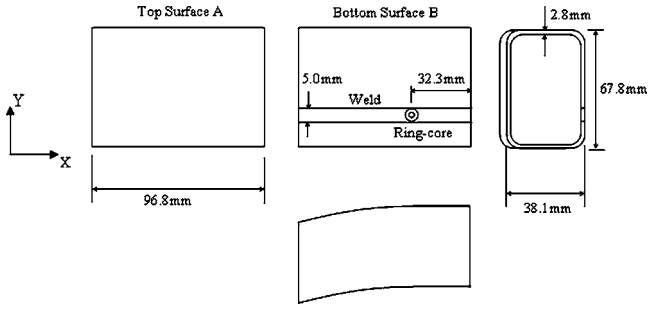

Fig. 8 Sample with a ring-core cut in plan, elevation, and side views

Table 7 Measured incremental relieved strains for laser weld

Depth (mm)	ε_{xx} ($\mu\varepsilon$)	ε_{yy} ($\mu\varepsilon$)	γ_{xy} ($\mu\varepsilon$)
0.102	9.1	−10.4	−20.7
0.2032	48.9	−19.7	32.1
0.3048	96.7	−56.8	5.6
0.4064	169.4	−77.8	24.1
0.5588	278.4	−198.3	100.4

vary across the weld with steep gradients, a smaller core radius is preferred to measure the residual stress distribution along the width of the weld.

The coefficients calculated with the thick plate model are applied to solve for the stresses because the total cutting depth is only one-fifth of the thickness of hydroformed tube. Since the diameter of central core is comparable to the thickness of hydroformed tube, more accurate stress results can be obtained by using the coefficients of a thin plate model. If the model is modified for this thin plate case, only the thickness of the model needs to be changed to a dimension 1.3 times of the central core diameter while the other dimensions remain unchanged.

The relieved strains measured by the ISSR are recorded in Table 7. In Fig. 9(*a*), the measured strains of five steps of cutting are cumulated till the completion of each increment and plotted at the end of each cutting increment as the marked symbols. The strains are also fitted by the third-order polynomials and shown in Fig. 9(*a*). With the same setup, the error ranges for the measurement of the relieved strains are close to those of the tests on the titanium blocks. The fitted strains are used to calculate residual stresses. The stress-strain coefficients in Table 1 of Part I [1] are used to calculate the residual stresses. In Fig. 9(*b*), the results of residual stresses are plotted at the middle position of each depth increment. Stress distributions are obtained by fitting the calculated residual stresses with high-order polynomials.

The residual stress results shown in Fig. 9(*b*) are compared with the results obtained by the ISSR/hole-drilling method in the same laser weld at a different location [5]. Distributions of the longitudinal stress σ_{xx} obtained by both methods compare well. Since σ_{xx} is in the longitudinal direction of the welding, the close σ_{xx} values at different locations show a uniform stress distribution along the weld. The transverse stress σ_{yy} measured by the ISSR/ring-core cutting method is in tension, increasing from zero to 200 MPa, while it is in compression from 0 to 0.12 mm and in tension from 0.12 mm to 0.48 mm and it increases from −300 MPa to 100 MPa as measured by the hole-drilling method. Noting that the location of the ring-core cutting is different from that of the hole-drilling experiment, the results of the transverse stress σ_{yy} obtained from the two methods are different. Despite the difference of values, tensile stresses along the transverse direction of the weld were measured by both methods. The tensile stress in σ_{yy} is the most concerned stress component for the hydroformed part because it could add to the operation stress and reduce the fatigue life. The tensile residual stress is induced due to the manufacture processing of the part. First, the weld cools rapidly and attempts to shrink during cooling. But the base material is cooler, stronger, and resistant to the shrink. As a result, the weld is essentially "stretched" by the base material [3]. Second, the welded tubular part would tend to spring back and open the weld joint. The weld joint resists this tendency and is stretched by the

Table 6 Parameters of the ring-core on the laser weld

Ring-core outer radius R_{out}	Central core radius R	ISSR position in polar coordinates	
2.384±0.002 mm	1.094±0.002 mm	$r=0.248\pm0.002$ mm	$\theta=-84.1\pm0.2°$

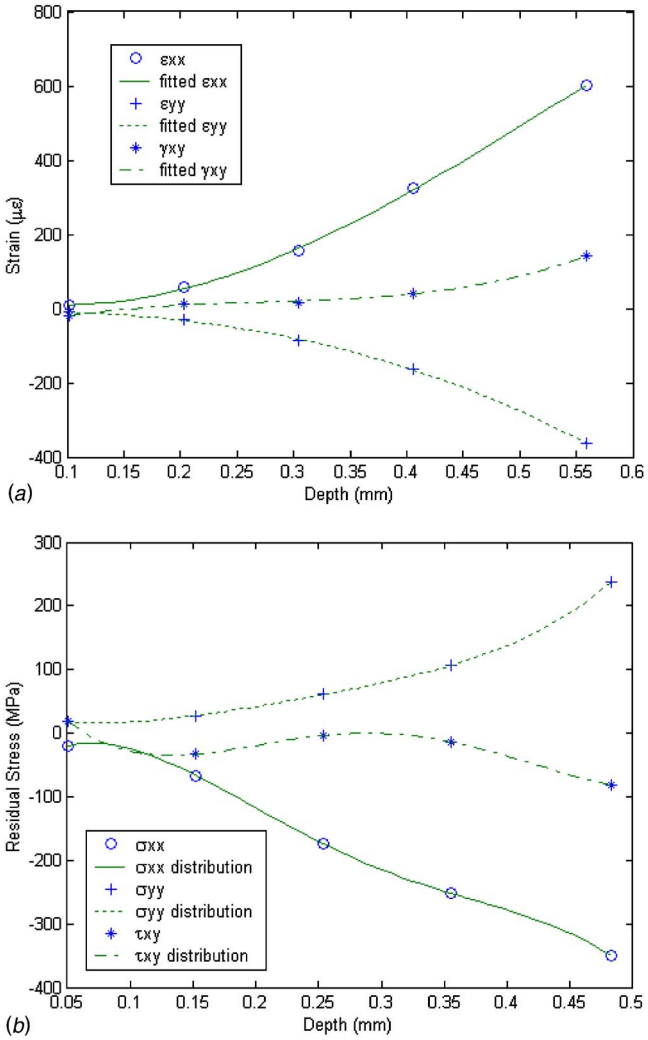

Fig. 9 Cumulative relieved strains and residual stresses for the laser weld of the hydroformed frame

surrounding structure. Third, more tensile residual stresses are induced due to the plastic expansion of hydroforming process. Since the stress σ_{yy} represents the stretch effect by the surrounding area in the transverse direction of the weld, it is much dependent on the joining conditions. Therefore, different spot joints along the same weld could have large differences in stress values.

As a newly developed measurement method, the ISSR/ring-core method is successfully applied to the residual stress measurement on the laser weld of hydroformed frame. Since the ISSR is tiny, the method is suitable to the measurement over small areas with high stress gradients. The experiment on the laser weld has demonstrated its advantages over the conventional methods. Because fundamental mechanics and material behavior associated with hydroforming operation have not been thoroughly understood [6], the test results provide important references for the improvement of the hydroforming process.

3.5 Discussions on Cutting Depth. The ill-conditioning problem for the coefficient matrix **K** in Eq. (8) of Part I [1] is caused by either deep cutting or small increments which can lead to the appearance of small elements in the diagonal bands of the coefficient matrix. When the matrix with ill-conditioning coefficients is employed to solve for the residual stresses, the solutions appear to be radically scattering or oscillating due to the magnified errors. Therefore, both the maximum cutting depth and the minimum depth increment need to be discussed.

Through the numerical analysis, the maximum cutting depth ratio $H_{max}/D=0.35$ (or $H_{max}/R=0.7$) has been found for the ISSR/ring-core method, where H_{max} is the maximum cutting depth and D is the central core diameter. In the RSR/ring-core method, the maximum cutting depth was provided as a 5 mm maximum cutting depth for a ring-core with 14 mm inner diameter [7]. The sensitivity of the measurement decreases as the cutting deepens. The coefficients for a cutting increment at the deep depths are relatively small. To reduce solution errors and validate test results, all H_{max} values in the tests are controlled to be smaller than $0.3D$. If the ring-core has a larger diameter D, a larger maximum cutting depth H_{max} can be reached and the stress distribution at the deep depths can be measured. But the resolution for stress determination would be decreased.

Once high stress spatial resolution or large measurement depth is required, the calculation errors are easily magnified. High spatial resolution and large measurement depth cannot be achieved at the same time [8]. As discussed above, the total cutting depths for the presented tests are less than $0.3D$. Hence, for the ISSR/ring-core method, all $\mathbf{K}_{ij}$ matrices in the tests are still well conditioned when high spatial resolution is reached.

If the maximum cutting depth H_{max} is fixed, the error sensitivity grows much higher when the total cutting step number N is increased. Since decreasing the error sensitivity is contradictory to increasing the spatial resolution, the suitable number N needs to be chosen as a compromise. If both the maximum cutting depth H_{max} and the total cutting step number N are fixed, the distribution of depth increments can be varied. For the RSR/ring-core method, three types of distributions were compared [9]: Constant depth-increment distribution, increasing depth-increment distribution, and optimized depth-increment distribution. The optimized depth increment distribution was obtained through decreasing the condition number of the coefficient matrix. Through the numerical analysis for the ISSR/ring-core method in this study, it can be concluded that there are no large differences among the condition numbers for the three types of distributions if the cutting steps are less than ten, and there is no extremely small depth-increment to cause ill-conditioning problems. The cutting steps for the tests presented in this paper are equal to or less than ten steps and the depth increments are appropriate. The constant depth increment and the increasing depth increment are used in the study because the two types of distributions are convenient to perform and easy to calculate.

3.6 Discussions on Error Propagation. The analysis performed for the RSR/ring-core method shows that the error of the measured strain at the nth step has an appreciable influence only on the residual stress at the n and $n+1$ steps [9]. Although the schemes of the ISSR/ring-core method are very different from those of the RSR/ring-core method, it has been found that the above conclusion is still valid for the ISSR/ring-core method. The stress error, caused by the strain perturbation at the n step, appears in the first term of Eq. (17) of Part I [1] at the n step. At the subsequent $n+1$ step, the stress errors appear in the second term. If there is a strain perturbation $\Delta\psi_1$ in the first step of cutting and the corresponding stress perturbation is ΔI_1, then the stress error vectors for the first three steps would be

$$\Delta I_1 = K_{11}^{-1}\Delta\psi_1$$

$$\Delta I_2 = (-K_{22}^{-1}K_{21}K_{11}^{-1})\Delta\psi_1$$

$$\Delta I_3 = (K_{33}^{-1}(-K_{31}K_{11}^{-1} + K_{32}K_{22}^{-1}K_{21}K_{11}^{-1}))\Delta\psi_1 \quad (1)$$

Given a strain error vector with unit microstrains $\Delta\psi_1=[1,1,1]^T$ and the parameters r and θ of Test No. 1 on a titanium block, the calculated stress error ratios are $\Delta I_2/\Delta I_1=[-1.24,-0.85,-1.27]^T$ and $\Delta I_3/\Delta I_1=[0.07,0,0.05]^T$. In the example, error at the first step only propagates to the second step, and it quickly damps at the third step. In comparison with the errors at the first step, the caused errors at the second step are nearly the reflection with an inverted sign. This can cause the back-and-forth oscillations of residual stresses. The above analysis for the example can be generalized to the subsequent steps of cutting.

The experiments on the titanium block have also found that the stress results calculated by the third-order-polynomial fitted strains are close to those by the second-order-polynomial fitted strains. The residual stress solutions directly calculated from the relieved strains are unstable and start to oscillate after the third step, while the smooth residual stress distributions can be obtained from the fitted strain data. In both fitted-strain and unfitted-strain cases, the same $\mathbf{K}_{ij}$ matrices have been used for calculation. All the depth increments are equal. Each K_{ij} matrix is well conditioned and has a small condition number. Therefore, polynomial fitting based on the least-squares technique can restrain the error propagation and stabilize the solutions. For the ring-core cutting with many steps, the second- or third-order-polynomial fitting for strains can be adopted to diminish the error propagation. If the measured strains are dispersing high-order polynomial fittinges, other fitting methods should be considered.

4 Conclusion

The ISSR/ring-core cutting method has been developed to measure residual stresses. The test system of the ISSR/ring-core cutting was constructed. A two-step measurement procedure and software were evaluated by the uniaxial loading tests.

Test procedures of the ISSR/ring-core method have been developed and tested. The stress coefficients determined in Part I [1] are used to calculate residual stresses from the strains measured by the ISSR. The cutting depth, cutting increments, and limitations were discussed. Measurement accuracy, resolution, and sensitivity were evaluated. Measurement error ranges were estimated. The strain measurement error can propagate only in the current and the next step of cutting increment in stress calculation. Fitting the strain data by polynomial functions can reduce error propagation and stabilize the results of residual stresses.

Experiments on the shot-peened titanium block show excellent repeatability and reliability of the method. The experiment on laser weld demonstrates the advantages of the ISSR being extremely small and applicable to local areas with high stress gradients. The ISSR/ring-core cutting method overcomes the shortcomings of the RSR/ring-core cutting method because of its miniature size and noncontacting nature.

Acknowledgment

The authors would like to thank Mr. Forrest Wright, a machine specialist, for the design of the ring-core cutter, and Mr. Xi Zhang, a visiting scholar, for the design of the adjustable arms to support the six photodiode sensors of the ISSR system. The authors also acknowledge the laboratory assistance received from Ms. Ming Yu and Mr. Liangdao Xia. Financial support for this work is provided by NSF Career Award No. CMS-9734522.

References

[1] Li, K., and Ren, W., 2007, "Application of Miniature Ring-Core and Interferometric Strain/Slope Rosette to Determine Residual Stress Distribution With Depth—Part I: Theories," ASME J. Appl. Mech., **74**(2), pp. 298–306.

[2] Li, K., 1996, "Out-of-Plane Displacement Derivative Measurements Using Interferometric Strain/Slope Gage," ASME J. Appl. Mech., **63**(4), pp. 1033–1038.

[3] Molzen, M., and Hornbach, D., 2001, "Shot Peening and Heat Treatment Reduce Stress," Weld. J. (Miami, FL, U. S.), **80**(1), pp. 38–42.

[4] Tjhung, T., and Li, K., 2003, "Measurement of In-Plane Residual Stresses Varying With Depth by the Interferometric Strain/Slope Rosette and Incremental Hole-Drilling," ASME J. Eng. Mater. Technol., **125**(2), pp. 153–162.

[5] Tjhung, T., Li, K., Knoerr, L., and Jin, G. C., 2002, "A Study of Residual Stresses in a Hydroformed Truck Frame," *Abstract Proceedings of SEM Conference*, Society of Experimental Mechanics, Milwaukee, WI, pp. 76–80.

[6] Dong, P., Zhang, J., Yang, Y., and Cao, Z., 1999, "Computational Simulation From Hydroforming to Welding Assembley for Rapid Virtual Prototyping," Document No. 1999-01-3190, *Proceedings of SAE IBEC International Conference*, Society of Automotive Engineers, Detroit, MI.

[7] Ajovalasit, A., Petrucci, G., and Zuccarello, B., 1996, "Determination of Nonuniform Residual Stresses Using the Ring-Core Method," ASME J. Eng. Mater. Technol., **118**(2), pp. 224–228.

[8] Schajer, G. S., and Altus, E., 1996, "Stress Calculation Error Analysis for Incremental Hole-Drilling Residual Stress Measurement," ASME J. Eng. Mater. Technol., **118**(1), pp. 120–128.

[9] Zuccarello, B., 1996, "Optimization of Depth Increment Distribution in the Ring-Core Method," J. Strain Anal. Eng. Des., **31**(4), pp. 251–258.

P. D. Spanos
R. B. Ryon Chair in Engineering
Fellow ASME
Rice University,
6100 Main Street,
MS 321,
Houston, TX 77005
e-mail: spanos@rice.edu

A. Sofi[1]
Dipartimento di Arte,
Scienza e Tecnica del Costruire,
Università "Mediterranea" di Reggio Calabria,
Via Melissari Feo di Vito,
I-89124 Reggio Calabria,
Italy
e-mail: alba.sofi@unirc.it

M. Di Paola
Dipartimento di Ingegneria Strutturale e Geotecnica,
Università di Palermo,
Viale delle Scienze,
90128, Palermo,
Italy
e-mail: dipaola@diseg.unipa.it

Nonstationary Response Envelope Probability Densities of Nonlinear Oscillators

The nonstationary random response of a class of lightly damped nonlinear oscillators subjected to Gaussian white noise is considered. An approximate analytical method for determining the response envelope statistics is presented. Within the framework of stochastic averaging, the procedure relies on the Markovian modeling of the response envelope process through the definition of an equivalent linear system with response-dependent parameters. An approximate solution of the associated Fokker-Planck equation is derived by resorting to a Galerkin scheme. Specifically, the nonstationary probability density function of the response envelope is expressed as the sum of a time-dependent Rayleigh distribution and of a series expansion in terms of a set of properly selected basis functions with time-dependent coefficients. These functions are the eigenfunctions of the boundary-value problem associated with the Fokker-Planck equation governing the evolution of the probability density function of the response envelope of a linear oscillator. The selected basis functions possess some notable properties that yield substantial computational advantages. Applications to the Van der Pol and Duffing oscillators are presented. Appropriate comparisons to the data obtained by digital simulation show that the method, being nonperturbative in nature, yields reliable results even for large values of the nonlinearity parameter. [DOI: 10.1115/1.2198253]

1 Introduction

The response of nonlinear oscillators subjected to random excitations has been extensively studied over a period of several decades. Indeed, problems encountered in various engineering fields have shown that in many circumstances the adoption of a linear model, though convenient, may fail to accurately predict the main features of the system behavior. Furthermore, it is well known that a realistic mathematical representation of environmental loads, such as ground motion, atmospheric turbulence, sea waves, etc., can be pursued by using stochastic processes. Well-established techniques have been developed for the analysis of randomly excited linear systems and are available in standard textbooks [1–3]. However, much research effort is still needed to provide accurate and efficient tools for estimating the response statistics of nonlinear systems subjected to stochastic excitations. Exact solutions of the Fokker-Planck (FP) equation, governing the transient probability density function (PDF) of the response, are available only for some special first-order nonlinear systems [4–6]. Analytical solutions for second- and higher-order systems are restricted to the reduced FP equation, namely, the FP equation without time derivative (see, e.g., [7–10]). Therefore, several approximate methods for solving nonlinear random vibration problems have been proposed in the literature. Among such procedures, stochastic averaging has proved to be a useful tool for analyzing the response of lightly damped nonlinear systems subjected to broadband stochastic excitations (see, e.g., [11]). This method was originally introduced by Stratonovich [12] and subsequently elucidated mathematically by Khasminskii [13] through a limit theorem. It may be viewed as an extension to stochastic differential equations of the well-known Bogoliubov-Mitropolski technique [14] for solving deterministic nonlinear vibration problems. A main feature of the method is that it enables replacement of the original system by a lower-dimensional one through a combination of time averaging and ensemble averaging. In the case of a single-degree-of-freedom system, the original two-dimensional Markov vector of displacement and velocity is approximated by a one-dimensional Markov process governing the response envelope. The associated FP equation is much more tractable mathematically than the original two-dimensional equation governing the joint PDF of the displacement and velocity processes. In particular, exact solutions can be derived for the stationary PDF of the response envelope [15], while the evaluation of the nonstationary PDF is a quite difficult task and approximate solution procedures are required. An envelope-based approach has been developed in [15,16] for a general class of nonlinear oscillators under white noise excitation by combining the concepts of equivalent linearization and stochastic averaging. Recently, this approach has been applied to Preisach hysteretic systems [17]. Furthermore, the definition of an equivalent linear system in the framework of stochastic averaging has also been employed by Bouc [18] to evaluate the response power spectral density function of strongly nonlinear oscillators. In [15], the nonstationary response envelope statistics have been estimated by a perturbation technique approximating the PDF as a series expansion in terms of the eigenvalues and eigenfunctions of the boundary-value problem associated with the FP equation governing the evolution of the envelope PDF of a linear oscillator. An analogous procedure has been applied in [19] to oscillators with nonlinear damping subjected to broadband stochastic excitations. However, since this approach relies on perturbation, it yields accurate results only for small values of the nonlinearity parameter. A Galerkin technique has been adopted in [20] to determine the nonstationary PDF of the response envelope by selecting as basis functions the eigenfunctions pertaining to the envelope of a linear oscillator. Indeed, such functions possess no-

[1]Visiting Scholar at Rice University, Houston, TX.

Contributed by the Applied Mechanics Division of ASME for publication in the JOURNAL OF APPLIED MECHANICS. Manuscript received June 1, 2005; final manuscript received February 6, 2006. Review conducted by M. P. Mignolet. Discussion on the paper should be addressed to the Editor, Prof. Robert M. McMeeking, Journal of Applied Mechanics, Department of Mechanical and Environmental Engineering, University of California—Santa Barbara, Santa Barbara, CA 93106-5070, and will be accepted until four months after final publication of the paper itself in the ASME JOURNAL OF APPLIED MECHANICS.

table properties that may provide substantial computational advantages in the implementation of approximate procedures based on eigenfunction expansions [21].

The present paper deals with random vibration analysis of a class of lightly damped nonlinear oscillators subjected to Gaussian white noise. The response envelope is modeled as a Markov process by using the averaging procedure presented in [15]. A general Galerkin scheme is adopted to find an approximate solution of the associated FP equation, without resorting to any perturbation analysis. In particular, the nonstationary PDF of the response envelope is expressed as the sum of a time-dependent Rayleigh distribution (approximate solution for the linear oscillator [22]) and of a series expansion in terms of a set of properly selected basis functions with time-dependent coefficients. These functions are the eigenfunctions of the boundary-value problem associated with the FP equation governing the evolution of the PDF of the response envelope of a linear oscillator. In this manner, a set of linear ordinary differential equations governing the unknown time-dependent series coefficients is obtained. Applications concerning a Van der Pol oscillator and a Duffing oscillator subjected to Gaussian white noise excitation are discussed. The accuracy of the proposed procedure is demonstrated through appropriate comparisons to Monte Carlo simulation data.

2 Mathematical Formulation

2.1 Markovian Model of Response Envelope. Consider a randomly excited nonlinear single-degree-of-freedom system whose motion is governed by

$$\ddot{x}(t) + 2\zeta_0\omega_0\dot{x}(t) + \omega_0^2 x(t) + \varepsilon f[x(t),\dot{x}(t)] = w(t) \tag{1}$$

where a dot over a variable denotes differentiation with respect to time t; ω_0 and ζ_0 represent the natural angular frequency and the ratio of critical damping, respectively; ε is a real number; $f[x(t),\dot{x}(t)]$ is an arbitrary nonlinear function of the response displacement and velocity; and the symbol $w(t)$ denotes a Gaussian white noise process with zero mean and power spectral density S_0. It is assumed that $\zeta_0 \ll 1$ and S_0 is $O(\zeta_0)$. Under these assumptions, it can be argued that the response of the nonlinear oscillator (1) exhibits a pseudoharmonic behavior described by

$$x(t) = a(t)\cos[\omega_n t + \vartheta(t)] \tag{2}$$

and

$$\dot{x}(t) = -a(t)\omega_n \sin[\omega_n t + \vartheta(t)] \tag{3}$$

where the envelope $a(t)$ and phase $\vartheta(t)$ are assumed to be slowly varying functions of time. The symbol ω_n denotes the effective angular frequency of the system, which is taken to be different from the angular frequency ω_0 in order to partly account for the effect of the nonlinear function $\varepsilon f[x(t),\dot{x}(t)]$. Once the form of the response has been defined using Eqs. (2) and (3), attention can be focused on the envelope process $a(t)$, which is particularly useful in estimating the failure probability of a system. Specifically, a first-order differential equation governing approximately the time evolution of $a(t)$ and the associated FP equation can be determined by applying the general averaging technique presented in [15–19], which is briefly reviewed here for completeness.

The first step of the aforementioned procedure involves replacing the nonlinear system (1) by an equivalent linear one by linearizing the function $f[x(t),\dot{x}(t)]$. That is,

$$\ddot{x}(t) + 2\omega_0[\zeta_0 + \varepsilon\zeta_e(a)]\dot{x}(t) + [\omega_0^2 + \varepsilon\omega_e^2(a)]x(t) = w(t) \tag{4}$$

where $\zeta_e(a)$ and $\omega_e(a)$ represent the response-dependent contributions of the nonlinear function to the effective damping and stiffness, respectively. Assuming that the envelope and phase remain essentially constant over one period of oscillation, such quantities can be determined through the relationships

$$2\omega_0\zeta_e(a) = -\frac{1}{\omega_n \pi a}\int_0^{2\pi} f(a\cos\psi, -a\omega_n \sin\psi)\sin\psi \mathrm{d}\psi \tag{5}$$

and

$$\omega_e^2(a) = \frac{1}{\pi a}\int_0^{2\pi} f(a\cos\psi, -a\omega_n \sin\psi)\cos\psi \mathrm{d}\psi \tag{6}$$

In view of Eq. (4), the effective natural frequency of the nonlinear system is therefore given by

$$\omega_n^2(a) = \omega_0^2 + \varepsilon\omega_e^2(a) \tag{7}$$

Squaring and summing both sides of Eqs. (2) and (3) yields

$$a(t) = \left[x^2(t) + \frac{\dot{x}^2(t)}{\omega_n^2(a)}\right]^{1/2} \tag{8}$$

Differentiating the previous equation with respect to time and taking into account Eqs. (2)–(4), the first-order stochastic differential equation

$$\dot{a}(t) = -2\omega_0[\zeta_0 + \varepsilon\zeta_e(a)]a(t)\sin^2[\omega_n(a)t + \vartheta(t)] - \frac{w(t)}{\omega_n(a)}\sin[\omega_n(a)t + \vartheta(t)] \tag{9}$$

governing, approximately, the time evolution of $a(t)$ is obtained. Equation (9) can be further simplified by applying an averaging procedure based on deterministic and stochastic averaging [12]. Thus, the averaged equation, which approximately governs $a(t)$, reads

$$\dot{a}(t) = -\omega_0[\zeta_0 + \varepsilon\zeta_e(a)]a(t) + \frac{\pi S_0}{2a(t)\omega_n^2(a)} + \frac{(\pi S_0)^{1/2}}{\omega_n(a)}\eta(t) \tag{10}$$

where $\eta(t)$ is a unitary white noise process with zero mean, i.e., $E[\eta(t)\eta(t+\tau)] = \delta(\tau)$, with $E[\cdot]$ and $\delta(\tau)$ being the mathematical expectation operator and the Dirac delta function, respectively. Note that Eq. (10) is decoupled from the phase $\vartheta(t)$. Thus, it provides the basis for modeling the response envelope as a one-dimensional Markov process, which is much more tractable mathematically, as will be shown next.

2.2 Fokker-Planck Equation. The FP equation associated with the stochastic differential equation (10) is given by [15]

$$\frac{\partial p(a,t)}{\partial t} = -\frac{\partial}{\partial a}[Y(a)p(a,t)] + \frac{1}{4}\frac{\partial}{\partial a}\left\{Z(a)\frac{\partial p(a,t)}{\partial a} + \frac{\partial}{\partial a}[Z(a)p(a,t)]\right\} \tag{11}$$

where $p(a,t)$ is the PDF of the random process $a(t)$, while $Y(a)$ and $Z(a)$ are defined as

$$Y(a) = -\zeta_0\omega_0\left(a - \frac{\sigma_s^2}{a}\frac{\omega_0^2}{\omega_n^2(a)}\right) - \varepsilon\zeta_e(a)\omega_0 a \tag{12}$$

$$Z(a) = 2\zeta_0\omega_0\sigma_s^2\left(\frac{\omega_0}{\omega_n(a)}\right)^2 \tag{13}$$

The symbol σ_s^2 in Eqs. (12) and (13) denotes the stationary variance of $x(t)$ for $\varepsilon = 0$

$$\sigma_s^2 = \frac{\pi S_0}{2\zeta_0\omega_0^3} \tag{14}$$

As outlined in [15], the stationary PDF, $p_s(a)$, solution of Eq. (11) for $\partial p(a,t)/\partial t = 0$, can be expressed in closed form

$$p_s(a) = \frac{C}{\sqrt{Z(a)}} \exp\left[2 \int \frac{Y(a)}{Z(a)} \mathrm{d}a \right] \tag{15}$$

where C is a normalization constant. However, the FP equation (11), in general, is not amenable to exact solutions in terms of the nonstationary PDF, $p(a,t)$. Therefore the development of accurate and efficient approximate solution procedures is desirable.

Equation (11) can be rewritten as

$$\frac{\partial p(a,t)}{\partial t} = \mathcal{L}_L[p(a,t)] + \mathcal{L}_{NL}[p(a,t)] \tag{16}$$

where $\mathcal{L}_L[\cdot]$ and $\mathcal{L}_{NL}[\cdot]$ are the following linear differential operators:

$$\mathcal{L}_L[\cdot] = \zeta_0 \omega_0 \frac{\partial}{\partial a}\left[\left(a - \frac{\sigma_s^2}{a} \right)(\cdot) \right] + \zeta_0 \omega_0 \sigma_s^2 \frac{\partial^2(\cdot)}{\partial a^2} \tag{17}$$

$$\mathcal{L}_{NL}[\cdot] = \zeta_0 \omega_0 \sigma_s^2 \frac{\partial}{\partial a}\left[\frac{1}{a}\left(1 - \frac{\omega_0^2}{\omega_n^2(a)} \right)(\cdot) \right] + \varepsilon \omega_0 \frac{\partial}{\partial a}[\zeta_e(a) a(\cdot)] + \frac{1}{2}\zeta_0 \omega_0 \sigma_s^2 \frac{\partial}{\partial a}\left[(\cdot)\frac{\partial}{\partial a}\left(\frac{\omega_0}{\omega_n(a)} \right)^2 + 2\left(\frac{\omega_0^2}{\omega_n^2(a)} - 1 \right)\frac{\partial(\cdot)}{\partial a} \right] \tag{18}$$

In particular, $\mathcal{L}_L[\cdot]$ is the FP operator for a linear oscillator ($\varepsilon = 0$), such that the PDF of the response envelope for $\varepsilon = 0$, $p_L(a,t)$, satisfies the partial differential equation

$$\frac{\partial p_L(a,t)}{\partial t} = \mathcal{L}_L[p_L(a,t)] \tag{19}$$

In [22], it has been shown that the solution of Eq. (19) is a time-dependent Rayleigh distribution

$$p_L(a,t) = \frac{a}{\sigma^2(t)} \exp\left[-\frac{a^2}{2\sigma^2(t)} \right] \tag{20}$$

in which

$$\sigma^2(t) = \sigma_s^2[1 - \exp(-2\zeta_0 \omega_0 t)] \tag{21}$$

Furthermore, under the restriction $0 \leqslant a \leqslant \infty$, it can be verified that the eigenvalues, λ_r, and the eigenfunctions, $A_r(a)$, of the boundary-value problem devised by applying a separation of variable procedure to Eq. (19) are given by

$$\lambda_r = 2\zeta_0 \omega_0 r, \quad r = 0, 1, \ldots \tag{22}$$

and

$$A_r(a) = \frac{1}{r!}\frac{a}{\sigma_s^2} \exp\left(-\frac{a^2}{2\sigma_s^2} \right) L_r\left(\frac{a^2}{2\sigma_s^2} \right), \quad r = 0, 1, \ldots \tag{23}$$

where L_r is the Laguerre polynomial of order r. Using the properties of Laguerre polynomials it can be readily proved that the eigenfunctions $A_r(a)$ satisfy the orthonormality condition

$$\int_0^\infty \frac{A_r(a) A_k(a)}{A_0(a)} \mathrm{d}a = \delta_{rk} \tag{24}$$

where δ_{rk} is the Kronecker delta symbol.

2.3 Computational Aspects of Eigenfunction Expansion. A solution of the FP equation (16) based on a series expansion in terms of the eigenfunctions $A_r(a)$ has been proposed in the past for both the case of linear [22] and nonlinear oscillators [15,19,20]. In [21], a detailed study of the computational aspects related to approximate procedures based on the use of the eigenfunctions $A_r(a)$ has been carried out. Specifically, analytical formulas that allow one to significantly reduce the computational effort associated with the implementation of the eigenfunction expansion have been derived. Some useful results, which will be used in the following, are briefly summarized here.

Using the properties of Laguerre polynomials, it can be proved that the recursive formula

$$(r+1)A_{r+1}(a) = \left(2r + 1 - \frac{a^2}{2\sigma_s^2} \right) A_r(a) - r A_{r-1}(a) \tag{25}$$

holds, which affords an easily mechanized numerical computation of the eigenfunctions $A_r(a)$.

Furthermore, the first-order derivative of $A_r(a)$ with respect to a can be conveniently expressed in terms of $A_{r+1}(a)$ and $A_r(a)$, as follows:

$$\frac{\mathrm{d}A_r(a)}{\mathrm{d}a} = \frac{1}{a}[2(r+1)A_{r+1}(a) - (2r+1)A_r(a)] \tag{26}$$

Using the recursive formula (25) and the orthonormality condition (24), it can be verified that integrals of the form

$$I_{n,r,k} = \int_0^\infty a^n \frac{A_r(a) A_k(a)}{A_0(a)} \mathrm{d}a \tag{27}$$

with n, r, and k being arbitrary integers, may be computed recursively by means of

$$I_{n+2,r,k} = 2\sigma_s^2[(2k+1)I_{n,r,k} - k I_{n,r,k-1} - (k+1)I_{n,r,k+1}] \tag{28}$$

It can be seen that for n even, the values of $I_{0,r,k}$, given by Eq. (24), are needed to start the recursive scheme, whereas for n odd, the numerical evaluation of $I_{1,r,k}$ is required.

A recursive computation of the integral

$$I_{n,r} = \int_0^\infty a^n A_r(a) \mathrm{d}a \tag{29}$$

can be accomplished by using

$$I_{n,r+1} = \frac{r - \frac{n}{2}}{r+1} I_{n,r} \tag{30}$$

A notable property, which simplifies the determination of the statistical moments of the response envelope when $p(a,t)$ is approximated in terms of the eigenfunctions $A_r(a)$, is

$$I_{n,r} = 0 \text{ for } r > \frac{n}{2} \tag{31}$$

with n being an even integer.

3 Approximate Solution of the Fokker-Planck Equation

In the present section, an approximate procedure is presented for estimating the nonstationary PDF of the response envelope of the class of lightly damped nonlinear oscillators considered herein. This procedure may be viewed as an appropriate generalization of the approach proposed in [15,16], which is based on the joint use of the eigenfunction expansion and perturbation technique. Numerical results have shown the limitation of the aforementioned method to handle large values of the nonlinearity parameter. In [15], the authors have suggested that the lack of accuracy detected for highly nonlinear systems is not related to the approximations involved in the linearization of the system, but it is a consequence of the perturbation solution of Eq. (11). In context with this notion, herein Eq. (11) is solved approximately by using a general Galerkin scheme without resorting to any perturbation analysis.

Specifically, relying on the mathematical structure of Eq. (16), a solution is attempted by expressing the PDF of the response envelope as the sum of the solution for $\varepsilon = 0$, $p_L(a,t)$ (Eq. (20)), and of an unknown function, $g(a,t)$, which accounts for the deviation of $p(a,t)$ from $p_L(a,t)$ due to the nonlinearity. That is,

$$p(a,t) = p_L(a,t) + g(a,t) \tag{32}$$

Furthermore, the function $g(a,t)$ is approximated by a truncated series expansion in terms of the eigenfunctions $A_r(a)$. That is,

$$g(a,t) = \sum_{r=0}^{N} c_r(t) A_r(a) \tag{33}$$

where N is an appropriate integer and $c_r(t)$ are functions of time to be determined. As shown in [22], an eigenfunction expansion can be used to express $p_L(a,t)$ as well.

It is assumed that the system is initially at rest, so that using Eqs. (32) and (33), the initial condition for Eq. (16) can be expressed as

$$p(a,0) = \hat{\delta}(a) = p_L(a,0) + \sum_{r=0}^{N} c_r(0) A_r(a) \tag{34}$$

in which $\hat{\delta}(a)$ denotes the one-sided Dirac delta function. Taking into account that $p_L(a,0) = \hat{\delta}(a)$, Eq. (34) yields

$$c_r(0) = 0, \quad r = 0,1,2,\ldots,N \tag{35}$$

Substituting Eq. (32) into Eq. (16) with $g(a,t)$ given by Eq. (33), the residual error

$$\begin{aligned} R[a,\mathbf{c}(t)] = {} & \frac{\partial p_L(a,t)}{\partial t} + \sum_{r=0}^{N} \dot{c}_r(t) A_r(a) - \mathcal{L}[p_L(a,t)] \\ & - \mathcal{L}_L\left[\sum_{r=0}^{N} c_r(t) A_r(a)\right] - \mathcal{L}_{NL}[p_L(a,t)] \\ & - \mathcal{L}_{NL}\left[\sum_{r=0}^{N} c_r(t) A_r(a)\right] \end{aligned} \tag{36}$$

is obtained, where $\mathbf{c}(t) = [c_0(t), c_1(t), \ldots, c_N(t)]^{\mathrm{T}}$. Taking into account Eq. (19) and that the relationship

$$\mathcal{L}_L\left[\sum_{r=0}^{N} c_r(t) A_r(a)\right] = -\sum_{r=0}^{N} \lambda_r c_r(t) A_r(a) \tag{37}$$

holds, Eq. (36) can be rewritten as

$$\begin{aligned} R[a,\mathbf{c}(t)] = {} & \sum_{r=0}^{N} \dot{c}_r(t) A_r(a) + \sum_{r=0}^{N} \lambda_r c_r(t) A_r(a) - \mathcal{L}_{NL}[p_L(a,t)] \\ & - \mathcal{L}_{NL}\left[\sum_{r=0}^{N} c_r(t) A_r(a)\right] \end{aligned} \tag{38}$$

According to the Galerkin method, the $N+1$ unknown functions $c_r(t)$ can be evaluated by imposing that the projection of the residual error $R[a,\mathbf{c}(t)]$ on a properly selected set of independent functions is zero. Then, selecting $A_k(a)/A_0(a)$ as weighting functions this condition can be expressed as

$$\int_0^{\infty} \frac{A_k(a)}{A_0(a)} R[a,\mathbf{c}(t)]\mathrm{d}a = 0, \quad k = 0,1,2,\ldots,N \tag{39}$$

Substituting Eq. (38) into Eq. (39), the set of linear first-order ordinary differential equations governing the unknown functions $c_r(t)$

$$\dot{\mathbf{c}}(t) = \mathbf{D}\mathbf{c}(t) + \mathbf{F}(t) \tag{40}$$

is obtained. In Eq. (40), $\mathbf{D}$ and $\mathbf{F}(t)$ denote a matrix of order $(N+1)\times(N+1)$ and an $(N+1)$-vector, respectively, whose generic elements are given by

$$D_{kr} = -\lambda_k \delta_{kr} + \int_0^{\infty} \frac{A_k(a)}{A_0(a)} \mathcal{L}_{NL}[A_r(a)]\mathrm{d}a \tag{41}$$

and

$$F_k(t) = \int_0^{\infty} \frac{A_k(a)}{A_0(a)} \mathcal{L}_{NL}[p_L(a,t)]\mathrm{d}a \tag{42}$$

Obviously, in the stationary case, Eq. (40) reduces to a set of linear algebraic equations governing the unknown constant coefficients c_k. In particular, it can be seen that as t tends to infinity the function $p_L(a,t)$ approaches the Rayleigh distribution (see Eq. (20)) and the elements of $\mathbf{F}(t)$ become constant.

Note that the computation of the integrals in Eqs. (41) and (42) can be readily accomplished in a mechanized way by exploiting the properties of the eigenfunctions $A_r(a)$ listed in Sec. 2, as will be outlined in detail next through applications. In particular, if $p_L(a,t)$ is expressed in terms of the eigenvalues λ_r and the eigenfunctions $A_r(a)$, as [22]

$$p_L(a,t) = \sum_{r=0}^{N} e^{-\lambda_r t} A_r(a) \tag{43}$$

Equation (42) can be rewritten in the form

$$F_k(t) = \sum_{r=0}^{N} e^{-\lambda_r t} \int_0^{\infty} \frac{A_k(a)}{A_0(a)} \mathcal{L}_{NL}[A_r(a)]\mathrm{d}a \tag{44}$$

which involves the evaluation of the same integrals appearing in Eq. (41). This fact, obviously, induces substantial computational savings.

Note that the solution of Eq. (40) under the initial condition $\mathbf{c}(0) = \mathbf{0}$ can be pursued either numerically or in a closed form as

$$\mathbf{c}(t) = \int_0^{t} \exp(\mathbf{D}\tau)\mathbf{F}(t-\tau)\mathrm{d}\tau \tag{45}$$

Once the differential equations (40) are integrated, an approximate analytical expression of $p(a,t)$ can be obtained by back substitution of $\mathbf{c}(t)$ into Eqs. (33) and (32).

The selected form of the approximate solution (32) proves advantageous for the determination of the statistical moments of the response envelope. Specifically, the jth order moment of $a(t)$ can be expressed as

$$m_j(t) = E[a^j(t)] = m_{L,j}(t) + \sum_{r=0}^{N} c_r(t) I_{j,r} \tag{46}$$

where

$$m_{L,j}(t) = \int_0^{\infty} a^j(t) p_L(a,t)\mathrm{d}a \tag{47}$$

and

$$I_{j,r} = \int_0^{\infty} a^j(t) A_r(a)\mathrm{d}a \tag{48}$$

The integrals $I_{j,r}$ can be readily computed by using the recursive formula (30). Furthermore, in view of property (31) it can be argued that if j is even, then only the first $r \leqslant j/2$ terms of the summation in Eq. (46) are different from zero. For instance, the first- and second-order statistical moments of the response envelope are given by

$$m_1(t) = E[a(t)] = \int_0^{\infty} a(t) p_L(a,t)\mathrm{d}a + \sum_{r=0}^{N} c_r(t) I_{1,r} \tag{49}$$

and

$$m_2(t) = E[a^2(t)] = \int_0^\infty a^2(t) p_L(a,t)\mathrm{d}a + \sum_{r=0}^{1} c_r(t) I_{2,r} \qquad (50)$$

where $I_{1,r}$ and $I_{2,r}$ with $r>0$ can be computed by the recursive formula (30), taking into account that $I_{1,0}=\sigma_s\sqrt{\pi/2}$ and $I_{2,0}=2\sigma_s^2$. It must be emphasized that the result in Eq. (50) does not imply that the PDF $p(a,t)$ can be approximated by retaining only the first two terms in Eq. (33). In fact, since the nonlinearity makes the differential equations (40) coupled (see Eq. (41)), in general, Eq. (50) provides more accurate estimates of the second-order moment $m_2(t)$ as a greater number of eigenfunctions is considered in the Galerkin solution of the FP equation.

4 Applications

4.1 Van der Pol Oscillator. Consider the special case in which

$$f[x(t),\dot{x}(t)] = 2\zeta_0\omega_0\left[-\frac{2}{\varepsilon}+\frac{x^2(t)}{\sigma_s^2}\right]\dot{x}(t), \quad \varepsilon>0 \qquad (51)$$

so that Eq. (1) represents a Van der Pol oscillator subjected to random excitation. That is, the equation of motion becomes

$$\ddot{x}(t) + 2\zeta_0\omega_0\left[-1+\frac{\varepsilon x^2(t)}{\sigma_s^2}\right]\dot{x}(t) + \omega_0^2 x(t) = w(t) \qquad (52)$$

Based on the procedure described in Sec. 2, Eq. (52) is linearized according to the scheme

$$f[x(t),\dot{x}(t)] \to 2\omega_0\zeta_e(a)\dot{x}(t) \qquad (53)$$

Using Eqs. (5) and (6), it can be proved that

$$\zeta_e(a) = \zeta_0\left(-\frac{2}{\varepsilon}+\frac{a^2}{4\sigma_s^2}\right); \quad \omega_e(a) = 0 \qquad (54)$$

Hence, in this case, there is no contribution by the nonlinear function to the effective stiffness of the system, namely, $\omega_n(a)\equiv\omega_0$.

Relying on the results in Eq. (54), it is readily found that for the system (52), the differential operator $\mathcal{L}_{NL}[\cdot]$ reduces to

$$\mathcal{L}_{NL}[\cdot] = \varepsilon\omega_0\frac{\partial}{\partial a}[\zeta_e(a)a(\cdot)] \Rightarrow \mathcal{L}_{NL}[\cdot] = -2\zeta_0\omega_0\frac{\partial}{\partial a}[a(\cdot)] + \frac{\varepsilon\zeta_0\omega_0}{4\sigma_s^2}\frac{\partial}{\partial a}[a^3(\cdot)] \qquad (55)$$

while, obviously, the differential operator $\mathcal{L}_L[\cdot]$ is still given by Eq. (17). In this context, it should be noted that the function $p_L(a,t)$ satisfying Eq. (19) does not represent the PDF of the response envelope of the oscillator for $\varepsilon=0$ and, consequently, the function $g(a,t)$ (Eq. (32)) cannot be viewed as the deviation from the linear solution due to nonlinearity. In fact, it is known that the linear part of the Van der Pol oscillator is unstable. Therefore, in this case the split of the differential operator of the FP equation (Eq. (16)) and of the PDF $p(a,t)$ (Eq. (32)) does not possess a physical meaning.

The stationary solution of the FP equation, $p_s(a)$, may be determined in closed form by applying Eq. (15). Following the procedure presented in Sec. 3, the nonstationary PDF, $p(a,t)$, can be approximated by means of Eq. (32). Then, on account of Eq. (55) the associated residual error (38) takes the form

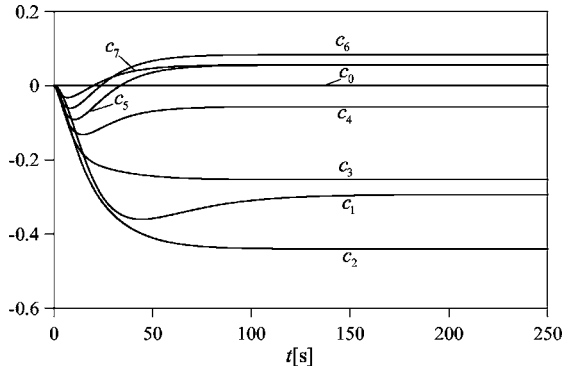

Fig. 1 Time evolution of the series coefficients $c_i(t)$, $i=0,1,\ldots,7$ (Van der Pol oscillator Eq. (52))

$$R[a,\mathbf{c}(t)] = \sum_{r=0}^{N}\dot{c}_r(t)A_r(a) + \sum_{r=0}^{N}\lambda_r c_r(t)A_r(a) + 2\zeta_0\omega_0\left[p_L(a,t) + a\frac{\partial p_L(a,t)}{\partial a} + \sum_{r=0}^{N}c_r(t)A_r(a) + a\sum_{r=0}^{N}c_r(t)\frac{\mathrm{d}A_r(a)}{\mathrm{d}a}\right] - \frac{\varepsilon\zeta_0\omega_0}{4\sigma_s^2}\frac{\partial}{\partial a}\left[a^3 p_L(a,t) + a^3\sum_{r=0}^{N}c_r(t)A_r(a)\right] \qquad (56)$$

Finally, using the orthonormality condition (24) and Eq. (26), Eq. (39) yields the set of linear ordinary differential equations

$$\dot{c}_k(t) = [-\lambda_k + 4\zeta_0\omega_0 k]c_k(t) + \frac{\varepsilon\zeta_0\omega_0}{4\sigma_s^2}\left\{2\sum_{r=0}^{N}c_r(t)[(1-r)I_{2,k,r} + (r+1)I_{2,k,r+1}] + 3L_k^{(1)}(t) + L_k^{(2)}(t)\right\} - 2\zeta_0\omega_0\left\{2\sum_{r=0}^{N}(r+1)c_r(t)\delta_{k,r+1} + L_k^{(3)}(t) + L_k^{(4)}(t)\right\}; \quad k=0,1,2,\ldots,N \qquad (57)$$

for the functions $c_r(t)$, where $I_{2,k,r}$ is given by Eq. (28) for $n=0$, while the time-dependent functions $L_k^{(j)}(t)$ $(j=1,\ldots,4)$ are defined by

$$L_k^{(1)}(t) = \int_0^\infty a^2\frac{A_k(a)}{A_0(a)}p_L(a,t)\mathrm{d}a; \quad L_k^{(2)}(t) = \int_0^\infty a^3\frac{A_k(a)}{A_0(a)}\frac{\partial p_L(a,t)}{\partial a}\mathrm{d}a$$

$$L_k^{(3)}(t) = \int_0^\infty \frac{A_k(a)}{A_0(a)}p_L(a,t)\mathrm{d}a; \quad L_k^{(4)}(t) = \int_0^\infty a\frac{A_k(a)}{A_0(a)}\frac{\partial p_L(a,t)}{\partial a}\mathrm{d}a \qquad (58)$$

To assess the accuracy of the present procedure, a Van der Pol oscillator characterized by the following parameters is considered: $\zeta_0=0.02$, $\omega_0=1$ rad/s and $\varepsilon=2$. It is assumed that the oscillator is subjected to a Gaussian white noise with power spectral density $S_0=0.1\ \mathrm{m}^2/\mathrm{s}^3$.

In Fig. 1, the time evolution of the series coefficients $c_i(t)$, $(i=0,1,\ldots,7)$, solution of the differential equations (40) for $N=7$, is plotted. It can be seen that as time increases the coefficients tend to constant values, which pertain to the stationary solution. Furthermore, the first coefficients dominate the higher-order ones whose contribution becomes negligible as larger values of N are considered.

Figure 2 displays the PDF $p(a,t)$ evaluated at different time instants by means of the proposed procedure retaining 20 terms in

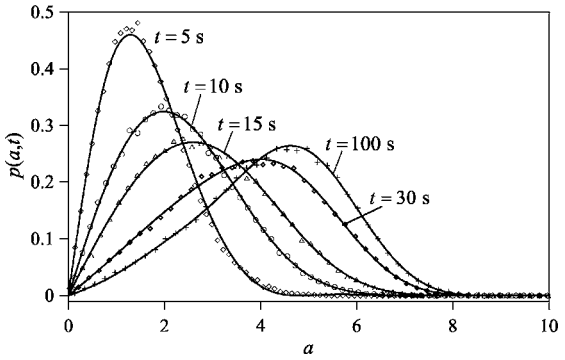

Fig. 2 Nonstationary PDF of the response envelope evaluated at different time instants by the proposed method setting *N* =19 (continuous line) and by MCS (symbols) (Van der Pol oscillator Eq. (52))

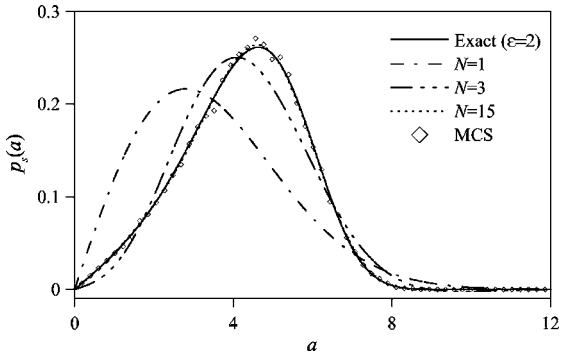

Fig. 4 Proposed approximation of the stationary PDF of the response envelope for different values of *N* compared to the exact solution (Eq. (15)) and MCS data (Van der Pol oscillator Eq. (52))

Eq. (33) ($N=19$) along with the results obtained by applying Monte Carlo simulation (MCS) to Eq. (52). It is noted that related comparisons have demonstrated that the present solution is in good agreement with digital simulation at each time instant even for $N=15$.

In Fig. 3, the PDF of the response envelope at $t=5$ s is shown. The estimates provided by the proposed procedure, including an increasing number of series terms in Eq. (33), are compared to MCS data. Note that, despite the large value of the nonlinearity parameter, 16 terms ($N=15$) are enough to achieve a good agreement with digital simulation. No significant improvement is obtained by further increasing the number of series terms over $N=19$. An analogous comparison for the stationary PDF, $p_s(a)$, is shown in Fig. 4, where the present solution is also compared to the exact one (Eq. (15)). It can be seen that the approximate stationary PDF corresponding to $N=15$ matches closely both the exact solution and MCS data.

Figure 5 shows the time evolution of the first- and second-order statistical moments of the response envelope (Eqs. (49) and (50)). It can be seen that the proposed estimates of $m_1(t)$ and $m_2(t)$ are in good agreement with digital simulation even for $N=3$. For comparison purpose, the exact stationary values of the first- and second-order statistical moments computed by means of the analytical expression of $p_s(a)$ are also plotted. As already mentioned, though $m_2(t)$ is evaluated by means of Eq. (50) where $I_{2,r}=0$ for $r>1$, a more accurate approximation is obtained by retaining a number of eigenfunctions greater than two in the series expansion (33).

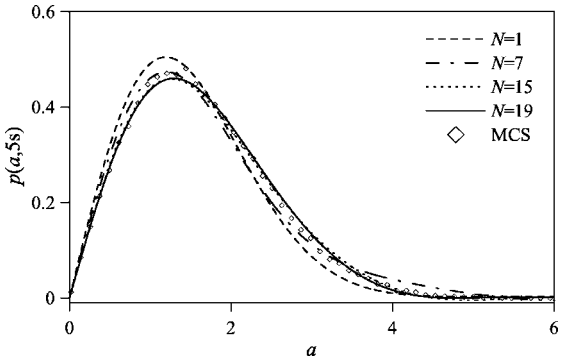

Fig. 3 Proposed approximation of the nonstationary PDF of the response envelope evaluated at *t*=5 s retaining *N* series terms contrasted with MCS data (Van der Pol oscillator Eq. (52))

4.2 Duffing Oscillator. The second application concerns a randomly excited Duffing oscillator

$$\ddot{x}(t)+2\zeta_0\omega_0\dot{x}(t)+\omega_0^2\left[1+\frac{\varepsilon x^2(t)}{\sigma_s^2}\right]x(t)=w(t),\quad \varepsilon>0 \quad (59)$$

for which the nonlinear function $f[x(t),\dot{x}(t)]$ is defined as

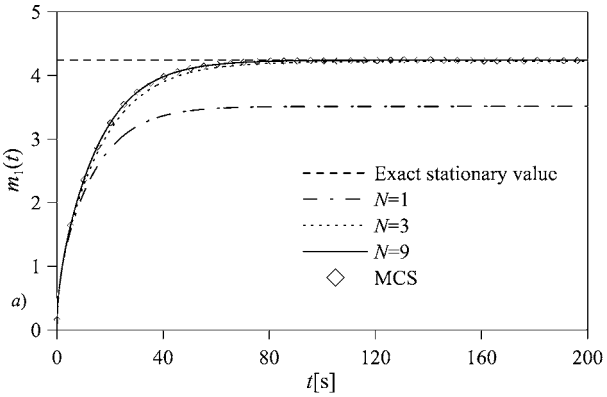

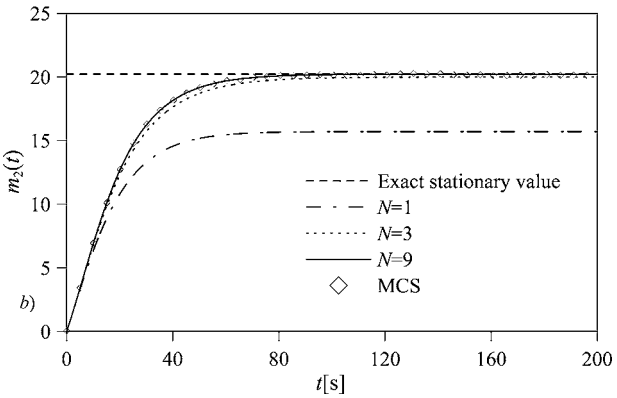

Fig. 5 Proposed estimates of the first- (*a*) and second-order (*b*) statistical moments of the response envelope obtained by applying Eqs. (49) and (50) for different values of *N* compared to MCS data (Van der Pol oscillator Eq. (52))

$$f[x(t),\dot{x}(t)] = \frac{\omega_0^2 x^3(t)}{\sigma_s^2} \tag{60}$$

Then, using Eqs. (5) and (6), the equivalent damping and stiffness are found to be, respectively,

$$\zeta_e(a) = 0; \quad \omega_e^2(a) = \frac{3}{4}\frac{\omega_0^2 a^2}{\sigma_s^2} \tag{61}$$

Replacing Eq. (61) into Eq. (18), the following expression of the linear differential operator $L_{NL}[\cdot]$ is obtained:

$$\begin{aligned}\mathcal{L}_{NL}[\cdot] = \zeta_0\omega_0\sigma_s^2\frac{\partial}{\partial a}\left[\frac{1}{a}\left(\frac{3\varepsilon a^2/4\sigma_s^2}{1+3\varepsilon a^2/4\sigma_s^2}\right)(\cdot)\right] \\ + \frac{1}{2}\zeta_0\omega_0\sigma_s^2\frac{\partial}{\partial a}\left[(\cdot)\frac{\partial}{\partial a}\left(\frac{1}{1+3\varepsilon a^2/4\sigma_s^2}\right)\right. \\ \left. - 2\left(\frac{3\varepsilon a^2/4\sigma_s^2}{1+3\varepsilon a^2/4\sigma_s^2}\right)\frac{\partial(\cdot)}{\partial a}\right]\end{aligned} \tag{62}$$

The stationary solution of the FP equation, $p_s(a)$, can be expressed in a closed form [15] by applying the general formula (15). However, to find an approximate expression for the nonstationary PDF, $p(a,t)$, a solution of the form (32) is assumed. Based on Eq. (62), it can be readily shown that the associated residual error (Eq. (38)) becomes

$$\begin{aligned}R[a,\mathbf{c}(t)] = \sum_{r=0}^{N}\dot{c}_r(t)A_r(a) + \sum_{r=0}^{N}\lambda_r c_r(t)A_r(a) \\ + \frac{3\varepsilon\sigma_s^2\zeta_0\omega_0}{h(a)}\left\{l(a)\sum_{r=0}^{N}c_r(t)A_r(a) + m(a)\sum_{r=0}^{N}c_r(t)\frac{\mathrm{d}A_r(a)}{\mathrm{d}a}\right. \\ + n(a)\sum_{r=0}^{N}c_r(t)\frac{\mathrm{d}^2A_r(a)}{\mathrm{d}a^2} + l(a)p_L(a,t) + m(a)\frac{\partial p_L(a,t)}{\partial a} \\ \left. + n(a)\frac{\partial^2 p_L(a,t)}{\partial a^2}\right\}\end{aligned} \tag{63}$$

where

$$l(a) = 9\varepsilon a^2(a^2\varepsilon - 4\sigma_s^2); \quad m(a) = a(3a^2\varepsilon + 4\sigma_s^2)(8\sigma_s^2 - 3a^2\varepsilon)$$

$$n(a) = a^2(3a^2\varepsilon + 4\sigma_s^2)^2; \quad h(a) = (3a^2\varepsilon + 4\sigma_s^2)^3 \tag{64}$$

Using the orthonormality condition (24) and applying Eq. (39), the set of linear ordinary differential equations

$$\begin{aligned}\dot{c}_k(t) = -\lambda_k c_k(t) - 3\varepsilon\sigma_s^2\zeta_0\omega_0\left\{\sum_{r=0}^{N}[B_{kr}^{(1)} + B_{kr}^{(2)} + B_{kr}^{(3)}]c_r(t) + L_k^{(1)}(t)\right. \\ \left. + L_k^{(2)}(t) + L_k^{(3)}(t)\right\} \quad k = 0,1,2,\ldots,N\end{aligned} \tag{65}$$

governing the unknown functions $c_k(t)$ is obtained, where

$$B_{kr}^{(1)} = \int_0^\infty \frac{l(a)}{h(a)}\frac{A_k(a)A_r(a)}{A_0(a)}\mathrm{d}a;$$

$$B_{kr}^{(2)} = \int_0^\infty \frac{m(a)}{h(a)}\frac{A_k(a)}{A_0(a)}\frac{\mathrm{d}A_r(a)}{\mathrm{d}a}\mathrm{d}a;$$

$$B_{kr}^{(3)} = \int_0^\infty \frac{n(a)}{h(a)}\frac{A_k(a)}{A_0(a)}\frac{\mathrm{d}^2A_r(a)}{\mathrm{d}a^2}\mathrm{d}a \tag{66}$$

and

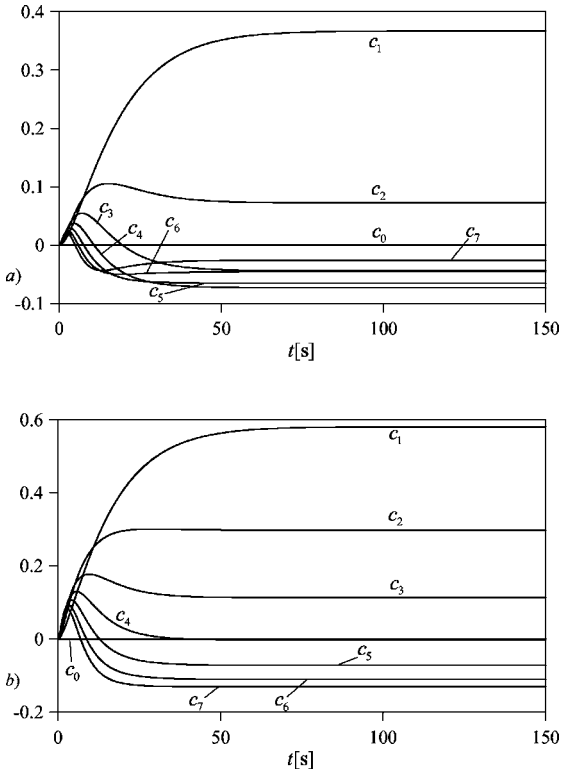

Fig. 6 Time evolution of the series coefficients $c_i(t)$, $i=0,1,\ldots,7$ (Duffing oscillator Eq. (59)): (*a*) $\varepsilon=0.5$; (*b*) $\varepsilon=2$

$$L_k^{(1)}(t) = \int_0^\infty \frac{l(a)}{h(a)}\frac{A_k(a)}{A_0(a)}p_L(a,t)\mathrm{d}a;$$

$$L_k^{(2)}(t) = \int_0^\infty \frac{m(a)}{h(a)}\frac{A_k(a)}{A_0(a)}\frac{\partial p_L(a,t)}{\partial a}\mathrm{d}a;$$

$$L_k^{(3)}(t) = \int_0^\infty \frac{n(a)}{h(a)}\frac{A_k(a)}{A_0(a)}\frac{\partial^2 p_L(a,t)}{\partial a^2}\mathrm{d}a \tag{67}$$

Because of the presence of ratios of the polynomials defined in Eq. (64), the above integrals cannot be evaluated taking advantage of the recursive formula (28). Nevertheless, the required computations can be significantly reduced by approximating the function $p_L(a,t)$ in terms of the eigenvalues λ_r and eigenfunctions $A_r(a)$, according to Eq. (43). In this manner, the functions $L_k^{(i)}(t)$, $(i=1,2,3)$, defined in Eq. (67), can be expressed as

$$L_k^{(1)}(t) = \sum_{r=0}^{N} e^{-\lambda_r t}B_{kr}^{(1)}; \quad L_k^{(2)}(t) = \sum_{r=0}^{N} e^{-\lambda_r t}B_{kr}^{(2)};$$

$$L_k^{(3)}(t) = \sum_{r=0}^{N} e^{-\lambda_r t}B_{kr}^{(3)} \tag{68}$$

where the dependence on time is explicit. It appears that only the evaluation of the integrals (66) is required, thus allowing substantial computational savings.

The preceding formulation is applied to a Duffing oscillator with $\zeta_0=0.02$ and $\omega_0=2$ rad/s, for two different values of the nonlinearity parameter, say $\varepsilon=0.5$ and $\varepsilon=2$. It is assumed that the oscillator is subjected to a Gaussian white noise with power spectral density $S_0=0.1$ m^2/s^3.

Figure 6 displays the time evolution of the series coefficients $c_i(t)$, $(i=0,1,\ldots,7)$, solution of the differential equations (40) for

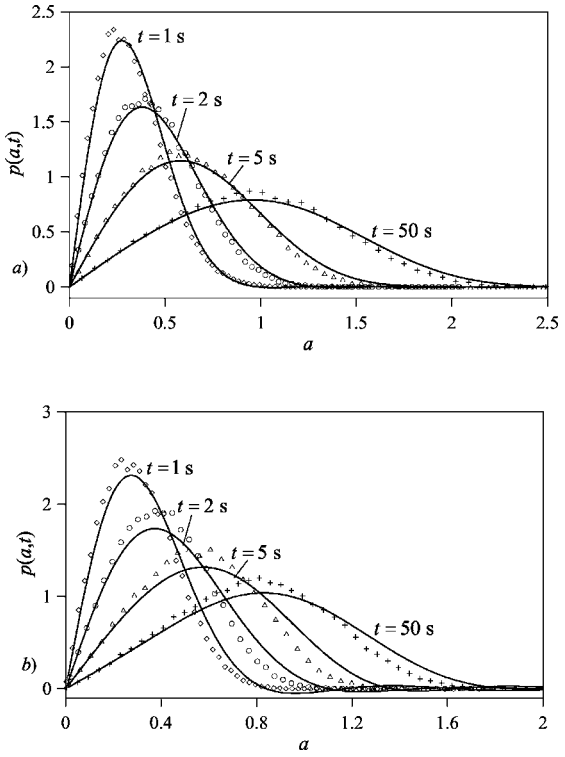

Fig. 7 Nonstationary PDF of the response envelope evaluated at different time instants by the proposed method setting $N=19$ (continuous line) and by MCS (symbols) (Duffing oscillator Eq. (59)): (*a*) $\varepsilon=0.5$; (*b*) $\varepsilon=2$

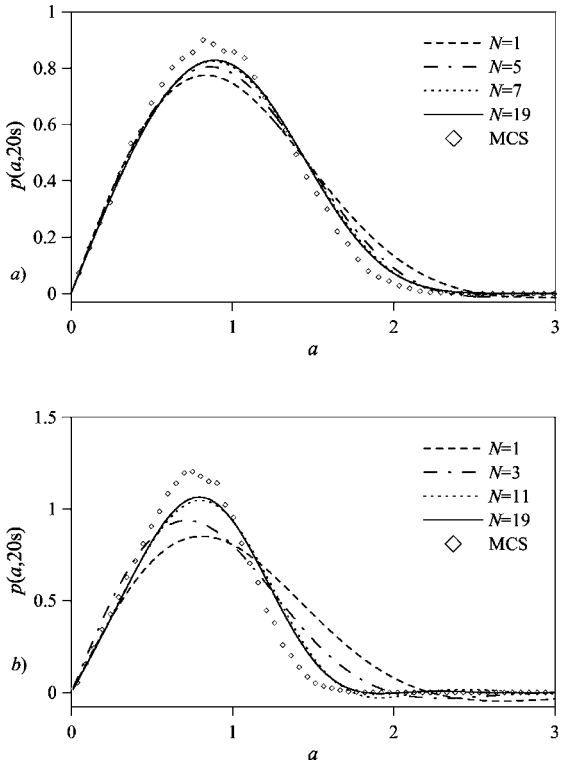

Fig. 8 Proposed approximation of the nonstationary PDF of the response envelope evaluated at $t=20$ s retaining N series terms contrasted with MCS data (Duffing oscillator Eq. (59)): (*a*) $\varepsilon=0.5$; (*b*) $\varepsilon=2$

$N=7$. Note that for $\varepsilon=0.5$ the values of the coefficients $c_i(t)$ with $i>4$ become smaller as the order i increases. A similar trend is also observed for $\varepsilon=2$ by retaining a number of series terms $N>7$. This implies that the proposed solution converges to the exact one more rapidly when the nonlinearity parameter is smaller, as will be shown next.

In Fig. 7, the PDF $p(a,t)$ evaluated at different time instants by means of the present procedure setting $N=19$ in Eq. (33) is compared to the results obtained by applying MCS to the original nonlinear system (59). As expected, the estimates pertaining to $\varepsilon=0.5$ are more accurate than those retrieved for $\varepsilon=2$ by retaining the same number of series terms. Nevertheless, numerical investigations have demonstrated that for values of $N>19$ slight improvements of the accuracy are achieved. In this context, it should be emphasized that when quite strong nonlinearities are considered, the proposed solution is inevitably affected by the approximations involved in both the definition of the equivalent linear system and the Markovian modeling of the response envelope process.

Figure 8 displays the estimates of $p(a,t)$ at $t=20$ s obtained by the proposed procedure, including an increasing number of series terms. The comparison to MCS data shows that for $\varepsilon=0.5$ a rather good accuracy is achieved by retaining only eight terms ($N=7$). For $\varepsilon=2$, despite the large nonlinearity involved, 12 terms ($N=11$) are enough to obtain a reasonable agreement with digital simulation, though small negative values of probability still appear. This drawback can be overcome by further increasing N. In particular, for $N\geqslant 13$ the proposed solution remains almost unchanged, so that no further improvement of the accuracy can be obtained.

In Fig. 9, different approximations of the stationary PDF, $p_s(a)$, determined by the proposed approach by retaining an increasing number of series terms in Eq. (33) are compared to both the exact solution (Eq. (15)) and MCS data. The exact stationary PDF per-

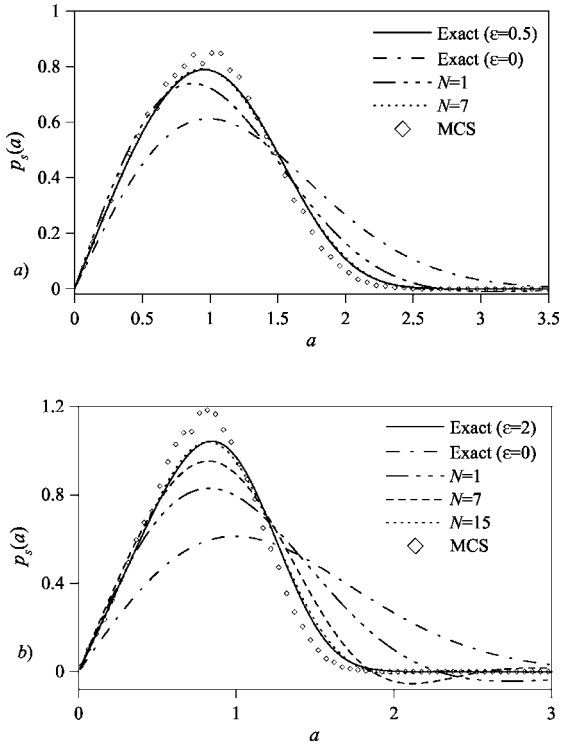

Fig. 9 Proposed approximation of the stationary PDF of the response envelope for different values of N compared to the exact solution (Eq. (15)), the solution pertaining to $\varepsilon=0$ and MCS data (Duffing oscillator Eq. (59)): (*a*) $\varepsilon=0.5$; (*b*) $\varepsilon=2$.

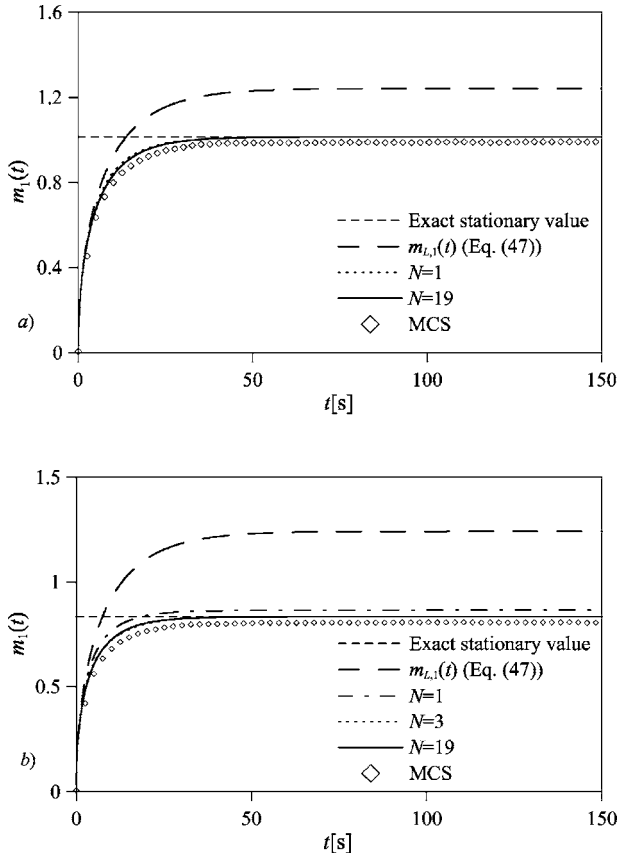

Fig. 10 Proposed estimate of the first-order statistical moment of the response envelope obtained by applying Eq. (49) for different values of *N* compared to MCS data (Duffing oscillator Eq. (59)): (*a*) $\varepsilon=0.5$; (*b*) $\varepsilon=2$

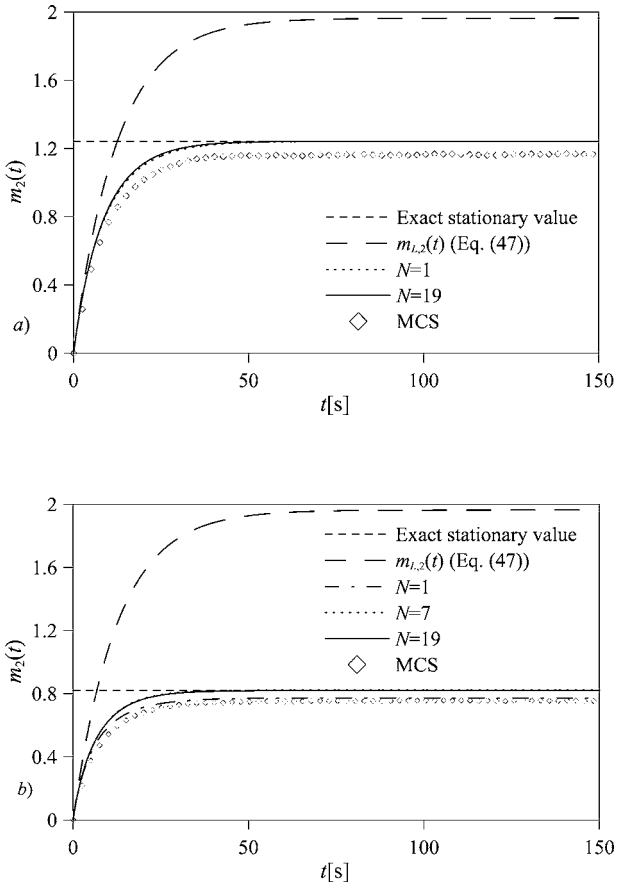

Fig. 11 Proposed estimate of the second-order statistical moment of the response envelope obtained by applying Eq. (50) for different values of *N* compared to MCS data (Duffing oscillator Eq. (59)): (*a*) $\varepsilon=0.5$; (*b*) $\varepsilon=2$

taining to the linear oscillator ($\varepsilon=0$) is also plotted. As expected, the present approximation converges more rapidly to the exact solution when a smaller nonlinearity is involved. In particular, it can be seen that for $\varepsilon=0.5$, the estimate of the stationary PDF obtained by retaining only the first eight series terms ($N=7$) is almost coincident with the exact one. However, for $\varepsilon=2$ a similar level of accuracy is achieved by setting $N=15$. In this regard, it is worth noting the capability of the present procedure to accurately describe the deviation of the PDF from the linear solution.

In Fig. 10, the time evolution of the first-order statistical moment of the response envelope (Eq. (49)) is plotted. Appropriate comparisons to both the exact stationary value, computed by using the analytical expression of $p_s(a)$, and digital simulation demonstrate that for $\varepsilon=0.5$ and $\varepsilon=2$, accurate estimates of $m_1(t)$ are obtained by setting $N=1$ and $N=3$, respectively. The statistical moment $m_{1,L}(t)$ pertaining to the linear oscillator ($\varepsilon=0$) is also plotted. Figure 11 displays the time evolution of the second-order statistical moment of the response envelope (Eq. (50)). Note that for $\varepsilon=0.5$, the proposed approximations of $m_2(t)$ corresponding to $N=1$ and $N=19$ are almost coincident, and as time increases they approach the exact stationary value deduced from the closed-form expression of $p_s(a)$. Hence, only the first two series terms are enough to achieve a good agreement with MCS. Furthermore, for $\varepsilon=2$ the comparison to the exact stationary value shows that, though only the contributions of the coefficients $c_0(t)$ and $c_1(t)$ to the second-order moment are different from zero (Eq. (50)), a more accurate approximation of $m_2(t)$ is obtained by setting $N=7$ in the series expansion (33). An inspection of Fig. 11(*b*) also reveals that the solution corresponding to $N=1$ is fortuitously closer to MCS data. For comparison purpose, the statistical moment $m_{2,L}(t)$ pertaining to the linear oscillator ($\varepsilon=0$) is also displayed. As already mentioned, the deviation of the results provided by the proposed method from MCS data is partly attributable to the approximations inherent in the linearization and averaging procedures. It should be observed, however, that the present estimates of the response envelope statistics are much more accurate than those obtained by a perturbation solution of the relevant FP equation [15].

5 Concluding Remarks

The nonstationary response of a class of lightly damped nonlinear oscillators subjected to Gaussian white noise excitation has been studied. The response envelope has been modeled as a Markov process by defining an equivalent linear system with response-dependent parameters and applying stochastic averaging. An approximate solution of the associated Fokker-Planck equation has been pursued resorting to the Galerkin method. Specifically, the nonstationary probability density function of the response envelope has been approximated by a time-dependent Rayleigh distribution plus a series expansion in terms of a set of properly selected basis functions with time-dependent coefficients. These functions are the eigenfunctions of the Fokker-Planck equation governing the evolution of the probability density function of the response envelope of a linear oscillator. A set of coupled linear ordinary differential equations governing the time-dependent series coefficients has been obtained. It has been shown that the computational time required by the derivation of such equations can be substantially reduced by exploiting the properties of the eigenfunctions. Furthermore, the selected form of the probability

density function proves quite advantageous in determining the statistical moments of the nonstationary response envelope.

Numerical results concerning a Van der Pol oscillator and a Duffing oscillator under Gaussian white noise excitation have demonstrated that the estimates of the nonstationary probability density function and statistical moments of the response envelope provided by the present procedure are in close agreement with Monte Carlo simulation data even when large nonlinearities are involved.

It is noted that the proposed Galerkin approach for determining an approximate expression for the nonstationary probability density of the system response envelope may yield reliable solutions for even stronger degrees of nonlinearity than the ones considered herein, if it is applied to more refined averaging schemes, such as, for instance, the one discussed in [18]. Furthermore, the presented approach should be deemed as supplementary to other more versatile, nevertheless more computationally intensive, purely numerical methods, such as the ones in [23–25]. Finally, it should be mentioned that the concepts of the proposed procedure are also applicable in the framework of alternative stochastic averaging approaches involving the energy envelope (see, e.g., [26,27]).

Acknowledgment

The partial support of this work by a contract from ONR (USA) its gratefully acknowledged.

References

[1] Crandall, S. H., and Mark, W. D., 1963, *Random Vibration in Mechanical Systems*, Academic Press, San Diego, CA.
[2] Lin, Y. K., 1967, *Probabilistic Theory of Structural Dynamics*, McGraw-Hill, New York.
[3] Clough, R. W., and Penzien, J., 1993, Dynamics of Structures, 2nd ed., McGraw-Hill, New York.
[4] Caughey, T. K., 1971, "Nonlinear Theory of Random Vibrations," *Advances in Applied Mechanics*, Vol. 11, C. S. Yih, ed. Academic Press, San Diego, CA, pp. 209–235.
[5] Caughey, T. K., and Dienes, J. K., 1961, "Analysis of a Nonlinear First-Order System With a White Noise Input," J. Appl. Phys., **32**(11), pp. 2476–2479.
[6] Gardiner, C. W., 1983, *Handbook of Stochastic Methods for Physics, Chemistry and the Natural Sciences*, Springer-Velarg, Berlin.
[7] Andronov, A., Pontryagin, L., and Witt, A., 1933, "On the Statistical Investigation of Dynamical Systems," Zh. Eksp. Teor. Fiz., **3**, pp. 165–180 (in Russian).
[8] Kramers, H. A., 1940, "Brownian Motion in a Field of Force and Diffusion Model of Chemical Reactions," Physica (Utrecht), **7**, pp. 284–304.
[9] Caughey, T. K., and Ma, F., 1982, "The Exact Steady-State Solution of a Class of Non-Linear Stochastic Systems," Int. J. Non-Linear Mech., **17**(3), pp. 137–142.
[10] Dimentberg, M. F., 1982, "An Exact Solution to a Certain Non-Linear Random Vibration Problem," Int. J. Non-Linear Mech., **17**(4), pp. 231–236.
[11] Roberts, J. B., and Spanos, P. D., 1986, "Stochastic Averaging: an Approximate Method of Solving Random Vibration Problems," Int. J. Non-Linear Mech., **21**, pp. 111–134.
[12] Stratonovich, R. L., 1986, *Topics in the Theory of Random Noise*, Vols. 1 and 2, Gordon & Breach, New York.
[13] Khasminskii, R. Z., 1966, "A Limit Theorem for Solutions of Differential Equations With Random Right Hand Sides," Theor. Probab. Appl., **11**, pp. 390–405.
[14] Bogoliubov, N., and Mitropolski, A., 1961, *Asymptotic Methods in the Theory of Non-linear Oscillations*, Gordon & Breach, New York.
[15] Iwan, W. D., Spanos, P.-T., 1978, "Response Envelope Statistics for Nonlinear Oscillators with Random Excitation," ASME J. Appl. Mech., **100**(1), pp. 170–174.
[16] Spanos, P.-T. D., 1976, "Linearization Techniques for Non-Linear Dynamical Systems," Report No. EERL 70-04, Earthquake Engineering Research Laboratory, California Institute of Technology, Pasadena, CA.
[17] Spanos, P. D., Cacciola, P., and Muscolino, G., 2004, "Stochastic Averaging of Preisach Hysteretic Systems," J. Eng. Mech. Div., Am. Soc. Civ. Eng., **130**(11), pp. 1257–1267.
[18] Bouc, R., 1994, "The Power Spectral Density of Response for a Strongly Non-Linear Random Oscillator," J. Sound Vib., **175**(3), pp. 317–331.
[19] Spanos, P.-T. D., 1978, "Stochastic Analysis of Oscillators with Non-Linear Damping," Int. J. Non-Linear Mech., **13**, pp. 249–259.
[20] Spanos, P.-T. D., 1981, "A Method for Analysis of Non-Linear Vibrations Caused by Modulated Random Excitation," Int. J. Non-Linear Mech., **16**, pp. 1–11.
[21] Spanos, P.-T. D., and Iwan, W. D., 1978, "Computational Aspects of Random Vibration Analysis," J. Eng. Mech. Div., Am. Soc. Civ. Eng., **104**(EM6), pp. 1043–1415.
[22] Spanos, P.-T. D., 1978, "Non-Stationary Random Vibration of a Linear Structure," Int. J. Solids Struct., **14**, pp. 861–867.
[23] Spencer, Jr. B. F., and Bergman, L. A., 1993, "Numerical Solutions of the Fokker-Planck Equations for Nonlinear Stochastic Systems," Nonlinear Dyn., **4**, pp. 357–372.
[24] Wojtkiewicz, S. F., Johnson, E. A., Bergman, L. A., Grigoriu, M., and Spencer, Jr., B. F., 1999, "Response of Stochastic Dynamical Systems Driven by Additive Gaussian and Poisson White Noises: Solution of a Forward Generalized Kolmogorov Equation by a Spectral Finite Difference Method," Comput. Methods Appl. Mech. Eng., **168**(1–4), pp. 73–89.
[25] Masud, A., and Bergman, L. A., 2005, "Application of Multi-Scale Finite Element Methods to the Solution of the Fokker-Planck Equation," Comput. Methods Appl. Mech. Eng. **194**, pp. 1513–1526.
[26] Zhu, W., and Lin, Y. K., 1991, "Stochastic Averaging of Energy Envelopes," J. Eng. Mech., **117**, pp. 1890–1905.
[27] Krenk, S., and Roberts, J. B., 1999, "Local Similarity in Non-Linear Random Vibration," ASME J. Appl. Mech., **66**, pp. 225–235.

Quasi-Periodic Response Regimes of Linear Oscillator Coupled to Nonlinear Energy Sink Under Periodic Forcing

O. V. Gendelman[1]
e-mail: ovgend@tx.technion.ac.il

Yu. Starosvetsky
e-mail: stryuli@techunix.technion.ac.il

Faculty of Mechanical Engineering,
Technion—Israel Institute of Technology,
Haifa 32000, Israel

Quasi-periodic response of a linear oscillator attached to nonlinear energy sink with relatively small mass under external sinusoidal forcing in a vicinity of main (1:1) resonance is studied analytically and numerically. It is shown that the quasi-periodic response is exhibited in well-defined amplitude-frequency range of the external force. Two qualitatively different regimes of the quasi-periodic response are revealed. The first appears as a result of linear instability of the steady-state regime of the oscillations. The second one occurs due to interaction of the dynamical flow with invariant manifold of damped-forced nonlinear normal mode of the system, resulting in hysteretic motion of the flow in the vicinity of this mode. Parameters of external forcing giving rise to the quasi-periodic response are predicted by means of simplified analytic model. The model also allows predicting that the stable quasi-periodic regimes appear for certain range of damping coefficient. All findings of the simplified analytic model are verified numerically and considerable agreement is observed. [DOI: 10.1115/1.2198546]

1 Introduction

Recently it has been demonstrated that various systems comprised of linear substructures and strongly nonlinear attachments demonstrate localization and irreversible transient transfer (pumping) of energy to prescribed fragments of structure dependent on initial conditions and external forcing [1–3]. Addition of a relatively small and spatially localized attachment leads to essential changes in the properties of the whole system. Unlike common linear and weakly nonlinear systems, systems with strongly nonlinear elements are able to react efficiently on the amplitude characteristics of the external forcing in a wide range of frequencies [4–6]. Thus, the systems under consideration give rise to a new concept of nonlinear energy sink (NES).

It was demonstrated [2,3] that the possibility of the energy pumping phenomenon in nonconservative systems can be understood and explained by studying the energy dependence of the nonlinear undamped free periodic solutions (nonlinear normal modes (NNM)) of the corresponding conservative system which are obtained when all damping forces are eliminated. Recent investigation [7] based on the approach of invariant manifolds [8,9] has introduced an asymptotic procedure suitable for explicit inclusion of damping within the framework of nonlinear normal modes.

Steady-state responses (i.e., the responses with almost constant amplitude) of the primary oscillator with NES attached were studied previously [10] for somewhat different design of the NES than we use. In recent studies, it was demonstrated [11] that in close vicinity of the main resonance the system with NES can exhibit quasi-periodic rather than steady-state response, leading to qualitatively different dynamical behavior. Besides, it was demonstrated that it is possible to use the NES in the quasi-periodic regime as a vibration absorber. Quasi-periodic response regimes in weakly nonlinear vibration absorbers were studied in papers [12–14], but it seems than no such results exist for strongly nonlinear absorbers. Detailed study of such regimes is a primary goal of present paper.

The structure of the paper is as follows. Section 2 is devoted to description and preliminary investigation of the model. In Secs. 3 and 4, two possible mechanisms for the quasi-periodic response are investigated analytically. Section 5 contains numeric verifications of the results, and Sec. 6 offers some concluding remarks and discussion.

2 Description of the Model

Analytic treatment of the model generally follows the procedure developed earlier [7,11] with modifications due to presence of the external forcing. Let us consider the system, which consists of a linear oscillator and small strongly nonlinear attachment (pure cubic nonlinearity) and is forced harmonically. The system is described by the following equations:

$$\ddot{y}_1 + \varepsilon\lambda(\dot{y}_1 - \dot{y}_2) + y_1 + \tfrac{4}{3}\varepsilon(y_1 - y_2)^3 = \varepsilon A \cos t$$

$$\varepsilon\ddot{y}_2 + \varepsilon\lambda(\dot{y}_2 - \dot{y}_1) + \tfrac{4}{3}\varepsilon(y_2 - y_1)^3 = 0 \tag{1}$$

where y_1 and y_2 are the displacements of the linear oscillator and the attachment, respectively, $\varepsilon\lambda$ is the damping coefficient, and εA is the amplitude of external force. For the sake of simplicity, the frequency of the external force is adopted to be exactly equal to linear frequency of the linear oscillator. $\varepsilon \ll 1$ is a small parameter that establishes the order of magnitude for coupling, damping, mass of the nonlinear attachment, and the amplitude of the external forcing; coefficients λ and A are adopted to be of order unity. Rigidity of the nonlinear spring is adopted to be equal to $4\varepsilon/3$ and linear frequency of the linear oscillator, to unity. Both these adoptions do not affect a generality of a treatment below, since they may be changed independently by proper rescaling of the variables.

Mass of the attachment is considered to be small related to the mass of the main oscillator. This condition has obvious motivation

[1]Author to whom correspondence should be addressed.

Contributed by the Applied Mechanics Division of ASME for publication in the JOURNAL OF APPLIED MECHANICS. Manuscript received May 18, 2005; final manuscript received February 9, 2006. Review conducted by N. Sri Namachchivaya. Discussion on the paper should be addressed to the Editor, Prof. Robert M. McMeeking, Journal of Applied Mechanics, Department of Mechanical and Environmental Engineering, University of California—Santa Barbara, Santa Barbara, CA 93106-5070, and will be accepted until four months after final publication of the paper itself in the ASME JOURNAL OF APPLIED MECHANICS.

from the viewpoint of possible applications: NES is designed to have small mass compared to the main system and does not require alternative grounding.

Change of variables

$$v = y_1 + \varepsilon y_2, \quad w = y_1 - y_2 \tag{2}$$

reduces Eqs. (1) to the following form:

$$\ddot{v} + \frac{v}{1+\varepsilon} + \frac{\varepsilon w}{1+\varepsilon} = \varepsilon A \cos t$$

$$\ddot{w} + \frac{v}{1+\varepsilon} + \frac{\varepsilon w}{1+\varepsilon} + (1+\varepsilon)\lambda \dot{w} + \frac{4}{3}(1+\varepsilon)w^3 = \varepsilon A \cos t \tag{3}$$

Complex variables are introduced according to following relationship:

$$\varphi_1 \exp(it) = \dot{v} + iv$$

$$\varphi_2 \exp(it) = \dot{w} + iw \tag{4}$$

With account of this change of variables, Eqs. (3) are rewritten as:

$$\begin{aligned}
&\dot{\varphi}_1 + \frac{i\varepsilon}{2(1+\varepsilon)}[\varphi_1 - \varphi_2 - \varphi_1^* \exp(-2it) + \varphi_2^* \exp(-2it)] \\
&= \frac{\varepsilon A}{2}[1 + \exp(-2it)] \\
&\times \dot{\varphi}_2 + \frac{i}{2(1+\varepsilon)}[\varphi_2 - \varphi_1 - \varphi_2^* \exp(-2it) + \varphi_1^* \exp(-2it)] \\
&+ \frac{\lambda(1+\varepsilon)}{2}[\varphi_2 + \varphi_2^* \exp(-2it)] + \frac{i(1+\varepsilon)}{6} \\
&\times \exp(-it)[\varphi_2 \exp(it) - \varphi_2^* \exp(-it)]^3 = \frac{\varepsilon A}{2}[1 + \exp(-2it)]
\end{aligned} \tag{5}$$

where the asterisk denotes complex conjugation.

The problem under investigation is the response regime of system described by Eqs. (5) in the vicinity of 1:1 resonance. Therefore, it is possible to suggest that the evolution of the modulation variables φ_1 and φ_2 may be considered as slow compared to the fast oscillations of the external force. Thus, the first approximation for the modulation variables may be obtained by averaging Eqs. (5) with respect to this fast time scale. The averaged system is as follows

$$\varphi_1' + \frac{i\varepsilon}{2(1+\varepsilon)}(\varphi_1 - \varphi_2) = \frac{\varepsilon A}{2}$$

$$\varphi_2' + \frac{i}{2(1+\varepsilon)}(\varphi_2 - \varphi_1) + \frac{\lambda(1+\varepsilon)}{2}\varphi_2 - \frac{i(1+\varepsilon)}{2}|\varphi_2|^2\varphi_2 = \frac{\varepsilon A}{2} \tag{6}$$

The differentiation with respect to time is denoted by the prime, to distinguish it formally from the fast time of the original problem. It should be mentioned that the smallness of parameter ε was not used at this stage.

Fixed points of Eqs. (6) correspond to steady-state response regimes of Eqs. (1). The condition for fixed point is written as

$$\frac{i\varepsilon}{2(1+\varepsilon)}(\varphi_{10} - \varphi_{20}) = \frac{\varepsilon A}{2}$$

$$\frac{i}{2(1+\varepsilon)}(\varphi_{20} - \varphi_{10}) + \frac{\lambda(1+\varepsilon)}{2}\varphi_{20} - \frac{i(1+\varepsilon)}{2}|\varphi_{20}|^2\varphi_{20} = \frac{\varepsilon A}{2} \tag{7}$$

where φ_{10} and φ_{20} denote the constant values of the modulation functions at the fixed points. System of equations (7) may be easily solved and yields the following result for the fixed point:

$$\lambda^2 N_0^2 + N_0^6 = A^2, \quad \theta_0 = -\tan^{-1}\frac{N_0^2}{\lambda}$$

$$\varphi_{20} = N_0 \exp(i\theta_0), \quad \varphi_{10} = \varphi_{20} - i(1+\varepsilon)A \tag{8}$$

where N_0 and θ_0 are real vaues. It is easy to see that for any A and λ, Eq. (8) yields exactly one solution for value $Z_0 = N_0^2$.

3 Linear Stability Analysis and Weak Quasi-periodic Regime

The standard approach to exploration of quasi-periodic responses of nonlinear vibration absorbers [13,14] involves the instability of the steady-state response regime. To perform such an investigation, one should linearize modulation equations (6) in the vicinity of the steady-state response and investigate the stability of the fixed point. Let us introduce small perturbations of the fixed point

$$\varphi_1 = \varphi_{10} + \delta_1, \quad \varphi_2 = \varphi_{20} + \delta_2 \tag{9}$$

The system of linearized equations is expressed as

$$\delta_1' + \frac{i\varepsilon}{2(1+\varepsilon)}(\delta_1 - \delta_2) = 0$$

$$\begin{aligned}
&\delta_2' + \frac{i}{2(1+\varepsilon)}(\delta_2 - \delta_1) + \frac{\lambda(1+\varepsilon)}{2}\delta_2 - i(1+\varepsilon)\delta_2|\varphi_{20}|^2 \\
&- \frac{i(1+\varepsilon)}{2}\varphi_{20}^2\delta_2^* = 0
\end{aligned} \tag{10}$$

Because of linearity, it is possible to express the solutions of Eqs. (10) in the following form:

$$\delta_1 = p_+ \exp(\mu t) + p_- \exp(\mu^* t)$$

$$\delta_2 = q_+ \exp(\mu t) + q_- \exp(\mu^* t) \tag{11}$$

Substituting Eqs. (11) into (10) and performing some simple algebraic transformations, one obtains the solvability conditions for exponent μ

$$\begin{aligned}
&\left[\mu + \frac{i\mu}{2\mu(1+\varepsilon) + i\varepsilon} + \frac{\lambda(1+\varepsilon)}{2} - i(1+\varepsilon)|\varphi_{20}|^2\right] \\
&\times\left[\mu - \frac{i\mu}{2\mu(1+\varepsilon) - i\varepsilon} + \frac{\lambda(1+\varepsilon)}{2} + i(1+\varepsilon)|\varphi_{20}|^2\right] \\
&= \frac{1}{4}(1+\varepsilon)^2|\varphi_{20}|^4
\end{aligned} \tag{12}$$

Equation (12) has the fourth degree and is solvable by standard methods. It is even easier to establish the boundary of stability by assuming $\mu = i\Omega$, where Ω is real modulation frequency. The condition of Ω being the real number greatly simplifies the treatment of (12) and yields the following expression for the frequency and the stability boundary:

$$\Omega = \frac{1}{2}\sqrt{\frac{\varepsilon}{1+\varepsilon}}$$

$$[1 - 2(1+\varepsilon)N_0^2]^2 + \lambda^2(1+\varepsilon)^2 - (1+\varepsilon)^2 N_0^4 = 0 \tag{13}$$

N_0 in Eqs. (13) is the solution of Eqs. (8). Therefore, the second equation of (13) constitutes the equation for stability boundary of

the steady-state solution in the space of variables (A,λ,ε). If the steady-state solution loses its stability by this mechanism, then in addition to main harmonic with unit frequency, two additional harmonics appear with frequencies $1+\Omega$ and $1-\Omega$. This response regime is clearly quasi-periodic since 1 and Ω are, generally speaking, incommensurate. Numeric examples of this quasi-periodic regime are presented in Sec. 5. We refer to this regime as weak quasi-periodic, since it emerges due to loss of stability of the periodic steady-state response regime.

4 Invariant Manifolds of Averaged Modulation Equations and Strong Quasi-Periodic Response

The above treatment did not take into account specific asymptotic structure of modulation equations (6). The loss of stability of the steady-state solution described by Eqs. (10) involved equal exponents for variables δ_1 and δ_2 despite strong mass asymmetry of the initial system. The purpose of this section is to demonstrate that the above asymmetry brings about possibility of additional qusiperiodic response regimes not related to perturbation of the steady-state response.

Crude approximation which allows estimating the boundaries for these nontrivial response regimes may be constructed with the help of asymptotic analysis of system (6) with respect to small parameter ε. For this sake, let us consider that typical time scale for the modulation is $O(\varepsilon)$. Therefore, slow time may be introduced as

$$\frac{d}{dt}=\varepsilon\frac{\partial}{\partial\tau} \tag{14}$$

Rescaling of Eqs. (6) with account of (14) yields

$$\frac{\partial\varphi_1}{\partial\tau}+\frac{i}{2(1+\varepsilon)}(\varphi_1-\varphi_2)=\frac{A}{2}$$

$$\varepsilon\frac{\partial\varphi_2}{\partial\tau}+\frac{i}{2(1+\varepsilon)}(\varphi_2-\varphi_1)+\frac{\lambda(1+\varepsilon)}{2}\varphi_2-\frac{i(1+\varepsilon)}{2}|\varphi_2|^2\varphi_2=\frac{\varepsilon A}{2} \tag{15}$$

The system of equations (15) is singular and therefore should be described with the help of both regular and singular asymptotic approaches. The singular asymptotic regime corresponds to fast evolution of variable φ_2 and, in fact, is described by the second equation of system (6) without rescaling; in the lowest approximation of the singular asymptotic regime, variable φ_1 should be considered as constant. Qualitative behavior of the solution may be established with the help of Bendixon criterion [15]. By splitting the last equation of (6) to real and imaginary parts, one gets

$$x'=\frac{1}{2(1+\varepsilon)}y-\frac{\lambda(1+\varepsilon)}{2}x-\frac{1+\varepsilon}{2}y(x^2+y^2)-\frac{1}{2(1+\varepsilon)}\,\mathrm{Im}(\varphi_1)+\frac{\varepsilon A}{2}=P(x,y)$$

$$y'=-\frac{1}{2(1+\varepsilon)}x-\frac{\lambda(1+\varepsilon)}{2}y+\frac{1+\varepsilon}{2}x(x^2+y^2)+\frac{1}{2(1+\varepsilon)}\,\mathrm{Re}(\varphi_1)=Q(x,y)$$

$$x=\mathrm{Re}(\varphi_2),\quad y=\mathrm{Im}(\varphi_2) \tag{16}$$

One obtains $\partial P/\partial x+\partial Q/\partial y=-\lambda(1+\varepsilon)<0$ for any values of x and y. The Bendixon criterion leads to the conclusion that the asymptotic solutions related to the singular regime must end (or begin) at fixed points of the equation and cannot be periodic. Consequently, in the singular regime variable φ_2 rapidly evolutes toward the equilibrium value Φ defined as follows:

$$\frac{i}{2(1+\varepsilon)}(\Phi-\varphi_1)+\frac{\lambda(1+\varepsilon)}{2}\Phi-\frac{i(1+\varepsilon)}{2}|\Phi|^2\Phi=\frac{\varepsilon A}{2} \tag{17}$$

provided that the limit manifold is stable. In fact, the limit manifold (Φ,Φ^*) constitutes the limit invariant manifold of system (15) [7].

The regular asymptotic regime of Eqs. (15) is thus related to evolution of variables Φ and φ_1 (or, equivalently, evolution of the invariant manifold descried above) with respect to slow time τ. To get explicit expression, one substitutes Eq. (17) to the first equation of system (15) and gets

$$\frac{\partial\Phi}{\partial\tau}[1-i\lambda(1+\varepsilon)^2-2(1+\varepsilon)^2|\Phi|^2]-\frac{\partial\Phi^*}{\partial\tau}(1+\varepsilon)^2\Phi^2=\frac{i(1+\varepsilon)}{2}\Phi|\Phi|^2+\frac{(1+\varepsilon)}{2}A-\frac{\lambda(1+\varepsilon)}{2}\Phi \tag{18}$$

By splitting modulus and argument of function $\Phi(\tau)=P(\tau)\exp[i\chi(\tau)]$ where P and χ are real functions, after simple but lengthy algebraic calculations one gets

$$\frac{\partial P}{\partial\tau}=-\frac{\nu}{2D}[A(2\nu^2P^2\cos\chi-\nu P^2\cos\chi-\cos\chi-\nu^2\lambda\sin\chi)+\lambda P+\nu\lambda P^3-\nu^2\lambda P^3]$$

$$P\frac{\partial\chi}{\partial\tau}=-\frac{\nu}{2D}[A(\sin\chi-\nu P^2\sin\chi-2\nu^2P^2\sin\chi-\nu^2\lambda\cos\chi)+\nu^2\lambda^2P+\nu P^5+2\nu^2P^5-P^3]$$

$$\nu=1+\varepsilon$$

$$D=1+\lambda^2\nu^2-4\nu^2P^2+3\nu^4P^4 \tag{19}$$

Equations for fixed points (χ_0,P_0) of system (19) are written as

$$A(2\nu^2P_0^2\cos\chi_0-\nu P_0^2\cos\chi_0-\cos\chi_0-\nu^2\lambda\sin\chi_0)=-\lambda P_0-\nu\lambda P_0^3+\nu^2\lambda P_0^3$$

$$A(\sin\chi_0-\nu P_0^2\sin\chi_0-2\nu^2P_0^2\sin\chi_0-\nu^2\lambda\cos\chi_0)=-\nu^2\lambda^2P_0-\nu P_0^5-2\nu^2P_0^5+P_0^3 \tag{20}$$

System (20) has two families of solutions. The first one is described by the following expressions:

$$P_0^2(P_0^4+\lambda^2)=A^2$$

$$\tan\chi_0=\frac{P_0^2}{\lambda} \tag{21}$$

In fact, this solution coincides with steady-state regime described by (8) and does not require any additional investigation. The second family of two possible solutions is described by the expressions:

$$P_{01,2}=\sqrt{\frac{2\nu\mp\sqrt{1+\lambda^2\nu^4-4\lambda^2\nu^6}}{\nu(4\nu^2-1)}}$$

$$\cos(\chi_{01,2}+\sigma_{1,2})=-\frac{1}{A}\frac{\lambda P_{01,2}+\nu\lambda P_{01,2}^3-\nu^2\lambda P_{01,2}^3}{\sqrt{\lambda^2\nu^4+(1+\nu P_{01,2}^2-2\nu^2P_{01,2}^2)^2}}$$

$$\sigma_{1,2}=-\tan^{-1}\frac{\lambda\nu^2}{1+\nu P_{01,2}^2-2\nu^2P_{01,2}^2} \tag{22}$$

Families of solutions (22) exist if the expressions at the right-hand side of cosine have modulus less than unity. Only the value -1 or limit value of the cosine function is considered; switch to 1 amounts to insufficient change of sign for A. Consequently, there

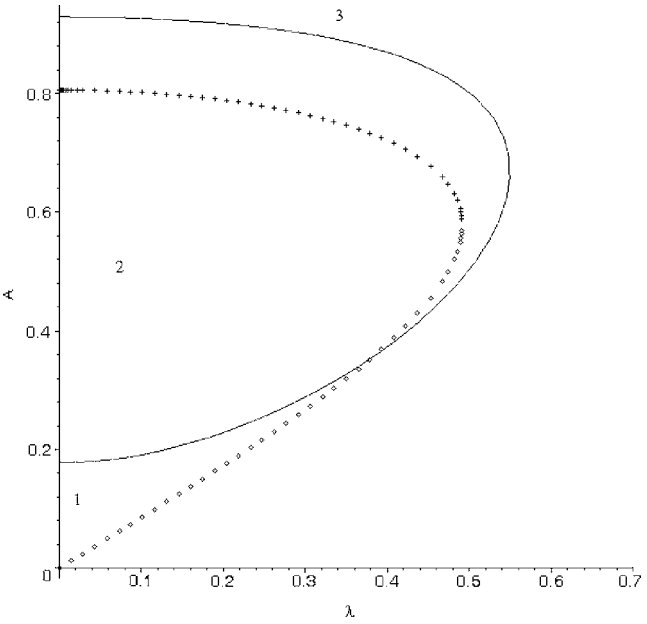

Fig. 1 Zones for weakly and strongly quasi-periodic responses at the plane of parameters. Weakly quasi-periodic responses can exist within the red boundary (Eq. (13)), family (23) of the strongly quasi-periodic attractors exists above blue curve, family (24)—above green curve.

are two boundaries for two families of the solutions in the space of parameters (A,λ,ε). The boundary for the first family of solutions is expressed as

$$\frac{1}{A}\frac{\lambda P_{01}+\nu\lambda P_{01}^3-\nu^2\lambda P_{01}^3}{\sqrt{\lambda^2\nu^4+(1+\nu P_{01}^2-2\nu^2 P_{01}^2)^2}}=1$$

$$P_{01}=\sqrt{\frac{2\nu-\sqrt{1+\lambda^2\nu^4-4\lambda^2\nu^6}}{\nu(4\nu^2-1)}} \tag{23}$$

Similarly, the boundary for the second family of solutions is expressed as

$$\frac{1}{A}\frac{\lambda P_{02}+\nu\lambda P_{02}^3-\nu^2\lambda P_{02}^3}{\sqrt{\lambda^2\nu^4+(1+\nu P_{02}^2-2\nu^2 P_{02}^2)^2}}=1$$

$$P_{02}=\sqrt{\frac{2\nu+\sqrt{1+\lambda^2\nu^4-4\lambda^2\nu^6}}{\nu(4\nu^2-1)}} \tag{24}$$

It is possible to conclude that saddle-node bifurcation occurs at each of two boundaries, described by Eqs. (23) and (24), resulting in appearance of an attractor-repeller pair at the invariant manifold. Presence of additional attractors at the invariant manifold provides the possibility for nontrivial quasi-periodic response regimes, not related to the loss of stability of the steady-state response regime. It is worthwhile to mention that the characteristic modulation frequency of the weakly quasi-periodic response is of order $\varepsilon^{1/2}$; the above consideration demonstrates that for the regimes related to families of attractors at the invariant manifold, the modulation frequency should be of order ε. The latter response regime is referred to as strongly quasi-periodic one.

5 Numeric Verification

For the sake of numeric simulation, the value $\varepsilon=0.05$ has been chosen. For given value of ε, the boundaries for weakly and strongly quasi-periodic regimes may be presented at the plane of parameters (λ,A). Boundary for weakly quasi-periodic regime in accordance with Eq. (13) and boundaries for strongly quasi-periodic response in accordance with Eqs. (23) and (24) are presented at Fig. 1.

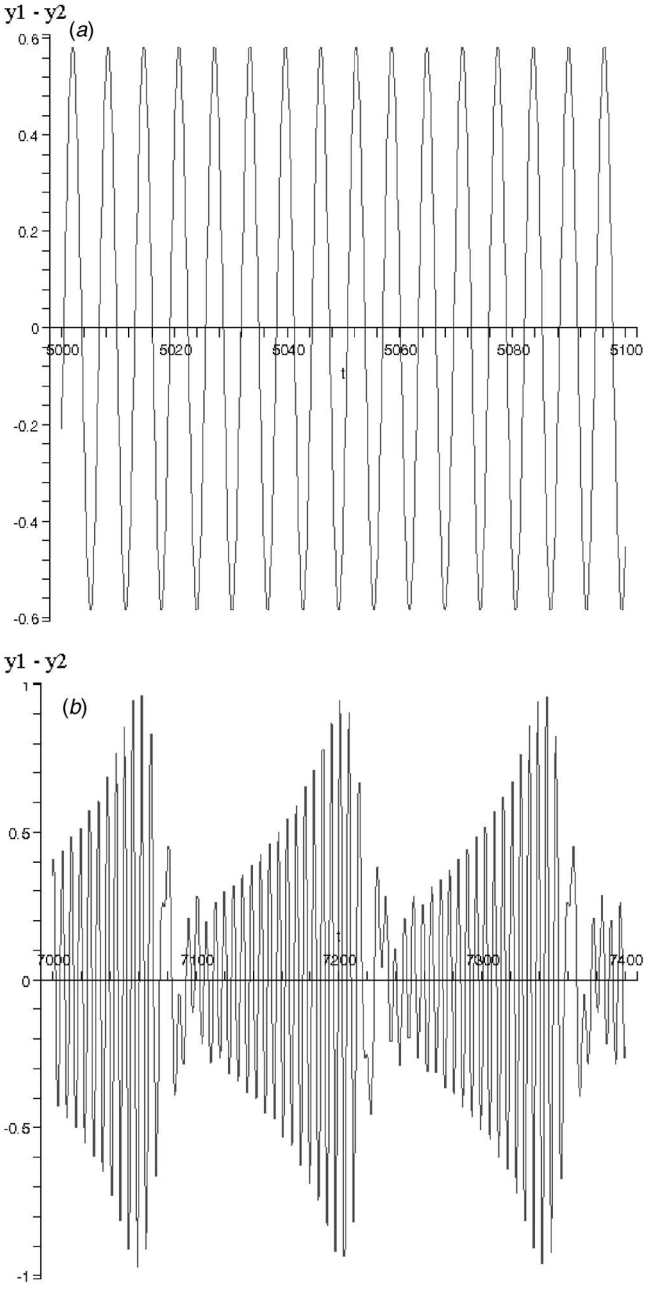

Fig. 2 (*a*) Steady-state response of system (1) for $A=0.225$, $\lambda=0.2$, and $\varepsilon=0.05$. Initial conditions are $y_1(0)=0.29$, $dy_1/dt(0)=0.25$, $y_2(0)=0$, and $dy_2/dt(0)=-0.15$, and (*b*). Strongly quasi-periodic response of system (1) for $A=0.225$, $\lambda=0.2$, and $\varepsilon=0.05$. Initial conditions are $y_1(0)=0$, $dy_1/dt(0)=0$, $y_2(0)=0$, and $dy_2/dt(0)=0$.

To verify the above conclusions numerically, we choose three points within three different zones at the plane of parameters. The value of the damping coefficient is adopted to be $\lambda=0.2$ and the amplitude of the external forcing A is modified.

For the point in zone 1, one expects both stable steady-state response and possibility of strongly quasi-periodic response for different initial conditions. Value $A=0.225$ is chosen. At Figs. 2(*a*) and 2(*b*), the results of appropriate numeric simulations are pre-

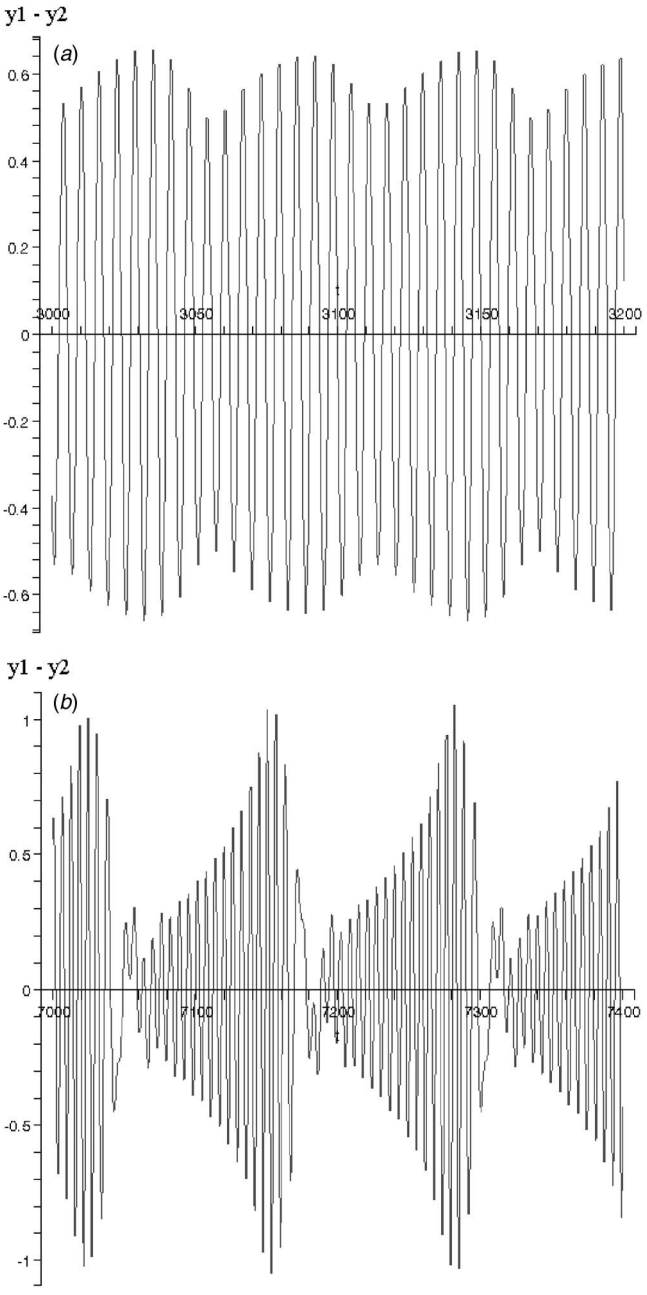

Fig. 3 (*a*) **weakly quasi-periodic response of system** (1) **for** $A=0.24$, $\lambda=0.2$, **and** $\varepsilon=0.05$. **Initial conditions are** $y_1(0)=0.29$, $dy_1/dt(0)=0.25$, $y_2(0)=0$, **and** $dy_2/dt(0)=-0.15$, **and** (*b*) **strongly quasi-periodic response of system** (1) **for** $A=0.24$, $\lambda=0.2$, $\varepsilon=0.05$. **Initial conditions are** $y_1(0)=0$, $dy_1/dt(0)=0$, $y_2(0)=0$, **and** $dy_2/dt(0)=0$.

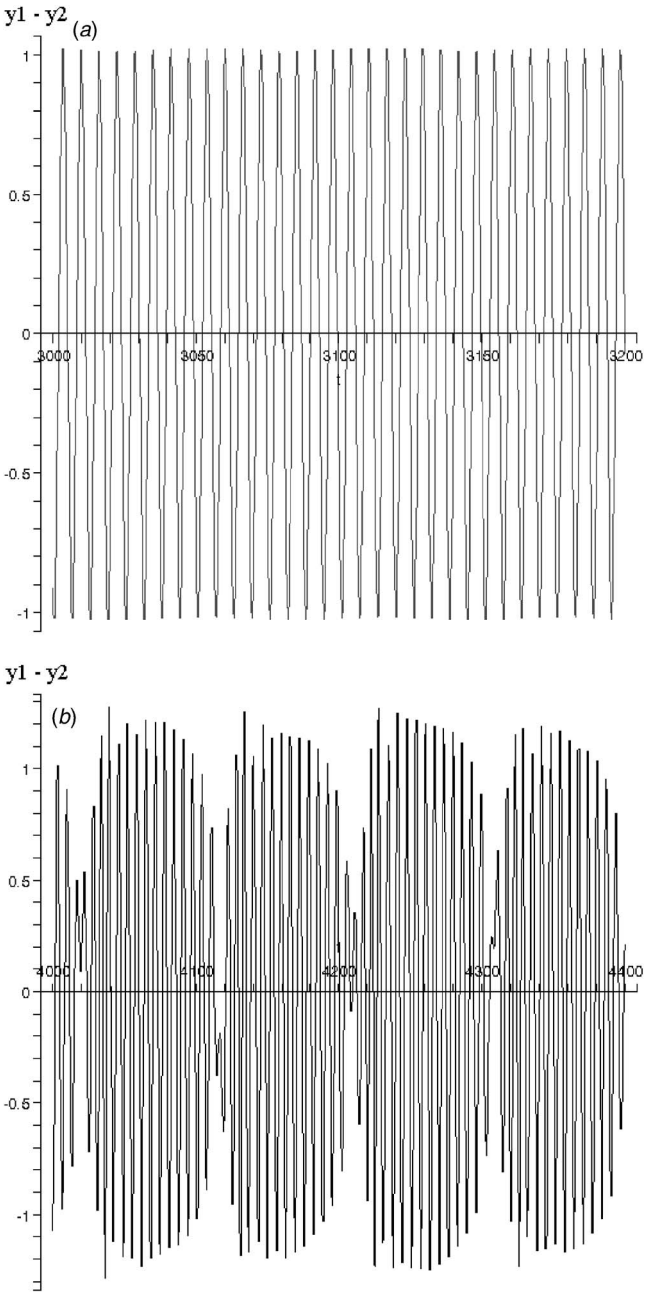

Fig. 4 (*a*) **Steady-state response of system** (1) **for** $A=1$, $\lambda=0.2$, **and** $\varepsilon=0.05$. **Initial conditions are** $y_1(0)=-0.052$, $dy_1/dt(0)=0.187$, $y_2(0)=-1$, $dy_2/dt(0)=0$, **and** (*b*) **strongly quasi-periodic response of system** (1) **for** $A=1$, $\lambda=0.2$, **and** $\varepsilon=0.05$. **Initial conditions are** $y_1(0)=0$, $dy_1/dt(0)=0$, $y_2(0)=0$, **and** $dy_2/dt(0)=0$.

sented for initial system (1) for the internal displacement of the attachment y_1-y_2 versus time t.

For the point from zone 2 at Fig. 1 both weakly and strongly quasi-periodic regimes are expected to be possible. $A=0.24$ is chosen and the results of numeric simulations are presented at Figs. 3(*a*) and 3(*b*).

For the point in zone 3 both stable steady-state and strongly quasi-periodic response are expected. Still, the strongly quasi-periodic response will be related to family of attractors different from one for regimes at Figs. 2(*b*) and 3(*b*), since this point is above the green line at Fig. 1. Therefore, the shape of the strongly quasi-periodic response in this case will be rather different from those at Figs. 2(*b*) and 3(*b*). Appropriate simulation results are presented at Figs. 4(*a*) and 4(*b*).

The response curves presented above support the findings concerning two possible scenarios of quasi-periodic response. Still, in order to get deeper understanding of the structure of the response, Fourier spectra of three out of six response curves presented above were analyzed.

Figure 5 demonstrates a fast Fourier transform (FFT) of the steady response presented at Fig. 4(*a*).

The response has one very strong central peak at unit frequency.

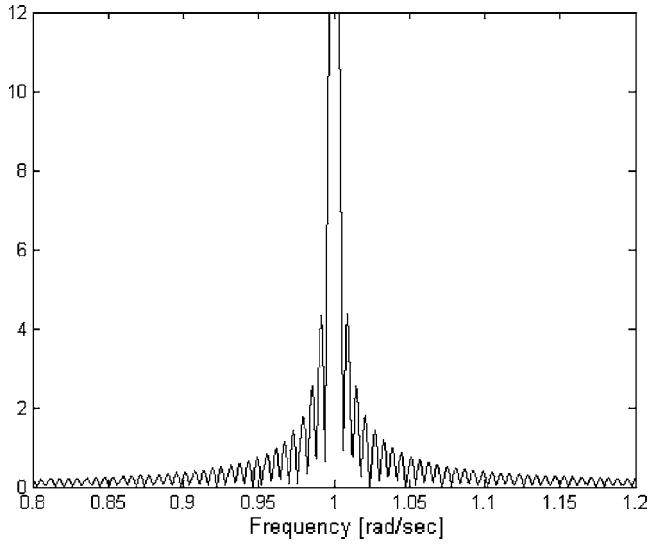

Fig. 5 Fast Fourier transform of the response for parameter values $A=1$, $\lambda=0.2$, and $\varepsilon=0.05$. Initial conditions are $y_1(0)=-0.052$, $dy_1/dt(0)=0.187$, $y_2(0)=-1$, and $dy_2/dt(0)=0$.

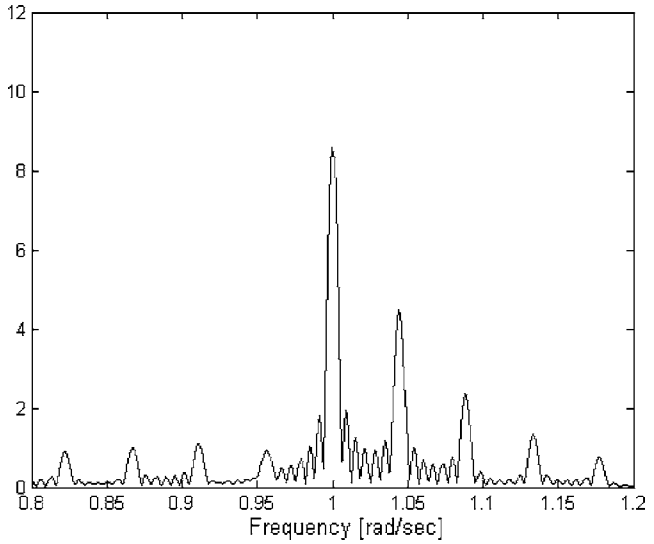

Fig. 7 Fast Fourier transform of the response for parameter values $A=0.24$, $\lambda=0.2$, and $\varepsilon=0.05$. Initial conditions are $y_1(0)=0$, $dy_1/dt(0)=0$, $y_2(0)=0$, and $dy_2/dt(0)=0$.

All other minor peaks are related to the finite size of the sample used for FFT. Such structure of the spectrum is consistent with steady character of the response.

FFT for weakly quasi-periodic response is presented at Fig. 6. The parameters and initial conditions (IC) are chosen to be the same as for the simulation presented at Fig. 3(*a*).

In addition to the central peak at unit frequency, two new peaks appear at frequencies equal to 0.89 and 1.11, shifted by ±0.11 with respect to the central peak. These additional peaks are related to the modulation of the response. The modulation frequency for $\varepsilon=0.05$ in accordance with Eq. (13) is $\Omega=0.109$. Accordingly, the prediction of the theory is in excellent agreement with the simulation results.

FFT for the case of strongly quasi-periodic response is presented at Fig. 7. The parameters and IC were chosen to be equal to those used for simulation at Fig. 3(*b*).

In addition to the central peak, a periodic structure of smaller peaks appears. The distance between neighboring small peaks is ~0.045. This value represents the characteristic frequency of the modulation; as suggested by the theoretical analysis, it is of order ε. Multiplicity of the peaks is related to strongly anharmonic shape of the modulation function in the case of a strongly quasi-periodic response.

The last test for verification of the approach developed above is to compare the shape of the modulation function computed in accordance with Eqs. (19) to the result of direct numeric simulation of system (1). Such a comparison is presented at Fig. 8.

It is clear from Fig. 8 that Eq. (19) predicts the shape of the modulation function with rather good accuracy up to the value $y_1-y_2=0.55$, which corresponds to the singularity P_{01}. Obviously, if the singularity of the invariant manifold is approached, the approximation (17) and (18) is no longer valid and an alternative analytic approach is required.

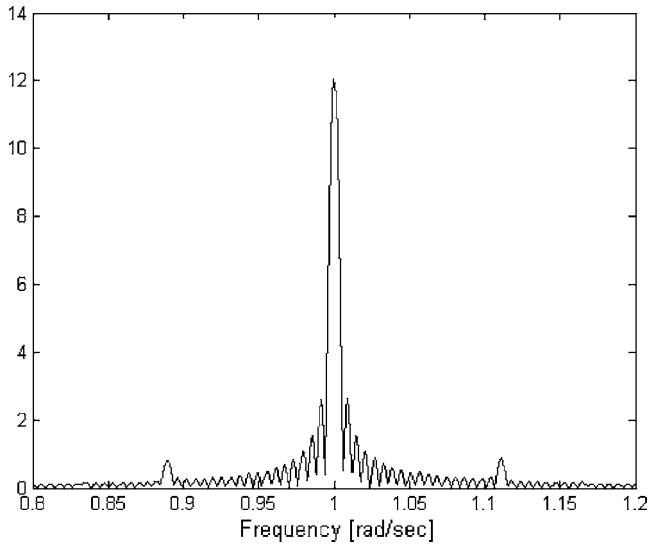

Fig. 6 Fast Fourier transform of the response for parameter values $A=0.24$, $\lambda=0.2$, and $\varepsilon=0.05$. Initial conditions are $y_1(0)=0.29$, $dy_1/dt(0)=0.25$, $y_2(0)=0$, and $dy_2/dt(0)=-0.15$.

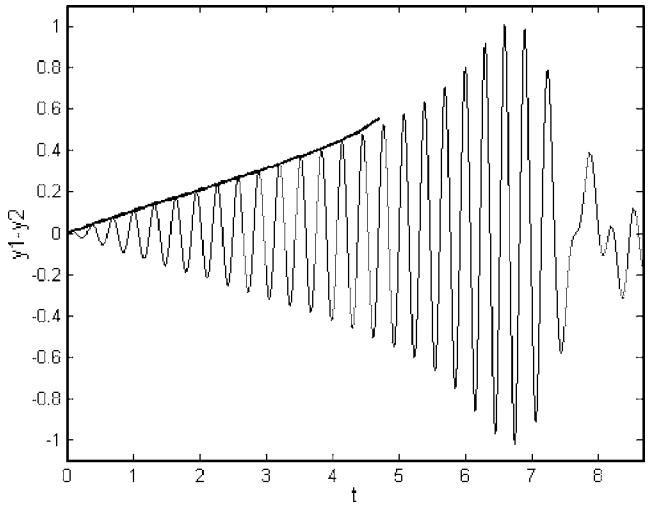

Fig. 8 Direct numeric simulation of system (1) for $A=0.225$, $\lambda=0.2$, and $\varepsilon=0.05$ (thin line) and modulation shape obtained from solution of Eq. (19) (thick line). The time scale is shifted to zero and scaled by factor ε.

6 Concluding Remarks and Discussion

The results presented above demonstrate that the quasi-periodic response regimes are very typical for a periodically forced linear oscillator with the NES attached. It is possible to distinguish two qualitatively different types of such responses. The first is similar to one revealed in weakly nonlinear vibration absorbers and is related to instability of the steady-state response regime. This regime has a typical modulation frequency of order $\varepsilon^{1/2}$. The other possible quasi-periodic response regime is related to the formation of additional attractors at invariant manifolds of the averaged system and has the modulation frequency of order ε. This mechanism is similar to well-known relaxation oscillations in multiple-branch systems. It seems that no such mechanism has been revealed to date in weakly nonlinear vibration absorbers. Approximate analytic models demonstrate good coincidence with numeric findings.

It was also revealed that stable response regimes of different types may coexist for the same parameters of the system under different initial conditions. The latter observation poses essential problem of the domains of attraction for different quasi-periodic response regimes. This issue may be crucial for possible use of the NES as vibration absorber.

Acknowledgment

The authors are grateful to Israel Science Foundation (Grant No. 486/05) for the financial support.

References

[1] Gendelman, O. V., 2001, "Transition of Energy to Nonlinear Localized Mode in Highly Asymmetric System of Nonlinear Oscillators," Nonlinear Dyn., **25**, pp. 237–253.

[2] Gendelman, O. V., Vakakis, A. F., Manevitch, L. I., and McCloskey, R., 2001, "Energy Pumping in Nonlinear Mechanical Oscillators. I: Dynamics of the Underlying Hamiltonian System," ASME J. Appl. Mech., **68**(1), pp. 34–41.

[3] Vakakis, A. F., and Gendelman, O. V., 2001, "Energy Pumping in Nonlinear Mechanical Oscillators. II: Resonance Capture," ASME J. Appl. Mech., **68**(1), pp. 42–48.

[4] Vakakis, A. F., 2001, "Inducing Passive Nonlinear Energy Sinks in Linear Vibrating Systems," ASME J. Vibr. Acoust., **123**(3), pp. 324–332.

[5] Vakakis, A. F., Manevitch, L. I., Gendelman, O., and Bergman, L., 2003, "Dynamics of Linear Discrete Systems Connected to Local Essentially Nonlinear Attachments," J. Sound Vib., **264**, pp. 559–577.

[6] Georgiadis, F., Vakakis, A. F., McFarland, M., and Bergman, L., 2003, "Shock Isolation Through Passive Energy Pumping in a System With Piecewise Linear Stiffnesses," *Proceedings of DETC.03 ASME Design Engineering Technical Conferences and Computers and Information in Engineering Conference*, Chicago, September 2–6, ASME, New York, ASME Paper No. VIB-48490, CD-ROM.

[7] Gendelman, O. V., 2004, "Bifurcations of Nonlinear Normal Modes of Linear Oscillator With Strongly Nonlinear Damped Attachment," Nonlinear Dyn., **37**(2), pp. 115–128.

[8] Shaw, S. W., and Pierre, C., 1993, "Normal Modes for Nonlinear Vibratory Systems," J. Sound Vib., **164**, pp. 85–124.

[9] Vakakis, A. F., Manevitch, L. I., Mikhlin, Yu. V., Pilipchuk, V. N., and Zevin, A. A., 1996, *Normal Modes and Localization in Nonlinear Systems*, Wiley, New York.

[10] Jang, X., McFarland, M., Bergman, L. A., and Vakakis, A. F., 2003, "Steady State Passive Nonlinear Energy Pumping in Coupled Oscillators: Theoretical and Experimental Results," Nonlinear Dyn., **33**, pp. 7–102.

[11] Gendelman, O. V., Gourdon, E., and Lamarque, C. H., 2005, "Quasi-periodic Energy Pumping in Coupled Oscillators Under Periodic Forcing," J. Sound Vib., (in press).

[12] Shaw, J., Shaw, S. W., and Haddow, A. G., 1989, "On the Response of the Nonlinear Vibration Absorber," Int. J. Non-Linear Mech., **24**, pp. 281–293.

[13] Natsiavas, S., 1992, "Steady State Oscillations and Stability of Non-Linear Dynamic Vibration Absorbers," J. Sound Vib., **156**(2), pp. 227–245.

[14] Rice, H. J., and McCraith, J. R., 1987, "Practical Non-Linear Vibration Absorber Design," J. Sound Vib., **116**(3), pp. 545–559.

[15] Jackson, E. A., 1994, *Perspectives of Nonlinear Dynamics*, Vol. 1, Cambridge University Press, Cambridge, UK.

Mechanical Steering Compensators for High-Performance Motorcycles

Simos Evangelou
e-mail: s.evangelou@imperial.ac.uk

David J. N. Limebeer[1]
e-mail: d.limebeer@imperial.ac.uk

Robin S. Sharp
e-mail: robin.sharp@imperial.ac.uk

Department of Electrical and Electronic Engineering,
Imperial College London,
London SW7 2AZ, UK

Malcolm C. Smith
Department of Engineering,
University of Cambridge,
Cambridge CB2 1PZ, UK
e-mail: mcs@eng.cam.ac.uk

This paper introduces the idea of using mechanical steering compensators to improve the dynamic behavior of high-performance motorcycles. These compensators are seen as possible replacements for a conventional steering damper and comprise networks of springs, dampers, and a less familiar component called the inerter. The inerter was recently introduced to allow the synthesis of arbitrary passive mechanical impedances, and finds a potential application in the present work. The design and synthesis of these compensation systems make use of the analogy between passive electrical and mechanical networks. This analogy is reviewed alongside the links between passivity, positive reality, and network synthesis. Compensator design methods that are based on classical Bode-Nyquist frequency-response ideas are presented. Initial designs are subsequently optimized using a sequential quadratic programing algorithm. This optimization process ensures improved performance over the machine's entire operating regime. The investigation is developed from an analysis of specific mechanical networks to the class of all biquadratic positive real functions. This aspect of the research is directed to answering the question: "What is the best possible system performance achievable using any simple passive mechanical network compensator?" The study makes use of computer simulations, which exploit a state-of-the-art motorcycle model whose parameter set is based on a Suzuki GSX-R1000 sports machine. The results show that, compared to a conventional steering damper, it is possible to obtain significant improvements in the dynamic properties of the primary oscillatory modes, known as "wobble" and "weave."
[DOI: 10.1115/1.2198547]

1 Introduction

The dynamics of motorcycles and their possible modes of instability have been studied for decades. In the case that one or more of these modes is stable, but lightly damped, the potential exists for undesirable responses to uneven road surfaces. Early research on motorcycle dynamics was confined to the relatively simple case of small perturbations from straight running [1–3]. In later work, models were extended to include small perturbations from a steady-state cornering condition [4–9]. It is clear from these studies that under certain operating conditions some of the machine's modes can be lightly damped, or even unstable. It is also clear that the lightly damped modes can be excited by road undulations [10]. Reference [10] refers to several real-life incidents in which resonant-forcing-type phenomena ended unhappily for the rider. In addition to this theoretical work, motorcycle oscillations have been widely studied via measurement programs [11–25].

The main lateral oscillations in two-wheeled vehicles are "wobble" and "weave." In straight running, the weave mode is well damped at moderate speeds, but becomes less so as the machine's forward speed increases. The natural frequency rises from zero at very low speed to somewhere in the range 2–4 Hz, depending on the mass and size of the machine, the lower frequencies corresponding to heavier motorcycles. The only properly documented wobble oscillations involve moderate speeds, although there are many anecdotal accounts of wobble at high speeds [26]. Theoretical results indicate that the torsional stiffness of the motorcycle frame at the steering head determines whether a machine will be prone to wobbling at medium speeds (compliant frame) or at high speeds (stiff frame) [27,28]. The frequency of the wobble mode is relatively independent of speed and is governed primarily by the mechanical trail, the front tire cornering stiffness and the front frame steer inertia. The wobble mode's frequency is normally in the range 6–9 Hz. Stiff framed machines, being prone to wobbling at high speed, often depend on a steering damper for satisfactory wobble-mode damping. Normally, however, a steering damper will destabilize the high-speed weave mode. In cornering, the above lateral modes and the in-plane modes associated with tire deflections and suspension motions become coupled, as was first shown in any detail by Koenen [4]. The motorcycle becomes prone to resonant forcing via regular road undulations when the displacement forcing they produce is tuned to lightly damped modal frequencies of the machine. Moderate roll angles are likely to represent the worst-case conditions [10].

The free steering system of a single-track vehicle is essential to its stability and control behavior [7]. It enables the machine to self-steer, to some extent, and it allows the rider to operate in free control, or provide a steering torque input for directional control purposes. Modifications to the machine in the steering head region that impact the steering geometry, the frame compliance, and the steering damping are particularly influential. The question naturally arises: "are there better ways of influencing the self-steering action than through the use of conventional steering dampers?" One approach to the problem posed by this question is described in [29], where an adaptive damper is considered as a means of alleviating a wobble-related phenomenon known as "kickback." Kickback is a sharp change is steering angle that results from high-speed running over rough surfaces. An interesting feature of this work is the preservation of the low-speed light handling of the

[1]Author to whom correspondence should be addressed.

Contributed by the Applied Mechanics Division of ASME for publication in the JOURNAL OF APPLIED MECHANICS. Manuscript received November 4, 2004; final manuscript received March 1, 2006. Review conducted by O. M. O'Reilly. Discussion on the paper should be addressed to the Editor, Prof. Robert M. McMeeking, Journal of Applied Mechanics, Department of Mechanical and Environmental Engineering, University of California – Santa Barbara, Santa Barbara, CA 93106-5070, and will be accepted until four months after final publication of the paper itself in the ASME JOURNAL OF APPLIED MECHANICS.

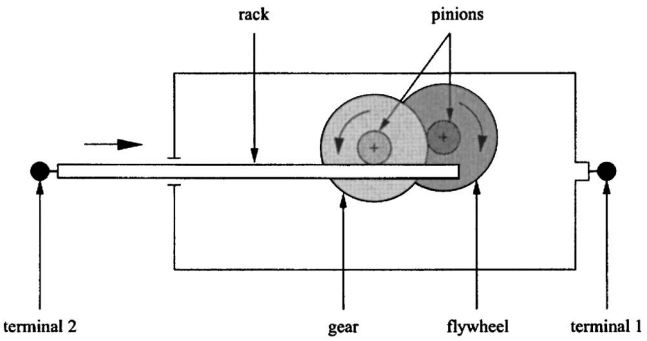

Fig. 1 Schematic of an inerter embodiment

Mechanical	Electrical
$Y(s)=\frac{k}{s}$ $\frac{dF}{dt}=k(v_2-v_1)$ spring	$Y(s)=\frac{1}{Ls}$ $\frac{di}{dt}=\frac{1}{L}(v_2-v_1)$ inductor
$Y(s)=bs$ $F=b\frac{d(v_2-v_1)}{dt}$ inerter	$Y(s)=Cs$ $i=C\frac{d(v_2-v_1)}{dt}$ capacitor
$Y(s)=c$ $F=c(v_2-v_1)$ damper	$Y(s)=\frac{1}{R}$ $i=\frac{1}{R}(v_2-v_1)$ resistor

Fig. 2 Circuit symbols and electromechanical correspondences with defining equations and admittances $Y(s)$

machine. The simultaneous suppression of kickback and low-speed maneuverability preservation led to the speed- and acceleration-based adaptive damping scheme described. The purpose of the present paper is to introduce a phase-compensation-based approach to the design question posed earlier in the paragraph. This compensation is achieved using passive mechanical networks consisting of springs, dampers, and inerters.

The paper is organized as follows. Section 2 reviews the nature and properties of the inerter, which is still a relatively unfamiliar mechanical component. Some of the basic elements of electrical-mechanical circuit analogies, passive network synthesis, and positive reality are briefly reviewed. In Sec. 3, the background to the motorcycle model is described. Some of the important characteristics of the reference motorcycle-rider system are described in Sec. 4. Frequency-response-based design procedures for simple mechanical networks are given in Sec. 5. A procedure for optimizing the parameter values of arbitrary passive steering compensators is given in Sec. 6. Both time- and frequency-domain approaches to parameter optimization are studied. The influence and performance of the base motorcycle fitted with various steering compensators are evaluated in Sec. 7. Conclusions are drawn in Sec. 8.

2 Network Synthesis

2.1 The Inerter. A two-terminal mechanical element called the inerter was introduced in [30] with the property that the (equal and opposite) force applied at the terminals is proportional to the relative acceleration between them. The inerter obeys the force-velocity law $F=b(\dot{v}_1-\dot{v}_2)$, where the constant of proportionality b is called the inertance and has the units of kilograms. In order to be practically useful, the device should have a small mass (relative to b) and its inertance should be adjustable independently of the mass. Also, the device should function properly in any spatial orientation, it should support adequate linear travel and should have reasonable overall dimensions. One way in which such a device can be made with the required properties is illustrated in Fig. 1. It comprises a plunger that is constrained to translate relative to a housing, which then drives a flywheel via a rack and pinion, and gears. For such devices, the value of the inertance b is easy to compute in terms of the various gear ratios and the flywheel's moment of inertia [30]. In general, if the device gives rise to a flywheel rotation of α radians per meter of relative displacement between the terminals, then the inertance of the device is given by $b=J\alpha^2$ where J is the flywheel's moment of inertia. Various embodiments of inerters are described in [31], and several prototype devices have been built and tested in the Engineering Department at Cambridge University.

A rotational version of the inerter can also be defined, namely, a device where the (equal and opposite) torque applied at each terminal (which can be separately rotated) is proportional to the relative angular acceleration between the terminals. The inertance of such a device is measured in kilogram meter squared. Embodiments in pure rotational form can be devised, by making use of epicyclic gears, for example [31]. For an ideal device of this type in which there is a gear ratio of n between rotations of the terminals and rotations of a flywheel with moment of inertia J, the inertance is given by Jn^2.

2.2 Passive Circuit Synthesis. One of the principal motivations for the introduction of the inerter in [30] was the synthesis of passive mechanical networks. It was pointed out that the standard form of the electrical-mechanical analogy (in which the spring, mass, and damper are analogous to the inductor, capacitor, and resistor) was restrictive for this purpose, because the mass element effectively has one terminal connected to ground. In order that the full power of electrical circuit synthesis theory be translated over to mechanical networks, it is necessary to replace the mass element by a genuine two-terminal element—the inerter. Figure 2 shows the new table of element correspondences in the force-current analogy where force and current are the "through" variables, and velocity and voltage are the "across" variables. The admittance $Y(s)$ is the ratio of through to across quantities, where s is the standard Laplace transform variable. For mechanical networks in rotational form, the through and across variables are torque and angular velocity, respectively. For further background on network analogies, the reader is referred to [32].

The theory of passive circuits has been widely studied in the electrical engineering literature [33,34]. The concept of passivity can be translated over directly to mechanical networks as follows. Suppose that (F,v) represents the force-velocity pair associated with a two-terminal mechanical network, then passivity requires

$$E(T)=\int_{-\infty}^{T}F(t)v(t)dt\geq 0 \tag{1}$$

for all admissible force-velocity pairs. The integral in (1) represents the energy supplied to the mechanical network. An important class of (rational) functions that relate to passivity are the positive real functions.

The following theorem is taken from [33,34]; see, for example, page 96 of [34].

THEOREM 1. *Let $Z(s)$ be the real rational immittance[2] function of a linear time-invariant two-terminal network. Then the network is passive if and only if*

1. *$Z(s)$ has no pole in $Re(s)>0$;*
2. *$Re[Z(j\omega)]\geq 0$ for all real ω, in the case that $j\omega$ is not a pole of $Z(s)$;*
3. *If $j\omega_0$ is a pole of $Z(s)$, it is at most a simple pole, and the residue $Z_{j\omega_0}=\lim_{s\to j\omega_0}(s-j\omega_0)Z(s)$ in the case that ω_0 is fi-*

[2]The immittance function of a network refers to either its impedance or admittance function.

nite, and $Z_\infty = \lim_{s\to\infty} Z(s)/s$ *in the case that* $Z(s)$ *has a pole at infinity, is non-negative.*

Real rational functions satisfying the above conditions are termed *positive real*. If $Z(s)$ is positive real, there exists a two-terminal mechanical network whose impedance equals $Z(s)$, which consists of a finite interconnection of springs, dampers, and inerters [30].

The work presented here will make use of a characterization of biquadratic positive-real functions. This result is often quoted without proof in the electrical circuit literature (e.g., [35], problem 4-18, and [36]). A full proof of necessity and sufficiency is provided in the Appendix.

THEOREM 2. *Consider the biquadratic real rational function*

$$Z(s) = \frac{a_2 s^2 + a_1 s + a_0}{d_2 s^2 + d_1 s + d_0}$$

where $a_2, a_1, a_0, d_2, d_1, d_0$ *are all non-negative and at least one of* d_0, d_1, d_2 *is positive. Then* $Z(s)$ *is positive real if and only if*

$$a_1 d_1 \geqslant (\sqrt{a_0 d_2} - \sqrt{d_0 a_2})^2$$

2.3 Applications. Various inerter-based mechanical network applications are outlined in [30]. These include (i) the simulation of a mass element without the need for a large mass, (ii) an alternative solution to vibration absorption problems, but without the requirement to mount additional mass-spring elements on the main body, and (iii) a new element in road vehicle suspension systems. In traditional four-wheeled vehicle suspension problems, the suspension system makes use of springs and dampers to connect together the sprung and unsprung masses. The limitations of such an approach are analogous to attempts to synthesize a driving-point impedance via resistors and inductors alone—it is possible to achieve a far broader class of passive circuits if capacitors are also available. The inerter allows a similar broadening for mechanical impedances. The possible benefits of using inerters in passive vehicle suspensions have been explored in [37]. In the present paper, the application of the inerter to motorcycles is considered only in respect of the steering system.

3 Motorcycle Model

The dynamics of motorcycles and the model used to represent them involve three translational and three rotational freedoms of the main frame, a steering freedom associated with the rotation of the front frame relative to the main frame, and the influences of spinning road wheels. The mathematical model employed here also accommodates front and rear suspension freedoms, frame twisting, aerodynamic forces and moments, and the rolling of the rider's upper body relative to the main frame. The forces and moments associated with the tires are modeled using "magic formulas" whose parameters have been optimized to fit measured rig data [38–41]. The tire models used here have been qualified against the contemporary measured data given in [6,42]; these details can be found in [43]. A motorcycle model incorporating all of the above features is described in detail elsewhere; it begins in [5] and is extended in [8,9]. The simulation model is written in LISP and makes use of the multibody modeling code AUTOSIM [44]. The source code can be obtained from the web site http://www.imperial.ac.uk/controlandpower/motorcycles/. The motorcycle's physical geometry is shown in Fig. 3, in which the masses are represented by circles, each with diameter proportional to the mass involved. The AUTOSIM™ [44] model can be configured as either "linear" or "nonlinear." In the latter case, a simulation program results in which the describing equations of motion are solved using numerical integration. The simulation program is used to find equilibrium trim states, which typically involve a fixed target lean angle and a fixed target speed. In the linear configuration, the system is symbolically linearized for small perturbations about a general trim condition. A MATLAB "M" file that sets up the linear model in state-space form is generated automatically. The parameters used in the model derive from laboratory experiments conducted on a contemporary commercially available sports machine [9], the Suzuki GSX-R1000. The effects of a steering damper or a more general steering compensator can be incorporated via the differential equations that describe it. For the particular purposes of the study presented here, the steering compensation system is separated from the rest of the model in the generalized regulator feedback structure [45] shown in Fig. 4. See [46] for a similar use of a control systems paradigm applied to car suspensions. Although this figure shows a frequency-domain model of the linearized system, it is equally applicable to nonlinear time-domain studies. The steering compensator appears as $K(s)$. If $P(s)$ is partitioned as

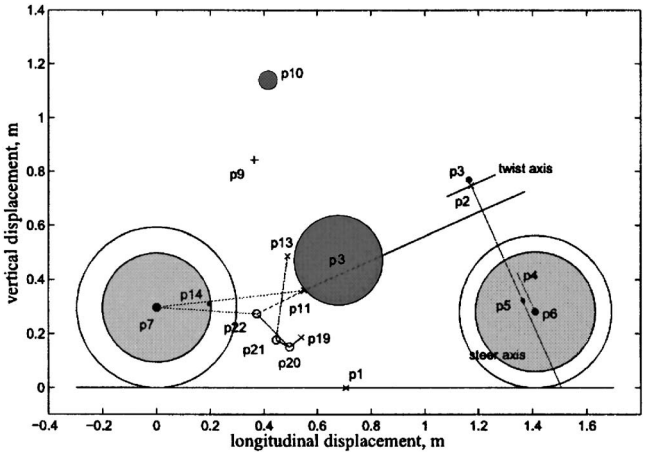

Fig. 3 Scaled diagrammatic motorcycle and rider in side view. The motorcycle-and-rider model shows the machine layout with each of the masses depicted as a proportionately scaled shaded circle.

$$P(s) = \begin{bmatrix} P_{11}(s) & P_{12}(s) \\ P_{21}(s) & P_{22}(s) \end{bmatrix}$$

then the generalized regulator configuration is defined by

$$\begin{bmatrix} \delta(s) \\ s\delta(s) \end{bmatrix} = \begin{bmatrix} P_{11}(s) & P_{12}(s) \\ P_{21}(s) & P_{22}(s) \end{bmatrix} \begin{bmatrix} d(s) \\ T_s(s) \end{bmatrix}$$

and

$$T_s(s) = K(s) s\delta(s)$$

which gives

$$\delta(s) = [I - sP_{12}(s)K(s)]^{-1} P_{11}(s) d(s)$$

since $P_{21}(s) = sP_{11}(s)$ and $P_{22}(s) = sP_{12}(s)$. Repeated reference will be made to Nyquist diagrams and the Nyquist criterion (for an elementary account, see [47], Sec. 9.3) of the open-loop system

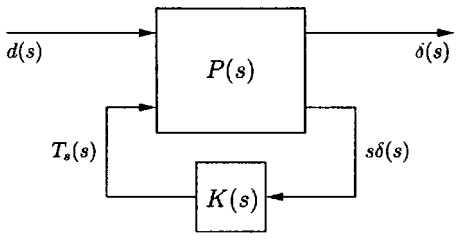

Fig. 4 Feedback arrangement in which $P(s)$ is the linearized motorcycle model and $K(s)$ is the steering compensator. The signal $d(s)$ represents vertical road displacement disturbances, $T_s(s)$ is the steering torque and $\delta(s)$ is the steering angle.

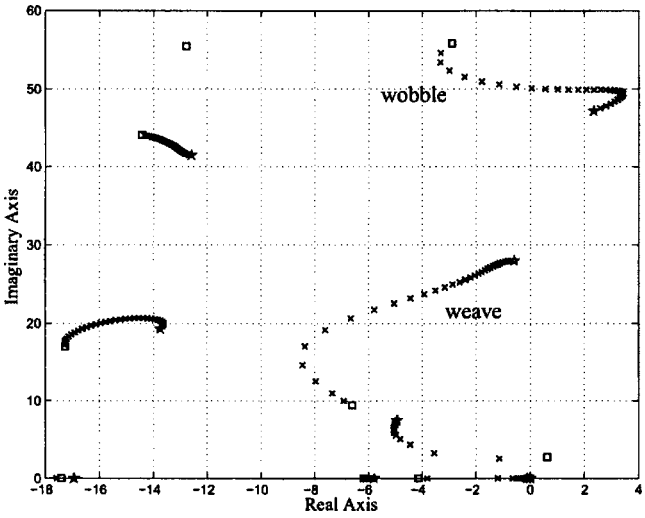

Fig. 5 Root-locus plot for the straight-running motorcycle with speed the varied parameter. No steering damper is fitted. The speed is increased from 5 m/s (□) to 85 m/s (⋆).

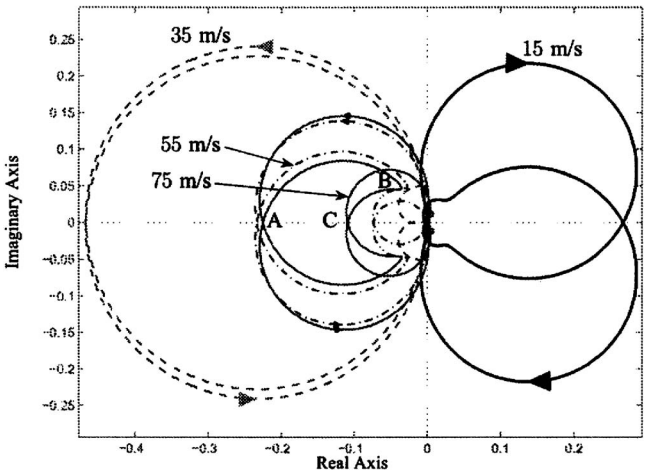

Fig. 7 Straight-running Nyquist diagrams for the open-loop motorcycle model for four different values of forward speed. On the 75 m/s locus, the frequency at A is 47.6 rad/s, at B it is 33.8 rad/s, and at C it reduces to 28.4 rad/s.

$sK(s)P_{12}(s)$, in which $P_{12}(s)$ maps the steering torque $T_s(s)$ into the steering angle $\delta(s)$.

As has been explained elsewhere [5,8,10], speed and steering torque controllers are used in the nonlinear model to establish the steady-state equilibrium state. The reader should understand that these controllers are not included in any of the linearized models or any of the results presented here.

4 Characteristics of the Standard Machine

The important oscillatory modes associated with "wobble" and "weave" are illustrated in the root-locus diagrams of Figs. 5 and 6. Figure 5 corresponds to the straight-running machine with the steering damper removed. It can be seen from this diagram that the wobble-mode frequency varies between 47 and 57 rad/s, while the weave mode's resonant frequency varies between 10 and 28 rad/s. It is clear that the damping of the wobble mode decreases with increased speed, and the mode becomes unstable at ~25 m/s. Figure 6 shows root-loci for the machine with the nominal steering damper fitted for four values of lean angle.

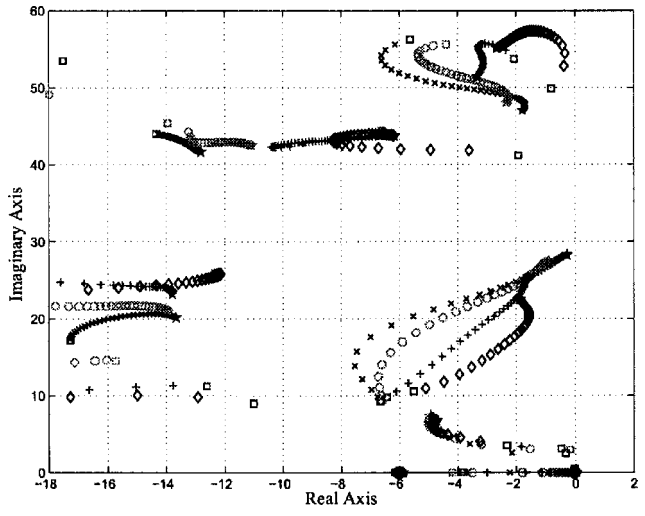

Fig. 6 Root-locus plots for: Straight running (×), 15 deg (∘), 30 deg (+), and 45 deg (◇) of roll angle with speed the varied parameter. The nominal steering damper is fitted. The speed is increased from 7 m/s (□) to 75 m/s (⋆).

Figures 5 and 6 show that the steering damper stabilizes the wobble mode. It also reduces the damping of the weave mode. Figure 6 also shows that increased values of roll angle tend to increase the high-speed weave-mode damping. Since the coupling between the in-plane and out-of-plane dynamics increases with roll angle, one expects the weave mode's vulnerability to road displacement forcing to maximize at an intermediate value (of ~15 deg [10]). It can also be seen from Fig. 6 that for roll angles of up to 30 deg, the high-speed wobble-mode damping increases with roll angle. Further increases in roll angle then destabilize this mode. At low speeds, the wobble-mode damping decreases monotonically with roll angle, and the vulnerability of this mode is worst at low speed and high roll angles.

The open-loop linearized motorcycle model can also be used to generate the Nyquist diagrams shown in Fig. 7. Frequency response plots for straight running at four different values of forward speed are considered. In the case of a steering damper as the compensator in the feedback loop of Fig. 4, $K(s)$ becomes a constant, K, say. It follows from the well-known Nyquist criterion [47] that closed-loop stability requires N anticlockwise encirclements of the $-1/K$ point, where N is the number of unstable poles of the open-loop system and K is the value of the steering damping. At low speeds, both the wobble and weave modes are stable (see Fig. 5), and therefore, no encirclements of the $-1/K$ point are required for the 15 m/s case as shown in Fig. 7. At 35 m/s, the wobble mode of the nominal motorcycle, without its steering damper, becomes unstable as the corresponding complex conjugate pair of poles crosses the imaginary axis into the right-half plane. Under these operating conditions, two counterclockwise encirclements of the $-1/K$ point are therefore required. For higher speeds, two counterclockwise encirclements of the $-1/K$ point are also required, but the range of damper values that will achieve this reduces. Indeed, if the steering damping value is too low, the wobble mode becomes unstable and if it is set too high, the weave mode becomes unstable. In order to appreciate this aspect of the motorcycle's behavior, the reader is referred to the 75 m/s locus in Fig. 7. If the steering damping is set at a low value such that the $-1/K$ point is located at A, the system is on the stability boundary and will oscillate at 47.6 rad/s, which is the wobble-mode frequency. If the steering damper is now increased, two counterclockwise encirclement of the $-1/K$ point result and the machine will be stable. If the steering damper is increased further so that the $-1/K$ point is coincident with the point C, the machine will oscillate at 28.4 rad/s, indicating that the weave mode is on the stability boundary. Any further increases in the steering damper

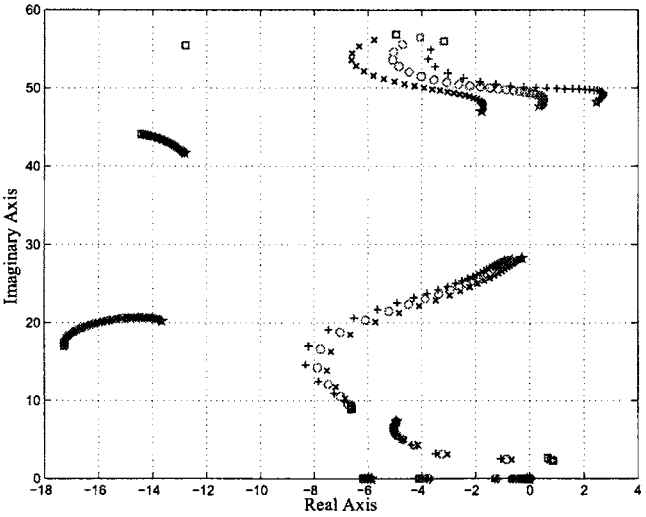

Fig. 8 Straight-running root-loci with speed the varied parameter. The speed is increased from 5 m/s (□) to 75 m/s (⋆). The × locus represents the nominal machine damping value, ∘ refers to a steering damping decrease of 3 Nms/rad, and + to a steering damping reduction of 6 Nms/rad.

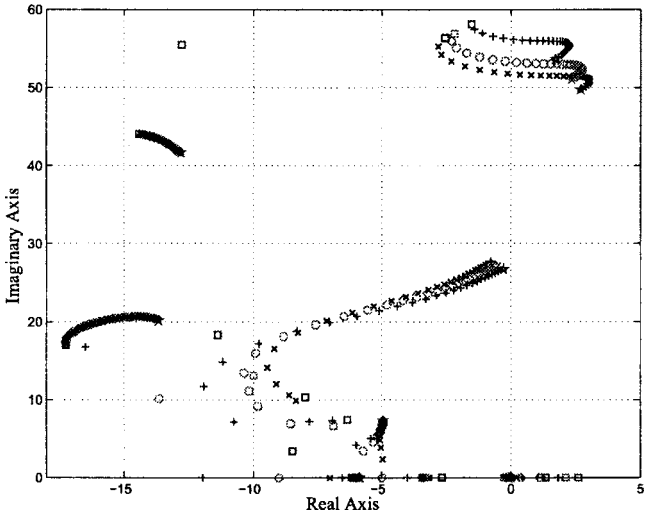

Fig. 9 Straight-running root-loci with speed the varied parameter. The speed is increased from 5 m/s (□) to 75 m/s (⋆). The × locus represents the nominal machine without a steering damper, but fitted instead with a torsional spring of 100 Nm/rad, ∘ represents a spring of 200 Nm/rad, and + corresponds to a spring of 400 Nm/rad.

will render the machine unstable because the $-1/K$ point is not encircled at all. The nominal steering damper value is 6.944 Nms/rad thereby locating the $-1/K$ point at −0.144, which is approximately midway between points *A* and *C* in Fig. 7.

5 Frequency Response Design

5.1 Preliminary Observations. In order to develop design methodologies for passive steering compensators, the influences of the damper, the spring, and the inerter, as isolated components, are studied briefly. This will be done by investigating their effect on the wobble- and weave-mode damping and stability. It can be seen from Fig. 8 that the introduction of a steering damper improves the damping of the wobble mode. When the steering damper coefficient value is reduced, the wobble mode becomes unstable at high speed, while the high-speed weave-mode damping increases. The damper has almost no effect on the natural frequency of either of these modes.

Figure 9 shows the effect of a simple torsional spring on the machine's modal damping. As the torsional stiffness is increased, the wobble-mode natural frequency increases and the mode becomes less unstable. At intermediate and high speeds, the wobble mode is unstable for all spring stiffness values. The spring has almost no effect on the weave mode, particularly at high speed, where the weave-mode damping is low.

Figure 10 illustrates the effect on the machine's modal damping characteristics of introducing an inerter. It may be observed that the wobble mode natural frequency reduces as the value of inertance is increased. This is to be expected, since the wobble mode chiefly involves rotation of the front frame assembly; thus, the change is similar to increasing its moment of inertia. It also makes the wobble mode more unstable and increases the damping of the weave mode. When comparing Figs. 8 and 10, one is drawn to the idea that an effective steering compensator should "look like" an inerter at low frequencies in order to improve the damping of the weave mode, while taking on the mantle of a damper at higher frequencies in order to stabilize the wobble mode. This can be interpreted as a form of lead compensation [47].

5.2 Candidate Networks. Beyond the three simple one-element networks considered in Sec. 5.1, the next simplest possibilities are those containing two components. It is easy to show that the three possible pairwise parallel networks have admittance functions: $c+k/s$, $c+sb$, and $(s^2+k/b)/(s/b)$; b, c, and k are used to denote inertance, damping coefficient, and spring stiffness, respectively. The first of these networks takes the form of a proportional-plus-integral compensator, the second is a proportional-plus-derivative compensator, and the third is a notch filter with blocking frequency k/b. Only the second provides the desirable phase-advance property identified in Sec. 5.1 for weave-mode stability, but this occurs above rather than below a specified frequency. The third network suggests the interesting idea of a compensator that is "tuned" to block the high-speed weave-mode range of frequencies. However, this network does not provide damper-like characteristics over the wobble range of frequencies.

The three possible pairwise series networks have transfer functions: $ck/(sc+k)$, $scb/(sb+c)$, and $sk/(s^2+k/b)$. The first of these networks is a lag compensator, the second is a lead compensator,

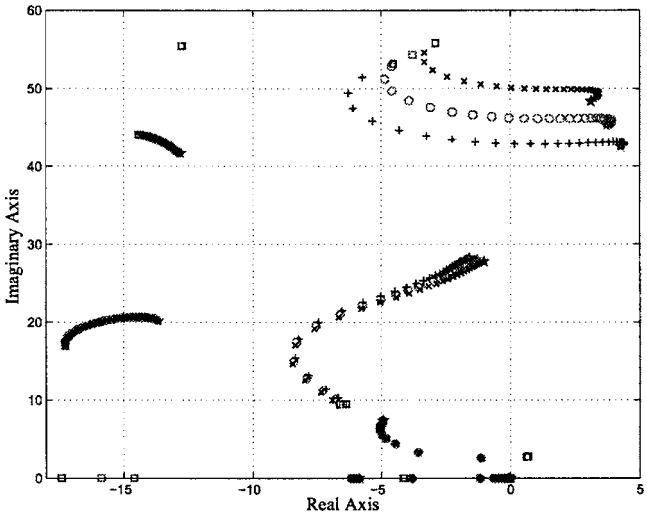

Fig. 10 Straight-running root-loci with speed the varied parameter; the speed is increased from 5 m/s (□) to 75 m/s (⋆). The × locus represents the nominal machine without a steering damper, ∘ represents the effect of an inertance of 0.1 kgm^2, and + the influence of an inertance of 0.2 kgm^2.

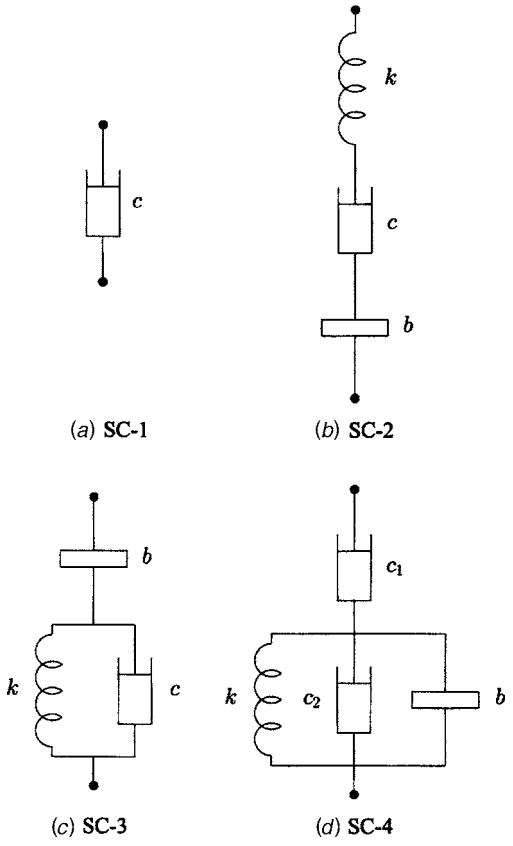

Fig. 11 Simple steering compensation networks

while the third has a resonant frequency at $\omega_0=\sqrt{k/b}$. Among these, the second is the most promising because it has inerter-like (phase-lead) characteristics at low frequencies and damper-like behavior at higher ones. The preliminary observations in Sec. 5.1 have identified such a frequency characteristic as being potentially suitable.

Extending the above type of reasoning to networks with three or four components allows a number of networks to be selected as potentially promising candidate steering compensators for further study. These are shown in Fig. 11. Alongside the conventional damper (steering compensator) SC-1, is the compensation network comprising a damper, spring, and inerter in series (SC-2). This network is a generalization of the two-component device $scb/(sb+c)$ identified above. The important added generality afforded by SC-2 facilitates a rapid phase change in the neighborhood of the resonant frequency $\omega_n=\sqrt{k/b}$. As with the series connected damper-inerter combination, SC-2 has the characteristics of an inerter at low frequencies. The SC-2 network is damper-like in the neighborhood of ω_n and spring-like at high frequencies. In our application, ω_n will be tuned to the wobble-mode frequency so as to introduce damping there.

Network SC-3 has lead networklike properties, and the spring allows fast phase changes through the transition region. Since a damper improves the wobble-mode damping, while having a deleterious effect on the weave-mode characteristics, benefit might be derived from a network which "notches out" the effect of a damper over the weave-mode frequency band. A mechanical network with notch filter characteristics is shown as SC-4 in Fig. 11.

The admittance functions for the networks in Fig. 11 are as follows:

$$Y_1(s)=c$$

$$Y_2(s)=k\frac{s}{s^2+sk/c+k/b}$$

$$Y_3(s)=c\frac{s(s+k/c)}{s^2+sc/b+k/b}$$

$$Y_4(s)=c_1\frac{s^2+sc_2/b+k/b}{s^2+s(c_1+c_2)/b+k/b}$$

It may be observed that the above admittances are at most second-order rational functions and are special cases of the positive-real biquadratic functions of Theorem 2. This class may still be synthesized using springs, dampers, and inerters (although the number of elements may be larger than that required in the networks shown in Fig. 11). It is appropriate to add the idealized case

$$Y_5(s)=\frac{a_2s^2+a_1s+a_0}{d_2s^2+d_1s+d_0}$$

as a further candidate admittance, with the parameters a_0, a_1, a_2, d_0, d_1, d_2 constrained by the conditions of Theorem 2. Although we will not show a circuit realization of $Y_5(s)$, we will refer to this configuration as SC-5.

It is possible to re-parameterize each of the networks SC-2, SC-3, SC-4, and SC-5 in terms of undamped natural frequencies and damping ratios. The admittance function for the network SC-2 may be reparametrized as

$$Y_2(s)=k\frac{s}{s^2+2\zeta\omega_ns+\omega_n^2}$$

in which

$$\omega_n=\sqrt{k/b},\quad \zeta=\frac{\sqrt{bk}}{2c} \tag{2}$$

In the case of SC-3,

$$Y_3(s)=c\frac{s\left(s+\dfrac{\omega_n}{2\zeta}\right)}{s^2+2\zeta\omega_ns+\omega_n^2}$$

in which $\omega_n=\sqrt{k/b}$ and $\zeta=c/(2\sqrt{kb})$.

Similarly,

$$Y_4(s)=c_1\frac{s^2+2\zeta_1\omega_ns+\omega_n^2}{s^2+2\zeta_2\omega_ns+\omega_n^2}$$

in which $\omega_n=\sqrt{k/b}$, $\zeta_1=c_2/(2\sqrt{bk})$ and $\zeta_2=(c_1+c_2)/(2\sqrt{bk})$, and so $\zeta_1<\zeta_2$ is enforced by this network.

In the case of the positive real biquadratic compensator, with a_0, a_2, d_0, $d_2>0$, one obtains

$$Y_5(s)=k\frac{s^2+2\zeta_1\omega_1s+\omega_1^2}{s^2+2\zeta_2\omega_2s+\omega_2^2}$$

in which $k=a_2/d_2$, $\omega_1=\sqrt{a_0/a_2}$, $\omega_2=\sqrt{d_0/d_2}$, $\zeta_1=a_1/(2\sqrt{a_0a_2})$, and $\zeta_2=d_1/(2\sqrt{d_0d_2})$. Then in essence, positive reality comes from satisfaction of the inequality

$$\zeta_1\zeta_2\geqslant\frac{(\omega_1-\omega_2)^2}{4\omega_1\omega_2} \tag{3}$$

As compared to the network SC-4, one is allowed two independent resonant frequencies (rather than one) and the damping ratios need to satisfy the less restrictive constraint (3) instead of $\zeta_2>\zeta_1$.

In the studies which follow, the steering compensator admittance $K(s)$ will be set equal to each of the admittances $Y_1(s),\ldots,Y_5(s)$. For $Y_1(s),\ldots,Y_4(s)$ the parameter values will be

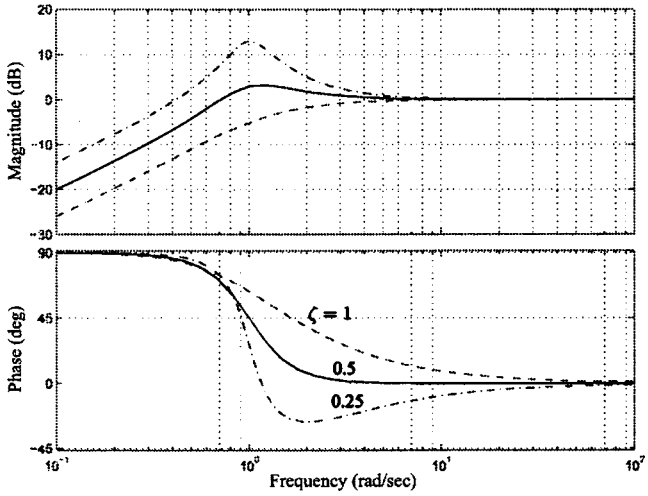

Fig. 12 Normalized frequency responses for SC-3 with unity gain and resonant frequency $\omega_n=1$ for three values of damping ratio ζ

required to be nonnegative, while for $Y_5(s)$ the passivity constraint of Theorem 2 will be imposed; additional networks are considered in the report [48].

5.3 Lead Network Design. The frequency-response characteristics of the compensator SC-3 in Fig. 11 are illustrated in Fig. 12, which has been normalized to $\omega_n=1$. As one would expect, the resonant peak becomes more and more pronounced as the value of ζ is reduced. At the same time, one observes an increasingly rapid phase transition in the neighborhood of ω_n and a smaller value of $\phi_n=\arctan(2\zeta)$, which is the network's phase shift at $s=j\omega_n$.

We now turn to the development of design guidelines for the SC-3 network. A careful examination of the 75 m/s Nyquist plot in Fig. 7 reveals that, for this high-speed straight-running condition, it is advantageous for the steering compensator to introduce phase lead up to the cusp frequency at point B (33.8 rad/s) and proportional gain thereafter; we therefore set $\omega_n=33.8$.

This observation is faithful to the notion that weave requires derivative action, whereas wobble requires proportional compensation. It was established by trial that a damping ratio of $\zeta=0.5$ was suitable. The influence of this unity-gain compensator is illustrated in Fig. 13. As desired, the derivative action has moved the negative-axis crossing point associated with weave-mode instability toward the origin and the crossing point linked to wobble to the left of the diagram. This "opens up" the interval over which two counterclockwise encirclements of the $-1/K$ point can be achieved. In order to maximize the radius of a circle centered at -1, and which can be encircled twice by the Nyquist diagram, the damper coefficient was chosen to be $c=1/0.1741=5.744$. This places the -1 point at the midpoint between the two negative real-axis crossing points. Given these values for c, ζ, and ω_n, the b and k parameters can be found via back substitution using

$$b=\frac{c}{2\zeta\omega_n}$$

$$k=\frac{c\omega_n}{2\zeta}$$

This gives the network parameter values listed in Table 1, and the root-locus plot that results with this mechanical network is shown in Fig. 14. Although the design was based on a single high-speed straight-running linearized model, it is evident that, in comparison with the nominal machine behavior given in Fig. 6, substantial improvements in the damping of the weave mode, under all operating conditions, have been achieved. Greatly improved wobble-mode damping has also been obtained. The improvement in the high-roll-angle (45 deg) case is worthy of particular note.

Table 1 Parameters for network SC-3 given in Fig. 11

c	b	k
5.744	0.1699	194.14

5.4 Notch Filter Design. The frequency-response characteristics of the notch filter network SC-4 in Fig. 11 are illustrated in Fig. 15, in which the depth of the notch is set via ζ_1. Trial and error design studies suggested that the notch frequency should be set below the weave-mode crossing frequency (28.4 rad/s) at point C in Fig. 7 in order that phase lead be introduced above the chosen ω_n value. The following were found to be suitable: ζ_1

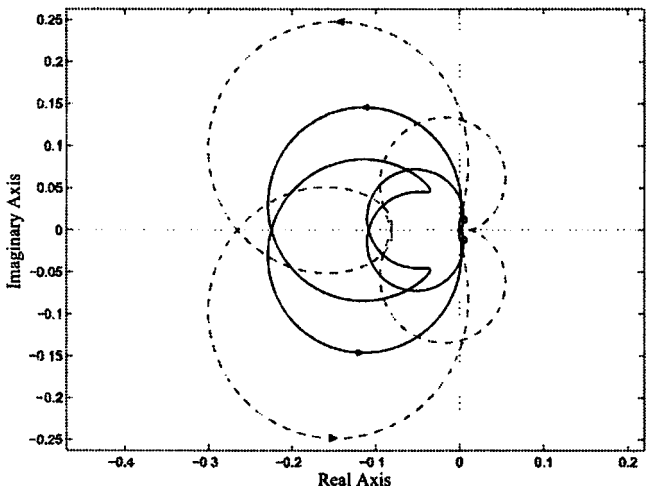

Fig. 13 Nyquist diagram for the straight-running open-loop motorcycle at a forward speed of 75 m/s. The solid line represents the nominal machine with a unity-gain steering damper and the dashed line the compensated system using the SC-3 network given in Fig. 11 ($\omega_n=33.8$, $\zeta=0.5$, c=1).

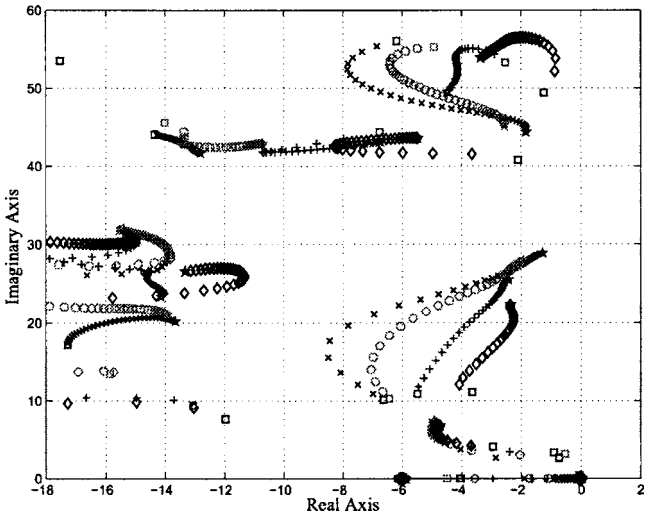

Fig. 14 Root-locus plots for: Straight running (×), 15 deg (∘), 30 deg (+), and 45 deg (◇) with speed the varied parameter from 7 m/s (□) to 75 m/s (⋆). The machine is fitted with the SC-3 network with the parameter values given in Table 1.

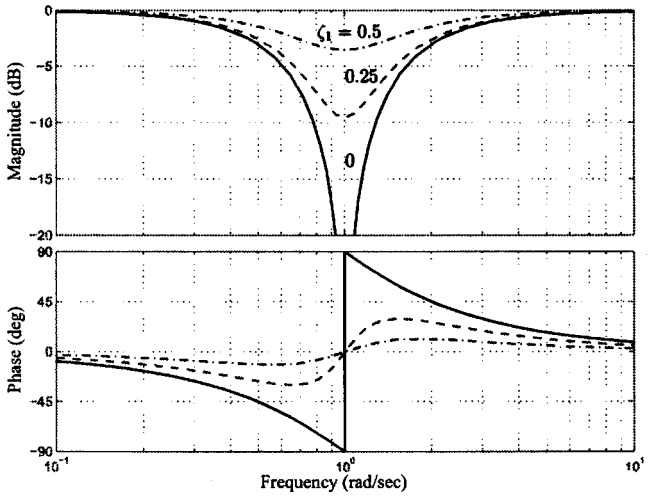

Fig. 15 Frequency responses for SC-4 with unity gain, resonant frequency ω_n=1, denominator damping ratio ζ_2=0.75 for three values of numerator damping ratio ζ_1

=0.1, ζ_2=0.4 and ω_n=25.

In the second phase of the design process, the unity-gain compensated Nyquist diagram is computed; the outcome is illustrated in Fig. 16. By studying the position of the $-1/K$ point as a function of K in Fig. 16, it can be seen that c_1=10 is a suitable damper value. As before, the other parameter values can be found by back substitution and are shown in Table 2.

As with the lead network illustrated above in Sec. 5.3, the notch compensator has good global properties which are demonstrated in Fig. 17. Again, good wobble- and weave-mode damping characteristics are evident.

5.5 Series Resonant Filter Design. The frequency-response characteristics of the SC-2 network are illustrated in Fig. 18. It is apparent from this figure that this network has the characteristics of an inerter at low frequencies and will introduce damping in the vicinity of ω_n, which should be tuned to the wobble-mode frequency. The damping ratio ζ is a free design parameter that can be chosen by trial and is used to provide the required phase compensation. As compared to the 90 deg of phase shift of SC-3, this network introduces 180 deg of phase and potentially has a fast phase transition in the vicinity of ω_n. These characteristics are useful in the present context. The correct value of the spring constant k can be derived from a compensated Nyquist plot in a manner analogous to the procedure explained in Secs. 5.3 and 5.4. Once k has been fixed, b can be found from ω_n and c from ζ; these details are left to the reader.

Table 2 Parameters for notch compensator (SC-4)

c_1	c_2	b	k
10	3.33	0.667	416.67

6 Optimization

The optimization of the mechanical networks in Fig. 11 will be studied from both a time- and a frequency-domain perspective. In order to do this, one has to deal with passivity constraints on the compensator parameters, the stability of the uncontrolled machine, as well as optimization across multiple linearized motorcycle models that "grid" the machine's operating envelope. The optimization studies will make use of the MATLAB sequential quadratic programing algorithm FMINCON [49], which accepts both linear and nonlinear equality and inequality constraints. In the case of the mechanical networks given in Fig. 11, passivity is ensured via the non-negativity of the network parameters. In the case of positive-real biquadratic functions, the constraints alluded to in Theorem 2 must be enforced.

6.1 Time Domain Criterion. The time-domain optimization of the networks in Fig. 11 seeks to maximize the motorcycle's lowest modal damping ratio for all the linearized models in the model set. In order to specify formally this optimization problem, it is helpful to refer to Fig. 19. In addition to the (hard) passivity constraints associated with the network parameter values, it is necessary to introduce stability constraints and a performance criterion for minimization. Recognizing that the low-frequency stability of the machine will be ensured by the rider, and not the compensation network, the stability constraint used here allows unstable low-frequency modes to remain in the right-half plane.

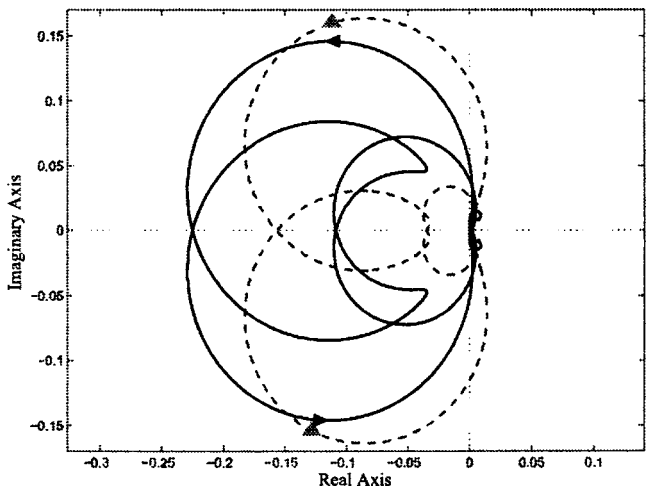

Fig. 16 Nyquist diagram for the straight-running open-loop motorcycle at a forward speed of 75 m/s. The solid line represents the nominal machine with a unity-gain steering damper and the dashed line the compensated system using the SC-4 network given in Fig. 11. The network parameters are c_1=1, ζ_1=0.1,ζ_2=0.4, and ω_n=25.

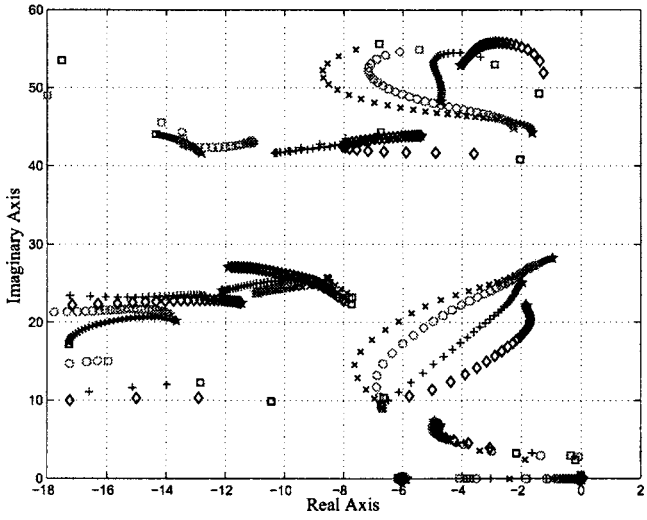

Fig. 17 Root-locus plots for: Straight running (×), 15 deg (∘), 30 deg (+), and 45 deg (◇) with speed the varied parameter for the compensated machine fitted with the network SC-4 with the parameters of Table 2. The speed is increased from 7 m/s (□) to 75 m/s (⋆).

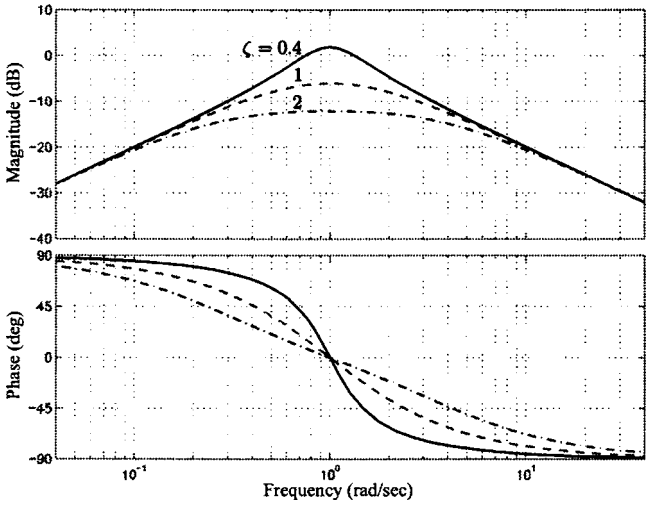

Fig. 18 Normalized frequency-response characteristics of the network SC-2 for three values of damping ratio

This is achieved via the requirement that only closed-loop eigenvalues with an imaginary part greater than j must be confined to the left-half of the complex plane. For illustration, this stability-related hard constraint is shown pictorially in Fig. 19(a) via the cross-hatching of the imaginary axis for values above j. As can be seen from Fig. 5 there is a low-frequency mode that is associated with rider upper-body oscillations. This mode is unstable for low speeds, and since it crosses the imaginary axis at $\sim 2.5j$, the optimization problem demands that the compensator stabilizes it. In contrast, no attempt is made to stabilize the marginally unstable capsize mode whose eigenvalue(s) is/are either real or has/have a very small imaginary part.

The set of linear motorcycle models used in solving the optimization problem grids the important part of the machine's operating conditions. This set is denoted Ω and contains linearized

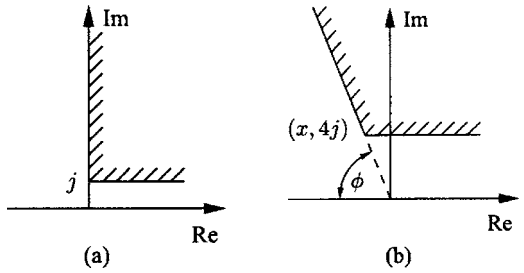

Fig. 19 (a) Stability constraint region and (b) damping ratio optimization region

models corresponding to trim roll angles of $0,3,6,\ldots,45$ deg and trim speeds of $7,9,11,\ldots,75$ m/s. The time-domain index for minimization is

$$J_t = \max_{\Omega} \max_{i} \{\tan(\phi_i)\} \tag{4}$$

in which the index i ranges over those modes with an imaginary part $>4j$. It is recognized that minimizing J_t will minimize ϕ_i for $0 \leqslant \phi_i \leqslant \pi/2$, and thus maximize the damping ratios, which are given by $\zeta_i = \cos(\phi_i)$. Geometrically, the optimizing algorithm will try to rotate the constant-damping-ratio line illustrated in Fig. 19(b) counterclockwise around the origin toward the negative real axis. The achieved minimum in J_t is associated with the least damped mode across the model set Ω.

6.2 Frequency-Domain Criterion. The optimization of linear systems via $\mathcal{H}_\infty$ frequency-response performance measures is a well-developed subject [45]. In the present context these measures are motivated by the role played by road displacement forcing in stability-related road traffic accidents [10]. The objective is to minimize the worst-case closed-loop gain from road forcing disturbances to steering angle (see Sec. 3 and Fig. 4) for all operating conditions, while simultaneously ensuring that the open-loop Nyquist diagram does not get "too close" to the -1 point. For each frequency ω_i, the

$$J_f = \max_{\Omega} \left\{ \max \left[\max_{\omega_i} \left| \frac{P_{11}(j\omega_i)}{1 - j\omega_i K(j\omega_i) P_{12}(j\omega_i)} \right|, \max_{\omega_i} \left| \frac{\gamma}{1 - j\omega_i K(j\omega_i) P_{12}(j\omega_i)} \right| \right] \right\} \tag{5}$$

distance between the Nyquist diagram and the -1 point is given by $|1 - j\omega_i K(j\omega_i) P_{12}(j\omega_i)|$. This is the modulus of the classical sensitivity function, which plays a central role in the subject of sensitivity and robustness of control systems [45]. In the work presented here, the multiobjective $\mathcal{H}_\infty$ index given in Eq. (5) will be used. The first term in (5) is the closed-loop transfer function between road forcing disturbances and the steering angle, while the second is a fixed constant times the inverse of the distance of closest approach between the Nyquist diagram and the -1 point. The positive reality constraints, the stability constraint, and the model set Ω used here are the same as those employed in the time-domain optimization problem described in Sec. 6.1. When evaluating J_f, a 100-point frequency list was used. These points were placed on a logarithmic scale that covered the range $\omega = 10^{1.3}$ to $\omega = 10^{1.85}$. This range was selected to include all the maxima in the index (5). The weighting factor on the second term was set by trial to $\gamma = 16$.

7 Optimization Results

Results pertaining to the performance of the optimized networks in Fig. 11, as well as the general positive real biquadratic function (SC-5) will now be given. The time-domain optimization results for the criterion described in Sec. 6.1 will be described first followed by the frequency-domain approach of Sec. 6.2. In appropriate cases, the optimization processes were initialized using the loop-shaping design methods described in Secs. 5.3–5.5.

7.1 Time-Domain Optimization. The results of optimizing each of the networks in Fig. 11 with the time-domain index (4) are given in Table 3. In addition to the optimal parameter values, the table also provides the minimum values achieved for the performance index (4), the trim condition at which the minimum was achieved, and the damped natural frequency of the least-damped mode at that trim state. The eigenvalues associated with this least-damped mode will lie against the damping ratio line in Fig. 19(b), while all the others will lie to the left of it. It can be seen from the

Table 3 Optimal Time-domain network parameter values

	Parameters	J_t	Maximum		
			(deg)	(m/s)	(rad/s)
SC-1	c=7.2526	112.99	45	11	54.56
SC-2	k=773.31	16.646	45	21	65.81
	c=22.723				
	b=0.32673				
SC-3	c=11.987	16.683	45	7	48.69
	k=416.54				
	b=0.32771				
SC-4	c_1=22.518	21.102	15	75	37.25
	c_2=0				
	k=101.74				
	b=0.6536				
SC-5	a_2=19.053	14.55	45	7	48.43
	a_1=180.29				
	a_0=11030.5				
	d_2=1.0				
	d_1=21.352				
	d_0=929.51				

table that the "best" network in this case is SC-2, and the least satisfactory is the conventional damper (SC-1). The performance of SC-2 (J_t=16.646) is only slightly worse than that of the general biquadratic positive real function SC-5 (J_t=14.55). Referring to Fig. 20, one observes the influence of the optimized SC-2 network on the compensated motorcycle's root-locus plot. As expected, the damping ratios of all the lightly damped motorcycle modes have been substantially increased with the wobble mode at ~66 rad/s against the constant damping ratio line. It can be shown that the networks SC-2, SC-3, and SC-4 substantially increase the highest achievable stable straight-running speed for the motorcycle modeled here ([48], Table 4).

Figure 21 shows the variation of J_t with operating point in the case of the optimal damper SC-1. The figure reflects the fact that there is a compromise between high-speed-weave and low-speed-wobble operating conditions with conventional dampers. In particular, at a speed of 11 m/s and a roll angle of 45 deg, the wobble damping ratio is only ζ=0.009. For high-speed straight-running, the weave mode is similarly lightly damped. A J_t performance surface for SC-2 is given in Fig. 22. It is clear from this figure that although the machine retains its tendency to have a lightly damped weave mode under high-speed straight-running conditions, and a lightly damped wobble mode under lower-speed high-roll-angle conditions, the worst case damping ratio has increased significantly to ζ=0.06. The general biquadratic positive real compensator increases this value only slightly to ζ=0.069.

Before leaving the time-domain results, it is interesting to consider the sensitivity of the designs obtained. Figure 23 shows the Nyquist diagrams associated with the nominal damper and the series resonant network SC-2. It is clear that in the latter case the optimized network offers poor gain and phase margins; indeed these were not included in the optimization problem formulation. This suggests the possibility that parameter variations and/or modeling inaccuracies may result in the instability of the weave mode.

Figure 24 shows the sensitivity of the wobble mode at 11 m/s and 45 deg to variations in the nominal steering damper parameter value, and the parameter values of each of the networks SC-2 to SC-4 inclusive. As compared to the other networks, the SC-2 network wobble-mode damping performance appears especially sensitive to variations in each of its three parameters. This is particularly true in the case of the spring constant and the inertance value, which together dictate the network's resonant frequency;

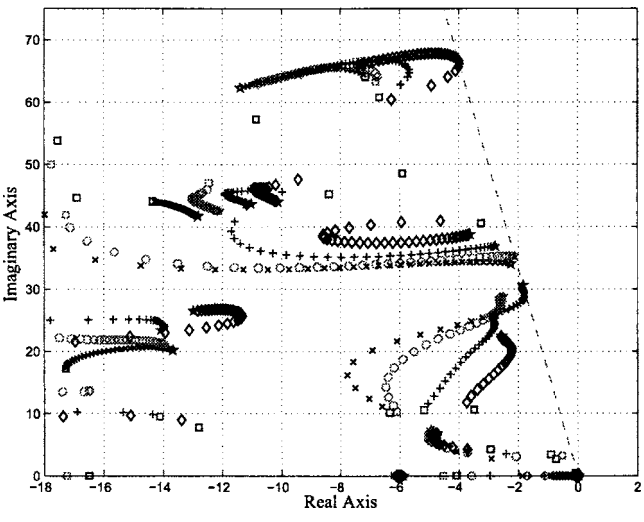

Fig. 20 Root-locus plots for: Straight running (×), 15 deg (∘), 30 deg (+), and 45 deg (◇) of roll angle with speed the varied parameter. The network SC-2 is fitted and was optimized to minimize the performance index (4). The speed is increased from 7 m/s (□) to 75 m/s (⋆).

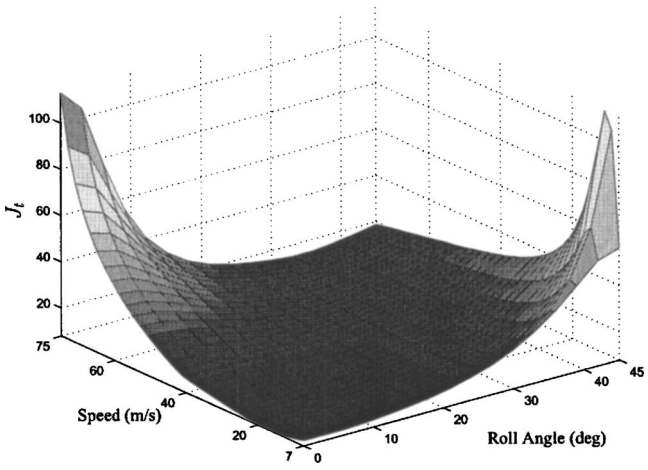

Fig. 21 Cost function J_t for 7–75 m/s and 0–45 deg lean with the motorcycle fitted with the optimized SC-1 compensated system

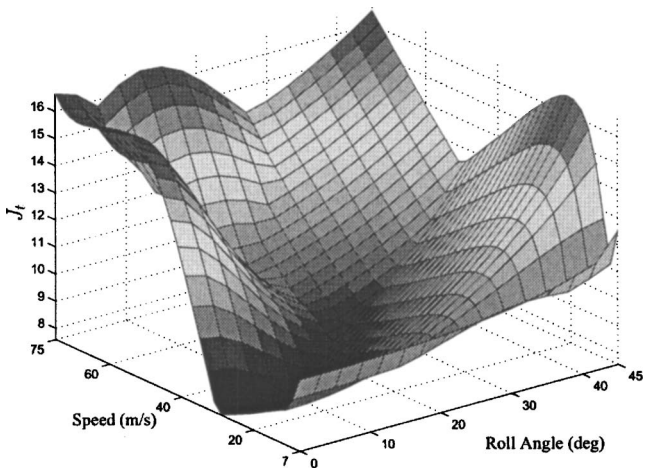

Fig. 22 Cost function J_t for 7–75 m/s and 0–45 deg lean with the motorcycle fitted with the optimized SC-2 compensated system

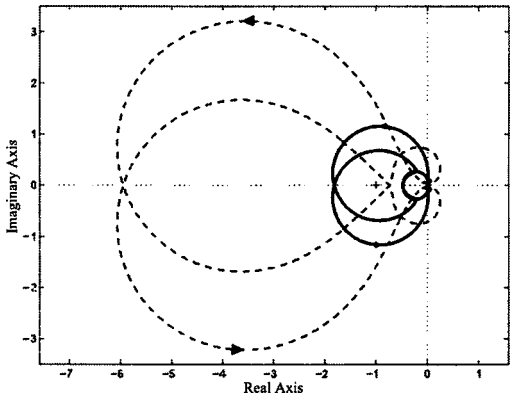

Fig. 23 Nyquist diagrams for the open-loop motorcycle with a forward speed of 75 m/s and a roll angle of 15 deg. The solid line represents the machine fitted with the nominal steering damper, and the dashed line represents the machine fitted with the time-domain optimized SC-2 network.

see (2). A similar calculation of sensitivities will also be done in the next section where the cost criterion (5) specifically includes a robustness enhancing term.

7.2 Frequency-Domain Optimization. The results of optimizing each of the networks in Fig. 11 with the frequency-domain index (5) are given in Table 4. In addition to the optimal parameter values the table also provides the minimum values achieved for the performance index (5), the trim condition at which the minimum was achieved, and the frequencies corresponding to the frequency-response peaks associated with the limiting value of J_f. It is evident from the table that the "best" network in this case is again SC-2 and the least satisfactory is the conventional steering damper SC-1. As one would now expect, a marginally better performance is achieved by the general biquadratic positive real compensator SC-5. It is also clear that in each case the wobble mode is dictating the lowest achievable value of J_f. In the case of SC-2, J_f=40.576 was obtained, and so the closest distance of approach between the Nyquist plot and the -1 point is $\geqslant 16/40.576 = 0.394$; recall that $\gamma = 16$ was used in (5). As a result, improved gain and phase margins have been achieved as compared with the time-domain optimized SC-2 network.

Table 4 Optimal frequency-domain network parameter values

	Parameters	J_f	Maximum		
			(deg)	(m/s)	(rad/s)
SC-1	c=8.0695	109.8412	45	9	52.97
SC-2	k=594.08	40.576	45	7	49.95
	c=13.716				
	b=0.24252				
SC-3	c=8.0941	49.05	45	7	49.21
	k=281.2483				
	b=0.2387				
SC-4	c_1=13.322	46.155	45	7	48.89
	c_2=0.00070281				
	k=256.66				
	b=0.71191				
SC-5	a_2=13.944	37.5896	45	7	49.16
	a_1=85.172				
	a_0=11167				
	d_2=1.0				
	d_1=13.535				
	d_0=941.83				

Figure 25 shows the locus of the motorcycle's important modes for a wide range of speeds and roll angles in the case that the optimized SC-2 network is fitted. As with the time-domain optimized parameters, this network achieves improved damping ratios for each of the machine's lightly damped modes. Figure 26 shows the road-forcing response

$$\max_{\omega_i} \left| \frac{P_{11}(j\omega_i)}{1 - j\omega_i K(j\omega_i) P_{12}(j\omega_i)} \right|$$

as the trim state ranges over the motorcycle's cornering regime; under straight-running conditions, the road-forcing response goes to zero. In common with each of the other networks, the highest gain values occur at low speeds and high roll angles, and correspond to the excitation of the wobble mode. As one would expect, relatively high values of road forcing gain are also achieved under high-speed low-roll-angle conditions (see 75 m/s and 15 deg roll

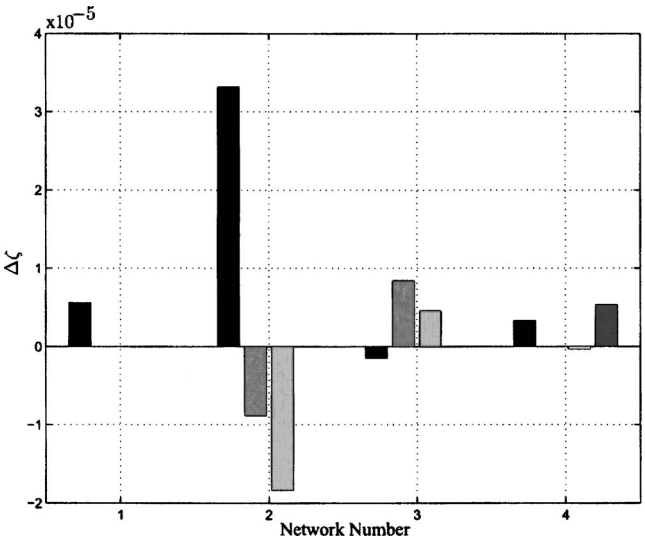

Fig. 24 The vertical axis shows changes in the damping ratio of the wobble mode for single-parameter variations in each of the time-domain optimized networks: nominal steering damper SC-1 to SC-4. The trim condition is 45 deg and 11 m/s; the parameter values are adjusted by 0.01%. The order of the parameters in each group is the same as that given in Table 3.

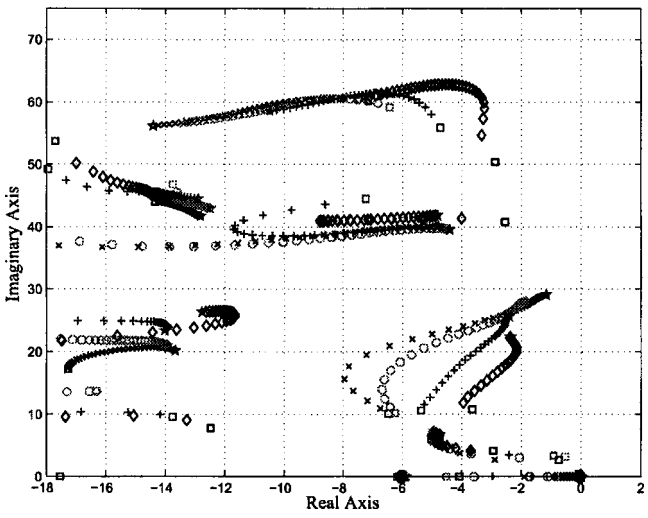

Fig. 25 Root-locus plots for: Straight running (×), 15 deg (∘), 30 deg (+), and 45 deg (◇) of roll angle, with the speed varied from 7 m/s (□) to 75 m/s (⋆). The network SC-2 is fitted with its parameters set to minimize J_f in (5).

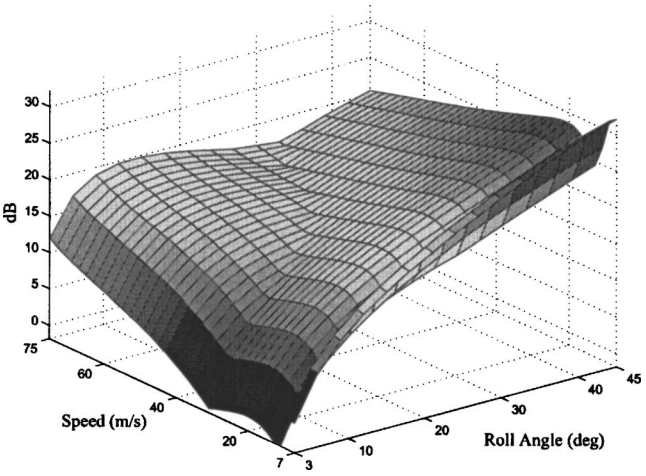

Fig. 26 Road forcing gain for 7–75 m/s and 3–45 deg roll angle for the frequency-domain optimized SC-2 compensated system

angle); this is a feature shared by each of the other networks. The road forcing characteristics of the machine are also illustrated by the frequency-response plots shown in Figs. 27 and 28. As is evident from the first of these figures, the SC-2 network decreases the peak wobble-mode road-forcing gain by ~15 dB. The trim condition selected corresponds to an equilibrium state in which the wobble mode is particularly vulnerable to road displacement forcing. The second of these figures corresponds to a high-speed trim condition in which the weave mode is particularly vulnerable to road displacement forcing. In this case the SC-2 network is seen to reduce the weave-mode peak by ~3 dB as compared to the nominal damper that is fitted to the production machine.

In order to further investigate the robustness of the frequency-domain optimized networks, a study was carried out that investigates the range over which the network parameters can be varied, one at a time, without destabilizing the machine. Table 5 shows the effect of changing individual network parameters. As expected, in the case of the damper, the wobble mode will be destabilized if the damper value is too low, while the weave mode is

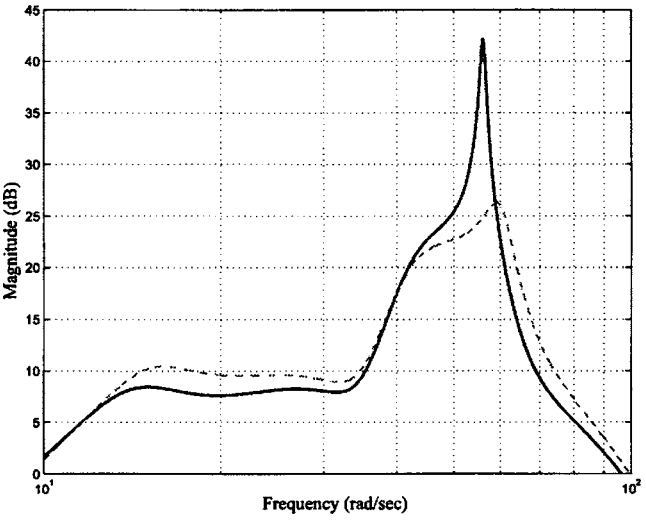

Fig. 27 Bode magnitude plot for road displacement forcing (0 dB=1 rad/m). The machine is operating at a forward speed of 15 m/s and a roll angle of 45 deg. The solid line represents the nominal machine, and the dashed line the machine fitted with the frequency-domain optimized SC-2 network.

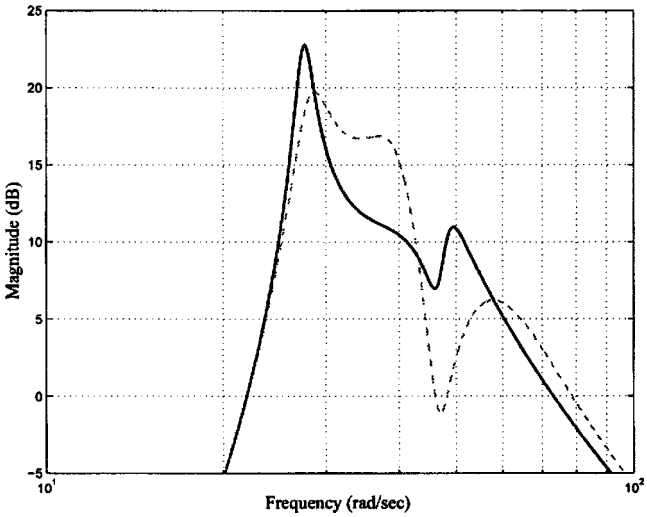

Fig. 28 Bode magnitude plot for road displacement forcing (0 dB=1 rad/m). The machine is operating at a forward speed of 75 m/s and a roll angle of 15 deg. The solid line represents the nominal machine, and the dashed line the machine fitted with the frequency-domain optimized SC-2 network.

destabilized if it is too large. In comparison to the other networks, the stable range of the SC-1 damper values is relatively small. Without exception, in the case of the other networks, the various parameter values can be varied over a much larger range without instability.

Figure 29 shows that the frequency-domain optimized SC-2 network has improved wobble-mode sensitivity properties as compared to its time-domain counterpart (Fig. 24). With that said, compared to the other networks, the need to "tune" this network to the low-speed high-roll-angle, wobble-mode frequency renders it relatively sensitive to parameter variations under these conditions. This relatively high low-speed high-roll-angle sensitivity characteristic has to be set against its excellent overall nominal performance.

We conclude with a brief examination of the motorcycle's sensitivity to machine parameter variations. Intuitively, one would expect any difficulty to be most apparent in the parameters which specify the dynamics of the steering system and the "front-end" of the motorcycle. These include geometry-related parameters, the front-frame stiffness and the steering system inertia parameters. The sensitivities to variations in a selection of these parameters is given in Fig. 30. It is apparent from this diagram that the damping ratio sensitivity of the wobble mode, at the indicated trim condition, for the network SC-2, is particularly large in respect of the front wheel attachment point, the x-axis component of the twist axis joint with the main frame, the front tire crown radius, and the steering head angle. The wobble-mode damping ratio sensitivities to the front frame stiffness, and the mass and moment of inertia parameters are comparatively low. It is important to note from Fig. 30 that the frequency-domain optimized networks have sensitivities that are comparable with those of the conventional damper. This indicates that the robustness of these networks will be no worse than that of the conventional damper.

8 Conclusions

This paper has introduced the idea of replacing a conventional steering damper with a mechanical network comprising spring(s), damper(s), and inerter(s) [30] on a high-performance motorcycle. The study has used an advanced motorcycle simulation model [5,8,9] to demonstrate that this can lead to clear performance benefits in the wobble- and weave-mode damping. Methods of passive electrical circuit synthesis [33,34] that have been recast into a

Table 5 Stable ranges for single parameter variations. The frequency of oscillation at instability and the associated trim states are also noted. The frequency-domain optimized network parameters are used. The operating conditions considered include forward speeds from 7 to 75 m/s and roll angles from 0 to 45 deg.

Network	Parameters	Stable range	Lower instability	Upper instability
SC-1	$c=8.0695$	$6.1328 \leqslant c \leqslant 9.1992$	(45 deg,11 m/s) 54.4036 rad/s	(0 deg,75 m/s) 28.3597 rad/s
SC-2	$k=594.08$	$433.6784 \leqslant k \leqslant 1969.4$	(45 deg,15 m/s) 60.0887 rad/s	(0 deg,73 m/s) 42.3941 rad/s
	$c=13.716$	$6.3779 \leqslant c \leqslant 27.0205$	(45 deg,11 m/s) 54.7304 rad/s	(0 deg,75 m/s)36.5001 rad/s
	$b=0.24252$	$0.1601 \leqslant b \leqslant 0.3771$	(0 deg,73 m/s) 42.4039 rad/s	(0 deg,75 m/s) 29.3787 rad/s
SC-3	$c=8.0941$	$4.4518 \leqslant c \leqslant 13.0315$	(0 deg,75 m/s) 31.1644 rad/s	(0 deg,73 m/s) 41.2790 rad/s
	$k=281.2483$	$32.3436 \leqslant k \leqslant 442.9661$	(0 deg,69 m/s) 45.1722 rad/s	(0 deg,75 m/s)37.4435 rad/s
	$b=0.2387$	$0.1719 \leqslant b \leqslant 0.3103$	(0 deg,73 m/s) 42.4861 rad/s	(0 deg,75 m/s) 30.2920 rad/s
SC-4	$c_1=13.322$	$5.9949 \leqslant c_1 \leqslant 26.644$	(45 deg,11 m/s) 53.9057 rad/s	(0 deg,75 m/s) 36.7354 rad/s
	$c_2=0.00070281$	$0 \leqslant c_2 \leqslant 29.5$		(0 deg,75 m/s) 28.5082 rad/s
	$k=256.66$	$0 \leqslant k \leqslant 730.1977$		(0 deg,75 m/s) 42.396 rad/s
	$b=0.71191$	$0.4485 \leqslant b \leqslant 1.1569$	(0 deg,73 m/s) 42.5535 rad/s	(0 deg,75 m/s) 29.3067 rad/s

mechanical engineering setting via the introduction of the inerter play a central role in this research. Classical frequency-response methodologies [47] also play an important role. A number of steering compensators are optimized and analyzed in the spirit of classical time-domain and $\mathcal{H}_\infty$ control systems design ideas [45].

The investigation in this paper was prompted by the often reported poor performance of high-powered sports motorcycles operating at high speed. The results of Sec. 4 show that the nominal machine is vulnerable to high-speed weave, particularly under straight-running or low-roll-angle conditions, and low-speed wobble, particularly at high roll angles. This initial study shows why there is only a small usable range of steering damper parameter values and illustrates why conventional motorcycles are dogged by an apparently intractable wobble-weave-mode damping compromise.

The results in Sec. 5.1 show that a steering damper is an effective means of damping the wobble mode, but that it has a deleterious effect on the weave mode. These results also show that a steering inerter can improve the damping of the weave mode. Taken in combination, these observations motivated the study of the simple mechanical networks presented in Fig. 11. In each case the network parameters can be selected so that they "look like" a damper above the weave-mode frequency band, while adopting the mantle of an inerter at lower frequencies. Three network configurations with these general characteristics were analyzed in detail. The network SC-2 introduces low-frequency inertance and narrowband wobble-mode damping, SC-3 is in essence a mechanical lead compensator [47], while the notch filter characteristics of SC-4 are used to shield the weave mode from the negative effect of a steering damper. Simple frequency-response design procedures are presented for each of these networks. In a first design step, each compensation network's natural frequency and damping ratio(s) are chosen. In a second step, which is conducted after the unity-gain compensated Nyquist diagram is plotted, the network's spring constant (SC-2), or (one of) the network's damper values is selected (SC-3 and SC-4). The remaining parameters are found by back substitution. It is demonstrated that these hand-designed networks have greatly improved performance characteristics as compared to the nominal machine.

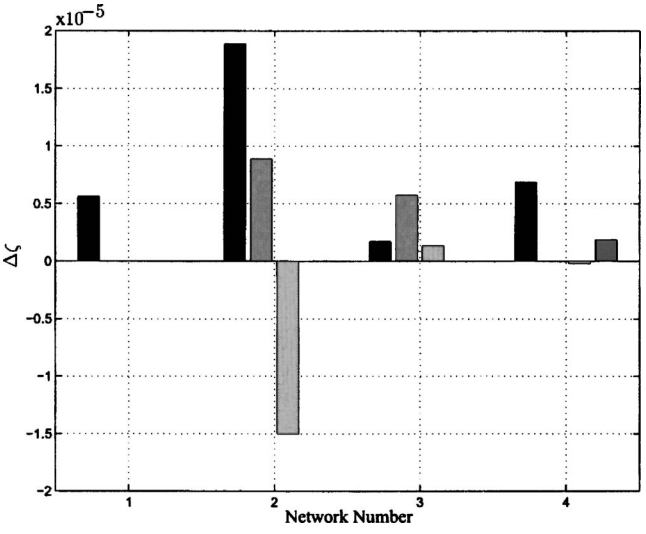

Fig. 29 Compensator parameter sensitivities for the wobble mode at 45 deg and 11 m/s. The vertical axis shows the change in the damping ratio for a 0.01% change in each parameter. The frequency-domain optimized networks are used; the first network is the nominal steering damper. The parameters in each of the four network groups (SC-1 to SC-4) adopt the ordering in Table 4.

Time- and frequency-domain design optimization frameworks are described in Sec. 6, which accommodate passivity and robust stability. The philosophy behind these frameworks comes from traditional second-order system ideas [47] and robust control theory [45]. The parameter optimization is achieved via a sequential quadratic programing algorithm [49]. Given the nonlinear characteristics of motorcycles, as they range over their operating envelope, it is vital that the steering compensator networks are optimized across the machine's entire working regime. This was achieved using a set of linearized models that grid the motorcycle's operating domain.

The results presented in Sec. 7 show that substantial global performance improvements, as compared to conventional steering dampers, are achievable using the various network configurations given in Fig. 11. In the case of both time- and frequency-domain optimization criteria, the nominal performance of the network SC-2 is excellent and only slightly worse than that of the ideal biquadratic positive real compensator SC-5. Important facets of this improved performance come in the form of substantially improved wobble- and weave-mode damping, as well as improvements in the motorcycle's straight-running top-speed stability. Sensitivity studies, and gain and phase margin considerations, indicated that parameter optimization exercises should be "robustified" against modeling uncertainties and parameter drift. In the case of the frequency-domain criterion J_f, given in Eq. (5), an explicit robust stability property is introduced. The operating conditions associated with worst-case wobble- and weave-mode damping are identified, and the road disturbance rejection properties of the various steering compensators are studied and greatly improved there. Worst-case wobble performance occurs under low-speed high-roll-angle conditions, while worst-case weave performance occurs when the machine is operating under high-speed low-roll-angle circumstances. As expected, each of the steering compensators is particularly effective against wobble. Impor-

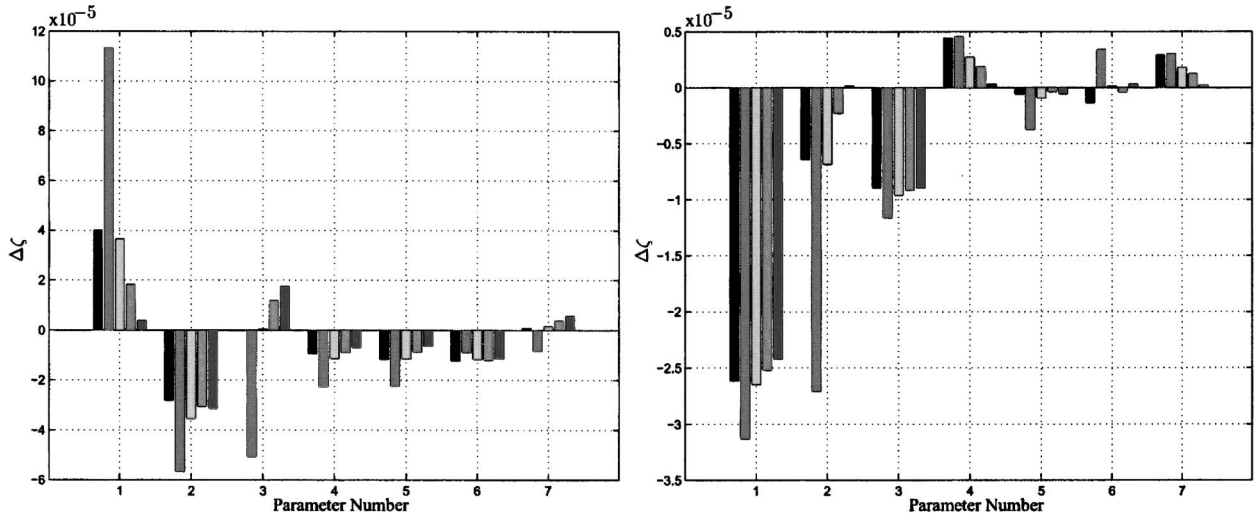

Par. Number	Symbol	Name
1	x6	x co. of front wheel attachment point
2	z6	z co. of front wheel attachment point
3	x2	x co. of twist axis joint with main frame
4	x5	x co. of center of mass of front susp. body
5	x3	x co. of center of mass of front steer body
6	x8	x co. of center of mass of the main frame
7	z2	z co. of twist axis joint with main frame

Par. Number	Symbol	Name
1	f_tcrad	Front tire crown radius
2	head_ang	Head angle
3	Mmain	Main body mass
4	Iff_strz	Front frame steering inertia
5	Kp_twst	Twist flexibility stiffness
6	Imnz	Main body yaw inertia
7	Ifwx	Front wheel x moment of inertia

Fig. 30 Wobble-mode damping ratio sensitivities at 45 deg and 11 m/s. The vertical axis shows the change in the damping ratio for a 0.01% change in each of the parameters shown in the tables below the subfigures. The bars are shown in groups of five; each group represents the steering-compensated vehicle with the frequency-domain optimized networks in the order: nominal steering damper, SC-2, SC-3, SC-4, and SC-5.

tantly, enhanced weave-mode performance can be achieved simultaneously. In each case, the network performance is more sensitive to front-end parameter variations than to those that do not directly affect the machine's steering behavior.

The general issue of the practical implementation of passive mechanical compensators is the subject of ongoing investigation. A prototype for the SC-2 network has been built and tested at the Cambridge University Engineering Department comprising an epicyclic gear mechanism. For steering compensators to be deployed on production motorcycles, issues such as the selection of optimal gear ratios for the inerters, correct dimensioning of the device in order that it is robust enough to withstand the wear and tear of normal usage, and packaging will be important to consider.

It has not escaped our notice that the use of active steering compensation is a potentially attractive possibility by, for example, making use of a steering torque motor, a digital signal processing chip set, and a speed- and steer-angle sensing arrangement. In this case, the correct dimensioning of the torque motor and its associated gearing and power electronics is likely to be of central importance. This approach has several potential advantages: one is no longer restricted to positive-real compensators, it is no longer necessary for the device to be low-order, and finally, adaptive systems are a practical possibility. This topic is the subject of ongoing research.

Appendix

Proof of Theorem 2. Suppose that $Z(s)$ is positive real. By calculation

$$Z(j\omega) = \frac{(a_0 - a_2\omega^2) + j\omega a_1}{(d_0 - d_2\omega^2) + j\omega d_1} = \frac{a_2 d_2 \omega^4 + \omega^2(a_1 d_1 - a_0 d_2 - a_2 d_0) + a_0 d_0}{(d_0 - d_2\omega^2)^2 + \omega^2 d_1^2} + \text{Im} \quad \text{(A1)}$$

in which Im is the imaginary part of $Z(j\omega)$. Since the real part of $Z(j\omega)$ is non-negative, after setting $x=\omega^2$, we obtain

$$f(x) = a_2 d_2 x^2 + (a_1 d_1 - a_0 d_2 - a_2 d_0)x + a_0 d_0 \geq 0$$

for all $x \geq 0$. In the case that $a_2 d_0 + a_0 d_2 - a_1 d_1 \geq 0$, it follows from the properties of quadratic equations that $f(x) \geq 0$ implies

$$4a_2 a_0 d_2 d_0 \geq (a_1 d_1 - a_0 d_2 - a_2 d_0)^2$$

$$\Leftrightarrow 2\sqrt{a_0 d_2}\sqrt{a_2 d_0} \geq a_0 d_2 + a_2 d_0 - a_1 d_1$$

$$\Leftrightarrow a_1 d_1 \geq (\sqrt{a_0 d_2} - \sqrt{a_2 d_0})^2 \quad \text{(A2)}$$

which shows that the inequality in the theorem is necessary. In the case that $a_0 d_2 + a_2 d_0 - a_1 d_1 \leq 0$, we observe that the inequality is again necessary.

Let us now turn to the sufficiency of the inequality in the theorem. Since d_0, d_1 and d_2 are all nonnegative, $Z(s)$ has no poles in the open right-half plane. If the inequality is satisfied, it follows that (A2) holds, which implies that $f(x) \geq 0$ for all x. Hence, $\text{Re}[Z(j\omega)] \geq 0$ for all $j\omega$ values that are not poles of $Z(s)$. To complete the proof we need to check the residue condition for all cases in which $Z(s)$ has poles on the imaginary axis, or infinity.

Case 1. Poles at the origin. This situation occurs when $d_2 \geqslant 0$, $d_1 \geqslant 0$ and $d_0 = 0$, in which case

$$Z_0 = \lim_{s \to 0} \frac{s(a_2 s^2 + a_1 s + a_0)}{s(d_2 s + d_1)} = \frac{a_0}{d_1}$$

when $d_1 > 0$. If $d_1 = 0$ and $d_2 > 0$, the inequality in the theorem $\Rightarrow a_0 = 0$ and $Z_0 = a_1/d_2$. In each case $Z_0 \geqslant 0$.

Case 2. Poles at infinity. This occurs when $d_2 = 0$, $d_1 \geqslant 0$ and $d_0 \geqslant 0$, in which case

$$Z_\infty = \lim_{s \to \infty} \frac{a_2 s^2 + a_1 s + a_0}{s(d_1 s + d_0)} = \frac{a_2}{d_1}$$

when $d_1 > 0$. If $d_1 = 0$, the inequality in the theorem $\Rightarrow a_2 = 0$ and $Z_\infty = a_1/d_0$. In each case, $Z_\infty \geqslant 0$.

Case 3. Poles on the imaginary axis with finite positive modulus. This occurs when $d_2 > 0$, $d_1 = 0$ and $d_0 > 0$, in which case

$$Z_{j\omega_0} = \lim_{s \to j\omega_0 = j\sqrt{d_0/d_2}} (s - j\omega_0) \frac{a_2 s^2 + a_1 s + a_0}{d_2 s^2 + d_0}$$

$$= \frac{a_0 d_2 - a_2 d_0 + j\sqrt{d_2 d_0}\, a_1}{2 j d_2 \sqrt{d_0 d_2}}.$$

Since $d_1 = 0$, it follows from the inequality in the theorem that $a_0 d_2 = a_2 d_0$ and so $Z_{j\omega_0} = a_1/2d_2 \geqslant 0$. A similar calculation also shows that $Z_{-j\omega_0} = a_1/2d_2 \geqslant 0$.

References

[1] Sharp, R. S., 1971, "The Stability and Control of Motorcycles," J. Mech. Eng. Sci., **13**(5), pp. 316–329.

[2] Sharp, R. S., 1994, "Vibrational Modes of Motorcycles and Their Design Parameter Sensitivities," *Vehicle NVH and Refinement, Proc Int Conf.* Mech. Eng. Publications, London, May 3–5, pp. 107–121.

[3] Limebeer, D. J. N., Sharp, R. S., and Evangelou, S., 2001, "The stability of motorcycles under acceleration and braking," Proc. Inst. Mech. Eng., Part C: J. Mech. Eng. Sci., **215**(9), pp. 1095–1109.

[4] Koenen, C., 1983, "The Dynamic Behaviour of Motorcycles When Running Straight Ahead and When Cornering," Ph.D. dissertation, Delft University of Technology.

[5] Sharp, R. S., and Limebeer, D. J. N., 2001, "A Motorcycle Model for Stability and Control Analysis," Multibody Syst. Dyn., **6**(2), pp. 123–142.

[6] Cossalter, V., and Lot, R., 2002, "A Motorcycle Multi-Body Model for Real Time Simulations Based on the Natural Coordinates Approach," Veh. Syst. Dyn., **37**(6), pp. 423–447.

[7] Sharp, R. S., 2001, "Stability, Control and Steering Responses of Motorcycles," Veh. Syst. Dyn., **35**(4–5), pp. 291–318.

[8] Sharp, R. S., Evangelou, S., and Limebeer, D. J. N., 2003, "Improved Modelling of Motorcycle Dynamics," *ECCOMAS Thematic Conference on Advances in Computational Multibody Dynamics*, J. Ambrósio, ed., Lisbon, July 1–4, Paper No. MB2003-029 (CD-ROM).

[9] Sharp, R. S., Evangelou, S., and Limebeer, D. J. N., 2004, "Advances in the Modelling of Motorcycle Dynamics," Multibody Syst. Dyn., **12**(3), pp. 251–281.

[10] Limebeer, D. J. N., Sharp, R. S., and Evangelou, S., 2002, "Motorcycle Steering Oscillations Due to Road Profiling," ASME J. Appl. Mech., **69**(6), pp. 724–739.

[11] Döhring, E., 1956, "Steering Wobble in Single-Track Vehicles," ATZ, **58**(10), pp. 282–286.

[12] Eaton, D. J., 1973, "Man-Machine Dynamics in the Stabilization of Single-Track Vehicles," Ph.D. dissertation, University of Michigan.

[13] Watanabe, Y., and Yoshida, K., 1973, "Motorcycle Handling Performance for Obstacle Avoidance," *2nd Int. Congress on Automotive Safety*, San Francisco.

[14] Jennings, G., 1974, "A Study of Motorcycle Suspension Damping Characteristics," SAE Paper No. 740628.

[15] Roe, G. E., and Thorpe, T. E., 1976, "A Solution of the Low-Speed Wheel Flutter Instability in Motorcycles," J. Mech. Eng. Sci., **18**(2), pp. 57–65.

[16] Verma, M. K., 1978, "Theoretical and Experimental Investigation of Motorcycle Dynamics," Ph.D. dissertation, University of Michigan.

[17] McKibben, J. S., 1978, "Motorcycle Dynamics – Fact, Fiction and Folklore," SAE Paper No. 780309.

[18] Aoki, A., 1979, "Experimental Study on Motorcycle Steering Performance," SAE Paper No. 790265.

[19] Weir, D. H., and Zellner, J. W., 1979, "Experimental Investigation of the Transient Behaviour of Motorcycles," SAE Paper No. 790266.

[20] Thomson, B., and Rathgeber, H., 1984, "Automated Systems Used for Rapid and Flexible Generation of System Models Exemplified by a Verified Passenger Car and a Motorcycle Model," *Dynamics of Vehicles on Roads and on Railway Tracks*, J. K. Hedrick, ed., Swets and Zeitlinger, Lisse, pp. 645–654.

[21] Bayer, B., 1988, "Flattern und Pendeln bei Krafträdern," Auto. Indust., **2**, pp. 193–197.

[22] Takahashi, T., Yamada, T., and Nakamura, T., 1984, "Experimental and Theoretical Study of the Influence of Tires on Straight-Running Motorcycle Weave Response," Paper No. SAE 840248.

[23] Otto, W. M., 1980, "Effect of Motorcycle Accessories on Stability," *Proc. International Motorcycle Safety Conference*, Linthicum, MD May, Motorcycle Safety Foundation, Washington, DC, pp. 1560–1581.

[24] Sugizaki, M., and Hasegawa, A., 1988, "Experimental Analysis of Transient Response of Motorcycle Rider Systems," SAE 881783.

[25] Biral, F., Bortoluzzi, D., Cossalter, V., and Da Lio, M., 2003, "Experimental Study of Motorcycle Transfer Functions for Evaluating Handling," Veh. Syst. Dyn., **39**(1), pp. 1–26.

[26] Foale, T., (2002), "Motorcycle Handling and Chassis Design—The Art and Science," available at http://www.tonyfoale.com

[27] Sharp, R. S., and Alstead, C. J., 1980, "The Influence of Structural Flexibilities on the Straight Running Stability of Motorcycles," Veh. Syst. Dyn., **9**(6), pp. 327–357.

[28] Spierings, P. T. J., 1981, "The Effects of Lateral Front Fork Flexibility on the Vibrational Modes of Straight-Running Single-Track Vehicles," Veh. Syst. Dyn., **10**(1), pp. 21–35.

[29] Wakabayashi, T., and Sakai, K., 2004, "Development of Electronically Controlled Hydraulic Rotary Steering Damper for Motorcycles," *International Motorcycle Safety Conference*, IFZ, Munich, pp. 1–22.

[30] Smith, M. C., 2002, "Synthesis of Mechanical Networks: The Inerter," IEEE Trans. Autom. Control, **47**(10), pp. 1648–1662.

[31] Smith, M. C., 2001, "Force-Controlling Mechanical Device," patent pending, International Application No. PCT/GB02/03056, July 4.

[32] Shearer, J. L., Murphy, A. T., and Richardson, H. H., 1967, *Introduction to System Dynamics*, Addison-Wesley, Reading, MA.

[33] Anderson, B. D. O., and Vongpanitlerd, S., 1973, *Network Analysis and Synthesis*, Prentice-Hall, Englewood Cliffs, NJ.

[34] Newcomb, R. W., 1966, *Linear Multiport Synthesis*, McGraw-Hill, New York.

[35] Valkenburg, M. E. V., 1960, *Introduction to Modern Network Synthesis*, Wiley, New York.

[36] Foster, R. M., and Ladenheim, E. L., 1963, "A Class of Biquadratic Impedances," IEEE Trans. Circuit Theory, **10**, pp. 262–265.

[37] Smith, M. C., and Wang, F.-C., 2004, "Performance Benefits in Passive Vehicle Suspensions Employing Inerters," Veh. Syst. Dyn., **42**(4), pp. 235–257.

[38] de Vries, E. J. H., and Pacejka, H. B., 1998, "The Effect of Tyre Modeling on the Stability Analysis of a Motorcycle," *Proc. AVEC'98*, SAE of Japan, Nagoya, pp. 355–360.

[39] de Vries, E., and Pacejka, H., 1998, "Motorcycle Tyre Measurements and Models," Proc. 15th IAVSD Symposium on the Dynamics of Vehicles on Roads and on Tracks, L. Palkovics, ed., Budapest, August 25–29 1997, Veh. Syst. Dyn., **28**(Suppl.), pp. 280–298.

[40] Pacejka, H. B., 2002, *Tyre and Vehicle Dynamics*, Butterworth Heinemann, Oxford.

[41] Tezuka, Y., Ishii, H., and Kiyota, S., 2001, "Application of the Magic Formula Tire Model to Motorcycle Maneuverability Analysis," JSAE Rev., **22**, pp. 305–310.

[42] Cossalter, V., Doria, A., Lot, R., Ruffo, N., and Salvador, M., 2003, "Dynamic Properties of Motorcycle and Scooter Tires: Measurement and Comparison," Veh. Syst. Dyn., **39**(5), pp. 329–352.

[43] Evangelou, S., 2004, "The Control and Stability Analysis of Two-Wheeled Road Vehicles," Ph.D. thesis, Imperial College, London.

[44] Anon, , 1998, *Autosim* 2.5+ *Reference Manual*, Mechanical Simulation Corp., Ann Arbor, http://www.carsim.com

[45] Green, M., and Limebeer, D. J. N., 1995, *Linear Robust Control*, Prentice-Hall, Englewood Cliffs, NJ.

[46] Papageorgiou, C., and Smith, M. C., 2004, "Positive Real Synthesis Using Matrix Inequalities for Mechanical Networks: Application to Vehicle Suspension," *43rd IEEE Conference on Decision and Control*, Dec. 14–17.

[47] Dorf, R. C., and Bishop, R. H., 2001, *Modern Control Systems*, Prentice-Hall, Englewood Cliffs, NJ.

[48] Evangelou, S., Limebeer, D. J. N., Sharp, R. S., and Smith, M. C., 2005, "Mechanical Steering Compensators for High-Performance Motorcycles," Cambridge Engineering Department, Tech. Report No. CUED/F-INFENG/TR 535.

[49] The Mathworks Inc., 2000, *MATLAB 6 Reference Manual* http://www.mathworks.com

X. Guo

A. Y. T. Leung[1]
e-mail: bcaleung@cityu.edu.hk

Department of Building and Construction,
City University of Hong Kong,
Hong Kong, China

H. Jiang
Department of Mechanical and Aerospace Engineering,
Arizona State University,
Tempe, AZ 85287-6106

X. Q. He
Department of Building and Construction,
City University of Hong Kong,
Hong Kong, China

Y. Huang
Department of Mechanical and Industrial Engineering,
University of Illinois at Urbana-Champaign,
1206 West Green Street,
Urbana, IL 61801

Critical Strain of Carbon Nanotubes: An Atomic-Scale Finite Element Study

This paper employs the atomic-scale finite element method (AFEM) to study critical strain of axial buckling for carbon nanotubes (CNTs). Brenner et al. "second-generation" empirical potential is used to model covalent bonds among atoms. The computed energy curve and critical strain for (8, 0) single-walled CNT (SWNT) agree well with molecular dynamics simulations. Both local and global buckling are achieved, two corresponding buckling zones are obtained, and the global buckling behavior of SWNT with a larger aspect ratio approaches gradually to that of a column described by Euler's formula. For double-walled CNTs with smaller ratio of length to outer diameter, the local buckling behavior can be explained by conventional shell theory very well. AFEM is an efficient way to study buckling of CNTs. [DOI: 10.1115/1.2198548]

Introduction

By atomic force microscope, Falvo et al. observed reversible high-strain deformation and periodic buckling of multiwalled carbon nanotubes (MWNT) [1]. Examining slices of MWNT embedded within a polymeric film by transmission electron microscopy, Lourie et al. reported experimental results of various deformation and fracture modes under compression [2]. To investigate buckling behavior of carbon nanotubes (CNTs), extensive theoretical research has been carried out. In general, the widely used theoretical methods can be divided into atomistic-based methods and continuum mechanics. Using molecular dynamics (MD), Yakobson et al. found that single-walled CNT (SWNT) switches into different morphological patterns when subject to large deformation [3]. Srivastava et al. investigated axial compression of SWNT using generalized tight-binding MD [4]. By MD simulation, Xiao et al. [5] and Liew et al. [6] studied instability of CNTs under axial compression, Sears and Batra [7] and Wang et al. [8] investigated critical strain for global and local buckling of CNTs, and further, Liew et al. [9] simulated the critical strain and buckling loads of CNT bundles. The atomistic-based methods are currently limited to very small length and time scales, due to insufficient computing power [6,9,10]. Several elasticity models can be comparatively easily used. Pantano et al. presented a nonlinear structural mechanics model and studied wrinkling of MWNT [11]. Based on explicit formula for the van der Waals (vdW) interaction between any two layers of MWNT, He et al. established a shell buckling model [12] and Kitipornchai et al. studied buckling behavior of triple-walled CNTs embedded in an elastic matrix [13]. In the above continuum models, interatomic potential is not employed directly and multibody interactions cannot be considered accurately, so the behavior of discrete atoms and concrete configuration of CNT can hardly be achieved. Huang and his colleagues proposed a three-dimensional atomic-scale finite element method (AFEM) [14,15]. Using interatomic potential to consider the multibody interactions, AFEM is as accurate as molecular mechanics simulation. It is much faster than molecular mechanics because it uses the first and second order of derivative of total energy, while molecular mechanics employs the conjugate gradient method, which only uses its first order of derivative.

This paper employs AFEM to study critical strain of axial buckling for CNTs. The achieved energy curve and critical strain for (8, 0) SWNT agree well with recent MD simulations, which verifies the application of AFEM to study buckling of CNTs. It is found that there are two kinds of buckling: local and global. With the aspect ratio (ratio of length to diameter) increasing, CNTs first locally buckle and then globally buckle. The local and global buckling zones can be searched in detail, and the critical strain shows different characteristics in two zones. The global buckling behavior of SWNT with a larger aspect ratio can be explained by Euler's buckling formula for column. For double-walled CNTs (DWNTs) with smaller ratio of length to outer diameter, the local buckling behavior is consistent with conventional shell theory.

Potential Function and AFEM for CNTs

As for the CNTs, covalent bonds among atoms can be modeled according to Brenner et al. "second-generation" empirical potentials [16]. For SWNT, covalent bonds are dominant interaction, so in the following simulations on SWNT, vdW interaction is not considered. For MWNT, vdW interaction is expressed according

[1]Author to whom correspondence should be addressed.

Contributed by the Applied Mechanics Division of ASME for publication in the JOURNAL OF APPLIED MECHANICS. Manuscript received September 30, 2005; final manuscript received February 22, 2006. Review conducted by R. M. McMeeking. Discussion on the paper should be addressed to the Editor, Prof. Robert M. McMeeking, Journal of Applied Mechanics, Department of Mechanical and Environmental Engineering, University of California—Santa Barbara, Santa Barbara, CA 93106-5070, and will be accepted until four months after final publication of the paper itself in the ASME JOURNAL OF APPLIED MECHANICS.

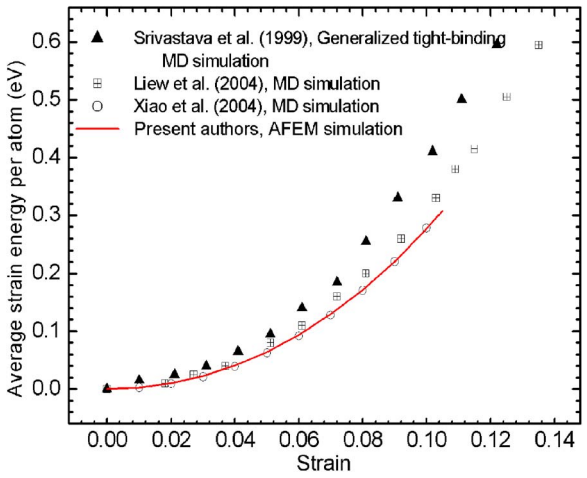

Fig. 1 Comparison among the strain energy curves for (8, 0) SWNT

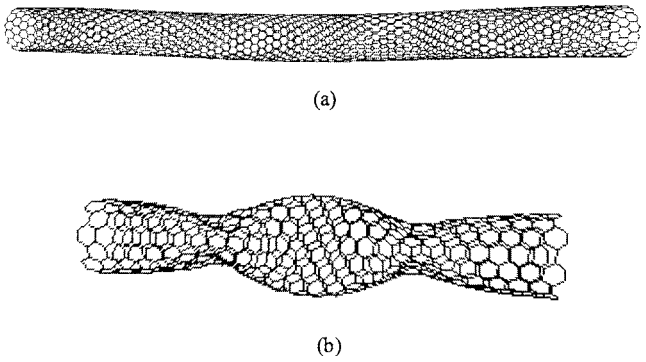

Fig. 2 (*a*) Morphology of (16, 0) SWNT after global buckling, (*b*) morphology of (7, 7) SWNT after local buckling. Two kinds of buckling for CNTs with different aspect ratios.

to the Lennard-Jones 12-6 model [17] and is taken as a nonlinear spring when the distance between two carbon atoms in the different layer is less than the cutoff radius.

In AFEM for CNTs proposed by Huang and his colleagues [14,15], the AFEM element consists of ten atoms because each carbon atom has three nearest-neighboring atoms and six second nearest-neighboring atoms. A schematic diagram of AFEM element, the associated element stiffness matrix, and the nonequilibrium force vector are therein [14,15]. Such an element captures the interactions among the central atom and other atoms. The number of nonzero entries in the global stiffness matrix K is of order N, so is the computational effort to solve $Ku=P$, while the conjugate gradient method widely used in atomistic studies is of order N^2.

Simulation on Buckling of CNTs

Consider an initial equilibrium configuration of CNT. Unless direct specification, one end of the CNT is fixed and the in-plane displacements of the other end are prohibited in our paper. An axial displacement can be applied to compress it, and AFEM can be performed to obtain new equilibrium configuration; then a further displacement can be applied. It deforms linearly when the strain is small. With the strain increasing, the stiffness matrix will lose positive definiteness at a certain point, which is the critical strain for axial buckling. The post-buckling configuration of CNT can also be achieved. All calculation is performed by ABAQUS via its UEL subroutine [18].

First, we study axial buckling of a (8, 0) zigzag SWNT, with length 4.07 nm and diameter 0.63 nm. The average strain energy per atom is calculated as the difference in the average energy per atom in the strained and unstrained system as a function of strain shown in Fig. 1. In Srivastava et al. [4], its structural deformation strained at 0.12 in the generalized tight-binding MD is completely spontaneous and leads to plastic collapse. By MD simulation using Brenner et al. "second-generation" empirical potential, Xiao et al. investigated nonlinear elastic properties and instability of SWNT under axial compression and found that (8, 0) SWNT can deform elastically to the strain 0.10 [5], while Liew et al. have shown that it can be compressed up to a strain 0.135 before buckling [6]. In our AFEM simulation, the critical strain is 0.105. For comparison, the strain energy curves of Srivastava et al. [4], Xiao et al. [5], and Liew et al. [6] are compared in Fig. 1. It can be easily found that our energy curve approaches theirs closely. Especially, the energy curve of Xiao et al. and ours almost coincide with each other. Srivastava et al. used the tight-binding MD scheme of Menon et al. [19], resulting in the highest strain energy in comparison to the others. Although the same Brenner et al. potential was employed in Liew et al., that their SWNT is a bit longer explains the slight difference. Thus, the application of AFEM to study the critical strain of axial buckling for CNTs is verified. The time needed really depends on the applied total displacement step size and the initial step size. Here only tens of seconds are needed to achieve the final critical strain 0.105. To show the effect of the boundary condition on the buckling behavior, we still keep one end of the (8, 0) SWNT fixed, but allow for the in-plane displacement at the other end. It is found that the new boundary conditions almost do not affect the strain energy, but reduce the critical strain to 0.03, less than one-third of the former one. The phenomenon that the release of the constraint will facilitate the buckling is consistent with the continuum mechanics.

As for CNT, there are two kinds of buckling. The first one is column buckling, where CNT approximately keeps the circular cross section and buckles sideways as a whole. The second one is shell buckling, where CNT buckles with lobes and half waves along the tube and the axis remains straight. It was the same with Wang et al. [8], the former and latter is named the global buckling and local buckling, respectively. For a (16, 0) zigzag SWNT, with length 17.1 nm and diameter 1.254 nm, by MD simulation, Sears and Batra found that critical strain is 0.02784 and it is global buckling [7]. In our AFEM simulation, its critical strain is 0.029, which represents 4.2% relative error with theirs, and it is also global buckling, shown in Fig. 2(*a*) [20]. In our AFEM simulation on a (7, 7) armchair SWNT, with length 6 nm and diameter 0.95 nm under axial compression, there is local buckling in good agreement with MD simulation of Yakobson et al. [3]. Its morphology after buckling is shown in Fig. 2(*b*) [20].

Figure 3 shows the various critical strains ε_{cr} of (5, 5), (10, 10), and (15, 15) armchair SWNTs at different length l, while their aspects ratios change from <5 to >20. It is obvious that the shorter SWNTs buckle locally and the longer ones buckle globally. There is an inflexion point in each curve of Fig. 3, and the aspect ratio is 7.1, 12.0, and 14.4, while the corresponding length is 4.788 nm, 16.35 nm, and 29.39 nm, respectively. With the diameter increasing, the length associated with inflexion point increases and so does the local buckling zone. The MD simulation of Wang et al. shows the length associated with its inflexion point for (10, 10) SWNT is 15.79 nm [8], and the result in our AFEM simulation has $<4\%$ relative error with theirs. In the local buckling zone, the critical strain decreases very slowly. In the global buckling zone, the critical strain first decreases fast, and then decreases slowly when the length is comparatively larger, which is consistent with MD simulation of Liew et al. [6]. Thus, to show this important characteristic of critical strain in the global buckling zone, the exponential decay function is chosen to fit the corresponding data, i.e.,

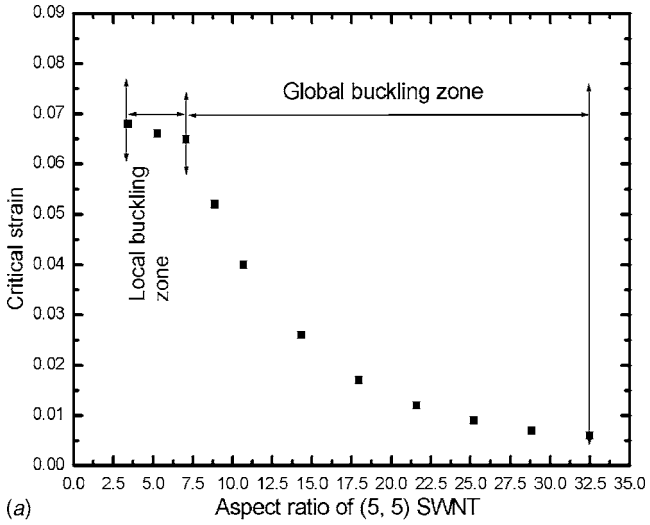

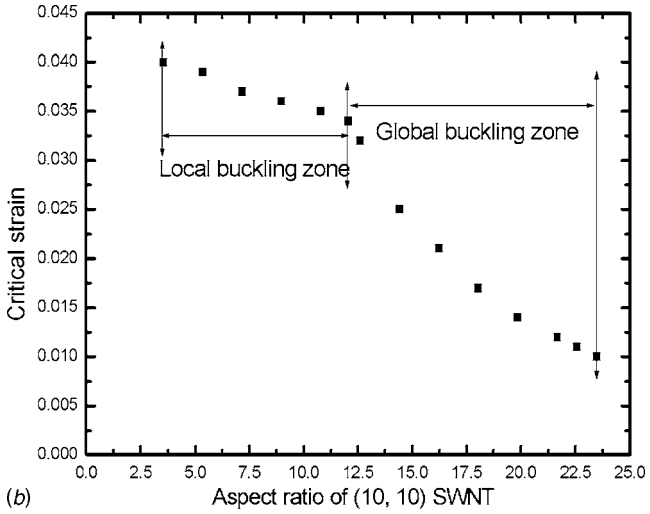

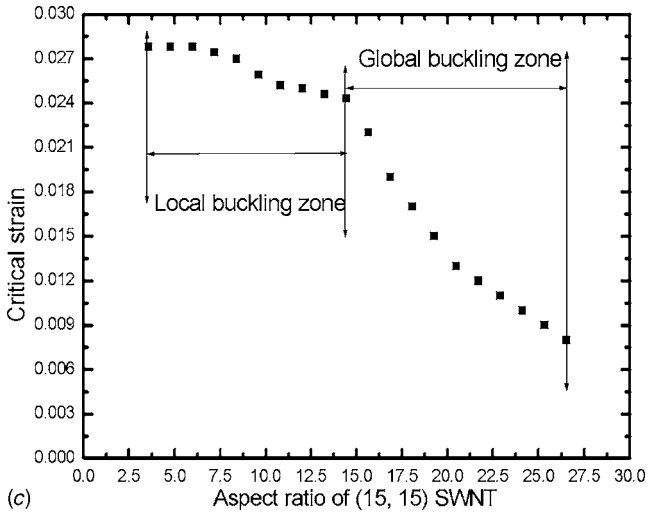

Fig. 3 Critical strain versus aspect ratio for (*a*) (5, 5) SWNT with diameter of 0.678 nm, (*b*) (10, 10) SWNT with diameter of 1.357 nm, and (*c*) (15, 15) SWNT with diameter of 2.036 nm

$$\varepsilon_{cr} = C + A\exp\left(-\frac{l}{B}\right) \tag{1}$$

where A, B, and C are fitting parameters. $1/B$ shows the decay of critical strain ε_{cr} with the length l, so it is named as decay rate.

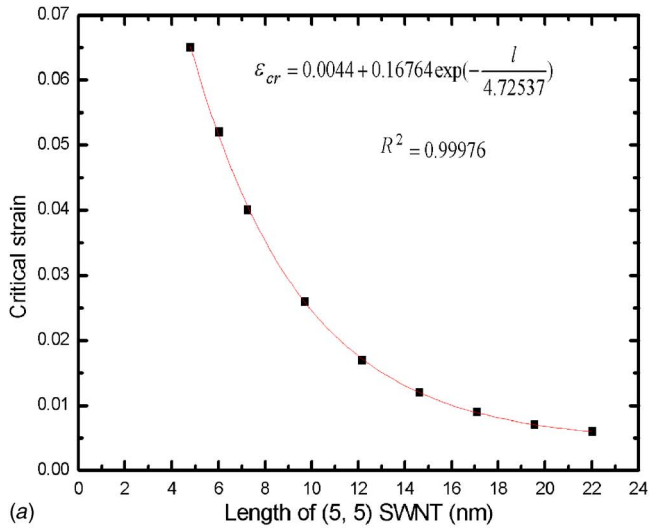

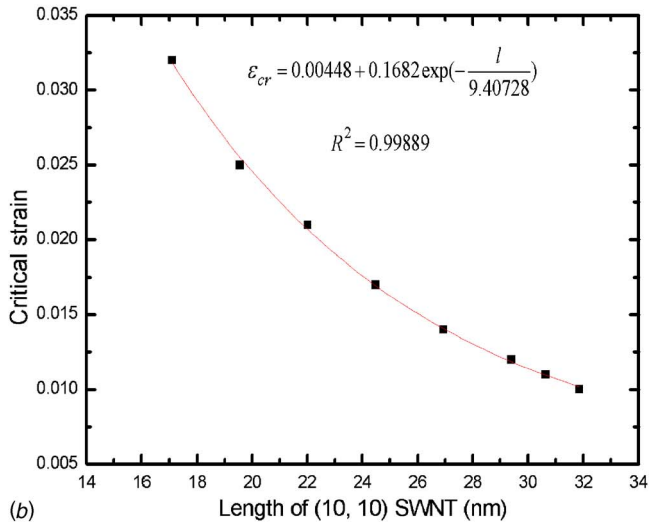

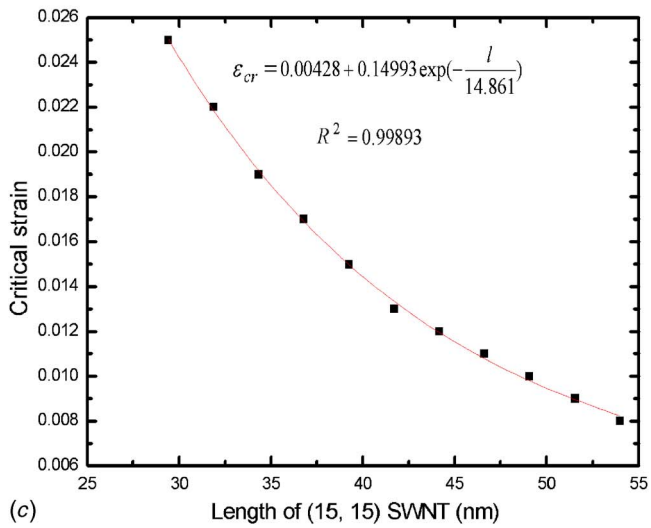

Fig. 4 Critical strain and fitting result by Eq. (1) for global buckling of (*a*) (5, 5), (*b*) (10, 10), and (*c*) (15, 15) SWNTs with different length

The fitting curves and the associated correlation coefficients are shown in Fig. 4. From Fig. 4, it can be found that Eq. (1) fits the data very well. With the diameter increasing, B increases, and so

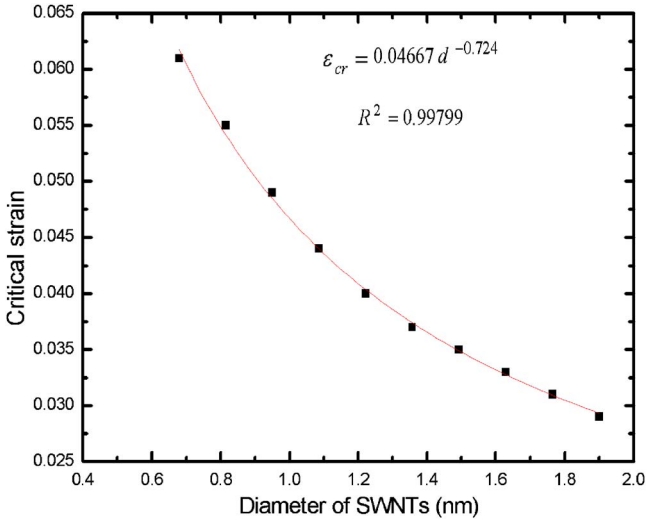

Fig. 5 Critical strain versus the diameter of SWNT with approximate aspect ratio of 7.6

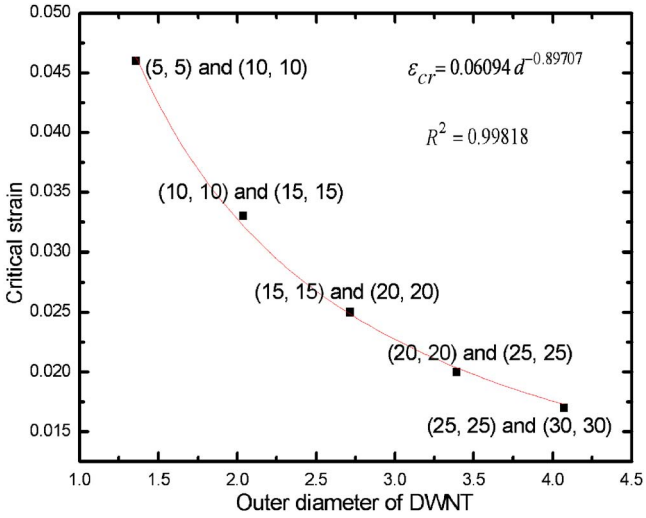

Fig. 6 Critical strain versus the outer diameter of DWNT. The ratio of length to the corresponding outer diameter is kept as ~4.5

the decay rate decreases, which is because, for SWNT with larger diameter, more length is needed to realize the same change of aspect ratio.

As shown in Fig. 2(*a*), the morphology of CNT after global buckling is similar to the buckled column, and quantitative discussion on the critical strain is performed as follows. According to Euler's formula, the critical strain ε_{cr} of column with both ends built in is given by [21]

$$\varepsilon_{cr} = \frac{4\pi^2 I}{Al^2} \tag{2}$$

where A is the cross-sectional area and I is moment of inertia of the column. Equation (2) shows that the critical strain ε_{cr} will be inversely proportional to the square of the length, given the constant A and I. As shown in Fig. 3, the data associated with global buckling are the right part of whole curve; thus, a power function with a shift term is chosen to fit the data in Fig. 4, i.e.,

$$\varepsilon_{cr} = al^b + c \tag{3}$$

where a, b, c are fitting parameters. It is found that Eq. (3) can also fit each curve in Fig. 4 very well and all correlation coefficients are larger than 0.997. b is −1.01412, −1.44938, and −1.62841; thus, the critical strain ε_{cr} is linearly related to the length to power of −1.01412, −1.44938, and −1.62841 for (5, 5), (10, 10), and (15, 15) SWNT, respectively. With the diameter increasing, number of the atoms in each circumference increase, and b approaches to −2.0 gradually, which shows that the global buckling behavior of SWNT with a larger aspect ratio approaches gradually to that of a column described by Euler's formula.

For armchair SWNTs with an approximate fixed aspect ratio 7.6, the relationship between critical strain in our AFEM simulation and the diameter is shown in Fig. 5. From Fig. 5, it is observed that as the diameter increases, the critical strain decreases. The power function is used to fit the critical strain, and it is found that the critical strain is inversely proportional to the diameter to power of 0.724.

Finally, we employ AFEM to study buckling behavior of DWNTs. They are (5, 5) and (10, 10), (10, 10) and (15, 15), (15, 15) and (20, 20), (20, 20) and (25, 25), (25, 25) and (30, 30), sequentially. The ratio of length to the corresponding outer diameter is kept as ~4.5. Their critical strain ε_{cr} versus the outer diameter is shown in Fig. 6. It shows that as the length increases, the critical strain decreases. As shown in Fig. 2(*b*), the morphology of CNT after local buckling is similar with the buckled thin shell, and quantitative discussion on the critical strain is performed as follows. For the buckling of a compressed thin shell, the critical strain is [21]

$$\varepsilon_{cr} = \frac{2h}{d\sqrt{3(1-\nu^2)}}\alpha \quad (\alpha = 0.6 - 1) \tag{4}$$

where h is the effective thickness, d is the diameter of the shell, ν is the Poisson's ratio, and α is correction coefficient. Usually, $\alpha = 1$ if it buckles into short longitudinal waves, otherwise it decreases with longer waves. Equation (4) shows that the critical strain will be inversely proportional to the diameter d, given constant effective thickness h. The fitting results on MD simulation of Xiao et al. [5] also reach that same conclusion on the critical strain for shorter SWNTs. Because the ratio of length to the corresponding outer diameter keeps constant, we fit the critical strain with the length in Fig. 6 and found that the critical strain is inversely proportional to the length to power of 0.897. There are different definitions of effective thickness of CNTs [3,11,22–24]. In our above analysis, the effective thickness of different DWNT is assumed as a constant and the DWNT is taken as thin shell. Further considering the vague definition on the diameter of DWNT, the buckling behavior of DWNTs with a smaller ratio of length to outer diameter can be explained very well by the conventional shell theory.

In order to show the effect of the intertube vdW interaction, we study the buckling of the above (5, 5) and (10, 10) DWNT without intertube vdW interaction. It is found that it does not affect the strain energy, but reduces the critical strain to 0.04, which is 15% smaller than the former one. The attractive intertube vdW interaction explains the larger critical strain when the vdW interaction is considered.

Conclusions

This paper employs the atomic-scale finite element method (AFEM) to study critical strain of the axial buckling for SWNTs and DWNTs. Comparison of the energy curve and critical strain for (8, 0) SWNT with MD simulations validates the application of AFEM. There are two kinds of buckling: local and global. With the aspect ratio increasing, SWNT first locally buckles and then globally buckles. With its diameter increasing, the length associated with inflexion point increases, decay rate of critical strain with length in the global buckling zone slows down, and its global buckling behavior gradually approaches that of a column described by Euler's formula. The relationship between critical

strain and the diameter for armchair SWNTs with an approximate fixed aspect ratio is obtained. For DWNTs with smaller ratio of length to outer diameter, the dependence of the critical strain on diameter is explained by conventional shell theory very well. AFEM is much faster in terms of computation because it is within the theoretical framework of the conventional FEM. It is an efficient way to study buckling of CNTs.

Acknowledgment

The research is supported by City University of Hong Kong Grant No. SRG7001824.

References

[1] Falvo, M. R., Clary, G. J., Taylor, R. M., II, Chi, V., Brooks, F. P., Jr., Washburn, S., and Superfine, R., 1997, "Bending and Buckling of Carbon Nanotubes Under Large Strain," Nature (London), **389**, pp. 582–584.
[2] Lourie, O., Cox, D. M., and Wagner, H. D., 1998, "Buckling and Collapse of Embedded Carbon Nanotubes," Phys. Rev. Lett., **81**, pp. 1638–1641.
[3] Yakobson, B. I., Brabec, C. J., and Bernholc, J., 1996, "Nanomechanics of Carbon Tubes: Instabilities Beyond Linear Response," Phys. Rev. Lett., **76**, pp. 2511–2514.
[4] Srivastava, D., Menon, M., and Cho, K., 1999, "Nanoplasticity of Single-Wall Carbon Nanotubes Under Uniaxial Compression," Phys. Rev. Lett., **83**, pp. 2973–2976.
[5] Xiao, T., Xu, X., and Liao, K., 2004, "Characterization of Nonlinear Elasticity and Elastic Instability in Single-Walled Carbon Nanotubes," J. Appl. Phys., **95**, pp. 8145–8148.
[6] Liew, K. M., Wong, C. H., He, X. Q., Tan, M. J., and Meguid, S. A., 2004, "Nanomechanics of Single and Multiwalled Carbon Nanotubes," Phys. Rev. B, **69**, p. 115429.
[7] Sears, A., and Batra, R. C., 2004, "Macroscopic Properties of Carbon Nanotubes From Molecular-Mechanics Simulations," Phys. Rev. B, **69**, p. 235406.
[8] Wang, Y., Wang, X. X., Ni, X. G., and Wu, H. A., 2005, "Simulation of the Elastic Response and the Buckling Modes of Single-Walled Carbon Nanotubes," Comput. Mater. Sci., **32**, pp. 141–146.
[9] Liew, K. M., Wong, C. H., and Tan, M. J., 2006, "Tensile and Compressive Properties of Carbon Nanotube Bundles," Acta Mater., **54**, pp. 225–231.
[10] Liew, K. M., He, X. Q., and Wong, C. H., 2004, "On the Study of Elastic and Plastic Properties of Multi-Walled Carbon Nanotubes Under Axial Tension Using Molecular Dynamics Simulation," Acta Mater., **52**, pp. 2521–2527.
[11] Pantano, A., Parks, D. M., and Boyce, M. C., 2004, "Mechanics of Deformation of Single- and Multi-Wall Carbon Nanotubes," J. Mech. Phys. Solids, **52**, pp. 789–821.
[12] He, X. Q., Kitipornchai, S., and Liew, K. M., 2005, "Buckling Analysis of Multi-Walled Carbon Nanotubes: A Continuum Model Accounting for van der Waals Interaction," J. Mech. Phys. Solids, **53**, pp. 303–326.
[13] Kitipornchai, S., He, X. Q., and Liew, K. M., 2005, "Buckling Analysis of Triple-Walled Carbon Nanotubes Embedded in an Elastic Matrix," J. Appl. Phys., **97**, p. 114318.
[14] Liu, B., Huang, Y., Jiang, H., Qu, S., and Hwang, K. C., 2004, "The Atomic-Scale Finite Element Method," Comput. Methods Appl. Mech. Eng., **193**, pp. 1849–1864.
[15] Liu, B., Jiang, H., Huang, Y., Qu, S., Yu, M. F., and Hwang, K. C., 2005, "Atomic-Scale Finite Element Method in Multiscale Computation With Applications to Carbon Nanotubes," Phys. Rev. B, **72**, p. 035435.
[16] Brenner, D. W., Shenderova, O. A., Harrison, J. A., Stuart, S. J., Ni, B., and Sinnott, S. B., 2002, "A Second-Generation Reactive Empirical Bond Order (Rebo) Potential Energy Expression for Hydrocarbons," J. Phys.: Condens. Matter, **14**, pp. 783–802.
[17] Girifalco, L. A., Hodak, M., and Lee, R. S., 2000, "Carbon Nanotubes, Buckyballs, Ropes, and a Universal Graphitic Potential," Phys. Rev. B, **62**, pp. 13104–13110.
[18] ABAQUS, ABAQUS *Theory Manual and Users Manual*, 2002, version 6.2, Hibbit, Karlsson and Sorensen Inc., Pawtucket, RI.
[19] Menon, M., Richter, E., and Subbaswamy, K. R., 1996, "Structural and Vibrational Properties of Fullerenes and Nanotubes in a Nonorthogonal Tight-Binding Scheme," J. Chem. Phys., **104**, pp. 5875–5882.
[20] Humphrey, W., Dalke, A., and Schulten, K., 1996, "VMD—Visual Molecular Dynamics," J. Mol. Graphics, **14**, pp. 33–38.
[21] Timoshenko, S. P., and Gere, J. M., 1961, *Theory of Elastic Stability*, 2nd ed., McGraw-Hill, New York.
[22] Zhou, X., Zhou, J. J., and Ou-Yang, Z. C., 2000, "Strain Energy and Young's Modulus of Single-Wall Carbon Nanotubes Calculated From Electronic Energy-Band Theory," Phys. Rev. B, **62**, pp. 13692–13696.
[23] Kundin, K. N., Scuseria, G. E., and Yakobson, B. I., 2001, "C_2F, BN, and C Nanoshell Elasticity From Ab Initio Computations," Phys. Rev. B, **64**, p. 235406.
[24] Tu, Z. C., and Ou-Yang, Z. C., 2002, "Single-Walled and Multiwalled Carbon Nanotubes Viewed as Elastic Tubes With the Effective Young's Moduli Dependent on Layer Number," Phys. Rev. B, **65**, p. 233407.

The Underwater Blast Resistance of Metallic Sandwich Beams With Prismatic Lattice Cores

G. J. McShane
V. S. Deshpande
N. A. Fleck[1]

Department of Engineering,
University of Cambridge,
Trumpington Street,
Cambridge, CB2 1PZ, UK

The finite element method is used to evaluate the underwater blast resistance of monolithic beams and sandwich beams containing prismatic lattice cores (Y-frame and corrugated core) and an ideal foam core. Calculations are performed on both free-standing and end-clamped beams, and fluid-structure interaction effects are accounted for. It is found that the degree of core compression in the free-standing sandwich beam is sensitive to core strength, yet the transmitted impulse is only mildly sensitive to the type of sandwich core. Clamped sandwich beams significantly outperform clamped monolithic beams of equal mass, particularly for stubby beams. The Fleck and Deshpande analytical model for the blast response of sandwich beams is critically assessed by determining the significance of cross-coupling between the three stages of response: in stage I the front face is accelerated by the fluid up to the point of first cavitation, stage II involves compression of the core until the front and back faces have an equal velocity, and in stage III the sandwich beam arrests by a combination of beam bending and stretching. The sensitivity of the response to the relative magnitude of these time scales is assessed by appropriately chosen numerical simulations. Coupling between stages I and II increases the level of transmitted impulse by the fluid by 20–30% for a wide range of core strengths, for both the free-standing and clamped beams. Consequently, the back face deflection of the clamped sandwich beam exceeds that of the fully decoupled model. For stubby beams with a Y-frame and corrugated core, strong coupling exists between the core compression phase (stage II) and the beam bending/stretching phase (stage III); this coupling is beneficial as it results in a reduced deflection of the back (distal) face. In contrast, the phases of core compression (stage II) and beam bending/stretching (stage III) are decoupled for slender beams. The significance of the relative time scales for the three stages of response of the clamped beams are summarized on a performance map that takes as axes the ratios of the time scales. [DOI: 10.1115/1.2198549]

1 Introduction

The underwater blast resistance of sandwich beams remains an active research subject of obvious practical importance to the marine industry. The prototypical problem is sketched in Fig. 1, where a planar underwater blast wave impinges the entire sandwich beam. This is representative of the loading on the outermost structure of a ship by a remote explosion. A number of low strength prismatic sandwich cores have been proposed for application in blast resistant sandwich beams, including the Y-frame of Schelde Shipbuilding[2], the corrugated core and the I-core[3]. The overall aim of this study (and that of the recent investigations reviewed below) is to develop sandwich beams whose blast resistance exceeds that of monolithic beams of equal mass.

Fleck and Deshpande [1] and Xue and Hutchinson [2] have used analytical methods and three-dimensional (3D) finite element (FE) simulations, respectively, to demonstrate that sandwich beams have superior shock resistance to monolithic beams. Fleck and Deshpande [1] developed an analytical model for the shock resistance of clamped sandwich beams by separating the response of these beams into three sequential stages comprising the fluid-structure interaction stage I up to the point of first cavitation, the core compression stage II and finally a combined beam bending and stretching stage III. Both studies decoupled the fluid-structure interaction phase from the structural response and employed the Taylor [3] analysis for a free-standing front face-sheet of the sandwich beam to estimate the momentum transmitted into the beam from the underwater blast wave. A detailed examination of the coupling between the fluid-structure interaction and core compression phases by Deshpande and Fleck [4] demonstrated that the Taylor analysis based upon a free-standing front face-sheet typically underestimates the transmitted momentum for sandwich beams comprising cores with high compressive strengths. This additional fluid-structure interaction was used to explain the difference in predictions between the fully-coupled finite element fluid-structure interaction simulations of Rabczuk et al. [5] and the Fleck and Deshpande [1] analytical model.

Deshpande and Fleck [4] tentatively suggested that low strength sandwich cores endow sandwich beams with enhanced underwater blast resistance: they argue that the low strength core causes sandwich action to begin during the core compression phase, and consequently the back face deflection is reduced. This hypothesis could not be confirmed from the free-standing sandwich beam calculations of Deshpande and Fleck [4]: fully coupled fluid-structure interaction simulations of clamped sandwich beams are required in order to investigate this coupling. In a parallel study, Liang et al. [6] investigated the blast resistance of the sandwich beams with a corrugated core and I-core via fully coupled FE fluid-structure interaction simulations. Their calculations also suggest that weak cores can enhance the blast resistance of sandwich beams. However, the reasons for this enhanced performance are

[1]Author to whom correspondence should be addressed.
[2]Royal Schelde, P.O. Box 16 4380 AA Vlissingen, The Netherlands.
[3]Jos. L. Meyer GmbH, I-Core panels, Industriegebiet Süd, D-26871 Papenburg, Germany.

Contributed by the Applied Mechanics Division of ASME for publication in the JOURNAL OF APPLIED MECHANICS. Manuscript received October 20, 2005; final manuscript received February 16, 2006. Review conducted by R. M. McMeeking. Discussion on the paper should be addressed to the Editor, Prof. Robert M. McMeeking, Journal of Applied Mechanics, Department of Mechanical and Environmental Engineering, University of California – Santa Barbara, Santa Barbara, CA 93106-5070, and will be accepted until four months after final publication of the paper itself in the ASME JOURNAL OF APPLIED MECHANICS.

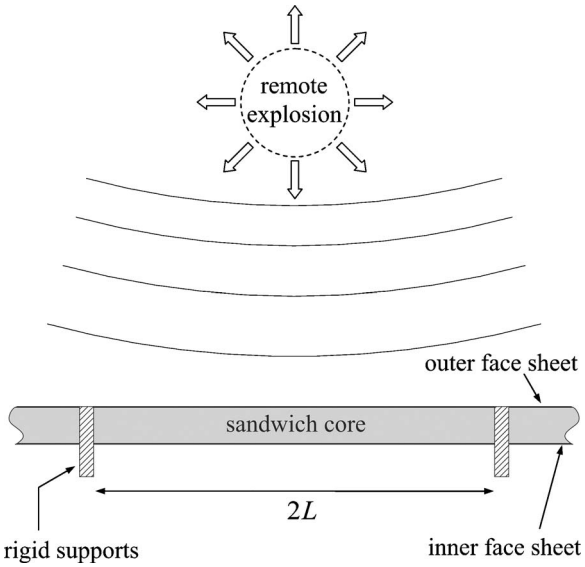

Fig. 1 Schematic of the underwater blast loading of a clamped sandwich beam

unclear from the Liang et al. [6] investigation as the fully coupled simulations are difficult to interpret. In the current study, a set of numerical calculations are reported that switch on and off the coupling between the three stages of response; thereby, the reasons for enhanced performance are determined unambiguously.

Scope of Study

The main aims of this study are:

(i) To compare the underwater blast resistance of sandwich beams with a prismatic Y-frame core, a corrugated core and a foam core of "ideal" strength as defined by Fleck and Deshpande [1], and detailed below.
(ii) To contrast the blast resistance of these sandwich beams with monolithic beams of equal mass.
(iii) To develop an understanding of the effect of cross-coupling between the stages of response in beams with prismatic cores and an ideal foam core. To elucidate this, simulations are performed on both free-standing and end-clamped beams.

The three sandwich cores were chosen in order to span the expected response of a wide range of lattice materials. The Y-frame has a much lower transverse static strength than the corrugated core and ideal foam core, while its longitudinal axial strength and longitudinal shear strength are comparable to those of the other cores. Here the ideal strength foam core with a well-defined isotropic core strength is used solely as a means to clarify the effect of core strength on the sandwich beam response. It gives a useful reference solution by which various topologies can be compared. The ideal strength foam might be representative of stacked cores such as the diamond core [7], and the square honeycomb core [8], but direct comparisons are beyond the scope of the current investigation.

The outline of this paper is as follows. First, the geometries of the sandwich beams are defined. The underwater blast resistance of *free-standing* monolithic and sandwich beams is investigated to determine the transmitted momentum, degree of core compression and the duration of the core compression phase. The use of free-standing beams gives unambiguous results for stages I and II. Next, the fully coupled fluid structure interaction response of *clamped* monolithic and sandwich beams is described. These calculations include stage III. The results for the clamped beams are then contrasted with three sets of decoupled simulations in which we systematically decouple one or more stages of the beam response. Finally, a blast mechanism map is constructed with axes comprising the ratios of the durations of the various phases of beam response.

2 Conceptual Framework

We shall make extensive use of the Fleck-Deshpande [1] framework in order to devise numerical calculations for the sandwich beam response, including a study on the role of overlapping time scales from stage to stage.

Stage I - The Initial Fluid-Structure Interaction Phase. Taylor [3] obtained the solution for a one-dimensional wave in an acoustic fluid impinging a free-standing plate. He demonstrated that fluid cavitation limits the momentum conveyed to the plate; when the plate is light, cavitation occurs early and only a small proportion of the free-wave impulse is transmitted to the plate. Fleck and Deshpande [1] and Xue and Hutchinson [2] followed this approach and similarly computed the momentum transmitted to the sandwich beam by treating the front face of the sandwich beam as a free-standing plate. We briefly review the relevant equations as we shall make use of them below. Consider a representative fluid particle engulfed by a pressure wave traveling at a velocity c_w. The pressure p on the particle of the fluid, of density ρ_w, rises from zero at time $t<0$ to the transient value

$$p = p_0 e^{-t/\theta} \tag{1}$$

for $t \geqslant 0$. Here, p_0 is the peak pressure and θ is the decay constant of the wave. (The values of (p_0, θ) depend upon the details of the underwater explosion.) When this pressure wave hits a stationary rigid plate at normal incidence it imparts an impulse

$$I_0 = 2\int_0^\infty p_0 e^{-t/\theta} dt = 2p_0\theta, \tag{2}$$

to the plate. The factor of 2 arises in (2) due to full reflection of the wave.

If instead, the pressure wave impacts a free-standing plate, the imparted impulse is less than I_0 and can be estimated as follows. When the pressure wave strikes a free-standing plate of thickness h made from a material of density ρ_f, it sets the plate in motion and is partly reflected. The reflected wave causes the pressure in the fluid to drop to zero, and thereby trigger cavitation. This occurs first at the interface between the plate and the fluid after a time

$$\frac{T_1}{\theta} = \frac{1}{\psi - 1} \ln \psi \tag{3}$$

where $\psi \equiv \rho_w c_w \theta/(\rho_f h)$. The momentum per unit area I_t transmitted to the structure is

$$I_t = \zeta I_0, \tag{4a}$$

where

$$\zeta \equiv \psi^{\psi/(1-\psi)} \tag{4b}$$

Fleck and Deshpande [1] assumed that this transmitted impulse imparts a uniform velocity

$$v_0 = I_t/(\rho_f h) \tag{5}$$

to the outer face of the sandwich plate. Now assume some representative values. The sandwich beam has steel faces of density $\rho_f = 7850\ \text{kgm}^{-3}$ and is of thickness $h = 10$ mm. The fluid medium is water of density $\rho_w = 1000\ \text{kgm}^{-3}$ and wave speed $c_w = 1400\ \text{m s}^{-1}$. The primary wave is assumed to possess a decay time $\theta = 0.1$ ms. Then, the fluid-structure interaction parameter has the value $\psi = 1.8$, resulting in a transmitted impulse of $I_t = 0.27 I_0$ from Fig. 4, and a duration of loading $T_1 \approx 0.74\theta = 0.07$ ms via (3).

Stage II–Core Compression Phase. At the start of this phase, the front face has a velocity v_0, while the core and back face are stationary. The finite compressive strength of the core causes the front face to be decelerated and the back face to be accelerated. The final common velocity of the faces and core is dictated by momentum conservation. Fleck and Deshpande [1] derived simple approximate expressions for the degree of core compression and the duration of this phase[4]. They argued that the duration of the core compression phase is

$$T_2 \approx \frac{I_t}{2\sigma_c} \tag{6}$$

where σ_c is the transverse compressive strength of the core. Now substitute some typical values. Upon taking $p_0=100$ MPa for an intense shock, and σ_c in the range 0.5 to 15 MPa, we estimate T_2 to lie in the range 0.1 to 5 ms.

Stage III–Beam Bending and Stretching Phase. At the end of stage II, the sandwich beam has a uniform velocity except for a boundary layer near the supports. The remaining problem to be solved is the classical problem of the impulsive response of a monolithic beam, and Fleck and Deshpande [1] presented an analytical solution by extending the Symmonds [9] analysis to finite deflections. The beam is brought to rest by plastic bending and stretching at a time T_3 given by

$$T_3 \approx L\sqrt{\frac{\rho_{\text{hom}}}{\sigma_{\text{hom}}}} \tag{7}$$

where L is the half-span of the beam and ρ_{hom} and σ_{hom} are the homogenized values of density and longitudinal strength of the beam, respectively. Now consider representative values for the material and geometric parameters. The average axial strength over the cross section of a sandwich beam is of order 60 MPa, and ρ_{hom} is of order 2000 kgm^{-3}. Consequently, T_3 ranges from 5 to 25 ms for beams of half-span 1 to 5 m, respectively.

Fleck and Deshpande [1] derived analytical expressions for the underwater blast response of sandwich beams by assuming that $T_1 \ll T_2 \ll T_3$. With the above choice of physical properties, the three time scales decouple for a slender beam with a strong core. In contrast, the three time scales overlap for a stubby beam with a weak core. We shall investigate the significance of overlapping time scales in some detail below.

2.1 An Hypothesis for the Effect of the Cross-Coupling Between the Stages of Response. It is now argued that the cross-coupling of the three stages of response can be parametrized in terms of the nondimensional groups T_1/T_2 and T_2/T_3 for a sandwich beam. The parameter T_1/T_2 gives a measure of fluid-structure interaction during core compression, while the parameter T_2/T_3 gives a measure of the degree to which beam bending/stretching occurs simultaneously with core compression. Deshpande and Fleck [4] have already investigated the sensitivity of the blast resistance of a free-standing sandwich beam with a foam core to the parameter T_1/T_2. Upon noting that T_1/T_2 is approximately equal to σ_c/p_0 via (3) and (6), we can reinterpret their results for the dependence of transmitted impulse and degree of core crush upon σ_c/p_0. In brief, they noted that the transmitted impulse is almost insensitive to σ_c/p_0 provided this ratio is less than 0.1, while the core compressive strain acquired in stage II is sensitive to σ_c/p_0 over the full range[5]. We conclude that the degree of core crush is much more sensitive to the ratio T_1/T_2 than the level of transmitted impulse.

Define $\bar{w}_p$ as the peak value over the time history of the mid-span back-face deflection, normalized by the corresponding value from a fully decoupled analysis, such as the analytical model of Fleck and Deshpande [1]. In broad terms, we can consider four regimes of behavior for $\bar{w}_p$, depending upon the values of T_1/T_2 and T_2/T_3. These four regimes are summarized in Fig. 2 in the form of a blast mechanism map for the underwater blast response of sandwich beams. The regimes are:

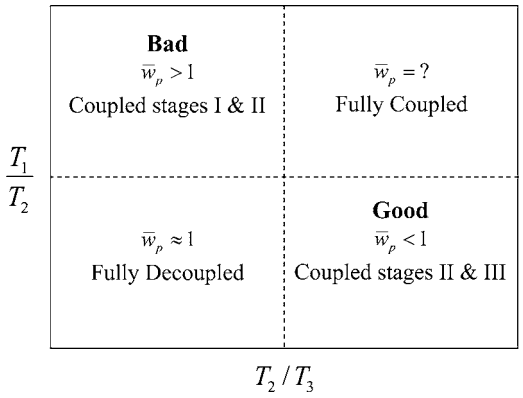

Fig. 2 Schematic of the deformation mechanism map for the underwater blast loading of a sandwich beam. Four regimes of behavior are expected depending on the ratios of the durations of the stages: T_1/T_2 and T_2/T_3. The anticipated values of $\bar{w}_p$ (peak deflection of the beams normalized by the prediction of the decoupled analysis) are included in the sketch.

(i) Low T_1/T_2 and low T_2/T_3, giving $\bar{w}_p \approx 1$. This corresponds to a fully decoupled response from one stage to the next, in the manner assumed by Fleck and Deshpande [1].

(ii) High T_1/T_2 and low T_2/T_3, giving $\bar{w}_p > 1$. Coupling exists between the fluid-structure interaction stage I and the core compression stage II, while the beam bending/stretching phase (stage III) is decoupled. This scenario has already been considered by Deshpande and Fleck [4] for the case of a foam core. They demonstrated that the momentum transmitted into the beam exceeds that predicted by the Taylor analysis (4) based upon a free-standing front face-sheet. In this regime, we expect the beams to undergo larger deflections than that predicted by a decoupled analysis.

(iii) Low T_1/T_2 and high T_2/T_3, giving $\bar{w}_p < 1$. The fluid-structure interaction stage is decoupled from the core compression phase, but the core compression and beam bending and stretching phases are coupled. The response resembles the one-dimensional buffer plate/crushable core as analyzed by Ashby et al. [10]. The front face arrests with little deflection of the back face, and sandwich action (that is, cooperative bending deformation of the faces) does not arise. Consequently, a decoupled analysis is expected to overpredict the back face deflection in this regime.

(iv) High T_1/T_2 and high T_2/T_3. Full coupling exists between all stages and it is difficult to make simplifying approximations. Additional 3D calculations are needed to determine the value of $\bar{w}_p$ in this regime, but this is beyond the scope of this study.

We conclude from the above discussion that the preferred small value of $\bar{w}_p$ is achieved by arranging for a small T_1/T_2 and a high T_2/T_3.

[4]More accurate calculations are reported by Radford et al. [12] but these involve numerical quadratures rather than explicit formulae.

[5]The interested reader is referred to Figs. 14(*a*) and 14(*b*) of Deshpande and Fleck [4].

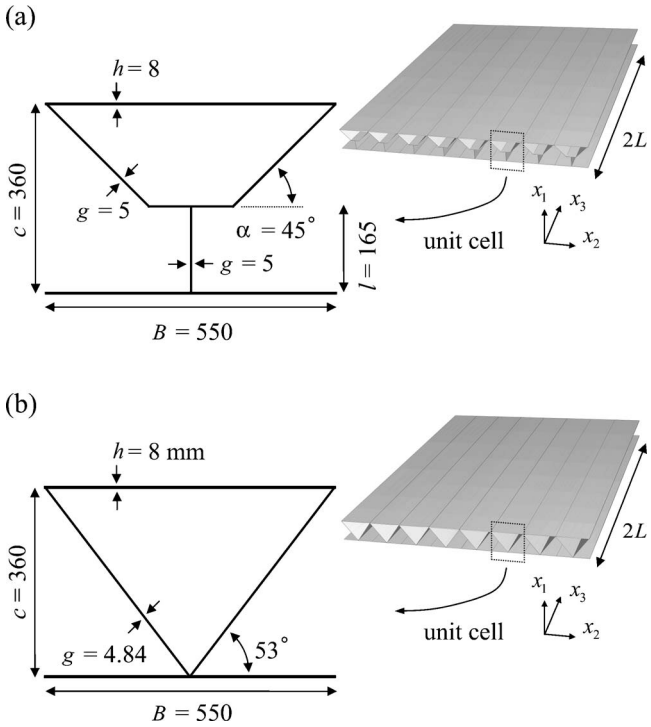

Fig. 3 Sketches of the (*a*) Y-frame (*b*) corrugated core sandwich beams, comprising a large number of repeating units. The prismatic axes of these cores are along the length of the beams. The cross-sectional beam dimensions employed in the FE calculations for the shell reference planes are given in the figure. All dimensions are in millimeters.

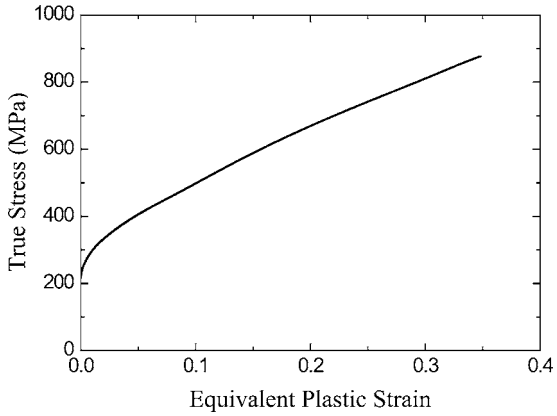

Fig. 4 The uniaxial tensile stress versus strain response of 304 stainless steel as measured by Côté et al. [7,8] and employed in all the calculations reported here

3 Geometry and Material Properties of Sandwich and Monolithic Beams

All beams of span $2L$ are assumed to be made from steel (density of steel $\rho_f = 8000\ \text{kgm}^{-3}$) with a fixed mass per unit area $m_{\text{tot}} = 192\ \text{kgm}^{-2}$, corresponding to a monolithic beam of thickness $d = 24$ mm. The sandwich beams comprise identical front and back face-sheets of thickness $h = 8$ mm and a core of depth $c = 360$ mm. The relative density of the core is $\bar{\rho} = 0.022$. Thus, the only difference between the three types of sandwich beams is the core topology.

The sandwich beams comprise a large number of repeating units, see, for example, the sketches of the Y-frame and corrugated core beams in Figs. 3(*a*) and 3(*b*), respectively. A single unit cell suffices to describe the Y-frame and corrugated core topologies:

(a) The *Y-frame* is sketched in Fig. 3(*a*). It comprises a Y-shaped frame with the prismatic x_3 axis along the beam length. The cross section of the Y-frame is described by the height l of the Y-frame leg, the inclination α of the Y-angles, the thickness g of all the constituent members, the overall core thickness c and the width B of the unit cell. In this study we restrict attention to the Y-frame design as employed by Royal Schelde (the dimensions are detailed in Fig. 3(*a*)).

(b) The *corrugated core* is chosen to ensure a fair comparison between the Y-frame and corrugated core sandwich beams. Both sets of beams have the same overall dimensions, face-sheet thickness, and overall mass. This dictates the sheet thickness of the corrugations to be $g = 4.84$ mm, with a corrugation angle of 53 deg, as sketched in Fig. 3(*b*).

(c) The *ideal foam core*, described as follows. The Y-frame and corrugated cores described above have a relative density (ratio of mass of smeared-out core to the mass of the solid material from which the core is made) of $\bar{\rho} = 0.022$. As a reference case, we also analyze the blast response of a sandwich beam with an "ideal" strength foam core of relative density $\bar{\rho} = 0.022$. As introduced by Fleck and Deshpande [1], this foam core has an isotropic response with a compressive strength $\sigma_c = \bar{\rho}\sigma_Y$, where σ_Y is the yield strength of the solid from which the foam is made and a nominal densification strain $1 - \bar{\rho}$. This is the Voigt upper bound on the strength of the cellular material of relative density $\bar{\rho}$ made from a solid material with yield strength σ_Y. The constitutive response of the foam core is detailed in Sec. 3.1.

In addition to these sandwich beams, a reference *monolithic* steel beam of thickness $d = 24.0$ mm (mass per unit area equal to that of the sandwich beams) is also considered. For each beam geometry, we assume two beam spans: $L = 1$ m and $L = 3$ m.

3.1 Material Properties. The sandwich beams (face-sheets and core) are made from 304 stainless steel of density $\rho_f = 8000\ \text{kgm}^{-3}$. The stainless steel is modeled as a rate independent J2 flow theory solid with Young's modulus $E_s = 210$ GPa, and Poisson's ratio $\nu = 0.3$. The uniaxial tensile true stress versus equivalent plastic strain response of 304 stainless steel has been measured by Côté et al. [7,8] at an applied strain rate of $10^{-3}\ \text{s}^{-1}$, and the measured response is plotted in Fig. 4. This uniaxial tensile curve was assumed in all calculations presented here. Although the actual curve was used, it is clear from Fig. 4 that the material behaves in a bilinear manner, with a Young's modulus of 210 GPa, a yield strength of $\sigma_Y = 217$ MPa and a post-yield linear hardening modulus of $E_t = 2.1$ GPa.

The ideal strength foam core was modeled as a compressible continuum using the metal foam constitutive model of Deshpande and Fleck [11]. Write s_{ij} as the usual deviatoric stress and the von Mises effective stress as $\sigma_e \equiv \sqrt{3 s_{ij} s_{ij}/2}$. The isotropic yield surface for the metal foam is then specified by

$$\hat{\sigma} - Y = 0, \tag{8}$$

where the equivalent stress $\hat{\sigma}$ is a homogeneous function of σ_e and mean stress $\sigma_m \equiv \sigma_{kk}/3$ according to

$$\hat{\sigma}^2 \equiv \frac{1}{1 + (\alpha/3)^2}\left[\sigma_e^2 + \alpha^2 \sigma_m^2\right] \tag{9}$$

The material parameter α denotes the ratio of deviatoric strength to hydrostatic strength, and the normalization factor on the right hand side of relation (9) is chosen such that $\hat{\sigma}$ denotes the stress in

a uniaxial tension or compression test. An over-stress model is employed with the yield stress Y specified by

$$Y = \eta\dot{\hat{\epsilon}}^p + \sigma_c \tag{10}$$

in terms of the viscosity η and the plastic strain-rate $\dot{\hat{\epsilon}}^p$ (work conjugate to $\hat{\sigma}$). The characteristic $\sigma_c(\hat{\epsilon}^p)$ is the static uniaxial stress versus plastic strain relation. Normality of plastic flow is assumed, and this implies that the "plastic Poisson's ratio" $\nu_p = -\dot{\varepsilon}^p_{22}/\dot{\varepsilon}^p_{11}$ for uniaxial compression in the 1-direction is given by

$$\nu_p = \frac{1/2 - (\alpha/3)^2}{1 + (\alpha/3)^2} \tag{11}$$

In the simulations, the ideal strength foam is assumed to have a Young's modulus $E_c = \bar{\rho}E_s$, an elastic Poisson's ratio $\nu = 0.3$, and a plastic Poisson's ratio $\nu_p = 0$ [10]. The static strength σ_c versus equivalent plastic strain $\hat{\varepsilon}^p$ history is taken as

$$\sigma_c = \begin{cases} \bar{\rho}\sigma_Y, & \hat{\varepsilon}^p \leqslant \epsilon_D \\ \bar{\rho}\sigma_Y + E_f(\hat{\varepsilon}^p - \varepsilon_D), & \text{otherwise} \end{cases} \tag{12}$$

where $\epsilon_D \equiv -\ln(\bar{\rho})$ is the logarithmic densification strain beyond which negligible plastic straining of the foam occurs. The viscosity η in the foam core was set to 0.86×10^{-3} MPa s. This ensures that the shock width is approximately $c/10$ for the range of the calculations reported here; see Radford et al. [12] for details of the shock width calculation.

4 Finite Element Calculations

The explicit time integration version of the commercial finite element package ABAQUS was used to calculate the underwater blast response of (i) a free-standing sandwich beam (Fig. 5(*a*)) and (ii) a clamped sandwich beam (Fig. 5(*b*)). Two-dimensional analyses sufficed to investigate the underwater blast response of the free-standing beams. The clamped beam simulations required three-dimensional analyses for the Y-frame and corrugated core beams while two-dimensional plane strain analyses sufficed for the clamped sandwich beams with an ideal strength foam core. Perfect bonding between core and face-sheets is assumed in all sandwich beams. The ABAQUS "general contact" option (which includes self-contact) was used to enforce a hard contact between all surfaces for the lattice cores in order to include the effect of core densification.

The monolithic beams were modeled using four-noded plane strain quadrilaterals (CPE4R in the ABAQUS notation). Typically, ten elements were used in the through-thickness direction of the beam and about 200 elements exist along the beam length.

4.1 The Fluid Column. All calculations were performed using the free-field pressure versus time characteristic (1) with $\theta = 0.1$ ms and p_0 in the range 60 to 180 MPa. The fluid was taken to be water, treated here as an acoustic medium with density $\rho_w = 1.0$ Mg m^{-3}, bulk modulus $E_w = 1.96$ GPa, and wave speed $c_w \equiv \sqrt{E_w/\rho_w} = 1400$ m s^{-1}. The fluid is assumed to be unable to sustain tensile loading, which implies that the cavitation pressure is $p_c = 0$ MPa.

The fluid column (in both the free-standing and clamped beam simulations) was modeled using acoustic elements: eight-node bricks in 3D, and four-node quadrilaterals in the plane strain analyses (AC3D8R and AC2D4R, respectively, in ABAQUS notation). The fluid column represents a semi-infinite fluid in order to model a far field explosion. However, refinement of the mesh in the fluid is necessary to ensure minimal numerical dispersion of the blast wave. As discussed by Sprague [13], it is desirable to have a small fluid-column with the pressure history (1) applied as close to the structure as possible. We thus employ a fluid-column of height $H = 1$ m in all calculations and use the following prescription to ensure minimal reflections from the top of the column,

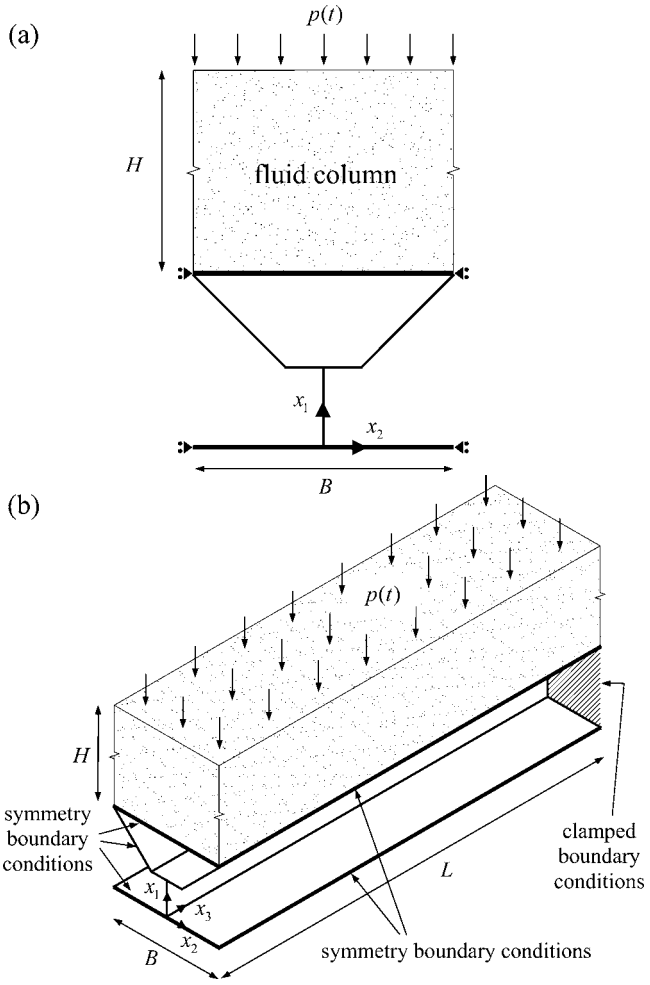

Fig. 5 Boundary value problems analyzed for the underwater blast loading of (*a*) the free-standing and (*b*) the clamped sandwich beam. Only the Y-frame core beams are shown in this figure.

thereby simulating a semi-infinite column.

The fluid column was divided into two equal halves, each of height 0.5 m with a horizontal layer of nodes along the interface. The bottom half in contact with the structure was discretized by elements of height 10 mm and the pressure boundary condition (1) was applied on the surface separating the two halves of the fluid column. The top half of the column was discretized using elements of height 40 mm and an impendence boundary condition

$$\dot{u} = \frac{p}{\rho_w c_w} \tag{13}$$

on the top surface of the column, where $\dot{u}$ is the particle velocity normal to the top surface and p is the fluid pressure. This boundary condition ensures no reflection of the waves from the top surface thereby simulating a semi-infinite column.

The pressure boundary condition (1) was applied to the horizontal layer of nodes separating the two halves of the column, in two steps. Step 1 has duration 0.69 ms and the pressure history (1) is applied throughout this step. The duration of this step is less than the time required for the wave reflected from the structure to reach the horizontal layer of nodes where the pressure boundary condition is specified. In step 2, no pressure was specified on the boundary separating the two halves of the fluid-column. This permits the reflected wave to pass through unimpeded. Note that although we only specify the pressure history (1) for 0.69 ms, 99.9% of the blast impulse is applied in this period since we have

made the choice $\theta=0.1$ ms in all calculations.

This prescription for the fluid column and application of the pressure wave (1) gave excellent agreement between analytically known fluid-structure interaction solutions and the numerical results. For example, the cavitation time and transmitted impulse predicted by the FE simulations were nearly identical to the Taylor [3] prediction for a variety of thicknesses of steel plate.

4.2 Free-Standing Beam Simulations. A sketch of the boundary value problem analyzed to investigate the underwater blast response of free-standing beams is shown in Fig. 5(*a*). In these two-dimensional calculations, the sandwich beam is free to move in the x_1-direction and constrained from motion in the x_2-direction via symmetry boundary conditions. The beams with an ideal foam core were modeled using four-noded quadrilaterals (CPE4R in the ABAQUS notation) in both the faces and core, with about 180 elements in the x_1-direction. The beams with a Y-frame core and a corrugated core were modeled using two-dimensional linear Timoshenko beam elements (B21 in ABAQUS notation) with elements of thickness 8 mm and 10 mm used to discretize each core strut and face-sheet, respectively. The symmetry boundary conditions for the Y-frame core and corrugated core entail zero rotation and zero displacement in the x_2-direction.

4.3 Clamped Beam Simulations. The boundary value problem comprises a clamped beam subjected to a far-field underwater explosion, as sketched in Fig. 5(*b*). Only half of the beam is analyzed and symmetry boundary conditions are specified on the x_1-x_2 plane at midspan ($x_3=0$); the beam (core and face-sheets) is clamped at the other end ($x_3=L$). These fully clamped boundary conditions have been employed in prior investigations (see for example Fleck and Deshpande [1] and Xue and Hutchinson [2]) and are considered appropriate for ship hulls where the bulkhead extends to the outer hull. We note that Liang et al. [6] have employed boundary conditions wherein only the inner face is fixed at the two outer supports. The effect of the choice of boundary conditions on the sandwich beam response is not within the scope of the present investigation, but clearly is important.

The beams with an ideal foam core are again modeled using plane strain elements (approximately 180 and 200 elements in the x_1- and x_3-directions, respectively). The Y-frame and corrugated core beams for the clamped beam analysis were generated in ABAQUS by extruding the respective cross sections (Figs. 3(*a*) and 3(*b*)) to the required lengths. These beams were then discretized using the 3D shell elements (S4R in the ABAQUS notation). Typically, 5500 elements were used to discretize each face-sheet and 11,000 elements were used in the core. In these 3D analyses, symmetry boundary conditions are specified on the x_1-x_3 planes at $x_2=\pm B/2$ in order to represent repeating units of the Y-frame and corrugated core in the x_2-direction (see Fig. 3).

5 Blast Response of Free-Standing Sandwich Beams

We first consider the blast response of free-standing sandwich beams due to an underwater blast wave impinging the front face, as sketched in Fig. 5(*a*). The beams are free to move in the x_1-direction but are constrained from motion in the x_2-direction via symmetry boundary conditions (consistent with the notion that we are analyzing a representative section of a panel comprising a large number of repeating units). Beam bending and stretching (stage III) effects are absent, and we use these calculations to investigate the coupling between stages I and II of the beam response and hence determine the (i) transmitted momentum, (ii) degree of core compression and (iii) times at which stages I and II end.

5.1 Results. The progressive increase in normalized momentum I/I_o of the entire sandwich beam with increasing normalized time t/θ (measured from the instant of the shock wave impinging on the structure) is plotted in Figs. 6(*a*) and 6(*b*) for peak blast pressures $p_o=100$ MPa and 180 MPa, respectively. Each of the

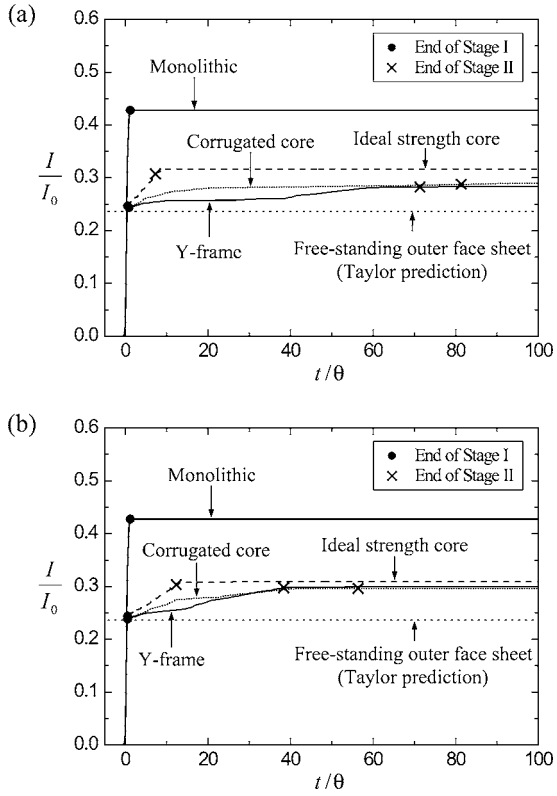

Fig. 6 The time variations of the momenta of the free-standing sandwich and monolithic plates for blast pressures (*a*) $p_0=100$ MPa and (*b*) $p_0=180$ MPa. The Taylor prediction of the final transmitted momentum into the sandwich plate based on a free-standing front face-sheet is also included.

sandwich beams rapidly acquires momentum, followed by a more gradual increase. Finally, the sandwich plate separates from the water and the ensuing momentum remains constant. Stage I of the response ends (by definition at the first cavitation of the water) at $t/\theta\approx 1$ for the monolithic and sandwich beams, while Stage II ends (as defined by the peak core compression being attained) much later at $t/\theta\sim 10-80$ for the various sandwich beams. The end of each stage is marked on the plots of Fig. 6. The beam with an ideal strength core acquires a slightly higher transmitted momentum over a much shorter time than the Y-frame and corrugated core beams. The momentum transmitted into each of the sandwich beams is less than that for a monolithic beam of equal mass but exceeds the Fleck and Deshpande [1] prediction based upon a free-standing front face-sheet.

The through-thickness core compression is related to the average reduction Δc in core thickness by $\epsilon_{fs}(t)\equiv\Delta c/c$, and is plotted in Fig. 7 (the core compression was obtained by averaging the displacements of the front and back faces over the beam width B). For both values of p_0, the Y-frame undergoes the maximum core compression, while the ideal core compresses least. The ends of stages I and II are also in Fig. 7. For each beam, and at both pressure levels, the time to maximum core compression in Fig. 7 defines the duration of stage II and approximates the time for the transmitted momentum to asymptote to the maximum value in Fig. 6. (The end of stage II marked in Fig. 6 corresponds to the time at which this maximum core compression is achieved.)

The effect of the free-field impulse I_0 upon the transmitted impulse I_t/I_0, duration of stage II T_2/θ and degree of core compression $\epsilon_{fs}^{\max}$ are summarized in Fig. 8 for the free-standing beams. These calculations have been performed by varying p_0 with θ held fixed at 0.1 ms. Observe that the normalized transmitted impulse is reasonably independent of the level of blast impulse and is

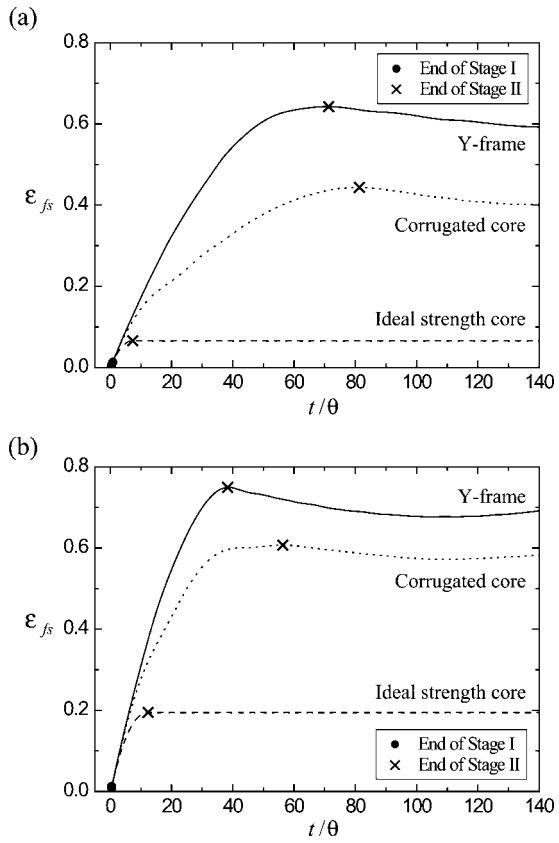

Fig. 7 The time evolution of core compression ε_{fs} in the free-standing sandwich beams for blast pressures (*a*) p_0=100 MPa and (*b*) p_0=180 MPa

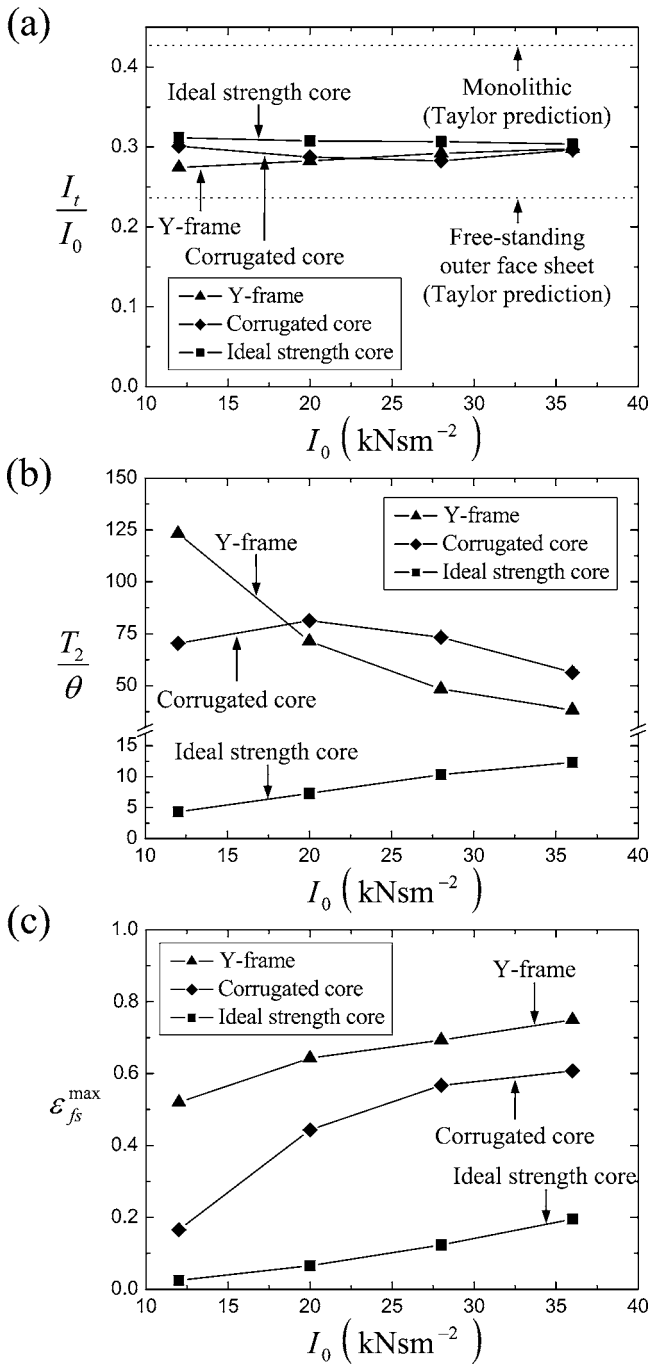

Fig. 8 Finite element predictions of the (*a*) normalized transmitted momentum I_t/I_0, (*b*) normalized duration of core compression T_2/θ and (*c*) peak core compression ε_{fs}^{max} as a function of the blast impulse for free-standing monolithic and sandwich beams

approximately equal for all beams; I_t is intermediate between that predicted for a free-standing front face and that transmitted into a monolithic beam of mass equal to that of the sandwich beam. In contrast, the duration of stage II, T_2, and the core compression strain ϵ_{fs}^{max} are sensitive to the level of applied impulse I_0. Both T_2 and the peak core compression ϵ_{fs}^{max} are much greater for the sandwich beams with corrugated and Y-frame cores than for the sandwich beams with an ideal strength foam core.

Recall that the Taylor analysis predicts a fluid-structure interaction period up to first cavitation in stage I of duration about θ. The present free-standing beam calculations reveal that an additional 20–30% momentum is transmitted during the stage II period of core compression. After first cavitation, the fluid continues to load the structure. The duration of stage II is 5θ–80θ for the corrugated and Y-frame sandwich beams and 5θ–10θ for the ideal strength foam core. Since the duration of stage III scales with the length L of the beam by (7), we anticipate that time-decoupling of stages II and III may not hold for short span corrugated and Y-frame sandwich beams. The significance of this temporal overlap is explored below where we investigate the blast response of clamped sandwich beams.

6 Blast Response of Clamped Sandwich Beams

Consider the underwater blast response of clamped sandwich beams with geometry and material properties described in Sec. 3. The boundary value problem under consideration is sketched in Fig. 5(*b*). A one-dimensional blast wave as defined by (1) loads a clamped sandwich beam. Both the core and the face-sheets of the sandwich beam are fully clamped, as in the analyses of Fleck and Deshpande [1] and Xue and Hutchinson [2]. In order to investigate the coupling between stages II and III of the response, we consider two sandwich configurations with L=1 m and 3 m, and all other parameters are held fixed at the reference values detailed in Sec. 3.

6.1 Fully Coupled Calculations for Clamped Sandwich Beams. The normalized transverse midspan deflections w/L of the back face-sheet of the L=1 m sandwich and monolithic beams (p_0=100 MPa) are plotted in Fig. 9(*a*) as a function of the normalized time $\bar{t}=t/(L\sqrt{\rho_f/\sigma_Y})$, where t is measured from the instant of the shock wave impinging the beams. The corresponding transient mid-span core compression $\epsilon_c(\bar{t})$ is given in Fig. 9(*b*) for the

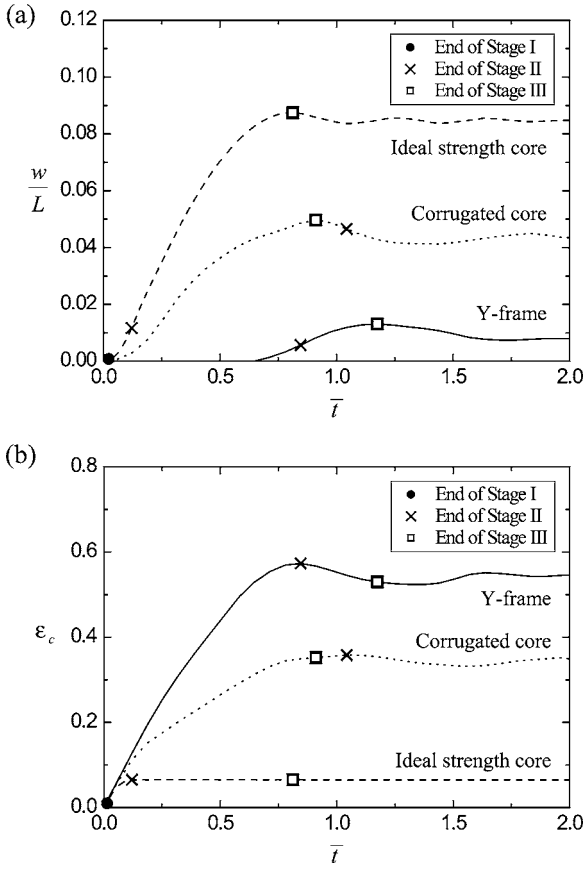

Fig. 9 The time variation of (*a*) normalized deflections of the midspan of the back face *w*/*L* and (*b*) midspan core compression of the *L*=1 m clamped beams subject to a p_0=100 MPa blast. Both the back face deflections and core compressions are obtained by spatially averaging the deflections over the width *B* at the midspans.

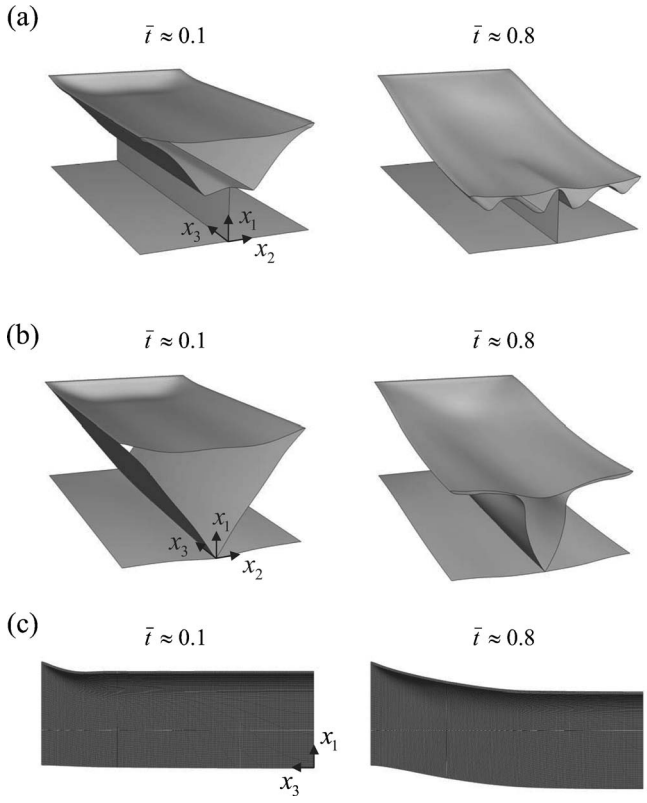

Fig. 10 Finite element predictions of the deformation modes of the *L*=1 m. (*a*) Y-frame, (*b*) corrugated core, and (*c*) ideal strength foam core clamped sandwich beams at $\bar{t} \approx 0.1$ and 0.8 for p_0=100 MPa.

three sandwich beams. Both the back face deflections and core compressions were obtained by averaging the midspan deflections over the width *B* of the sandwich beams. Stage I ends early at $\bar{t} \approx 0.02$ for all three types of sandwich beams. For the beam with an ideal foam core, maximum core compression signifies the end of stage II at $\bar{t} \approx 0.1$ while stage III ends at the point of peak back face deflection at $\bar{t} \approx 0.8$. The stage II response of the beams with a Y-frame and a corrugated core is simultaneous with stage III and ends at $\bar{t} \approx 1.0$. Note the reverse ordering of the three cores in Fig. 9(*a*) and 9(*b*): the Y-frame core has the lowest back face deflection, and this is associated with the largest degree of core crush. This is reminiscent of the behavior noted by Liang et al. [6] for stubby beams with a weak core: their assumed boundary conditions were such that the front face behaved as a flyer plate against the weak core, and produced minimal back face deflection.

The FE predictions of the deformation modes (at two selected values of time $\bar{t}$) of the *L*=1 m sandwich beams subjected to a p_0=100 MPa blast are shown in Fig. 10. The core compression of the Y-frame (Fig. 10(*a*)) is accommodated mainly by the deformation of the webs of the Y-frame while the compression of the corrugated core is more uniform (Fig. 10(*b*)). The ideal strength beams undergo smaller core compression (Fig. 10(*c*)), with almost complete densification near the front face-sheet and nearly no deformation adjacent to the back face-sheet due to the propagation and arrest of a plastic shock wave.

The peak midspan back face deflection w_p/L is plotted as a function of blast impulse I_0 in Fig. 11(*a*) for the *L*=1 m monolithic and sandwich beams. Additionally, the core compressive strain $\epsilon_c^{\max}$ (normalized by the corresponding maximum core compressions in the free-standing sandwich beams $\epsilon_{fs}^{\max}$ of Fig. 8(*c*)) is plotted against I_0 in Fig. 11(*b*); and the time T_3 required to achieve peak back face deflection (normalized by the time T_2 required to achieve maximum core compression in the corresponding free-standing sandwich beam calculations of Fig. 8(*b*)) is plotted against I_0 in Fig. 11(*c*). It is evident from Fig. 11(*a*) that the midspan deflection of the sandwich beams is significantly less than that of the monolithic beam of equal mass. With back face deflection taken as the performance metric, the Y-frame and corrugated core beams have a comparable performance and outperform the sandwich beam with an ideal strength core. For the sandwich beams with an the ideal strength core we find that $T_3 \gg T_2$, and so the beam bending/stretching stage III is decoupled from the core compression stage II. This is consistent with the fact that the degree of core compression in the free-standing and clamped beams are similar (see Fig. 11(*b*)). In contrast, the degree of core compression in the clamped Y-frame and corrugated core sandwich beam calculations differs from that in the free-standing sandwich beam calculations (see Fig. 11(*b*)). This is due to the fact that the structural response time T_3 is comparable to the core compression time T_2 for the sandwich beams with a Y-frame core or corrugated core.

The blast response of the *L*=3 m sandwich and monolithic beams is shown in Fig. 12: w_p/L, $\epsilon_c^{\max}/\epsilon_{fs}^{\max}$, and T_3/T_2 are each plotted against I_0 for each beam. Again, the sandwich beams outperform the monolithic beam in the sense that w_p/L is reduced. There is only a minor variation in rear face deflection for the different sandwich beams, in contrast to the case of *L*=1 m shown in Fig. 11(*a*). The structural response time of the *L*=3 m sandwich beams is about three times greater than that of the *L*=1 m beams, as anticipated by relation (7). The ratios T_3/T_2 exceed unity for all

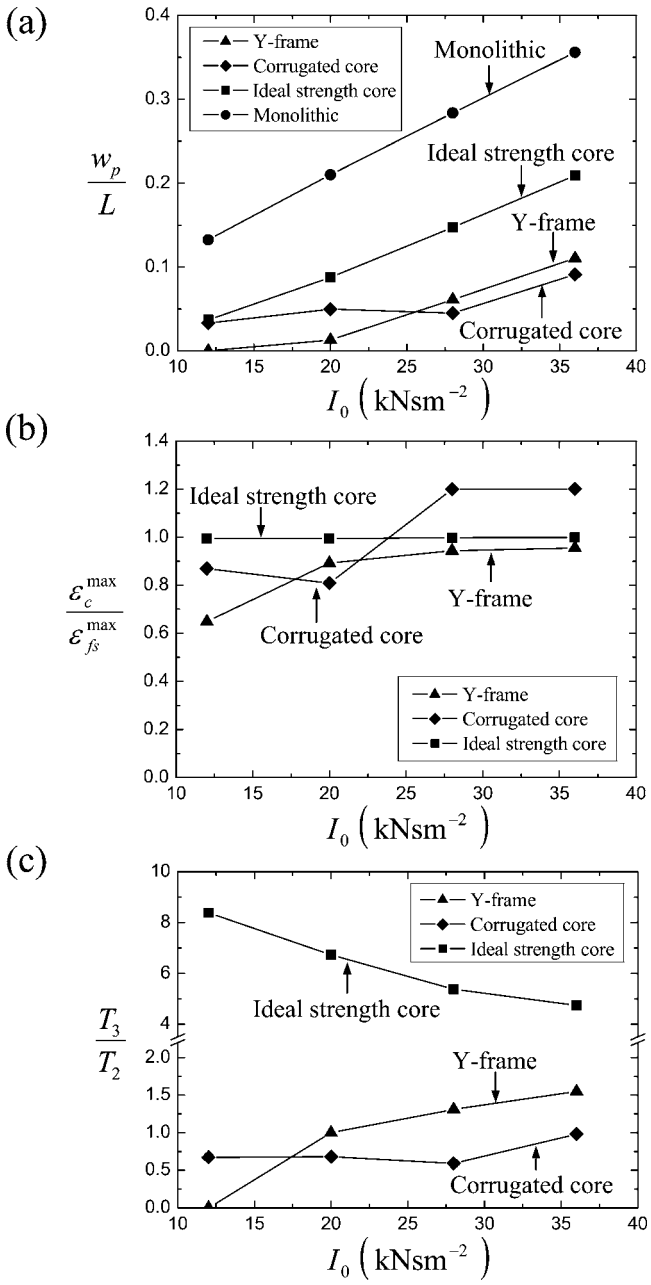

Fig. 11 Finite element predictions of the (*a*) peak normalized back face deflections w_p/L, (*b*) normalized peak core compression $\varepsilon_c^{max}/\varepsilon_{fs}^{max}$, and (*c*) normalized time required to attain the maximum deflection T_3/T_2 as a function of blast impulse for the $L=1$ m clamped monolithic and sandwich beams

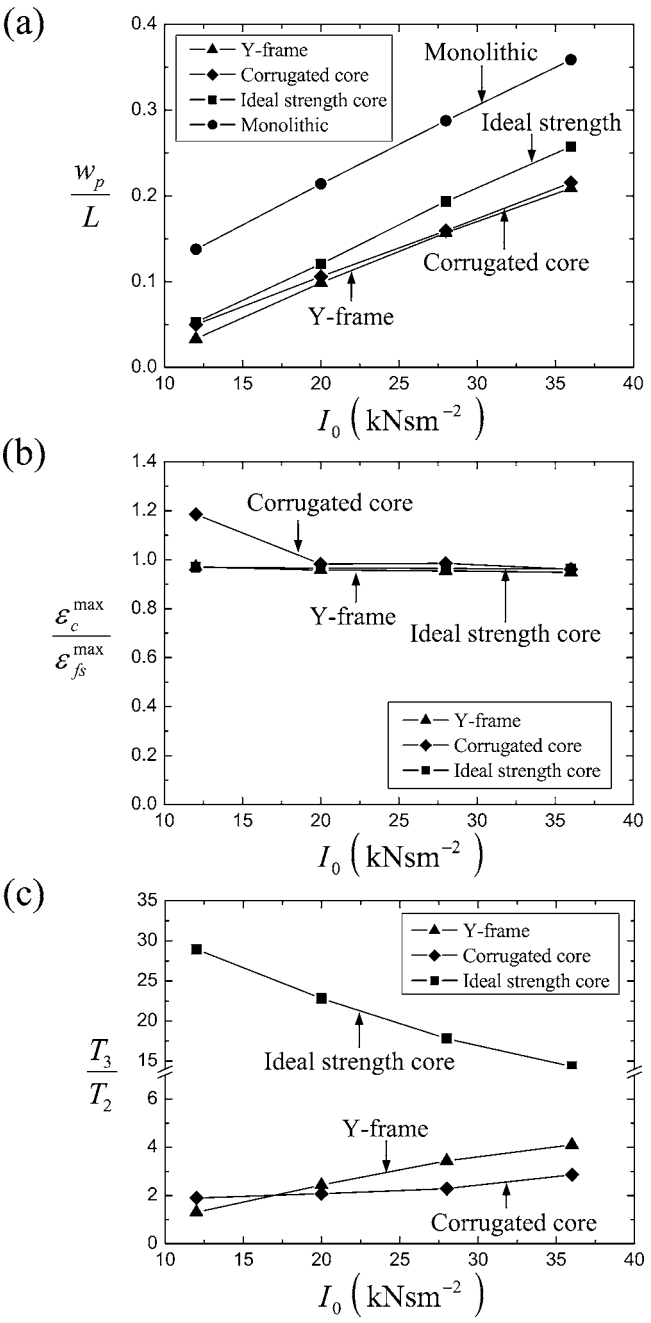

Fig. 12 Finite element predictions of the (*a*) peak normalized back face deflections w_p/L, (*b*) normalized peak core compression $\varepsilon_c^{max}/\varepsilon_{fs}^{max}$ and (*c*) normalized time required to attain the maximum deflection T_3/T_2 as a function of blast impulse for the $L=3$ m clamped monolithic and sandwich beams

the sandwich beams (Fig. 12(*c*)), implying that stages II and III are decoupled. Consistently, the core compression predictions from the free-standing and clamped beam simulation are almost identical for all the sandwich cores considered here (refer to Fig. 12(*b*)).

7 An Assessment of the Cross-Coupling Between the Three Stages of Response for the Clamped Sandwich Beam

The superior performance of the Y-frame and corrugated core beams over both the ideal strength foam core sandwich beams and monolithic beams of equal mass is evident from the above calculations for a fully clamped sandwich beam over a wide range of imposed impulses. Here we attempt to explain this performance enhancement within the Fleck and Deshpande [1] conceptual framework. For this purpose we consider the following three sets of calculations for the sandwich beams.

(i) Decoupled Stage I, Denoted by I/II+III. These simulations decouple stage I from the remaining stages by applying an initial uniform velocity to the front face only of the sandwich beam in accordance with the Taylor prediction (5), with no subsequent interaction between the clamped sandwich beam and the fluid. This type of loading was assumed in the previous finite element studies of Xue and Hutchinson [2] and Qiu et al. [14]. A decoupled stage I response is achieved when T_1/T_2 is much less than

unity, or equivalently when σ_c/p_0 is small via (2), (3), and (6). Recall that the full simulations reported above demonstrate that continued fluid loading occurs during stages II and III. Consequently, a comparison of the results for the fully coupled case and for the decoupled stage I case provides an assessment of the significance of fluid-structure interaction in stages II and III. The fully coupled simulations reveal that an additional 20–30% impulse is transmitted during stage II, and thus it is anticipated that the decoupled stage I simulations will result in somewhat smaller back face deflections than the fully coupled case. (For consistency of notation, we shall refer to the fully coupled case by *I+II+III*.)

For the monolithic beams, the only meaningful decoupled calculation is the decoupled stage I calculation, *I//II+III* (or equivalently *I//III* as no core compression exists for monolithic beams), where we impart the velocity (5) to the monolithic beam based upon the Taylor [3] free-standing plate analysis. This corresponds to impulsive loading of the monolithic beam with the impulse given by the Taylor [3] analysis.

(ii) Decoupled Stage III, Denoted by I+II/III. This is achieved by fluid-loading of the free standing beam in stages I and II. At the instant when the faces and core of the sandwich beam share a common velocity, the ends of the sandwich beam are clamped and the beam is allowed to be brought to rest by a combination of plastic bending and stretching in the absence of a fluid. Thus, these simulations switch off any fluid-structure interaction in stage III, and additionally switch off any beneficial coupling between stages II and III. We shall show below that the contribution to the beam displacement is negligible due to pressure loading by the fluid in stage III. However, the cross-coupling between stages II and III significantly reduces the rear face deflection of the clamped sandwich beam for stubby beams with a weak core. We anticipate that the simulations that decouple stage III will produce a greater deflection than the fully coupled case *I+II+III*.

(iii) Fully decoupled, Denoted by I/II/III. The fully decoupled case considers a freely supported beam with its front face given an initial velocity according to the Taylor [3] result (5). The fluid is absent in stages II and III. After the core has finished compressing in stage II, end clamps are applied instantaneously to the beam and the beam is allowed to arrest by bending/stretching in stage III. Now compare this analysis to the fully coupled case *I+II+III*. The fully coupled problem involves 20–30% additional momentum transfer in stage II than that given by the Taylor prediction, but the coupled analysis includes the beneficial coupling between stages II and III, particularly for stubby beams with a weak core. Consequently, it is anticipated that the decoupled numerical analysis will give predictions which are reasonably close to the predictions of the fully coupled analysis. Recall that the analytical model of Fleck and Deshpande [1] also assumes decoupling from one stage to the next.

These decoupled calculations were performed using the finite element meshes described in Sec. 4. The boundary conditions are as specified above (all other boundary conditions being the same as those in the fully coupled simulations). We proceed to present numerical predictions for the maximum midspan back face deflections w_p/L from the above partially and fully decoupled simulations and compare them with the fully coupled predictions. Note that the transverse deflection w is always measured from the clamped supports. The fully coupled finite element calculations reported above for the free-standing and clamped beams have revealed that the deformation mode of the Y-frame resembles that of the corrugated core, while the beams with an ideal foam core display a markedly different behavior. We first explore the significance of cross-coupling between the three stages of response for the Y-frame and corrugated cores and then consider the beams with an ideal foam core.

7.1 The Y-frame and Corrugated Core Beams. Comparisons between the decoupled and fully coupled predictions for the

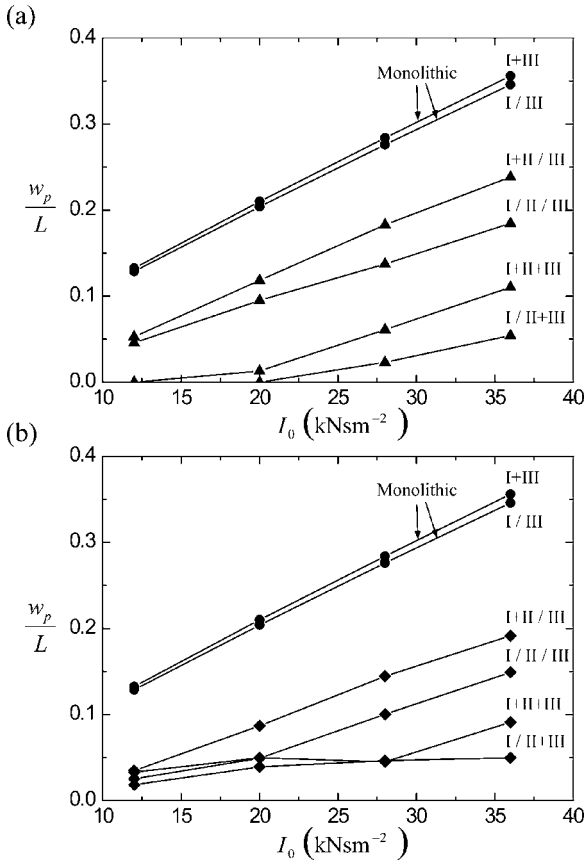

Fig. 13 Comparisons between the fully coupled (*I+II+III*) and decoupled finite element predictions of the peak normalized back face deflections w_p/L of the $L=1$ m (*a*) Y-frame and (*b*) corrugated core clamped sandwich beams. The decoupled calculations for the sandwich beams are the (i) fully decoupled (*I//II//III*), (ii) the decoupled stage I (*I//II+III*), and (iii) the decoupled stage III (*I+II//III*) calculations. The fully coupled and decoupled stage I predictions for the $L=1$ m monolithic beams are included.

$L=1$ m Y-frame and corrugated core beams are shown in Figs. 13(*a*) and 13(*b*), respectively. In general, the fully decoupled analysis *I//II//III* and decoupled stage III analysis *I+II//III* overpredict the maximum midspan deflection w_p while the decoupled stage I analysis underpredicts w_p for the $L=1$ m sandwich beams. On the other hand, the decoupled stage I calculation *I//II+III* for the monolithic beam is in good agreement with the fully coupled predictions *I+II+III*. These results are rationalized as follows.

(a) The decoupled stage I calculation underpredicts the deflection because the Taylor prediction based on a free-standing outer-face-sheet underpredicts the momentum transmitted to the Y-frame and corrugated core beams (see Fig. 8(*a*)).

(b) Peak core compression and back face deflection are attained approximately simultaneously in the $L=1$ m Y-frame and corrugated core beams (Fig. 9). This strong coupling between stages II and III results in reduced back face deflections: the bending action in the sandwich beam occurs at the same time as core crush. Thus, the decoupled stage III calculations overpredict the deflection.

(c) The fully decoupled calculations *I//II//III* only slightly overpredict the deflections as the competing effects (a) and (b) mitigate against each other.

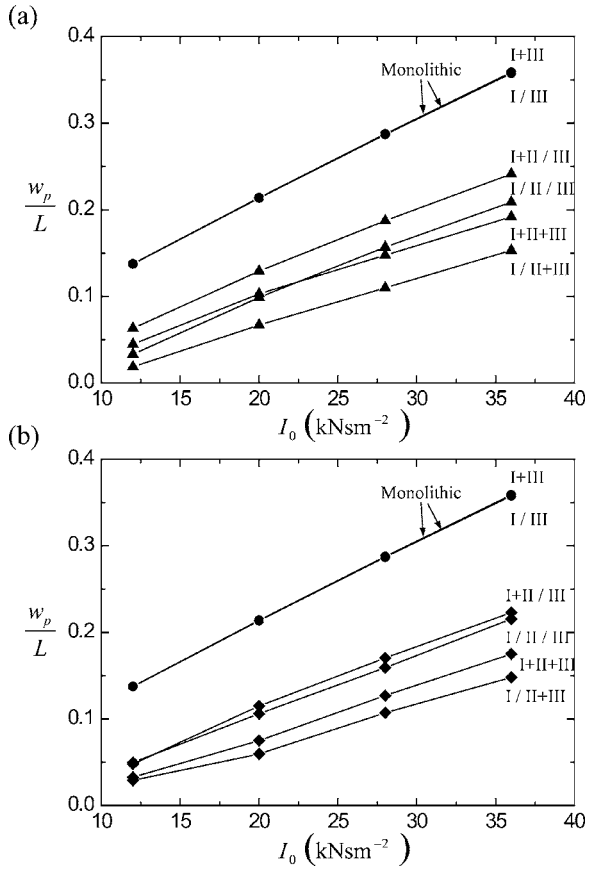

Fig. 14 Comparisons between the fully coupled (*I+II+III*) and decoupled finite element predictions of the peak normalized back face deflections w_p/L of the $L=3$ m (*a*) Y-frame and (*b*) corrugated core clamped sandwich beams. The decoupled calculations for the sandwich beams are the (i) fully decoupled (*I/II/III*), (ii) the decoupled stage I (*I/II+III*), and (iii) the decoupled stage III (*I+II/III*) calculations. The fully coupled and decoupled stage I predictions for the $L=1$ m monolithic beams are included.

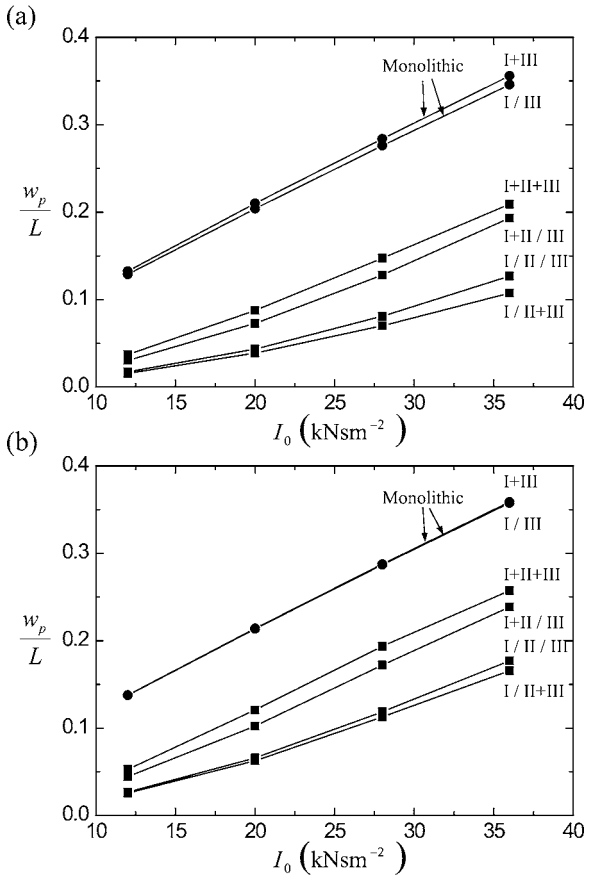

Fig. 15 Comparisons between the fully coupled (*I+II+III*) and decoupled finite element predictions of the peak normalized back face deflections w_p/L of the (*a*) $L=1$ m and (*b*) $L=3$ m ideal strength core clamped sandwich beams. The decoupled calculations for the sandwich beams are the (i) fully decoupled (*I/II/III*), (ii) the decoupled stage I (*I/II+III*), and (iii) the decoupled stage III (*I+II/III*) calculations. The fully coupled and decoupled stage I predictions for the $L=1$ m and $L=3$ m monolithic beams are included.

Similar comparisons between the decoupled and fully coupled predictions of the $L=3$ m Y-frame and corrugated core beams are shown in Figs. 14(*a*) and 14(*b*), respectively. For these slender sandwich beams, there is negligible coupling between stages II and III, and so the decoupled stage III calculations are in good agreement with the fully coupled predictions. On the other hand, the decoupled stage I calculations (and the fully decoupled calculations) underpredict the deflection as the transmitted impulse is underestimated by a Taylor analysis based on the free-standing front face-sheet. Note that the decoupled and fully coupled monolithic beam calculations are in excellent agreement for the $L=3$ m sandwich beams.

7.2 Ideal Strength Core. Comparisons between the various decoupled and fully coupled predictions for the maximum midspan back face deflections of the ideal strength core beams are shown in Figs. 15(*a*) and 15(*b*) for the $L=1$ and 3 m beams, respectively. Unlike the Y-frame and corrugated core beams, the degree of cross-coupling between the three stages of response is similar for the two lengths of sandwich beam. The decoupled stage III calculations slightly underpredict the deflections, while the decoupled stage I and fully decoupled predictions are substantially lower than the fully coupled estimates. These results are understood as follows.

(a) The duration of the beam bending and stretching phases greatly exceeds the duration of the core compression phase in these beams with strong cores (Figs. 11 and 12). Thus, stage III is decoupled from stages I and II and the decoupled stage III calculation only slightly underestimates the fully coupled predictions for both beam lengths.

(b) Similar to the Y-frame and corrugated core beams, the Taylor analysis based on a free-standing front face-sheet underestimates the momentum transmitted into the ideal strength foam core beams (Fig. 8(*a*)). Thus, the decoupled stage I and fully decoupled calculations under-predict the deflection. Since there is negligible coupling between stage III and stages I and II, the fully decoupled calculation and the decoupled stage I calculation predict approximately equal deflections.

7.3 Effect of Transmitted Impulse in Stage III. The transmitted impulse is plotted in Fig. 16 as a function of $\bar{t}$ for the case of a 100 MPa blast wave impinging the clamped sandwich beams (Y-frame, corrugated core and ideal strength foam core) and clamped monolithic beams with half-span $L=1$ m. In order to define the impulse, first define $\bar{p}$ as the spatial average of the fluid pressure on the front face of the monolithic or sandwich beams. The accumulated transmitted impulse is $I(\bar{t})=\int_0^{\bar{t}}\bar{p}(\tau)d\tau$. We have

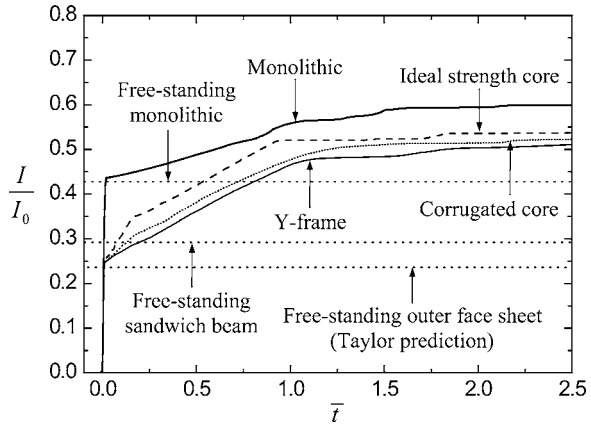

Fig. 16 Time variation of the normalized transmitted momentum I/I_o for the L=1 m clamped monolithic and sandwich beams subject to the p_o=100 MPa blast. Predictions for the final transmitted impulse in the free-standing cases are shown (for the sandwich beams an average value is given).

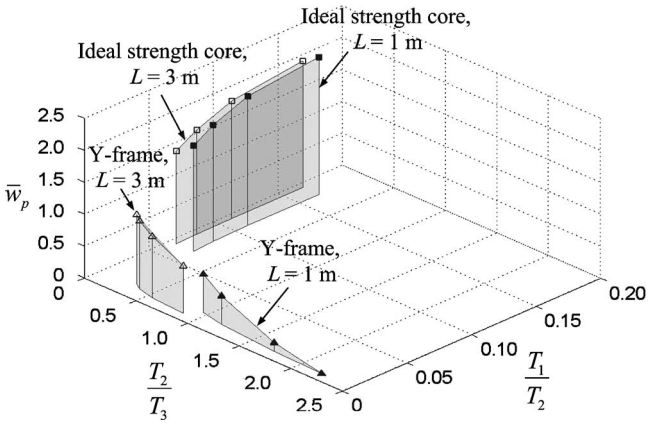

Fig. 17 A synopsis of the normalized peak deflections $\bar{w}_p$ of the Y-frame and ideal strength core sandwich beams. The axes employed are the ratios T_1/T_2 and T_2/T_3 of the durations of stages I and II and II and III, respectively, as predicted from a fully decoupled analysis. ($\bar{w}_p$ is defined as the ratio of the peak deflection as predicted from the fully coupled analysis to that predicted by a fully decoupled analysis.)

marked on Fig. 16 the final transmitted momentum as predicted by the free-standing beam analyses. Clearly, there is continued loading of the beam by the water beyond stage II, but at a much reduced pressure (for the sandwich beams, $\bar{p} \approx 0.2$ MPa for $\bar{t} > 0.25$). This pressure has a negligible effect upon the response for all beams considered, by the following argument. First, consider the sandwich beam with an ideal foam core, in which stages II and III are temporally decoupled; in the fully coupled simulations *I+II+III* of these beams, continued fluid loading is present in stage III and leads to a small additional deflection compared to the response for decoupled stage III analysis *I+II/III* (in which fluid loading is absent in stage III). This confirms that fluid loading in stage III has a negligible effect upon beam deflection. Second, consider the sandwich beams with a Y-frame or corrugated core. The beneficial coupling between stages II and III has a major effect upon the back face deflection, and the small increase in deflection due to fluid loading in stage III is masked.

7.4 Assembly of Results Into a Performance Map for Blast. Consider again the maximum midspan back face deflections of the beams with an ideal core and a Y-frame core. The dependence of these deflections upon the relative durations of the three stages of response is summarized in the three-dimensional plot of Fig. 17. The horizontal axes are T_1/T_2 and T_2/T_3[6], while the vertical axis is the ratio $\bar{w}_p$ of deflection from the fully coupled calculations *I+II+III* and from the fully decoupled calculations *I/II/III*. The predictions of $\bar{w}_p$ for the sandwich beams with a corrugated core are omitted as they lay close to the results for the beams with a Y-frame core.

The beams with an ideal foam core have high values of T_1/T_2 and a low value of T_2/T_3 due to the high transverse strength of the core. The low value of T_2/T_3 implies that the stages II and III are decoupled. The values of T_1/T_2 are sufficiently high for additional momentum transfer to occur in stage II, and thus the fully coupled calculations *I+II+III* have 50–100% larger deflections than the fully decoupled calculations *I/II/III*. This is emphasized by replotting the data in a two-dimensional graph of $\bar{w}_p$ versus T_1/T_2 in Fig. 18(*a*). It is seen that fluid loading in stage II enhances the beam deflection unless T_1/T_2 is very small (less than 0.05).

The sandwich beams with a Y-frame core lie in a different domain of the performance map (Fig. 17). The L=3 m Y-frame beams have low values of T_1/T_2 and T_2/T_3, resulting in a decoupled response from one stage to the next. Consequently, good agreement exists between the predictions of the fully coupled and fully decoupled analyses. In contrast, the L=1 m Y-frame sandwich beams display a high value of T_2/T_3, resulting in a beneficial

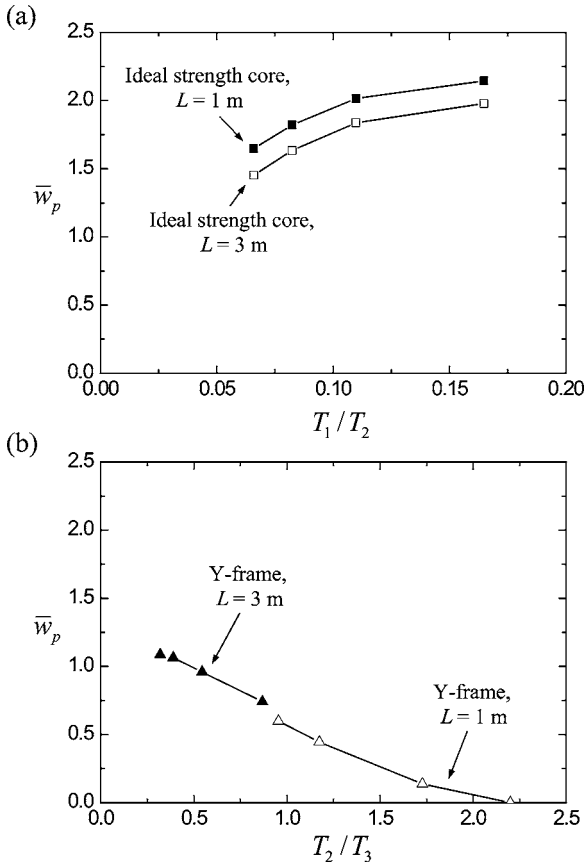

Fig. 18 The variation of $\bar{w}_p$ (*a*) with T_1/T_2 (ratio of the duration of stages I and II) for the ideal strength core beams and (*b*) with T_2/T_3 (ratio of the durations of stages II and III) for the Y-frame core beams. ($\bar{w}_p$ is defined as the ratio of the peak deflection as predicted from the fully coupled analysis to that predicted by a fully decoupled analysis.)

[6]Here the durations T_1, T_2, and T_3 are obtained from the fully decoupled analysis *I/II/III*.

coupling between stages II and III and a small deflection in the fully coupled simulations. The correlation of $\bar{w}_p$ with T_2/T_3 is summarized in Fig. 18(*b*) for the sandwich beams with a Y-frame core.

The results in Figs. 17 and 18 confirm the hypothesis presented in Sec. 2.1, viz.:

(i) the fully decoupled model underpredicts deflections when there is coupling between stages I and II (i.e., high values of T_1/T_2);
(ii) the decoupled model overpredicts deflections when coupling between stages II and III exists (i.e., high values of T_2/T_3), and
(iii) the decoupled model is adequate in the low T_1/T_2 and T_2/T_3 limit.

8 Concluding Remarks

The underwater blast response of clamped sandwich beams with a Y-frame, corrugated core and an ideal strength isotropic foam core has been investigated. The beams with a Y-frame core and corrugated core outperform the beams with an ideal foam core on the basis of rear face deflection for a beam of given mass. This is particularly true for stubby beams. All sandwich beams investigated here outperform monolithic beams of equal mass.

The Fleck and Deshpande [1] framework has been used to devise and interpret the finite element simulations. For all sandwich beams explored, the Taylor analysis based on a free-standing front face-sheet underestimates the transmitted momentum by 20–30%. This is due to continued fluid loading during the core compression phase, and leads to enhanced sandwich beam deflections.

A beneficial coupling can occur between the core compression stage and the final beam bending/stretching stage of the response for the case of stubby beams with a weak core. Consequently, cores made from a Y-frame or corrugations are superior to the stronger foam core.

The regimes of behavior of the underwater blast response of sandwich beams are usefully summarized in a performance map which takes as axes the relative duration of the three stages of response. The optimal regime is located where the initial stage of response (up to the point of first cavitation in the fluid) is decoupled from that of core compression, while the core compression phase is coupled to the beam bending/stretching phase.

Acknowledgment

The authors are grateful to ONR for their financial support through US-ONR IFO grant number N00014-03-1-0283 on "The Science and Design of Blast Resistant Sandwich Structures" and to the NIMR for support on the project "The optimal design of Y-core sandwich structures."

References

[1] Fleck, N. A., and Deshpande, V. S., 2004, "The Resistance of Clamped Sandwich Beams to Shock Loading," ASME J. Appl. Mech., **71**(3), pp. 386–401.
[2] Xue, Z., and Hutchinson, J. W., 2004, "A Comparative Study of Blast-Ressistant Metal Sandwich Plates," Int. J. Impact Eng., **30**(11), pp. 1283–1305.
[3] Taylor, G. I., 1941, "The Pressure and Impulse of Submarine Explosion Waves on Plates," *The Scientific Papers of G I Taylor* (1963), Vol. III, Cambridge University Press, Cambridge, pp. 287–303.
[4] Deshpande, V. S., and Fleck, N., 2005, "A One-dimensional Response of Sandwich Plates to Underwater Shock Loading," J. Mech. Phys. Solids, **53**(11), pp. 2347–2383.
[5] Rabczuk, T., Kim, J. Y., Samaniego, E., and Belytschko, T., 2004, "Homogenization of Sandwich Structures," Int. J. Numer. Methods Eng., **61**(7), pp. 1009–1027.
[6] Liang, Y., Spuskanyuk, A. V., Flores, S. E., Hayhurst, D. R., Hutchinson, J. W., McMeeking, R. M., and Evans, A. G., 2005, "The Response of Metallic Sandwich Panels of Water Blast," ASME J. Appl. Mech., submitted for publication.
[7] Côté, F., Deshpande, V. S., Fleck, N. A., and Evans, A. G., 2005, "The Compressive and Shear Responses of Corrugated and Diamond Lattice Materials," Int. J. Solids Struct., to appear.
[8] Côté, F., Deshpande, V. S., Fleck, N. A., and Evans, A. G., 2004, "The Out-of-Plane Compressive Behaviour of Metallic Honeycombs," Mater. Sci. Eng., A, **380**, pp. 272–280.
[9] Symmonds, P. S., 1954, "Large Plastic Deformations of Beams Under Blast Type Loading," *Proceedings of the Second US National Congress of Applied Mechanics*, University of Michigan, Ann Arbor, MI, June, pp. 505–515.
[10] Ashby, M. F., Evans, A. G., Fleck, N. A., Gibson, L. J., Hutchinson, J. W., and Wadley, H. N. G., 2000, *Metal Foams: A Design Guide*, Butterworth Heinemann, Boston.
[11] Deshpande, V. S., and Fleck, N. A., 2000, "Isotropic Constitutive Models for Metallic Foams," J. Mech. Phys. Solids **48**, pp. 1253–1283.
[12] Radford, D. D., Deshpande, V. S., and Fleck, N. A., 2005, "The Use of Metal Foam Projectiles to Simulate Shock Loading on a Structure," Int. J. Impact Eng., **31**(9), pp. 1152–1171.
[13] Sprague, M. A., 2002, "Advanced Computational Techniques for the Analysis of 3-D Fluid-Structure Interaction with Cavitation," PhD thesis, Department of Mechanical Engineering, University of Colorado.
[14] Qiu, X., Deshpande, V. S., and Fleck, N. A., 2003, "Finite Element Analysis of the Dynamic Response of Sandwich Beams Subject to Shock Loading," Eur. J. Mech. A/Solids, **22**, p. 801–814.

An Asymptotic Framework for the Analysis of Hydraulic Fractures: The Impermeable Case

S. L. Mitchell[1]
e-mail: sarah@iam.ubc.ca

R. Kuske

A. P. Peirce

Department of Mathematics,
University of British Columbia,
Vancouver, BC, V6T 1Z2,
Canada

This paper presents a novel asymptotic framework to obtain detailed solutions describing the propagation of hydraulic fractures in an elastic material. The problem consists of a system of nonlinear integro-differential equations and a free boundary problem. This combination of local and nonlocal effects leads to transitions on a small scale near the crack tip, which control the behavior across the whole fracture profile. These transitions depend upon the dominant physical process(es) and are identified by simultaneously scaling the associated parameters with the distance from the tip. A smooth analytic solution incorporating several physical processes in the crucial tip region can be constructed using this new framework. In order to clarify the exposition of the new methodology, this paper is confined to considering the impermeable case in which only the two physical processes of viscous dissipation and structure energy release compete.
[DOI: 10.1115/1.2200653]

1 Introduction

Hydraulic fracturing involves the propagation of a fracture in a brittle material, such as rock, due to the pressure exerted on the fracture surfaces by a viscous fluid that is pumped into the fracture. Hydraulic fractures occur naturally as a result of magma driven flows [1–3] as well as in several industrial and environmental applications such as the deliberate propagation of fractures in oil and gas reservoirs to enhance oil recovery; the generation of free-surface parallel hydraulic fractures in block caving mining operations as an alternative to explosive blasting [4]; and the generation of hydraulic fractures that are subsequently filled with impermeable material to isolate toxic waste or environmentally sensitive regions.

In many of these applications it is important to determine the progress of the fracture surface over time, which cannot be obtained from the few quantities that can easily be monitored, such as the fluid volume and pressure. It is, therefore, desirable to develop mathematical models that will predict the evolution of hydraulic fractures under given pumping conditions and geological situations [3,5–14]. The objective of these models is to calculate the fluid pressure, fracture width, and footprint given the properties of the rock, the injection rate, and the fluid characteristics. These models typically assume that: (i) the intact rock is linear elastic having a Young's modulus E and a Poisson's ratio ν; (ii) the fluid has viscosity μ; (iii) the progress of the fracture is controlled by rock toughness K_{Ic}; (iv) the loss of fluid to the reservoir (not considered in this paper) is determined by the leak-off coefficient C_l.

While the most general hydraulic fracture situations require numerical solution of these models, analytic and asymptotic methods also provide solutions for simple geometries. The highly nonlinear terms in the fluid flow equations, the nonlocal elastic response of the fracture, and the history-dependence of a sink term governing the fluid-loss present considerable challenges to mathematical analysis. The analytic solutions are important as they provide: benchmarks against which to test numerical algorithms; detailed information about the singular near-tip behavior of the solution in order to design suitable basis functions for numerical models; and the parameter values and length scales that characterize the transitions between distinct combinations of physical processes.

The purpose of this paper is to present a novel asymptotic framework that enables us to determine the different propagation regimes as well as an asymptotic solution. The ultimate strength of the new methodology is its capacity for developing asymptotic solutions when more than two physical processes compete or, for situations in which the solution is not self-similar, for example, when a fracture passes through a bi-material interface. For clarity of exposition of the new methodology we concentrate here on self-similar solutions as in [15], in which only two physical processes (viscosity and toughness) compete.

The fracture geometry considered here, known as the KGD (plane strain) model, was developed independently by Geertsma and de Klerk [8] and Khristianovic and Zheltov [12]. It assumes the fracture is an infinite vertical strip so that horizontal cross-sections are in a state of plane strain, see Fig. 1. This model is applicable to large aspect ratio rectangular planar fractures and was extended in [16] to include toughness. A major contribution to this mathematical modeling was by Spence and Sharp [16] who initiated the work on self-similar solutions and scaling for a KGD crack propagating in an elastic, impermeable medium with finite toughness. Their approach has been continued through asymptotic analyses of near-tip processes, yielding results for zero-toughness in an impermeable rock [17]; and for zero-toughness when leak-off is dominant [18]. Several papers [19–21] have extended this analysis to include toughness and fluid lag, where regions devoid of fluid develop close to the crack tip, along with transitional regions. This paper assumes that fluid lag is negligible and so these effects can be ignored.

Certain phases of hydraulic fracture propagation are characterized within a dimensionless parametric space [15,22], with boundaries controlled by the dominant processes, namely viscosity, energy release/toughness, or leak-off. This framework has been the basis for semi-analytical solutions for simple geometries (KGD and penny-shaped) which have provided benchmarks for numerical simulators. These include the following asymptotic regimes: impermeable with zero toughness [23–25], small toughness [26], finite toughness [16,27], and large toughness [25,28]; and permeable with zero toughness [29].

[1]Author to whom correspondence should be addressed.

Contributed by the Applied Mechanics Division of ASME for publication in the JOURNAL OF APPLIED MECHANICS. Manuscript received October 31, 2005; final manuscript received March 13, 2006. Review conducted by R. M. McMeeking. Discussion on the paper should be addressed to the Editor, Prof. Robert M. McMeeking, Journal of Applied Mechanics, Department of Mechanical and Environmental Engineering, University of California—Santa Barbara, Santa Barbara, CA 93106-5070, and will be accepted until four months after final publication of the paper itself in the ASME JOURNAL OF APPLIED MECHANICS.

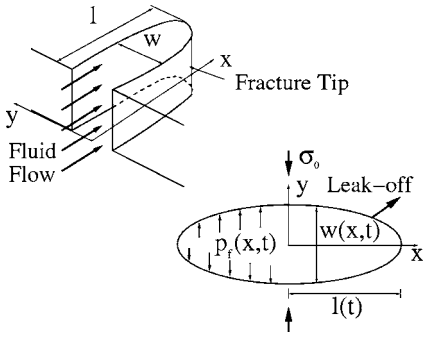

Fig. 1 The KGD profile and its cross-section

The analysis in this paper is closely related and complementary to these most recent studies; thus we describe here how our framework is different and more far-reaching. Previous analyses [21,23,24,26,28,30] have been limited to parameter regimes in which one or two physical processes dominate the dynamics, with the remainder of the related nondimensional quantities set to zero. A different set of scaling parameters is defined depending on which process is dominant, corresponding to the edges and corners of the parameter space [22,31]. We develop an asymptotic method which handles different scaling limits within a single framework, and so it is not necessary to redefine scaling parameters to consider the effect of different dominant processes. Although this study also only considers two physical processes, our analysis can be directly applied in situations where several processes are in balance, for example, including leak-off [32]. It can also be extended to other geometries, such as the PKN model [33], which assumes an elliptical vertical cross-section in contrast to the KGD model.

We avoid the semi-infinite approximations used in previous studies and consider parameter regimes which allow an asymptotic expansion with self-similar solutions. The method involves the simultaneous scaling of the physical processes relative to a parameter denoting the distance from the tip. A uniform asymptotic solution is then constructed in the tip region by rescaling the governing equations in terms of this small parameter. We determine the regions where the different processes are dominant, and relate them back to physical space. The process also identifies an important parameter combination quantifying these spatial transitions, which is used to match the local expansions analytically. This is in contrast to [26], where matching is done numerically. We find that the flexibility of the method is valuable for understanding the nonlocal and local effects in the model.

1.1 Governing Equations. We describe the governing equations for the propagation of an impermeable, KGD fracture driven by a viscous fluid in a uniform elastic medium under conditions of plane strain, as shown in Fig. 1. The solution is constructed to determine the fracture opening $w(x,t)$, net pressure $p(x,t)$ (the difference between the fluid pressure p_f and the far-field stress σ_0), and the fracture half-length, $l(t)$. We define three combined parameters E', μ', and K', in terms of the material parameters E, ν, μ, and K_{Ic}, as

$$E' = \frac{E}{1-\nu^2}, \quad \mu' = 12\mu, \quad K' = 4\left(\frac{2}{\pi}\right)^{1/2} K_{Ic} \tag{1}$$

Along with the volumetric fluid injection rate Q_0, these parameters govern the fracture propagation. Consistent with linear elastic fracture mechanics, we assume that the rock toughness K_{Ic} equals the stress intensity factor K_I, which, for a symmetric crack in a state of plane strain subjected to a pressure p, is given by

$$K_{Ic} = K_I := 2\sqrt{\frac{l}{\pi}}\int_0^l \frac{p}{\sqrt{l^2-x^2}}\mathrm{d}x \tag{2}$$

The governing equations are given as follows: The conservation of the fluid mass for an incompressible fluid with zero leak-off is described by the *lubrication equation*

$$\frac{\partial w}{\partial t} = \frac{1}{\mu'}\frac{\partial}{\partial x}\left[w^3\frac{\partial p}{\partial x}\right] + Q_0\delta(x) \tag{3}$$

For a state of plane strain, the *elasticity equation*

$$p(x,t) = -\frac{E'}{4\pi}\int_{-l}^{l}\frac{\partial w}{\partial s}\frac{\mathrm{d}s}{s-x} \tag{4}$$

expresses the force balance through a nonlocal relationship between the fracture opening and the net pressure. Equations (2) and (4) imply the local *propagation condition*

$$w = (K'/E')\sqrt{l-x} + O[(l-x)^{3/2}], \quad x \to \pm l \tag{5}$$

which determines the asymptotic behavior of the fracture opening close to the tip. Finally, we have *boundary conditions*, which ensure zero width and zero fluid loss at the tip

$$w = 0, \quad w^3\frac{\partial p}{\partial x} = 0, \quad \text{at } x = \pm l \tag{6}$$

The *global volume balance condition*

$$Q_0 t = \int_{-l}^{l} w(s,t)\mathrm{d}s \tag{7}$$

results from integrating (3) and using (6). The solution is constructed asymptotically by alternatively solving the lubrication equation (3) and the elasticity equation (4). In the near-tip region the dominant physical process is the energy release which is captured by the propagation condition (5). The remaining unknown constants are then found by applying the global volume balance condition (7); this also confirms the balance of dominant physical processes that arise.

1.2 Scaling and Dimensionless Equations. We seek a self-similar solution in the form $w(x,t) \propto l(t)\Omega(x/l,t)$ and, therefore, write the governing Eqs. (3)–(7) with nondimensionalized width, pressure and length scales

$$\xi = x/l, \quad l = L\gamma, \quad w = \epsilon L\Omega, \quad p = \epsilon E'\Pi \tag{8}$$

as used in [31,28,26]. The nondimensional quantities Ω (the opening), Π (the net pressure), and γ (a fracture length) are all $O(1)$. The parameter ϵ is introduced here for comparison with [26,28,31], where it is used to relate w/l to p/E'. However, it could be set to unity in our analysis. The parameter L denotes a length scale and is of the same order as l. We assume that γ =constant in our analysis below and show that this assumption is valid in Sec. 2.5, for the impermeable case of zero leak-off.

The three nondimensional quantities, which play important roles in our analysis, are

$$\mathcal{G}_k = \frac{K'}{\epsilon E' L^{1/2}}, \quad \mathcal{G}_m = \frac{\mu'}{\epsilon^3 E' t}, \quad \mathcal{G}_v = \frac{Q_0 t}{\epsilon L^2} \tag{9}$$

representing toughness/energy release, viscosity, and injected fluid volume, respectively. We simultaneously balance these parameters with the distance from the tip which allows us to consider regimes where both toughness and viscosity compete. The method can also be extended to consider multiple competing physical processes in balance, as in [32] where leak-off is included. Note that we have not introduced a nondimensionalized time scaling since it does not affect this balance approach. Here we examine the case where $\mathcal{G}_k \neq 0$ and $\mathcal{G}_m \neq 0$; the analysis for $\mathcal{G}_m = 0$ is the so called Griffiths crack solution [34], and $\mathcal{G}_k = 0$ is the viscosity solution [17,26].

The governing Eqs. (3)–(7) can, therefore, be written as

$$\frac{t(\epsilon L)_t}{\epsilon L}\Omega + t\frac{\partial \Omega}{\partial t} - \xi\frac{t(L\gamma)_t}{L\gamma}\frac{\partial \Omega}{\partial \xi} = \frac{1}{\mathcal{G}_m}\frac{1}{\gamma^2}\frac{\partial}{\partial \xi}\left[\Omega^3\frac{\partial \Pi}{\partial \xi}\right] \tag{10}$$

$$\Pi = -\frac{1}{4\pi\gamma}\int_{-1}^{1}\frac{\partial \Omega}{\partial \chi}\frac{\mathrm{d}\chi}{\chi - \xi} \tag{11}$$

$$\Omega = \mathcal{G}_k\gamma^{1/2}(1 \mp \xi)^{1/2}, \quad \xi \to \pm 1 \tag{12}$$

$$\mathcal{G}_v = \gamma\int_{-1}^{1}\Omega \mathrm{d}\chi \tag{13}$$

$$\Omega = 0, \quad \text{at } \xi = 1^{\pm} \tag{14}$$

We determine different local expansions depending on which physical process is dominant, and then construct a uniform near-tip solution analytically. The regions where these expansions are valid depend on a critical parameter which is a combination of the dimensionless $\mathcal{G}_{(\,)}$ quantities (9), and the transition in behavior can be related to the dominant physical processes. We determine this parameter as part of the process by scaling Eqs. (10)–(14) with a parameter controlling the distance from the tip $\xi=1$. Our method relies on analyzing the governing equations in this nondimensional form but we also quote the results in the original dimensional variables at the end of Sec. 2 to more easily give a physical interpretation.

Some of the expansions in this paper have been found previously, see [16,17,26,28,31] for example. We obtain the well-known results that the fracture width has $(1-x/l)^{1/2}$ and $(1-x/l)^{2/3}$ asymptotic behavior for the toughness and viscosity dominated regions, respectively. We also show that the fracture grows as $t^{2/3}$ and the fracture width is proportional to $t^{1/3}$. Although we confirm previous work, our new approach gives the construction in a transition region, where the solution consists of several terms in the expansion and thus is not purely a power law. It is also has the flexibility to handle behavior dominated by different physical processes simultaneously. When considering two or more physical processes, we do not rely on a scaling in which any one process is dominant: This is in contrast to other studies, [26,28,31] amongst others, where the nondimensional quantities $\mathcal{G}_{(\,)}$ corresponding to the controlling processes are set to unity. In our method the critical parameters are determined as part of the expansion. In Sec. 2 we describe the approach of the method in detail and in Sec. 3 we briefly describe how the methodology can be extended to include leak-off and in [33] it is applied to the PKN model.

2 Analytical Solution Method

We now describe the new approach, which provides a unified framework to balance viscosity and toughness simultaneously.

2.1 Re-scaled Equations and Balancing Approach. First we scale the key dimensionless quantities in (9) with a parameter $\delta \ll 1$ related to the distance from the tip $\xi=1$. Then we define an asymptotic expansion for both Ω and Π in terms of this parameter, and balance δ with the nondimensionless quantities $\mathcal{G}_{(\,)}$ (9). Through this procedure we can locate changes in the behavior of the solution and the spatial regions characterized by the different dominant physical processes. Thus we define

$$1 - \delta z = \xi \tag{15}$$

$$\mathcal{G}_k = \delta^{\beta_k}\hat{\mathcal{G}}_k, \quad \mathcal{G}_m = \delta^{\beta_m}\hat{\mathcal{G}}_m, \quad \mathcal{G}_v = \delta^{\beta_v}\hat{\mathcal{G}}_v \tag{16}$$

where the $\hat{\mathcal{G}}_{(\,)}$ quantities are all $O(1)$. The construction of the asymptotic expansion determines inequalities between the values of the exponents $\beta_{(\,)}$, which characterize the different regimes. The parameter $\delta \ll 1$ is essentially the distance from the tip, since we assume that z is $O(1)$. Previous work, for example [26,28,31], assumes a semi-infinite approximation; however, the parameter δ allows us to be more general in the analysis of the fracture tip behavior as we have not assigned the exact distance from the tip. The semi-infinite approximation does not allow extensions to include stress jumps, for example, whereas the methodology described in this paper can incorporate such modifications. Note that the parameter δ is used for bookkeeping to balance terms in the expansion, but does not appear in the final solution.

We assume that the solution is symmetric about $\xi=0$ (see Fig. 1) and so, without loss of generality, we consider the interval $0 < \xi < 1$. Then the integral in (11) is written as (and similarly for the integral in (13))

$$\Pi = -\frac{1}{4\pi\gamma}\int_{-1}^{1}\frac{\mathrm{d}\Omega}{\mathrm{d}\chi}\frac{\mathrm{d}\chi}{\chi - \xi} = -\frac{1}{2\pi\gamma}\int_{0}^{1}\frac{\mathrm{d}\Omega}{\mathrm{d}\chi}\frac{\chi \mathrm{d}\chi}{\chi^2 - \xi^2} \tag{17}$$

The governing Eqs. (10)–(14) are now written in terms of z by substitutions of (15) and (16)

$$\frac{t(\epsilon L)_t}{\epsilon L}\Omega + (1-\delta z)\frac{t(L\gamma)_t}{L\gamma}\delta^{-1}\frac{\mathrm{d}\Omega}{\mathrm{d}z} = \frac{\delta^{-\beta_m - 2}}{\hat{\mathcal{G}}_m\gamma^2}\frac{\mathrm{d}}{\mathrm{d}z}\left[\Omega^3\frac{\mathrm{d}\Pi}{\mathrm{d}z}\right] \tag{18}$$

$$\Pi = -\frac{1}{2\pi\gamma}\delta^{-1}\int_{0}^{1/\delta}\frac{\mathrm{d}\Omega}{\mathrm{d}r}\frac{(1-\delta r)}{r(2-\delta r) - z(2-\delta z)}\mathrm{d}r \tag{19}$$

$$\Omega = \hat{\mathcal{G}}_k\gamma^{1/2}\delta^{\beta_k + 1/2}z^{1/2}, \quad z \to 0 \tag{20}$$

$$\delta^{\beta_v}\hat{\mathcal{G}}_v = 2\gamma\delta\int_{0}^{1/\delta}\Omega \mathrm{d}r \tag{21}$$

$$\Omega = 0, \quad \text{at } z = 0 \tag{22}$$

As mentioned above, we expand Ω and Π in terms of δ. The terms in these expansions can then be combined with the powers of δ appearing explicitly in (18)–(22). Hence we set

$$\Omega = \delta^{\beta_k + 1/2}(\Omega_0 + \delta^{\alpha_1}\Omega_1 + \cdots) \tag{23}$$

$$\Pi = \delta^{\beta_k}\Pi_0 + \delta^{\sigma_1}\Pi_1 + \cdots \tag{24}$$

The exponents α_i and σ_i are unknown at present and determined below in terms of the exponents $\beta_{(\,)}$ in (16) as part of the asymptotic construction. The method involves substituting (23) and (24) into (18)–(22) and matching terms in powers of δ using the exponents $\beta_{(\,)}$. This determines the exponents α_i and σ_i and shows how the relative magnitudes of the dimensionless parameters (9) compared with δ influences the solution.

The sign of α_1 determines the leading order behavior of the solution, and we see more clearly how this arises in the expansions (23) and (24) by considering the lubrication Eq. (18). The leading order terms in δ satisfy

$$\lambda\delta^{-1}\frac{\mathrm{d}\Omega}{\mathrm{d}z} = \frac{1}{\hat{\mathcal{G}}_m\gamma^2}\delta^{-\beta_m - 2}\frac{\mathrm{d}}{\mathrm{d}z}\left[\Omega^3\frac{\mathrm{d}\Pi}{\mathrm{d}z}\right] \tag{25}$$

where we have assumed that the length scale L satisfies $L = C_L t^{\lambda}$.

The two situations which arise are either (i) the right-hand side of (25) is dominant and thus set to zero, so that to leading order Π=constant, and Ω is determined using the propagation condition (20). This corresponds to $\alpha_1 > 0$ and so Ω_0 is dominant and obtained from the propagation condition (20) which gives the classical square root term associated with a dominant toughness [28,31]. This in turn also defines Π_0 via (19). Note that the prefactor δ^{β_k} incorporated explicitly in (23) and (24) comes from the dimensionless toughness $\mathcal{G}_k$. Also, we show below that the other solution in (25), namely $\Omega^3\Pi'$=constant, cannot arise. Or, (ii) the two terms in Eq. (25) balance. This corresponds to $\alpha_1 < 0$ where

viscosity dictates the leading order behavior of $z^{2/3}$, as in [17,26,31] and discussed here in Sec. 2.3. Then the leading order terms in (23) and (24) are Ω_1 and Π_1, and we find that $\Omega_0, \Pi_0 = 0$. Hence the square root behavior is not leading order, implying that toughness is not dominant. Our expansion ties this change in leading order behavior to physical space.

To give the details and higher order terms of expansions (23) and (24) we substitute these expressions into the lubrication equation (18) to give

$$\frac{t(\epsilon L)_t}{\epsilon L}\delta^{\beta_k+1/2}(\Omega_0+\delta^{\alpha_1}\Omega_1+\cdots)+\lambda(1-\delta z)\delta^{\beta_k-1/2} \times\left(\frac{d\Omega_0}{dz}+\delta^{\alpha_1}\frac{d\Omega_1}{dz}+\cdots\right) = \frac{\delta^{-\beta_m-1/2+3\beta_k}}{\hat{\mathcal{G}}_m\gamma^2}\cdot\frac{d}{dz}\left[(\Omega_0+\delta^{\alpha_1}\Omega_1+\cdots)^3 \times\left(\delta^{\beta_k}\frac{d\Pi_0}{dz}+\delta^{\sigma_1}\frac{d\Pi_1}{dz}+\cdots\right)\right] \tag{26}$$

and into the elasticity equation (19)

$$\delta^{\beta_k}\Pi_0+\delta^{\sigma_1}\Pi_1+\cdots=-\frac{\delta^{\beta_k-1/2}}{2\pi\gamma}\cdot\int_0^{1/\delta}\left(\frac{d\Omega_0}{dr}+\delta^{\alpha_1}\frac{d\Omega_1}{dr}+\cdots\right)\frac{(1-\delta r)}{r(2-\delta r)-z(2-\delta z)}dr \tag{27}$$

In Secs. 2.2 and 2.3 we use (26) and (27) to determine local expansions in the different asymptotic limits, $\alpha_1>(<)0$, by balancing terms according to powers of δ, and in Sec. 2.4 we match to obtain a uniform near-tip expansion. Finally, in Sec. 2.5 we substitute Ω from (23) into the global volume balance equation (21) to determine remaining unknown coefficients.

2.2 The Near-Tip Behavior ($\alpha_1>0$). First we look for an expansion where $\alpha_1>0$, and determine the conditions under which this is valid. The leading order terms in (26) and (27) for $\delta\ll 1$ are

$$0=\frac{\delta^{-\beta_m-1/2+4\beta_k}}{\hat{\mathcal{G}}_m\gamma^2}\frac{d}{dz}\left[\Omega_0^3\frac{d\Pi_0}{dz}\right] \tag{28}$$

$$\delta^{\beta_k}\Pi_0=-\frac{\delta^{\beta_k-1/2}}{2\pi\gamma}\int_0^{1/\delta}\frac{d\Omega_0}{dr}\frac{(1-\delta r)}{r(2-\delta r)-z(2-\delta z)}dr \tag{29}$$

and the solution is determined as

$$\Omega_0(z)=C_0\sqrt{z(2-\delta z)},\quad \Pi_0(z)=\frac{C_0}{4\gamma} \tag{30}$$

where Π_0 is found by integrating (28) (see [32].) The solution (30) is the eigenfunction of (29) which, with Π_0=constant, is symmetric about $\xi=0$. It satisfies the propagation condition (20) to yield $C_0=\hat{\mathcal{G}}_k\sqrt{\gamma/2}$. Comparison of the two leading terms in (26), namely the $\delta^{\beta_k-1/2}$ and $\delta^{-\beta_m-1/2+4\beta_k}$ terms, shows that we are in the toughness regime. We assume $\delta^{\beta_k-1/2}<\delta^{-\beta_m-1/2+4\beta_k}$ and then use (16) to deduce that $\mathcal{G}_k^3$ is large compared with $\mathcal{G}_m$, since the $\hat{\mathcal{G}}_0$ are $O(1)$. From the constant C_0 observe that the leading order term in the expansion for Ω (for $\alpha_1>0$) involves the re-scaled toughness parameter $\mathcal{G}_k$; this, together with the square root behavior, also implies that the toughness is dominant in this region. Note that we disregard the solution $\Omega_0^3\Pi_0'$=constant in (28). Using the propagation condition (20) for Ω_0 implies that Π_0 is $O(z^{-1/2})$ to leading order, but this contradicts Π_0=constant, which arises from (29).

The next order terms in (26) and (27) for $\delta\ll 1$ are

$$\lambda\delta^{\beta_k-1/2}\frac{d\Omega_0}{dz}=\frac{\delta^{-\beta_m+3\beta_k-1/2+\sigma_1}}{\hat{\mathcal{G}}_m\gamma^2}\frac{d}{dz}\left[\Omega_0^3\frac{d\Pi_1}{dz}\right] \tag{31}$$

$$\delta^{\sigma_1}\Pi_1=-\frac{\delta^{\beta_k-1/2+\alpha_1}}{2\pi\gamma}\int_0^{1/\delta}\frac{d\Omega_1}{dr}\frac{(1-\delta r)}{r(2-\delta r)-z(2-\delta z)}dr \tag{32}$$

Equating exponents of δ in (31) and (32) defines α_1 and σ_1 explicitly

$$\alpha_1=1/2+\beta_m-3\beta_k,\quad \sigma_1=\beta_m-2\beta_k \tag{33}$$

The condition $\alpha_1>0$ can be written as $\mathcal{G}_k^3/\mathcal{G}_m>\delta^{1/2}$, using (16), and violation of this condition means we are no longer in the toughness dominated regime.

We can now obtain Ω_1 and Π_1: Solving (31) gives

$$\Pi_1=-\frac{C_1}{4\pi\gamma}\ln\left(1-\frac{1}{2-\delta z}\right)-\frac{C_1}{4\pi\gamma}[\ln(1-\delta z)-\ln(\delta z)] \tag{34}$$

for $z=O(1)$, and then $\Omega_1(z)=C_1 z$ follows from (32). Note that the integration constant in (31) must be zero, otherwise Π_1 has infinite energy, deduced from integrating (31), also discussed in [32]: a non-zero constant means that Π_1 includes a $z^{-1/2}$ term, but substitution into the integral (2) would then yield an infinite stress intensity factor K_I. We can then find C_1 by substituting (34) into (31), considering the leading order terms only.

Hence the first two terms in the expansion (23) for Ω are

$$\Omega=\delta^{\beta_k}\hat{\mathcal{G}}_k\left[\sqrt{\frac{\gamma}{2}}\sqrt{\delta z(2-\delta z)}+4\pi\gamma^2\lambda\frac{\hat{\mathcal{G}}_m}{\hat{\mathcal{G}}_k^3}\delta^{\beta_m-3\beta_k}(\delta z)\right] \tag{35}$$

which is valid when $\alpha_1>0$ or $\mathcal{G}_k^3/\mathcal{G}_m>\delta^{1/2}$, i.e., close to the tip for ξ near 1. The square root term is dominant, but in the transition region both terms in (35) become the same order, which is when toughness and viscosity balance.

2.3 The Intermediate-Tip Behavior ($\alpha_1<0$). The leading order terms in (26) for $\delta\ll 1$ are now

$$\lambda\delta^{\beta_k-1/2+\alpha_1}\frac{d\Omega_1}{dz}=\frac{\delta^{-\beta_m+3\beta_k-1/2+3\alpha_1+\sigma_1}}{\hat{\mathcal{G}}_m\gamma^2}\frac{d}{dz}\left[\Omega_1^3\frac{d\Pi_1}{dz}\right] \tag{36}$$

which is coupled with the expression for Π_1 in (32). Equating exponents of δ in (32) and (36) gives

$$\alpha_1=1/6+\beta_m/3-\beta_k,\quad \sigma_1=-1/3+\beta_m/3 \tag{37}$$

The condition $\alpha_1<0$ then becomes $\mathcal{G}_k^3/\mathcal{G}_m<\delta^{1/2}$, which holds in the viscosity dominated regime; combining this with the analysis in Sec. 2.2 shows that the transition region occurs when $\mathcal{G}_k^3/\mathcal{G}_m=O(\delta^{1/2})$, and will be discussed in the following section.

Again we look for Ω_1 as a power law in z, namely

$$\Omega_1=\bar{C}_1 z^m+\Omega_2 \tag{38}$$

where Ω_2 is a small correction term found below. This is equivalent to a perturbation expansion for the solution of (36) for $\Omega_2\ll 1$, which we confirm in the matching.

The elasticity equation (32) can then be used to obtain

$$\Pi_1=\cot\pi m\frac{\bar{C}_1 m}{4\gamma}z^{m-1}+\frac{\bar{C}_1 m\delta^{1-m}(2-\delta z)^{-1}}{4\pi\gamma}+O(\delta^{1-m})+\Pi_2 \tag{39}$$

where the leading term is the standard result for the integral (32) of Ω_1 for $\delta\to 0$, as given in [35] and discussed in the Appendix, and Π_2 is the term corresponding to Ω_2. We integrate (36) and substitute Ω_1 and Π_1 from (38) and (39), respectively; then the leading order terms are

$$\lambda \bar{C}_1 z^m = \frac{\bar{C}_1^4 \mu_m}{4\hat{\mathcal{G}}_m \gamma^3} z^{4m-2} \tag{40}$$

where, for convenience, we have defined $\mu_m := m(m-1)\cot \pi m$. Equating exponents of z yields $m=2/3$ and the remaining expression determines $\bar{C}_1$. The equation for Ω_2 is then

$$\frac{\lambda d\Omega_2}{dz} = \frac{1}{\hat{\mathcal{G}}_m \gamma^2} \frac{d}{dz}\left[\frac{3\bar{C}_1^3 \mu_{2/3}}{4\gamma} \Omega_2 + \bar{C}_1^3 z^2 \frac{d\Pi_2}{dz} \right] \tag{41}$$

We look for solutions to (41) of the form $\Omega_2 = \hat{\mathcal{A}}_1 z^h + \hat{\mathcal{A}}_2 z^p$, with Π_2 following directly from (32). Substitution of Ω_2 and Π_2 into (41) leads to

$$\lambda \hat{\mathcal{A}}_1 z^{(h-1)} + \lambda p \hat{\mathcal{A}}_2 z^p = \frac{h\bar{C}_1^3 \hat{\mathcal{A}}_1}{4\hat{\mathcal{G}}_m \gamma^3}[h(h-1)\cot \pi h + 3\mu_{2/3}] z^{h-1} + \frac{p\bar{C}_1^3 \hat{\mathcal{A}}_2}{4\hat{\mathcal{G}}_m \gamma^3}[p(p-1)\cot \pi p + 3\mu_{2/3}] z^{p-1} \tag{42}$$

The coefficients $\hat{\mathcal{A}}_1$ and $\hat{\mathcal{A}}_2$ are unknown as they correspond to coefficients of homogeneous solutions to the linear Eq. (41). These are found below, by matching with (35). Setting $p=0$ gives one independent solution $\Omega_2 = \hat{\mathcal{A}}_2$. The other independent solution is found by solving a transcendental equation from matching the coefficients of z^{h-1} in (42). This reduces to

$$h(h-1)\cot \pi h + 2\mu_{2/3} = 0 \tag{43}$$

We find that $h \approx 0.138673$, which confirms the result in [26]. The solution does not satisfy the $z^{1/2}$ behavior described by the propagation condition (20) for $\hat{\mathcal{G}}_k > 0$ (since $m \neq 1/2$ and $h \neq 1/2$), and so toughness is not dominant in the region where this solution holds. The terms Ω_0 and Π_0 are, therefore, set to zero in (23) and (24).

Then the first term in the expansion (23) for Ω is

$$\Omega = \delta^{\beta_m/3} \hat{\mathcal{G}}_m^{1/3} \left[\left\{ \frac{4\gamma^3 \lambda}{\mu_m} \right\}^{1/3} (\delta z)^{2/3} + \frac{\hat{\mathcal{A}}_1 \delta^{2/3-h}}{\hat{\mathcal{G}}_m^{1/3}} (\delta z)^h + \frac{\hat{\mathcal{A}}_2 \delta^{2/3}}{\hat{\mathcal{G}}_m^{1/3}} \right] \tag{44}$$

for $\alpha_1 < 0$ or $\mathcal{G}_k^3/\mathcal{G}_m < \delta^{1/2}$. This expression is valid only away from $\xi = 1$, since the propagation condition (20) is not satisfied.

It should be noted that the next term in the expansion for Ω in (23), for $\alpha_1 < 0$, is given by $\Omega_2 = z^{5/3}$. It can be shown to be higher order in the construction of the uniform near-tip expansion and so is not included in (44).

2.4 Transition Region and Matching. We now consider the local expansions (35) for $\alpha_1 > 0$ and (44) for $\alpha_1 < 0$, to determine the transitions in spatial behavior, find the unknown coefficients by matching, and construct the uniform near-tip asymptotic expansion. Motivated by the balance Eqs. (33) and (37), we define a combined parameter $\mathcal{P}_{km}$ involving $\mathcal{G}_k$ and $\mathcal{G}_m$, namely

$$\mathcal{P}_{km} := \mathcal{G}_k^3/\mathcal{G}_m \tag{45}$$

which appears explicitly in both expansions. These expansions can be written in the ξ scaling, without δ, in terms of $\mathcal{P}_{km}$ as

$$\Omega \sim \mathcal{G}_k[C_0\sqrt{1-\xi^2} + C_1 \mathcal{P}_{km}^{-1}(1-\xi)] \tag{46}$$

$$\Omega \sim \mathcal{G}_m^{1/3}[\bar{C}_1(1-\xi)^{2/3} + \mathcal{A}_1(\mathcal{P}_{km})(1-\xi)^h + \mathcal{A}_2(\mathcal{P}_{km})] \tag{47}$$

for $\alpha_1 > (<) 0$, respectively. The coefficients C_0, C_1, and $\bar{C}_1$ have been re-defined without the $\hat{\mathcal{G}}_0$ terms as these are combined with δ^{β_0} to give the dimensionless $\mathcal{G}_0$. Also, the coefficients $\mathcal{A}_1(\mathcal{P}_{km})$ and $\mathcal{A}_2(\mathcal{P}_{km})$ are re-defined, observed by comparing (44) and (47). These depend on the parameter $\mathcal{P}_{km}$ since they are determined by matching (46) and (47) in a transition region which is related to $\mathcal{P}_{km}$, as discussed below. Some of the terms in (46) and (47) have also been found in previous work. The terms in (46) were given in [16,26,31], and also in [28] in the asymptotic limit of large toughness, with the second given for $x \to \pm l$, i.e., in limit close to the tip. The first term in (47) is found in [17], and the first two terms in (47) are used in local expansions in [26,31], in the asymptotic limit of small toughness as $x \to \pm l$. However, the constant term in (47) is not found in [26]. This new parameter is important in the matching, as shown below.

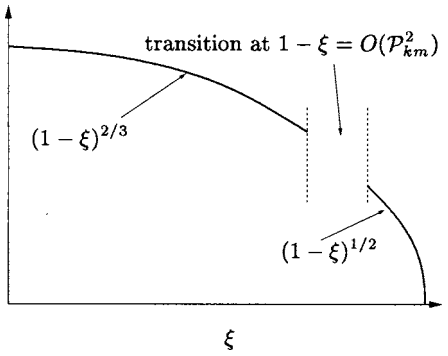

Fig. 2 Diagram of the solution Ω versus ξ near the fracture tip with transition region at $1-\xi = O(\mathcal{P}_{km}^2)$

The definition of the parameter $\mathcal{P}_{km}$ follows naturally from the two different regimes where either toughness or viscosity dominates the behavior. These two regimes correspond to $\alpha_1 > (<) 0$, as seen by re-examining (33) and (37). Recalling that $1-\xi = O(\delta)$, we can rewrite the condition on α_1 in terms of the physical parameters $\mathcal{G}_0$ and the distance from the tip. The solution for $\alpha_1 > 0$ is physically significant when toughness is dominant ($\mathcal{G}_k^3 \gg \mathcal{G}_m$), which in physical space is close to the tip and translates to $\mathcal{P}_{km} \gg (1-\xi)^{1/2}$. As $(1-\xi)^{1/2}$ approaches $\mathcal{P}_{km}$, the terms in (46) and (47) are the same order of magnitude; we observe a transition to an intermediate-tip region (see Fig. 2), which is found by considering $\alpha_1 < 0$ in (47). This is valid when the viscosity is dominant ($\mathcal{G}_k^3 \ll \mathcal{G}_m$), which in the physical space is away from the tip and translates to $\mathcal{P}_{km} \ll (1-\xi)^{1/2}$. Thus the expansion (46) holds for $1-\xi < \mathcal{P}_{km}^2$ and the expansion (47) for $1-\xi = O(\mathcal{P}_{km}^s)$, with $0 < s < 2$, and $\mathcal{P}_{km} \ll 1$.

The results confirm work carried out in [26] where the expansion is in terms of a parameter $\mathcal{K}^6 \ll 1$ with $\mathcal{G}_k = \mathcal{K}$ for $\mathcal{G}_v = \mathcal{G}_m = 1$; the relationship $\mathcal{P}_{km}^2 = O(1-\xi)$ can be shown to be equivalent to their scalings with $\mathcal{K}$. Also, our expansion for the toughness dominated solution (46) agrees with that found in [28] where a series expansion is obtained in terms of a parameter $\mathcal{M}$ with $\mathcal{G}_m = \mathcal{M}$ for $\mathcal{G}_v = \mathcal{G}_k = 1$. However, one difference between the two approaches is that in both [26,28] the matching is done by numerical calculation of a series expansion, while below we construct a uniform near-tip expansion analytically. The other main differences are that our framework can be extended to consider cases with more than two physical processes in balance, for example, including leak-off [32], and extended to cases in which the solution is not self-similar.

We construct a uniform near-tip asymptotic approximation by matching in the transition region where $\mathcal{G}_k^3/\mathcal{G}_m = O((1-\xi)^{1/2})$. In this region the leading order terms in the lubrication equation satisfy (25), coupled with the propagation condition (20). Note that both (46) and (47) are solutions of (25) in the two asymptotic limits. A closed form solution to (25) cannot be given in this

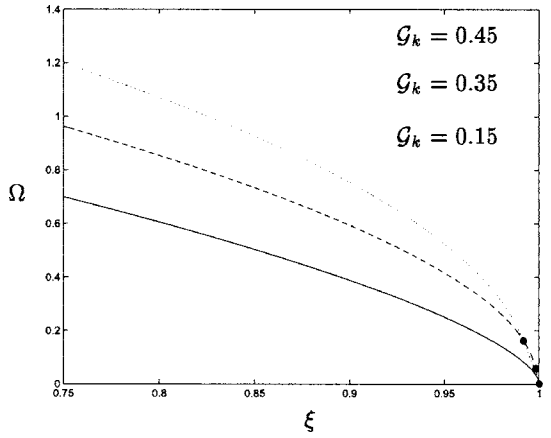

Fig. 3 Solution profiles of Ω versus ξ in the viscosity dominated regime with $\mathcal{G}_m$=1 and $\mathcal{G}_k$=0.45,0.35,0.15 (and so $\mathcal{P}_{km}$ =0.091,0.043,0.003)

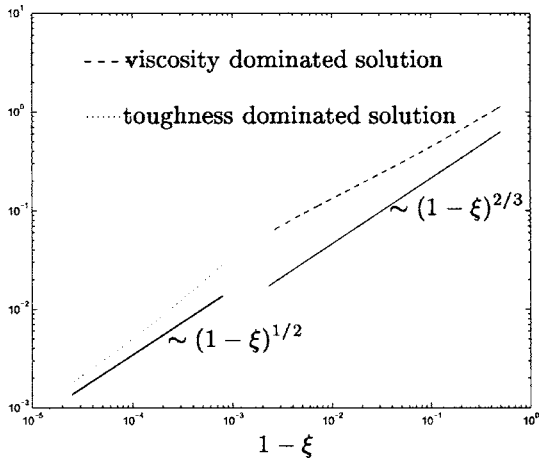

Fig. 4 Plot of $\log \Omega$ versus $\log(1-\xi)$ in the viscosity dominated regime with $\mathcal{G}_m$=1, $\mathcal{G}_k$=0.35 (and so $\mathcal{P}_{km}$=0.043). The solid line denotes the leading order power law solutions, as indicated above.

region, but it can be constructed computationally where $1-\xi = O(\mathcal{P}_{km}^2)$ for $0<\mathcal{P}_{km}\ll 1$, providing the basis for numerical matching in [26].

However, the identification of $\mathcal{P}_{km}$ and the correct form of Ω_2 allows us to determine the remaining unknown coefficients $\mathcal{A}_1(\mathcal{P}_{km})$ and $\mathcal{A}_2(\mathcal{P}_{km})$ to give an analytical expression for the matching. The critical scaling is $1-\xi=\mathcal{P}_{km}^2\zeta$ for $\zeta=0(1)$, and substitution into (46) and (47) yields, respectively

$$\Omega \sim \mathcal{G}_k[C_0\mathcal{P}_{km}\zeta^{1/2}\sqrt{2-\mathcal{P}_{km}^2\zeta}+C_1\mathcal{P}_{km}\zeta] \tag{48}$$

$$\Omega \sim \mathcal{G}_m^{1/3}[\bar{C}_1\mathcal{P}_{km}^{4/3}\zeta^{2/3}+\mathcal{A}_1(\mathcal{P}_{km})\mathcal{P}_{km}^{2h}\zeta^h+\mathcal{A}_2(\mathcal{P}_{km})] \tag{49}$$

Equating (48) and (49) and their first derivatives gives

$$\mathcal{A}_1(\mathcal{P}_{km}) = \frac{1}{h}\mathcal{P}_{km}^{-2h+4/3}\left[\frac{C_0}{\sqrt{2}}+C_1-\frac{2\bar{C}_1}{3}\right] \tag{50}$$

$$\mathcal{A}_2(\mathcal{P}_{km}) = \mathcal{P}_{km}^{4/3}\left[\frac{(2h-1)\sqrt{2}C_0}{2h}+\frac{(h-1)C_1}{h}-\frac{(3h-2)\bar{C}_1}{3h}\right] \tag{51}$$

which is equivalent to writing a Taylor series for (46) and (47) about $1-\xi=O(\mathcal{P}_{km}^2)$ where Ω is regular, and matching the first two terms. The coefficient of the error is proportional to $\Omega''(\zeta)$ which is bounded for $\zeta=O(1)$ with respect to $\mathcal{P}_{km}\ll 1$, so that terms are matched up to $O(\mathcal{P}_{km}^{4/3})$. Figure 3 shows solution profiles of Ω against ξ for several values of $\mathcal{P}_{km}$. The location of the match point within the transition region is identified in the figure by asterisks enclosed in circles. The majority of the solution in these cases follows the 2/3 power law characteristic of the viscosity dominated propagation. To further emphasize this transition we provide a log-log plot of Ω in Fig. 4. The asymptotic 1/2 and 2/3 power law behaviors for the toughness and viscosity dominated regions can be clearly seen, while in the transition region the solution does not follow a simple power law.

The elasticity equation (19) determines Π, which is used above in the lubrication equation as part of the solution process. The corresponding expansions to (46) and (47) are

$$\Pi \sim \mathcal{G}_k\left[\Pi_0-\mathcal{P}_{km}^{-1}\frac{C_1}{4\pi\gamma}\left\{\ln\left|1-\frac{1}{1+\xi}\right|+\ln\left|\frac{1}{1-\xi}\right|+\ln\xi\right\}\right] \tag{52}$$

$$\Pi \sim \mathcal{G}_m^{1/3}\left[m\cot\pi m\frac{\bar{C}_1}{4\gamma}(1-\xi)^{m-1}+h\cot\pi h\frac{\mathcal{A}_1(\mathcal{P}_{km})}{4\gamma}(1-\xi)^{h-1}\right] \tag{53}$$

for $\mathcal{P}_{km}\gg(\ll)(1-\xi)^{1/2}$, respectively, and the calculations are outlined in the Appendix. In Fig. 5 we graph Π for different values of $\mathcal{P}_{km}$. Note that Π is a monotonically decreasing function of ξ in each case, which is consistent with gradient driven fluid flow and dynamic, viscosity driven, fracture propagation. However, as $\mathcal{G}_k$ is increased Π becomes close to a constant in spite of the fact that the propagation regime is considered viscous owing to the 2/3 power law behavior of Ω over the majority of the fracture. Indeed, this pressure profile is surprisingly close to that in the toughness dominated regime which is characterized by a zero pressure gradient to leading order owing to the quasi-static mode fracture propagation in a tough material. We also note the presence of the region close to the fracture tip where the pressure becomes negative. This "cavitation region" is an artifact of the model which deviates from the physical situation where the fluid front lags behind the fracture front. Such fluid lag regions, which can be significant in fractures propagating in low confinement environments, are beyond the scope of the model considered in this paper as the appropriate zero pressure boundary condition and unknown lag boundary would have to be included. The phenomenon of fluid

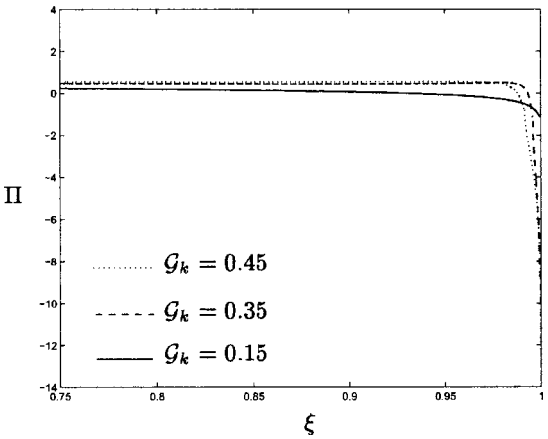

Fig. 5 Solution profiles of Π versus ξ corresponding to Ω in Fig. 3

lag has been studied analytically in [21,36] and numerically in [37], both for separate toughness and viscosity regimes, and analytically and numerically in [19] for the stationary problem with dominant toughness.

2.5 The Global Volume Balance Condition. We now use the global volume balance condition (13) to determine the dimensionless length parameter γ, defined in (8). The expression incorporates the dimensionless quantities $\mathcal{G}_{()}$ in (9) which involve powers of t. We can thus find the parameter λ, the power law exponent for $L=C_L t^{\lambda}$, with C_L constant, and justify the use of the self-similar solution. The condition also checks the ordering of the terms in the expansion. When $\mathcal{P}_{km} \gg 1$, clearly $\mathcal{P}_{km} \gg (1-\xi)^{1/2}$ and the solution for Ω in (46) holds for all ξ. Then the global volume balance condition becomes

$$\mathcal{G}_v = \gamma\pi\mathcal{G}_k C_0/2 + \gamma\mathcal{G}_k C_1 \mathcal{P}_{km}^{-1} \tag{54}$$

In the limit $\mathcal{G}_m \to 0$, the resulting value of γ in (54) agrees with the value obtained numerically in previous studies [31,28], which include computational results of Ω for $\xi \sim 0$. We substitute $L=C_L t^{\lambda}$ into (54) using the definitions of $\mathcal{G}_v$ and $\mathcal{G}_k$ from (9), and the expression for C_1 from (35), to give

$$\frac{Q_0}{\epsilon C_L^2} t^{1-2\lambda} = \pi\left(\frac{\gamma}{2}\right)^{3/2} \frac{K'}{\epsilon E' C_L^{1/2}} t^{-\lambda/2} + 4\pi\gamma^3 \frac{C_L^2 \mu' E'}{\epsilon K'^2} t^{\lambda-1} \tag{55}$$

Then, in this toughness dominated regime, we find that $\lambda = 2/3$.

Now we examine the situation $\mathcal{P}_{km} \ll 1$, away from the toughness dominated regime, where the solution for Ω in (46) is valid for $1-\xi < \mathcal{P}_{km}^2$, and (47) is valid for $\mathcal{P}_{km}^s > 1-\xi > \mathcal{P}_{km}^2$, for $0 < s < 2$. For the remainder of the integral (13), Ω must be computed numerically as in [23,26,31], yielding $\gamma \approx 0.61524$, which is used in Figs. 4 and 5. Although a numerical approximation of the solution is required near $\xi=0$ to find γ, this computation is straightforward and the significance of our method is that we can obtain an analytical result for the solution near the tip, where numerical computation is more difficult.

For $\mathcal{P}_{km} \ll 1$, the leading contribution to the integral in (13) is given by the part for ξ away from 1. For these values of ξ, the forms of the lubrication and elasticity equations indicate that Ω and Π must scale with $\mathcal{G}_m^{1/3}$, so that (13) reduces to $\mathcal{G}_v = \text{const} \cdot \mathcal{G}_m^{1/3}$. Substituting $L=C_L t^{\lambda}$ and the definitions of $\mathcal{G}_v$ and $\mathcal{G}_m$ from (9) then also yields $\lambda = 2/3$. The time dependence of the leading order terms are all $t^{-1/3}$, confirming that the self-similar solution, with γ is constant, is appropriate to leading order. In practice if leak-off is included, this assumption could break down and some time dependence in γ may have to be considered, as discussed in [32].

We summarize the main results (46) and (47) in the original dimensional variables. For $\mathcal{P}_{km} := (K'^3 t)/(\mu' E'^2 L^{3/2}) \gg (\ll) (1-x/l)^{1/2}$, respectively

$$w \sim \frac{K'}{E'} l^{1/2} \left\{ \left(1-\frac{x}{l}\right)^{1/2} + \frac{8\pi}{3}\gamma^{3/2}\mathcal{P}_{km}^{-1}\left(1-\frac{x}{l}\right) \right\} \tag{56}$$

$$w \sim \left(\frac{\mu'}{E'}\right)^{1/3} \frac{l}{t^{1/3}} \left\{ 2^{2/3}\sqrt{3}\left(1-\frac{x}{l}\right)^{2/3} + C_{11}\gamma^{-1}\mathcal{P}_{km}^{-2h+4/3}\left(1-\frac{x}{l}\right)^{h} + C_{12}\gamma^{-1}\mathcal{P}_{km}^{4/3} \right\} \tag{57}$$

Observe that these expansions confirm the well-known results regarding the time dependence of the fracture, as discussed in [17,23]; the fracture half-length $l(t)$ is proportional to $t^{2/3}$ and, therefore, the dimensional fracture width w is proportional to $t^{1/3}$. Also, the spatial dependence in (56) and (57) agrees with previous work: the first two terms in both these expansions were obtained in [26]; the leading order terms in both and the second term in (57) (in the asymptotic limit $x \to \pm l$) were obtained in [31]; and [28], which considers large toughness, obtained both terms in (56), again in the asymptotic limit $x \to \pm l$ for the latter. However, our analysis shows that the additional terms in (56) and (57) are needed to construct a uniform asymptotic near-tip solution between the two expansions.

3 Conclusions and Extensions

In this paper we have presented a new technique to analyze the system of integro-differential equations that arise when fluid-driven fractures are generated in an impermeable elastic solid. Our theoretical approach gives detailed solutions of the crack tip region and identifies the important processes controlling the fracture growth, namely viscosity and toughness. The combined parameter which quantifies these processes can be identified from critical scaling relationships between the nondimensional distance from the tip $1-\xi$ and the key nondimensional quantities $\mathcal{G}_k$, $\mathcal{G}_m$, and $\mathcal{G}_v$, representing toughness/energy release, viscosity, and injected fluid volume, respectively. This allows us to construct a uniform near-tip asymptotic expansion analytically instead of numerically as in [26]. From the expansion we can highlight the dominant physical processes through the parameter combination $\mathcal{P}_{km} = \mathcal{G}_k^3/\mathcal{G}_m$, relate these processes to the distance from the tip, and locate the transition region $\mathcal{P}_{km} = O((1-\xi)^{1/2})$.

It is straightforward to extend the method to the permeable case when leak-off is included. A similar analysis in [32] leads to expansions which we quote here in the original variables. For $\mathcal{P}_{ckm} := (K'^4 t^{1/2})/(C' \mu' E'^3 L^{1/2}) \gg (\ll) (1-x/l)^{1/2}$, respectively

$$w \sim \frac{K'}{E'} l^{1/2} \left\{ \left(1-\frac{x}{l}\right)^{1/2} + \left[\frac{8\pi}{3}\gamma^{3/2}\mathcal{P}_{km}^{-1} + 4\sqrt{2}\pi\gamma\mathcal{P}_{ckm}^{-1} \right] \left(1-\frac{x}{l}\right) \right\} \tag{58}$$

$$w \sim \left(\frac{C'\mu'}{E'}\right)^{1/4} \frac{l^{3/4}}{t^{1/8}} \gamma^{-3/4} \left\{ \tilde{C}_{01}\left(1-\frac{x}{l}\right)^{5/8} + \mathcal{B}_1\left(1-\frac{x}{l}\right)^{1/8} + \mathcal{B}_2\left(\frac{\mu'\gamma^{-3}}{C'^3 E'}\right)^{1/4} \frac{l^{3/4}}{t^{5/8}} \left(1-\frac{x}{l}\right)^{3/4} + \mathcal{B}_3\left(1-\frac{x}{l}\right)^{r} \right\} \tag{59}$$

where C' is the leak-off parameter, and $\mathcal{P}_{ckm}$ is a combination of $\mathcal{G}_k$, $\mathcal{G}_m$, and the corresponding dimensionless leak-off parameter. Observe that the fracture width w is now proportional to $t^{1/4}$, as opposed to $t^{1/3}$ for zero leak-off, which is deduced using the result that the fracture grows as $t^{1/2}$ for the permeable case. The results in (58) and (59) are found from balancing these three parameters simultaneously with the distance from the tip. The coefficients $\mathcal{B}_1$ and $\mathcal{B}_3$, analogous to $\mathcal{A}_1$ and $\mathcal{A}_2$ in this study, are determined by matching in the transition region. The expansion (58) gives the toughness dominated limit, and is analogous to (47) with an extra leak-off term. The expansion in (59) gives the leak-off dominated limit, where the leading order 5/8 term was established by [18] for the stationary solution. The other terms in (59) are new and again necessary in order to match the expansions in the two limits analytically.

Our methodology has also been applied to fracture propagation with a finger-like geometry, known as the PKN fracture [13,14]. The results show a transition between $(1-\xi)^{1/3}$ and $(1-\xi)^{2/3}$ power laws which correspond to the leading terms in the far- and near-tip expansions for zero toughness [33].

Acknowledgment

The authors gratefully acknowledge Emmanuel Detournay, José Adachi, and Dmitry Garagash for sharing a number of pre-prints with us and for their insightful comments. The authors would like to acknowledge the support of NSERC for this research through the Discovery Grant Program.

Appendix: Calculation of Π

To calculate Π we substitute expansions (46) and (47) into the elasticity equation (17). A parameter ξ^* is introduced which is in the transition region $1-\xi=O(P_{km}^2)$, for example $1-\xi^*=\mathcal{P}_{km}^2$. Then (17) becomes

$$\Pi = -\frac{\mathcal{G}_k}{4\pi\gamma}\int_{\xi^*}^{1}\{C_0[(1-\chi^2)^{1/2}]' + C_1\mathcal{P}_{km}^{-1}[(1-\chi)]'\}\frac{2\chi d\chi}{\chi^2-\xi^2}$$
$$-\frac{\mathcal{G}_m^{1/3}}{4\pi\gamma}\int_{0}^{\xi^*}\{\bar{C}_1[(1-\chi)^{2/3}]' + \mathcal{A}_1(\mathcal{P}_{km})[(1-\chi)^h]'\}\frac{2\chi d\chi}{\chi^2-\xi^2}$$
$$=: I_1 + I_2 \qquad \text{(A1)}$$

Different asymptotic expansions for I_1 and I_2 are found depending on the position of ξ relative to the interval of integration. In the near-tip region $\xi > \xi^*$, the integral I_2 gives $O(1)$ terms and the leading order contribution comes from the singularity in I_1. Hence the near-tip expansion for Π is

$$\Pi \sim \mathcal{G}_k\left[\frac{C_0}{4\gamma} - \frac{C_1\mathcal{P}_{km}^{-1}}{4\pi\gamma}\left\{\ln\left|\frac{\xi^2-\xi^{*2}}{1-\xi^2}\right|\right\}\right]$$

for $\mathcal{P}_{km} \gg 1$, which to leading order corresponds to (52) with $\xi^*=0$ in the correction.

For intermediate values $\xi < \xi^*$, the leading order expansion for Π comes from I_2 in (A1). Consider the general integral

$$J = \int_0^{\xi^*}\frac{(1-\chi)^{a-1}}{\chi-\xi}d\chi - \int_{-\xi^*}^{0}\frac{(1+\chi')^{a-1}}{\chi'-\xi}d\chi' =: J^A + J^B$$

where $0<a<1$. Then the result for I_2 follows by setting $a=2/3$ and $a=h$ in the integral J, since these exponents correspond to Π_1 and Π_2 from Sec. 2.3. Introducing variables $\delta Z = 1-\xi$ and $\delta R = 1-\chi$ means J^A can be written as

$$J^A = -\delta^{a-1}\left(\int_0^{\infty} - \int_{1/\delta}^{\infty} - \int_0^{(1-\xi^*)/\delta}\right)\frac{R^{a-1}}{R-Z}dR \qquad \text{(A2)}$$

Then the leading order contribution to Π in the intermediate-tip region $\xi < \xi^*$ is determined by the first integral in (A2) for $\delta = \mathcal{P}_{km}^2 \ll 1$, see [35]. Hence $J^A = (\delta Z)^{a-1}\pi\cot\pi a + O(1)$ and a similar calculation gives J^B. Thus

$$\Pi \sim \frac{\mathcal{G}_m^{1/3}}{4\gamma}\left\{\frac{m\cot\pi m\bar{C}_1}{4\gamma}(1-\xi)^{m-1} + \frac{h\cot\pi h\mathcal{A}_1(\mathcal{P}_{km})}{4\gamma}(1-\xi)^{h-1}\right\}$$

for $\mathcal{P}_{km} \ll 1$, where $m=2/3$ and $h \approx 0.138673$, and corresponds to leading order to (39).

References

[1] Lister, J. R., 1990, "Buoyancy-Driven Fluid Fracture: Similarity Solutions for the Horizontal and Vertical Propagation of Fluid-Filled Cracks," J. Fluid Mech., **217**, pp. 213–239.

[2] Lister, J. R., 1990, "Buoyancy-Driven Fluid Fracture: The Effects of Material Toughness and of Low-Viscosity Precursors," J. Fluid Mech., **210**, pp. 263–280.

[3] Spence, D. A., and Turcotte, D. L., 1985, "Magma-Driven Propagation of Cracks," J. Geophys. Res., **90**, pp. 575–580.

[4] Van As, A., and Jeffrey, R. G., 2000, "Caving induced by Hydraulic Fracturing at Northparkes Mines," in *Proc. 4th North American Rock Mechanics Symp.*, J. E. A. Girard, ed., pp. 353–360.

[5] Abé, H., Mura, T., and Keer, L. M., 1976, "Growth Rate of a Penny-Shaped Crack in Hydraulic Fracturing of Rocks," J. Geophys. Res., **81**, pp. 5335–5340.

[6] Barenblatt, G., 1962, "The Mathematical Theory of Equilibrium Cracks in Brittle Fracture," Adv. Appl. Mech., **7**, pp. 55–129.

[7] Crittendon, B. C., 1959, "The Mechanics of Design and Interpretation of Hydraulic Fracture Treatments," J. Pet. Technol., **11**(10), pp. 21–29.

[8] Geertsma, J., and de Klerk, F., 1969, "A Rapid Method of Predicting Width and Extent of Hydraulically Induced Fractures," J. Pet. Technol., **246**, pp. 1571–1581.

[9] Harrison, E., Kieschnick, W. F., and McGuire, W. J., 1954, "The Mechanics of Fracture Induction and Extension," Trans. Am. Inst. Min., Metall. Pet. Eng., **201**, pp. 252–263.

[10] Howard, G. C., and Fast, C. R., 1957, "Optimum Fluid Characteristics for Fracture Extension," Drill. & Prod. Prac., **24**, pp. 261–270.

[11] Hubbert, M. K., and Willis, D. G., 1957, "Mechanics of Hydraulic Fracturing," Trans. Am. Inst. Min., Metall. Pet. Eng., **210**, pp. 153–166.

[12] Khristianovic, S., and Zheltov, Y., 1955, "Formation of Vertical Fractures by Means of Highly Viscous Fluids," in *Proc., 4th World Petroleum Congress*, pp. 579–586.

[13] Nordgren, R., 1972, "Propagation of Vertical Hydraulic Fractures," SPEJ, **12**, pp. 306–314.

[14] Perkins, T. K., and Kern, L. R., 1961, "Widths of Hydraulic Fractures," J. Pet. Technol., **222**, pp. 937–949.

[15] Detournay, E., and Garagash, D. I., 2004, "General Scaling Laws for Fluid-Driven Fractures," Preprint.

[16] Spence, D. A., and Sharp, P., 1985, "Self-Similar Solutions for Elastohydro Dynamic Cavity Flow," Proc. R. Soc. London, Ser. A, **400**, pp. 289–313.

[17] Desroches, J., Detournay, E., Lenoach, B., Papanastasiou, P., Pearson, J. R. A., Thiercelin, M., and Cheng, A. H.-D., 1994, "The Crack Tip Region in Hydraulic Fracturing," Proc. R. Soc. London, Ser. A, **447**, pp. 39–48.

[18] Lenoach, B., 1995, "The Crack Tip Solution for Hydraulic Fracturing in a Permeable Solid," J. Mech. Phys. Solids, **43**(7), pp. 1025–1043.

[19] Detournay, E., and Garagash, D. I., 2003, "The Near-Tip Region of a Fluid-Driven Fracture Propagating in a Permeable Elastic Solid," J. Fluid Mech., **494**, pp. 1–32.

[20] Detournay, E., Adachi, J. I., and Garagash, D. I., 2002, "Asymptotic and Intermediate Asymptotic Behavior Near the Tip of a Fluid-Driven Fracture Propagating in a Permeable Elastic Medium," in *Structural Integrity and Fracture*, Dyskin, Hu, and Sahouryeh, eds., Swets and Zeitlinger, Lisse.

[21] Garagash, D., and Detournay, E., 2000, "The Tip Region of a Fluid-Driven Fracture Propagating in an Elastic Medium," ASME J. Appl. Mech., **67**, pp. 183–192.

[22] Detournay, E., 2004, "Propagation Regimes of Fluid-Driven Fractures in Impermeable Rocks," Int. J. Geomech., **4**, pp. 1–11.

[23] Adachi, J. I., and Detournay, E., 2002, "Self-Similar Solution of a Plane-Strain Fracture Driven by a Power-Law Fluid," Int. J. Numer. Analyt. Meth. Geomech., **26**, pp. 579–604.

[24] Carbonell, R. S., Desroches, J., and Detournay, E., 1999, "A Comparison Between a Semi-Analytical and a Numerical Solution of a Two-Dimensional Hydraulic Fracture," Int. J. Solids Struct., **36**, pp. 4869–4888.

[25] Savitski, A. A., and Detournay, E., 2002, "Propagation of a Penny-Shaped Fluid-Driven Fracture in an Impermeable Rock: Asymptotic Solutions," Int. J. Solids Struct., **39**, pp. 6311–6337.

[26] Garagash, D. I., and Detournay, E., 2005, "Plane-Strain Propagation of a Fluid-Driven Fracture: Small Toughness Solution," ASME J. Appl. Mech., **72**, pp. 916–928.

[27] Adachi, J. I., and Detournay, E., 2005, "Plane-Strain Propagation of a Fluid-Driven Fracture: Finite Toughness Self-Similar Solution," (in preparation).

[28] Garagash, D. I., 2005, "Plane-Strain Propagation of a Hydraulic Fracture During Injection and Shut-In: Asymptotics of Large Toughness," Eng. Fract. Mech., **73**(4), pp. 456–481.

[29] Adachi, J. I., and Detournay, E., 2006, "Propagation of a Fluid-Driven Fracture in a Permeable Medium," Int. J. Fract. (submitted).

[30] Garagash, D. I., 2000, "Hydraulic Fracture Propagation in Elastic Rock with Large Toughness," in *Proc. 4th North American Rock Mechanics Symp.*, J. Girard, M. Liebman, C. Breeds, and D. T, eds., pp. 221–228.

[31] Adachi, J. I., 2001, "Fluid-Driven Fracture in Permeable Rock," PhD. thesis, University of Minnesota, Department of Civil Engineering (available at www.umi.com), December.

[32] Mitchell, S. L., Kuske, R., and Peirce, A. P., 2005, "An Asymptotic Framework for Finite Hydraulic Fractures Including Leak-Off," to SIAM J. Appl. Math. (under review).

[33] Mitchell, S. L., Kuske, R., Peirce, A. P., and Adachi, J. I., 2005, "An Asymptotic Analysis of a Finger-Like Fluid-Driven Fracture," (in preparation).

[34] Griffith, A. A., 1921, "The Phenomena of Rupture and Flow in Solids," Philos. Trans. R. Soc. London, Ser. A, **221**, pp. 163–198.

[35] Martin, P. A., 1991, "End-Point Behavior of Solutions to Hypersingular Integral Equations," Proc. R. Soc. London, Ser. A, **432**, pp. 301–320.

[36] Garagash, D. I., 2005, "Propagation of a Plane-Strain Hydraulic Fracture With a Fluid Lag: Early Time Solution," Int. J. Solids Struct. (in press).

[37] Lecampion, B., and Detournay, E., 2006, "An Implicit Algorithm for the Propagation of a Hydraulic Fracture With a Fluid Lag," Computer Methods in Applied Mechanics and Engineering (submitted).

Journal of Applied Mechanics

Technical Briefs

An Extension of Hertz's Theory in Contact Mechanics

Guanghui Fu
Lam Research Corporation,
4540 Cushing Parkway,
Fremont, CA 94538
e-mail: guanghui.fu@lamrc.com

Hertz's theory, developed in 1881, remains the foundation for the analysis of most contact problems. In this paper, we consider the axisymmetric normal contact of two elastic bodies, and the body profiles are described by polynomial functions of integer and noninteger positive powers. It is an extension of Hertz's solution, which concerns the contact of two elastic spheres. A general procedure on how to solve this kind of problem is presented. As an example, we consider the contact between a cone and a sphere. The relations among the radius of the contact area, the depth of the indentation, the total load, and the contact pressure distribution are derived. [DOI: 10.1115/1.2188017]

1 Introduction

Contact pressure distribution between two surfaces has always been of great interest to engineers. The widely used equation for bearing application is Hertz's solution. Boussinesq's solution for a flat-ended punch finds its application in the safety evaluation of foundations in civil engineering. Recently, researchers used the Love and Sneddon solution for a conical punch to explain nanoindentation experimental data (e.g., Fu and Fischer-Cripps [1]). For the better understanding of fretting fatigue, Ciavarella investigated the pressure distribution for indenters with rounded corners [2].

Perhaps the most famous solution in contact mechanics is Hertz's formula for the contact of two elastic bodies. Hertz derived the solution in 1881; later, he tried to extend it to a hardness definition [3]. Hertz's solution is based on the linear theory of elasticity. The materials of the two bodies are homogenous and isotropic. Their surfaces are smooth and continuous. The normal contact of the two bodies is frictionless, and the load is static. The distance between the two bodies is zero within the contact region, and is finite outside. Without the external force, the contact zone is a point. The contact pressure is localized, and disappears at great distance from the contact area. This leads to Hertz's assumption that each body may be considered as a half-space in order to calculate the local deformations. Although Hertz's theory has been used in wide ranges of applications, it has some limitations; e.g., it considers mainly the nonconformal contact of spheres, while in reality, body profiles may be complicated. In this paper, we consider the axisymmetric normal contact of two elastic bodies, and extend Hertz's theory to bodies with polynomial profiles. The results for the contact between a cone and a sphere are presented as an example.

2 Problem Formulation in the Theory of Linear Elasticity

We use Hertz's assumptions, except that the shapes of the bodies are not necessarily spherical. Following the standard procedure in contact mechanics, this problem is reduced to the axisymmetric normal indentation of a flat elastic half-space with a rigid smooth frictionless punch [4]. In our frame of reference, the x-y plane is the common plane tangent to the surfaces of the two bodies before the deformation, and the z axis is directed into one of the solids. The shape of the punch is defined as

$$f(r) = z_1(r) - z_2(r) \tag{1}$$

where $z_1(r)$ and $z_2(r)$ describe individual body profiles.

The elastic modulus of the half-space is related to the elastic properties of the two bodies by the following equation:

$$\frac{1}{E} = \frac{1-\nu_1^2}{E_1} + \frac{1-\nu_2^2}{E_2} \tag{2}$$

where E_i is Young's modulus and ν_i Poisson's ratio of body i. Poisson's ratio of the half-space is zero.

The punch described by Eq. (1) has the axis of revolution as the z axis. It indents into the plane $z=0$ of the elastic half-space $z \geqslant 0$. The problem is considered in the linear theory of elasticity, and the half-space is assumed to be isotropic and homogeneous. The contact region between the punch and the half-space is simply connected. The following equations give the relevant displacement and stresses for the half-space. The vertical component of the displacement is denoted by u_z, and the stress components have two subscripts corresponding to the appropriate coordinates.

The boundary conditions for the half-space at $z=0$ are

$$\tau_{zr} = \tau_{z\theta} = 0, \quad (0 \leqslant r < \infty) \tag{3}$$

$$\sigma_{zz} = 0, \quad (r > a) \tag{4}$$

$$u_z = h + f(r), \quad (0 \leqslant r \leqslant a) \tag{5}$$

where a is the radius of the contact area, and h is the depth of the indentation ($h \geqslant 0$). Equation (3) describes the frictionless contact (zero shear stresses and discontinuity of tangential displacements at the interface). The second term at the right-hand side of Eq. (5) describes the shape of the punch, which depends on the geometries of the two bodies, and is given by Eq. (1). $f(0)=0$; if $f'(0) \neq 0$, the punch will have a sharp tip at its apex.

Because the two bodies are smooth, $f(r)$ will be a smooth function, and can be expressed as a polynomial series. The analytical solution to the problem of normal indentation of a flat elastic half-space with a rigid axisymmetric polynomial punch is avail-

Contributed by the Applied Mechanics Division of ASME for publication in the JOURNAL OF APPLIED MECHANICS. Manuscript received November 8, 2005; final manuscript received January 20, 2006. Review conducted by M. R. Begley.

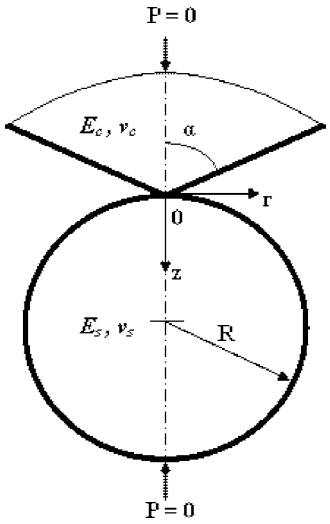

Fig. 1 Cone-sphere contact under zero load

able [5]. From Ref. [5], it will not be difficult to find those relations: (a) the radius of the contact area versus the depth of the indentation, (b) the total load versus the depth of the indentation, and (c) the contact pressure distribution. To illustrate the procedure, we consider a special case: the contact between a cone and a sphere.

3 Cone-Sphere Contact

Following the method given above, the original cone-sphere contact problem is converted to the axisymmetric normal indentation of a flat elastic half-space by a rigid second-order polynomial punch (Figs. 1 and 2). Equation (5) becomes

$$u_z = h - \cot\alpha \cdot r - \frac{r^2}{2R}, \quad (0 \leqslant r \leqslant a) \tag{6}$$

where α is the half-included angle of the cone, and R is the radius of the sphere.

The radius of the contact area a and the depth of the penetration h are related by the following equation:

$$h - \frac{\pi}{2}\cot\alpha \cdot a - \frac{a^2}{R} = 0 \tag{7}$$

Solving a from the quadratic equation, we have

$$a = -\frac{R}{4}\left(\pi\cot\alpha \pm \sqrt{(\pi\cot\alpha)^2 + \frac{16h}{R}}\right) \tag{8}$$

Three conditions have to be satisfied in order to make Eq. (8) physically meaningful: (a) the radius of the contact area should be a non-negative number, (b) the radius of the contact area should not be a complex number, and (c) the contact area is a simply connected domain. Under these conditions, the radius of the contact area can only be

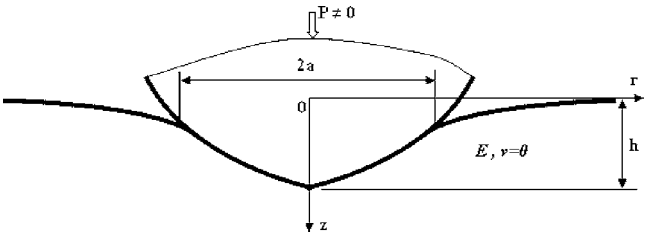

Fig. 2 Indentation of an elastic half-space with a rigid second-order polynomial punch

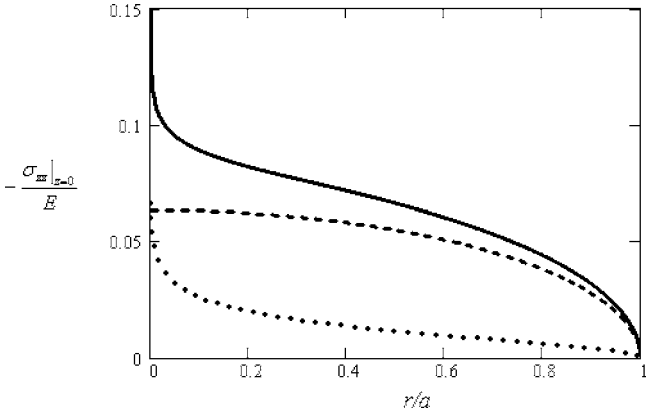

Fig. 3 Contact pressure distributions: solid line is for the cone-sphere contact, dotted line is for the cone–half-space contact, and dashed line is for the sphere–half-space contact

$$a = -\frac{R}{4}\left(\pi\cot\alpha - \sqrt{(\pi\cot\alpha)^2 + \frac{16h}{R}}\right) \tag{9}$$

The total vertical load P, which causes the displacement h, is

$$P = E\left(2ah - \frac{\pi}{2}\cot\alpha \cdot a^2 - \frac{2}{3R}a^3\right) \tag{10}$$

where

$$\frac{1}{E} = \frac{1-\nu_c^2}{E_c} + \frac{1-\nu_s^2}{E_s}.$$

c in the subscript refers to the cone, and s the sphere.

Under the condition given by Eq. (7), the contact pressure between the cone and the sphere is

$$\sigma_{zz}|_{z=0} = -E\left(\frac{\cot\alpha}{4}\ln\frac{a+\sqrt{a^2-r^2}}{a-\sqrt{a^2-r^2}} + \frac{2}{\pi R}\sqrt{a^2-r^2}\right),$$

$$(0 \leqslant r \leqslant a) \tag{11}$$

The first term in Eq. (11) shows the influence of cone geometry on the pressure distribution, and the second term indicts the effect of sphere geometry. The shape of the pressure profile is governed solely by α and R. The logarithmic singularity in the pressure profile happens at the tip of the cone, and it is due to the nonsmoothness of the cone tip.

The solid line in Fig. 3 shows a typical pressure distribution of the cone-sphere contact. In the simulation, we choose $\alpha = 89$ deg and $R = 10$ m. In the same figure, we also put two other pressure distributions: the dotted line is for the contact between a rigid cone with the same half-included angle α, and a flat half-space; the dashed line is for the contact between a rigid sphere with the same radius R and a flat half-space. In both cases, the half-space has the same Young's modulus E. Figure 3 shows clearly that the pressure singularity is due to the cone.

References

[1] Fu, G., and Fischer-Cripps, A. C., 2005, "On Sneddon's Boundary Conditions Used in the Analysis of Nanoindentation Data," J. Mater. Sci., **40**, pp. 1789–1791.

[2] Ciavarella, M., 1999, "Indentation by Nominally Flat or Conical Indenters with Rounded Corners," Int. J. Solids Struct., **36**, pp. 4149–4181.

[3] Hertz, H., 1896, *Miscellaneous Papers by Heinrich Hertz*, MacMillan & Co, London, UK, p. 146–183.

[4] Johnson, K. L., 1985, *Contact Mechanics*, Cambridge University Press, Cambridge, UK, Chap. 4.

[5] Fu, G., and Chandra, A., 2002, "Normal Indentation of Elastic Half-Space With a Rigid Frictionless Axisymmetric Punch," ASME J. Appl. Mech., **69**, pp. 142–147.

Wavelet-Based Sensitivity Analysis of the Impulse Response Function for Damage Detection

S. S. Law

X. Y. Li

Civil and Structural Engineering Department,
Hong Kong Polytechnic University,
Hunghom, Kowloon,
Hong Kong, P.R.C.

This paper discusses the extraction of the wavelet-based impulse response function from the acceleration response using the discrete wavelet transform (DWT). The analytical formulation of the sensitivity of the DWT coefficient of the impulse response function with respect to a system parameter is then presented for structural damage detection. A numerical example with a 31-bar *plane truss structure is used to verify the proposed method with different damage scenarios with or without model error and noise effect.*
[DOI: 10.1115/1.2189875]

1 Introduction

Numerous methods for damage detection have been developed based on the observation of the dynamic behavior of a structure. Cattarius and Inman [1] used the time history of structural vibration response to identify damage in smart structures. More recently the sensitivity matrix of response is computed using Newmark method [2], and it was used directly in an inverse problem for structural damage identification. The results were subject to the effect of measurement noise and model error. This deficiency was significantly alleviated later in an approach using the sensitivity of the wavelet coefficient of structural responses [3]. All these approaches require approximately equal excitation for the testing the different states of the structure. To remove this restriction, the impulse response function (IRF) is studied in the damage detection process in this paper. IRFs are intrinsic functions of the system given the excitation location, and they can be easily extracted from the measured response. The analytical formulation of the sensitivity of the discrete wavelet transform coefficient of the impulse response function with respect to a system parameter is derived. The identification equation is then solved using the damped least-squares method. Numerical example with a 31-bar plane truss structure is used to verify the proposed method with different damage scenarios with and without model error and noise effects.

2 Sensitivity of Wavelet-Based Unit Impulse Response

The equation of motion of a N–degree-of-freedom (DOF) damped structural system under the unit impulse excitation is

$$M\ddot{x} + C\dot{x} + Kx = D\delta(t) \tag{1}$$

where M, C, and K are the $N\times N$ mass, damping, and stiffness matrices, respectively. D is the mapping matrix relating the force excitation location to the corresponding degrees of freedom of the system. x, $\dot{x}$, and $\ddot{x}$ are the $N\times 1$ displacement, velocity, and acceleration vectors, respectively. $\delta(t)$ is the Dirac delta function. Assuming the system is in static equilibrium, initially, the unit impulse response function can be computed from the following equation using the Newmark method:

$$\begin{cases} M\ddot{h} + C\dot{h} + Kh = 0 \\ h(0) = 0, \quad \dot{h}(0) = M^{-1}D \end{cases} \tag{2}$$

where h, $\dot{h}$, and $\ddot{h}$ are the unit impulse displacement, velocity, and acceleration vectors, respectively. We express local damage in the structural system as $\Delta K=\Sigma_{i=1}^{ne}\alpha_i K_i$, with $0\leqslant\alpha_i\leqslant 1.0$, and ne is the number of elements in the structure. Differentiating Eq. (2) with respect to α_i, we get

$$\begin{cases} M\dfrac{\partial\ddot{h}}{\partial\alpha_i} + C\dfrac{\partial\dot{h}}{\partial\alpha_i} + K\dfrac{\partial h}{\partial\alpha_i} = -\dfrac{\partial K}{\partial\alpha_i}h \\ \dfrac{\partial h(0)}{\partial\alpha_i} = 0, \quad \dfrac{\partial\dot{h}(0)}{\partial\alpha_i} = \dfrac{\partial M^{-1}D}{\partial\alpha_i} \end{cases} \tag{3}$$

The sensitivities $\partial h/\partial\alpha_i$, $\partial\dot{h}/\partial\alpha_i$, and $\partial\ddot{h}/\partial\alpha_i$ can be obtained from Eq. (3) using the Newmark method.

A response $f(t)$ when expressed in terms of the Daubechies wavelets [4] can be approximated in terms of its discrete wavelet transform (DWT) as

$$f(t) = f_0^{\mathrm{DWT}}\varphi(t) + f_1^{\mathrm{DWT}}\psi(t) + f_2^{\mathrm{DWT}}\psi(2t) + \cdots + f_{2^j+k}^{\mathrm{DWT}}\psi(2^j t - k) \tag{4}$$

where $\varphi(t)$ and $\psi(t)$ are the scaling function and the mother wavelet function, respectively. $f_{2^j+k}^{\mathrm{DWT}}$ is the wavelet transform coefficients. For real wavelets, $f_0^{\mathrm{DWT}}=\int f(t)\varphi(t)dt$ and $f_{2^j+k}^{\mathrm{DWT}}=\int f(t)\psi_{j,k}(t)dt$. Differentiating $f_{2^j+k}^{\mathrm{DWT}}$ with respect to the stiffness parameter of an element, we have [3]

$$\left(\frac{\partial\ddot{h}}{\partial\alpha_i}\right)_{2^j+k}^{\mathrm{DWT}} = \int\frac{\partial\ddot{h}}{\partial\alpha_i}\psi_{j,k}(t)dt \tag{5}$$

The sensitivity matrix can then be obtained from Eq. (5)

$$S = \left[\frac{\partial\ddot{h}_l^{\mathrm{DWT}}}{\partial\alpha_1}\ \frac{\partial\ddot{h}_l^{\mathrm{DWT}}}{\partial\alpha_2}\ \cdots\ \frac{\partial\ddot{h}_l^{\mathrm{DWT}}}{\partial\alpha_m}\right] \tag{6}$$

where $\ddot{h}_l^{\mathrm{DWT}}$ is the DWT coefficient of $\ddot{h}_l$, and $\ddot{h}_l$ denotes the acceleration impulse response function at location l, and m is the number of the structural parameters.

3 Impulse Response Function via Discrete Wavelet Transform

When the N-DOF damped structural system is under general excitation $F(t)$ with zero initial conditions, the acceleration response $\ddot{x}_l(t_n)$ from location l at time t_n is

$$\ddot{x}_l(t_n) = \int_0^{t_n}\ddot{h}_l(\tau)F(t_n-\tau)d\tau \tag{7}$$

Applying the DWT to $\ddot{h}_l(\tau)$ and $F(t_n-\tau)$ separately, we get

$$\ddot{x}_l(t_n) = \int_0^{t_n}[\ddot{h}_{l,0}^{\mathrm{DWT}}\varphi(\tau) + \ddot{h}_{l,1}^{\mathrm{DWT}}\psi(\tau) + \cdots + \ddot{h}_{l,2^j+k}^{\mathrm{DWT}}\psi(2^j\tau-k)] \times[F_0^{\mathrm{DWT}}(t_n)\varphi(\tau) + F_1^{\mathrm{DWT}}(t_n)\psi(\tau) + \cdots + F_{2^j+k}^{\mathrm{DWT}}(t_n)\psi(2^j\tau - k)]d\tau \tag{8}$$

Contributed by the Applied Mechanics Division of ASME for publication in the JOURNAL OF APPLIED MECHANICS. Manuscript received February 3, 2005; final manuscript received February 3, 2006. Review conducted by O. M. O'Reilly.

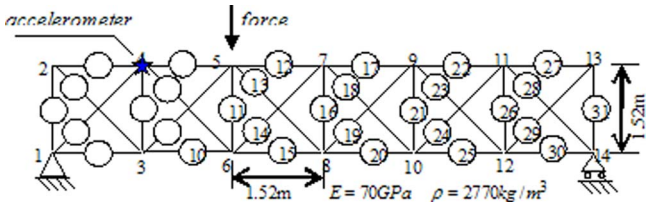

Fig. 1 31-bar plane truss structure

Using the orthogonal conditions for both the translation and scale of the Daubechies wavelets, Eq. (8) can be rewritten in matrix form for a time series

$$\ddot{x}_l = F^{\mathrm{DWT}} \ddot{h}_l^{\mathrm{DWT}} \tag{9}$$

where

$$\ddot{x}_l = [\ddot{x}_l(t_1)\ \ddot{x}_l(t_2)\ \cdots\ \ddot{x}_l(t_n)]^T, \quad F^{\mathrm{DWT}} = \begin{bmatrix} F^{\mathrm{DWT}}(t_1) \\ F^{\mathrm{DWT}}(t_2) \\ \cdots \\ F^{\mathrm{DWT}}(t_n) \end{bmatrix}$$

$$F^{\mathrm{DWT}}(t_n) = [F_0^{\mathrm{DWT}}(t_n)\ F_1^{\mathrm{DWT}}(t_n)\ \cdots\ F_{2^j+k}^{\mathrm{DWT}}(t_n)/2^j],$$

$$\ddot{h}_l^{\mathrm{DWT}} = [\ddot{h}_{l,0}^{\mathrm{DWT}}\ \ddot{h}_{l,1}^{\mathrm{DWT}}\ \cdots\ \ddot{h}_{l,2^j+k}^{\mathrm{DWT}}]^T$$

Finally, $\ddot{h}_l^{\mathrm{DWT}}$ can be computed using a pseudoinverse as

$$\ddot{h}_l^{\mathrm{DWT}} = (F^{\mathrm{DWT}^T} F^{\mathrm{DWT}})^{-1} F^{\mathrm{DWT}^T} \ddot{x}_l \tag{10}$$

4 Damage Identification Equation

In Eq. (10), $\ddot{h}_{l0}^{\mathrm{DWT}}$ and $\ddot{h}_{ld}^{\mathrm{DWT}}$ are vectors of the DWT coefficients of the impulse response function from the two states of the structure. $\partial \ddot{h}_{l0}^{\mathrm{DWT}} / \partial \alpha$ is the sensitivity matrix of the DWT coefficient with respect to the structural parameter of the intact state. $\Delta\alpha$ is the vector of parameter change of the system. We can express the identification equation as

$$\ddot{h}_{ld}^{\mathrm{DWT}} - \ddot{h}_{l0}^{\mathrm{DWT}} = \frac{\partial \ddot{h}_{l0}^{\mathrm{DWT}}}{\partial \alpha} \Delta\alpha = S\Delta\alpha \tag{11}$$

The solution of Eq. (11) is ill conditioned, and the damped least-squares method [5] is adopted for the solution. When measurements from the intact state of the structure are obtained, $\ddot{h}_{l0}^{\mathrm{DWT}}$ is the vector of the DWT coefficients computed from the analytical model. $\ddot{h}_{ld}^{\mathrm{DWT}}$ is computed with the measured responses and the input forces obtained in experiment from the intact state from Eqs. (2) and (6). The sensitivity matrix $\partial \ddot{h}_{l0}^{\mathrm{DWT}} / \partial \alpha$ is computed from the analytical model of the structure at the initial state. The analytical model is then updated, and the corresponding wavelet coefficient and its sensitivity are again computed for the next iteration. Convergence is considered achieved when both the norms of fractional difference between successive iterations of the $\ddot{h}_l^{\mathrm{DWT}}$ and $\Delta\alpha$ are smaller than some prescribed values. When measurement from the damaged state is obtained, the updated analytical model is used in the iteration in the same way as that using the measurement from the intact state. The final set of identified parameter increments correspond to the changes that have occurred between the two states of the structure.

5 Simulation

The 31-bar plane truss shown in Fig. 1 is modeled using 31 finite elements without internal nodes in the bars giving 28 degrees of freedom. The cross-sectional area of the bar is 0.0025 m^2.

Table 1 Damage scenarios

Damage scenario	Damage extent (%)	Damage locations	Noise	Model error
1	5,10	22nd, 26th element	no	no
2	5 10,10	28th, 30th, 31st element	no	no
3	10	28th element	1%	no
4	10	28th element	5%	no
5	5,10	22nd, 26th element	no	2% reduction in the stiffness in all elements
6	5,10	22nd, 26th element	no	50% increase in the support stiffness at two supports
7	5,10	22nd, 26th element	no	2% decrease in the Rayleigh damping coefficients
8	5,10	22nd, 26th element	5%	Include all the above model errors

Damage in the structure is defined as a reduction in the axial stiffness of individual bars with the inertial properties unchanged. The translational restraints at the supports are represented by large stiffnesses of 1.0×10^{10} kN/m. Rayleigh damping of $\xi_1=0.01$ and $\xi_2=0.01$ is adopted. The first 12 natural frequencies of the structure range from 36.415 Hz to 547.393 Hz.

Excitation is applied in the downward direction at node 5 while the vertical acceleration measurement at node 4 is recorded. Two different excitations are used in the different states of the structure. Note that this is different from those in Refs. [2,3]. Excitation for the intact state is an impulsive force with 320.4 N peak value and it lasts for 0.005 s. Excitation for the damaged state is a sinusoidal force of $F=20\sin(2\pi 20t)$ *N*. Sampling rate is 2000 Hz and the first 0.25 s of the acceleration response is used for the damage identification. The tolerance limits for both convergence criteria have been set equal to 1.0×10^{-6}.

Table 1 shows eight damage scenarios with and without noise and model error effects. The latter group of scenarios is studied with one IRF, while the former group of scenarios is studied with an averaged IRF from 20 samples. Results in Fig. 2 show that both the damage location and extent are identified very accurately without any alarm in other elements for scenarios without noise and model errors. The random noise is seen to cause error in the damaged element and with alarm in several other elements in scenarios 3 and 4. The identified results for scenarios 5–8 are acceptable for the damaged elements while there is alarm in several other elements in the last scenario with the combined noise and model error effects. The presence of random noise in the "measured" data is noted to amplify the erroneous effect due to the model errors.

6 Discussion

The noise effect can be further reduced by averaging from longer duration of measurement with more and better located sensors. However, the initial model errors associated with a sticky joint, material nonlinearity, cracks and fissures in a member, etc., cannot be addressed using the present approach of modeling the damage with an averaged damage parameter. Separate damage models should be included in the initial model for proper identification. This, however, is optimistic since there are few damage models. The wavelet is known to have a full bandwidth of the responses, and further benefit can be sought by employing sensitivity of wavelet coefficients from different bandwidth in the inverse analysis, as the noise effect and model error would have different contributions to the different bandwidths of the responses [3].

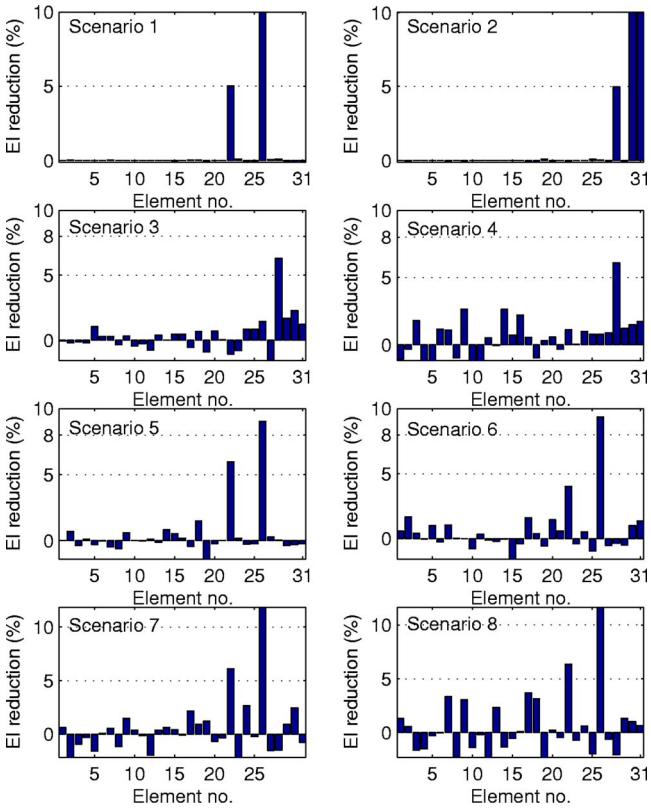

Fig. 2 Identified results for scenarios

7 Conclusions

A new method is developed for damage detection using the sensitivity of the DWT coefficient of the impulse response function. It removes the restriction of requiring approximately equal excitation in testing the different states of the structure. The analytical formulation of the sensitivity with respect to a system parameter is derived. Numerical example with a 31-bar plane truss structure is studied with different damage scenarios. The new approach is shown to be effective for damage detection, but the results are subject to the effect of measurement noise and model errors.

Acknowledgment

The work described in this paper was supported by a grant from the Hong Kong Research Grant Council Project No. PolyU 5043/02E and a research grant from the Hong Kong Polytechnic University.

References

[1] Cattarius, J., and Inman, D. J., 1997, "Time Domain Analysis for Damage Detection in Smart Structures," Mech. Syst. Signal Process., **11**(3), pp. 409–423.
[2] Lu, Z. R., and Law, S. S., 2007, "Features of Dynamic Response Sensitivity and Its Application in Damage Detection," J. Sound Vib., under review.
[3] Law, S. S., and Li, X. Y., 2007 "Structural Damage Detection from Wavelet Coefficient Sensitivity with Model Errors," J. Eng. Mech. Div., Am. Soc. Civ. Eng., in press.
[4] Daubechies, I., 1992, *Ten Lectures on Wavelets*, SIAM, Philadelphia.
[5] Tikhonov, A. N., and Arsenin, V. Y., 1997, "Solution of Ill-Posed Problems," Winston and Sons, Washington, DC.

Dynamic *T*-Stress for a Mode-I Crack in an Infinite Elastic Plane

Xian-Fang Li
Institute of Mechanics and Sensor Technology,
School of Civil Engineering and Architecture,
Central South University,
Changsha, Hunan 410083, China
e-mail: xfli@mail.csu.edu.cn

An integral equation method is presented to determine dynamic elastic T-stress. Special attention is paid to a single crack in an infinite elastic plane subjected to impact loading. By using the Laplace and Fourier transforms, the associated initial-boundary value problem is transformed to a Fredholm integral equation. The dynamic T-stress in the Laplace transform domain can be expressed in terms of its solution. Moreover, an explicit expression for initial T-stress is derived in closed form. Numerically solving the resulting equation and performing the inverse Laplace transform, the transient response of T-stress is determined in the time space, and the response history of the T-stress is shown graphically. Results indicate that T-stress exhibits apparent transient characteristic. [DOI: 10.1115/1.2190232]

1 Introduction

In describing crack growth for brittle materials with cracks, in addition to well-known stress intensity factors (SIFs), elastic *T*-stress at a crack tip is also a significant fracture parameter [1]. The so-called elastic *T*-stress [2] refers to a nonsingular constant term at the crack tip parallel to the crack plane, which is firstly derived by Williams [3] using an eigenvalue expansion method. So far, it has been observed that the *T*-stress plays an important role in predicting crack propagation and changing apparent fracture toughness in brittle materials [4] and in predicting shape and size of small scale yielding around a crack tip in elastic-plastic materials [5].

Considerable researches are devoted to the elastic *T*-stress at the crack tip under static case. For dynamic *T*-stress, Jayadevan et al. [6] studied the transient response of *T*-stress for single edge notched tension specimens, and three point bend specimens under the action of impact loading. Shin and Lee [7] investigated the *T*-stress of an interfacial crack of a bi-material subjected to dynamic loading. However, the methods they adopted are based on the numerical finite element method. Up to now, a simple, efficient analytical approach is still absent for the determination of dynamic *T*-stresses, although there are several analytical approaches for static *T*-stresses [2,8].

An integral equation method is proposed to determine dynamic *T*-stress in this note. Special attention is paid to a single crack in an infinite elastic plane subjected to impact loading. Similar to obtaining dynamic SIFs, by means of integral transform methods, the associated initial-boundary value problem is converted to a Fredholm integral equation. The *T*-stress can be expressed in terms of an integral involving the solution of the resulting Fredholm integral equation. A simple expression for initial *T*-stress is given by asymptotic analysis.

Contributed by the Applied Mechanics Division of ASME for publication in the JOURNAL OF APPLIED MECHANICS. Manuscript received September 30, 2005; final manuscript received February 2, 2006. Review conducted by H. Gao. Discussion on the paper should be addressed to the Editor, Prof. Robert M. McMeeking, Journal of Applied Mechanics, Department of Mechanical and Environmental Engineering, University of California—Santa Barbara, Santa Barbara, CA 93106-5070, and will be accepted until four months after final publication of the paper itself in the ASME JOURNAL OF APPLIED MECHANICS.

2 Formulation of the Problem

For an infinite isotropic elastic medium, dynamic elastic displacements u and v in the x- and y-axes, respectively, can be expressed by

$$u = \varphi_{,x} + \psi_{,y}, \quad v = \varphi_{,y} - \psi_{,x}, \tag{1}$$

where a comma denotes differentiation with respect to the suffixed space variable, φ and ψ are governed by two decoupled wave equations [9]

$$\nabla^2\varphi = s_l^2\ddot{\varphi}, \quad \nabla^2\psi = s_s^2\ddot{\psi}, \tag{2}$$

where a dot over a function stands for differentiation with respect to time. Here s_l and s_s are the slownesses of longitudinal and shear waves, respectively, which are related to the velocities of longitudinal and shear waves c_l and c_s by $c_l s_l = 1$ and $c_s s_s = 1$. Here c_l and c_s are defined as

$$c_l = \sqrt{(2\mu + \lambda)/\rho}, \quad c_s = \sqrt{\mu/\rho}, \tag{3}$$

μ and λ are elastic moduli, and ρ the mass density. Under these circumstances, the stress components can be expressed in terms of φ and ψ as follows:

$$\sigma_{xx} = \mu[c_l^2 s_s^2 \nabla^2\varphi - 2(\varphi_{,yy} - \psi_{,xy})], \tag{4}$$

$$\sigma_{yy} = \mu[c_l^2 s_s^2 \nabla^2\varphi - 2(\varphi_{,xx} + \psi_{,xy})], \tag{5}$$

$$\sigma_{xy} = \mu(\varphi_{,xy} + \psi_{,yy} - \psi_{,xx}). \tag{6}$$

For an infinite isotropic elastic solid with a crack located at $|x| \leq a, y = 0$, it is assumed that the crack surfaces are loaded suddenly by impacts. Hence, the associated boundary conditions for a mode-I crack can be stated below

$$\sigma_{yy}(x,0,t) = -\sigma_{yy}^0(x)H(t), \quad \sigma_{xy}(x,0,t) = 0, \quad |x| < a, \tag{7}$$

where $\sigma_{yy}^0(x)$ is a prescribed function, and $H(t)$ is the Heaviside unit step function. In what follows, for simplicity $\sigma_{yy}^0(x)$ is assumed to be an even function. Other cases can be similarly treated, and a detailed procedure is omitted here.

3 Derivation of Fredholm Integral Equation

To solve an elastodynamic problem, it is convenient to employ the Laplace transform technique. For this purpose, it is imposed that a cracked elastic body is at rest initially and stress-free. Applying the Laplace and Fourier transforms to (2) yields ordinary differential equations in y

$$\hat{\varphi}^{*\prime\prime} - (\xi^2 + p^2 s_l^2)\hat{\varphi}^* = 0, \quad \hat{\psi}^{*\prime\prime} - (\xi^2 + p^2 s_s^2)\hat{\psi}^* = 0, \tag{8}$$

p and ξ being the Laplace and Fourier parameters, and $(\,)' = d/dy$.

Clearly, due to symmetry of the problem, attention may be restricted to the upper half-plane. Under the regular conditions at infinity, the solutions of Eqs. (8) are readily found, and by performing the inverse Fourier transform, displacement potentials in the transformed space can be represented as

$$\varphi^* = -\int_{-\infty}^{\infty} A(\xi,p)e^{-\alpha_l y}\cos(\xi x)\mathrm{d}\xi,$$
$$\psi^* = -\int_{-\infty}^{\infty} B(\xi,p)e^{-\alpha_s y}\sin(\xi x)\mathrm{d}\xi, \tag{9}$$

where $A(\xi,p)$ and $B(\xi,p)$ are two unknown functions, and

$$\alpha_l = \sqrt{\xi^2 + p^2 s_l^2}, \quad \alpha_s = \sqrt{\xi^2 + p^2 s_s^2}. \tag{10}$$

Using these representations, the components of displacement and stress can be expressed in terms of A, B,

$$u^* = \int_0^\infty [\xi A e^{-\alpha_l y} + \alpha_s B e^{-\alpha_s y}]\sin(\xi x)\mathrm{d}\xi,$$
$$v^* = \int_0^\infty [\alpha_l A e^{-\alpha_l y} + \xi B e^{-\alpha_s y}]\cos(\xi x)\mathrm{d}\xi, \tag{11}$$

and

$$\sigma_{xx}^* = \int_0^\infty [[(2\mu+\lambda)\xi^2 - \lambda\alpha_l^2]A e^{-\alpha_l y} + 2\mu\xi\alpha_s B e^{-\alpha_s y}]\cos(\xi x)\mathrm{d}\xi, \tag{12}$$

$$\sigma_{yy}^* = \int_0^\infty [[\lambda\xi^2 - (2\mu+\lambda)\alpha_l^2]A e^{-\alpha_l y} - 2\mu\xi\alpha_s B e^{-\alpha_s y}]\cos(\xi x)\mathrm{d}\xi, \tag{13}$$

$$\sigma_{xy}^* = -\mu\int_0^\infty [2\xi\alpha_l A e^{-\alpha_l y} + (\xi^2+\alpha_s^2)B e^{-\alpha_s y}]\sin(\xi x)\mathrm{d}\xi. \tag{14}$$

Therefore, dynamic T-stresses in the transformed space can be determined through [10]

$$\tilde{T}^* = \lim_{x\to a^+}(\sigma_{xx}^*(x,0) - \sigma_{yy}^*(x,0)) = 2\mu\int_0^\infty [(\xi^2+\alpha_l^2)A + 2\xi\alpha_s B]\cos(\xi a)\mathrm{d}\xi, \tag{15}$$

where $\tilde{T}$ denotes the T-stress caused by loading acting at the crack surfaces, and T corresponds to that caused by loading applied at infinity. It is noted that the above result is only suitable to an open crack. For a closed crack, it has been shown in [11] that there are two T-stresses parallel to and perpendicular to the crack plane, which is beyond the scope of this note since in this note an opening crack is concerned.

For a mode-I crack, we have $\sigma_{xy}(x,0,t)=0$, which leads to

$$B = -\frac{2\xi\alpha_l}{\xi^2+\alpha_s^2}A. \tag{16}$$

Put this result into the expressions (11) and (13). In particular, at $y=0$, we get

$$v^*(x,0,p) = \frac{p^2}{c_s^2}\int_0^\infty \frac{\alpha_l}{\xi^2+\alpha_s^2}A\cos(\xi x)\mathrm{d}\xi, \tag{17}$$

$$\sigma_{yy}^*(x,0,p) = -\int_0^\infty [(\mu+\lambda)s_l^2p^2 + \mu q(\xi)]A\cos(\xi x)\mathrm{d}\xi, \tag{18}$$

$$\sigma_{xx}^*(x,0,p) = -\int_0^\infty [(\mu+\lambda)s_l^2p^2 - \mu q(\xi)]A\cos(\xi x)\mathrm{d}\xi, \tag{19}$$

where

$$q(\xi) = \frac{(\xi^2+\alpha_l^2)(\xi^2+\alpha_s^2) - 4\xi^2\alpha_l\alpha_s}{\xi^2+\alpha_s^2}. \tag{20}$$

From symmetry of the problem in question, the displacement component v should satisfy

$$v^*(x,0,p) = 0, \quad |x| > a, \tag{21}$$

which allows us to represent A in terms of the following integral

$$A = \frac{c_s^2(\xi^2+\alpha_s^2)}{\alpha_l p^2}\int_0^a r\chi(r,p)J_0(r\xi)\mathrm{d}r, \tag{22}$$

where $J_0(\cdot)$ is the zeroth-order Bessel function of the first kind, and $\chi(r,p)$ is a new auxiliary function.

Taking into account the well-known identity

$$\int_0^\infty J_0(\xi r)\cos(\xi x)\mathrm{d}\xi = 0, \quad x > r, \tag{23}$$

it is easily shown that Eq. (21) is automatically fulfilled when substituting (22) into (21). In addition, inserting (22) into (18) and applying the remaining boundary condition (7), we get

$$\int_0^a r\chi(r,p)\mathrm{d}r\int_0^\infty \frac{(\xi^2+\alpha_s^2)[(\mu+\lambda)s_l^2p^2+\mu q(\xi)]}{\alpha_l s_s^2 p^2}J_0(r\xi)J_0(x\xi)\mathrm{d}\xi = \frac{2}{\pi p}\int_0^x \frac{\sigma_{yy}^0(r)}{\sqrt{x^2-r^2}}\mathrm{d}r, \tag{24}$$

which can be further transformed to a Fredholm integral equation of the second kind:

$$\chi(x,p) + \int_0^a rN(x,r,p)\chi(r,p)\mathrm{d}r = \frac{4(1-\nu^2)}{E}\frac{1}{\pi p}\int_0^x \frac{\sigma_{yy}^0(r)}{\sqrt{x^2-r^2}}\mathrm{d}r, \tag{25}$$

for $0 \leqslant x < a$, where

$$N(x,r,p) = \int_0^\infty \left[\frac{(\xi^2+\alpha_s^2)[(\mu+\lambda)s_l^2p^2+\mu q(\xi)]}{2(\mu+\lambda)\alpha_l\xi s_l^2p^2} - 1\right]\xi J_0(r\xi)J_0(x\xi)\mathrm{d}\xi. \tag{26}$$

Hereafter we also use alternative pair of material constants: Young's modulus E and Poisson's ratio ν, related to μ and λ by the relations $\mu = E/[2(1+\nu)]$, $\lambda = E\nu/[(1+\nu)(1-2\nu)]$ for a state of plane strain.

4 Dynamic T-Stress

Once a solution of Eq. (25) is obtained, the transient behavior of a cracked elastic medium can be determined. Especially, of importance is the response history of the crack-tip field, which contains commonly two terms, one is related to a singular field and the other is related to a nonsingular field. They are often characterized by SIFs and T-stresses at the crack tips, respectively. Most existing researches on dynamic problems related to cracks are concentrated on dynamic SIFs.

Taking into account (18) and (19), $\sigma_{yy}^*(x,0,p)$ and $\sigma_{xx}^*(x,0,p)$ are found to be

$$\sigma_{yy}^*(x,0,p) = \frac{E}{2(1-\nu^2)}\frac{x\chi(a,p)}{\sqrt{x^2-a^2}} + \tilde{\sigma}_{yy}^*(x,0,p), \tag{27}$$

$$\sigma_{xx}^*(x,0,p) = \frac{E}{2(1-\nu^2)}\frac{x\chi(a,p)}{\sqrt{x^2-a^2}} + \tilde{\sigma}_{xx}^*(x,0,p), \tag{28}$$

where $\tilde{\sigma}_{yy}^*(x,0,p)$ and $\tilde{\sigma}_{xx}^*(x,0,p)$ are nonsingular terms, expressions for which can be given and omitted here. Accordingly, from the crack-tip field, dynamic SIFs for a mode-I crack is easily found to be represented as

$$K_{\mathrm{I}}^* = \frac{E}{2(1-\nu^2)}\sqrt{\pi a}\chi(a,p). \tag{29}$$

Furthermore, dynamic T-stresses in the transformed space can be evaluated by subtracting (27) from (28), after some algebra one deduces

Table 1 Material properties

	E (GPa)	ν	ρ (kg/m^3)	c_l (km/s)	c_s (km/s)	c_R (km/s)
PMMA	3.02	0.35	1190	2.0182	0.9695	0.9065
Aluminum	80	0.33	2710	6.6135	3.3313	3.1049
Steel	208	0.3	7833	5.9788	3.1958	2.9638
Glass	70	0.25	2500	5.7966	3.3466	3.0769

$$\widetilde{T}^* = \frac{2\mu c_s^2}{p^2}\int_0^a x\chi(x,p)V(x,p)\mathrm{d}x, \tag{30}$$

where

$$V(x,p) = \int_0^\infty \frac{(\xi^2+\alpha_l^2)(\xi^2+\alpha_s^2)-4\xi^2\alpha_l\alpha_s}{\alpha_l}J_0(\xi x)\cos(\xi a)\mathrm{d}\xi. \tag{31}$$

In particular, consider the case of constant uniaxial tension impact loading, $\sigma_{yy}^0(x)=\sigma_{yy}^\infty$. By superposition of a uniform field arising from impact load $\sigma_{yy}^\infty H(t)$ at infinity, we get

$$T^* = \frac{2\mu}{p^2 s_s^2}\int_0^a x\chi(x,p)V(x,p)\mathrm{d}x - \frac{\sigma_{yy}^\infty}{p}. \tag{32}$$

From the above, the corresponding static results of T-stress $T=-\sigma_{yy}^\infty$ can be also derived from the following property

$$T = \lim_{p\to 0} pT^*. \tag{33}$$

This is due to the fact

$$\lim_{p\to 0}\frac{(\xi^2+\alpha_l^2)(\xi^2+\alpha_s^2)-4\xi^2\alpha_l\alpha_s}{p^2} = 0. \tag{34}$$

On the other hand, from the asymptotic behaviors of $\chi(x,p)$ and $V(x,p)$ as $p\to\infty$, one can similarly deduce dynamic T-stresses during the earlier period of the application of impact loading. To this end, as p is large enough, Eq. (24) with $\sigma_{yy}^0(x)=\sigma_{yy}^\infty$ becomes

$$\frac{E(1-\nu)ps_l}{(1+\nu)(1-2\nu)}\int_0^a r\chi(r,p)\mathrm{d}r\int_0^\infty J_0(\xi x)J_0(\xi r)\mathrm{d}\xi = \frac{\sigma_{yy}^\infty}{p}, \tag{35}$$

which, after some derivations, has a solution

$$\chi(x,p) = \frac{2(1+\nu)(1-2\nu)\sigma_{yy}^\infty}{\pi E(1-\nu)p^2 s_l}\frac{1}{\sqrt{a^2-x^2}}. \tag{36}$$

Consequently, substituting the above into (30) we find that as p is sufficiently large,

$$\widetilde{T}^* = \frac{2(1-2\nu)\sigma_{yy}^\infty}{\pi(1-\nu)p}\int_0^a \frac{x}{\sqrt{a^2-x^2}}\mathrm{d}x\int_0^\infty J_0(\xi x)\cos(\xi a)\mathrm{d}\xi$$
$$= \frac{(1-2\nu)\sigma_{yy}^\infty}{\pi(1-\nu)p}\int_0^\infty \frac{1}{\xi}\sin(2a\xi)\mathrm{d}\xi. \tag{37}$$

Therefore, since $\int_0^\infty \xi^{-1}\sin(\xi)\mathrm{d}\xi=\pi/2$, from the above along with Eq. (32) we get

$$\widetilde{T} = \frac{(1-2\nu)\sigma_{yy}^\infty}{2(1-\nu)}, \quad T = -\frac{\sigma_{yy}^\infty}{2(1-\nu)}, \quad c_l t/a \ll 1. \tag{38}$$

5 Results and Discussions

In this section we appeal to a numerical technique to treat Eq. (25). To compute efficiently a solution, one can split N into two parts

$$N(x,r,p) = \frac{(7-12\nu+8\nu^2)E}{4(1-2\nu)}p^2 s_l^2 R(x,r) + \int_0^\infty Z(\xi,p)\xi J_0(r\xi)J_0(x\xi)\mathrm{d}\xi, \tag{39}$$

where $R(x,r)=I_0(rp/c_l)K_0(xp/c_l)$ for $r<x$, $R(x,r)=I_0(xp/c_l)K_0(rp/c_l)$ for $x<r$, and

$$Z(\xi,p) = \frac{(\xi^2+\alpha_s^2)[(\mu+\lambda)s_l^2p^2+\mu q(\xi)]}{2(\mu+\lambda)\alpha_l\xi s_l^2 p^2} - \left[1+\frac{7-12\nu+8\nu^2}{4(1-2\nu)}\frac{p^2s_l^2}{\alpha_l^2}\right]. \tag{40}$$

Here $I_0(\cdot)$ and $K_0(\cdot)$ are the modified zeroth-order Bessel functions of the first and the second kinds, respectively. By applying the asymptotic expansion

$$(\xi^2+\alpha_l^2)(\xi^2+\alpha_s^2)-4\xi^2\alpha_l\alpha_s = 0.5(p^4s_l^4+p^4s_s^4)+O(p^2\xi^{-2}), \tag{41}$$

it is easily shown that $Z(\xi,p)$ behaves like ξ^{-4} as $\xi\to\infty$, which leads to a rapid convergence of the involved infinite integral. For the purpose of computation, introduce the following normalized variables

$$\bar{x}=\frac{x}{a}, \quad \bar{r}=\frac{r}{a}, \quad \Omega(\bar{x},p)=\frac{E\chi(x,p)}{2(1-\nu^2)a}, \quad \bar{N}(\bar{x},\bar{r},p)=a^2N(x,r,p). \tag{42}$$

Consequently, Eq. (25) is rewritten in the form

$$\Omega(\bar{x},p)+\int_0^1 \bar{r}\bar{N}(\bar{x},\bar{r},p)\Omega(\bar{r},p)\mathrm{d}\bar{r} = \frac{2}{\pi p}\int_0^{\bar{x}}\frac{\sigma_{yy}^0(a\bar{r})}{\sqrt{\bar{x}^2-\bar{r}^2}}\mathrm{d}\bar{r}, \tag{43}$$

for $0\leqslant\bar{x}<1$, the solution of which is straightforward and is omitted here.

Once the solution of the above equation is determined, from (29) and (32), one can get desired SIFs and T-stresses in the transformed space,

$$K_{\mathrm{I}}^* = \sqrt{\pi a}\,\Omega(1,\bar{p}), \tag{44}$$

$$T^* = \frac{(1-2\nu)c_l^2}{p^2}\int_0^1 \bar{x}\Omega(\bar{x},p)\bar{V}(\bar{x},p)\mathrm{d}\bar{x} - \frac{\sigma_{yy}^\infty}{p}, \tag{45}$$

where $\bar{V}(\bar{x},p)$ is readily derived from (31) and so omitted. Obviously, the result of K_{I}^* is in exact agreement with that obtained in [12]. Nevertheless, for T^*, it can be determined based on all the values of $\Omega(\bar{x},p)$ over [0,1].

In order to present dynamic T-stresses in the physical space, the inverse Laplace transform must be performed. To achieve this, a numerical inversion of the Laplace transform by use of the Fourier series approximation [13] is adopted here. Several different isotropic elastic materials with relevant material properties listed in Table 1 are used to evaluate dynamics T-stresses.

The variation of normalized dynamic T-stresses $T(t)/\sigma_{yy}^\infty$ against $c_s t/a$ is plotted in Fig. 1. During the early stage of the

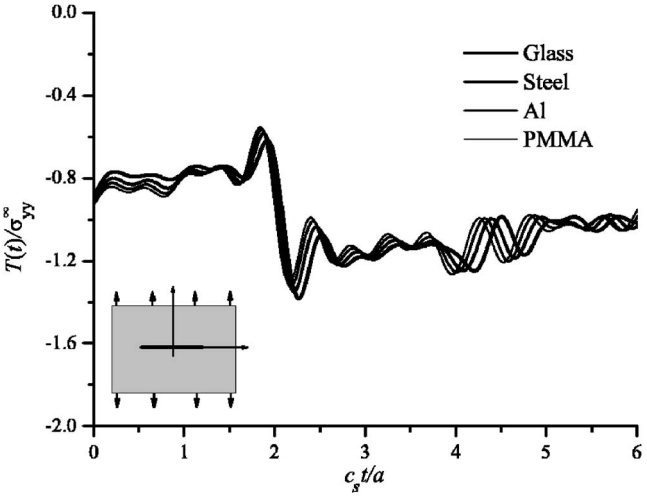

Fig. 1 $T(t)/\sigma_{yy}^{\infty}$ **versus** $c_s t/a$

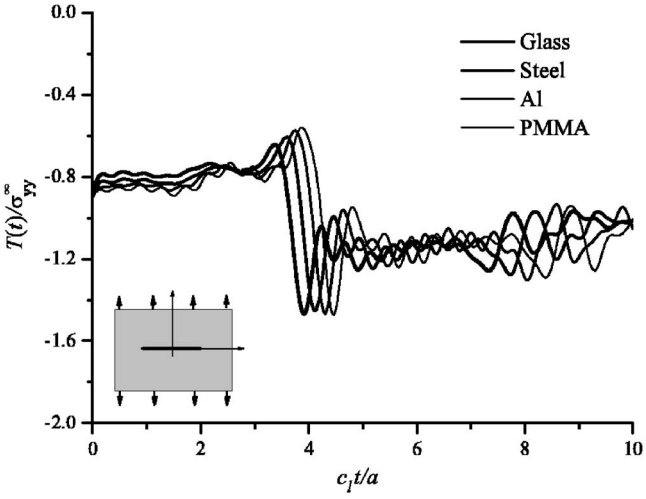

Fig. 2 $T(t)/\sigma_{yy}^{\infty}$ **versus** $c_l t/a$

action of impact loading, dynamic T-stresses vary slightly with small oscillation, climbing rapidly a peak at about $c_s t/a=1.86$ corresponding to the arrival time of a surface wave starting from the other crack tip, then drops abruptly to a minimum at a certain value at about $c_s t/a=2.2$, which has a slight difference for different Poisson's ratios, and finally exhibits oscillatory behavior approaching -1, i.e., the corresponding static result. Moreover, it is found that the difference between response curves of dynamic T-stress arises only from Poisson's ratio of respective materials. The larger Poisson's ratio is, the slower the arrival of the maximum or minimum of dynamic T-stress is. A similar trend can be found in Fig. 2, which displays $T(t)/\sigma_{yy}^{\infty}$ versus $c_l t/a$. Since c_l is larger than c_s, the arrival order of the peak value of dynamic T-stress is more pronounced, but opposite to the arrival order in Fig. 1. In addition, an initial value of $T(t)/\sigma_{yy}^{\infty}$ for $\nu=0.3$ is given about -0.85 [9], which is in satisfactory agreement with our calculated result -0.91 for Steel. Moreover, after a very small period of time, $T(t)/\sigma_{yy}^{\infty}$ oscillates between -0.85 and -0.74, which is also close to -0.71 by using (38).

6 Conclusions

Dynamic T-stresses at the tip of a crack embedded in an isotropic elastic medium have been analyzed by an integral equation approach. Transient response of T-stress is determined, which strongly depends on Poisson's ratio. The results indicate that there exists a significant difference between T-stresses for dynamic and static cases. For an internally pressured crack, elastic T-stress is absent for static case, while it is present for the corresponding dynamic case, inferring a remarkable transient feature of T-stress.

Acknowledgment

The author would like to thank the reviewers for helpful suggestions to improve this paper.

References

[1] Betegon, C., Belzunce, F. J., and Rodriguez, C., 1996, "A Two Parameter Fracture Criterion for High Strength Low Carbon Steel," Acta Mater., **44**, pp. 1055–61.

[2] Rice, J. R., 1974, "Limitations to the Small Scale Yielding Approximation for Crack Tip Plasticity," J. Mech. Phys. Solids, **22**, pp. 17–26.

[3] Williams, M. L., 1957, "On the Stress Distribution at the Base of Stationary Crack," ASME J. Appl. Mech., **24**, pp. 109–114.

[4] Smith, D. J., Ayatollahi, M. R., and Pavier, M. J., 2001, "The Role of T-stress in Brittle Fracture for Linear Elastic Materials Under Mixed-Mode Loading," Fatigue Fract. Eng. Mater. Struct., **24**, pp. 137–150.

[5] Larsson, S. G., and Carlsson, A. J., 1973, "Influence of Nonsingular Stress Terms and Specimen Geometry on Small Scale Yielding at Crack Tips in Elastic-Plastic Materials," J. Mech. Phys. Solids, **21**, pp. 263–277.

[6] Jayadevan, K. R., Narasimhan, R., Ramamurthy, T. S., and Dattaguru, B., 2001, "A Numerical Study of T-Stress in Dynamically Loaded Fracture Specimens," Int. J. Solids Struct., **38**, pp. 4987–5005.

[7] Shin, D. K., and Lee, J. J., 2001. "Fracture Parameters of Interfacial Crack of Bimaterial Under the Impact Loading," Int. J. Solids Struct., **38**, pp. 5303–5322.

[8] Broberg, K. B., 2005, "A Note on T-Stress Determination Using Dislocation Arrays," Int. J. Fract., **131**, pp. 1–14.

[9] Freund, L. B., 1990, *Dynamic fracture mechanics*, Cambridge University Press, Cambridge, UK.

[10] Yang, B., and Ravi-Chandar, K., 1999, "Evaluation of Elastic T-Stress by the Stress Difference Method," Eng. Fract. Mech., **64**, pp. 589–605.

[11] Leblond, J.-B., and Frelat, J., 2000, "Crack Kinking From an Initially Closed Crack," Int. J. Solids Struct., **37**, pp. 1595–1614.

[12] Chen, E. P., and Sih, G. C., 1977, "Transient Response of Cracks to Impact Loads," in *Elastodynamic Crack Problems*, G. C. Sih, ed., Noordhoff, Groningen.

[13] Crump, K. S., 1976, "Numerical Inversion of Laplace Transforms Using a Fourier Series Approximation," J. Assoc. Comput. Mach., **23**, pp. 89–96.

Dynamic Stress Concentration of a Circular Cutout Buried in Semi-Infinite Plates Subjected to Flexural Waves

Xueqian Fang[1]
e-mail: fangxueqian@163.com

Chao Hu

Wenhu Huang

Department of Aerospace Engineering and Mechanics,
Harbin Institute of Technology,
Harbin 150001,
China

In this paper, based on the theory of elastic thin plates, applying the image method and the wave function expansion method, multiple scattering of elastic waves and dynamic stress concentration in semi-infinite plates with a circular cutout are investigated, and the general solutions of this problem are obtained. As an example, the numerical results of dynamic stress concentration factors are graphically presented and discussed. Numerical results show that the analytical results of scattered waves and dynamic stress in semi-infinite plates are different from those in infinite plates when the distance ratio b/a is comparatively small. In the region of low frequency and long wavelength, the maximum dynamic stress concentration factors occur on the illuminated side of scattered body with $\theta=\pi$, but not on the side of cutout with $\theta=\pi/2$. As the incidence frequency increases (the wavelength becomes short), the dynamic stress on the illuminated side of cutout becomes little, and the dynamic stress on the shadow side becomes great.
[DOI: 10.1115/1.2198545]

1 Introduction

Plate structures are widely used in aviation, aerospace, shipping, and civil construction engineering. To satisfy the engineering designs, it is inevitable to design plate structures containing cutouts, which can cause stress concentrations. Stress concentrations greatly decrease the bearing capacity of structures and reduce the service life of structures. So, the scattering of elastic waves and dynamic stress concentrations have received a considerable amount of interest over the last few decades [1–8].

It is known from researches of wave dynamics that in a certain frequency range of waves, the dynamic stress concentration factors are greater than static stress concentration factors. Dynamical loads of the same amplitude can produce greater stress concentration factors than static loads. Pao studied elastic wave scattering and dynamic stress concentrations in thin plates with cutouts; analytical and numerical solutions of the problem were presented [1–3]. Kung also studied dynamic stress concentrations in thin plates and gave expressions of bending moment and shearing force versus frequency [4]. Klyukin et al. studied scattering of flexural waves produced by a row of circular inclusions in plates [5]. By making use of complex function method, Chao et al. analyzed the dynamic stress concentrations produced by cutouts of arbitrary shape in thin plates and presented general and numerical results [6,7]. Hayir and Bakirtas applied the image method to analyze the scattering and dynamic stress concentrations of elastic waves in plates having a circular cavity subject to plane harmonic SH waves [8].

It can be seen that up to the present time the researches on elastic waves and dynamic stress in plates are mainly focused on structure models of infinite plates. However, models of semi-infinite plates are more familiar in engineering. But, because of the effects of the boundaries of the investigating areas, complex problems of multiple scattering in structures arise. In this paper, based on the dynamical theory of the elastic thin plate, applying the image method and the wave function expansion method, multiple scattering of elastic waves and dynamic stress concentrations in plates with a circular cutout are investigated, and the general solutions of the problem are presented.

2 Equations of Wave Motion and its Solution

The incidence of flexural waves in semi-infinite plates is considered, which is depicted in Fig. 1. The flexural wave equation in elastic plates may be described as

$$D\nabla^2\nabla^2 w + \rho h\frac{\partial^2 w}{\partial t^2} = q \tag{1}$$

where D is the bending stiffness of plates, $D=Eh^3/12(1-\nu^2)$, ρ is the density of plates, h is the thickness of plates, t is the time, q is the transverse load, and $q=0$.

Steady solutions of the problem are investigated. Let $w=\mathrm{Re}[W\exp(-i\omega t)]$. Then the displacement components determined by steady flexural waves are

$$u_x = -z\frac{\partial w}{\partial x},\quad u_y = -z\frac{\partial w}{\partial y},\quad u_z = w = \mathrm{Re}[W(x,y)e^{-i\omega t}] \tag{2}$$

Here ω is incident frequency and $i=\sqrt{-1}$ is an imaginary unit.

Simultaneously, $W(x,y)$ should satisfy the following equations:

$$\nabla^2\nabla^2 W - k^4 W = (\nabla^2 + k^2)(\nabla^2 - k^2)W = 0 \tag{3}$$

$$(\nabla^2 + k^2)W_1 = 0,\quad (\nabla^2 - k^2)W_2 = 0 \tag{4}$$

where k is the wave number of elastic waves, and $k=(\rho h\omega^2/D)^{1/4}$.

In Eq. (4), it is noted that $W_1e^{-i\omega t}$ denotes the propagating elastic waves in plates and $W_2e^{-i\omega t}$ denotes the localized periodical vibration. The two parts are integrated and form the motion of flexural waves and vibration modes in thin plates.

The general solution of the scattered field of elastic waves determined by Eq. (3) can be described as

$$W = W_1 + W_2 = \sum_{n=-\infty}^{\infty} A_{n1}H_n^{(1)}(kr)e^{in\theta} + A_{n2}K_n(kr)e^{in\theta} \tag{5}$$

where A_{n1}, A_{n2} are the mode coefficients of scattered waves produced by the cutout and can be determined by the boundary conditions, $H_n^{(1)}(\cdot)$ is the nth-order Hankel function of the first kind, and $K_n(\cdot)$ is the nth-order modified Bessel function of the second kind.

3 Excitation of Incident Waves and Total Wave Field

Assume that a periodical steady elastic wave impinges along the positive x direction at the edge of semi-infinite plates. One is the propagating waves, the other is the localized vibration. According to the propagating theory of Bloch waves, the incident waves may be described as

[1]Author to whom correspondence should be addressed.

Contributed by the Applied Mechanics Division of ASME for publication in the JOURNAL OF APPLIED MECHANICS. Manuscript received October 10, 2005; final manuscript received February 4, 2006. Review conducted by H. D. Espinosa.

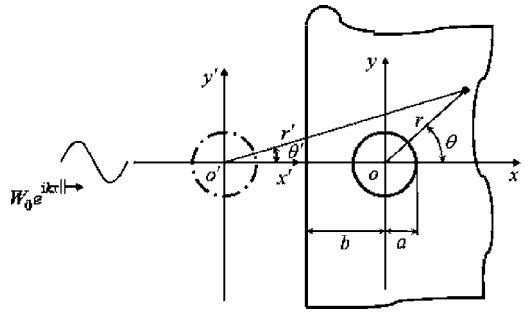

Fig. 1 Sketch of elastic waves incident in plates

$$W_1^{(i)} = W_{10}\exp(\mathrm{i}kb)\exp[\mathrm{i}(kx-\omega t)] + W_{20}\exp(-kb)\exp(-kx-\mathrm{i}\omega t)$$
$$= W_{10}\exp(\mathrm{i}kb)\sum_{n=-\infty}^{\infty}\mathrm{i}^n J_n(kr)e^{\mathrm{i}n\theta}\exp(-\mathrm{i}\omega t)$$
$$+ W_{20}\exp(-kb)\sum_{n=-\infty}^{\infty} I_n(kr)e^{\mathrm{i}n\theta}\exp(-\mathrm{i}\omega t) \tag{6}$$

where W_{10}, W_{20} are the transverse vibration amplitudes of incident flexural waves, $J_n(\cdot)$ is the nth-order Bessel function, and $I_n(\cdot)$ is the nth-order modified Bessel function of the first kind.

The reflected waves at the edge of semi-infinite plates are described by the virtual image. To the image cutout, the waves propagate in the negative x' direction and can be expressed as

$$W_2^{(i)} = W_{10}\exp(\mathrm{i}kb)\exp[-\mathrm{i}(kx'+\omega t)] + W_{20}\exp(-kb)$$
$$\times\exp(kx'-\mathrm{i}\omega t) = W_{10}\exp(\mathrm{i}kb)\sum_{n=-\infty}^{\infty}\mathrm{i}^{-n}J_n(kr')e^{\mathrm{i}n\theta}$$
$$\times\exp(-\mathrm{i}\omega t) + W_{20}\exp(-kb)$$
$$\times\sum_{n=-\infty}^{\infty}(-1)^n I_n(kr')e^{\mathrm{i}n\theta}\exp(-\mathrm{i}\omega t) \tag{7}$$

When the exciting source is far enough from the cutout, one may consider $W_{20}=0$, and then the incident waves for the real and the image cutouts are described as, respectively,

$$W_1^{(i)} = W_{10}\exp(\mathrm{i}kb)\exp[\mathrm{i}(kx-\omega t)]$$
$$= W_{10}\exp(\mathrm{i}kb)\sum_{n=-\infty}^{\infty}\mathrm{i}^n J_n(kr)e^{\mathrm{i}n\theta}\exp(-\mathrm{i}\omega t) \tag{8}$$

$$W_2^{(i)} = W_{10}\exp(\mathrm{i}kb)\exp[-\mathrm{i}(kx'+\omega t)]$$
$$= W_{10}\exp(\mathrm{i}kb)\sum_{n=-\infty}^{\infty}\mathrm{i}^{-n}J_n(kr')e^{\mathrm{i}n\theta'}\exp(-\mathrm{i}\omega t) \tag{9}$$

Considering the multiple scattering between the real and the image cutouts, the scattered fields of elastic waves produced by the real cutout in the localized coordinate system (r,θ) of the real cutout are described as

$$W_1^{(s)} = \sum_{l=1}^{\infty}\sum_{n=-\infty}^{\infty} A_{n1}^l H_n^{(1)}(kr)e^{\mathrm{i}n\theta}\exp(-\mathrm{i}\omega t)$$
$$+ \sum_{l=1}^{\infty}\sum_{n=-\infty}^{\infty} A_{n2}^l K_n(kr)e^{\mathrm{i}n\theta}\exp(-\mathrm{i}\omega t) \tag{10}$$

And that the scattered waves produced by the image cutout, in the localized coordinate system (r',θ') of the image cutout, are described as

$$W_2^{(s)} = \sum_{l=1}^{\infty}\sum_{n=-\infty}^{\infty} B_{n1}^l H_n^{(1)}(kr')e^{\mathrm{i}n\theta'}\exp(-\mathrm{i}\omega t)$$
$$+ \sum_{l=1}^{\infty}\sum_{n=-\infty}^{\infty} B_{n2}^l K_n(kr')e^{\mathrm{i}n\theta'}\exp(-\mathrm{i}\omega t) \tag{11}$$

where $A_{n1}^l, A_{n2}^l, B_{n1}^l, B_{n2}^l$ are the lth mode coefficients of scattered waves of the real cutout and the image cutout, respectively. They are determined by satisfying boundary conditions. In fact, they are related to the boundary conditions of the edge of plates.

To make computation tractable, the expressions of elastic waves in the localized coordinate system (r',θ') may be changed into coordinate system (r,θ). According to the addition theorem of Graf [9], the following relations can be derived:

$$H_n^{(1)}(kr')e^{\mathrm{i}n\theta'} = \sum_{m=-\infty}^{\infty}(-1)^{m-n}H_{m-n}^{(1)}(2kb)J_m(kr)e^{\mathrm{i}m\theta}$$
$$K_n(kr')e^{\mathrm{i}n\theta'} = \sum_{m=-\infty}^{\infty}(-1)^m K_{m-n}(2kb)I_m(kr)e^{\mathrm{i}m\theta} \tag{12}$$

$$H_n^{(1)}(kr)e^{\mathrm{i}n\theta} = \sum_{m=-\infty}^{\infty} H_{m-n}^{(1)}(2kb)J_m(kr')e^{\mathrm{i}m\theta'}$$
$$K_n(kr)e^{\mathrm{i}n\theta} = \sum_{m=-\infty}^{\infty}(-1)^n K_{m-n}(2kb)I_m(kr')e^{\mathrm{i}m\theta'} \tag{13}$$

Thus, the total field of elastic waves in plates should be produced by the superposition of the incident field, the scattered field, and the reflected field at the edge of plates.

$$W = W_1^{(i)} + W_1^{(s)} + W_1^{(f)} = W_1^{(i)} + W_1^{(s)} + W_2^{(s)} \tag{14}$$

4 Boundary Conditions

Without loss of generality, we investigate the given generalized force around the cutout, and then the boundary conditions expressed by the generalized force are [1]

$$M_r = -D\left[\frac{\partial^2 W}{\partial r^2} + \nu\left(\frac{1}{r}\frac{\partial W}{\partial r} + \frac{1}{r^2}\frac{\partial^2 W}{\partial\theta^2}\right)\right] = \bar{M}_r \tag{15}$$

$$V_r = Q_r + \frac{1}{r}\frac{\partial M_{r\theta}}{\partial\theta} = \bar{V}_r \tag{16}$$

where $\bar{M}_r$ and $\bar{V}_r$ are the bending moment and the equivalent shearing force around the cutout, respectively.

5 Mode Coefficients of Elastic Waves

Multiple scattering of elastic waves takes place between the real cutout and the image cutout. By satisfying the boundary conditions around cutout, mode coefficients of elastic waves are determined. When $l=1$, and the time factor is omitted, the relations among every mode coefficient of scattered waves are

$$A_{n1}^1 k^2[(1-\nu)H_n''(ka) - \nu H_n(ka)] + A_{n2}^1 k^2[(1-\nu)K_n''(ka) + \nu K_n(ka)] \tag{17}$$
$$= -W_{10}\exp(\mathrm{i}kb)\mathrm{i}^n k^2[(1-\nu)J_n''(ka) - \nu J_n(ka)]$$

$$A_{n1}^1[n^2(1-\nu)H_n(ka) - n^2 ka(1-\nu)H_n'(ka) - (ka)^3 H_n'(ka)]$$
$$+ A_{n2}^1[n^2(1-\nu)K_n(ka) - n^2 ka(1-\nu)K_n'(ka) + (ka)^3 K_n'(ka)]$$
$$= -W_{10}\exp(\mathrm{i}kb)\mathrm{i}^n[n^2(1-\nu)J_n(ka) - n^2 ka(1-\nu)J_n'(ka)$$
$$- (ka)^3 J_n'(ka)] \tag{18}$$

$$B_{n1}^{1}k^2[(1-\nu)H_n''(ka)-\nu H_n(ka)]+B_{n2}^{1}k^2[(1-\nu)K_n''(ka)+\nu K_n(ka)]$$

$$=-W_{10}\exp(\mathrm{i}kb)\mathrm{i}^{-n}k^2[(1-\nu)J_n''(ka)-\nu J_n(ka)] \quad (19)$$

$$B_{n1}^{1}[n^2(1-\nu)H_n(ka)-n^2ka(1-\nu)H_n'(ka)-(ka)^3H_n'(ka)]$$

$$+B_{n2}^{1}[n^2(1-\nu)K_n(ka)-n^2ka(1-\nu)K_n'(ka)+(ka)^3K_n'(ka)]$$

$$=-W_{10}\exp(\mathrm{i}kb)\mathrm{i}^{-n}[n^2(1-\nu)J_n(ka)-n^2ka(1-\nu)J_n'(ka)$$
$$-(ka)^3J_n'(ka)] \quad (20)$$

When $l=2,3,\ldots,\infty$, and the time factor is omitted, the relations among every mode coefficient of scattered waves are

$$A_{n1}^{l}k^2[(1-\nu)H_n''(ka)-\nu H_n(ka)]+A_{n2}^{l}k^2[(1-\nu)K_n''(ka)+\nu K_n(ka)]$$

$$=-\sum_{m=-\infty}^{\infty}B_{m1}^{l-1}H_{m-n}(2kb)k^2[(1-\nu)J_n''(ka)-\nu J_n(ka)]$$

$$-\sum_{m=-\infty}^{\infty}(-1)^nB_{m2}^{l-1}K_{m-n}(2kb)k^2[(1-\nu)I_n''(ka)+\nu I_n(ka)] \quad (21)$$

$$A_{n1}^{l}[n^2(1-\nu)H_n(ka)-n^2ka(1-\nu)H_n'(ka)-(ka)^3H_n'(ka)]$$

$$+A_{n2}^{l}[n^2(1-\nu)K_n(ka)-n^2ka(1-\nu)K_n'(ka)+(ka)^3K_n'(ka)]$$

$$=-\sum_{m=-\infty}^{\infty}B_{m1}^{l-1}H_{m-n}(2kb)[n^2(1-\nu)J_n(ka)-n^2ka(1-\nu)J_n'(ka)$$
$$-(ka)^3J_n'(ka)]$$

$$-\sum_{m=-\infty}^{\infty}(-1)^nB_{m2}^{l-1}K_{m-n}(2kb)[n^2(1-\nu)I_n(ka)-n^2ka(1-\nu)I_n'(ka)$$
$$+(ka)^3I_n'(ka)] \quad (22)$$

$$B_{n1}^{l}[(1-\nu)k^2H_n''(ka)-\nu k^2H_n(ka)]+B_{n2}^{l}[(1-\nu)k^2K_n''(ka)$$
$$+\nu k^2K_n(ka)]$$

$$=-\sum_{m=-\infty}^{\infty}A_{m1}^{l-1}H_{n-m}(2kb)[(1-\nu)k^2J_n''(ka)-\nu k^2J_n(ka)]$$

$$=-\sum_{m=-\infty}^{\infty}(-1)^nA_{m2}^{l-1}K_{n-m}(2kb)[(1-\nu)k^2I_n''(ka)+\nu k^2I_n(ka)] \quad (23)$$

$$B_{n1}^{l}[n^2(1-\nu)H_n(ka)-n^2ka(1-\nu)H_n'(ka)-(ka)^3H_n'(ka)]$$

$$+B_{n2}^{l}[n^2(1-\nu)K_n(ka)-n^2ka(1-\nu)K_n'(ka)+(ka)^3K_n'(ka)]$$

$$=-\sum_{m=-\infty}^{\infty}A_{m1}^{l-1}H_{n-m}(2kb)[n^2(1-\nu)J_n(ka)-n^2ka(1-\nu)J_n'(ka)$$
$$-(ka)^3J_n'(ka)]$$

$$-\sum_{m=-\infty}^{\infty}(-1)^nA_{m2}^{l-1}K_{n-m}(2kb)[n^2(1-\nu)I_n(ka)-n^2ka(1-\nu)I_n'(ka)$$
$$+(ka)^3I_n'(ka)] \quad (24)$$

Equations (17)–(24) are the system of algebra equations determining mode coefficients $A_{n1}^{l},A_{n2}^{l},B_{n1}^{l},B_{n2}^{l}$ of multiple scattering of elastic waves.

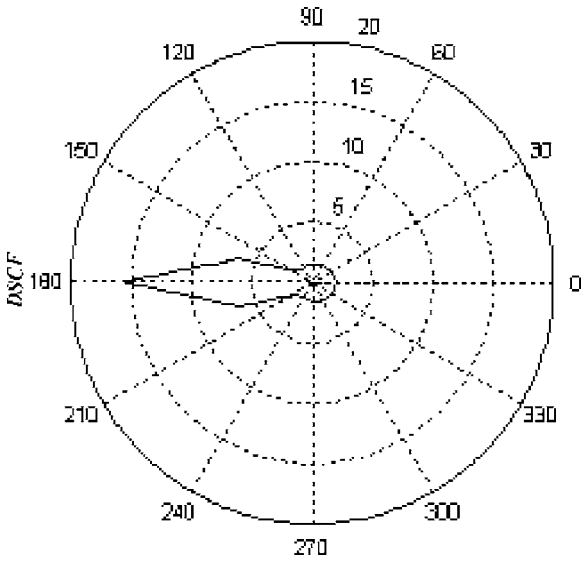

Fig. 2 Dynamic stress concentration factors around a circular cutout ($ka=0.1, b/a=2.0$)

We determine the characteristic scale of the problem: assuming that the characteristic length is the radius a of the circular cutout, the displacement amplitude of incident waves is $|W_{10}|$ and $|W_{20}|=0$. When computing, the following dimensionless variables are adopted: the ratio of Poisson is $\nu=0.30$, the wave number of incident waves is $ka=0.01-1.0$, and the relative distance between the cutout and the edge of plates is $b/a=1.1-10$.

Without loss of generality, the boundary of the circular cutout is assumed to be free of traction. According to the definition of dynamic stress concentration factor (DSCF) [10], the dynamical bending moment concentration factor is the ratio of the amplitude hoop bending moment around the cutout and the bending moment in the incident direction of elastic waves. Thus, the expression of the dynamic bending moment concentration factor around the circular cutout is described as

$$\mathrm{DSCF}=M_\theta^*=M_\theta/M_0=-\frac{1}{W_{10}k^2}[\nabla^2W-(1-\nu)\partial^2W/\partial r^2] \quad (25)$$

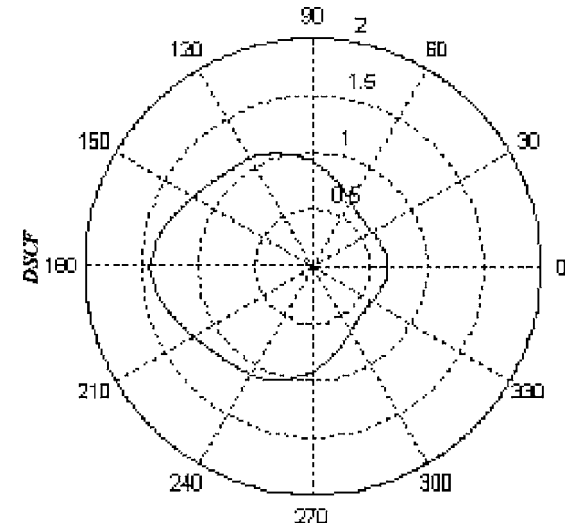

Fig. 3 Dynamic stress concentration factors around a circular cutout ($ka=0.5, b/a=2.0$)

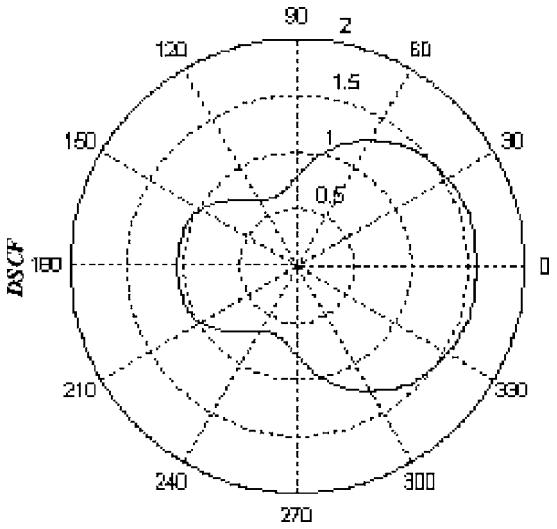

Fig. 4 Dynamic stress concentration factors around a circular cutout ($ka=1, b/a=2.0$)

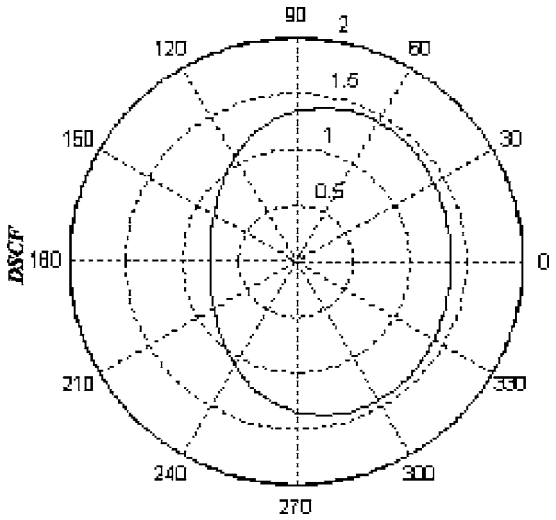

Fig. 6 Dynamic stress concentration factors around a circular cutout ($ka=0.5, b/a=5.0$)

$$M_\theta^* = \sum_{l=1}^{\infty}\sum_{n=-\infty}^{\infty} A_{n1}^l[(1-\nu)H_n''(ka) + H_n(ka)]e^{in\theta} + \sum_{l=1}^{\infty}\sum_{n=-\infty}^{\infty} A_{n2}^l[(1-\nu)K_n''(ka) - K_n(ka)]e^{in\theta} + \sum_{l=1}^{\infty}\sum_{n=-\infty}^{\infty}\sum_{m=-\infty}^{\infty} B_{m1}^l H_{m-n}(2kb)[(1-\nu)J_n''(ka) + J_n(ka)]e^{in\theta} + \sum_{l=1}^{\infty}\sum_{n=-\infty}^{\infty}\sum_{m=-\infty}^{\infty} (-1)^n B_{m2}^l K_{m-n}(2kb)[(1-\nu)I_n''(ka) - I_n(ka)]e^{in\theta} + e^{ikb}(\sin^2\theta + \nu\cos^2\theta) \quad (26)$$

where M_0 is the amplitude of the bending moment of incident waves, and $M_0 = Dk^2 W_{10}$.

6 Numerical Examples

According to the expression of DSCF, the DSCFs around the circular cutout are computed. It should be noted that the number of l truncated at 10 is enough for computation, and the numbers of n and m are truncated at 12. Figures 2–7 illustrate the angular distribution of DSCFs around the cutout when the values of ka and b/a are different.

From Figs. 2–7, one can see that the analytical results of dynamic stress in semi-infinite plates are different from those in infinite plates. In the region of low frequency and long wavelength, the maximum DSCF occurs on the illuminated side of the scattered body with $\theta=\pi$, but not on the side of cutout with $\theta=\pi/2$. The dynamic stress on the illuminated side around the cutout is great, and the dynamic stress on the shadow side is little. However, at higher frequency, the dynamic stress on the illuminated side around the cutout becomes little, and the dynamic stress on the shadow side becomes great.

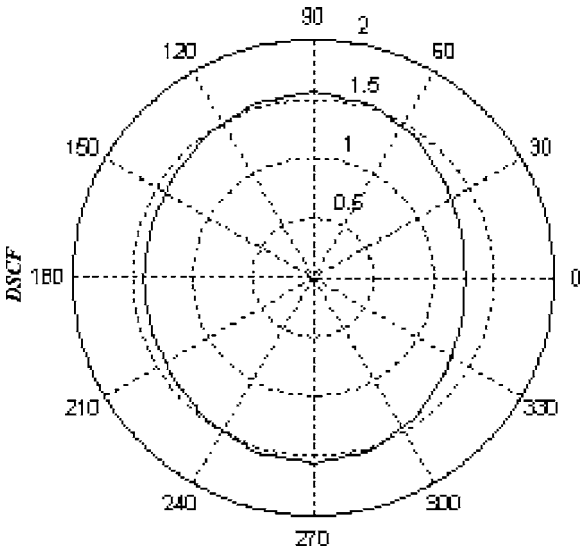

Fig. 5 Dynamic stress concentration factors around a circular cutout ($ka=0.1, b/a=5.0$)

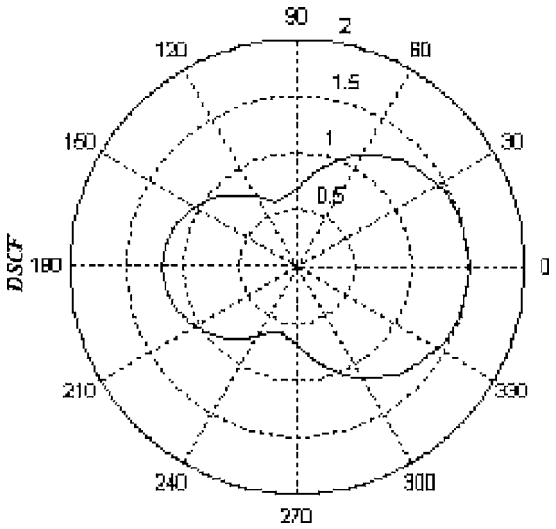

Fig. 7 Dynamic stress concentration factors around a circular cutout ($ka=1, b/a=5.0$)

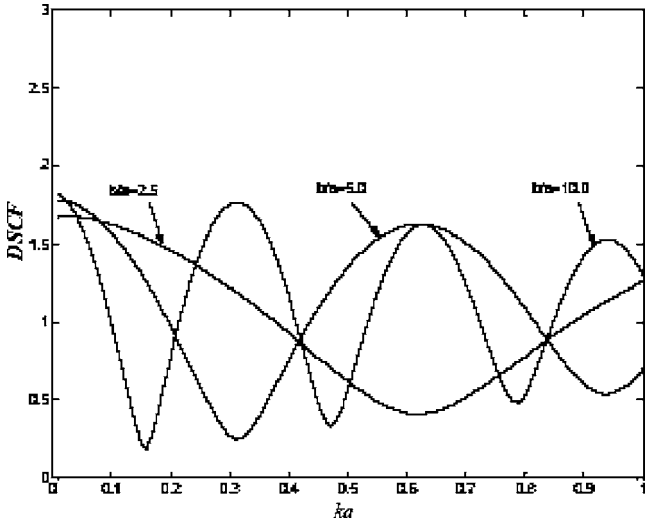

Fig. 8 Dynamic stress concentration factors versus incident wave number ($\theta=\pi/2$)

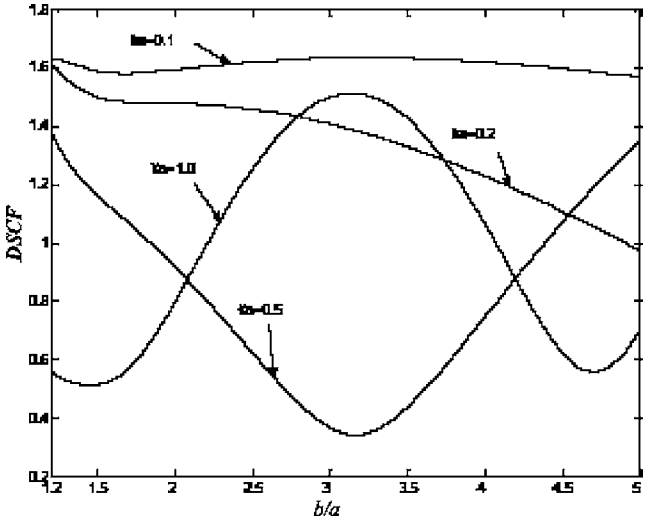

Fig. 10 Dynamic stress concentration factors versus b/a($\theta=\pi/2$)

Figure 8 shows the DSCFs on the side of the cutout with $\theta=\pi/2$ as a function of the incident wave number when the relative distance b/a between the cutout and the edge of plates is different. From Fig. 8, one can see that when the incident wave number is $ka\rightarrow 0$, the DSCF is the maximum, and its value is $M^{*}_{\theta}=1.86$, which is consistent with the analytical results of infinite plates in the literature [6]. Figure 9 shows the DSCFs on the side of the cutout with $\theta=\pi$ as a function of the incident wave number when the relative distance b/a between the cutout and the edge of plates is different. From Fig. 9, one can see that when the relative distance b/a between the cutout and the edge of plates is comparatively small, the DSCFs on the side of the cutout with $\theta=\pi$ become much greater, and the values are far greater than 1.86.

Figure 10 illustrates the effect of incident wave number on the DSCFs on the side of the cutout with $\theta=\pi/2$ as a function of the ratio of distance b/a. When the wavelength of incident waves is longer, the DSCFs vary slowly with the variation of b/a. However, the DSCFs vary sharply when the wavelength is shorter. Figure 11 illustrates the effect of incident wave number on the DSCFs on the side of the cutout with $\theta=\pi$ as a function of the ratio of distance b/a. From Fig. 11, it can be seen that when the wavelength of the incident waves is long, the DSCFs vary slowly with the variation of the values of b/a. However, the DSCFs around the cutout are extremely nonhomogeneous. It is noted that when the value of b/a is small, the DSCFs on the side of the cutout with $\theta=\pi$ will become quite great, and the smaller the wave number is, the greater the maximum DSCF is.

7 Conclusion

In this paper, based on the dynamical equation of flexural waves in elastic thin plates, applying the image method and the wave function expansion method, the multiple scattering of elastic waves and dynamic stress concentrations in semi-infinite plates with a circular cutout are investigated. The boundary conditions of the cutout are free of tractions. Analytical solutions and numerical results of the problem are presented.

It can be seen from the analytical results that the results of scattering of elastic waves and dynamic stress in semi-infinite plates are different from those in infinite plates. When the ratio of distance is the same, and the incident waves are in the region of

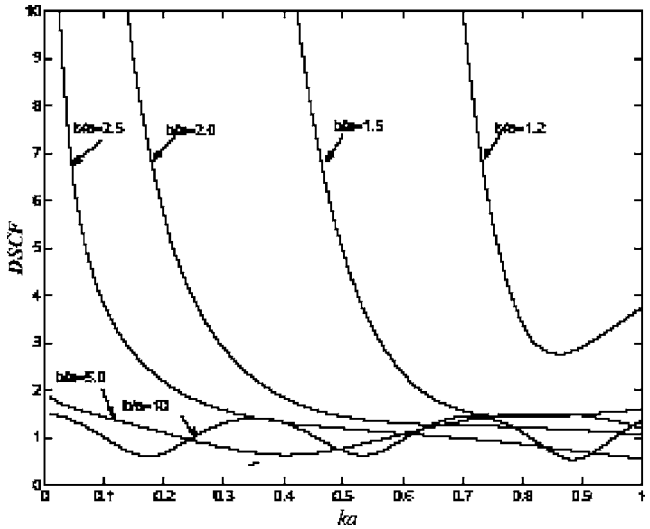

Fig. 9 Dynamic stress concentration factors versus incident wave number ($\theta=\pi$)

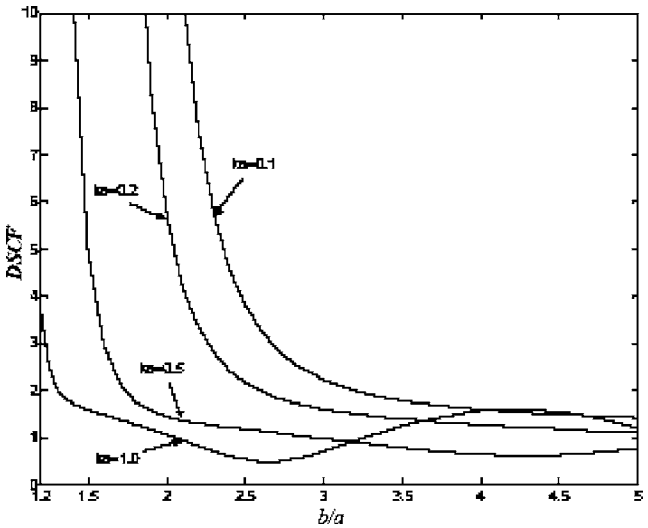

Fig. 11 Dynamic stress concentration factors versus b/a($\theta=\pi$)

low frequency, the maximum DSCF occurs on the illuminated side of the scattered body. However, in the region of short waves, the dynamic stress on the illuminated side around the cutout becomes little, and the dynamic stress on the shadow side becomes great. It is obvious that the problem of elastic propagating expresses the wave property in the region of long wavelength, while it has the corpuscular property in the region of short wavelength.

The conclusions of this paper can provide theoretical basis and reference data for dynamical analyses, strength designs, and nondestructive evaluation of structures.

Acknowledgment

The paper is supported by the National Natural Science Foundation of China (Foundation No. 10572045) and the Outstanding Youth Foundation of Hei Longjiang Province of China (Foundation No. JC-9).

References

[1] Pao, Y. H., and Mow, C. C., 1973, *Diffraction of Elastic Waves and Dynamic Stress Concentrations*, Crane, Russak, New York, Chap. 4.
[2] Pao, Y. H, 1962, "Dynamical Stress Concentration in an Elastic Plate," ASME J. Appl. Mech., **10**(2), pp. 299–305.
[3] Pao, Y. H., and Chao, C. C., 1964, "Diffractions of Flexural Waves by a Cavity in an Elastic Plate," AIAA J., **2**(11), pp. 2004–2010.
[4] Kung, G. C. S., 1964, "Dynamical Stress Concentration in an Elastic Plate", M.S. thesis, Cornell University, Ithaca, NY.
[5] Klyukin, I. I., Satedkin, B. H., and Tirbln, D. C., 1964, "Scattering of Flexural Waves by Antivibrators on a Plate," Sov. Phys. Acoust., **10**, pp. 49–53.
[6] Hu, C., and Liu, D. K., 1995, "Application of Method of the Complex Function to Dynamic Stress Concentrations in Thin Plates With a Cavity," Acta Mech. Sin., **27**, pp. 125–134 (in Chinese).
[7] Liu, D. K., and Hu, C., 1996, "Scattering of Flexural Wave and Dynamic Stress Concentrations in Mindlin's Thick Plates," Acta Mech. Sin., **12**(2), pp. 69–185.
[8] Hayir, A., and Bakirtas, I., 2004, "A Note on Plate Having a Circular Cavity Excited by Plane Harmonic SH Waves," J. Sound Vib., **271**, pp. 241–255.
[9] Wang, Z-X., and Guo, D-R., 1962, *Summary of Special Functions*, Science Press, Beijing, Chap. 7 (in Chinese).
[10] Hu, C., Ma, X-R., and Huang, W-H., 1998, "Dynamic Stress Concentrations in Thin Plates With Two Circular Cutouts," Acta Mech. Sin., **30**(5), pp. 587–596.